SPATIAL AND TEMPORAL VARIABILITY OF SEAWATER CHEMISTRY IN COASTAL ECOSYSTEMS IN THE CONTEXT OF GLOBAL CHANGE

EDITED BY: Tyler Cyronak, Andrea J. Fassbender, Yuichiro Takeshita,
Raquel Vaquer-Sunyer, Iris Eline Hendriks and David Koweek
PUBLISHED IN: Frontiers in Marine Science

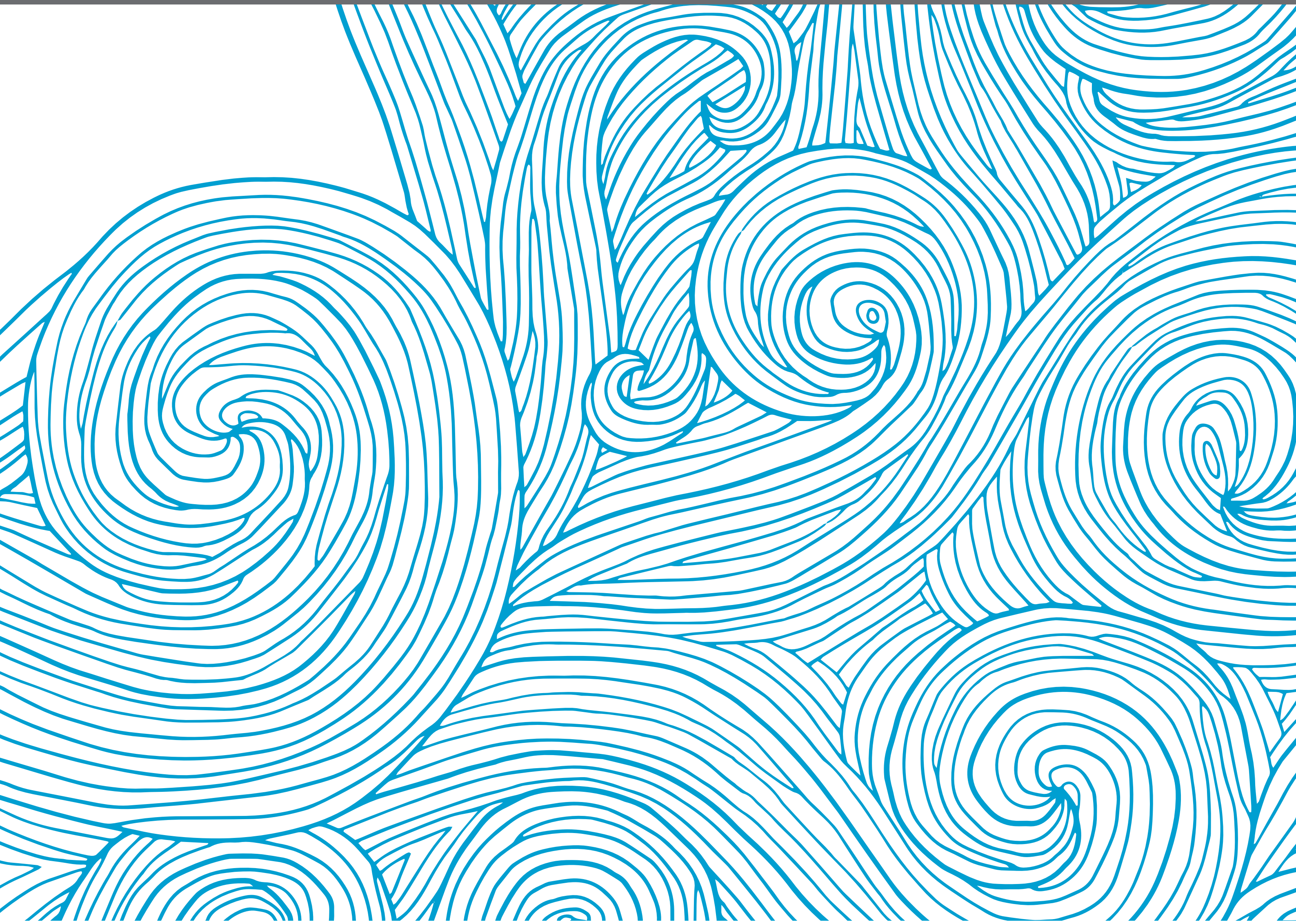

frontiers Research Topics

ISSN 1664-8714
ISBN 978-2-88963-071-4
DOI 10.3389/978-2-88963-071-4

About Frontiers

Frontiers is more than just an open-access publisher of scholarly articles: it is a pioneering approach to the world of academia, radically improving the way scholarly research is managed. The grand vision of Frontiers is a world where all people have an equal opportunity to seek, share and generate knowledge. Frontiers provides immediate and permanent online open access to all its publications, but this alone is not enough to realize our grand goals.

Frontiers Journal Series

The Frontiers Journal Series is a multi-tier and interdisciplinary set of open-access, online journals, promising a paradigm shift from the current review, selection and dissemination processes in academic publishing. All Frontiers journals are driven by researchers for researchers; therefore, they constitute a service to the scholarly community. At the same time, the Frontiers Journal Series operates on a revolutionary invention, the tiered publishing system, initially addressing specific communities of scholars, and gradually climbing up to broader public understanding, thus serving the interests of the lay society, too.

Dedication to Quality

Each Frontiers article is a landmark of the highest quality, thanks to genuinely collaborative interactions between authors and review editors, who include some of the world's best academicians. Research must be certified by peers before entering a stream of knowledge that may eventually reach the public - and shape society; therefore, Frontiers only applies the most rigorous and unbiased reviews.
Frontiers revolutionizes research publishing by freely delivering the most outstanding research, evaluated with no bias from both the academic and social point of view. By applying the most advanced information technologies, Frontiers is catapulting scholarly publishing into a new generation.

What are Frontiers Research Topics?

Frontiers Research Topics are very popular trademarks of the Frontiers Journals Series: they are collections of at least ten articles, all centered on a particular subject. With their unique mix of varied contributions from Original Research to Review Articles, Frontiers Research Topics unify the most influential researchers, the latest key findings and historical advances in a hot research area! Find out more on how to host your own Frontiers Research Topic or contribute to one as an author by contacting the Frontiers Editorial Office: researchtopics@frontiersin.org

SPATIAL AND TEMPORAL VARIABILITY OF SEAWATER CHEMISTRY IN COASTAL ECOSYSTEMS IN THE CONTEXT OF GLOBAL CHANGE

Topic Editors:
Tyler Cyronak, Nova Southeastern University, Dania Beach, United States
Andrea J. Fassbender, Monterey Bay Aquarium Research Institute (MBARI), United States
Yuichiro Takeshita, Monterey Bay Aquarium Research Institute (MBARI), United States
Raquel Vaquer-Sunyer, Instituto Mediterráneo de Estudios Avanzados (IMEDEA), Spain
Iris Eline Hendriks, University of the Balearic Islands, Spain
David Koweek, Carnegie Institution for Science (CIS), United States

Citation: Cyronak, T., Fassbender, A. J., Takeshita, Y., Vaquer-Sunyer, R., Hendriks, I. E., Koweek, D., eds. (2019). Spatial and Temporal Variability of Seawater Chemistry in Coastal Ecosystems in the Context of Global Change. Lausanne: Frontiers Media. doi: 10.3389/978-2-88963-071-4

Table of Contents

05 ***Marine Bacterial Diversity in Coastal Sichang Island, the Upper Gulf of Thailand, in 2011 Wet Season***
Naraporn Somboonna, Alisa Wilantho, Panan Rerngsamran and Sissades Tongsima

11 ***Hawaii Coastal Seawater CO_2 Network: A Statistical Evaluation of a Decade of Observations on Tropical Coral Reefs***
Gerianne J. Terlouw, Lucie A. C. M. Knor, Eric Heinen De Carlo, Patrick S. Drupp, Fred T. Mackenzie, Yuan Hui Li, Adrienne J. Sutton, Albert J. Plueddemann and Christopher L. Sabine

29 ***Seasonal Carbonate Chemistry Dynamics on Southeast Florida Coral Reefs: Localized Acidification Hotspots From Navigational Inlets***
Ian C. Enochs, Derek P. Manzello, Paul R. Jones, S. Jack Stamates and Thomas P. Carsey

41 ***Riverine Calcium End-Members Improve Coastal Saturation State Calculations and Reveal Regionally Variable Calcification Potential***
Sean T. Beckwith, Robert H. Byrne and Pamela Hallock

53 ***Decadal-Scale Acidification Trends in Adjacent North Carolina Estuaries: Competing Role of Anthropogenic CO_2 and Riverine Alkalinity Loads***
Bryce R. Van Dam and Hongjie Wang

64 ***Variability of Seawater Chemistry in a Kelp Forest Environment is Linked to* in Situ *Transgenerational Effects in the Purple Sea Urchin,* Strongylocentrotus purpuratus**
Umihiko Hoshijima and Gretchen E. Hofmann

82 ***Chesapeake Bay Inorganic Carbon: Spatial Distribution and Seasonal Variability***
Jean R. Brodeur, Baoshan Chen, Jianzhong Su, Yuan-Yuan Xu, Najid Hussain, K. Michael Scaboo, Yafeng Zhang, Jeremy M. Testa and Wei-Jun Cai

99 ***Carbon Isotopic Fractionation in Organic Matter Production Consistent With Benthic Community Composition Across a Coral Reef Flat***
David A. Koweek, Atleigh Forden, Rebecca Albright, Yuichiro Takeshita, David A. Mucciarone, Aaron Ninokawa and Ken Caldeira

113 ***Marine CO_2 Patterns in the Northern Salish Sea***
Wiley Evans, Katie Pocock, Alex Hare, Carrie Weekes, Burke Hales, Jennifer Jackson, Helen Gurney-Smith, Jeremy T. Mathis, Simone R. Alin and Richard A. Feely

131 ***Modeled Effect of Coastal Biogeochemical Processes, Climate Variability, and Ocean Acidification on Aragonite Saturation State in the Bering Sea***
Darren J. Pilcher, Danielle M. Naiman, Jessica N. Cross, Albert J. Hermann, Samantha A. Siedlecki, Georgina A. Gibson and Jeremy T. Mathis

149 ***Improved Post-processing of Eddy-Covariance Data to Quantify Atmosphere–Aquatic Ecosystem CO_2 Exchanges***
Tatsuki Tokoro and Tomohiro Kuwae

160 ***The Dynamics of Coral-Algal Interactions in Space and Time on the Southern Great Barrier Reef***
Kristen T. Brown, Dorothea Bender-Champ, Andreas Kubicek, Rene van der Zande, Michelle Achlatis, Ove Hoegh-Guldberg and Sophie G. Dove

173 ***Coral Reef Carbonate Chemistry Variability at Different Functional Scales***
Yuichiro Takeshita, Tyler Cyronak, Todd R. Martz, Theodor Kindeberg and Andreas J. Andersson

frontiers
in Marine Science

BRIEF RESEARCH REPORT
published: 11 June 2019
doi: 10.3389/fmars.2019.00308

Marine Bacterial Diversity in Coastal Sichang Island, the Upper Gulf of Thailand, in 2011 Wet Season

Naraporn Somboonna[1,2], Alisa Wilantho[3], Panan Rerngsamran[1] and Sissades Tongsima[3]*

[1] Department of Microbiology, Faculty of Science, Chulalongkorn University, Bangkok, Thailand, [2] Microbiome Research Unit for Probiotics in Food and Cosmetics, Chulalongkorn University, Bangkok, Thailand, [3] Genome Technology Research Unit, National Center for Genetic Engineering and Biotechnology, Pathum Thani, Thailand

Tha Wang coast in Sichang island, Chonburi province, Thailand, serves a major pier, cargo transportation and is populated with anthropogenic activities. Hence, monitoring of environmental status, in part by microbial diversity, is essential. Previously, the coastal marine microbiota of this area in a dry season (February 2011) had been reported, but the database for a wet season is none. As marine microbiota in several sites were reported fluctuate between dry and wet seasons, specifically in the 2011 that one of the largest flood in Thailand history even occurred from July 2011 to January 2012; the present study thereby first revealed the coastal Sichang water microbiota in the 2011 wet season (July 2011) using metagenomic derived 16S rRNA gene sequencing. Wet and dry seasons showed differences in prokaryotic community richness and evenness: community similarity indices by Jaccard, Lennon, and Yue and Clayton were 2.06–58.28%. This resulted in differences in metabolic potentials, for instances the lower metabolisms for energy and nutrient cycling but the greater in pathogenesis in wet season. Our data were also compared against the flooding water microbiota nearby to Chonburi province to observe any possible correlation; and the coastal Sichang was found distinct given diverse sources of flooding water and local contamination might affect the diversity. In conclusion, this wet-season microbiota supported the better knowledge on the seasonal microbiota of coastal Sichang island.

Keywords: microbiome, biodiversity, prokaryote, 16S ribosomal RNA, Sichang, upper Gulf of Thailand

Edited by:
Raquel Vaquer-Sunyer,
Instituto Mediterráneo de Estudios
Avanzados (IMEDEA), Spain

Reviewed by:
Raghab Ray,
The University of Tokyo, Japan
Raul Martell-Dubois,
National Commission
for the Knowledge and Use
of Biodiversity (CONABIO), Mexico

****Correspondence:***
Naraporn Somboonna
Naraporn.S@chula.ac.th

Specialty section:
This article was submitted to
Coastal Ocean Processes,
a section of the journal
Frontiers in Marine Science

Received: *26 February 2019*
Accepted: *24 May 2019*
Published: *11 June 2019*

Citation:
Somboonna N, Wilantho A,
Rerngsamran P and Tongsima S
(2019) Marine Bacterial Diversity
in Coastal Sichang Island, the Upper
Gulf of Thailand, in 2011 Wet Season.
Front. Mar. Sci. 6:308.
doi: 10.3389/fmars.2019.00308

INTRODUCTION

Sichang island, Chonburi province, Thailand, situates around an equator, within 23.5 degree north and 23.5 degree south, of the upper Gulf of Thailand, and comprises two coasts. On an east side of Sichang coast, named Tha Wang (TW), is major local and international pier and cargo transportation, whereas on the west side coast named Tham Phang (TP) is quiet with neither pier and cargo transportation nor many human activities. TW also has rather close bay geography surrounding by the mainland of Thailand and two islands named Khaam Yai and Prong islands; and thus minimal water circulation compared with TP. More organic and non-organic wastes (e.g., glass bottles, plastics, biodegradable garbage, metals and hazardous materials) were reported at TW than TP (Piyatiratitivorakul and Rungsupa, personal communications and unpublished data; Chantanawisuti et al., 1996). Associated with these different coastal characteristics, Somboonna et al. (2012) reported dissimilar coastal marine microbial population structures between TW and TP in a dry season of year 2011: TW contain many harsh-living prokaryotic species with possible biotechnology application, meanwhile TP contain natural nutrient cyclers and some with possible pharmaceutical application.

In 2011, Thailand witnessed one largest floods in decades, covering over half of Thailand region (∼60,000 square kilometers), from July 2011 to January 2012. Thailand and other Southeast Asia countries, such as Philippines, Indonesia and Cambodia, generally occur flooding in a wet season due to tropical monsoon (Mhuantong et al., 2015). High water level in a wet season lowers concentration and availability of nutrients for marine microorganisms and organisms. Global ocean microbiome researches reported temperature and seasons as factors for changes of microbial structures, in open oceans and coral reefs (Gilbert et al., 2012; Somboonna et al., 2014; Campbell et al., 2015; Bulan et al., 2018); yet seasonal dynamics of microbial structures in coastal marine sites of the Gulf of Thailand remain limited. This study thereby described the Sichang coastal water microbiota in one period (July 2011) in a wet season of TW and TP (abbreviated TW-wet and TP-wet), and compared with our previous reports of dry season of TW and TP (abbreviated TW and TP) of the same corresponding year and analysis methods, metagenomics derived 16S rRNA gene sequencing (Somboonna et al., 2012).

Bacteria play crucial roles in marine food supplies, as initial producers (e.g., photosynthesis) and final recyclers (e.g., conversion of complex or toxic compounds to simple organic and inorganic substrates) (Moran et al., 2015). The latter is critical for coastal water where anthropogenic pollution is abundant. Our first culture-independent databases benefit marine biologists and environmentalists a better knowledge of microbial ecosystem and metabolic potentials, of wet season.

MATERIALS AND METHODS

Sample Collection

A minimum of triplicate water samples of TW-wet and TP-wet, at 5–100 cm depth, were collected into sterile glass containers on 17 July 2011, around 12:00–13:00 h. Measurements included GPS, water color, temperature, pH, salinity, and conductivity were recorded (**Supplementary Table S1**). The geographical location was consistent with Somboonna et al. (2012). The two coastal areas are not vast. All samples were stored at 4°C, and processed immediately upon laboratory arrival within 14 days.

Metagenomic Extraction

Each water sample was poured through four-layered sterile cheesecloths to remove ≥30 μm debris and large-size organisms, followed by a sterile 0.45-micron filter (Merck Millipore, MA, United States) to confine microorganisms of ≥0.45 μm (bacteria and archaea) onto the filter membrane. Then total nucleic acids were isolated using Metagenomic DNA Isolation Kit for Water (Epicentre, WI, United States), following the manufacturer's instructions, and isolated metagenomes should be randomly sheared and appear around 40 kb in size (Begum and Murray, 2008). The metagenomes were analyzed for metagenomic DNA yield and quality by agarose gel electrophoresis with a fosmid control of around 40 kb (Epicentre) and A_{260}/A_{280} nanodrop spectrophotometry.

Pyrotagged 16S rRNA Gene Sequencing

Universal prokaryote 338F (forward) and 803R (reverse) primers were used to amplify a 466-nucleotide sequence covering V3–V4 regions of 16S rRNA gene (Baker et al., 2003; Humblot and Guyoet, 2009). The forward and reverse pyrotagged-16S rDNA primers for TW-wet were 5′-*TCTCTGTG*ACTCCTACGGGAGGCAGCAG-3′ and 5′-*TCTCTGTG*CTACCAGGGTATCTAATC-3′, and TP-wet were 5′-*TCTACTCG*ACTCCTACGGGAGGCAGCAG-3′ and 5′-*TCTACTCG*CTACCAGGGTATCTAATC-3′, where italic sequences represent the tagged sequences (Meyer et al., 2008). For each sample, a 50-μl PCR comprised 1× EmeraldAmp®GT PCR Master Mix (TaKaRa, Shiga, Japan), 0.3 μM of each primer, and 100 ng of the metagenomic DNA. PCR conditions were 95°C for 4 min, and 30 cycles of 94°C for 45 s, 50°C for 55 s, and 72°C for 1 min 30 s, followed by 72°C for 10 min. To minimize PCR bias, a minimum of two independent reactions were performed. The PCR products were purified using PureLink®Quick Gel Extraction Kit (Invitrogen, NY, United States), and the products belonging the same sample site were pooled for 175 ng each for pyrotagged TW-wet and TP-wet sequencing. Pyrosequencing was performed on an eight-lane Picotiter plate, using the 454-Life Sciences GS FLX Genome Sequencer system (Roche, Branford, CT, United States), following the manufacturer's protocols. The datasets were deposited in NCBI Sequence Read Archive (SRA) under an accession number SRP095760.

Bacterial Diversity Analyses

Sequences were categorized TW-wet and TP-wet based on their pyrotag-sequences, then the pyrotagged and primer sequences were removed, and the sequences that do not pass the recommended quality parameters by Mothur (Schloss et al., 2009), including those of less than 100 nucleotides in length and chimera sequences, were removed. The sequences were annotated, visualized and computed for taxonomic compositions using VITCOMIC (Visualization tool for Taxonomic Compositions of Microbial Community) (Mori et al., 2010; Somboonna et al., 2012). BLASTN (Altschul et al., 1997) was performed with *E*-value ≤1E-08 and other default parameters, against 16S rDNA sequences from NCBI non-redundant (Sayers et al., 2010), RDP (Maidak et al., 2001), and Greengenes (McDonald et al., 2011) databases. Percent relative abundance for each phylum was computed from the frequency of reads in the phylum divided by the total number of identified reads. For community diversity estimates (Jaccard, Lennon, and Yue and Clayton (Thetayc) indices), phylogenetic clustering, and non-metric multidimensional scaling (NMDS) were computed using Mothur with default parameters (Schloss et al., 2009). These 16S rDNA data were compared with those of TW and TP of dry season of the same year (Somboonna et al., 2012), and of Thai flood water areas (Mhuantong et al., 2015). The comparing flood areas locate next and nearby provinces to Chonburi (Bangkok, Nonthaburi, Pathum Thani, and Nakhon

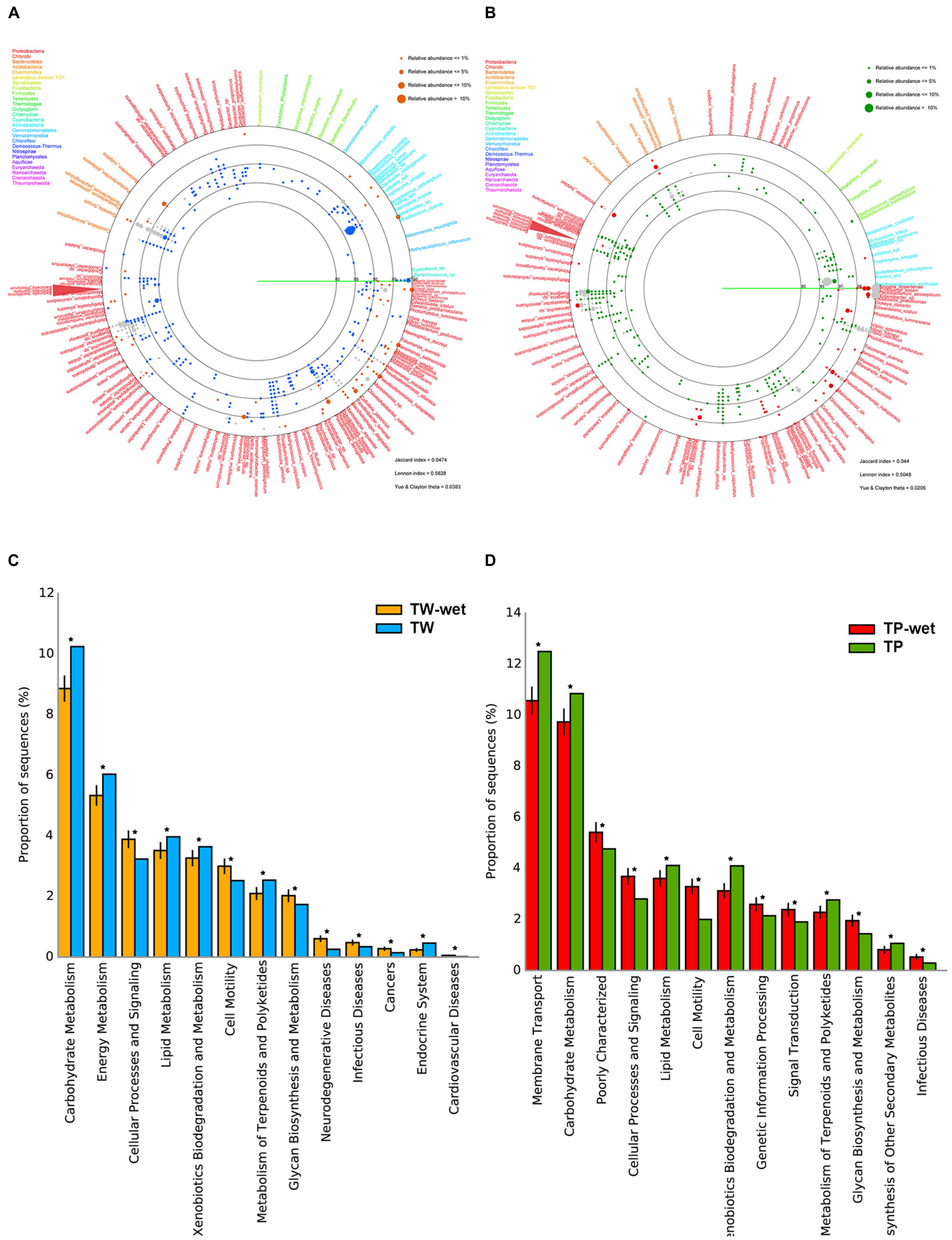

FIGURE 1 | Comparative bacterial diversity **(A,B)** and potential metabolisms **(C,D)** between TW-wet against TW, and TP-wet against TP, respectively. In **(A,B)**, each identified read as represented by orange (TW-wet), blue (TW), red (TP-wet), or green (TP) dot, is annotated to genus and species level along the percent sequence similarity between the read and the annotated sequences (80–100%). Dot size refers to percent relative abundance because multiple reads could be annotated the same species, and only ≥0.05% relative abundance was displayed to fit limited diagram space. Gray dot represents conserved species. Sequence is placed on a circular diagram following its relative genetic distances among one another. Different type font color represents species belonging to different phylum. In **(C,D)**, *represents *q*-value <0.05. See section "Materials and Methods" for details.

Pathom provinces), and the samples were collected 5–150 cm depth in December 2011.

Metabolic Potential Analysis

PICRUSt (Langille et al., 2013) was used to predict metabolic potentials of microbiota into KEGG (Kyoto Encyclopedia of genes and genomes) pathways from the 16S rDNA data. Statistics and visualization were performed at KEGG pathway level 2 using STAMP version 2.1.3 (Parks et al., 2014). Statistic comparison was based on Fisher's exact test and Benjamini-Hochberg False Discovery Rate (FDR) that yields q-value of <0.05 as significant.

RESULTS

Physical Properties and Metagenomic DNA

Temperature of coastal water of TW-wet and TP-wet were roughly equal as the two sites are only 0.010° latitude and 0.012° longitude apart (**Supplementary Table S1**). On-site visual observation for water color demonstrated TP-wet water was clearer than TW-wet. The water physical properties exhibited the slightly greater salinity, acidity (lower pH) and conductivity in TW-wet than TP-wet (**Supplementary Table S1**), partly consistent with previous reports (Somboonna et al., 2012) and the Sichang Marine Science Research and Training Station (SMaRT) monthly records (Rungsupa, personal communication and unpublished data). Comparing between the wet and dry seasons, dissimilarity was denoted, including the higher sea temperature and alkalinity pH while lower salinity and conductivity in the wet season (**Supplementary Table S1**: TW-wet vs. TW, TP-wet vs. TP). These different water physical properties and monsoon effect in wet season suggested microbial diversity between wet and dry seasons.

The metagenomic DNA appeared in proper size range (>12–40 kb) as described by manufacturer and included a size evaluation via a 40 kb fosmid (Begum and Murray, 2008). The metagenomic DNA yield per ml of seawater of TW-wet was higher than that of TP-wet (**Supplementary Figure S1**); nonetheless both were averagely half of that reported in a dry season: ~0.26 ng/ml in wet season vs. ~0.45 ng/ml in dry season (Somboonna et al., 2012).

Diversity of Microbial Communities and Functional Potentials Between Wet and Dry Seasons

The 16S rDNA profiles demonstrated a wet season had increase in bacterial members belonging Proteobacteria (TW-wet 70.71% vs. TW 56.84%, TP-wet 93.64% vs. TP 50.58%), but Actinobacteria (TW-wet 5.01% vs. TW 23.65%, TP-wet 2.34% vs. TP 41.16%), for both Tha Wang and Tham Phang; and specially for Tha Wang Bacteroidetes also became highly pronounced (TW-wet 24.27% vs. TW 13.68%, TP-wet 4.01% vs. TP 6.01%). Many species of Bacteroidetes are related to municipal wastes, such as feces; hence the finding might reflect Tha Wang's effect of populated residents and close bay geography.

For diversity of bacteria, the far fewer bacterial diversity was in the wet season (**Figures 1A,B**). In TW-wet, species such as Bacteroidetes *Gramella forsetii* (14.51%) remained relatively abundant. This specie has been reported one major marine microbial adaptation, because it can degrade polymeric organic matter and plays a key role in the decomposition of carbon complexes for carbon cycling food chains in several marine ecosystems (Bauer et al., 2006; Langille et al., 2013; Kabisch et al., 2014). Another reserved species in TW-wet are of Proteobacteria in genus *Ruegeria*, such as *R. pomeroyi* (1.34%) (**Figure 1A**). This specie was abundant in coastal elsewhere with versatile utilization ability and roles in cycling of sulfur, carbon, nitrogen and many other compounds (i.e., sulfonate, dimethylsulphoniopropionate, and trimethylamine *N*-oxide) (Reisch et al., 2013; Rivers et al., 2014; Li et al., 2015). This finding of bacteria with complex organic users and saprophytes were also reported in the 16S rRNA gene sequencing survey in other high-water level areas during the 2011 Thailand flood crisis (Mhuantong et al., 2015). Other

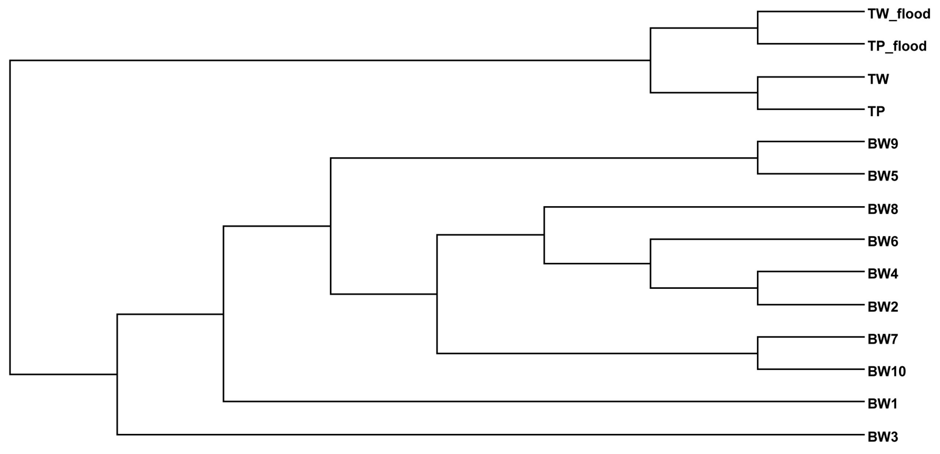

FIGURE 2 | Phylogenetic relationship of bacterial diversity in wet and dry TW and TP, and among diverse flood affected areas of Thailand.

abundant species in TW-wet included *Pseudoalteromonas haloplanktis* (5.54%), *Roseobacter denitrificans* (5.54%), *Marinomonas* sp. (5.01%), *Aeromonas salmonicida* (5.28%), *Pectobacterium atrosepticum* (5.01%), *Pseudomonas aeruginosa* (2.11%), and *Shigella dysenteriae* (0.79%) (**Figure 1A**). These first prior three species, albeit at the lower percent prevalence than in the dry season, function involve cycling of organic nutrients (Medigue et al., 2005; Swingley et al., 2007; Bai et al., 2014), while the latter four species were reported pathogens of aquatic animals and plants (i.e., starch) (Panda et al., 2016), and thus the KEGG pathways of diseases were denoted in **Figure 1C**.

In Tham Phang, prevalent species in the wet season were similar to those in TW-wet, including Bacteroidetes *Gramella forsetii* (TP-wet 2.68%) and Proteobacteria *Ruegeria* spp. (1.34%). Unlike TP, TP-wet had diminished members of Actinobacteria, whereas microbial pathogens such as *Shigella dysenteriae* (25.75%), *Pectobacterium atrosepticum* (16.05%), and *Vibrio vulnificus* (8.68%) became abundant (**Figure 1B**). Nonetheless, as the relative amount of microbial metagenomic DNA of TP-wet was much lower than TW-wet (**Supplementary Figure S1**), a percentage of pathogen in TP-wet (**Figure 1D**, infectious diseases) might remain minimal in term of the abundance in nature compared with TW-wet. Besides metabolisms of diseases that were high in wet season, other relatively greater metabolisms in TW-wet and TP-wet were cellular processes and signaling, cell motility, and glycan biosynthesis and metabolism (**Figures 1C,D**).

The diverse differences in the communities between the seasons arouse the low community similarity coefficients by all community similarity formulas, i.e., Jaccard index of 0.0474 for Tha Wang and 0.044 for Tham Phang as reported in the lower right of **Figures 1A,B**. The closer the community similarity coefficient to 0.000 indicated no community similarity.

Similarity of Microbial Communities With Other Thailand Flood Sites

The TW-wet and TP-wet microbiota were compared with those of reported flood areas in Thailand (Mhuantong et al., 2015). Tha Wang and Tham Phang microbial communities albeit seasons were clustered separated from flood water of different sites albeit next and nearby provinces (Bangkok, Nonthaburi, Pathum Thani, and Nakhon Pathom) (**Figure 2**). Supportively, in addition to differences by sources of flood water and local contamination, the physical properties between ours and flood water samples were found different by water conductivity and water temperature.

DISCUSSION

This study presented the first study to reveal coastal marine microbiome of the upper Gulf of Thailand, Sichang island, in wet season using metagenomics combined 16S rRNA gene sequencing. This year also signified the 2011 Thailand's high-water level in decades. As climate change contributes not only sea-level rise from land-to-ocean flux of freshwater and affects global hydrological cycle, but also release of dissolved organic carbon as a result of glacier mass loss (Hood et al., 2015), together these affected diversity of bacteria and their metabolisms (e.g., carbohydrate metabolism and energy metabolism). Comparison between seasons, and with other flood sites from diverse sources of flooding water and local contamination, indicated uniqueness in Tha Wang and Tham Phang microbial ecosystems. The finding of site dependence was consistent with many previous marine microbiome databases. Albeit minimal, a tip of an iceberg of bacteria with infectious diseases metabolism in the wet season suggested an awareness and if flood occurs, a source of nutrients in food webs, and contaminants, in residential and agricultural areas in part support growth of these infectious disease bacteria. Mhuantong et al. (2015) reported that flood crisis disturbed microbial population with overgrowth of pathogens.

DATA AVAILABILITY

The datasets generated for this study can be found in NCBI Sequence Read Archive (SRA), SRP0957.

AUTHOR CONTRIBUTIONS

NS conceived the study, carried out the molecular biology experiments, participated in and coordinated the data analysis, and drafted the manuscript. AW performed the data analysis. PR collected the samples. ST advised on the data analysis. All authors read and approved the final manuscript.

FUNDING

This research was supported Research Funds from the Faculty of Science, Chulalongkorn University, under the Project for Interdisciplinary Research, which Targeted to Collaborate with the Leading World Class University (to NS).

ACKNOWLEDGMENTS

The authors acknowledged S. Thaniyavarn and K. Kidmoa for experimental support, the National Center for Genetic Engineering and Biotechnology (BIOTEC) and the National Science and Technology Development Agency (NSTDA) for allowing us to compute the data on the server.

SUPPLEMENTARY MATERIAL

The Supplementary Material for this article can be found online at: https://www.frontiersin.org/articles/10.3389/fmars.2019.00308/full#supplementary-material

FIGURE S1 | Agarose-electrophoretic gels showing **(A)** TW-wet and **(B)** TP-wet. Left lane is 80 ng of a 40 kb fosmid control, and right lane is a 1 kb Plus DNA Ladder (Invitrogen) where the top band is at 12 kb.

TABLE S1 | Water sampling sites (GPS) and physical properties.

REFERENCES

Altschul, S. F., Madden, T. L., Schäffer, A. A., Zhang, J., Zhang, Z., Miller, W., et al. (1997). Gapped BLAST and PSI-BLAST: a new generation of protein database search programs. *Nucleic Acids Res.* 25, 3389–3402.

Bai, X., Lai, Q., Dong, C., Li, F., and Shao, Z. (2014). Marinomonas profundimaris sp. nov., isolated from deep-sea sediment sample of the Arctic Ocean. *Antonie Van Leeuwenhoek* 106, 449–455. doi: 10.1007/s10482-014-0213-5

Baker, G. C., Smith, J. J., and Cowan, D. A. (2003). Review and re-analysis of domain-specific 16S primers. *J. Microbiol. Methods* 55, 541–555.

Bauer, M., Kube, M., Teeling, H., Richter, M., Lombardot, T., Allers, E., et al. (2006). Whole genome analysis of the marine Bacteroidetes '*Gramella forsetii*' reveals adaptations to degradation of polymeric organic matter. *Environ. Microbiol.* 8, 2201–2213.

Begum, D., and Murray, J. (2008). Direct isolation of metagenomic DNA from environmental water samples. *EPICENTRE Forum* 15, 7–8.

Bulan, D. E., Wilantho, A., Krainara, P., Viyakarn, V., Chavanich, S., and Somboonna, N. (2018). Spatial and seasonal variability of reef bacterial communities in the upper Gulf of Thailand. *Front. Mar. Sci.* 5:441. doi: 10.3389/fmars.2018.00441

Campbell, A. M., Fleisher, J., Sinigalliano, C., White, J. R., and Lopez, J. V. (2015). Dynamics of marine bacterial community diversity of the coastal waters of the reefs, inlets, and wastewater outfalls of southeast Florida. *Microbiologyopen* 4, 390–408. doi: 10.1002/mbo3.245

Chantanawisuti, N., Piyatiratitivorakul, S., and Menasveta, P. (1996). Types and annual distribution of garbages around the shore of Sichang Islands. *Thai. J. Aquat. Sci.* 2, 108–116.

Gilbert, J. A., Steele, J. A., Caporaso, J. G., Steinbrück, L., Reeder, J., Temperton, B., et al. (2012). Defining seasonal marine microbial community dynamics. *ISME J.* 6, 298–308. doi: 10.1038/ismej.2011.107

Hood, E., Battin, T. J., Fellman, J., O'Neel, S., and Spencer, R. G. M. (2015). Storage and release of organic carbon from glaciers and ice sheets. *Nat. Geosci.* 8, 91–96.

Humblot, C., and Guyoet, J.-P. (2009). Pyrosequencing of tagged 16S rRNA gene amplicons for rapid diciphering of the microbiomes of fermented foods such as pearl millet slurries. *Appl. Environ. Microbiol.* 75, 4354–4361. doi: 10.1128/AEM.00451-09

Kabisch, A., Otto, A., König, S., Becher, D., Albrecht, D., Schüler, M., et al. (2014). Functional characterization of polysaccharide utilization loci in the marine Bacteroidetes '*Gramella forsetii*' KT0803. *ISME J.* 8, 1492–1502. doi: 10.1038/ismej.2014.4

Langille, M. G., Zaneveld, J., Caporaso, J. G., McDonald, D., Knights, D., Reyes, J. A., et al. (2013). Predictive functional profiling of microbial communities using 16S rRNA marker gene sequences. *Nat. Biotechnol.* 31, 814–821. doi: 10.1038/nbt.2676

Li, C. Y., Chen, X. L., Shao, X., Wei, T. D., Wang, P., Xie, B. B., et al. (2015). Mechanistic insight into trimethylamine N-oxide recognition by the marine bacterium *Ruegeria pomeroyi* DSS-3. *J. Bacterol.* 197, 3378–3387. doi: 10.1128/JB.00542-15

Maidak, B. L., Cole, J. R., Liburn, T. G., Parker, C. T. Jr., Saxman, P. R., Farris, R. J., et al. (2001). The RDP-II (ribosomal database project). *Nucleic Acids Res.* 29, 173–174.

McDonald, D., Price, M. N., Goodrich, J., Nawrocki, E. P., DeSantis, T. Z., Probst, A., et al. (2011). An improved Greengenes taxonomy with explicit ranks for ecological and evolutionary analyses of bacteria and archaea. *ISME J.* 6, 610–618. doi: 10.1038/ismej.2011.139

Medigue, C., Krin, E., Pascal, G., Barbe, V., Bernsel, A., Bertin, P. N., et al. (2005). Coping with cold: the genome of the versatile marine Antarctica bacterium *Pseudoalteromonas haloplanktis* TAC125. *Genome Res.* 15, 1325–1335.

Meyer, M., Stenzel, U., and Hofreiter, M. (2008). Parallel tagged sequencing on the 454 platform. *Nat. Protoc.* 3, 267–278. doi: 10.1038/nprot.2007.520

Mhuantong, W., Wongwilaiwalin, S., Laothanacharoen, T., Eurwilaichitr, L., Tangphatsornruang, S., Boonchayaanant, B., et al. (2015). Survey of microbial diversity in flood areas during Thailand 2011 flood crisis using high-throughput tagged amplicon pyrosequencing. *PLoS One* 10:e0128043. doi: 10.1371/journal.pone.0128043

Moran, M. A., Kujawinski, E. B., Stubbins, A., Fatland, R., Aluwihare, L. I., Buchan, A., et al. (2015). Deciphering ocean carbon in a changing world. *Proc. Natl. Acad. Sci. U.S.A.* 113, 3143–3151. doi: 10.1073/pnas.1514645113

Mori, H., Maruyama, F., and Kurokawa, K. (2010). VITCOMIC: visualization tool for taxonomic compositions of microbial communities based on 16S rRNA gene sequences. *BMC Bioinformatics* 11:332. doi: 10.1186/1471-2015-11-332

Panda, P., Vanga, B. R., Lu, A., Fiers, M., Fineran, P. C., Butler, R., et al. (2016). *Pectobacterium atrosepticum* and *Pectobacterium carotovorum* harbor distinct, independently acquired integrative and conjugative elements encoding coronafacic acid that enhance virulence on potato stems. *Front. Microbiol.* 7:397. doi: 10.3389/fmicb.2016.00397

Parks, D. H., Tyson, G. W., Hugenholtz, P., and Beiko, R. G. (2014). STAMP: statistical analysis of taxonomic and functional profiles. *Bioinformatics* 30, 3123–3124. doi: 10.1093/bioinformatics/btu494

Reisch, C. R., Crabb, W. M., Gifford, S. M., Teng, Q., Stoudemayer, M. J., Moran, M. A., et al. (2013). Metabolism of dimethylsulphoniopropionate by *Ruegeria pomeroyi* DSS-3. *Mol. Microbiol.* 89, 774–791. doi: 10.1111/mmi.12314

Rivers, A. R., Smith, C. B., and Moran, M. A. (2014). An update genome annotation for the model marine bacterium *Ruegeria pomeroyi*. *Stand. Genom. Sci.* 9:11. doi: 10.1186/1944-3277-9-11

Sayers, E. W., Barrett, T., Benson, D. A., Bolton, E., Bryant, S. H., Canese, K., et al. (2010). Database resources of the national center for biotechnology information. *Nucleic Acids Res.* 38, D5–D16. doi: 10.1093/nar/gkp967

Schloss, P. D., Westcott, S. L., Ryabin, T., Hall, J. R., Hartmann, M., Hollister, E. B., et al. (2009). Introducing mothur: open-source, platform-independent, community-supported software for describing and comparing microbial communities. *Appl. Environ. Microbiol.* 75, 7537–7541. doi: 10.1128/AEM.01541-09

Somboonna, N., Assawamakin, A., Wilantho, A., Tangphatsornruang, S., and Tongsima, S. (2012). Metagenomic profiles of free-living archaea, bacteria and small eukaryotes in coastal areas of Sichang island, Thailand. *BMC Genomics* 13:S29. doi: 10.1186/1471-2164-13-S7-S29

Somboonna, N., Wilantho, A., Assawamakin, A., Monanunsap, S., Sangsrakru, D., Tangphatsornruant, S., et al. (2014). Structural and functional diversity of free-living microorganisms in reef surface, Kra island, Thailand. *BMC Genomics* 15:607. doi: 10.1186/1471-2164-15-607

Swingley, W. D., Sadekar, S., Mastrian, S. D., Matthies, H. J., Hao, J., Ramos, H., et al. (2007). The complete genome sequence of *Roseobacter denitrificans* reveals a mixotrophic rather than photosynthetic metabolism. *J. Bacteriol.* 189, 683–690.

Conflict of Interest Statement: The authors declare that the research was conducted in the absence of any commercial or financial relationships that could be construed as a potential conflict of interest.

frontiers in Marine Science

ORIGINAL RESEARCH
published: 07 May 2019
doi: 10.3389/fmars.2019.00226

Hawaii Coastal Seawater CO_2 Network: A Statistical Evaluation of a Decade of Observations on Tropical Coral Reefs

Gerianne J. Terlouw[1], Lucie A. C. M. Knor[1]*, Eric Heinen De Carlo[1], Patrick S. Drupp[1], Fred T. Mackenzie[1], Yuan Hui Li[1], Adrienne J. Sutton[2], Albert J. Plueddemann[3] and Christopher L. Sabine[1]

[1] Department of Oceanography, SOEST, University of Hawai'i at Mānoa, Honolulu, HI, United States, [2] Pacific Marine Environmental Laboratory, National Oceanic and Atmospheric Administration, Seattle, WA, United States, [3] Woods Hole Oceanographic Institution, Woods Hole, MA, United States

A statistical evaluation of nearly 10 years of high-resolution surface seawater carbon dioxide partial pressure (pCO_2) time-series data collected from coastal moorings around O'ahu, Hawai'i suggest that these coral reef ecosystems were largely a net source of CO_2 to the atmosphere between 2008 and 2016. The largest air-sea flux (1.24 ± 0.33 mol m^{-2} yr^{-1}) and the largest variability in seawater pCO_2 (950 µatm overall range or 8x the open ocean range) were observed at the CRIMP-2 site, near a shallow barrier coral reef system in Kaneohe Bay O'ahu. Two south shore sites, Kilo Nalu and Ala Wai, also exhibited about twice the surface water pCO_2 variability of the open ocean, but had net fluxes that were much closer to the open ocean than the strongly calcifying system at CRIMP-2. All mooring sites showed the opposite seasonal cycle from the atmosphere, with the highest values in the summer and lower values in the winter. Average coastal diurnal variabilities ranged from a high of 192 µatm/day to a low of 32 µatm/day at the CRIMP-2 and Kilo Nalu sites, respectively, which is one to two orders of magnitude greater than observed at the open ocean site. Here we examine the modes and drivers of variability at the different coastal sites. Although daily to seasonal variations in pCO_2 and air-sea CO_2 fluxes are strongly affected by localized processes, basin-scale climate oscillations also affect the variability on interannual time scales.

Keywords: time series, CO_2, reef, coastal, ocean acidification, variability, fluxes

OPEN ACCESS

Edited by:
Tyler Cyronak,
University of California, San Diego,
United States

Reviewed by:
Wiley Evans,
Hakai Institute, Canada
Lester Kwiatkowski,
UMR8539 Laboratoire
de Météorologie Dynamique (LMD),
France

***Correspondence:**
Lucie A. C. M. Knor
luciek@hawaii.edu

Specialty section:
This article was submitted to
Coastal Ocean Processes,
a section of the journal
Frontiers in Marine Science

Received: *31 January 2019*
Accepted: *11 April 2019*
Published: *07 May 2019*

Citation:
Terlouw GJ, Knor LACM, De Carlo EH, Drupp PS, Mackenzie FT, Li YH, Sutton AJ, Plueddemann AJ and Sabine CL (2019) Hawaii Coastal Seawater CO_2 Network: A Statistical Evaluation of a Decade of Observations on Tropical Coral Reefs. Front. Mar. Sci. 6:226. doi: 10.3389/fmars.2019.00226

INTRODUCTION

Since the start of the industrial revolution, atmospheric CO_2 concentrations have increased steadily from ~280 ppm in preindustrial times, reaching 408 ppm in 2018 at the Mauna Loa Observatory, Hawai'i Island, Hawai'i[1] (Keeling et al., 1976, 2001; Tans and Kieling, 2017; Dlugokencky and Tans, 2018). The average annual growth rate of atmospheric CO_2 was 2 ppm yr^{-1} during the last decade (2007–2016), but varies from year to year (Dlugokencky and Tans, 2018). Through the process of air-sea gas exchange, the global ocean has taken up approximately one quarter of the CO_2

---

[1] https://www.esrl.noaa.gov/gmd/ccgg/trends/

emissions since the Industrial Revolution (Le Quéré et al., 2018). The trend of rising atmospheric CO_2 concentrations has been well documented for several decades at various geographic locations (Keeling et al., 1976, 2001; Thoning et al., 1989; Chamard et al., 2003). Over the last 20 years, the uptake of CO_2 by the ocean, the subsequent decrease in seawater pH (Ocean Acidification, OA), and the consequences of enhanced ocean acidity for the marine environment and its organisms has been an important topic of study (Kleypas et al., 1999; Caldeira and Wickett, 2003; Feely et al., 2004; Sabine et al., 2004; Kleypas and Langdon, 2006; Hoegh-Guldberg et al., 2007; Dore et al., 2009; Gattuso and Hansson, 2011; Andersson and Gledhill, 2013; Mackenzie and Andersson, 2013).

Quantifying CO_2 fluxes in the coastal ocean and particularly in coral reef ecosystems can be more challenging than in the open ocean owing to a variety of factors, including especially the larger variability observed in the former. To help resolve this problem, high-resolution monitoring of seawater partial pressure of CO_2 (pCO_2sw) on surface buoys in coastal regions began late in 2005 (see Massaro et al., 2012). Ocean carbonate chemistry research conducted in various coastal settings (Drupp et al., 2011, 2013; Yan et al., 2011, 2016; Massaro et al., 2012; Bates et al., 2014; Shaw et al., 2014; Sutton et al., 2014a, 2016) has shown that, in order to understand the drivers of natural variability and identify long-term trends, it is necessary to gain better insight into the processes that control marine CO_2 concentrations, including the direction and magnitude of the air-sea CO_2 flux.

The high temporal variability of the CO_2-carbonate system parameters in coral reefs is associated with changes in the magnitude of forcing mechanisms, and resultant changes in other water quality parameters (Kayanne et al., 1995; Gagliano et al., 2010; Drupp et al., 2011, 2013; Hofmann et al., 2011; Shamberger et al., 2011; Price et al., 2012; Shaw and McNeill, 2014; Courtney et al., 2017). Although great strides have been made over the past few years in adding time-series stations on coral reefs, and undertaking process-based studies at these locations (e.g., Yeakel et al., 2015; Drupp et al., 2016; Courtney et al., 2017; Page et al., 2017, 2018; Eyre et al., 2018), it is only at a relatively small number of sites that the biogeochemical conditions in waters of coral reefs have been successfully observed for extended periods of time. Hence, thorough characterization and unequivocal attribution of observed changes to ocean acidification (OA) remain elusive for most coral reef settings.

The biogeochemistry of Hawai'i's coastal waters is strongly influenced by land-derived nutrient inputs (Ringuet and Mackenzie, 2005; De Carlo et al., 2007; Fagan and Mackenzie, 2007; Hoover and Mackenzie, 2009), which drive primary productivity and impact the CO_2-carbonic acid system parameters (e.g., Fagan and Mackenzie, 2007; Drupp et al., 2011, 2013; Shamberger et al., 2011; Massaro et al., 2012). High-nutrient freshwater entering coastal waters causes increased phytoplankton growth, often leading to the drawdown of pCO_2sw (Fagan and Mackenzie, 2007; Drupp et al., 2011; Massaro et al., 2012). The duration of such phytoplankton blooms depends strongly on physical processes including water residence time and mixing (e.g., De Carlo et al., 2007; Tomlinson et al., 2011), as well as biotic effects such as predation (e.g., Hoover et al., 2006).

In an effort to characterize the dynamics of the CO_2–carbonic acid system in waters bathing coral reefs on short and long time scales, NOAA/PMEL and University of Hawai'i scientists established the first coastal seawater pCO_2 monitoring station at Kaneohe Bay in 2005. The Coral Reef Instrumented and CO_2 Monitoring Platform (CRIMP-CO_2) was first deployed in southern Kaneohe Bay, but was moved in 2008 to the inner edge of the barrier reef. Two additional buoys were also deployed in 2008 on the south shore of O'ahu, Hawai'i (see **Figure 1**). A fourth buoy was added in 2011 on the off-shore side of the Kaneohe Bay barrier reef to help characterize the source waters entering the bay. The buoys collect high temporal resolution (3-hourly) CO_2 time-series data that have been used to assess inorganic carbon variability (Massaro et al., 2012; Drupp et al., 2013). These now nearly decade-long time series provide a unique opportunity to quantify the influence of local climatic, geographic, and biogeochemical processes on CO_2 dynamics. An open ocean mooring, WHOI Hawaii Ocean Time Series (WHOTS), operated by the Woods Hole Oceanographic Institution (WHOI), 100 km North of O'ahu, in the North Pacific Subtropical Gyre, also collects high-resolution surface seawater pCO_2 (pCO_2sw) observations and provides an open ocean reference to compare to data from the coastal O'ahu sites (Dore et al., 2003; Sutton et al., 2017). The WHOTS mooring is located at the station ALOHA (A Long-term Oligotrophic Habitat Assessment) oceanographic observatory (Karl and Church, 2018).

This paper builds on earlier work (Drupp et al., 2013) and utilizes nearly 10 years of seawater pCO_2 data to investigate long-term changes and differences in variability across sites around O'ahu, Hawai'i. Due to the low signal-to-noise ratio in these highly variable coastal locations, the datasets are too short to discern statistically significant long-term trends in pCO_2sw, which underscores the importance of continuing high-quality observations. Regardless, data from these stations represent the longest running coordinated autonomous pCO_2 time series characterizing differing coral environments around a single island. The high-resolution data permit a detailed description and analysis of the variability of pCO_2sw in O'ahu's coastal waters. The results of this study enhance our understanding of the behavior of the tropical coastal ocean with respect to the CO_2-carbonic acid system and provide a basis to begin to refine regional coastal CO_2 budgets. Our observations and interpretation also contribute to the goals of the Global Ocean Acidification Observing Network (GOA-ON) to determine spatio-temporal patterns in carbon chemistry, and provide information for state and federal agency managers and decision makers with respect to coastal management.

MATERIALS AND METHODS

Environmental Setting

The CRIMP-2 buoy is a Moored Autonomous pCO_2 ($MAPCO_2$) buoy that was deployed in June 2008 over a sandy bottom in

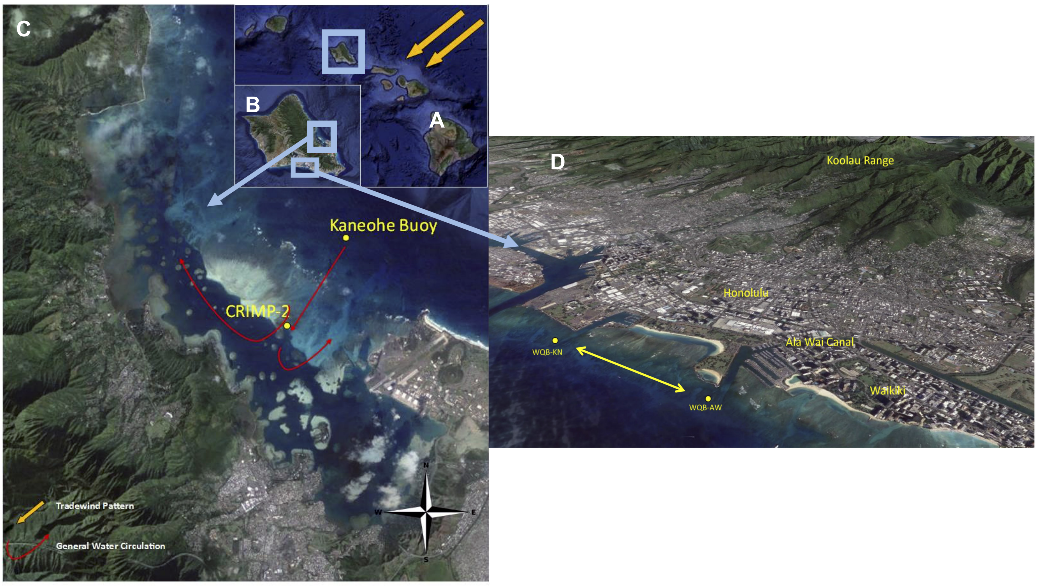

FIGURE 1 | Locations of the four O'ahu coral reef $MAPCO_2$ moorings. **(A)** The Hawaiian Islands, highlighting O'ahu. **(B)** The island of O'ahu, highlighting Kaneohe Bay on the windward (east) coast and the Honolulu watersheds on the southern coast. **(C)** Kaneohe Bay, with the CRIMP-2 buoy located on the back reef and the Kaneohe buoy on the deeper forereef. The red dot represents the previous CRIMP location. **(D)** Two south shore buoys, Ala Wai (WQB-AW) and Kilo Nalu (WQB-KN) are located 200 m offshore of urban Honolulu above fringing reefs. WQB-AW is located near the mouth of the Ala Wai Canal, which drains the Honolulu city watersheds. Adapted from Drupp et al. (2013).

three meters of water depth on the landward edge of the barrier reef of Kaneohe Bay (**Figure 1**). Kaneohe bay is the largest semi-enclosed water body on O'ahu and is located on the windward side of the island, where northeasterly trade winds blow most of the year (Giambelluca et al., 1986, 2011). The entire bay is relatively shallow, with a mean depth of 9.5 m. The depth of the barrier reef is quite variable with a significant area characterized by approximately 2 m water depth, and the mean tidal amplitude in the bay is 68 cm (Ringuet and Mackenzie, 2005). Water at the CRIMP-2 location has a variable residence time (hours to days: Lowe et al., 2009a,b; Ho et al., 2019), which is long compared to the two buoy locations on the South Shore of O'ahu. Generally, open ocean water crosses the barrier reef before reaching CRIMP-2, then enters the deeper lagoon and returns to the ocean through the shallow Sampan Channel (Lowe et al., 2009a,b). A fraction of the water, however, does not complete its trajectory across the reef and advects toward the Sampan channel, complicating exact residence time estimates (Courtney et al., 2017). Subsequently some of the water exiting the bay during outgoing tides is recirculated over the barrier reef, the amount depending on wind strength and direction and wave conditions.

Two other $MAPCO_2$ buoys, Ala Wai and Kilo Nalu, are located on sand patches within the spur and groove structure of fringing reefs offshore of Honolulu, in Mamala Bay on the South Shore of O'ahu (**Figure 1**). Compared to the CRIMP-2 location, this coastline is unprotected. It is directly affected by tides and winds, and is exposed to open ocean swells from the south, particularly during the Austral winter. The Ala Wai buoy (WQB-AW in **Figure 1**) is ∼300 m offshore of the mouth of the Ala Wai Canal, where freshwater discharge from a large part of urban Honolulu often delivers high nutrient and sediment loads to the buoy site (e.g., De Carlo et al., 2004; Tomlinson et al., 2011). The Kilo Nalu buoy (WQB-KN in **Figure 1**), located ∼400 m offshore, is not directly affected by stream discharge, although the local coastal waters receive urban overland runoff, input from nearby storm drains, and groundwater discharge. Depending on currents and wind conditions, some water from the Ala Wai canal occasionally advects toward the Kilo Nalu site. Water on the south shore fringing reefs is thought to have a short residence time because of significant tidal and wind-driven currents. Near bed current velocities at Kilo Nalu of nearly one knot have been reported (Fogaren et al., 2013). Stronger values are typically observed near the surface, particularly during rising tides, when the flow is in the same direction as the predominant wind driven flow. Data coverage for the 8-year record for all Hawaii sites ranged from 40% (Ala Wai) to 77% (CRIMP-2) for $p\text{CO}_2\text{sw}$. Data gaps were due to time spent off station for annual servicing and sensor/platform malfunctions.

The WHOTS buoy is the surface element of an open ocean mooring, located within the Station ALOHA circle, centered at 22° 45′ N, 158° W approximately 100 km due north of O'ahu in the oligotrophic North Pacific Ocean[2]. A $MAPCO_2$ system on the WHOTS buoy has provided a continuous time series since 2004, complementing the Hawai'i Ocean Time Series (HOT) ship-based program that has been operating at Station ALOHA for more than 25 years. OA and the fluxes of CO_2 have been well characterized at the HOT site (Dore et al., 2003, 2009; Sutton et al., 2017).

---

[2] http://uop.whoi.edu/currentprojects/whots/whots.html

To put the findings of this study in a more global context, the CRIMP-2 seawater pCO_2 time-series data from three other coral reef $MAPCO_2$ sites[3] are directly compared. Two are located in the Atlantic Ocean ("La Parguera" in Puerto Rico, and "Crescent reef" in Bermuda) and one is in the Pacific ("Chuuk K1" in Micronesia). These three sites were chosen mainly because of their relatively long and continuous CO_2 record and their different geographic locations. La Parguera and Crescent reef are both located in the North Atlantic Ocean. Crescent reef in Bermuda is a high latitude reef (32.40°N, 64.79°W), where the large seasonal sea surface temperature (SST) cycle drives the observed large seasonal pCO_2 cycle. The La Parguera site in Puerto Rico (17.95°N, 67.05°W) is located within a natural reserve on a shallow (1.5–5 m) fore-reef. Chuuk K1 in the equatorial Pacific is a low latitude (7.46°N, 151.90°E) reef located in Micronesia within a semi- enclosed atoll in ∼23 m water depth. Time frames evaluated were 2009–2016 for La Parguera, 2011–2016 for Chuuk-K1, and 2010–2016 for Crescent reef.

Measurements

At the above described locations, a $MAPCO_2$ system is deployed on each of the surface buoys. The $MAPCO_2$ measures the mole fraction of CO_2 (xCO_2) in the marine boundary layer and in air in equilibrium with surface seawater every 3 h using a non-dispersive infrared (NDIR) sensor, which is calibrated with standard reference gasses *in situ* before each measurement. The pCO_2 of air and seawater is calculated from the xCO_2 following the method of Weiss and Price (1980) with a resulting uncertainty of < 2 μatm [see Sutton et al. (2014b) for a more detailed description of the $MAPCO_2$ methodology]. Other water property data including sea surface temperature (SST), salinity (SSS), dissolved oxygen (DO), turbidity and fluorescence are collected by SeaBird 16V2 instruments at the same (or higher) frequency as the CO_2 observations. Finalized quality-controlled data from the buoys are publicly available and can be found online[4].

Ancillary Data

Wind data needed for CO_2 flux calculations at coastal locations were obtained from the NOAA-National Ocean Service Station OOUH1 in Honolulu, at the Hawai'i Institute for Marine Biology weather station on Moku o Loʻe (Coconut Island) in South Kaneohe Bay, and at the Kaneohe MCAS ID911760 (Kaneohe Marine Corps Base). Wind data for the WHOTS buoy are collected on site by an Air-Sea Interaction Meteorology (ASIMET) system (Weller, 2018).

Climate oscillation index data for the Pacific Decadal Oscillation (PDO) and the Oceanic Niño Index (ONI) were obtained from NOAA[5,6] and for the North Pacific Gyre Oscillation from E. Di Lorenzo (Di Lorenzo et al., 2008; Chhak and Di Lorenzo, 2009)[7].

Calculations

Air-sea CO_2 fluxes are calculated from the gas transfer (piston) velocity using the parameterization of Ho et al. (2006) and the sea-air pCO_2 difference (e.g., Weiss, 1974; Liss, 1983; Wanninkhof, 1992) according to equation (1):

$$\mathrm{F} = k\,\alpha\,\Delta\,pCO_2 \tag{1}$$

where k is the gas transfer (piston) velocity, α is the solubility of CO_2 in seawater at a specified salinity and temperature, and ΔpCO_2 is the difference between seawater and air pCO_2. The gas transfer velocity, k, was calculated using equation (2) (Ho et al., 2006):

$$k(600) = 0.266\,(U10)^2 \tag{2}$$

where k (600) is a scaling factor for the gas transfer velocity and U10 is the wind speed at 10 m altitude above the water surface. If wind speed was not measured at 10 m, it was converted to U10 using the wind profile power law (equation 3, Peterson and Hennessey, 1978):

$$U10 = \left(\frac{10}{z}\right)^{(1/7)} \tag{3}$$

where in (3), z is the altitude of the wind speed measurement and 1/7 is a scaling factor that is used when assuming neutral stability conditions of the overlaying atmosphere. Wind speed data were provided as hourly average values, and each wind speed value was matched with the closest buoy pCO_2 measurement. The uncertainty in the flux (1 standard deviation) was calculated by error propagation of 2 μatm uncertainty in the pCO_2 measurement (Sutton et al., 2014b) and an uncertainty of 0.019 in the gas transfer velocity, k (Ho et al., 2006). Other studies have described uncertainties in coastal CO_2 flux estimates due to the physical differences between nearshore and open ocean wind and current stresses (e.g., Tokoro et al., 2014). Although the gas transfer velocity is derived from an open ocean relationship, recent work by Ho et al. (2019) in Kaneohe Bay show its general applicability to coastal and lagoon waters. Further refinement of the gas exchange at shallow reef sites, however, would benefit from inclusion of the effect of current induced turbulence on k.

In order to isolate pCO_2 changes due to biogeochemical and physical factors from the direct temperature effect on solubility, the observed values were normalized to the mean temperature at each buoy over the full study period, using equation 4 (Takahashi et al., 1993, 2002). This methodology assumes that for every degree Celsius increase in temperature, the pCO_2sw will increase by 4.23%.

$$pCO_2\mathrm{sw\ at\ T_{mean}} = pCO_2\mathrm{obs} * \exp\left(0.0432 * (\mathrm{T_{mean}} - \mathrm{T_{obs}})\right) \tag{4}$$

where in (4), T is the temperature in °C and the subscripts "mean" and "obs" refer to the annual mean and the individual observed values, respectively.

To plot weekly (monthly) means in averaged time series graphs, a moving average filter was applied over 56 (243) data points, which is the number of measurements made per week

---

[3] https://www.pmel.noaa.gov/co2/story/Coral+Reef+Moorings

[4] https://www.nodc.noaa.gov/ocads/oceans/time_series_moorings.html

[5] https://www.ncdc.noaa.gov/teleconnections/pdo/

[6] http://origin.cpc.ncep.noaa.gov/products/analysis_monitoring/ensostuff/ONI_v5.php

[7] http://www.o3d.org/npgo/npgo.php

(month). Additionally, monthly means were calculated for each month of the study period, and "sub-monthly" variability (mostly diurnal and tidal fluctuation) was defined as the average of the standard deviations of the monthly means. Monthly means were then averaged over each year (to annual means), and "sub-annual" variability (mostly seasonal fluctuation) was defined as the average of the standard deviations of the annual means. Finally, annual means were averaged over two 4-year periods, and the standard deviation of these means was denoted "sub-decadal" variability, describing inter-annual changes.

Long-term trends were quantified using a linear least squares regression of monthly mean pCO_2 values over time, with beginning and end points chosen in the same month, to avoid biases resulting from different phases of the seasonal cycle. Trend significance was calculated by doing a two sample T-test between the time series and the linear regression using a 5% significance level.

RESULTS

Seawater pCO_2

Descriptive statistics of pCO_2sw at each site for the period from June 2008 through December 2016 are shown in **Table 1**. Mean ($\pm$1 standard deviation of the mean) of pCO_2sw values at CRIMP-2, Ala Wai, Kilo Nalu, and WHOTS were 457 ± 91, 399 ± 29, 386 ± 21, and 378 ± 13 μatm, respectively. Mean pCO_2sw values at Kilo Nalu and WHOTS were equal within one standard deviation, although the range in pCO_2sw at Kilo Nalu was nearly twice as large as that at the open ocean WHOTS buoy (**Table 1**). The largest range in pCO_2sw was observed at the CRIMP-2 buoy on the barrier reef of Kaneohe Bay, with an overall range of 950 μatm, which is nearly four times larger than the ranges at Ala Wai and Kilo Nalu (240 μatm, and 198 μatm, respectively) and about eight times the range of pCO_2sw observed at the WHOTS buoy (94 μatm). Additionally, the mean daily range in pCO_2sw at CRIMP-2 (**Table 2**) was nearly four times as large as at Ala Wai and Kilo Nalu, and more than an order of magnitude greater than that at WHOTS.

The time-series of pCO_2sw at the four O'ahu locations, from June 2008 through December 2016, is shown in **Figure 2A**. The greatest daily variations in pCO_2sw occurred at the CRIMP-2 buoy (green) while the smallest were at the WHOTS buoy (blue). A seasonal pattern was observed at all buoys, with generally higher pCO_2sw in summer (May through October) than in winter (November through April). A clear deviation from the seasonal pattern is visible at Ala Wai during the period October 2013–April 2014, with pCO_2sw increasing at Ala Wai, while decreasing at the other buoys. An opposite seasonal pattern was observed for atmospheric pCO_2 (pCO_2air), which is largely due to the large terrestrial carbon uptake (release) by vegetation during Northern Hemisphere summer (winter) (Keeling et al., 1976).

TABLE 1 | Descriptive statistics for seawater pCO_2 (pCO_2sw) at CRIMP-2, Ala Wai, Kilo Nalu, and WHOTS for the entire study period.

pCO_2sw (μatm)	Min	Max	Mean	Standard Deviation	Range	Mean
						Diurnal Range
CRIMP-2	196	1146	457	91	950	192
Ala Wai	298	539	399	29	240	49
Kilo Nalu	311	509	386	21	198	31
WHOTS	344	438	378	13	94	5

Range is defined as minimum – maximum of the entire study period. Diurnal range is defined as the maximum – minimum within a diurnal cycle.

The pCO_2sw normalized to the overall mean seawater temperature at each buoy (pCO_2 at T_{mean}, shown in **Figure 2B**) illustrates variations in pCO_2sw presumably due primarily to biological processes (Takahashi et al., 2002). Although the sub-seasonal variations are similar to the *in situ* data, the seasonal cycle due to temperature variations is dampened, as previously described by Drupp et al. (2013).

Long term trends are more readily visualized by plotting weekly mean pCO_2sw (**Figure 3**). pCO_2sw was increasing at CRIMP-2 between 2012 and 2015, from a maximum weakly mean of 480 μatm in summer 2011, to a maximum of 660 μatm in summer 2014, and a slightly lower maximum of 638 μatm in September 2015. This steep increase in pCO_2sw was not observed at the other buoys. **Figure 3B** also shows weekly mean pCO_2 at T_{mean}, with steeply increasing pCO_2 at Ala Wai during the winter of 2013/2014, in contrast to decreasing pCO_2 at T_{mean} at the other buoys during that period.

The coral reef MAPCO$_2$ sites from our study all display increasing pCO_2sw over time [7.5 ± 1.9 (1σ), 8.3 ± 1.0, and 2.6 ± 0.7 μatm yr^{-1} at CRIMP-2, Ala Wai, and Kilo Nalu, respectively, **Figure 3A**]. These trends are not statistically significant for $p < 0.05$ (n.s.).

Air-Sea Fluxes of CO_2

The magnitude of instantaneous air-sea CO_2 fluxes (**Figure 4**) is much greater at the CRIMP-2 buoy than at the South Shore buoys Ala Wai and Kilo Nalu. The larger (positive as well as

TABLE 2 | Year to year air-sea CO_2 fluxes (mol C m^{-2} yr^{-1}) at CRIMP-2, Ala Wai, Kilo Nalu, and WHOTS buoys.

Air-Sea CO_2 flux (mol C m^{-2}yr^{-1})	CRIMP-2	Ala Wai	Kilo Nalu	WHOTS
Jun08–May09	0.76	0.00	−0.03	−0.34
Jun09–May10	0.89	0.02	0.01	N/A
Jun10–May11	1.34	0.03	0.03	−0.41
Jun11–May12	1.04	0.08	−0.05	0.51
Jun12–May13	1.23	0.04	0.01	0.07
Jun13–May14	1.51	0.15	−0.01	0.27
Jun14–May15	1.89	0.02	0.02	0.11
Jun15–May16	1.38	N/A	0.01	−0.08
Overall	1.24	0.05	0.00	0.04

CO_2 fluxes are calculated from June of one year to May of the following year, because our data set starts in June 2008. Negative values indicate sink behavior (invasion of CO_2 into seawater) and positive values indicate source behavior (outgassing of CO_2 to the atmosphere).

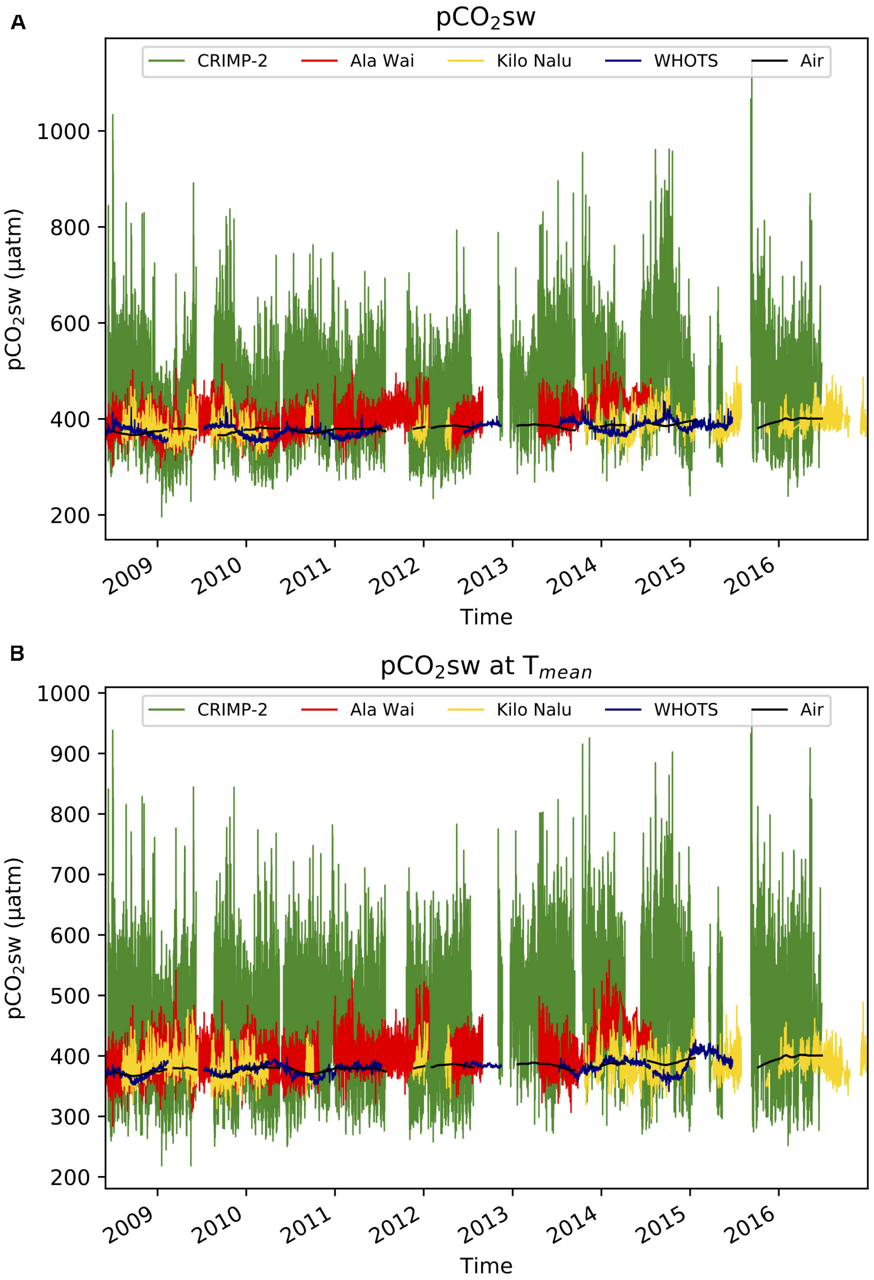

FIGURE 2 | Time-series of *in situ* (3-hourly) pCO_2sw in μatm at CRIMP2, Ala Wai, Kilo Nalu, and WHOTS from June 2008 to December 2016. Weekly mean air pCO_2 at CRIMP2 is displayed in black. **(A)** pCO_2sw at all sites. **(B)** pCO_2sw normalized to the mean annual seawater temperature (pCO_2 at T_{mean}).

negative) fluxes observed at the two South Shore sites in January and March 2009 coincided with storm events (see Tomlinson et al., 2011). The annual air-sea CO_2 fluxes at each buoy from June of a given year to May of the next (**Table 2**), are typically an order of magnitude larger at CRIMP-2 than at either south shore buoy. The annual CO_2 flux at Ala Wai is very small but positive, while at Kilo Nalu it is negative for three out of the 8 years. The CRIMP-2 location frequently switches between CO_2 source and sink behavior, but the net annual flux over the entire study period (flux estimate ± 1 standard deviation propagated error) at CRIMP-2 is positive (1.24 ± 0.33 mol m^{-2} yr^{-1}; **Table 2**) and much larger than the fluxes of 0.05 ± 0.02 and 0.00 ± 0.03 mol m^{-2} yr^{-1} at Ala Wai and Kilo Nalu, respectively.

Climatology

Box plots of monthly climatological pCO_2sw and air-sea CO_2 fluxes are presented in **Figures 5**, **6**, respectively. Although pCO_2sw ranges from 196 to 1146 μatm at CRIMP-2 (**Table 1**), 99.3% of the observed values are between approximately 220 and

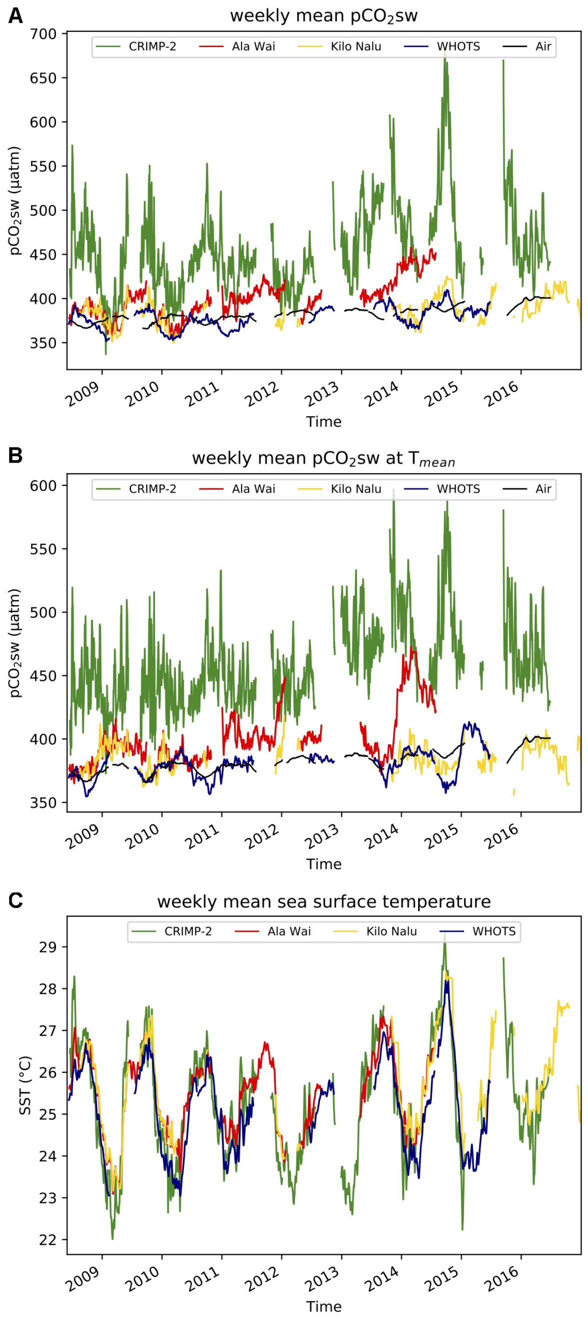

FIGURE 3 | Time-series of weekly mean values at CRIMP2, Ala Wai, Kilo Nalu, and WHOTS from June 2008 through December 2016. Weekly mean air pCO_2 is displayed in black. **(A)** pCO_2sw. **(B)** pCO_2sw normalized to the mean annual seawater temperature (pCO_2 at T_{mean}). **(C)** Seawater temperature.

790 µatm. The monthly climatological mean pCO_2sw at CRIMP-2 is higher and the range is slightly larger in the summer than in the winter. A much narrower range of pCO_2sw is observed at the south shore buoys (298–539 µatm at Ala Wai, 311–509 µatm at Kilo Nalu, **Table 1**), and 99.3% of the pCO_2sw values fall between 300 and 500 µatm at Ala Wai and between 320 and 450 µatm at Kilo Nalu.

The coral reef sites described here display a different extent of variability in pCO_2sw during different months. At CRIMP-2, the highest pCO_2sw and greatest variability is observed during the summer (May through October). In contrast, the most variable periods at Ala Wai occur during winter, especially in December through January. The pCO_2sw at Kilo Nalu exhibits consistently less variability than Ala Wai.

Instantaneous air-sea CO_2 fluxes (**Figure 6**) also show a slight seasonal pattern similar to that of pCO_2sw. At CRIMP-2, higher mean fluxes are observed during summer than winter, and the lowest variability in fluxes is observed during December.

DISCUSSION

To assess various drivers of variability on selected Hawaiian reefs, we compare pCO_2sw (see Variability in pCO_2sw) and air-sea CO_2 fluxes (see Variability in Air-Sea Fluxes) of our most open ocean-like coastal $MAPCO_2$ buoy, Kilo Nalu, to the offshore reference WHOTS mooring, and subsequently examine local differences between all three coral reef locations, as well as monthly climatological values.

Variability in pCO_2sw

Coastal vs. Open Ocean pCO_2sw

Kilo Nalu was originally selected as a coastal reference point that should reflect near open ocean waters with well mixed conditions. There are indeed similar trends in seasonal variability in pCO_2sw at Kilo Nalu and WHOTS (**Figure 7A**), which can largely be attributed to comparable seasonal SST changes at both sites. Daily pCO_2sw fluctuations, however, are much greater at Kilo Nalu's coastal reef ecosystem than in the open ocean. These diurnal variations in pCO_2sw at Kilo Nalu are mainly driven by greater benthic and water column photosynthesis and respiration, which reflect both the presence of a coral reef at Kilo Nalu, and the effect of discharge of nutrients and suspended solids on biogeochemical processes in proximity to land, with additional effects of calcification and dissolution on the reef (Tomlinson et al., 2011; Drupp et al., 2013). Consequently, the seasonal cycles of pCO_2sw in both a nearshore reef and the open North Pacific Ocean are similar in amplitude and driven by the temperature effect on CO_2 solubility, while short-term variability is much larger in the coral reef environment largely due to biological processes.

Local Drivers of pCO_2sw

Local geography, weather, and proximity to land all affect pCO_2sw at coastal coral reef sites. Ala Wai and Kilo Nalu buoys are both a few hundred meters from shore, moored in waters with the same depth. They differ, however, with respect to riverine input. The Ala Wai site receives direct runoff from the Ala Wai Canal, that usually does not strongly impact the Kilo Nalu buoy (Tomlinson et al., 2011). Consequently, the overall range of pCO_2sw on diurnal to seasonal time scales (**Table 1**) is substantially greater at Ala Wai than those observed at Kilo Nalu (**Figures 4**, **6**).

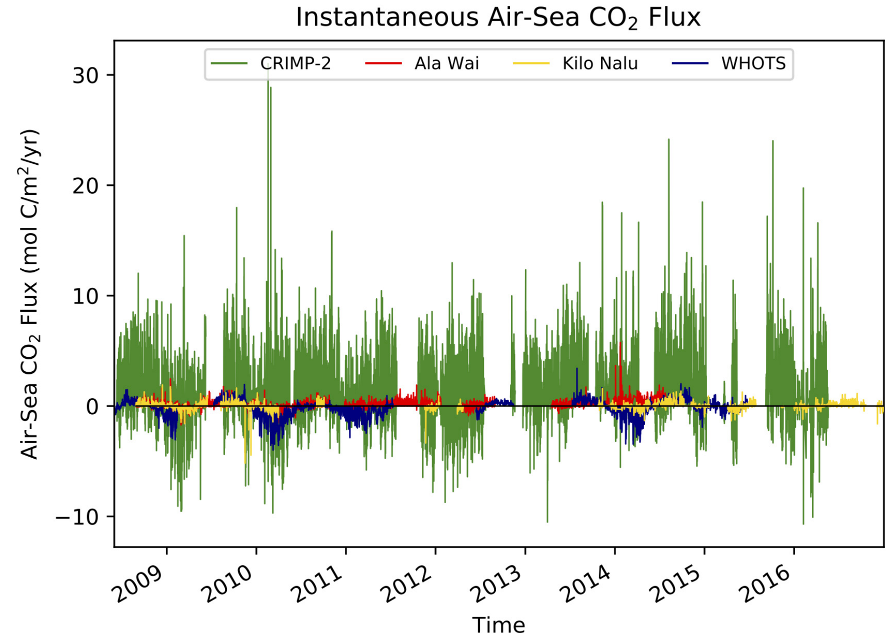

FIGURE 4 | Time-series of *in situ* (3-hourly) air-sea CO_2 fluxes at CRIMP-2, Ala Wai, Kilo Nalu, and WHOTS from June 2008 through December 2016 in units of mol C m^{-2} yr^{-1}. Positive values indicate a source of CO_2 to the atmosphere.

An unusual increase in pCO$_2$sw at the Ala Wai buoy was observed during the winter of 2013–2014 (**Figure 3A**). A decrease in seawater temperature during the winter, however, is expected to cause a decrease in the pCO$_2$sw (e.g., Takahashi et al., 1993; Massaro et al., 2012; Drupp et al., 2013). Despite the somewhat elevated seawater temperature at both south shore buoys during this period, higher pCO$_2$sw values were not observed at Kilo Nalu. In the temperature-normalized pCO$_2$sw record for this period (**Figure 3B**, e.g., Takahashi et al., 1993, 2002), the pCO$_2$sw increase at the Ala Wai buoy is even more apparent. Consequently, it is likely that there was increased respiration and organic matter degradation at the mouth of the Ala Wai Canal during this period. This biological activity was potentially triggered by riverine runoff, as suggested by the Kilo Nalu buoy's lack of a response to direct inputs from the Ala Wai Canal.

A distinguishing feature of the CRIMP-2 site is its extreme variability in pCO$_2$sw compared to the South Shore buoys (**Figures 2**, **4–6**). CRIMP-2 is located in shallow water (<3 m) on the inside edge of the highly productive barrier reef of Kaneohe Bay, and vigorous calcification/dissolution and primary production/respiration on the reef flat (e.g., Shamberger et al., 2011; Courtney et al., 2017) cause large and occasionally extreme daily swings in pCO$_2$sw. Page et al. (2018) found that organic carbon cycling (P/R) was dominating Kaneohe Bay barrier reef metabolism compared to inorganic carbon cycling (calcification/dissolution), especially in the winter, with very low pCO$_2$sw due to primary productivity during the day, and a strong respiration signal leading to high pCO$_2$sw at night. In addition, two physical factors result in a very large amplitude of these daily swings at CRIMP-2 compared to other coral reef sites in this study, residence time and water depth. The longer residence time of seawater on the barrier reef of Kaneohe Bay (up to several days, Lowe et al., 2009) relative to the Honolulu sites allows for a more pronounced signature of changes in CO_2 in the water column at CRIMP-2: the products of biological reactions have a longer time to accumulate in a given parcel of water. Additionally, the shallow depth (i.e., low volume of water) at CRIMP-2 may also enhance the effects of benthic productivity and carbonate mineral-seawater interactions (e.g., Drupp et al., 2016; Page et al., 2018) on the pCO$_2$ of surface seawater at this location, by reducing the effective volume of water into which accumulate this and other chemical constituents associated with metabolism.

Monthly pCO$_2$sw Climatology

The monthly pCO$_2$sw climatology for the O'ahu coastal and WHOTS buoys (**Figure 5**) is characterized by a clear seasonal trend with lower mean pCO$_2$sw during winter months and higher mean pCO$_2$sw during summer months. The range of the variability (illustrated by the size of the boxes and length of the whiskers of the box plots) differs between sites, and over time at each site, reflecting how differences in physical and biogeochemical processes influence CO_2 dynamics.

At CRIMP-2, higher SST and increased productivity/respiration cycles during the summer (May through October) result in higher pCO$_2$sw and greater fluctuations of pCO$_2$sw. Higher seawater temperature causes decreased CO_2 solubility, which increases the pCO$_2$sw. Productivity is enhanced by elevated seawater temperature during summer, and likely also by increased solar radiation, but this factor works in the opposite direction (CO_2 drawdown). Lower and less

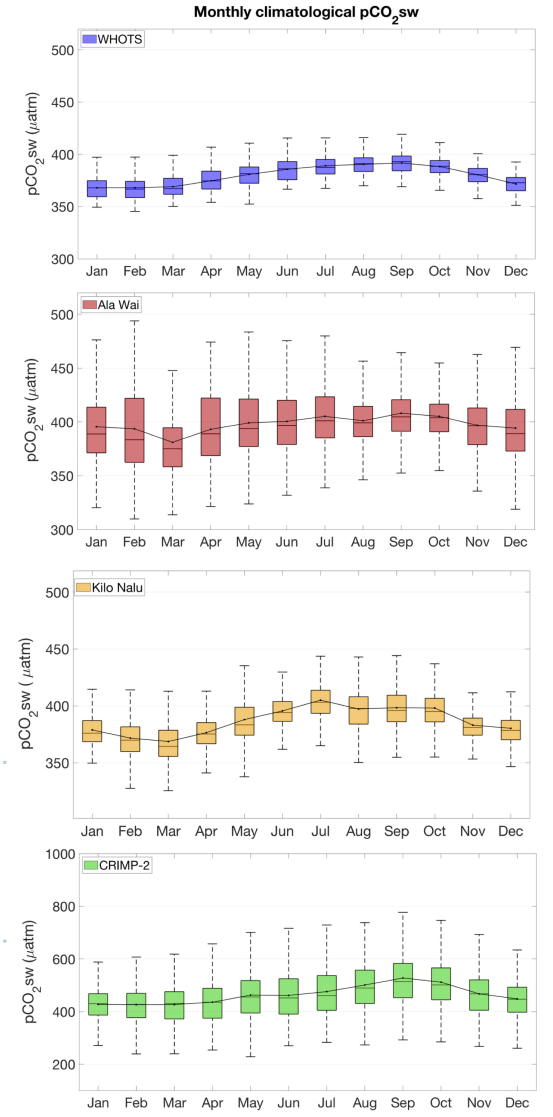

FIGURE 5 | Monthly climatological box plots of pCO_2sw, based on data from June 2008 through December 2016, at all sites. Box plots show median (line within the box), mean (dot, with a line drawn through the mean of each month), the bottoms and tops of the boxes are the 25th (q_1) and 75th (q_3) percentiles, respectively. The whiskers extend to 1.5 X interquartile range (q_3-q_1), corresponding to approximately ± 2.7 σ or 99.3% of the data (if normally distributed). Outliers are not included.

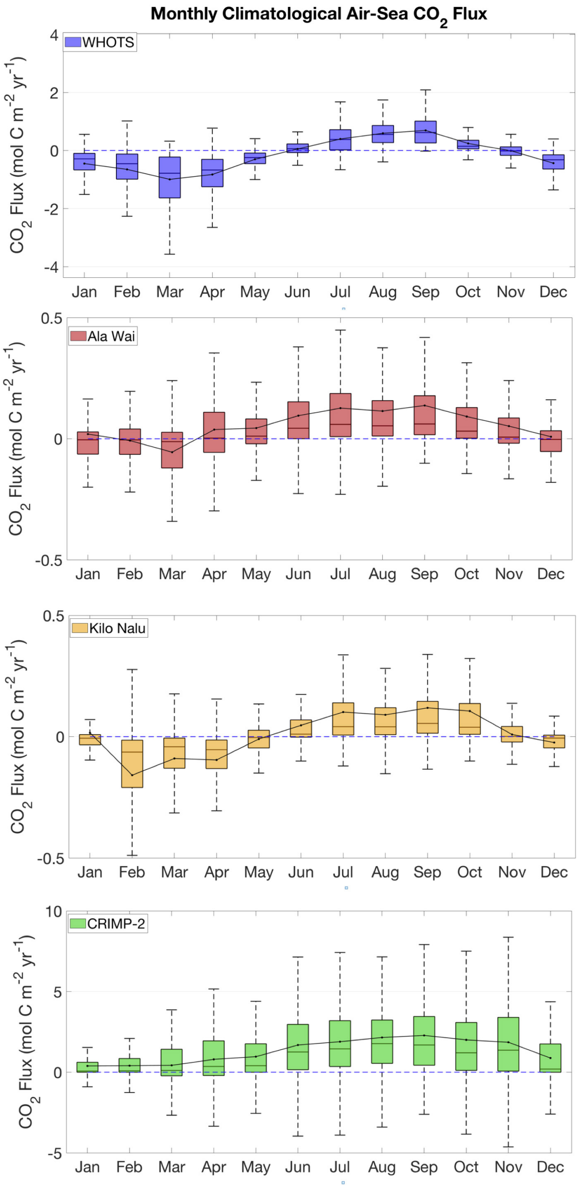

FIGURE 6 | Monthly climatological box plots of air-sea CO_2 fluxes, based on data from June 2008 through December 2016, at all sites. The blue dashed line illustrates a flux of zero, positive values indicates that the area is a source of CO_2 to the atmosphere. See **Figure 5** for plot description.

variable pCO_2sw during the winter months results from lower seawater temperature, lower insolation, and the concomitant effects on productivity/respiration and calcification/dissolution cycles. As mentioned earlier, the shallow depth and the relatively long residence time of water on the barrier reef of Kaneohe Bay allow for a pronounced accumulation (or depletion) of CO_2 in a given parcel of water from vigorous reef metabolism. The changes in pCO_2sw due to reef metabolism are most apparent during the summer, when wind speeds are often lower and gas exchange with the atmosphere is consequently diminished.

At the South Shore buoys, Ala Wai and Kilo Nalu, the pCO_2sw variability is considerably smaller than that at CRIMP-2 year-round. This reflects the less productive environment as well as the shorter water residence time and deeper water at the two fringing reef sites. At Ala Wai, pCO_2sw variability is somewhat greater during the winter months. This is likely due to increased rainfall leading to more runoff of nutrients and organic matter from the Ala Wai Canal, thereby enhancing productivity during the wet season. The monthly means and the seasonal cycles at Ala Wai and Kilo Nalu are similar, but the smaller variability during the rainy season at Kilo Nalu reflects the lack of direct riverine input

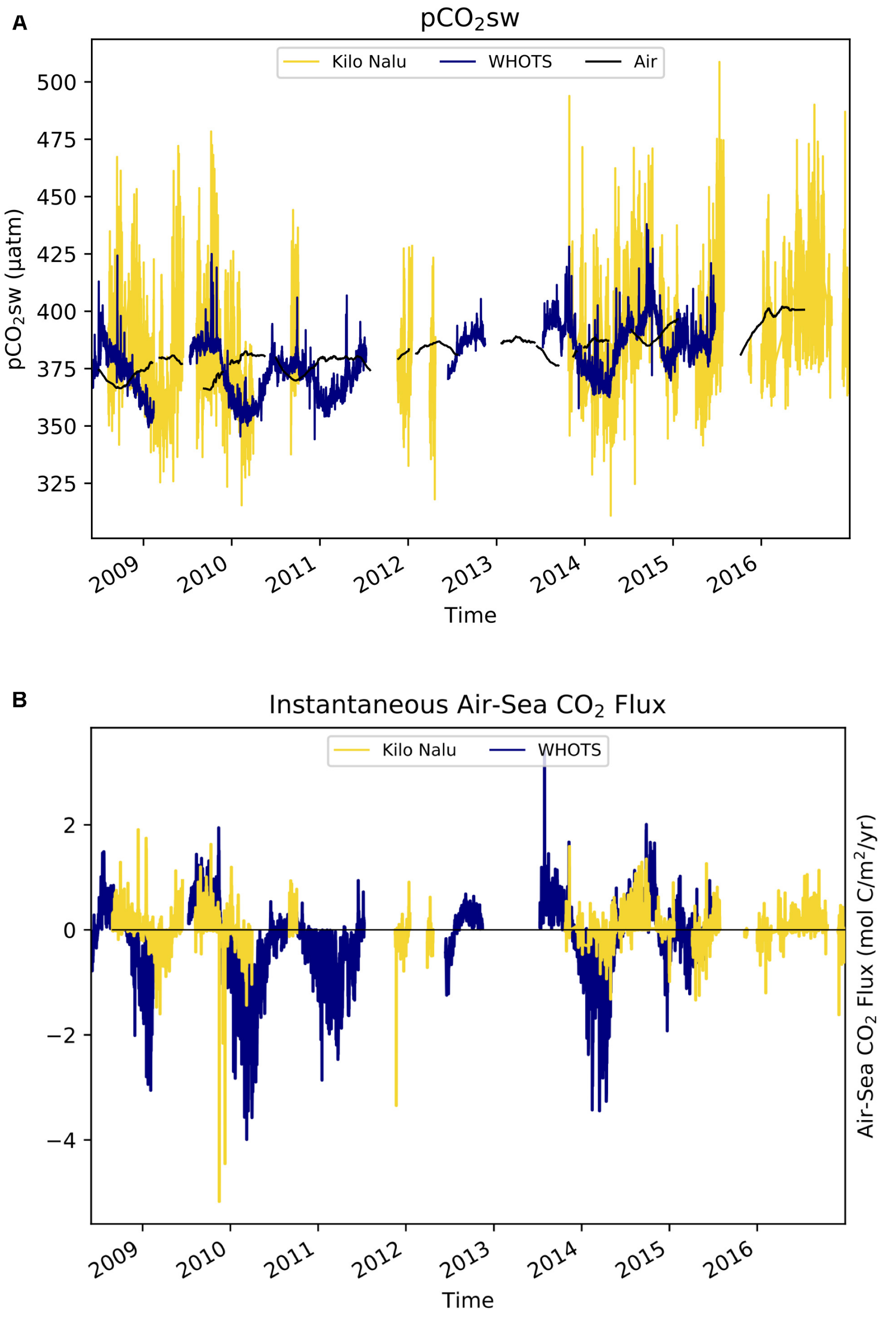

FIGURE 7 | Time-series of pCO$_2$sw and air-sea CO$_2$ fluxes at Kilo Nalu and WHOTS from June 2008 through December 2016. This figure is similar to **Figures 2A**, **4**, but plotted on a narrower y-axis range to highlight the differences in variability at Kilo Nalu and WHOTS. **(A)** *In situ* (3-hourly) pCO$_2$sw in units of µatm. **(B)** Air-sea CO$_2$ fluxes in units of mol C m^{-2} yr^{-1} where positive values indicate a source of CO$_2$ to the atmosphere.

at this site. The pCO$_2$sw in the open ocean (WHOTS) shows little variability throughout the year.

Variability in Air-Sea Fluxes

Coastal vs. Open Ocean Air-Sea CO$_2$ Fluxes

Although the air-sea CO$_2$ fluxes at Kilo Nalu and WHOTS are more similar than their pCO$_2$sw time series (**Figure 7B**), the dynamics driving these fluxes differ between locations. The magnitude and direction of the instantaneous air-sea flux of CO$_2$ depend primarily on the sea-air pCO$_2$ difference (ΔpCO$_2$) and the wind speed. Larger pCO$_2$sw fluctuations at Kilo Nalu due to the biogeochemical processes described above result in larger values of ΔpCO$_2$ as well as greater variability of ΔpCO$_2$ than observed at WHOTS. Annual median wind speeds at Kilo Nalu (2.2 ms^{-1}) are typically lower than at WHOTS (7.5 ms^{-1}), further increasing the relative importance of the ΔpCO$_2$ term in the flux equation for the Kilo Nalu coastal site. Storm events can enhance the biogeochemical processes driving $\Delta p\mathrm{CO_2}$ at Kilo Nalu, which often increases fluxes significantly. During and after storm events, Kilo Nalu is often exposed to diluted freshwater discharges of nutrients and suspended solids that are advected from the mouth of the Ala Wai canal (see Tomlinson et al., 2011, and **Figure 1**). For example, immediately after a storm that took place on March 13, 2009 (Tomlinson et al., 2011), instantaneous flux values reached a maximum of -5.43 mol C m^{-2} yr^{-1} at the Kilo Nalu buoy. This large ocean uptake can be attributed to a seawater CO$_2$ drawdown associated with a phytoplankton bloom (Drupp et al., 2013). Despite these events, the net CO$_2$ flux throughout the full study period at Kilo Nalu is near zero, because the daily positive and negative fluxes due to biogeochemical processes mostly cancel out.

Because wind speeds at WHOTS are approximately four-fold greater than at Kilo Nalu, even the very small $\Delta p\mathrm{CO_2}$ driven by weaker daily photosynthesis/respiration and SST cycles causes an instantaneous flux that is, with an average of 0.49 mol C m^{-2} yr^{-1}, considerably larger in magnitude (absolute value) at WHOTS than at Kilo Nalu. This is a result of the greater gas transfer velocity at higher wind speeds (Wanninkhof, 1992; Nightingale et al., 2000a,b; Ho et al., 2006). Nonetheless, the net annual area specific air-sea CO$_2$ flux at WHOTS remains small, because summer and winter changes mostly cancel out.

TABLE 3 | Area specific air-sea CO$_2$ fluxes in units of mol C m^{-2} yr^{-1} in tropical and subtropical coral reef environments.

Location	Mean annualized flux (mol C m^{-2} year^{-1})	References
CRIMP-2 (Kaneohe Bay, O'ahu, Hawai'i)	1.14	This work; Drupp et al., 2013
Southern Kaneohe Bay, O'ahu, Hawai'i	1.80	Massaro et al., 2012
Kaneohe Bay, O'ahu, Hawai'i	1.45	Fagan and Mackenzie, 2007
Ala Wai (Mamala Bay, O'ahu, Hawai'i	0.05	This work; Drupp et al., 2013
Kilo Nalu (Mamala Bay, O'ahu, Hawai'I	0.01	This work; Drupp et al., 2013
Hog Reef, Bermuda	1.2	Bates et al., 2001
Okinawa Reef flat, Japan	1.8	Ohde and van Woesik, 1999
Yonge Reef, N. Great Barrier Reef, Australia	1.5	Frankignoulle et al., 1996; Gattuso et al., 1996
Moorea, French Polynesia	0.1	Gattuso et al., 1993, 1996, 1997; Frankignoulle et al., 1996
Heron Island, Great Barrier Reef, Australia	0.9	Cyronak et al., 2014
Rarotonga, Cook Islands	3.2	Cyronak et al., 2014
Yongxing Island Reef atoll, Nansha Islands, South China Sea	0.1	Yan et al., 2011
Yongxing Island, Nansha Islands, South China Sea	1.7	Yan et al., 2011
Luhuitou Fringing Reef, South China Sea	3.6	Yan et al., 2011

A positive value indicates a source of CO$_2$ to the atmosphere.

Local Drivers of Air-Sea CO$_2$ Fluxes

On the south shore, despite larger variability in $p\mathrm{CO_2sw}$ at the Ala Wai site, the overall area specific air-sea CO$_2$ flux was close to zero at both Ala Wai and Kilo Nalu locations (**Tables 2**, **3**). The CRIMP-2 site in Kaneohe Bay, on the other hand, has been a persistent, albeit variable, annual source of CO$_2$ to the atmosphere (**Figure 6**). The additional years of data since the compilation of Drupp et al. (2013) also show that the flux from the ocean to the atmosphere at CRIMP-2 has increased since 2012.

Air-sea CO$_2$ fluxes in coastal waters of O'ahu are consistent with the range previously published for coral reef environments around the world (**Table 3**). The flux at CRIMP-2 is close to the flux of 1.30 mol C cm^{-2} yr^{-1}, observed at Hog Reef, Bermuda (Bates et al., 2001), a relatively wide and open water reef. It should be kept in mind that fluxes at CRIMP-2 may be even greater than we calculate here, because the current gas transfer velocity parameterization (k) in the flux calculation (Equation 3) does not account for any enhanced gas exchange due to turbulence over the shallow reef (Ho et al., 2016).

Monthly Air-Sea CO$_2$ Flux Climatology

The climatological differences in air-sea CO$_2$ fluxes (**Figure 6**) are determined by both the variabilities in $\Delta p\mathrm{CO_2}$ and in wind speed. A clear seasonal cycle is visible at all sites, with more positive fluxes during the summer (outgassing), and smaller or negative fluxes (ingassing) during the winter. This seasonal cycle in air-sea CO$_2$ fluxes is largely driven by the seasonal $p\mathrm{CO_2sw}$ cycle that determines the $\Delta p\mathrm{CO_2}$ values. At CRIMP-2, the monthly mean CO$_2$ flux is positive throughout the year and more than an order of magnitude greater than that at the South Shore buoys. There are also clear seasonal differences. The variability in fluxes is greatest in the summer, when the highest $p\mathrm{CO_2sw}$ is observed and trade winds are strong and nearly consistent. During the winter, especially in December and January, wind speed is generally lower and less consistent, and these months are characterized by smaller and less variable fluxes. At Ala Wai and Kilo Nalu, the monthly mean CO$_2$ fluxes are negative during the winter, and positive during the summer. The greatest variability also coincides with the months characterized by the largest fluxes. The largest positive fluxes are observed in the summer, between August and October, during periods of maximum SST and wind speed. The most negative fluxes, as well as the largest variability in winter months, are observed in February (Kilo Nalu) and March (Ala Wai). This is when strong rains and increased runoff, as well as occasional strong onshore winds, are the most frequent. The presence of riverine input from the Ala Wai Canal results in clear climatological differences in $p\mathrm{CO_2sw}$ at the Ala Wai buoy relative to Kilo Nalu, but this difference is not as evident in the air-sea CO$_2$ fluxes. The CO$_2$ flux at WHOTS is negative in winter and positive in summer, and the greatest flux variability at this site is also observed when the flux is the strongest, around

March, similar to what is observed at the South Shore sites (Ala Wai and Kilo Nalu).

Inter-annual Changes in $p\mathrm{CO}_2$sw

Although the multi-year record obtained at the O'ahu MAPCO$_2$ buoy network is too short to identify reliably long-term global climate change signals such as OA (Sutton et al., 2019), especially considering the low signal-to-noise ratio in highly variable coastal environments such as the coral reefs around O'ahu, it does allow one to make year to year comparisons and begin to identify inter-annual changes. On an inter-annual timescale, $p\mathrm{CO}_2$sw could be affected by climate change, or by climate oscillations such as the El Niño-Southern Oscillation (ENSO). These oscillations drive changes in ocean-atmosphere circulation patterns, as well as SST. They can affect biological productivity and calcification, and therefore should also affect $p\mathrm{CO}_2$sw (e.g. Alexander et al., 2002).

Seawater at both our coastal buoys (Ala Wai, Kilo Nalu, and CRIMP-2), and the open ocean WHOTS site, experienced rising maxima in weekly mean seawater temperatures between 2013 and 2015 (**Figure 3C**). Additionally, all sites display increasing $p\mathrm{CO}_2$sw over our time series, which is, however, not statistically significant (7.5 ± 1.9, 8.3 ± 1.0, 2.5 ± 0.7, 2.9 ± 0.6 ppm yr^{-1} at CRIMP-2, Ala Wai, and Kilo Nalu, and WHOTS respectively; **Figures 3A**, **8**). The increase at Ala Wai is greatest, but this is largely due to the limited dataset, with the anomalously high $p\mathrm{CO}_2$sw in the winter of 2013/2014, as discussed above, driving the (apparent) large annual increase. Raw data from more recent deployments at Ala Wai show that *in situ* and weekly mean $p\mathrm{CO}_2$sw have since decreased to approximately their previous magnitude (data not shown). This discussion will therefore focus on the CRIMP-2 site, which experienced a very large sustained increase in $p\mathrm{CO}_2$sw between 2013 and 2015, and a dramatic increase in the seasonal amplitude of $p\mathrm{CO}_2$sw in 2014/2015 to twice the amount observed in 2011 (**Figure 3**).

Due to the extreme variability in $p\mathrm{CO}_2$sw on all temporal scales, it is difficult to isolate possible effects of longer-term signals. To disentangle contributions of different timescales of $p\mathrm{CO}_2$sw variability at CRIMP-2, magnitudes of sub-monthly, sub-annual and sub-decadal variability were determined (**Table 4**). The amplitude of sub-monthly variations, which include diurnal changes from P/R and calcification/dissolution, and fluctuations associated with the effects of mixed tides on time scales of a few hours to 28 days, is the largest (78 μatm). Sub-annual and sub-decadal variability are 34 and 31 μatm, respectively. The main signal on the sub-annual time scale is the seasonal cycle. Consequently, the difference in $p\mathrm{CO}_2$sw between the first 4-year period and the second 4-year period of the CRIMP-2 time series has approximately the same magnitude as its average seasonal cycle.

TABLE 4 | Amplitude of $p\mathrm{CO}_2$sw variability at CRIMP-2 on different time scales, defined as the average standard deviation of monthly, annual and 4-year mean $p\mathrm{CO}_2$sw.

Timescale of variability	$p\mathrm{CO}_2$sw (μatm)
Sub-monthly	78
Sub-annual	34
Sub-decadal	31

To investigate the potential contribution of climatic oscillations to these sub-decadal variations, annual mean $p\mathrm{CO}_2$sw was plotted (**Figure 8**) with annual mean values of three predominant climate oscillation indices in the North Pacific; the El Niño Southern Oscillation (Oceanic Niño Index, ONI), Pacific Decadal Oscillation (PDO index), and the North Pacific Gyre Oscillation (NPGO index). Correlations between annual mean pCO$_2$sw and ENSO, PDO and NPGO were $R = 0.40$, $R = 0.69$, $R = -0.81$, respectively ($p < 0.01$), suggesting some control of $p\mathrm{CO}_2$sw from large-scale climate oscillations.

Changes in physical forcings such as climate oscillations can have an effect on the CO_2 chemistry of seawater on reefs, as has been observed in the open ocean and on coral reefs of Bermuda (Yeakel et al., 2015). A portion of the increase in $p\mathrm{CO}_2$sw at CRIMP-2 is also likely due to rising atmospheric CO_2 concentrations from anthropogenic carbon emissions, and penetration of this CO_2 into the surface ocean via air-sea gas exchange, as well as reduced outgassing during natural outgassing periods due to a smaller air-sea gradient. An additional fraction of the sub-decadal $p\mathrm{CO}_2$sw variability can likely be explained by the direct temperature effect on CO_2 solubility, which leads to higher (lower) $p\mathrm{CO}_2$sw at higher (lower) temperatures.

Temperature change and associated $p\mathrm{CO}_2$sw change may be driven partly by large scale inter-annual processes such as the ENSO. El Niño events are characterized by larger seasonal amplitudes in SST, while La Niña events have smaller amplitudes. The temperature effect on CO_2 solubility translates this pattern from SST to $p\mathrm{CO}_2$sw. The period from 2009 to 2010 was classified as a moderate El Niño event[8], and displays large SST swings, with a lower winter minimum and a higher summer maximum than subsequent years. The periods 2010–2011 and 2011–2012 were identified as moderate and weak La Niña events, respectively, and were characterized by relatively high winter and low summer SST, leading to smaller seasonal fluctuations in SST. The very strong El Niño in winter 2015 to 2016 shows the largest seasonal amplitude, as well as the highest SST of our dataset.

An additional factor in explaining rising SST between 2013 and 2016 is the North Pacific warm pool, a positive basin-wide SST anomaly beginning in the winter of 2013–2014 (Peterson et al., 2015). Sutton et al. (2017) also proposed that elevated seawater $p\mathrm{CO}_2$sw at the WHOTS buoy during the period 2013–2015 may have been driven by North Pacific warm anomalies, consistent with our observations at CRIMP-2 over a similar time period. Models and observations indicate that the amplitude of diurnal to seasonal $p\mathrm{CO}_2$sw variability in the oceans will likely increase with increasing anthropogenic CO_2 uptake (McNeil and Sasse, 2016; Kwiatkowski and Orr, 2018; Landschützer et al., 2018). This factor could lead to increasing prevalence of conditions similar to the higher and more variable $p\mathrm{CO}_2$sw regime of 2013–2016 at CRIMP-2.

---

[8] http://ggweather.com/enso/oni.htm

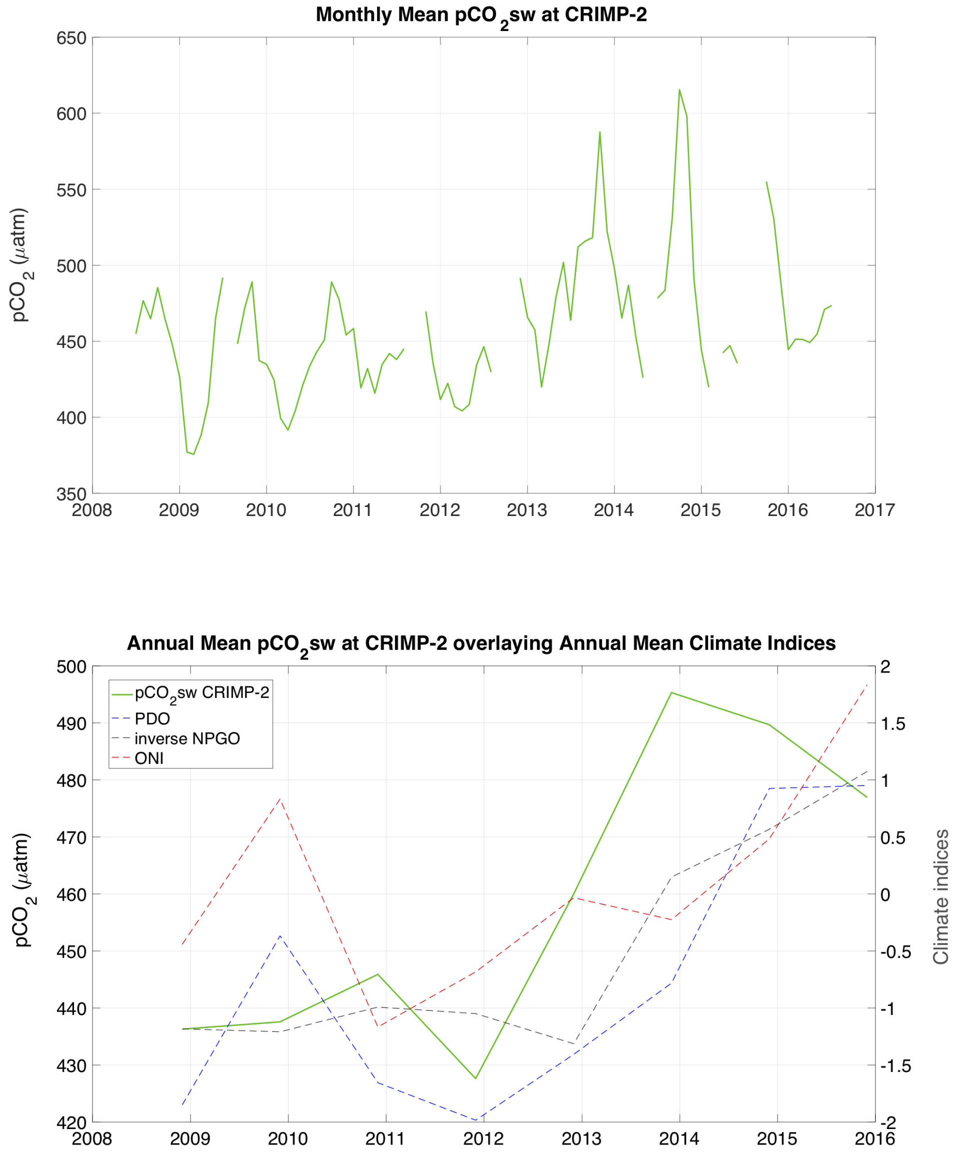

FIGURE 8 | Time-series of Monthly Mean **(top)** and Annual mean **(bottom)** pCO$_2$sw at CRIMP-2 from June 2008 through June 2016. Annual means of pCO$_2$sw calculated from June of 1 year to May of the next. The dashed curves in the bottom panel show annual mean values of the Pacific Decadal Oscillation index (PDO, blue), Oceanic Nino Index (ONI, red), and the inverse of the North Pacific Gyre Oscillation index (NPGO, gray).

El Niño events are also associated with lower trade wind speeds (Collins et al., 2010, and references therein). Weakening of the trade winds increases the residence time of water on the Kaneohe Bay reef flat (e.g., Lowe et al., 2009b) and also reduces air-sea gas exchange rates (e.g., Wanninkhof, 1992; Ho et al., 2006, 2019). Thus, both increased residence time and decreased air-sea gas exchange lead to a stronger buildup of biogeochemical signatures of primary productivity and dissolution (drawdown of pCO$_2$sw) and respiration and calcification (increase in pCO$_2$sw), respectively. Weaker trade winds are therefore likely partially responsible for the greater amplitude of fluctuations in pCO$_2$sw at CRIMP-2 during El Niño years.

Changes in biogeochemical processes on the reef that could cause an increase in pCO$_2$sw at CRIMP-2 between 2013 and 2016 include: (1) an increase in net ecosystem calcification (NEC) (e.g., Drupp et al., 2013; Courtney et al., 2017) and (2) an increase in respiration of organic matter relative to primary production (e.g., Drupp et al., 2011, 2013). An increase in NEC seems unlikely. The high SST during the summers of 2014 and 2015 caused widespread coral bleaching throughout the Hawaiian Islands, and led to lower calcification rates on the barrier reef of Kaneohe Bay. The reefs largely recovered by Courtney et al. (2017). An increase of respiration on the reef flat, however, is more likely responsible for the observed higher pCO$_2$sw between 2012 and 2016. Rates of biogeochemical processes typically increase with increasing (seawater) temperature, but respiration is more sensitive to temperature changes than primary production ("Q10 effect," e.g., Woodwell and Mackenzie, 1995; Ver et al., 1999). Higher SST consequently causes enhanced respiration relative to photosynthesis, which increases $p\mathrm{CO_2sw}$. The barrier reef ecosystem is perhaps shifting toward longer periods of heterotrophy as a result of elevated SST between 2013 and 2016. Photosynthesis/respiration cycles appear to be a more important driver of $p\mathrm{CO_2sw}$ at CRIMP-2 than calcification/dissolution (see Page et al., 2018). Therefore, the relative increase in the ratio of respiration to photosynthesis likely outweighs the decrease in $p\mathrm{CO_2sw}$ due to lower calcification, resulting in higher $p\mathrm{CO_2sw}$ values during periods of temperature-induced coral bleaching. Kayanne et al. (2005) also measured an increase in $p\mathrm{CO_2sw}$ in coral reefs with extensive bleaching, but observed a concomitant 50% decrease in diurnal variability associated with reduced metabolic performance. This does not apply to the bleaching

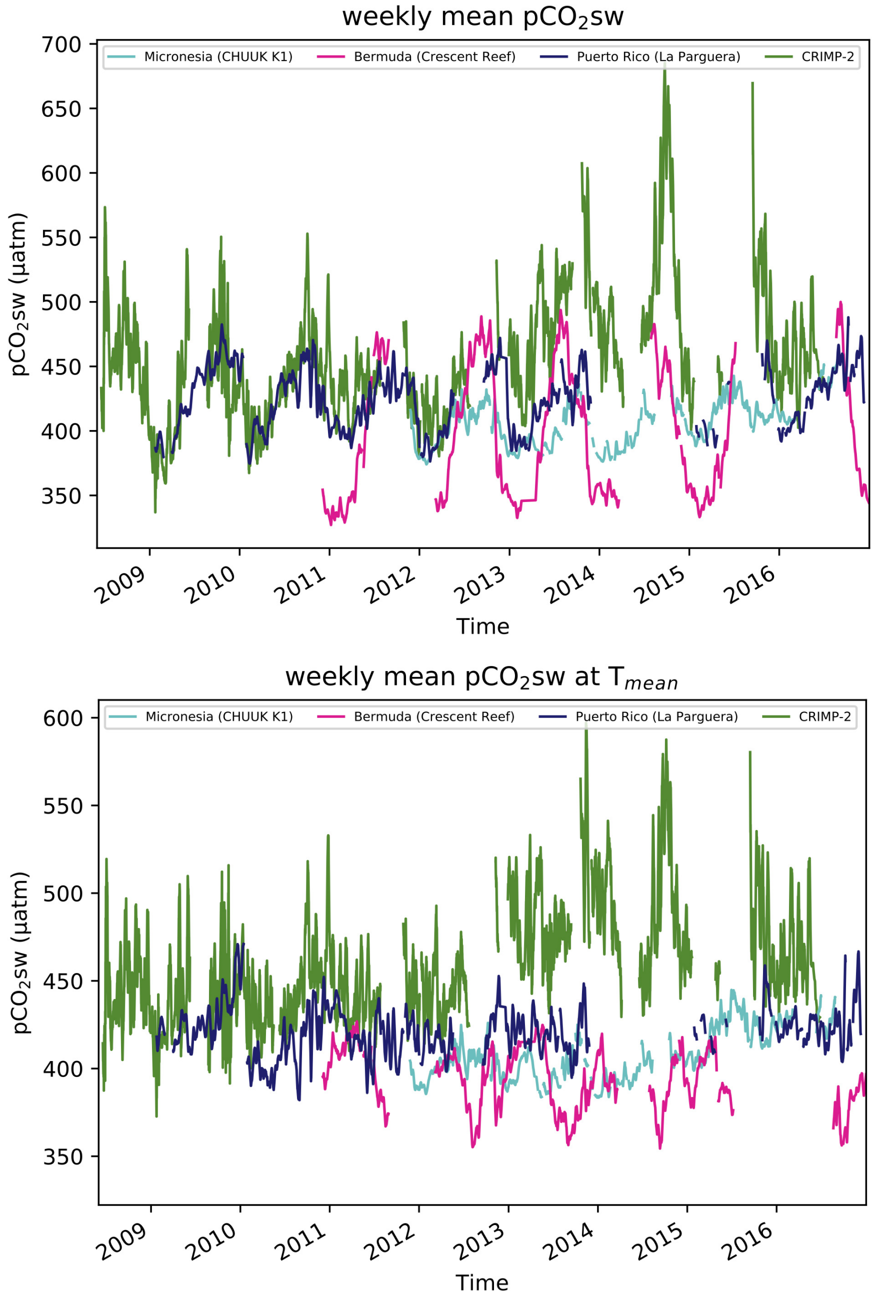

FIGURE 9 | Time-series of weekly mean $p\mathrm{CO_2sw}$ **(Top)** and temperature normalized $p\mathrm{CO_2sw}$ ($p\mathrm{CO_2sw}$ at T_{mean}, **Bottom**) at different reef sites for June 2008 through December 2016.

period in Kaneohe Bay, where CRIMP-2 diurnal variability did not decrease.

The pCO$_2$sw increase observed at CRIMP-2 was greater than those observed at MAPCO$_2$ sites at coral reefs in different parts of the world (**Figure 9** and online[9]). The records from La Parguera site, on the southwestern coast of Puerto Rico, and CRIMP-2 nearly overlap early (2009) in the time series: The maxima in summer are roughly 50 ppm higher at CRIMP-2, but the means and amplitudes are comparable. The similarity in the CRIMP-2 and La Parguera pCO$_2$sw records disappears after the winter of 2011–2012, when pCO$_2$sw at CRIMP-2 begins to rise considerably. Neither the Chuuk K1 site, a low latitude (7.5°N) reef in Micronesia, or the Crescent reef site in Bermuda showed a significant trend in pCO$_2$sw, or a baseline shift similar to the CRIMP-2 observations. Upon normalization to the overall mean temperature (**Figure 8**) at each site over the respective time periods, pCO$_2$sw at both moorings in tropical waters of the Pacific (CRIMP-2 and Chuuk K1) appears to rise toward the end of the time series, while pCO$_2$sw at T_{mean} at La Parguera and Crescent reef do not exhibit the same feature.

The observed similarity between both North Pacific reefs in temperature normalized pCO$_2$sw may be attributed partially to the influence of basin wide changes in physical processes, such as SST and wind speed variations. The larger variability of pCO$_2$sw at CRIMP-2 relative to other reefs around the world, however, is likely driven more by local changes in biogeochemistry on the Kaneohe Bay barrier reef, which are themselves influenced strongly by inter-annual changes in large scale ocean-atmosphere circulation patterns. The relative importance of these drivers can only be assessed with additional years of continuous monitoring that can resolve the time scales of inter-annual variability and long-term trends.

CONCLUSION

In this paper we presented a statistical evaluation and interpretation of nearly a decade of high-resolution CO$_2$ time-series data collected between June 2008 and December 2016 at three different coral reef environments off the island of O'ahu, Hawai'i. Our major findings are:

- Land-ocean interactions, water column and benthic photosynthesis/respiration and calcification/dissolution, as well as physical forcing (wind, waves, and water residence time), all exert controls on pCO$_2$sw and air-sea CO$_2$ fluxes, which are therefore more variable on coral reefs than in the open ocean.
- Diurnal pCO$_2$sw variability was, on average, 40 times greater on the Kaneohe Bay barrier reef than in waters of the North Pacific subtropical gyre, and comparatively less so (10 times) at the more exposed fringing reef sites of O'ahu, driven largely by daily cycles of photosynthesis and respiration. The temperature effect on CO$_2$ solubility is the largest driver of seasonal pCO$_2$sw variability, with additional impacts by biogeochemical processes that differ between reef locations.
- While seasonal variability determines the direction of air-sea CO$_2$ fluxes in the open ocean, which are negative in winter (sink for atmospheric CO$_2$) and positive in summer, large short-term changes occur in coastal coral reef systems. Instantaneous air-sea CO$_2$ fluxes on O'ahu's coral reefs are highly variable in magnitude and direction and, reflecting local dynamic conditions, often switch between being a source or a sink of CO$_2$ on timescales of hours to days. Overall estimated area specific air-sea CO$_2$ fluxes at CRIMP-2, Ala Wai and Kilo Nalu sites of 1.24, 0.05, 0.00 mol C m^{-2}yr^{-1}, respectively, are consistent with earlier work, indicating that the productive coral reefs of Hawai'i are generally a source of CO$_2$ to the atmosphere.
- Instantaneous air-sea CO$_2$ fluxes were most variable during the summer at CRIMP-2 due to higher SST enhancing biological productivity. At the south shore sites, on the other hand, the variability was greater in winter and spring, likely due to increased rainfall delivering nutrients to the coastal ocean.
- Relatively low peak pCO$_2$sw at CRIMP-2 in the early parts of our time-series (2008 and 2010) coincided with La Niña periods, whereas higher peak pCO$_2$sw later in our time series (2014–2016) coincided with El Niño.
- The observed inter-annual increase in pCO$_2$sw at CRIMP-2 over the study period may reflect the influence of climate oscillations on local conditions: Firstly, increased seawater temperature both directly increases pCO$_2$sw and may enhance rates of respiration, which also increase pCO$_2$sw. Secondly, reduced trade wind speed increases the water residence time on the reef, allowing for more build-up of CO$_2$ in seawater.
- Variability in pCO$_2$sw at CRIMP-2 is greatest at timescales shorter than a month (78 μatm), while average seasonal and inter-annual variations are 34 and 31 μatm, respectively. Consequently, there is a large magnitude of short-term changes due to reef metabolism and physical drivers overlaying a smaller amplitude seasonal cycle, and comparable inter-annual changes on a time-scale of approximately 5 years. This shows that inter-annual changes in pCO$_2$ are difficult to identify on a background of extremely large shorter-term variability at CRIMP-2.

AUTHOR CONTRIBUTIONS

GT, PD, EDC, FM, and CS contributed to the conception and design of the study. GT and EDC wrote an earlier version of the manuscript. LK and GT re-wrote the manuscript, performed statistical analysis, and generated figures and tables. AS and AP contributed to datasets. YL provided valuable insights into interpretations of the data. All authors contributed to manuscript revisions, read and approved the submitted version.

---

[9] http://www.pmel.noaa.gov/co2/story/Coral+Reef+Moorings

FUNDING

We acknowledge with gratitude the financial support of our research provided in part by a grant/cooperative agreement from the National Oceanic and Atmospheric Administration, Project R/IR-27, which is sponsored by the University of Hawaii Sea Grant College Program, SOEST, under Institutional Grant No. NA14OAR4170071 from NOAA Office of Sea Grant, Department of Commerce. Additional support was granted by the NOAA/Ocean Acidification Program (to EDC and AS) and the NOAA/Climate Program Office (AP), and the NOAA Ocean Observing and Monitoring Division, Climate Program Office (FundRef number 100007298) through agreement NA14OAR4320158 of the NOAA Cooperative Institute for the North Atlantic Region (AP). The views expressed herein are those of the author(s) and do not necessarily reflect the views of NOAA or any of its subagencies. This is SOEST contribution number 10684, PMEL contribution number 4845, and Hawai'i Sea Grant contribution UNIHI-SEAGRANT-JC-15-30.

ACKNOWLEDGMENTS

We are grateful to research groups working on NOAA MAPCO_2 moorings globally who supplied data for comparison: the Korea Institute of Ocean Science and Technology (Chuuk K1), University of Puerto Rico (La Parguera), and the Bermuda Institute of Ocean Science (Crescent Reef). We would like to thank Ryan Tabata, Noah Howins, and Anthony Barro (at UH), as well as Sylvia Musielewicz, Stacy Maenner-Jones, and Randy Bott (at NOAA/PMEL) who provided technical support and their efforts are deeply appreciated as this research would not have been possible without their able assistance. This manuscript also benefited from reviews from several reviewers who helped improve the quality of this manuscript.

REFERENCES

Alexander, M. A., Blade, I., Newman, M., Lanzante, J. R., Lau, N. C., and Scott, J. D. (2002). The atmospheric bridge: the influence of ENSO teleconnections on air–sea interaction over the global oceans. *J. Clim.* 15, 2205–2231. doi: 10.1175/1520-0442(2002)015\%3C2205\%3Atabtio\%3E2.0.co\%3B2

Andersson, A. J., and Gledhill, D. (2013). Ocean acidification and coral reefs: effects on breakdown, dissolution, and net ecosystem calcification. *Annu. Rev. Mar. Sci.* 5, 321–348. doi: 10.1146/annurev-marine-121211-172241

Bates, N. R., Astor, Y. M., Church, M. J., Currie, K., Dore, J. E., González-Dávila, M., et al. (2014). A time-series view of changing ocean chemistry due to ocean uptake of anthropogenic CO2 and ocean acidification. *Oceanography* 27, 126–141. doi: 10.5670/oceanog.2014.16

Bates, N. R., Samuels, L., and Merlivat, L. (2001). Biogeochemical and physical factors influencing seawater *f*CO2 and air-sea CO2 exchange on the Bermuda coral reef. *Limnol. Oceanogr.* 46, 833–846. doi: 10.4319/lo.2001.46.4.0833

Caldeira, K., and Wickett, M. E. (2003). Oceanography: anthropogenic carbon and ocean pH. *Nature* 425, 365–365. doi: 10.1038/425365a

Chamard, P., Thiery, F., Di Sarra, A., Ciattaglia, L., De Silverstri, L., Grigioni, P., et al. (2003). Interannual variability of atmospheric CO2 in the mediterranean: measurements at the island of lampedusa. *Tellus* 55, 83–93. doi: 10.1034/j.1600-0889.2003.00048.x

Chhak, K. C., and Di Lorenzo, E. (2009). Forcing of low-frequency ocean variability in the Northeast Pacific*. *J. Clim.* 22, 1255–1276. doi: 10.1175/2008jcli2639.1

Collins, M., An, S. I., Cai, W., Ganachaud, A., Guilyardi, E., Jin, F. F., et al. (2010). The impact of global warming on the tropical Pacific Ocean and El Niño. *Nat. Geosci.* 3, 391–397.

Courtney, T., De Carlo, E. H., Page, H. N., Bahr, K. D., Barro, A., Howins, N., et al. (2017). Recovery of reef-scale calcification following a bleaching event in Kaneʻohe Bay, Hawaiʻi. *Limnol. Oceanogr. Lett.* 3, 1–9. doi: 10.1002/lol2.10056

Cyronak, T., Santos, I. R., Erler, D. V., Maher, D. T., and Eyre, B. D. (2014). Drivers of *p*CO_2 variability in two contrasting coral reef lagoons: the influence of submarine groundwater discharge. *Global Biogeochem. Cycles* 28, 398–414. doi: 10.1002/2013gb004598

De Carlo, E. H., Beltran, V. L., and Tomlinson, M. S. (2004). Composition of water and suspended sediment in streams of urbanized subtropical watersheds in Hawaii. *Appl. Geochem.* 19, 1011–1037. doi: 10.1016/j.apgeochem.2004.01.004

De Carlo, E. H., Hoover, D. J., Young, C. W., Hoover, R. S., and Mackenzie, F. T. (2007). Impact of storm runoff from tropical watersheds on coastal water quality and productivity. *Appl. Geochem.* 22, 1777–1797. doi: 10.1016/j.apgeochem.2007.03.034

Di Lorenzo, E., Schneider, N., Cobb, K. M., Franks, P. J. S., Chhak, K., Miller, A. J., et al. (2008). North pacific gyre oscillation links ocean climate and ecosystem change. *Geophys. Res. Lett.* 35:L08607. doi: 10.1111/gcb.13171

Dlugokencky, E., and Tans, P. (2018). *Trends in Atmospheric Carbon Dioxide. NOAA/ESRL*. Available at: http://www.esrl.noaa.gov/gmd/ccgg/trends/global.html (accessed April 17, 2019).

Dore, J. E., Lucas, R., Sadler, D. W., Church, M. J., and Karl, D. M. (2009). Physical and biogeochemical modulation of ocean acidification in the central North Pacific. *PNAS* 106, 12235–12240. doi: 10.1073/pnas.0906044106

Dore, J. E., Lukas, R., Sadler, D. W., and Karl, D. M. (2003). Climate-driven changes to theatmospheric CO2 sink in the subtropical North Pacific Ocean. *Nature* 424, 754–757. doi: 10.1038/nature01885

Drupp, P., De Carlo, E. H., Mackenzie, F. T., Bienfang, P., and Sabine, C. L. (2011). Nutrient inputs, phytoplanton response, and CO2 variations in a semi-enclosed subtropical embayment, Kaneohe Bay, Hawaii. *Aquat. Geochem.* 17, 473–498. doi: 10.1007/s10498-010-9115-y

Drupp, P. S., De Carlo, E. H., and Mackenzie, F. T. (2016). Porewater CO2-carbonic acid geochemistry in sandy sediments. *Mar. Chem.* 185, 48–64. doi: 10.1016/j.marchem.2016.04.004

Drupp, P. S., DeCarlo, E. H., Mackenzie, F. T., Sabine, C. L., Feely, R. A., and Shamberger, K. E. (2013). Comparison of CO2 dynamics and air-sea gas exchange in differing tropical reef environments. *Aquat. Geochem.* 19, 371–397. doi: 10.1007/s10498-013-9214-7

Eyre, B., Cyronak, T., Drupp, P., De Carlo, E. H., Sachs, J., and Andersson, A. J. (2018). Coral reefs will transition to net dissolving before end of century. *Science* 359, 908–911. doi: 10.1126/science.aao1118

Fagan, K. E., and Mackenzie, F. T. (2007). Air-sea CO2 exchange in a subtropical estuarine-coral reef system, Kaneohe Bay, Oahu, Hawaii. *Mar. Chem.* 106, 174–191. doi: 10.1016/j.marchem.2007.01.016

Feely, R. A., Sabine, C. L., Lee, K., Berelson, W., Kleypas, J., Fabry, V. J., et al. (2004). Impact of anthropogenic CO_2 on the $CaCO_3$ system in the oceans. *Science* 305, 362–366. doi: 10.1126/science.1097329

Frankignoulle, M., Gattuso, J. P., Biondo, R., Bourge, I., Copin-Montégut, G., and Pichon, M. (1996). Carbon fluxes in coral reefs. II. Eulerian study of inorganic carbon dynamics and measurement of air-sea CO_2 exchanges. *Mar. Ecol. Prog. Ser.* 145, 123–132. doi: 10.3354/meps145123

Fogaren, K. E., Sansone, F. J., and De Carlo, E. H. (2013). Porewater temporal variability in a wave-impacted permeable nearshore sediment. *Mar. Chem.* 149, 74–84. doi: 10.1016/j.marchem.2012.12.005

Gagliano, M., McCormick, M. I., Moore, J. A., and Depczynski, M. (2010). The basics ofacidification: baseline variability of pH on Australian coral reefs. *Mar. Biol.* 157, 1849–1856. doi: 10.1007/s00227-010-1456-y

Gattuso, J. P., and Hansson, L. (2011). *Ocean Acidification*. Oxford: Oxford University Press.

Gattuso, J.-P., Payri, C. E., Pichon, M., Delesalle, B., and Frankignoulle, M. (1997). Primary production, calcification, and air-sea CO_2 fluxes of a macroalgal-dominated coral reef community in Moorea, French Polynesia. *J. Phycol.* 33, 729–738. doi: 10.1111/j.0022-3646.1997.00729.x

Gattuso, J. P., Pichon, M., Delesalle, B., Canon, C., and Frankignoulle, M. (1996). Carbon fluxes in coral reefs. I. Lagrangian measurement of community metabolism and resulting air-sea CO_2 disequilibrium. *Mar. Ecol. Prog. Ser.* 145, 109–121. doi: 10.3354/meps145109

Gattuso, J.-P, Pichon, M., Delesalle, B., and Frankignoulle, M. (1993). Community metabolism and air-sea CO_2 fluxes in a coral-reef ecosystem (Moorea, French-Polynesia). *Mar. Ecol. Prog. Ser.* 96, 259–267. doi: 10.3354/meps096259

Giambelluca, T. W., Chen, Q., Frazier, A. G., Price, J. P., Chen, Y.-L., Chu, P. S., et al. (2011). *The Rainfall Atlas of Hawai'i.*Available at: http://rainfall.geography.hawaii.edu (accessed April 17, 2019).

Giambelluca, T. W., Nullet, M. A., and Schroeder, T. A. (1986). *Rainfall atlas of Hawaii.* Hawaii, HI: Department of Land and Natural Resources.

Ho, D., De Carlo, E. H., and Schlosser, P. (2019). Air-sea gas exchange and CO2 fluxes in a tropical coral reef lagoon. *J. Geophys. Res. Oceans* 123, 8701–8713. doi: 10.1029/2018JC014423

Ho, D. T., Coffineau, N., Hickman, B., Chow, N., Koffman, T., and Schlosser, P. (2016). Influence of current velocity and wind speed on air-water gas exchange in a mangrove estuary. *Geophys. Res. Lett.* 43, 3813–3821. doi: 10.1002/2016gl068727

Ho, D. T., Law, C. S., Smith, M. J., Schlosser, P., Harvey, M., and Hill, P. (2006). Measurements of air-sea gas exchange at high wind speeds in the Southern Ocean: implications for global parameterization. *Geophys. Res. Lett.* 33:L16611 doi: 10.1029/2006GL026817

Hoegh-Guldberg, O., Mumby, P. J., Hooten, A. J., Steneck, R. S., Greenfield, P., Gomez, E., et al. (2007). Coral reefs under rapid climate change and ocean acidification. *Science* 318, 1737–1742.

Hofmann, G. E., Smith, J. E., Johnson, K. S., Send, U., Levin, L. A., Micheli, F., et al. (2011). High-frequency dynamics of ocean pH: a multi-ecosystem comparison. *PLoS One* 6:e28983. doi: 10.1371/journal.pone.0028983

Hoover, D. J., and Mackenzie, F. T. (2009). Fluvial fluxes of water, suspended particulate matter, and nutrients and potential impacts on tropical coastal water biogeochemistry: Oahu, Hawaii. *Aquat. Geochem.* 15, 547–570. doi: 10.1007/s10498-009-9067-2

Hoover, R. S., Hoover, D., Miller, M., Landry, M. R., DeCarlo, E. H., and Mackenzie, F. T. (2006). Zooplankton response to storm runoff in a tropical estuary: bottom-up and top-down controls. *Mar. Ecol. Prog. Ser.* 318, 187–201. doi: 10.3354/meps318187

Karl, D. M., and Church, M. J. (2018). Station ALOHA: a gathering place for discovery, education,and scientific collaboration. *Limnol. Oceanogr. Bull.* 28, 10–12. doi: 10.1002/lob.10285

Kayanne, H., Hata, H., Kudo, S., Yamano, H., Watanabe, A., Ikeda, Y., et al. (2005). Seasonal and bleaching-induced changes in coral reef metabolism and CO_2 flux. *Global Biogeochem. Cycles* 19. doi: 10.1029/2004GB002400

Kayanne, H., Suzuki, A., and Saito, H. (1995). Diurnal changes in the partial pressure of carbon dioxide in coral reef water. *Science* 269, 214–216. doi: 10.1126/science.269.5221.214

Keeling, C. D., Bacastow, R. B., Bainbridge, A. E., Ekdahl, C. A., Guenther, P. R., and Waterman, L. S. (1976). Atmospheric carbon dioxide variations at Mauna Loa Observatory, Hawaii. *Tellus* 28, 538–551. doi: 10.3402/tellusa.v28i6.11322

Keeling, C. D., Piper, S. C., Bacastow, R. B., Wahlen, M., Whorf, T. P., Heimann, M., et al. (2001). *Exchanges of Atmospheric CO2 and 13CO2 with the Terrestrial Biosphere and Oceans from 1978 to 2000. I. Global Aspects, SIO Reference Series, No. 01-06.* San Diego, CA: Scripps Institution of Oceanography.

Kleypas, J. A., Buddemeier, R. W., Archer, D., Gattuso, J. P., Langdon, C., and Opdyke, B. N. (1999). Geochemical consequences of increased atmospheric carbon dioxide on coral reefs. *Science* 284, 118–120. doi: 10.1126/science.284.5411.118

Kleypas, J. A., and Langdon, C. (2006). "Coral Reefs and changing seawater carbonate chemistry," in *Coral Reefs and Climate Change: Science and Management*, eds J. T. Phinney, O. Hoegh-Guldberg, J. Kleypas, W. Skirving, and A. Strong (Washington, DC: American Geophysical Union), doi: 10.1029/61CE06

Kwiatkowski, L., and Orr, J. C. (2018). Diverging seasonal extremes for ocean acidification during the twenty-first century. *Nat. Clim. Change* 8, 141–145. doi: 10.1038/s41558-017-0054-0

Landschützer, P., Gruber, N., Bakker, D. C. E., Stemmler, I., and Six, K. D. (2018). Strengthening seasonal marine CO2 variations due to increasing atmospheric CO2. *Nat. Clim. Change* 8, 146–150. doi: 10.1038/s41558-017-0057-x

Le Quéré, C. L., Andrew, R. M., Friedlingstein, P., Sitch, S., Pongratz, J., Manning, A. C., et al. (2018). Global Carbon Budget 2017. *Earth Syst. Sci. Data* 10, 405–448. doi: 10.5194/essd-10-405-2018

Liss, P. S. (1983). "Gas transfer: experiments and geochemical implications," in *Air–Sea Exchange of Gases and Particles*, eds P. S. Liss and W. G. N. Slinn (Dordrecht: D. Reidel), 241–298. doi: 10.1007/978-94-009-7169-1_5

Lowe, R. J., Falter, J. L., Monismith, S. G., and Atkinson, M. J. (2009a). A numerical study of circulation in a coastal reef–lagoon system. *J. Geophys. Res. Oceans* 114:C06022.

Lowe, R. J., Falter, J. L., Monismith, S. G., and Atkinson, M. J. (2009b). Wave-driven circulation of a coastal reef–lagoon system. *J. Phys. Oceanogr.* 39, 873–889.

Mackenzie, F. T., and Andersson, A. J. (2013). The marine carbon system and ocean acidification during Phanerozoic time. *Geochem. Perspect.* 2, 1–3.

Massaro, R. F., De Carlo, E. H., Drupp, P. S., Mackenzie, F. T., Maenner Jones, S., Shamberger, K. E., et al. (2012). Multiple factors driving variability of CO2 exchange between the ocean and atmosphere in a tropical coral reef environment. *Aquat. Geochem.* 18, 357–386. doi: 10.1007/s10498-012-9170-7

McNeil, B. I., and Sasse, T. P. (2016). Future ocean hypercapnia driven by anthropogenic amplification of the natural CO2 cycle. *Nature* 529, 383–386. doi: 10.1038/nature16156

Nightingale, P. D., Liss, P. S., and Schlosser, P. (2000a). Measurements of air-sea gas transfer during an open ocean algal bloom. *Geophys. Res. Lett.* 27, 2117–2120. doi: 10.1029/2000gl011541

Nightingale, P. D., Malin, G., Law, C. S., Watson, A. J., Liss, P. S., Liddicoat, M. I., et al. (2000b). In situ evaluation of air-sea gas exchange parameterizations using novel conservative and volatile tracers. *Glob. Biogeochem. Cycles* 14, 373–387. doi: 10.1029/1999gb900091

Ohde, S., and van Woesik, R. (1999). Carbon dioxide flux and metabolic processes of a coral reef, Okinawa. *Bull. Mar. Sci.* 65, 559–576.

Page, H. N., Courtney, T. A., Collins, A., De Carlo, E. H., and Andersson, A. J. (2017). Net community metabolism and seawater carbonate chemistry scale non-intuitively with coral cover. *Front. Mar. Sci.* 4:161. doi: 10.3389/fmars.2017.00161

Page, H. N., Courtney, T. A., De Carlo, E. H., Howins, N., Koester, I., and Andersson, A. J. (2018). Spatio-temporal variability in seawater carbon chemistry for a coral reef flat in Kaneohe Bay, Hawaii. *Limnol. Oceanogr.* 9999, 1–22. doi: 10.1002/lno.11084

Peterson, E. W., and Hennessey, J. P. (1978). On the use of power laws for estimates of wind power potential. *J. Appl. Meteorol.* 17, 390–394. doi: 10.1175/1520-0450(1978)017\%3C0390\%3Aotuopl\%3E2.0.co\%3B2

Peterson, W., Robert, M., and Bond, N. (2015). The warm blob-conditions in the northeastern Pacific Ocean. *North Pac. Mar. Sci. Organ.* 23, 36–38.

Price, N. N., Martz, T. R., Brainard, R. E., and Smith, J. E. (2012). Diel variability in seawater pH relates to calcification and benthic community structure on coral reefs. *PLoS One* 7:e43843. doi: 10.1371/journal.pone.0043843

Ringuet, S., and Mackenzie, F. T. (2005). Controls on nutrient and phytoplankton dynamics during normal flow and storm runoff conditions, Southern Kaneohe Bay, Hawaii. *Estuaries* 28, 327–337. doi: 10.1007/bf02693916

Sabine, C. L., Feely, R. A., Gruber, N., Key, R. M., Lee, K., Bullister, J. L., et al. (2004). The oceanic sink for anthropogenic CO2. *Science* 305, 367–371. doi: 10.1126/science.1097403

Shamberger, K. E., Feely, R. A., Sabine, C. L., Atkinson, M. J., De Caro, E. H., Mackenzie, F. T., et al. (2011). Calcification and organic production on a Hawaiian coral reef. *Mar. Chem.* 127, 64–75. doi: 10.1016/j.marchem.2011.08.003

Shaw, E. C., and McNeill, B. I. (2014). Seasonal variability in carbonate chemistry and air–sea CO2 fluxes in the southern Great Barrier Reef. *Mar. Chem.* 158, 49–58. doi: 10.1016/j.marchem.2013.11.007

Shaw, E., Tilbrook, B., Steven, A., and Phinn, S. (2014). *Carbonate Chemistry, Community Metabolism, PAR, Temperature and Salinity of One Tree Island Reef.* Bremen: Pangaea.

Sutton, A. J., Feely, R. A., Maenner-Jones, S., Musielwicz, S., Osborne, J., Dietrich, C., et al. (2019). Autonomous seawater $p\text{CO}_2$ and pH time series from 40 surface buoys and the emergence of anthropogenic trends. *Earth Syst. Sci. Data* 11, 421–439. doi: 10.5194/essd-11-421-2019

Sutton, A. J., Feely, R. A., Sabine, C. L., McPhadden, M. L., Takahashi, T., Chavez, F. P., et al. (2014a). Natural variability and anthropogenic change in equatorial Pacific surface ocean *p*CO2 and pH. *Glob. Biogeochem. Cycles* 28, 131–145. doi: 10.1002/2013GB004679

Sutton, A. J., Sabine, C. L., Feely, R. A., Cai, W. J., Cronin, M. F., McPhaden, M. J., et al. (2016). Using present-day observations to detect when anthropogenic change forces surface ocean carbonate chemistry outside preindustrial bounds. *Biogeosciences* 13, 5065–5083. doi: 10.5194/bg-13-5065-2016

Sutton, A. J., Sabine, C. L., Maenner-Jones, S., Lawrence-Slavas, N., Meinig, C., Feely, R. A., et al. (2014b). A high-frequency atmospheric and seawater *p*CO2 data set from 14 open-ocean sites using a moored autonomous system. *Earth Syst. Sci. Data* 6, 353–366. doi: 10.5194/essd-6-353-2014

Sutton, A. J., Wanninkhof, R., Sabine, C. L., Feely, R. A., Cronin, M. F., and Weller, R. A. (2017). Variability and trends in surface seawater *p*CO2 and CO2 flux in the Pacific Ocean. *Geophys. Res. Lett.* 44, 5627–5636. doi: 10.1002/2017GL073814

Takahashi, T., Olafsson, J., Goddard, J. G., Chipman, D. W., and Sutherland, S. C. (1993). Seasonal-variation of CO2 and nutrients in the high-latitude surface oceans—a comparative study. *Glob. Biogeochem. Cycles* 7, 843–878. doi: 10.1029/93gb02263

Takahashi, T., Sutherland, S. C., Sweeney, C., Poisson, A., Metzl, N., Tilbrook, B., et al. (2002). Global sea–air CO_2 flux based on climatological surface ocean $p\text{CO}_2$, and seasonal biological and temperature effects. *Deep Sea Res. Part 2 Top. Stud. Oceanogr.* 49, 1601–1622. doi: 10.1016/s0967-0645(02)00003-6

Tans, P. P., and Kieling, R. (2017). *NOAA/ESRL*. Available at: www.esrl.noaa.gov/gmd/ccgg/trends (accessed April 17, 2019).

Thoning, K. W., Tans, P. P., and Komhyr, W. D. (1989). Atmospheric carbon dioxide at mauna loa observatory 2. analysis of the NOAA GMCC data, 1974-1985. *J. Geophys. Res.* 94, 8549–8565. doi: 10.1029/jd094id06p08549

Tokoro, T., Hosokawa, S., Miyoshi, E., Tada, K., Watanabe, K., Montani, S., et al. (2014). Net uptake of atmospheric CO2 by coastal submerged aquatic vegetation. *Glob. Change Biol.* 20, 1873–1884. doi: 10.1111/gcb.12543

Tomlinson, M. S., De Carlo, E. H., McManus, M. A., Pawlak, G., and Steward, G. F. (2011). Characterizing the effects of two storms on the coastal waters of Oahu, Hawaii, using data from the Pacific Islands Ocean Observing System. *Oceanography* 24, 182–198.

Ver, L. M. B., Mackenzie, F. T., and Lerman, A. (1999). Biogeochemical responses of the carbon cycle to natural and human perturbation: past, present, and future. *Am. J. Sci.* 299, 762–801. doi: 10.2475/ajs.299.7-9.762

Wanninkhof, R. (1992). Relationship between wind speed and gas exchange over the ocean. *J. Geophys. Res.* 97, 7373–7382.

Weiss, R. F. (1974). Carbon dioxide in water and seawater: the solubility of a non-ideal gas. *Mar. Chem.* 2, 203–215. doi: 10.1016/0304-4203(74)90015-2

Weiss, R. F., and Price, B. A. (1980). Nitrous oxide solubility in water and seawater. *Mar. Chem.* 8, 347–359. doi: 10.1016/0304-4203(80)90024-9

Weller, R. A. (2018). "Observing Surface Meteorology and Air-Sea Fluxes," in *Observing the Oceans in Real Time*, eds R. Venkatesan, A. Tandon, E. D'Asaro, and M. A. Atmanand (New York, NY: Springer Oceanography), 17–35. doi: 10.1007/978-3-319-66493-4_2

Woodwell, G. M., and Mackenzie, F. T. (1995). *Biotic Feedbacks in the Global Climatic System: Will the Warming Feed the Warming?* New York, NY: Oxford University Press.

Yan, H., Yu, K., Shi, Q., Tan, Y., Lui, G., Zhao, M., et al. (2016). Seasonal variations of seawater pCO2 and sea-air CO2 fluxes in a fringing coral reef, northern South China Sea. *J. Geophys. Res. Oceans* 121, 998–1008. doi: 10.1002/2015jc011484

Yan, H., Yu, K., Shi, Q., Tan, Y., Zhang, H., Zhao, M., et al. (2011). Coral reef ecosystems in the South China Sea as a source of atmospheric CO_2 in summer. *Chin. Sci. Bull.* 56, 676–684. doi: 10.1007/s11434-011-4372-8

Yeakel, K. L., Nadersson, A. J., Bates, N. R., Noyes, T. J., Collins, A., and Garley, R. (2015). Shifts in coral reef biogeochemistry and resulting acidification linked to offshore productivity. *PNAS* 112, 14512–14517. doi: 10.1073/pnas.1507021112

Conflict of Interest Statement: The authors declare that the research was conducted in the absence of any commercial or financial relationships that could be construed as a potential conflict of interest.

frontiers in Marine Science

ORIGINAL RESEARCH
published: 10 April 2019
doi: 10.3389/fmars.2019.00160

Seasonal Carbonate Chemistry Dynamics on Southeast Florida Coral Reefs: Localized Acidification Hotspots From Navigational Inlets

Ian C. Enochs[1]*, *Derek P. Manzello*[1], *Paul R. Jones*[1,2], *S. Jack Stamates*[1] *and Thomas P. Carsey*[1]

[1] NOAA, Atlantic Oceanographic and Meteorological Laboratory, Ocean Chemistry and Ecosystem Division, Miami, FL, United States, [2] Cooperative Institute for Marine and Atmospheric Studies, University of Miami, Miami, FL, United States

Edited by:
Tyler Cyronak,
Scripps Institution of Oceanography,
University of California, San Diego,
United States

Reviewed by:
Coulson Lantz,
Southern Cross University, Australia
Yuri Artioli,
Plymouth Marine Laboratory,
United Kingdom
Yuichiro Takeshita,
Monterey Bay Aquarium Research
Institute (MBARI), United States

***Correspondence:**
Ian C. Enochs
ian.enochs@noaa.gov

Specialty section:
This article was submitted to
Global Change and the Future Ocean,
a section of the journal
Frontiers in Marine Science

Received: *01 November 2018*
Accepted: *14 March 2019*
Published: *10 April 2019*

Citation:
Enochs IC, Manzello DP, Jones PR,
Stamates SJ and Carsey TP (2019)
Seasonal Carbonate Chemistry
Dynamics on Southeast Florida Coral
Reefs: Localized Acidification
Hotspots From Navigational Inlets.
Front. Mar. Sci. 6:160.
doi: 10.3389/fmars.2019.00160

Seawater carbonate chemistry varies across temporal and spatial scales. Shallow-water environments can exhibit especially dynamic fluctuations as biological and physical processes operate on a smaller water volume relative to open ocean environments. Water was collected on a bi-monthly basis from seven sites off of southeast Florida (Miami-Dade and Broward counties), including four reefs, and three closely-associated inlets. Significant seasonal fluctuations in carbonate chemistry were observed on reef sites, with elevated pCO_2 in the warmer wet season. Inlets demonstrated a more dynamic range, with periodic pulses of acidified water contributing to, on average, more advanced acidification conditions than those found at nearby reefs. Within inlet environments, there was a significant negative correlation between seawater salinity and both total alkalinity (TA) and dissolved inorganic carbon (DIC), which was in contrast to the patterns observed on reefs. Elevated TA and DIC in low salinity waters likely reflect carbonate dissolution as a result of organic matter decomposition. Together, these data highlight the important role that inlets play on shallow-water carbonate chemistry dynamics within southeast Florida waters and underscore the degree to which engineered freshwater systems can contribute to coastal acidification on localized scales.

Keywords: ocean acidification, inlet, Port Everglades, Port of Miami, coral reef, SEFCRI

INTRODUCTION

Roughly 25% of anthropogenic carbon dioxide production is absorbed by seawater on an annual basis (Le Quéré et al., 2018), contributing to a global decline in pH known as ocean acidification or OA (Bates et al., 2014). This trend has important implications for the biology of marine organisms and has the potential to lead to large-scale shifts in ecosystem structure and function (Fabry et al., 2008; Enochs et al., 2015).

While patterns in OA are clear in the open ocean, data from near-shore and shallow-water environments are comparatively more complex (Hofmann et al., 2011). Smaller water volumes coupled with the biological activity of benthic communities can lead to alteration of seawater carbonate chemistry via respiration and photosynthesis, as well as calcification and dissolution. The effects of these processes can be further exacerbated by restricted flow and long residence times. Temporal variation in biological processes, such as diel fluctuations in photosynthesis and light-enhanced calcification alter seawater pH (Price et al., 2012). Seasonal variation in these biological processes can also manifest in the overlying waters (Shaw and McNeil, 2014). Additionally, comparatively brief storm events (Manzello et al., 2013) and upwelling (Manzello, 2010) impact and further obscure long-term trends in shallow-water acidification.

Natural variation in benthic community structure, across spatial scales ranging several orders of magnitude (cm to km), has been closely tied to changes in carbonate parameters. For example, various microhabitats within a reef environment such as filamentous algal gardens may locally elevate pH (Gagliano et al., 2010). Over larger scales (∼30 m), pH has been found to vary between reef zones, distance from shore, and depth within the same reef structure (Silbiger et al., 2014). Still larger-scale variation in the distribution of reef and seagrass habitats can lead to regional and shelf-scale variability on the order of 10's of kilometers (Manzello et al., 2012).

Abiotic processes may also influence seawater carbonate chemistry in shallow-water environments. Volcanic gas vents can locally enhance CO_2 concentration (Fabricius et al., 2011) and submarine freshwater seeps (Ojos; Crook et al., 2011) have been shown to lower seawater pH. Upwelling of deep CO_2-rich waters can drive periodic regional acidification (Feely et al., 2008; Manzello, 2010). Finally, freshwater systems can strongly impact the carbonate chemistry of adjacent marine ecosystems, either directly due to their export of inorganic carbon, or indirectly via perturbations (e.g., nutrients, organic carbon) that influence carbonate-chemistry-altering biota (Aufdenkampe et al., 2011; Duarte et al., 2013).

While a global rises in atmospheric CO_2 is an important driver of OA, it is not the only anthropogenic process contributing to coastal acidification (Duarte et al., 2013). The impact of human activities on both riverine and groundwater systems can lead to downstream effects for estuarine and coastal ecosystems. Eutrophication, for example, can lead to more rapid shifts in carbonate chemistry than global OA processes (Duarte et al., 2013). Algal blooms as the result of nutrient pollution can potentially offset the influences of OA (Borges and Gypens, 2010) but subsequent microbial breakdown of organic matter can lead to elevated CO_2 and hypoxia via increased respiration (Cai et al., 2011; Wallace et al., 2014). Highly eutrophied waters can therefore periodically experience pH values expected to occur at advanced states of global OA (Wallace et al., 2014), and given that their CO_2 buffering capacity is already compromised, may be more susceptible to future OA stress (Cai et al., 2011). In addition to eutrophication, agricultural practices and mining have been found to influence carbonate chemistry (Brake et al., 2001; Raymond and Cole, 2003; Oh and Raymond, 2006; Barnes and Raymond, 2009). Ultimately, urbanized watersheds have also been found to contribute twice as much DIC as agricultural areas and nearly eight times as much as those that are naturally forested, owing to elevated CO_2 production, along with increased weathering and organic matter contributions from septic and sewer sources (Barnes and Raymond, 2009). Together, these processes demonstrate the close relationship between human activity and the localized perturbation of carbonate chemistry.

The southeast Florida continental reef tract extends from south Miami (25°34′), ∼125 km north to West Palm Beach (26°43′) and is situated in close proximity to dense urban populations, with a heavily engineered system of canals and waterways (Banks et al., 2008). This high-latitude reef system is no longer actively accreting, but exist as a series of three parallel ridges which ceased upward growth between 3,700 and 8,000 years ago (Banks et al., 2007). Acroporid corals, important reef-builders in the Caribbean, were common as far north as Palm Beach County up until 6,000 years ago (Lighty et al., 1978). The range of these thermally sensitive species contracted south of Miami thereafter, likely due to climatic cooling at this time (Precht and Aronson, 2004). Less thermally sensitive species of coral continued to accrete on the middle reef until 3,700 years ago (Banks et al., 2007). It is still unclear what led to the termination of reef growth at this time; it has been suggested that seasonal cold fronts, elevated turbidity associated with flooding of the Florida shelf, and/or sea-level rise may have led to the cessation of accretion (Lighty et al., 1978; Banks et al., 2007). Hard bottom remains mostly uncolonized, though benthic communities are composed primarily of macroalgae, soft corals, and sponges (Moyer et al., 2003; Banks et al., 2008). Overall coral cover is low (<6%), comprised primarily of small colonies, that are depauperate in nature (27 species) compared with the Florida Keys and wider Caribbean (Goldberg, 1973; Moyer et al., 2003).

Three main navigational inlets, man-made marine passageways, influence the area from Miami to Ft. Lauderdale. The Port of Miami Inlet in the southern part of the region connects Biscayne Bay to the open ocean and is highly trafficked by large commercial vessels as well as recreational boat traffics (**Figure 1**). Baker's Haulover Inlet is located ∼15 km north and provides passage strictly for small vessels through the northern part of Biscayne Bay. Finally, the Port Everglades Inlet is located off of Ft. Lauderdale, ∼21 km further north. Like the Port of Miami, Port Everglades accommodates large commercial shipping vessels.

There is a long history of these inlets influencing the adjacent ocean water, reefs, and corals. For instance, skeletal records from massive corals in the region reveal a 30 year period of low extension, high density growth from 1940 to 1970, which correlates with canal construction and increased freshwater output (Banks et al., 2008). More recently (late 2013–early 2015), dredging activity, conducted to enlarge the Port of Miami for Panamax ships, was associated with large turbidity plumes (127–228 km^2) that encompassed ∼11 km^2 of coral habitat in the surrounding waters (Barnes et al., 2015; Miller et al., 2016).

Despite these anthropogenic stressors, southeast Florida coral reefs remain highly utilized for fishing and diving. In a year spanning 2000–2001, they generated 2.1 and 1.3 billion dollars in sales in Broward and Miami-Dade counties, respectively (Johns et al., 2003). As such, these coral reefs represent economically valuable ecosystems, closely associated with dense urban development and heavily engineered waterways. For these reasons, they have been specially targeted for monitoring and management through the Southeast Florida Coral Reef Initiative (SEFCRI). The goal of this study is to describe the temporal and spatial variability of carbonate chemistry of this region, both as a present-day baseline for future monitoring efforts, as well as a means of preliminarily investigating the magnitude of localized anthropogenic acidification.

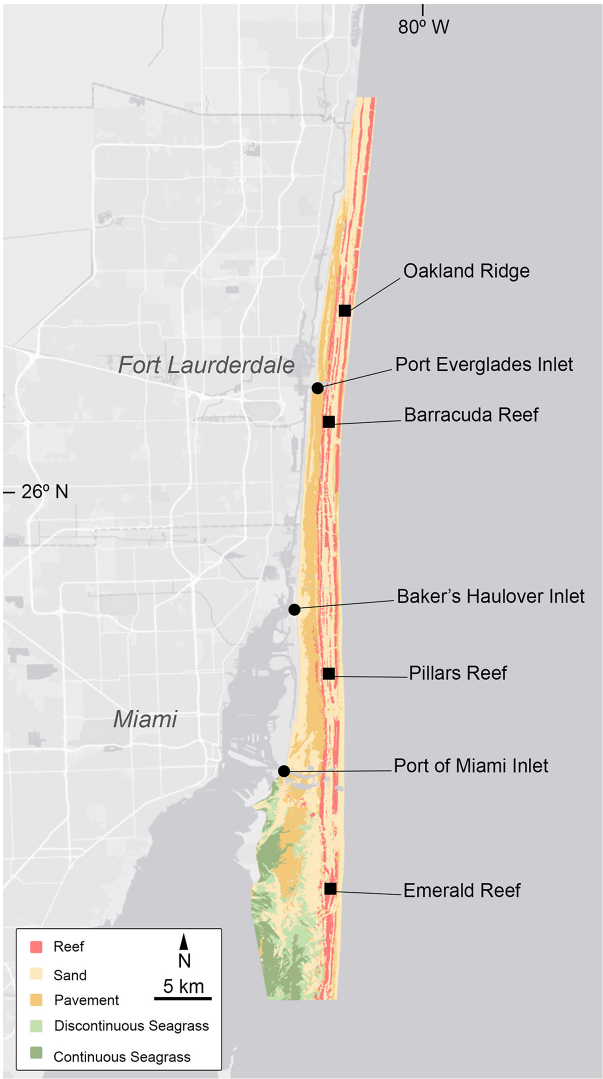

FIGURE 1 | Site map showing the four reef (squares) and three inlets (circles) sampling sites. Colors reflect the dominant benthic habitat type. GIS data obtained from Florida Fish and Wildlife Research Institute (FWRI). http://research.myfwc.com.

MATERIALS AND METHODS

Four reefs (Oakland Ridge, Barracuda, Pillars, and Emerald) and three inlets (Port Everglades, Bakers Haulover, and Port of Miami) were selected, spanning Miami-Dade and Broward Counties (**Figure 1**). Three replicate sampling sites were selected per reef, while a single sampling location was selected per inlet. Seawater samples were collected at each site on a bi-monthly basis from May 2014 to September 2015. Southeast Florida experiences a warm wet season from late May to October, and a cooler dry season from late October to early May. For analysis, data were binned by season and depth. All were collected between the hours of 8:11 and 14:31 and those collected in the vicinity of inlets were timed to occur during outgoing tides, though tidal range in the region is less than a meter.

Water samples were collected from the surface (~1 m depth) and immediately above the benthos (10.3–17.6 m depth, except Baker's Haulover) using a rosette sampler (ECO 55, Seabird). Temperature was recorded at each depth using a CTD (SBE 19V2, Seabird). Turbidity (NTU) was measured at the time of water collection using 90 degree infrared backscatter (Turner Designs). Once collected, water samples were transferred to borosilicate glass jars while minimizing turbulent water movement, bubbles, and gas exchange. Samples were fixed using 200 μL of $HgCl_2$, sealed using Apiezon grease and a ground glass stopper. Salinity was measured using a densitometer (DMA 5000M, Anton Paar). Total alkalinity (TA) was determined using automated Gran titration using an AS-ALK2 (Apollo SciTech). Dissolved inorganic carbon (DIC) was measured using an AS-C3 (Apollo SciTech) and a LI-7000 non-dispersive infrared CO_2 analyzer (LI-COR). Both TA and DIC values were measured in duplicate and corrected using certified reference materials following recommendations in Dickson et al. (2007). Aragonite saturation state ($\Omega_{Arag.}$), pH (Total scale), and the partial pressure of CO_2 (pCO_2) were calculated with CO2SYS (Lewis and Wallace, 1998) using the dissociation constants of Mehrbach et al. (1973) as refit by Dickson and Millero (1987) and Dickson (1990).

Water samples were reserved for nutrient analysis at the time of collection. Total Kjeldahl nitrogen (TKN) and total phosphorous (TP), were determined by semi-automated colorimetry (Methods 351.2 rev. 2, 365.1 rev. 2; EPA, 1993a,b TKN and TP, respectively). Chlorophyll-*a* was determined through fluorescence (Method 445.0 rev. 1.2, EPA, 1997). Analyses of TP, TKN and Chlorophyll-*a* were performed by the Florida Department of Environmental Protection (FDEP, Tallahassee, Florida).

Normalization of TA and DIC to a constant salinity (35) followed the recommendations of Friis et al. (2003) for normalization to a non-zero end member, which were determined using linear regression of sample data. Temperature, salinity, and carbonate chemistry data at each site were analyzed for normality and homoscedasticity using Shapiro-Wilk and Levene's tests, respectively. Data which did not conform to the assumptions of a parametric analysis were analyzed using a Kruskal-Wallis test, while all others were analyzed using a one way ANOVA, with unique combinations of season and depth as factors (e.g., dry shallow, dry deep, wet shallow, wet deep). Data were pooled across sites in order to compare conditions present at reefs vs. inlets. Non-parametric Wilcox signed-rank tests were performed to determine the significance of these differences. All statistical analyses were performed using R and R Studio (R Team, 2008; RStudio Team, 2015). All data are publicly available through NOAA's National Centers for Environmental Information (NCEI, https://www.nodc.noaa.gov/archivesearch/, accession 0185741).

RESULTS

Reef Water Chemistry

Averaged across depths and sites, temperature was higher in the wet 28.7 ± 1.26°C (mean ± SD) vs. the dry season 25.1 ± 1.33°C (**Table 1**; **Table S1**; **Figure 2**). No significant seasonal fluctuations

TABLE 1 | Environmental conditions and sample sizes at four reef and three inlet sites off of southeast Florida.

	Sample size		Depth (m)		Temperature (°C)		Salinity		Turbidity (NTU)	
	Wet	**Dry**	**Wet**	**Dry**	**Wet**	**Dry**	**Wet**	**Dry**	**Wet**	**Dry**
OAKLAND RIDGE										
Shallow	15	9	1.1	1.5	28.6 (1.35)	24.9 (0.53)	35.1 (1.43)	36.3 (0.16)	1.09 (1.054)	0.72 (0.445)
Deep	15	9	17.6	16.9	28.6 (1.32)	24.8 (0.71)	35.8 (0.80)	36.3 (0.18)	0.53 (0.045)	0.72 (0.333)
BARRACUDA REEF										
Shallow	15	9	1.1	1.3	28.8 (1.37)	24.9 (0.58)	35.3 (1.21)	36.3 (0.15)	1.12 (0.855)	1.34 (1.255)
Deep	14	9	10.3	10.7	28.8 (1.34)	24.8 (0.47)	35.5 (1.11)	36.3 (0.14)	0.60 (0.081)	0.88 (0.521)
PILLARS REEF										
Shallow	15	9	1	1.1	28.9 (1.25)	25.2 (0.56)	35.4 (1.44)	36.0 (0.31)	1.18 (0.754)	1.57 (0.978)
Deep	15	9	11.6	13.2	28.7 (1.32)	25.8 (3.43)	35.6 (1.25)	36.2 (0.26)	0.97 (0.712)	1.43 (0.784)
EMERALD REEF										
Shallow	15	9	1	1.2	28.8 (1.28)	25.3 (0.75)	35.4 (1.23)	36.3 (0.17)	1.57 (1.555)	2.95 (4.869)
Deep	15	9	12.8	13.8	28.6 (1.08)	25.2 (0.82)	35.7 (1.07)	36.3 (0.16)	1.06 (1.345)	0.73 (0.182)
PORT EVERGLADES INLET										
Shallow	5	3	1	1.3	29.5 (1.44)	24.8 (1.26)	32.3 (5.54)	34.8 (0.13)	2.25 (0.706)	2.77 (0.87)
Deep	4	3	13.3	13.1	29.5 (1.24)	24.7 (1.03)	34.7 (2.16)	35.5 (0.36)	1.35 (0.728)	2.21 (0.967)
BAKER'S HAULOVER INLET										
Shallow	5	3	1.5	1	29.7 (1.37)	24.7 (1.10)	34.6 (2.66)	35.1 (0.78)	2.16 (0.862)	3.97 (1.524)
Deep	0	0								
PORT OF MIAMI INLET										
Shallow	4	3	1	2.1	29.7 (1.39)	24.5 (1.53)	35.4 (2.47)	35.5 (0.26)	3.75 (1.724)	10.84 (4.119)
Deep	2	3	13.6	13.5	30.2 (1.25)	24.5 (1.53)	35.8 (4.40)	35.5 (0.22)	9.82 (9.634)	9.54 (2.523)

Values are means (±Std. Dev.) and are arranged according to season (Wet and Dry) as well as for two depth bins (Shallow and Deep).

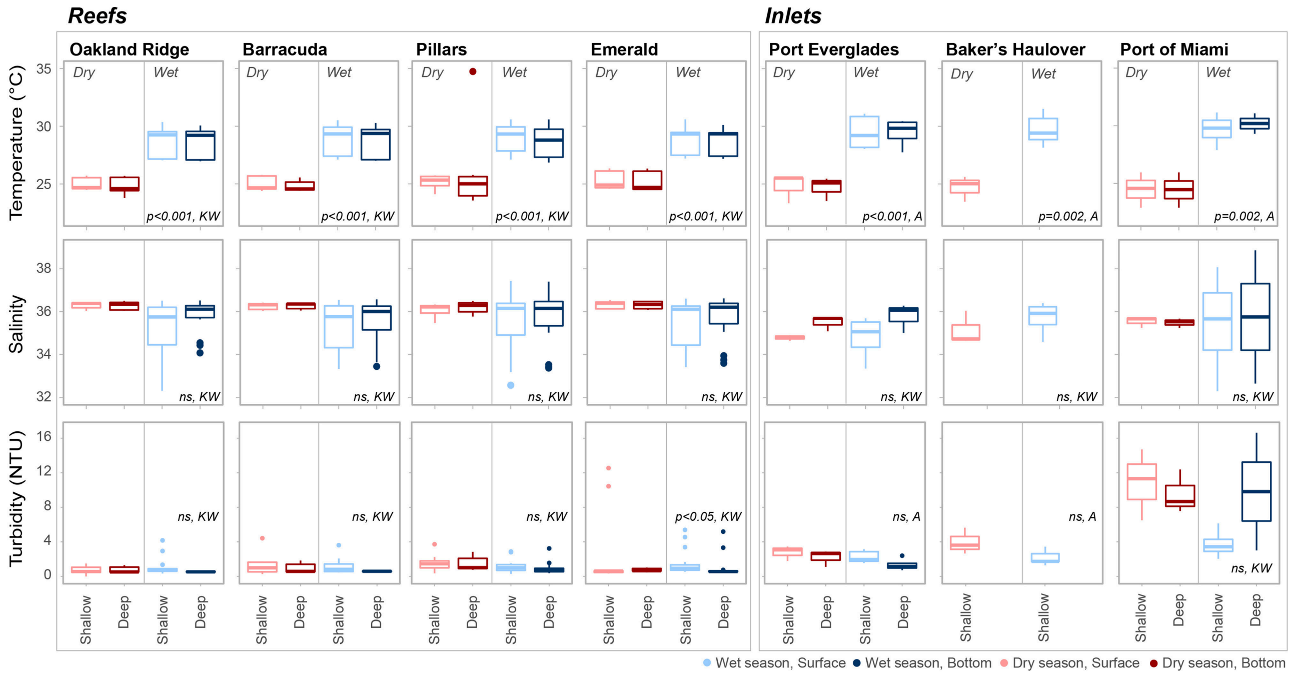

FIGURE 2 | Temperature (°C), salinity, and turbidity (NTU) at each of four reef and three inlet sampling sites. Data are divided into dry (red) and wet season (blue). Darker colors represent samples taken above the benthos while lighter colors represent samples taken at the surface. *P* values are given for significant differences as determined by ANOVA (A) or nonparametric Kruskal-Wallis (KW) tests. Non-significant ($p > 0.05$) are marked ns.

in salinity were detected within reef sites (**Table S1**; **Figure 2**), though averaged across all reef sites salinity was higher in the dry 36.25 ± 0.209, vs. the more variable wet season (35.48 ± 1.192, **Table 1**; **Figure 2**). Significant seasonal fluctuation in turbidity was only detected at the southern-most reef site (Emerald), which displayed extreme high-turbidity outliers that were present to a lesser extent at other reef sites (**Table 1**; **Table S1**; **Figure 2**).

There were significant seasonal fluctuations in temperature, TA, and DIC at reef sites (**Table 2**; **Table S2**; **Figures 3**, **4**). No clear trends were distinguishable between samples collected at the surface and those collected at depth. On average, the dry season was characterized by higher TA (2,384.3 ± 9.24 vs. 2,368.89 μmol kg^{-1}) and DIC (2,059.2 ± 18.05 vs. 2,041.6 ± 19.71 μmol kg^{-1}). TA and DIC were both positively correlated with salinity at reef sites, with zero salinity end members of 2,137.1 μmol kg^{-1} and 1,864.8 μmol kg^{-1}, respectively (**Figure 5**). The fit of these relationships, however, are low ($R^2 = 0.215$ and 0.058, TA and DIC, respectively) and predicted end members should therefore be treated with a degree of caution.

Seasonal variability of calculated carbonate chemistry parameters was more nuanced than that of TA and DIC (**Table 2**; **Table S2**; **Figure 6**). All reefs with the exception of Pillars had higher pCO$_2$ in the wet season, corresponding to a lower pH (**Table 2**; **Table S2**; **Figure 6**). Counterintuitively, the acidified wet-season waters at Oakland and Barracuda (as well as Pillars) had high $\Omega_{\text{Arag.}}$, which may be an effect of the elevated temperature (**Tables 1**, **2**; **Tables S1**, **S2**; **Figure 6**). Significant differences in nutrients across depths and seasons were only observed at Oakland, Barracuda, and Pillars reefs, which had higher TP in the dry season (**Tables S3, S4**; **Figure S2**).

Salinity normalized TA-DIC plots yielded significant linear relationships at Oakland and Pillars (**Figure 7**). Relationships were not significant at Barracuda and Emerald, which had a small range of salinity normalized DIC (nDIC) than the aforementioned reef sites. The slope of the nTA/nDIC line, was only slightly higher at Pillars (0.547) than Oakland Ridge (0.447).

Inlet Fluctuations

As with reef sites, temperature was significantly higher in the wet season and no clear stratification with depth was detected (**Table 1**; **Table S1**; **Figure 2**) The wet season resulted in more variable salinity at inlet sites (**Table 1**; **Figures 2**, **5**), though no significant differences were detected across depths and seasons (**Table S1**; **Figure 2**). While intra-site seasonal variation in turbidity was not significant, Port of Miami had much higher, and more variable turbidity compared with Port Everglades or Baker's Haulover (**Figure 2**).

Both TA ($R^2 = 0.665$, $P < 0.001$) and DIC ($R^2 = 0.678$, $P < 0.001$) were strongly negatively correlated with salinity at inlet sites, reflecting contributions from terrestrial freshwater sources (**Figure 5**). Across all considered inlets, the extremes in salinity (**Table 1**; **Figure 2**) experienced during the wet seasons were accompanied by the most extreme TA and DIC (**Table 2**; **Figures 3–5**). While there was a general trend of higher TA during the dry season, significant differences were only detected at Port Everglades (**Table S2**; **Figure 3**). The same site revealed strong depth stratification in TA, and to a lesser extent DIC, with higher values observed in surface waters (**Table 2**; **Figures 4**, **5**). These surface waters were generally less saline than those from the deep, though no significant differences were detected (**Table 1**; **Table S1**; **Figure 2**). No significant differences in DIC were detected between depth/season groupings at any of the inlet sites (**Table S2**).

Unlike many of the reef sites, which displayed strong seasonal fluctuations in mean pCO$_2$, pH, and $\Omega_{\text{Arag.}}$, no significant trends were detected in the calculated carbonate chemistry parameters (**Table S2**; **Figure 6**). This was largely due to much higher variability (**Table 2**; **Figure 6**) displayed in these parameters at the inlet sites. Extreme highs in pCO$_2$, accompanied by low pH, were especially apparent in surface waters during the wet season in Port Everglades (**Figure 6**). No significant seasonal/depth patterns were observed in TKN, TP, or Chlorophyll-*a* at inlet sites (**Tables S3, S4**; **Figure S2**).

Significant linear relationships between salinity-normalized nTA and nDIC were observed at the two larger Inlets (Port Everglades and Port of Miami) but not at Baker's Haulover (**Figure 7**). This may have been a function of sample size, as Baker's Haulover only included surface samples. Port of Miami had the highest slope (0.774) of all measured sites including reefs, while Port Everglades had the lowest (0.353).

Inlet vs. Reef Sites

Salinity was significantly lower ($P < 0.0001$, W = 1,867.5) at inlet (34.7 ± 2.67, mean ± SD) vs. reef sites (35.8 ± 1.02) but there was no significant difference detected in temperature ($P = 0.6167$). All carbonate chemistry parameters were found to be significantly different ($P < 0.0001$, $W_{\text{TA}} = 5{,}317$, $W_{\text{DIC}} = 5{,}424$, $W_{\text{pH}} = 5{,}376$, $W_{\text{pCO2}} = 1{,}436$, $W_{\Omega\text{Arag.}} = 1{,}104.5$) between site types. Both TA (2,425.6 ± 76.97 vs. 2,474.7 ± 14.44 μmol kg^{-1}, inlets vs. reefs, respectively) and DIC (2,137.0 ± 107.10 vs. 2,048.3 ± 20.89 μmol kg^{-1}) were higher at inlets vs. reef sites. These contributed to an elevated pCO$_2$, lower pH, and depressed $\Omega_{\text{Arag.}}$ at inlet sites vs. reefs. TKN ($P < 0.0001$, W = 5,241), TP ($P < 0.0001$, W = 5,735), and Chlorophyll-*a* ($P < 0.0001$, W = 6,158) were all higher at inlet vs. reef sites (6.84 ± 4.34 vs. 4.00 ± 1.90 μM TKN; 0.34 ± 0.14 vs. 0.25 ± 0.19 μM TP; 1.33 ± 0.65 vs. 0.42 ± 0.28 μg L^{-1} Chlorophyll-*a*).

DISCUSSION

Carbonate chemistry parameters at reef sites and seasonal variation thereof are consistent with those reported from off-shore reef sites in the Florida Keys (Manzello et al., 2012). Seasonal variability in pCO$_2$, however, was in line with that reported at offshore stations (Bermuda, Bates, 2007) and it is possible that fluctuations observed on reefs were due to large-scale open ocean processes. Benthic marine organisms and water chemistry are strongly interdependent and spatial variation in community composition can impact the carbonate chemistry of associated waters. For example, regions with high seagrass biomass such as inshore patch reefs of the Upper Florida Keys may exhibit net CO$_2$ sequestration, locally elevating saturation states and providing refugia for calcifying organisms such as corals (Manzello et al., 2012). Despite the prevalence of seagrass within nearby Biscayne Bay (**Figure 1**, Lirman and Cropper,

TABLE 2 | Environmental conditions and sample sizes at four reef and three inlet sites off of southeast Florida.

	Sample size		TA (μmol kg^{-1})		nTA (μmol kg^{-1})		DIC (μmol kg^{-1})		nDIC (μmol kg^{-1})		pCO$_2$ (μatm)		pH (Total)		$\Omega_{Arag.}$	
	Wet	**Dry**	**Wet**	**Dry**	**Wet**	**Dry**	**Wet**	**Dry**	**Wet**	**Dry**	**Wet**	**Dry**	**Wet**	**Dry**	**Wet**	**Dry**
OAKLAND RIDGE																
Shallow	15	9	2,371.1 (16.91)	2,384.4 (8.13)	2,370.3 (15.16)	2,375.6 (8.36)	2,041.7 (30.21)	2,053.7 (12.41)	2,041.2 (30.60)	2,047.0 (12.33)	429 (29.9)	383 (17.2)	8.03 (0.023)	8.07 (0.015)	3.81 (0.195)	3.70 (0.070)
Deep	15	9	2,376.4 (6.05)	2,382.8 (4.14)	2,371.0 (3.65)	2,374.2 (4.57)	2,042.5 (6.60)	2,056.6 (13.95)	2,038.6 (7.07)	2,049.9 (13.31)	428 (20.9)	388 (19.5)	8.03 (0.017)	8.06 (0.017)	3.82 (0.071)	3.64 (0.124)
BARRACUDA REEF																
Shallow	15	9	2,368.6 (11.57)	2,382.9 (8.35)	2,366.8 (8.92)	2,374.4 (8.30)	2,043.0 (17.61)	2,056.4 (10.61)	2,041.3 (13.90)	2,049.7 (10.05)	441 (39.6)	390 (14.2)	8.02 (0.033)	8.06 (0.013)	3.77 (0.215)	3.65 (0.095)
Deep	14	9	2,372.2 (10.38)	2,380.6 (8.96)	2,368.9 (8.50)	2,372.1 (9.07)	2,040.9 (7.82)	2,058.4 (13.42)	2,038.3 (4.67)	2,051.6 (13.37)	431 (29.5)	395 (20.9)	8.02 (0.025)	8.06 (0.018)	3.81 (0.150)	3.6 (0.110)
PILLARS REEF																
Shallow	15	9	2,363 (13.78)	2,396.8 (13.71)	2,360.5 (15.10)	2,389.3 (13.59)	2,037.3 (21.93)	2,084.7 (24.95)	2,035.3 (22.81)	2,078.4 (24.96)	443 (49.1)	425 (38.6)	8.01 (0.041)	8.03 (0.030)	3.76 (0.196)	3.53 (0.164)
Deep	15	9	2,363.9 (18.01)	2,385.8 (6.14)	2,360.0 (18.75)	2,377.4 (6.39)	2,033.0 (24.49)	2,063.9 (11.96)	2,030.1 (23.99)	2,057.3 (12.32)	430 (41.8)	418 (79.9)	8.02 (0.035)	8.04 (0.061)	3.79 (0.173)	3.62 (0.066)
EMERALD REEF																
Shallow	15	9	2,365.2 (17.23)	2,380.3 (5.22)	2,362.8 (12.16)	2,371.3 (4.50)	2,044.0 (16.89)	2,049.7 (18.47)	2,042.4 (17.70)	2,042.8 (17.16)	453 (71.4)	388 (24.0)	8.01 (0.053)	8.06 (0.021)	3.72 (0.263)	3.7 (0.161)
Deep	15	9	2,370.9 (10.65)	2,380.5 (6.28)	2,366.5 (8.76)	2,371.8 (5.52)	2,050.5 (19.83)	2,050.5 (12.31)	2,047.1 (20.60)	2,043.8 (11.22)	455 (63.8)	387 (13.7)	8.01 (0.048)	8.06 (0.013)	3.69 (0.250)	3.68 (0.115)
PORT EVERGLADES INLET																
Shallow	5	3	2,498.9 (121.72)	2,485.7 (14.44)	2,436.0 (27.67)	2,480.9 (13.29)	2,250.6 (173.21)	2,146.9 (138.27)	2,163.4 (48.66)	2,139.8 (138.26)	692 (184.9)	428 (189.3)	7.89 (0.063)	8.07 (0.180)	3.12 (0.404)	3.92 (1.322)
Deep	4	3	2,391.4 (25.38)	2,428.1 (22.93)	2,383.3 (36.67)	2,439.6 (16.62)	2,096.7 (55.48)	2,135.1 (31.05)	2,085.7 (61.48)	2,151.4 (19.35)	530 (98.5)	461 (49.5)	7.96 (0.064)	8.01 (0.039)	3.49 (0.352)	3.36 (0.133)
BAKER'S HAULOVER INLET																
Shallow	5	3	2,393.1 (94.76)	2,437.0 (26.51)	2,383.2 (48.85)	2,440.3 (13.32)	2,111.9 (107.43)	2,146.2 (58.07)	2,096.7 (58.11)	2,151.1 (32.03)	584 (180.0)	470 (91.1)	7.93 (0.107)	8.01 (0.068)	3.37 (0.536)	3.36 (0.315)
Deep	0	0														
PORT OF MIAMI INLET																
Shallow	4	3	2,367.8 (76.45)	2,433.4 (32.06)	2,378.7 (32.37)	2,445.7 (36.47)	2,068.5 (117.57)	2,142.9 (24.61)	2,084.3 (53.31)	2,160.5 (22.63)	527 (123.7)	469 (77.3)	7.96 (0.072)	8.01 (0.062)	3.49 (0.348)	3.34 (0.339)
Deep	2	3	2,373.8 (113.39)	2,433.4 (29.87)	2,392.5 (5.83)	2,444.2 (33.90)	2,089.8 (160.15)	2,142.7 (24.85)	2,115.8 (12.10)	2,158.1 (25.36)	576 (91.3)	466 (65.3)	7.92 (0.025)	8.01 (0.052)	3.32 (0.259)	3.34 (0.289)

Values are means (±Std. Dev.) and are arranged according to season (Wet and Dry) as well as for two depth bins (Shallow and Deep).

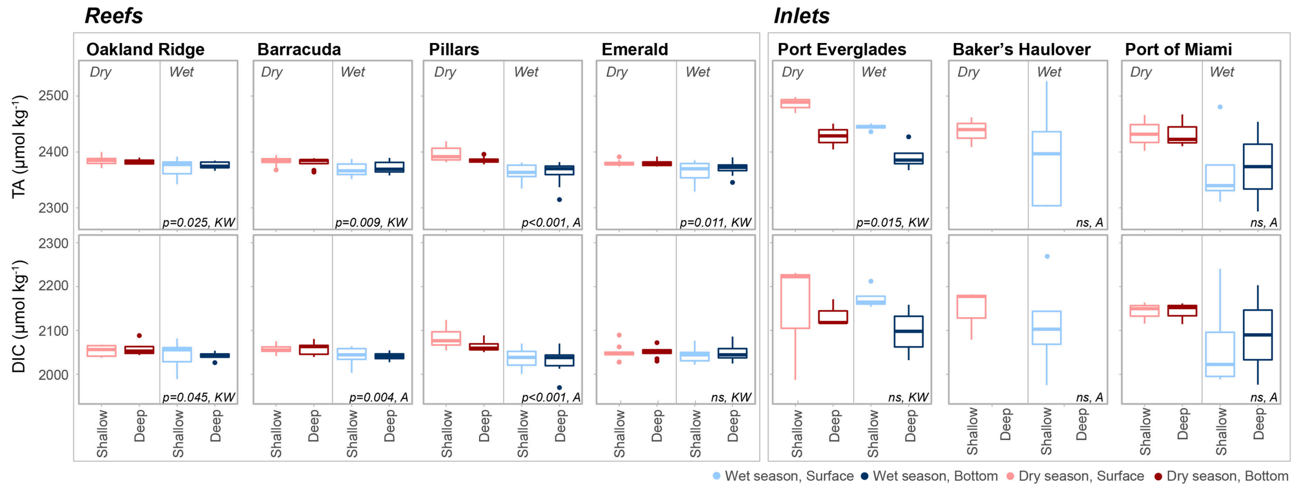

FIGURE 3 | Total alkalinity (TA, µmol kg^{-1}) and dissolved inorganic carbon (DIC, µmol kg^{-1}) at each of four reef and three inlet sampling sites. Data are divided into dry (red) and wet season (blue). Darker colors represent samples taken above the benthos while lighter colors represent samples taken at the surface. *P* values are given for significant differences as determined by ANOVA (A) or nonparametric Kruskal-Wallis (KW) tests. Non-significant ($p > 0.05$) are marked ns. An outlier surface sample (2,716.5, 2,557.8 µmol kg^{-1}, TA and DIC, respectively) from Port Everglades collected in September 2014 is not shown in order to be better visualize the dataset.

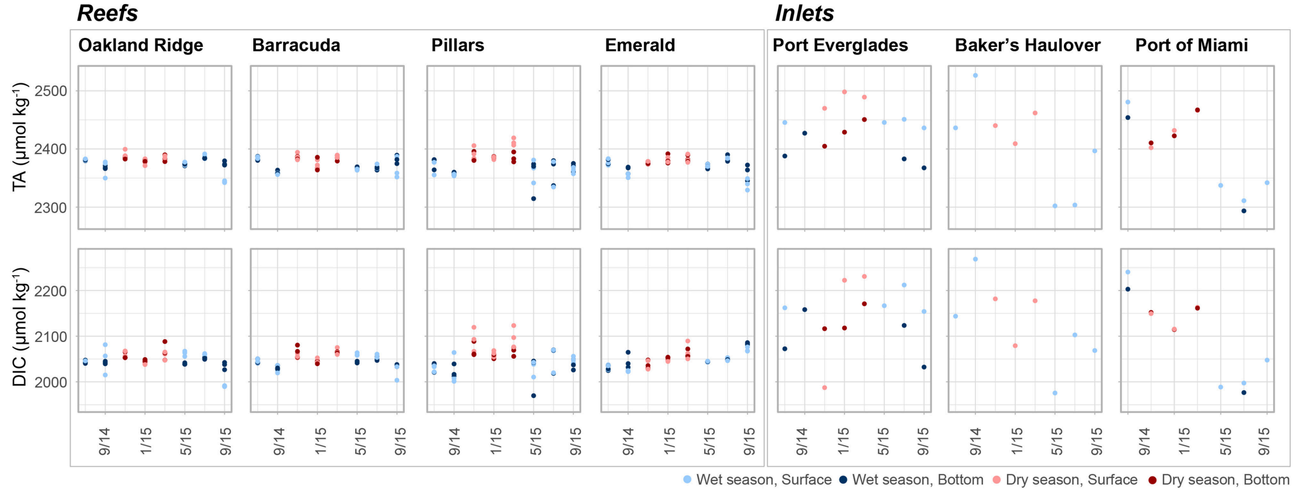

FIGURE 4 | Total alkalinity (TA, µmol kg^{-1}) and dissolved inorganic carbon (DIC, µmol kg^{-1}) at four reef and three inlet sites. Data represent each sampling trip, with blue and red points denoting wet and dry season, respectively. Darker colors represent samples taken above the benthos while lighter colors represent samples taken at the surface. An outlier surface sample (2,716.5, 2,557.8 µmol kg^{-1}, TA and DIC, respectively) from Port Everglades collected in September 2014 is not shown in order to be better visualize the dataset.

2003), Emerald Reef did not appear to demonstrate the OA-refugium characteristics of inshore Upper Keys reefs (Manzello et al., 2012). The slope (when significant) of nTA/nDIC plots of water from reef sites ranged from 0.447 to 0.547 (**Figure 7**), reflecting the importance of calcification/dissolution at these sites relative to photosynthesis/respiration (Lantz et al., 2013). Relative to open ocean endmembers for TA in the nearby Florida Keys (2,377 µmol kg^{-1}, Cyronak et al., 2018) reefs were not strongly skewed toward net calcification or dissolution, though Pillars Reef does appear to favor calcification in the wet vs. dry season (**Figure 7**; **Table 2**). These slopes and the importance of calcification/dissolution are interesting considering the low coral cover and high benthic algae prevalence on reefs in this region (Moyer et al., 2003; Banks et al., 2008).

Within southeast Florida, inlets (especially Port of Miami and Port Everglades) act as acidification hotspots. There was a significant negative relationship between both DIC and TA with salinity, as DIC and TA were elevated at the inlets despite depressed salinity (**Figure 5**). The increase in DIC was disproportionately higher than the increase in TA, which led

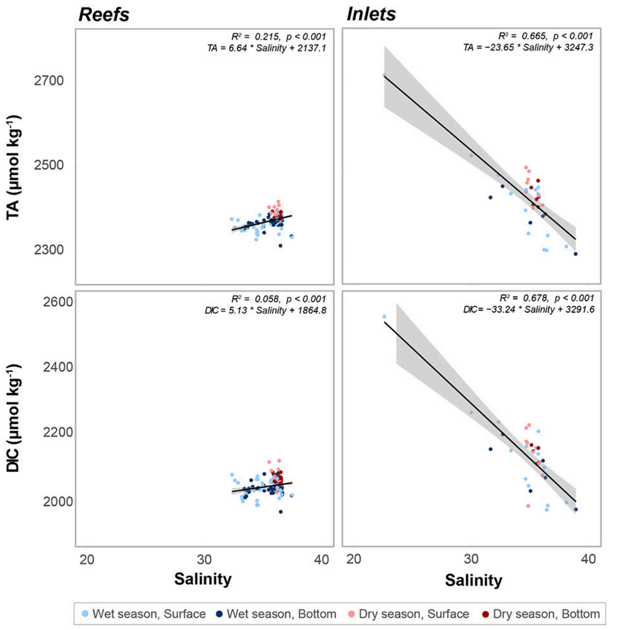

FIGURE 5 | Linear regression of total alkalinity (TA, µmol kg^{-1}) as a function of salinity at reef and inlet sites. Error bars in gray, R^2 and *p* values, as well as the equation for each fitted line given for each sampling site. Data are divided into dry (red) and wet season (blue). Darker colors represent samples taken above the benthos while lighter colors represent samples taken at the surface.

to the depressed pH at the inlets. This is shown by the greater slope in the regression of DIC with salinity when compared to TA (**Figure 5**). The negative relationship of these carbonate chemistry parameters with salinity stands out as anomalous when compared with other estuarine systems throughout the wider Atlantic and Caribbean, which demonstrate a clear positive correlation between TA and salinity (Cai et al., 2010). Even in river-dominated systems with the highest TA end members, values of roughly 2,400 µmol kg^{-1} (Mississippi River, Cai et al., 2010) have been reported, whereas here we calculate 3,247.3 µmol kg^{-1}. In this study, not only were low-salinity inlet samples high in TA and DIC relative to their high-salinity inlet counterparts, they represented extremes that exceeded values present on the more ocean-driven reefs.

Estuarine environments with high organic carbon respiration, such as salt marshes (Cai and Wang, 1998; Cai et al., 2000), mangrove habitats (Ho et al., 2017), or those with high plankton biomass (Borges and Frankignoulle, 1999) are known to export DIC. Some studies of estuarine systems have shown a break-down in the linearity of the TA/salinity relationship at low salinity (<2.5) and a steep rise over this range, but still a lower TA end member (e.g., Cai et al., 2004). Others have found a parabolic relationship, with an alkalinity peak at intermediate levels of salinity (Ho et al., 2017). Similar to data reported for inlets herein, spatial surveys of nearby Florida Bay, revealed high alkalinity, high DIC acidified waters correlated with lower salinity (Millero et al., 2001). Elevated levels of phosphate near the mangrove fringe of the Everglades indicated desorption during dissolution of $CaCO_3$ sediments, which was likely due to oxidation of abundant organic matter resulting in a rise in CO_2 and a decline in pH (Millero et al., 2001). These processes may also be contributing to localized acidification reported herein, as the inlets examined in this study are connected to Everglades waters, composed of carbonate sediments, and occupied by mangrove communities.

We note that the analysis of data from fixed-site time series (one per inlet) used here differs from the spatially distributed transects across ocean margins (Cai et al., 2010) or estuaries (Millero et al., 2001; Cai et al., 2004) even if those transects are repeated over time. Our data therefore represent a temporally dynamic system, with periodic low salinity fluxes correlated with high DIC, high TA water. This difference may help to explain the apparent incongruity of these data with some of the aforementioned studies because the continuum of salinity is not simply a function of steady mixing of fresh and ocean water, but rather the temporal variability in freshwater output and correlated alteration of carbonate chemistry. The relationships shown in **Figure 5** are therefore likely strongly influenced by extreme events and the explicit use of calculated end members should be done with care.

The origin of this variable high TA and DIC freshwater source (ground vs. surface) cannot be determined with absolute certainty within the scope of this study. While the carbonate-rich Biscayne Aquifer that covers both Miami-Dade and Broward counties is both surficial and highly porous (Back and Hanshaw, 1970; Fish and Stewart, 1991), development and extensive engineering projects have altered the natural water flow, contributing to accelerated clearance of storm water runoff, lowering the water table, and likely decreasing submarine discharge (Fish and Stewart, 1991). In support of this, Stalker et al. (2009) used geochemical tracers to determine the percent contribution of canals, precipitation, and groundwater to Biscayne Bay, which feeds both the Port of Miami and Baker's Haulover. They found that the greatest freshwater source was precipitation (53% and 55%, wet and dry season, respectively), followed by canals (37% and 40%) and lastly groundwater (10% and 5%). While these data do not reflect processes occurring at Port Everglades, given the presumably low TA and DIC of rain water and low contribution of groundwater, elevated TA and DIC tied to salinity fluxes could potentially be linked with input from eutrophied, organic-rich freshwater canals and rivers.

Prior studies have highlighted canals as the most important source of nutrients within Biscayne Bay (Caccia and Boyer, 2007). Those feeding more northern areas of the bay have characteristically low dissolved oxygen and nutrient signatures that reflect the highly urbanized nature of the surrounding land (Caccia and Boyer, 2005, 2007). Data on the impact of nutrients to the surrounding coastal waters and coral reefs of the SEFCRI region are limited though studies suggest that nearby reef environments off of Palm Beach County are influenced by nutrient enrichment from sewage and agricultural sources (Lapointe, 1997; Finkl and Krupa, 2003). We observed higher TKN, TP, and Chlorophyll-a at inlet sites vs. offshore reefs (**Table S3**; **Figure S2**), reflecting localized

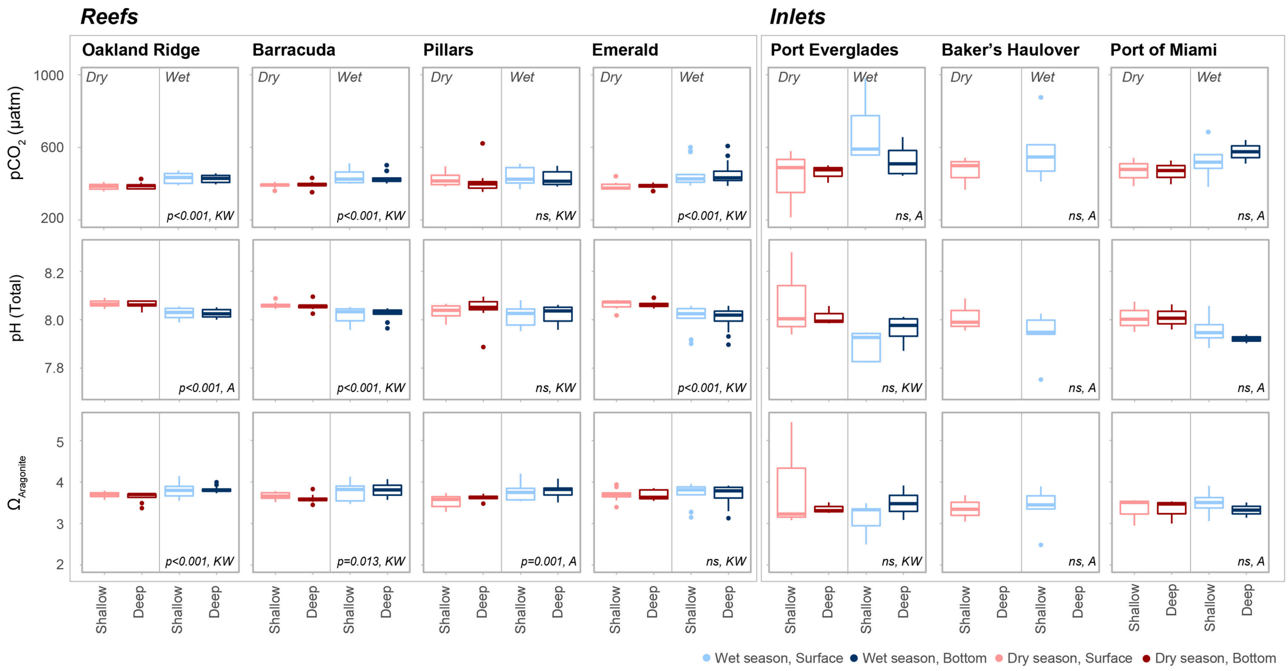

FIGURE 6 | The partial pressure of carbon dioxide (pCO_2, µatm), pH (Total scale), and aragonite saturation state ($\Omega_{Arag.}$) at each of four reef and three inlet sampling sites. Data are divided into dry (red) and wet season (blue). Darker colors represent samples taken above the benthos while lighter colors represent samples taken at the surface. *P* values are given for significant differences as determined by ANOVA (A) or nonparametric Kruskal-Wallis (KW) tests. Non-significant ($p > 0.05$) are marked ns.

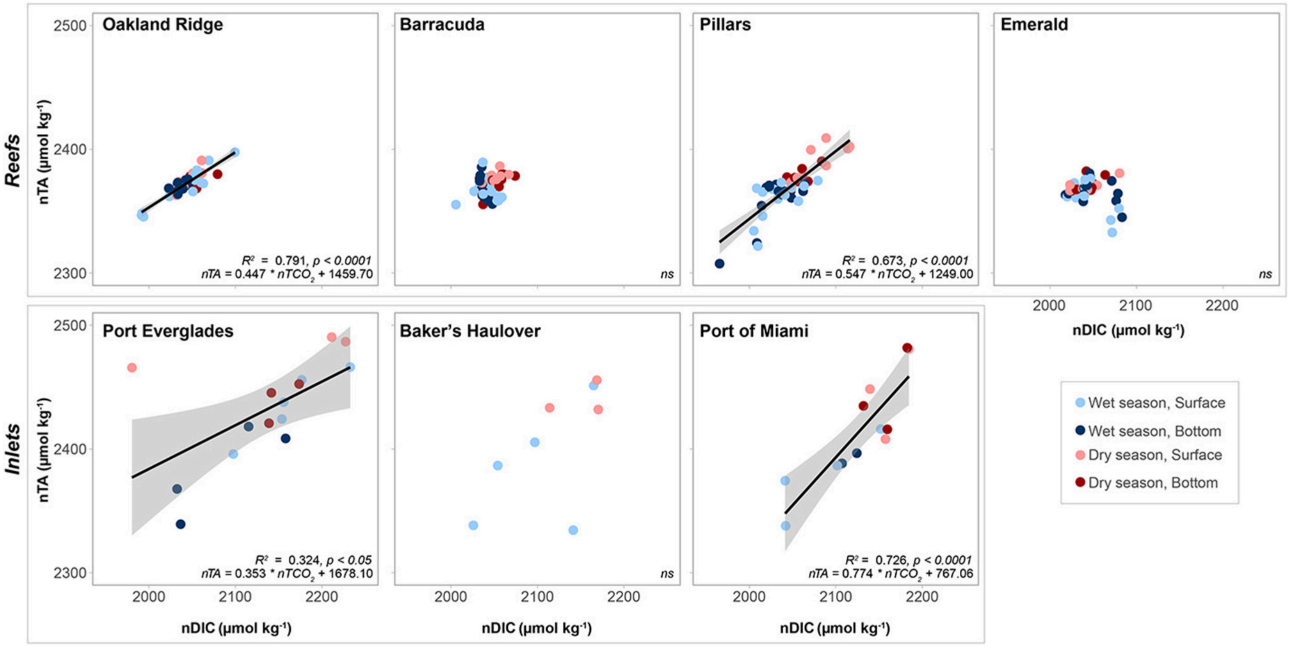

FIGURE 7 | Salinity normalized total alkalinity (nTA, µmol kg^{-1}) as a function of salinity normalized dissolved inorganic carbon (nDIC, µmol kg^{-1}).Lines represent linear regression, with error bars shown in gray. R^2 and *p* values, as well as the equation for each fitted line given for each sampling site where a significant relationship was observed. Non-significant ($p > 0.05$) are marked ns. Data are divided into dry (red) and wet season (blue) at each of four reef and three inlet sampling sites. Darker colors represent samples taken above the benthos while lighter colors represent samples taken at the surface.

eutrophication and elevated productivity. This enrichment was correlated with hotspots of coastal acidification and support the hypothesis that eutrophication can locally elevate pCO_2 (Cai et al., 2011; Wallace et al., 2014).

Coastal eutrophication should be considered when evaluating the present day and future impacts of OA on local carbonate chemistry. Curtailing nutrient pollution and organic matter enrichment could serve as a means for locally managing the large-scale impacts of global OA and should be incorporated into models which seek to determine the ecosystem outcomes of management strategies. Similarly, continued eutrophication or even dynamic fluctuations in nutrient output have the potential to impact carbonate chemistry monitoring efforts, and will render long-term trends due to OA more difficult to detect in coastal ecosystems. This is especially true in near-shore reef environments in close proximity to developed urban areas, such as those in southeast Florida, which are most heavily utilized by people.

Nutrients may also influence reef ecology more directly, via pathways outside of organic matter enrichment and localized acidification. Eutrophication can drive phase shifts from a state characterized by habitat-building corals to one dominated by less desirable macroalgae (McCook, 1999), further exacerbating the ecosystem-altering process of OA (Enochs et al., 2015). As previously noted, reefs in southeast Florida already exist in a state characterized by low coral cover and a high prevalence of benthic algae (Moyer et al., 2003). For this reason, they exist in a functionally compromised state and are potentially more prone to the multifarious and interwoven influences of eutrophication and acidification.

Other human activities have the potential to alter coastal water in the region. High turbidity was observed at the Port of Miami Inlet relative to all other collection sites and periodic spikes in turbidity were observed at Emerald Reef, which is located offshore of the inlet (S1). This elevated turbidity corresponds to a period of dredging conducted to expand the Port of Miami to be able to accommodate Panamax ships. From November 20, 2013 to March 16, 2016, roughly 4.39 million m^3 of sediment and rock was removed from the channel and deposited 2.4 km offshore (see **Figure S1** in Miller et al., 2016). The resulting sediment plumes were documented from satellites which reached nearby coral habitats (Barnes et al., 2015). During the same period, stretching into March of 2015, both TA and DIC were elevated at the Port of Miami compared to samples collected thereafter (**Figure 4**). The abrupt relative decline was not observed at any of the other inlet or reef sites. The pore waters of carbonate sediments, especially those high in organic matter may be high in DIC and TA due to metabolic dissolution (Andersson and Gledhill, 2013). This process can be oxygen-limited and processes which perturb and oxygenate sediment pore waters can therefore contribute to further organic matter decomposition and to greater dissolution (Andersson and Gledhill, 2013). Dredging activity may therefore act to release this high TA pore water into the above water column, as well as to further oxygenate previously buried sediments and organic matter, contributing to further dissolution. Additionally, higher water column turbidity resulting in lower light reaching the benthos, and greater metabolic stress due to direct sediment exposure may also lead to higher respiration and reduced photosynthesis, further contributing to elevated DIC (Manzello et al., 2013). Further dredging activities are planned for Port Everglades and it remains to be seen whether sediment disturbance will lead to alteration in seawater turbidity as well as carbonate chemistry parameters.

At present, inlet-driven acidification does not appear to be strongly impacting the carbonate chemistry of the nearby reef sites. While inlet carbonate chemistry was highly variable and strongly correlated with salinity, TA and DIC variation at reef sites was constrained to more subtle seasonal variation, reflecting a separation of processes driving the two site types. "Urban corals" (Heery et al., 2018) growing on anthropogenic hard substrates in the immediate vicinity of inlets are periodically experiencing acidification conditions predicted to occur in the future due to rising atmospheric CO_2. The physiology and genetics of these individuals may therefore provide insight into coral resilience to OA, though it is cautioned that dynamic pH fluctuations may result in different physiological responses than more-static conditions (Rivest et al., 2017; Enochs et al., 2018).

In conclusion, the seawater exiting the inlets of southeast Florida has highly variable carbonate chemistry that can include very low pH excursion. While reef environments revealed more characteristic seasonal fluctuations driven by biological processes, nearby inlets were periodic sources of low-salinity, high-CO_2 waters, and therefore potential sources of coastal acidification. Monitoring and management of carbonate chemistry parameters in tandem with nutrients is important going forward, along with further investigation into the degree to which inlets influence nearby reef ecosystems.

AUTHOR CONTRIBUTIONS

PRJ, SJS, and TPC collected water samples. All authors participated in analysis and manuscript preparation.

FUNDING

Field operations were funded by Florida's Department of Environmental Protection. NOAA's Coral Reef Conservation Program and Ocean Acidification Program provided funding for analysis of carbonate chemistry.

ACKNOWLEDGMENTS

We are grateful to J. Bishop, M. Doig, C. Featherstone, M. Gidley, R. Kotkowski, L. Valentino, B. Vandine, and M. Weekly for providing assistance with water collection. M. McDonald and K. Loggins provided important insights throughout manuscript preparation.

SUPPLEMENTARY MATERIAL

The Supplementary Material for this article can be found online at: https://www.frontiersin.org/articles/10.3389/fmars.2019.00160/full#supplementary-material

REFERENCES

Andersson, A. J., and Gledhill, D. (2013). Ocean acidification and coral reefs: effects on breakdown, dissolution, and net ecosystem calcification. *Ann. Rev. Mar. Sci.* 5, 321–348. doi: 10.1146/annurev-marine-121211-172241

Aufdenkampe, A. K., Mayorga, E., Raymond, P. A., Melack, J. M., Doney, S. C., Alin, S. R., et al. (2011). Riverine coupling of biogeochemical cycles between land, oceans, and atmosphere. *Front. Ecol. Environ.* 9, 53–60. doi: 10.1890/100014

Back, W., and Hanshaw, B. (1970). Comparison of chemical hydrogeology of the carbonate peninsulas of Florida and Yucatan. *J. Hydrol.* 10, 330–368. doi: 10.1016/0022-1694(70)90222-2

Banks, K. W., Riegl, B. M., Richards, V. P., Walker, B. K., Helmle, K. P., Jordan, L. K. B., et al. (2008). "The reef tract of continental Southeast Florida (Miami-Dade, Broward and Palm Beach Counties, USA)," in *Coral Reefs of the USA. Coral Reefs of the World*, Vol. 1, eds B. M. Riegl and R. E. Dodge (Dordrecht: Springer), 175–220.

Banks, K. W., Riegl, B. M., Shinn, E. A., Piller, W. E., and Dodge, R. E. (2007). Geomorphology of the Southeast Florida continental reef tract (Miami-Dade, Broward, and Palm Beach Counties, USA). *Coral Reefs* 26, 617–633. doi: 10.1007/s00338-007-0231-0

Barnes, B. B., Hu, C., Kovach, C., and Silverstein, R. N. (2015). Sediment plumes induced by the Port of Miami dredging: analysis and interpretation using Landsat and MODIS data. *Remote Sens. Environ.* 170, 328–339. doi: 10.1016/j.rse.2015.09.023

Barnes, R. T., and Raymond, P. A. (2009). The contribution of agricultural and urban activities to inorganic carbon fluxes within temperate watersheds. *Chem. Geol.* 266, 318–327. doi: 10.1016/j.chemgeo.2009.06.018

Bates, N., Astor, Y., Church, M., Currie, K., Dore, J., Gonaález-Dávila, M., et al. (2014). A time-series view of changing ocean chemistry due to ocean uptake of anthropogenic CO_2 and ocean acidification. *Oceanography* 27, 126–141. doi: 10.5670/oceanog.2014.16

Bates, N. R. (2007). Interannual variability of the oceanic CO_2 sink in the subtropical gyre of the North Atlantic Ocean over the last 2 decades. *J. Geophys. Res.* 112:26. doi: 10.1029/2006JC003759

Borges, A., and Frankignoulle, M. (1999). Daily and seasonal variations of the partial pressure of CO_2 in surface seawater along Belgian and southern Dutch coastal areas. *J. Mar. Syst.* 19, 251–266. doi: 10.1016/S0924-7963(98)00093-1

Borges, A., and Gypens, N. (2010). Carbonate chemistry in the coastal zone responds more strongly to eutrophication than to ocean acidification. *Limnol. Oceanogr.* 55, 346–353. doi: 10.4319/lo.2010.55.1.0346

Brake, S., Connors, K., and Romberger, S. (2001). A river runs through it: impact of acid mine drainage on the geochemistry of West Little Sugar Creek pre- and post-reclamation at the Green Valley coal mine, Indiana, USA. *Environ. Geol.* 40, 1471–1481. doi: 10.1007/s002540100373

Caccia, V. G., and Boyer, J. N. (2005). Spatial patterning of water quality in Biscayne Bay, Florida as a function of land use and water management. *Mar. Pollut. Bull.* 50, 1416–1429. doi: 10.1016/j.marpolbul.2005.08.002

Caccia, V. G., and Boyer, J. N. (2007). A nutrient loading budget for Biscayne Bay, Florida. *Mar. Pollut. Bull.* 54, 994–1008. doi: 10.1016/j.marpolbul.2007.02.009

Cai, W.-J., Dai, M., Wang, Y., Zhai, W., Huang, T., Chen, S., et al. (2004). The biogeochemistry of inorganic carbon and nutrients in the Pearl River estuary and the adjacent Northern South China Sea. *Cont. Shelf Res.* 24, 1301–1319. doi: 10.1016/j.csr.2004.04.005

Cai, W.-J., Hu, X., Huang, W.-J., Jiang, L.-Q., Wang, Y., Peng, T.-H., et al. (2010). Alkalinity distribution in the western North Atlantic Ocean margins. *J. Geophys. Res.* 115:C08014. doi: 10.1029/2009JC005482

Cai, W.-J., Hu, X., Huang, W.-J., Murrell, M. C., Lehrter, J. C., Lohrenz, S. E., et al. (2011). Acidification of subsurface coastal waters enhanced by eutrophication. *Nat. Geosci.* 4, 766–770. doi: 10.1038/ngeo1297

Cai, W.-J., Wiebe, W. J., Wang, Y., and Sheldon, J. E. (2000). Intertidal marsh as a source of dissolved inorganic carbon and a sink of nitrate in the Satilla River–estuarine complex in the southeastern U.S. *Limnol. Oceanogr.* 45, 1743–1752. doi: 10.4319/lo.2000.45.8.1743

Cai, W. J., and Wang, Y. (1998). The chemistry, fluxes, and sources of carbon dioxide in the estuarine waters of the Satilla and Altamaha Rivers, Georgia. *Limnol. Oceanogr.* 43, 657–668. doi: 10.4319/lo.1998.43.4.0657

Crook, E. D., Potts, D., Rebolledo-Vieyra, M., Hernandez, L., and Paytan, A. (2011). Calcifying coral abundance near low-pH springs: implications for future ocean acidification. *Coral Reefs* 31, 239–245. doi: 10.1007/s00338-011-0839-y

Cyronak, T., Andersson, A. J., Langdon, C., Albright, R., Bates, N. R., Caldeira, K., et al. (2018). Taking the metabolic pulse of the world's coral reefs. *PLoS ONE* 13:e0190872. doi: 10.1371/journal.pone.0190872

Dickson, A. G. (1990). Thermodynamics of the dissociation of boric acid in synthetic seawater from 273.15 to 318.15 K. *Deep Sea Res.* 37, 755–766. doi: 10.1016/0198-0149(90)90004-F

Dickson, A. G., and Millero, F. J. (1987). A comparison of the equilibrium constants for the dissociation of carbonic acid in seawater media. *Deep Sea Res.* 34, 1733–1743. doi: 10.1016/0198-0149(87)90021-5

Dickson, A. G., Sabine, C. L., and Christian, J. R. (2007). *Guide to Best Practices for Ocean CO_2 Measurements.* Sydney, BC: PICES Special Publication.

Duarte, C. M., Hendriks, I. E., Moore, T. S., Olsen, Y. S., Steckbauer, A., Ramajo, L., et al. (2013). Is ocean acidification an open-ocean syndrome? Understanding anthropogenic impacts on seawater pH. *Estuaries Coast* 36, 221–236. doi: 10.1007/s12237-013-9594-3

Enochs, I., Manzello, D., Donham, E., Kolodziej, G., Okano, R., Johnston, L., et al. (2015). Shift from coral to macroalgae dominance on a volcanically acidified reef. *Nat. Clim. Chang.* 5, 1083–1089. doi: 10.1038/nclimate2758

Enochs, I. C., Manzello, D. P., Jones, P. J., Aguilar, C., Cohen, K., Valentino, L., et al. (2018). The influence of diel carbonate chemistry fluctuations on the calcification rate of *Acropora cervicornis* under present day and future acidification conditions. *J. Exp. Mar. Biol. Ecol.* 506, 135–143. doi: 10.1016/j.jembe.2018.06.007

EPA (1993a). *Method 351.2, Revision 2.0: Determination of Total Kjeldahl Nitrogen by Semi-Automated Colorimetry.* Cincinnati, OH: U.S. Environmental Protection Agency, Environmental Monitoring Systems Laboratory, Office of Research and Development, US EPA.

EPA (1993b). *Method 365.1, Revision 2.0: Determination of Phosphorus by Semi-Automated Colorimetry.* Cincinnati, OH: U.S. Environmental Protection Agency, Environmental Monitoring Systems Laboratory, Office of Research and Development, US EPA.

EPA (1997). *In vitro Determination of Chlorophyll a and Pheophytin a in Marine and Freshwater Algae by Fluorescence.* Cincinnati, OH: U.S. Environmental Protection Agency, National Exposure Research Laboratory, Office of Research and Development, US EPA.

Fabricius, K. E., Langdon, C., Uthicke, S., Humphrey, C., Noonan, S., De'ath, G., et al. (2011). Losers and winners in coral reefs acclimatized to elevated carbon dioxide concentrations. *Nat. Clim. Chang.* 1, 165–169. doi: 10.1038/nclimate1122

Fabry, V. J., Seibel, B. A., Feely, R. A., and James, O. C. (2008). Impacts of ocean acidification on marine fauna and ecosystem processes. *ICES J. Mar. Sci.* 65, 414–432. doi: 10.1093/icesjms/fsn048

Feely, R. A., Sabine, C. L., Hernandez-Ayon, J. M., Ianson, D., and Hales, B. (2008). Evidence for upwelling of corrosive "acidified" water onto the continental shelf. *Science* 320, 1490–1492. doi: 10.1126/science.1155676

Finkl, C. W., and Krupa, S. L. (2003). Environmental impacts of coastal-plain activities on sandy beach systems: hazards, perception and mitigation. *J. Coast. Res.* 132–150.

Fish, J. E., and Stewart, M. (1991). *Hydrogeology of the Surficial Aquifer System Dade County, Florida.* Report 90-4108, US Geological Survey.

Friis, K., Körtzinger, A., and Wallace, D. W. R. (2003). The salinity normalization of marine inorganic carbon chemistry data. *Geophys. Res. Lett.* 30:1085. doi: 10.1029/2002GL015898

Gagliano, M., McCormick, M. I., Moore, J. A., and Depczynski, M. (2010). The basics of acidification: baseline variability of pH on Australian coral reefs. *Mar. Biol.* 157, 1849–1856. doi: 10.1007/s00227-010-1456-y

Goldberg, W. M. (1973). The ecology of the coral-octocoral communities off the southeast Florida coast: geomorphology, species composition, and zonation. *Bull. Mar. Sci.* 3, 465–488.

Heery, E. C., Hoeksema, B. W., Browne, N. K., Reimer, J. D., Ang, P. O., Huang, D., et al. (2018). Urban coral reefs: degradation and resilience of hard coral assemblages in coastal cities of East and Southeast Asia. *Mar. Pollut. Bull.* 135, 654–681. doi: 10.1016/j.marpolbul.2018.07.041

Ho, D. T., Ferrón, S., Engel, V. C., Anderson, W. T., Swart, P. K., Price, R. M., et al. (2017). Dissolved carbon biogeochemistry and export in mangrove-dominated rivers of the Florida Everglades. *Biogeosciences* 14, 2543–2559. doi: 10.5194/bg-14-2543-2017

Hofmann, G. E., Smith, J. E., Johnson, K. S., Send, U., Levin, L. A., Micheli, F., et al. (2011). High-frequency dynamics of ocean pH: a multi-ecosystem comparison. *PLoS ONE* 6:e28983. doi: 10.1371/journal.pone.0028983

Johns, G. M., Leeworthy, V. R., Bell, F. W., and Bonn, M. A. (2003). *Socioeconomic Study of Reefs in Southeast Florida (Final Report)*. Hollywood, FL: Hazen and Sawyer, Environmental Engineers and Scientists.

Lantz, C. A., Atkinson, M. J., Winn, C. W., and Kahng, S. E. (2013). Dissolved inorganic carbon and total alkalinity of a Hawaiian fringing reef: chemical techniques for monitoring the effects of ocean acidification on coral reefs. *Coral Reefs* 33, 105–115. doi: 10.1007/s00338-013-1082-5

Lapointe, B. E. (1997). Nutrient thresholds for bottom-up control of macroalgal blooms on coral reefs in Jamaica and southeast Florida. *Limnol. Oceanogr.* 42, 1119–1131. doi: 10.4319/lo.1997.42.5_part_2.1119

Le Quéré, C., Andrew, R. M., Friedlingstein, P., Sitch, S., Pongratz, J., Manning, A. C., et al. (2018). Global carbon budget 2017. *Earth Syst. Sci. Data* 10, 405–448. doi: 10.5194/essd-10-405-2018

Lewis, E., and Wallace, D. (1998). *Program Developed for CO_2 System Calculations.* Oak Ridge, TN: ORNL/CDIAC.

Lighty, R. G., Macintyre, I. G., and Stuckenrath, R. (1978). Submerged early Holocene barrier reef south-east Florida shelf. *Nature* 276, 59–60. doi: 10.1038/276059a0

Lirman, D., and Cropper, W. P. (2003). The influence of salinity on seagrass growth, survivorship, and distribution within Biscayne Bay, Florida: field, experimental, and modeling studies. *Estuaries* 26, 131–141. doi: 10.1007/BF02691700

Manzello, D., Enochs, I., Musielewicz, S., Carlton, R., and Gledhill, D. (2013). Tropical cyclones cause $CaCO_3$ undersaturation of coral reef seawater in a high-CO_2 world. *J. Geophys. Res. Oceans* 118, 5312–5321. doi: 10.1002/jgrc.20378

Manzello, D. P. (2010). Ocean acidification hot spots: spatiotemporal dynamics of the seawater CO_2 system of eastern Pacific coral reefs. *Limnol. Oceanogr.* 55:239. doi: 10.4319/lo.2010.55.1.0239

Manzello, D. P., Enochs, I. C., Melo, N., Gledhill, D. K., and Johns, E. M. (2012). Ocean acidification refugia of the Florida Reef Tract. *PLoS ONE* 7:e41715. doi: 10.1371/journal.pone.0041715

McCook, L. J. (1999). Macroalgae, nutrients and phase shifts on coral reefs scientific issues and management consequences for the Great Barrier. *Coral Reefs* 18, 357–367. doi: 10.1007/s003380050213

Mehrbach, C., Culberson, C. H., Hawley, J. E., and Pytkowicz, R. M. (1973). Measurement of the apparent dissociation constants of carbonic acid in seawater at atmospheric pressure. *Limnol. Oceanogr.* 18, 897–907. doi: 10.4319/lo.1973.18.6.0897

Miller, M. W., Karazsia, J., Groves, C. E., Griffin, S., Moore, T., Wilber, P., et al. (2016). Detecting sedimentation impacts to coral reefs resulting from dredging the Port of Miami, Florida USA. *PeerJ* 4:e2711. doi: 10.7717/peerj.2711

Millero, F. J., Hiscock, W. T., Huang, F., Roche, M., and Zhang, J. Z. (2001). Seasonal variation of the carbonate system in Florida Bay. *Bull. Mar. Sci.* 68, 101–123.

Moyer, R. P., Riegl, B., Banks, K., and Dodge, R. E. (2003). Spatial patterns and ecology of benthic communities on a high-latitude South Florida (Broward County, USA) reef system. *Coral Reefs* 22, 447–464. doi: 10.1007/s00338-003-0334-1

Oh, N.-H., and Raymond, P. A. (2006). Contribution of agricultural liming to riverine bicarbonate export and CO2sequestration in the Ohio River basin. *Global Biogeochem. Cycles* 20:GB3012. doi: 10.1029/2005GB002565

Precht, W. F., and Aronson, R. B. (2004). Climate flickers and range shifts of reefcorals. *Front. Ecol. Environ.* 2, 307–314. doi: 10.1890/1540-9295(2004)002[0307:CFARSO]2.0.CO;2

Price, N. N., Martz, T. R., Brainard, R. E., and Smith, J. E. (2012). Diel variability in seawater pH relates to calcification and benthic community structure on coral reefs. *PLoS ONE* 7:e43843. doi: 10.1371/journal.pone.0043843

R Team (2008). *R: A Language and Environment for Statistical Computing*. Vienna: R Foundation for Statistical Computing.

Raymond, P. A., and Cole, J. J. (2003). Increase in the export of alkalinity from North America's largest river. *Science* 301, 88–91. doi: 10.1126/science.1083788

Rivest, E. B., Comeau, S., and Cornwall, C. E. (2017). The role of natural variability in shaping the response of coral reef organisms to climate change. *Curr. Clim. Chang. Rep.* 3, 271–281. doi: 10.1007/s40641-017-0082-x

RStudio Team (2015). *RStudio: Integrated Development for R*. Boston, MA: RStudio, Inc.

Shaw, E. C., and McNeil, B. I. (2014). Seasonal variability in carbonate chemistry and air–sea CO_2 fluxes in the southern Great Barrier Reef. *Mar. Chem.* 158, 49–58. doi: 10.1016/j.marchem.2013.11.007

Silbiger, N. J., Guadayol, Ò., Thomas, F. I. M., and Donahue, M. J. (2014). Reefs shift from net accretion to net erosion along a natural environmental gradient. *Mar. Ecol. Prog. Ser.* 515, 33–44. doi: 10.3354/meps10999

Stalker, J. C., Price, R. M., and Swart, P. K. (2009). Determining spatial and temporal inputs of freshwater, including submarine groundwater discharge, to a subtropical estuary using geochemical tracers, Biscayne Bay, South Florida. *Estuaries Coast* 32, 694–708. doi: 10.1007/s12237-009-9155-y

Wallace, R. B., Baumann, H., Grear, J. S., Aller, R. C., and Gobler, C. J. (2014). Coastal ocean acidification: the other eutrophication problem. *Estuar. Coast. Shelf Sci.* 148, 1–13. doi: 10.1016/j.ecss.2014.05.027

Conflict of Interest Statement: The authors declare that the research was conducted in the absence of any commercial or financial relationships that could be construed as a potential conflict of interest.

frontiers in Marine Science

ORIGINAL RESEARCH
published: 03 April 2019
doi: 10.3389/fmars.2019.00169

Riverine Calcium End-Members Improve Coastal Saturation State Calculations and Reveal Regionally Variable Calcification Potential

Sean T. Beckwith*, Robert H. Byrne and Pamela Hallock

College of Marine Science, University of South Florida, Saint Petersburg, FL, United States

Carbonate-rich groundwater discharged from springs, seeps, and spring-fed rivers on carbonate platforms creates environments of potential refuge for calcifying organisms in coastal waters by supplying higher $[Ca^{2+}]$ and $[CO_3{}^{2-}]$ along with typically lower nutrient concentrations. The benefits associated with carbonate terrains are maximized in the presence of submerged aquatic vegetation (SAV), especially seagrasses. To improve the accuracy of carbonate saturation state (Ω) determinations, calculated values of $[CO_3{}^{2-}]$ and $K_{sp}{}^*$ were paired with $[Ca^{2+}]$ values determined using a model that incorporates directly measured riverine calcium end-members (model A). This model results in Ω values larger than those calculated by assuming that $[Ca^{2+}]$ is directly proportional to salinity (model B; e.g., using CO2SYS, CO2calc). As an example, for salinity (S) between 13.5 and 24, improvements in saturation states calculated as differences ($\Delta\Omega$) between model A and model B saturation states in the tidal mixing zone of the Weeki Wachee River (Florida, United States) ranged from 0.39 to 1.00 (aragonite) and 0.61–1.65 (calcite). Saturation state ratios ($\Omega_{(A)}/\Omega_{(B)}$) for coastal waters with enhanced $[Ca^{2+}]$ originating from carbonate-rich groundwater can be calculated from end-member calcium concentrations and salinity. Applied to several river systems in the conterminous United States, $\Omega_{(A)}/\Omega_{(B)}$ values calculated at S = 20 lead to $\Omega_{(A)}/\Omega_{(B)}$ ratios of 1.12 (Weeki Wachee), 1.09 (Anclote), 1.06 (Mississippi), and 1.03 (Columbia). These increases in saturation states can be used to identify potential calcification refugia for subsequent high resolution field studies that focus on, for example, the long-term viability of oyster communities and other calcifying organisms in brackish coastal waters.

Keywords: carbonate-rich groundwater, first-magnitude springs, riverine calcium, ocean acidification, west Florida coastal waters, seagrass

OPEN ACCESS

Edited by:
Tyler Cyronak,
University of California, San Diego,
United States

Reviewed by:
Zvi Steiner,
University of Cambridge,
United Kingdom
Emily E. Bockmon,
California Polytechnic State University,
United States

****Correspondence:***
Sean T. Beckwith
stbeckwith@mail.usf.edu

Specialty section:
This article was submitted to
Coastal Ocean Processes,
a section of the journal
Frontiers in Marine Science

Received: *16 October 2018*
Accepted: *18 March 2019*
Published: *03 April 2019*

Citation:
Beckwith ST, Byrne RH and Hallock P (2019) Riverine Calcium End-Members Improve Coastal Saturation State Calculations and Reveal Regionally Variable Calcification Potential. Front. Mar. Sci. 6:169. doi: 10.3389/fmars.2019.00169

INTRODUCTION

While it has been shown that the global ocean is acidifying due to anthropogenic emissions of greenhouse gases (Ciais et al., 2013), the evidence that this is potentially occurring faster than any ocean acidification (OA) event discernible in the geologic record (Kump et al., 2009; Honisch et al., 2012) should be of paramount concern. In light of the prospect that human intervention will not quickly or effectively limit or reverse greenhouse gas emissions (Ciais et al., 2013; Collins et al., 2013;

Kirtman et al., 2013) and avoid foreseeable hardships (including loss of marine species), resource management must focus on identifying and protecting coastal areas that have the potential to provide refuge for organisms most sensitive to changing environmental conditions. A pragmatic approach would be to map habitats around the globe that exhibit some resilience to global stressors such as warming and acidification.

Numerous studies have revealed deleterious effects that unabated OA is likely to have on organisms from corals to shellfish to foraminifera (e.g., Kleypas and Yates, 2009; Gaylord et al., 2011; Uthicke et al., 2013). Although relatively few studies have explored potential solutions to the problem of rapid OA, some insight may be gleaned from looking at the past. The long-recognized association between mass-extinction events and carbonate depositional hiatuses (e.g., Magaritz, 1991) indicates that ocean chemistry was sufficiently acidified to induce dissolution and prevent preservation of carbonate sediments. At times in the geologic past, species have disappeared from the fossil record, commonly at a mass-extinction horizon, but were subsequently found in a later interval within facies comparable to their pre-event habitats. Termed "Lazarus" taxa (Jablonski, 1996; Erwin, 1998), such surviving species withstood regional or global stressors, but existed in such low numbers or under conditions of minimal preservation that they essentially disappeared from a portion of the geologic record. Lazarus species likely survived in micro- or macrohabitats that buffered the changes caused by an unfavorable event. Such habitats are referred to as refugia.

Seagrasses significantly draw down CO_2, and coral reefs downstream of seagrass beds have shown resistance to OA (Manzello et al., 2012; Okazaki et al., 2013). Similarly, mangroves have been shown to harbor organisms sensitive to ocean warming and acidification. Yates et al. (2014) reported that corals living on mangrove prop roots are protected from photic stress by shade that the mangroves provide, protected from warming through adaptation to extremely shallow waters, and more resistant to OA owing to the variable water chemistry that is associated with a highly heterogeneous environment. In addition to seagrasses and mangroves, what other natural systems might favor the survival of organisms sensitive to increases in CO_2?

In an area known as the "Springs Coast" (Florida, United States), numerous spring-fed rivers emerge from Eocene and Oligocene limestone and dolostone substrata found along the Gulf of Mexico coastal region adjoining the Florida peninsula and panhandle. Florida hosts the largest assemblage of artesian springs in the world and the largest number of first-magnitude springs (Knight, 2017), most of which are concentrated in north central Florida. In coastal mixing zones associated with spring-fed rivers, *Archaias angulatus*, a symbiont-bearing, large benthic foraminifer (LBF), was commonly found living on seagrass blades and in sediments sampled during seagrass monitoring (2012–2014) by the Florida Fish and Wildlife Conservation Commission (FWC). Although *A. angulatus* occurs abundantly in warm, shallow waters of the Caribbean and Western Atlantic, in the low salinities and cooler temperatures of the Springs Coast its occurrence provoked curiosity. In previous work leading up to this study (Beckwith, 2016), we examined the prevalence and spatial distribution of *A. angulatus* in nearshore waters of the Springs Coast, hypothesizing that the water chemistry of the springs and spring-fed rivers increases calcium carbonate saturation states (Ω) in coastal waters and, to an extent, compensates for low salinity, allowing *A. angulatus* to thrive at salinities below their previously known range ($29 \leq S \leq 39$, Hallock and Peebles, 1993; Weinmann et al., 2013; Murray, 2014).

Carbonate rocks occur at or near the land surface at many locations around the world. Where these rocks form aquifers that feed springs and rivers, especially in coastal zones, they alter the water chemistry. Calcium is treated as a substantially conservative ion in marine waters, but, while constancy of calcium/salinity ratios is a good approximation for most of the open ocean, coastal waters can show significant variability (e.g., Chakrabarti et al., 2018). Previous studies have alluded to this observation and discussed a need for further analysis of carbonate system variability related to calcium concentrations (e.g., Keul et al., 2010; Wanninkhof et al., 2015). Similar in focus, the recent work of DeCarlo et al. (2018) linked OA resistance in corals to active increases in calcium concentration ($[Ca^{2+}]$) in internal calcifying fluids at the site of calcification.

It is notable that empirically derived calcium concentrations are rarely included in calculations of $CaCO_3$ saturation states (Ω). Accordingly, the contributions of freshwater sources to $CaCO_3$ saturation are typically overlooked. By considering calcium end-member contributions, this work provides a model to more effectively assess $CaCO_3$ saturation states for regions where $[Ca^{2+}]$ significantly deviates from direct proportion to salinity. A ratio of saturation states obtained with and without consideration of freshwater calcium contributions provides a useful examination of regional calcification potential.

MATERIALS AND METHODS

Saturation State Model for Mixing of Seawater and Calcium-Rich Freshwater

To account for the effects of riverine and groundwater contributions to $CaCO_3$ saturation states (Ω) in coastal waters, particularly in carbonate provinces, we propose use of a simple mixing model. Defining S_{sw} and $[Ca^{2+}]_{sw}$ as the seawater end-members of salinity and calcium specific to a particular coastal region and $[Ca^{2+}]_{fw}$ as the freshwater end-member specific to a river or other source, total calcium concentrations are derived as follows:

$$\textit{seawater fraction} + \textit{freshwater fraction} = 1 \tag{1a}$$

$$\left(\frac{S}{S_{sw}}\right) + \left(\frac{S_{sw} - S}{S_{sw}}\right) = 1 \quad \left(\textit{where } S_{fw} \cong 0\right) \tag{1b}$$

(A) model for $[Ca^{2+}]_{fw} > 0$:

$$\left[Ca^{2+}\right]_T = \left[Ca^{2+}\right]_{fw}\left(\frac{S_{sw} - S}{S_{sw}}\right) + \left[Ca^{2+}\right]_{sw}\left(\frac{S}{S_{sw}}\right) \tag{2}$$

$$\left[Ca^{2+}\right]_T = \left[Ca^{2+}\right]_{fw} + \frac{S}{S_{sw}}\left(\left[Ca^{2+}\right]_{sw} - \left[Ca^{2+}\right]_{fw}\right) \tag{3}$$

(B) model for $[Ca^{2+}]_{fw} = 0$:

$$\left[Ca^{2+}\right]_{\mathrm{T}} = \frac{S}{S_{\mathrm{sw}}}\,[Ca^{2+}]_{\mathrm{sw}} \tag{4}$$

$$\Omega = \frac{\left[Ca^{2+}\right]_{\mathrm{T}}\,[CO_3^{2-}]_{\mathrm{T}}}{K^{*}_{\mathrm{sp}}}$$

Dividing Equation (3) by Equation (4) and multiplying both the numerator and denominator by $[CO_3{}^{2-}]_T$, we obtain:

$$\frac{\Omega_{(A)}}{\Omega_{(B)}} = 1 + \frac{\left[Ca^{2+}\right]_{\mathrm{fw}}}{\left[Ca^{2+}\right]_{\mathrm{sw}}}\left(\frac{S_{\mathrm{sw}}}{S} - 1\right) \tag{5}$$

In this study, we use $[Ca^{2+}]_T$ from Equation (3) to calculate more accurate values of Ω in two coastal mixing zones, and use Equation (5) as a tool to highlight regional differences in Ω resulting from models that do and do not consider riverine $[Ca^{2+}]$ contributions. The dependence of $\Omega_{(A)}/\Omega_{(B)}$ on salinity reveals regions with disproportionately elevated $[Ca^{2+}]$ as a result of substantial inputs of freshwater calcium.

Acquisition of Riverine $[Ca^{2+}]$ Data

Although the primary focus of this study was the coastal rivers of west Florida, characteristics of other United States rivers and streams were investigated to provide comparisons. Calcium data were gathered from online data repositories, including WMIS (Southwest Florida Water Management District), DBHYDRO (South Florida Water Management District), and the Environmental Protection Agency's STORET Data Warehouse and Water Quality Portal. To locate sampling sites appropriately representative of riverine calcium (data unaffected by tidally influenced saltwater intrusion), downriver sites were limited to those with measured $S < 0.5$. Sites were included in the analysis only if they were sampled for $[Ca^{2+}]$ and salinity on the same day. Whenever possible, sites with records spanning several months or years were chosen.

Data were gathered for every mapped river in the Southwest Florida Water Management District (SWFWMD). For the Alafia and Hillsborough rivers, the most complete records were obtained from the Environmental Protection Commission Hillsborough County (EPCHC). For south Florida, $[Ca^{2+}]$ and salinity data were accessed from DBHYDRO for the Shark River and for Canal 111 (both located in the Everglades). For other locations in the conterminous United States, data were obtained through EPA portals by searching 'Rivers/Streams' station types within selected states or specific drainage basins. These data were used for comparisons between the Florida rivers and rivers found in non-carbonate provinces. The method for measuring $[Ca^{2+}]$ varied among agencies and over time, but the majority of calcium measurements, as reported by the respective laboratories, were made by either the flame atomic absorption spectrometric method [APHA 3500-CA(B)] or by the inductively coupled plasma-atomic emission spectrometric method (USEPA 200.7).

Data were filtered to meet the criteria mentioned above. For sites where only specific conductivity was reported, conversion to salinity was made. Using one sample per day from each site, $[Ca^{2+}]$ and salinity were averaged for every site within the timeframe requested in the data download (e.g., the most recent 20 years), although a few of the sites returned limited sampling records. The stations for the selected rivers were chosen as the most robust representation of individual freshwater end-members for each river (farthest downriver sites with a long measurement record), but distances between sampling stations and river mouths differ, with concomitant small variations in salinity ($S \leq 0.5$ at all sites). In contrast, Crystal River in the Springs Coast is an estuarine spring/river system where the salinity is rarely less than 0.5. Due to the limitations imposed by the data filter used in our analysis ($S \leq 0.5$), data for the Crystal River station were sparse and not fully indicative of the contributions of $[Ca^{2+}]$ to coastal waters by the many springs of King's Bay. Homosassa River (also in the Springs Coast) was excluded altogether due to a lack of available data, and, as this study is not an exhaustive analysis of the Gulf Coast of Florida, there are additional rivers not included in the analysis.

GIS Analysis

Substratum Type and $[Ca^{2+}]$ in Rivers

Subsequent to the acquisition process described above, data for all sampling sites were plotted in ArcMap (Esri™), and one site for each river was chosen for a representative riverine $[Ca^{2+}]$. The $[Ca^{2+}]$ for each river was symbolized by color, producing a gradient of concentrations for various rivers across the conterminous United States. Concentrations of Ca^{2+} were commonly reported in mg/L, so all units were converted to micromoles per kilogram (μmol/kg) to make direct comparisons to concentrations of marine waters. Averaging $[Ca^{2+}]$ over a sufficiently long sampling record accounts for any interannual, seasonal, or daily fluctuations in $[Ca^{2+}]$ and provides a signature end-member value for each river in order to assess regional differences in Ω enhancement through use of the $\Omega_{(A)}/\Omega_{(B)}$ model.

Rivers were superimposed on a lithology layer to examine the spatial connection between limestone substrata and riverine $[Ca^{2+}]$. The lithology layer, downloaded from the USGS Mineral Resources Online Spatial Data catalog[1], was modified from Dicken et al. (2005) for central-west Florida (CWF), and from Schweitzer (2011) for the conterminous United States, to include only substrata for which the primary rock type was limestone.

Interpolated Mapping of the Ω-Ratio Model

Values of $\Omega_{(A)}/\Omega_{(B)}$ for 14 coastal rivers along CWF and portions of north Florida were used to model differences in saturation state potential in coastal waters. Utilizing NOAA satellite derived 5-year mean salinity data for autumn (Allee et al., 2012)[2], salinity values corresponding to the mesohaline and polyhaline boundaries (S = 5–30) in the NOAA Gulf of Mexico Data Atlas were used to create points within the coastal waters to simulate the riverine output. By the Inverse Distance Weighted interpolation method (Watson and Philip, 1985), and given $[Ca^{2+}]_{sw} = 0.0103$ mol/kg for typical seawater of S = 35, $\Omega_{(A)}/\Omega_{(B)}$ values for the simulated coastal points were assessed

---

[1] http://mrdata.usgs.gov/geology/state/

[2] https://gulfatlas.noaa.gov/

to spatially examine any gradient in estuarine waters related to differences in calcium contributions of the rivers along CWF.

Quantifiable Improvements to Ω From Riverine Contributions

The difference between (a) Ω calculated by inclusion of directly measured calcium (Equation 3) and (b) a model wherein calcium is directly proportional to salinity (i.e., CO2SYS), represents the increase in Ω attributable to riverine calcium: $\Delta\Omega = \Omega_A - \Omega_B$. To calculate absolute values of Ω, $[CO_3{}^{2-}]_T$ must be known in addition to $[Ca^{2+}]_T$, salinity and temperature. Carbonate-system water-sampling data from Beckwith (2016) were utilized to compare $\Delta\Omega$ between the two mixing zones of the Weeki Wachee and Anclote rivers. For input variables of total alkalinity (TA) and dissolved inorganic carbon (DIC), the constants chosen in CO2SYS for the calculation of Ω_B, and likewise for the calculation of $[CO_3{}^{2-}]$ for Ω_A, include K_1^* and K_2^* (Millero, 2010), K_{HSO4-}^* (Dickson, 1990), and B_T (Uppstrom, 1974). To properly compute $\Delta\Omega$, it is necessary to use the same set of constants to obtain $[CO_3{}^{2-}]$ for both Ω_A and Ω_B. The constants should be chosen based on whether they are appropriate over the observed environmental range of salinity. If the same constants are used for both saturation state assessments, no bias should be introduced in the calculations. For absolute values of Ω_A, $[Ca^{2+}]_T$ (Equation 3) was paired with $[CO_3{}^{2-}]_T$ from CO2SYS, and calcium carbonate solubility products appropriate to seawater/freshwater mixtures were calculated using the K_{sp}^* model of Mucci (1983). Using this model, which is appropriate for $S \geq 5$, K_{sp}^* is expressed as a product of total calcium and total carbonate ion concentrations.

RESULTS

Calcium Concentrations for Representative Conterminous United States Rivers

Geologic maps compiled by the USGS for the conterminous United States (Schweitzer, 2011; Horton, 2017) classify lithologic units by primary and secondary rock type. Some limestone units contain a secondary rock type of sand, sandstone, clay, mudstone, or any one of the numerous non-$CaCO_3$ substrates. Examples of areas with the highest percentage of $CaCO_3$ include those where limestone is the primary rock type and the secondary rock type is dolostone [$CaMg(CO_3)_2$] or calcarenite (consolidated calcareous sand), as well as cases where the absence of a stated secondary rock type implies that the lithology is wholly limestone.

Figure 1 shows limestone substrata for the conterminous United States drawn in dark gray or black (for varying $CaCO_3$ content) and overlain by selected rivers whose colors depict calcium concentrations. This graphical description confirms logical expectations: rivers that traverse limestone substrata have elevated calcium concentrations. Likewise, higher carbonate/bicarbonate concentrations are expected for rivers that traverse limestone. Two river systems in central-west Florida (CWF), a carbonate province, were studied by Beckwith (2016), and carbonate-system data for the two were compared, as described in the section pertaining to $\Delta\Omega$.

Riverine [Ca^{2+}] Effects on Estuarine Ω

Dissolved calcium is elevated in rivers that traverse limestone substrata. New River in North Carolina and several rivers found along the Springs Coast of CWF are prime examples of increases in Ω attributed to riverine $[Ca^{2+}]$. This increase is quantified as a ratio ($\Omega_{(A)}/\Omega_{(B)}$) by Equation (5), and the values for all rivers in this study are shown in **Table 1**, along with riverine $[Ca^{2+}]$ end-members and lithology traversed. The Weeki Wachee River, in the Springs Coast, and New River had the highest $[Ca^{2+}]$ of natural rivers in this study ($[Ca^{2+}]$ = 1,594 and 1,534 μmol kg^{-1}, respectively), which translates to the highest Ω-ratios. **Table 1** shows a large difference in Ω-ratios between highlighted rivers of the Pacific Northwest that traverse mostly igneous and siliciclastic sedimentary rocks versus rivers to the East that traverse extensive limestone terrains.

A very stark contrast in Ω-ratios exists between New River, NC and nearby Santee River, in South Carolina. The Santee River, with one of the lowest $[Ca^{2+}]$ values in the East (although still an order of magnitude greater than the Willamette River of Oregon), produced almost no enhancement to estuarine waters (standardized to S = 20). By contrast, the New River, with one of the highest $[Ca^{2+}]$ values (2.5 orders of magnitude greater than the Willamette), had an Ω-ratio of 1.11 (or, an 11% increase in the value of Ω) at S = 20. Both the Weeki Wachee River in the Springs Coast, and Canal 111, which empties into Florida Bay, had an Ω-ratio of 1.12, the highest in this study. While there is little to no effect on the Ω-ratio model at oceanic salinity where riverine calcium contributions are negligible, substantial differences can be found in estuaries that receive high riverine calcium concentrations. As an example of the variation in $[Ca^{2+}]$ enhancements to Ω at lower salinities, **Figure 2** highlights improved Ω values for three rivers in this study that feed into the Gulf of Mexico. Saturation state enhancements in the waters around the Weeki Wachee River are profound at very low salinities, while at high salinities the regional differences become insignificant. Preliminary examination of SWFWMD data for coastal sampling sites (which are somewhat limited) confirmed $[Ca^{2+}]$ well above the mixing line for brackish waters and diminishing discrepancies for increases in salinity.

The interpolation created from $\Omega_{(A)}/\Omega_{(B)}$ values for several rivers along CWF shows the greatest $[Ca^{2+}]$ enhancement to Ω values in the zone encompassing the Springs Coast (**Figure 3**). Considering the maximum extent of brackish waters along portions of CWF coastal waters, a substantially large area exhibits elevated $[Ca^{2+}]$. The large areal extent of brackish waters in the Springs Coast is due to the cumulative discharge of many coastal rivers. The Springs Coast is also the largest estuarine seagrass habitat in the study area. Assessed at S = 20, the range of Ω-ratios in the Springs Coast was 1.08–1.12. Numerous springs infuse the rivers of this coastal region with groundwater rich in calcium and bicarbonate (Yobbi and Knochenmus, 1989). Submarine springs

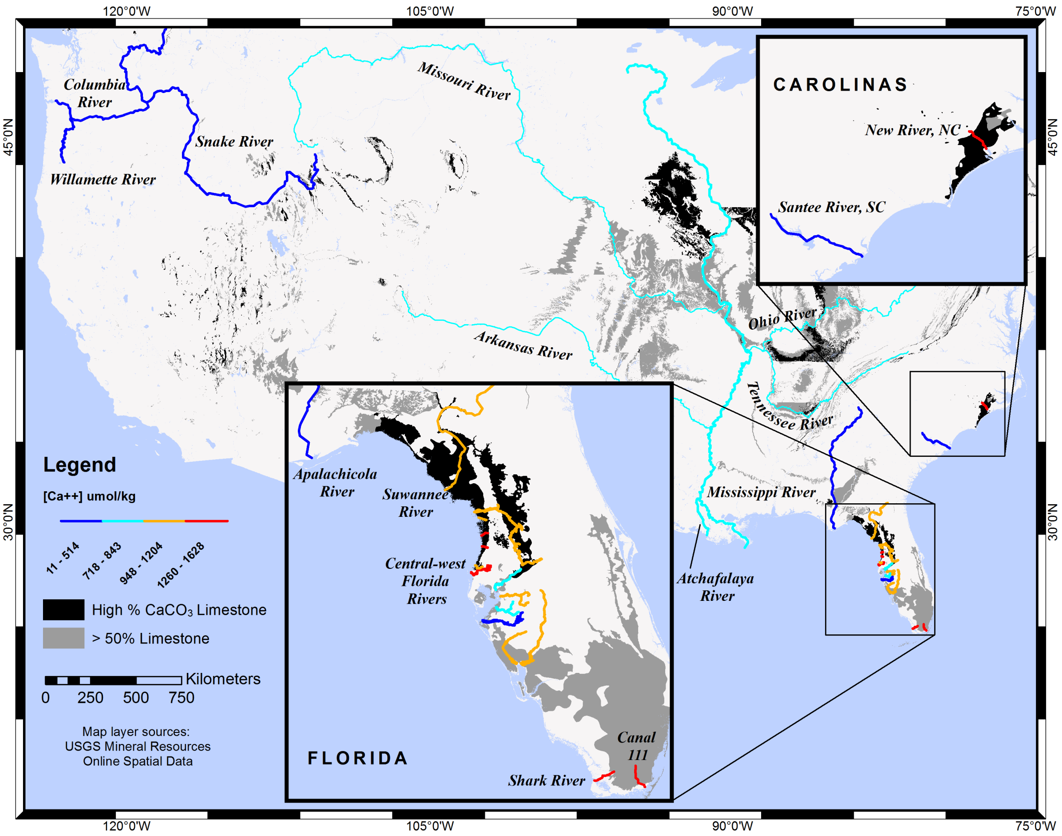

FIGURE 1 | Map of selected rivers in the conterminous United States showing riverine calcium concentrations and limestone lithology. Rivers with low calcium concentrations traverse few to no limestone substrata, while rivers with high [Ca^{2+}] traverse substrata composed primarily of limestone rock: dark gray areas symbolize rock that is primarily limestone (>50%) with a secondary rock type that is non-$CaCO_3$, while black areas symbolize main rock composed of limestone-dolostone, limestone-calcarenite, or exclusively limestone. Although rivers are symbolized uniformly along their entire lengths and tributaries are generalized, [Ca^{2+}] characterizations were determined from a single downstream sampling station. The limestone layer map was adapted from the USGS Geologic map of the conterminous United States (Schweitzer, 2011).

and seeps add an additional, although unquantified, contribution of water interacting with the limestone substrata.

In waters of central Tampa Bay, Ω-ratios were notably lower (1.03–1.07) than in adjacent regions to the north and south. Although some springs feed into the rivers of this central region, most of the river volume is associated with surface hydrology. In the northernmost portion of the Florida study region, a large contrast exists between the [Ca^{2+}], and therefore the Ω-ratio, of the Apalachicola and Suwannee Rivers. While the Apalachicola River flows alongside limestone substrata near the Alabama-Florida-Georgia border, the Suwannee River flows through substrata of high $CaCO_3$ composition over most of its length.

Errors (ΔΩ) in Calculation of Ω From Salinity-Dependent Calcium

While the value of $\Omega_{(A)}/\Omega_{(B)}$ is a ratio of the two models, increases in the value of Ω by inclusion of riverine [Ca^{2+}] can be obtained as a difference between Ω calculated with $[Ca^{2+}]_T$ from Equation (3) and Ω calculated in proportion to salinity. Focusing on two mixing zones, we examined the increase in the value of Ω at a number of locations near the Weeki Wachee and Anclote rivers (**Table 2**) using available carbonate-system chemical data from multiple seasons presented by Beckwith (2016). Improved determinations of Ω are especially evident at low to intermediate salinities. Calculations of $\Omega_{(calcite)}$ using $[Ca^{2+}]_T$ from Equation (3) ($[Ca^{2+}]_{sw}$ = 0.0103 mol/kg for S = 35) produced ΔΩ values of 0.10–0.26 near the Anclote River (S = 23–32) and 0.61–1.65 near the Weeki Wachee (S = 13–24) (**Figure 4**). Likewise, $\Delta\Omega_{(aragonite)}$ values were 0.06–0.16 near the Anclote River and 0.39–1.00 near the Weeki Wachee River.

The higher values of ΔΩ for all samples in the Weeki Wachee mixing zone are in part related to the lower salinities of the samples taken there; at lower salinities ΔΩ is substantially more pronounced (i.e., **Figure 2**). However, the high ΔΩ values are also attributable to higher end-member [Ca^{2+}] in the Weeki Wachee River. Both rivers have high [Ca^{2+}] and enhance the Ω of the coastal waters, but the [Ca^{2+}] of the Weeki Wachee River is roughly 20% greater. Comparing the two coastal mixing zones at roughly similar salinity revealed $\Delta\Omega_{(calcite)}$ = 0.71 (S = 24) for the Weeki Wachee area versus $\Delta\Omega_{(calcite)}$ = 0.22 (S = 23) for the Anclote area.

TABLE 1 | Freshwater calcium end-members, lithology, and Ω-ratios of rivers in this study.

River name by region	Lat/Lon of sampling station	$[Ca^{2+}]_{fw}$ μmol kg^{-1}	Ω/Ω at S = 20	Primary lithology traversed
Springs Coast (Florida)				
Withlacoochee	29.04566, −82.46475	1204	1.09 ± 0.01	Clay, Limestone, Sand
Crystal	28.89483, −82.59864	951	1.07 ± 0.01	Limestone
Chassahowitzka	28.71544, −82.57622	1357	1.10 ± 0.002	Limestone
Weeki Wachee	28.53226, −82.62704	1594	1.12 ± 0.03	Clay, Limestone, Sand
Pithlachascotee	28.257, −82.643	953	1.07 ± 0.04	Clay, Limestone
North Florida				
Apalachicola	29.94857, −85.0162	384	1.03 ± 0.01	Alluvium, Amphibole schist, Amphibolite, Augen gneiss, Biotite gneiss, Clay, Dolostone, Felsic gneiss, Gneiss, Granite, Granitic gneiss, Limestone, Mafic gneiss, Mica schist, Mylonite, Pyroxenite, Quartzite, Sand, Sandstone, Schist, Terrace
Suwannee	29.39917, −83.02278	995	1.07 ± 0.03	Clay, Limestone, Sand, Sandstone, Unconsolidated material
Central Florida				
Anclote	28.21466, −82.66596	1303	1.09 ± 0.05	Clay, Limestone, Sand
Hillsborough	28.02211, −82.43511	842	1.06 ± 0.01	Clay, Limestone
Alafia	27.8631, −82.137	1067	1.08 ± 0.02	Clay, Limestone, Sand, Sandstone
Little Manatee	27.67169, −82.35225	718	1.05 ± 0.02	Clay, Limestone, Sand, Sandstone
Manatee	27.51379, −82.36701	514	1.04 ± 0.01	Clay, Dolostone, Limestone, Sand, Sandstone
Myakka	27.24044, −82.31389	977	1.07 ± 0.03	Clay, Limestone, Sand, Sandstone
Peace	27.08944, −81.99583	948	1.07 ± 0.04	Limestone, Sand, Sandstone
South Florida				
Shark	25.46134, −80.86460	1260	1.09 ± 0.02	Limestone, Sand
Canal 111	25.28726, −80.44150	1628	1.12 ± 0.01	Limestone, Sand
Additional United States Rivers				
New (NC)	34.84897, −77.51961	1534	1.11 ± 0.06	Limestone, Sand
Santee (SC)	33.18390, −79.40582	164	1.01 ± 0.01	Clay, Peat, Sand
Mississippi	29.85369, −89.98104	843	1.06 ± 0.01	Alluvium, Arenite, Basalt, Clay, Claystone, Conglomerate, Dolostone, Gneiss, Granite, Graywacke, Iron formation, Limestone, Loess, Metavolcanic rock, Monzonite, Mudstone, Sand, Sandstone, Schist, Shale, Silt, Slate
Atchafalaya	29.85576, −91.19815	730	1.05 ± 0.01	Clay, Silt
Columbia	46.18122, −123.18345	351	1.03 ± 0.003	Alluvium, Andesite, Argillite, Arkose, Basalt, Biotite gneiss, Glacial drift, Glacial outwash sediment, Glaciolacustrine sediment, Granite, Lake/marine sediment, Landslide, Limestone, Loess, Quartzite, Rhyodacite, Sand, Sandstone, Schist, Silt, Tholeiite, Till, Wacke
Willamette	43.69486, −122.84504	11	1.00	Alluvium, Basalt, Clay, Mudstone, Sand, Sandstone, Silt

The Ω-ratios were computed from a typical seawater end-member, $[Ca^{2+}]_{sw}$, of 0.0103 mol/kg (S = 35) and from the freshwater end-members, $[Ca^{2+}]_{fw}$, listed in the table. The Ω-ratios are compared at S = 20 to represent the improvement to Ω at typical salinities found in estuaries and coastal mixing zones. The $[Ca^{2+}]_{fw}$ values are long-term, interannual means for downstream sampling stations. The standard errors associated with the $[Ca^{2+}]_{fw}$ means were incorporated into the Ω-ratios to express the sensitivity of the model to variability in riverine $[Ca^{2+}]$. Results were somewhat limited for the New, Chassahowitzka, and Hillsborough Rivers, and only 1 day of sampling results was found in the search timeframe for the Willamette River. Lithological descriptions are of the main rivers and exclude tributaries.

DISCUSSION

$\Omega_{(A)}/\Omega_{(B)}$ Interpolation Reveals Subregional Differences

The Ω-ratio represents corrections to Ω values owing to freshwater calcium sources. By spatially interpolating the results of this model, regional and subregional differences in calcification potential emerge. In general, riverine $[Ca^{2+}]$ is higher in rivers of the Eastern United States than in rivers of the Western United States due to greater abundance of limestone substrata. Comparing subregions or even individual river basins provides useful insight, as the $[Ca^{2+}]$ can change markedly from river to river. With a large number of rivers traversing substrata of varying $CaCO_3$ composition, CWF is an ideal location to demonstrate the contrast in riverine $[Ca^{2+}]$ contributions to coastal waters.

The coastal lithology of CWF transitions from Eocene and Oligocene limestones/dolostones in the north, to Miocene and younger clays, sand, and limestone around Tampa Bay, to Pliocene and Pleistocene limestones in the south. The Ω-ratios, significantly above 1.00 for all rivers in the region, highlight the need to include directly measured $[Ca^{2+}]$ in Ω calculations. River-by-river comparisons reveal that further variability is found within carbonate provinces.

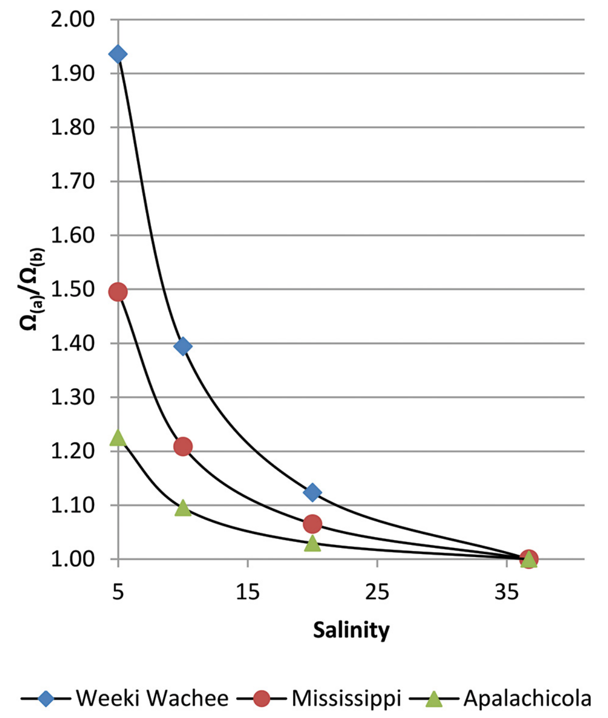

FIGURE 2 | Salinity versus $\Omega_{(A)}/\Omega_{(B)}$ for three rivers that discharge into the Gulf of Mexico; the seawater end-member ($S \cong 37$) is for the Loop Current (Wang et al., 2013). In addition to highlighting differences among river regions, this graph reveals an increasing disparity, as salinity decreases, between models that do and do not account for riverine [Ca^{2+}].

Similar to the contrast seen between the Carolina rivers (Santee and New), the underlying lithology in CWF explains much of the variation in [Ca^{2+}] seen among the rivers. Short, coastal rivers in the Springs Coast, such as the Weeki Wachee River, emerge from and flow entirely within Eocene-Oligocene limestone. In contrast to the Weeki Wachee River ([Ca^{2+}] = 1594 μmol/kg), the Manatee River ([Ca^{2+}] = 514 μmol/kg) traverses primarily clay, sand, and sandstone as well as some areas of dolostone and limestone.

While lithology appears to be a strong predictor of riverine calcium, other contributing factors exist. The Alafia River, for example, flows along a narrow section of limestone lithology, seemingly exposed by the action of the river (although, at the scale of **Figure 3**, this is not clearly visible among the surrounding lithology class representing clay, sand, and sandstone). An additional noteworthy factor is the high number of riparian springs that feed into the Alafia River. Seemingly, the additive effects of substrata type and groundwater activity give the Alafia the highest [Ca^{2+}] among the rivers feeding the Tampa Bay estuary. Thus, flow is an important factor to consider in addition to lithology. The Manatee River, which has the lowest [Ca^{2+}] among the CWF rivers examined, also has a very low rate of discharge. In the comparison of the Weeki Wachee and Anclote Rivers, the case is more subtle: the lack of major springs seems to contribute to a lower [Ca^{2+}] in the Anclote, which equates to the lower $\Delta\Omega$ seen in estuarine waters. More broadly, the Ω-ratios provide the best overview of regional differences, and the strongest influence of riverine calcium is attributed to the Springs Coast.

Taken together, the lithology of an area can influence the riverine chemistry and in turn the coastal chemistry to an extent that substantially increases calculated Ω. The Ω-ratio model does not provide actual Ω values for a given location but rather provides a useful tool for first-order examination of coastal Ω trends by region. The model, by obviating the need for carbonate-system measurements (TA, DIC, pCO_2, pH), reduces efforts in the field and laboratory that can instead be exerted on subsequent high-resolution studies of narrower regions of interest. Where [Ca^{2+}] and [$CO_3{}^{2-}$] data are available, however, improved Ω calculations can be made, as highlighted by the presentation of $\Delta\Omega$ in this study.

Biogeochemical Signals of Refugia: A Case Study

Synergy of Limestone Bedded Rivers and Submerged Aquatic Vegetation Enhances Coastal Ω for Calcifying Species

In spring-fed rivers buffered by the dissolution of $CaCO_3$ in the Springs Coast, the pH is typically high (≈ 8) (Yobbi and Knochenmus, 1989), and, as highlighted in this study, the riverine [Ca^{2+}] is high. Total alkalinity is also high in these rivers, typically around 3,000 μmol/kg (Beckwith, 2016). At pH 8 in freshwater, a greater proportion of the TA is in the form of bicarbonate, $HCO_3{}^-$, than is the case for seawater at pH 8. The high concentration of CO_2 found in groundwater bubbling from the headsprings and riparian springs is drawn down in part by degassing but primarily through the influence of SAV (Troester and White, 1986; de Montety et al., 2011).

Farther downstream, in the coastal mixing zone, prolific seagrass and macroalgae further draw down CO_2, raising the pH and shifting the relative proportions of carbonate species from $HCO_3{}^-$ to $CO_3{}^{2-}$. Based on higher TA found in the Weeki Wachee River relative to seawater, a gradual dilution of the TA might be expected to occur due to seawater mixing, yet an increase in [$CO_3{}^{2-}$] and TA occurs from the headwaters into the coastal waters, cresting to a maximum, for both [$CO_3{}^{2-}$] and TA, at intermediate salinities before decreasing further offshore (Beckwith, 2016). The increase in TA is possibly due to additional input from downstream springs. This maximum zone is reflected in the distribution of *Archaias angulatus* (a foraminifer) in the Springs Coast; the highest density (individuals per gram of sediment) was seen at sampling sites within a band of intermediate salinity along the coastline (**Figure 5**) that could be termed a calcification "sweet spot," referring to an ideal calcification environment. Similar sweet spots likely exist in any low latitude location where there is concurrence of limestone-influenced riverine discharge and extensive SAV, resulting in enhanced Ω.

Ideal calcification environments require additional contributing factors beyond high Ω. Environmental conditions in the Springs Coast that contribute to the abundance of *A. angulatus* include the low nutrient concentrations that are

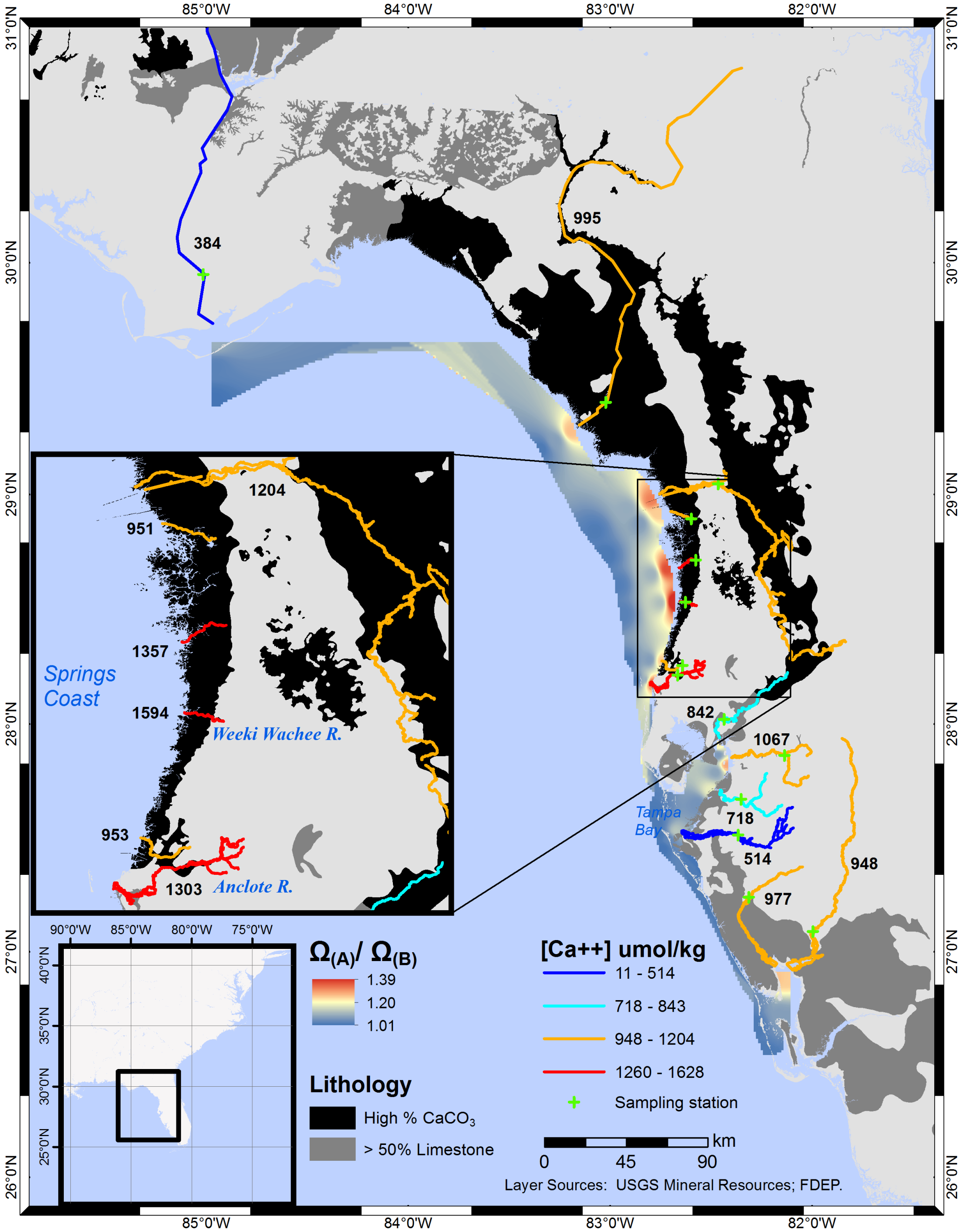

FIGURE 3 | Interpolated $\Omega_{(A)}/\Omega_{(B)}$ ratios for central-west and central-north Florida coastal waters. Averaged calcium ion concentrations for individual sampling stations, in µmol/kg, are labeled adjacent to each river. Comparing the Manatee and Weeki Wachee Rivers ($[Ca^{2+}]$ = 514 and 1594 µmol/kg, respectively), the Ω-ratio, assessed at S = 20, translates to a 4 and 12% increase, respectively, in calculated Ω values. The boundaries of the interpolation approximately encompass the mesohaline and polyhaline regions (S≅5–30) in Oct–Dec (5 years mean), as estimated from NOAA satellite imagery.

common in these spring-fed coastal rivers. In addition, these rivers receive little runoff due to their low-gradient drainage basins (Yobbi and Knochenmus, 1989). Low nutrients and low runoff result in high water clarity, providing ample light for benthic organisms in these shallow waters. Also, a lack of barrier islands in this region (a result of an extremely low sloping gradient on this portion of the west Florida shelf) eliminates the potential stagnation that can occur in bay and lagoonal waters during slack tides.

What Constitutes a Refugium?

As defined by Keppel et al. (2012), refugia are "habitats that components of biodiversity retreat to, persist in and can potentially expand from under changing environmental

TABLE 2 | The salinity, $\Delta\Omega_{(\text{aragonite})}$, $\Delta\Omega_{(\text{calcite})}$, carbonate ion concentration and total alkalinity for sampling sites in the mixing zones of the Anclote and Weeki Wachee Rivers in central-west Florida.

Site	S	$\Delta\Omega_{(\text{arag})}$	$\Delta\Omega_{(\text{calc})}$	$[CO_3{}^{2-}]$ μmol kg^{-1}	TA μmol kg^{-1}
Weeki Wachee	13.5	0.66	1.10	151	3114
	15	0.62	1.03	171	3121
	15	1.00	1.65	272	3227
	15.5	0.54	1.10	167	2896
	19.25	0.57	0.91	258	2788
	21.75	0.39	0.61	238	2656
	24	0.45	0.71	370	2926
Anclote	23	0.13	0.22	132	2740
	26	0.13	0.20	190	2654
	29	0.11	0.18	263	2351
	30	0.06	0.10	172	2393
	32	0.09	0.14	437	2421

Carbonate chemistry water sampling was performed in multiple seasons during 2014–16 and reported by Beckwith (2016); a few samples were taken subsequent to Beckwith (2016) following identical methods.

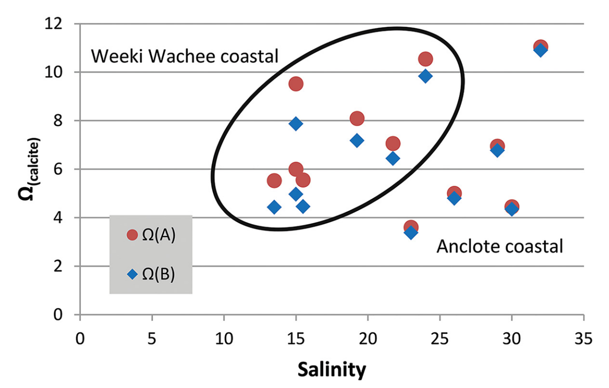

FIGURE 4 | Salinity versus $\Omega_{(\text{calcite})}$. Calcium carbonate saturation state measurements shown for two mixing zones in central-west Florida (Weeki Wachee coastal samples encircled). The red circle markers represent $\Omega_{(A)}$ calculated from total calcium (Equation 3) and the blue diamond markers represent $\Omega_{(B)}$ calculated in CO2SYS, which does not account for measured $[Ca^{2+}]$. The distance between the two marker types, $\Delta\Omega$, is the error created by not accounting for riverine calcium. The error is more profound at lower salinities but also varies by river region.

conditions" (p. 394). Kavousi and Keppel (2017) outlined two essential criteria and four additional criteria that must be met to deem an area a refugium for coral reefs: (1) long term buffering, (2) protection from multiple climatic stressors, (3) accessibility, (4) microclimatic heterogeneity, (5) size of the refugia, and (6) low exposure to other disturbances. By first-order examination, the Springs Coast seems to meet all of these criteria, although not necessarily for coral reefs in the present day. Other organisms, such as oysters, scallops, calcareous algae, and foraminifera, to name a few, thrive in the Springs Coast. Calculation of the enhancement to saturation state values (Ω-ratio) presents a new tool to search for additional locations around the globe that meet the criteria of a refugium for calcareous organisms in terms of calcification potential. Here, we have highlighted environments with such potential: limestone-bedded rivers that meet with substantial SAV in the coastal mixing zone.

Along with measures such as the ratio of ΔpH to ΔDO (dissolved oxygen), and either the TA/DIC ratio or the closely related $[CO_3{}^{2-}]/[HCO_3{}^{-}]$ ratio, the Ω-ratio can serve as a useful tool for comparing coastal habitats. Bach (2015) contends that the $[HCO_3{}^{-}]/[H^+]$ ratio may be a more robust indicator than Ω for assessments of OA on a global scale. In consideration of the direct impacts of carbonate system variables such as pH and pCO_2 on calcification in organisms, it is clear that Ω describes only a portion of the complex processes associated with OA. Cyronak et al. (2016) suggest that greater importance should be placed on pH in ambient seawater, owing to evidence of strong internal control of $[CO_3{}^{2-}]$ within organismal calcification fluids and concern that a reduced proton (H^+) gradient potential between internal fluids and ambient seawater can strain an organism's ability to maintain homeostasis. With respect to any of these indicators, carbonate springs and SAV are clearly beneficial factors that buffer the effects of OA.

Implications for Commercial Shellfish Harvesting

While the role of refugia may take many decades or longer to unravel, the case for conserving ecologically and economically-viable habitats is more compelling. A much more immediate benefit of locating areas of anomalously high saturation states exists for shellfish industries looking to sustainably harvest in locations that demonstrate longevity. Although the bay scallop (*Argopecten irradians*) meta-population in Florida has declined significantly since the 1960s, seemingly due to a combination of habitat loss, diminished water quality, overfishing, and recruitment failure (Barber and Blake, 1983; Arnold and Marelli, 1991; Blake et al., 1993; Sargent et al., 1995), a much needed reduction in harvesting pressures and environmental restoration efforts have subsequently facilitated a minor rejuvenation of key source populations of scallops (Arnold et al., 2005; Geiger et al., 2010). Factors that determine successful recovery of scallop populations include adequate adult density, suitable biological and environmental factors, and availability of seagrass beds (Arnold et al., 2005). The "Big Bend" coast of Florida, which includes the Springs Coast, is not immune to algal blooms that sometimes threaten shellfish populations, however, the coastal waters and benthic habitats of this area remain nearly pristine in other regards and provide the habitat and large-scale connectivity needed for successful restoration.

In this study, the rivers with the highest Ω-ratio were those fed by groundwater emerging from limestone. In the presence of SAV, this constant supply of calcium and carbonate creates essential buffering capacity to mediate changes in pH. While the rivers of the Springs Coast are a source of CO_2 to the atmosphere (Barrera and Robbins, 2017), and while a recent decreasing trend in pH has been shown for rivers in the Springs Coast (increased water consumption has led to shorter residence times of high CO_2 groundwater, and therefore lower pH)

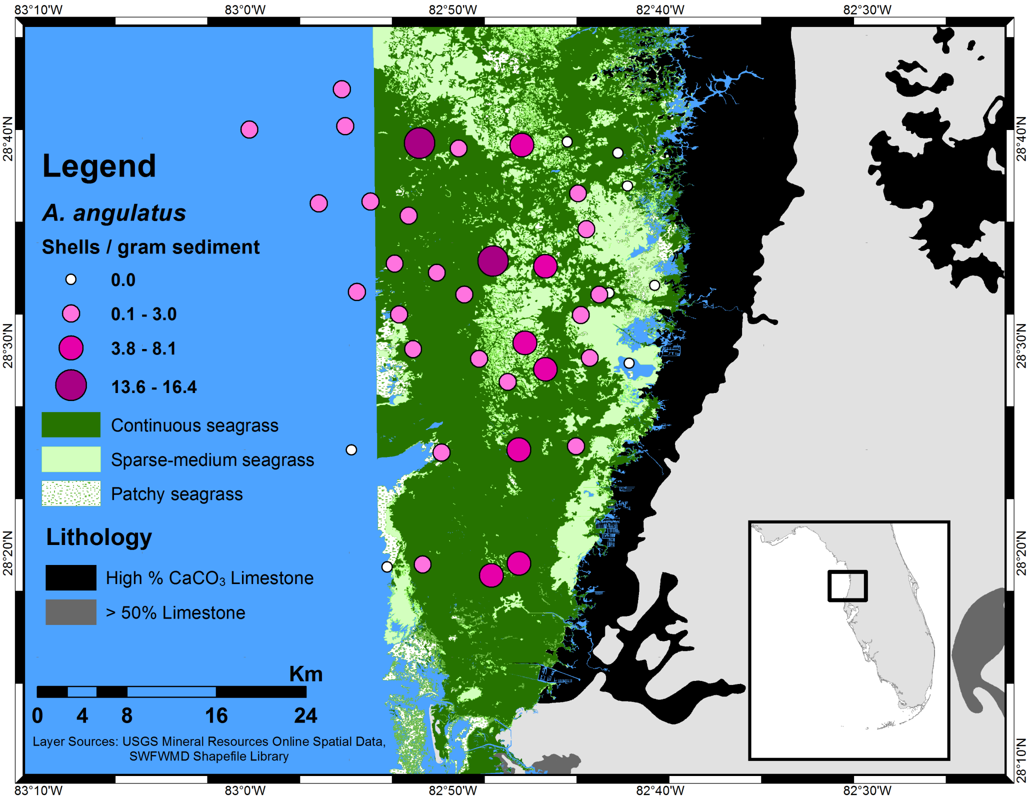

FIGURE 5 | Distribution of *A. angulatus* (by density) in the southern Springs Coast of central-west Florida. The larger, darker circles represent higher density; note the concentration of highest density along a band parallel with the coastline. The *A. angulatus* distribution is shown over seagrass of varying density. The foraminiferal abundances were determined from sediment analysis and presented in Beckwith (2016); a few additional samples were examined subsequent to Beckwith (2016) following identical methods.

(Barrera and Robbins, 2017), the SAV draws down CO_2 creating a relatively high pH coastal environment. The high TA of the riverine discharge provides long-term buffering potential, but the realization of the buffering effect is dependent on sufficient draw down of CO_2 by SAV. Because of their value as potential calcification refugia, the first priority in managing highly buffered areas should be protection and conservation. Through proper management and industry collaboration, it seems plausible that calcification refugia might also be ideal for shell-fish fisheries.

CONCLUSION

Consideration of freshwater contributions to saturation states reveals substantial enhancements in calcium carbonate saturation states (Ω). The model described in this study offers researchers and resource managers a tool to examine regional differences in calcification potential by utilizing riverine calcium data wherever available. Key points of this study are summarized as follows:

(1) Groundwater discharged by limestone bedded seeps, springs, and rivers results in highly non-conservative $[Ca^{2+}]$ at sub-regional and regional scales in coastal waters.
(2) Saturation state calculations can be improved by directly measuring $[Ca^{2+}]$; $\Delta\Omega_{(aragonite)} = {\sim}0.06–1.00$ and $\Delta\Omega_{(calcite)} = {\sim}0.10–1.65$ for the Anclote and Weeki Wachee River areas.
(3) Models using actual riverine end-members highlight regions of enhanced calcification potential: ~1.04–1.12 at $S = 20$ for CWF.
(4) Especially in combination with abundant SAV, carbonate springs and rivers may provide greater resistance to OA in coastal waters than offshore waters can provide.

DATA AVAILABILITY

The datasets generated for this study can be found in the United States Environmental Protection Agency's Water Quality Data online data warehouse, https://www.epa.gov/waterdata/water-quality-data-wqx.

AUTHOR CONTRIBUTIONS

SB performed the data collection and analysis. RB developed the calcium end-member and saturation state ratio models.

All authors contributed to the development of the study, interpretation of the data, and writing of the manuscript.

ACKNOWLEDGMENTS

A portion of this work was performed in fulfillment of SB's thesis, including carbonate system water sampling and sediment analysis of foraminiferal abundance. The Cushman Foundation for Foraminiferal Research provided partial funding of the thesis work through the Joseph A. Cushman Award for Student Research. Dr. Paul Carlson of the Florida Fish and Wildlife Conservation Commission Fish and Wildlife Research Institute provided sediment samples collected during the Springs Coast Seagrass Monitoring project, which was funded by a United States Fish and Wildlife Service State Wildlife Grant. SB thanks Marshall Lester, Christian Gfatter, and Kyle Amergian for help with sediment sample analysis.

REFERENCES

Allee, R., Finkbeiner, R., Gould, R., Ko, D.-S., Lary, D., Kurtz, J., et al. (2012). *Coastal and Marine Ecological Classification Standard (CMECS) Application for Sea Surface Salinity in the N Gulf of Mexico in GOM Data Atlas*. Asheville, NC: National Centers for Environmental Information.

Arnold, W. S., Blake, N. J., Harrison, M. M., Marelli, D. C., Parker, M. L., Peters, S. C., et al. (2005). Restoration of bay scallop (*Argopecten irradians* (Lamarck)) populations in Florida coastal waters: planting techniques and the growth, mortality and reproductive development of planted scallops. *J. Shellfish Res.* 24, 883–904. doi: 10.2983/0730-8000(2005)24[883:ROBSAI]2.0.CO;2

Arnold, W. S., and Marelli, D. C. (1991). *Assessment of Bay Scallop Populations on the West Coast of Florida*. Tallahassee, FL: Florida Department of Environmental Protection.

Bach, L. T. (2015). Reconsidering the role of carbonate ion concentration in calcification by marine organisms. *Biogeosciences* 12, 4939–4951. doi: 10.5194/bg-12-4939-2015

Barber, B. J., and Blake, N. J. (1983). Growth and reproduction of the bay scallop, *Argopecten irradians* (Lamarck) at its southern distributional limit. *J. Exp. Mar. Biol. Ecol.* 66, 247–256. doi: 10.1016/0022-0981(83)90163-6

Barrera, K. E., and Robbins, L. L. (2017). Historical patterns of acidification and increasing CO2 flux associated with Florida springs. *Limnol. Oceanogr.* 62, 2404–2417. doi: 10.1002/lno.10573

Beckwith, S. T. (2016). *Abundance of Archaias angulatus on the West Florida Coast Indicates the Influence of Carbonate Alkalinity Over Salinity*. Master's thesis, University of South Florida, Tampa, FL.

Blake, N. J., Lu, Y., and Moyer, M. (1993). *Evaluation of Tampa Bay Waters for the Survival and Growth of Southern Bay Scallop Larvae and Juveniles*. St. Petersburg, FL: Tampa Bay National Estuary Program Technical Publications, 04–93.

Chakrabarti, R., Mondal, S., Acharya, S. S., Lekha, J. S., and Sengupta, D. (2018). Submarine groundwater discharge derived strontium from the Bengal Basin traced in Bay of Bengal water samples. *Sci. Rep.* 8:4383. doi: 10.1038/s41598-018-22299-5

Ciais, P., Sabine, C., Bala, G., Bopp, L., Brovkin, V., Canadell, J., et al. (2013). "Carbon and other biogeochemical cycles," in *Climate Change 2013: The Physical Science Basis. Contribution of Working Group I to the Fifth Assessment Report of the Intergovernmental Panel on Climate Change*, eds T. F. Stocker, D. Qin, G.-K. Plattner, M. Tignor, S. K. Allen, J. Boschung, A. Nauels, Y. Xia, V. Bex and P. M. Midgley (Cambridge: Cambridge University Press), 465–570.

Collins, M., Knutti, R., Arblaster, J., Dufresne, J.-L., Fichefet, T., Friedlingstein, P., et al. (2013). "Long-term climate change: projections, commitments and irreversibility," in *Climate Change 2013: The Physical Science Basis. Contribution of Working Group I to the Fifth Assessment Report of the Intergovernmental Panel on Climate Change*, eds T. F. Stocker, D. Qin, G.-K. Plattner, M. Tignor, S. K. Allen, J. Boschung, A. Nauels, Y. Xia, V. Bex and P. M. Midgley (Cambridge: Cambridge University Press), 1029–1136.

Cyronak, T., Schulz, K. G., and Jokiel, P. L. (2016). The Omega myth: what really drives lower calcification rates in an acidifying ocean. *ICES J. Mar. Sci.* 73, 558–562. doi: 10.1093/icesjms/fsv075

de Montety, V., Martin, J., Cohen, M., Foster, C., and Kurz, M. (2011). Influence of diel biogeochemical cycles on carbonate equilibrium in a karst river. *Chem. Geol.* 283, 31–43. doi: 10.1016/j.chemgeo.2010.12.025

DeCarlo, T. M., Comeau, S., Cornwall, C. E., and McCulloch, M. T. (2018). Coral resistance to ocean acidification linked to increased calcium at the site of calcification. *Proc. R. Soc. B* 285:20180564. doi: 10.1098/rspb.2018.0564

Dicken, C. L., Nicholson, S. W., Horton, J. D., Foose, M. P., and Mueller, J. A. (2005). *Integrated Geologic Map Databases for the United States: Alabama, Florida, Georgia, Mississippi, North Carolina, and South Carolina: United States Geological Survey Open-File Report* 2005-1323. Reston, VA: United States Geological Survey.

Dickson, A. G. (1990). Standard potential of the reaction: AgCl(s) + 1/2 H2(g) = Ag(s) + HCl(aq), and the standard acidity constant of the ion HSO4- in synthetic sea water from 273.15 to 318.15 K. *J. Chem. Thermodynam.* 22, 113–127. doi: 10.1016/0021-9614(90)90074-Z

Erwin, D. H. (1998). The end and the beginning: recoveries from mass extinctions. *Trends Ecol. Evol.* 13, 344–349. doi: 10.1016/S0169-5347(98)01436-0

Gaylord, B., Hill, T. M., Sanford, E., Lenz, E. A., Jacobs, L. A., Sato, K. N., et al. (2011). Functional impacts of ocean acidification in an ecologically critical foundation species. *J. Exp. Biol.* 214, 2586–2594. doi: 10.1242/jeb.055939

Geiger, S. P., Stephenson, S. P., and Arnold, W. S. (2010). Protracted recruitment in the bay scallop *Argopecten irradians* in a west Florida estuary. *J. Shellfish Res.* 29, 809–817. doi: 10.2983/035.029.0414

Hallock, P., and Peebles, M. W. (1993). Foraminifera with chlorophyte endosymbionts: habitats of six species in the Florida Keys. *Mar. Micropaleontol.* 20, 277–292. doi: 10.1016/0377-8398(93)90037-X

Honisch, B., Ridgwell, A., Schmidt, D., Thomas, E., Gibbs, S., Sluijs, A., et al. (2012). The geological record of ocean acidification. *Science* 335, 1058–1063. doi: 10.1126/science.1208277

Horton, J. D. (2017). *The State Geologic Map Compilation (SGMC) Geodatabase of the Conterminous United States (ver.1.1)*. Reston, VA: United States Geological Survey.

Jablonski, D. J. (1996). "Causes and consequences of mass extinctions: a comparative approach," in *Dynamics of Extinction*, ed. D. K. Elliot (Hoboken, NJ: Wiley), 183–229.

Kavousi, J., and Keppel, G. (2017). Clarifying the concept of climate change refugia for coral reefs. *ICES J. Mar. Sci.* 75, 43–49. doi: 10.1093/icesjms/fsx124

Keppel, G., Van Niel, K. P., Wardell-Johnson, G. W., Yates, C. J., Byrne, M., Mucina, L., et al. (2012). Refugia: identifying and understanding safe havens for biodiversity under climate change. *Global Ecol. Biogeogr.* 21, 393–404. doi: 10.1111/j.1466-8238.2011.00686.x

Keul, N., Morse, J. W., Wanninkhof, R., Gledhill, D. K., and Bianch, T. S. (2010). Carbonate chemistry dynamics of surface waters in the Northern Gulf of Mexico. *Aquat. Geochem.* 16, 337–351. doi: 10.1007/s10498-010-9091-2

Kirtman, B., Power, S. B., Adedoyin, J. A., Boer, G. J., Bojariu, R., Camilloni, I., et al. (2013). "Near-term climate change: projections and predictability," in *Climate Change 2013: The Physical Science Basis. Contribution of Working Group I to the Fifth Assessment Report of the Intergovernmental Panel on Climate Change*, eds T. F. Stocker, D. Qin, G.-K. Plattner, M. Tignor, S. K. Allen, J. Boschung, A. Nauels, Y. Xia, V. Bex and P. M. Midgley (Cambridge: Cambridge University Press), 953–1028.

Kleypas, J. A., and Yates, K. K. (2009). Coral reefs and ocean acidification. *Oceanography* 22, 108–117. doi: 10.5670/oceanog.2009.101

Knight, R. L. (2017). *Florida, Land of 1,000 Springs*. Available at: FloridaSpringsInstitute.org (accessed March 2, 2017).

Kump, L. R., Bralower, T. J., and Ridgewell, A. (2009). Ocean acidification in deep time. *Oceanography* 22, 94–107. doi: 10.5670/oceanog.2009.100

Magaritz, M. (1991). Carbon isotopes, time boundaries and evolution. *Terra Nova* 3, 251–256. doi: 10.1111/j.1365-3121.1991.tb00142.x

Manzello, D. P., Enochs, I. C., and Melo, N. (2012). Ocean acidification refugia of the Florida Reef Tract. *PLoS One* 7:e41715. doi: 10.1371/journal.pone.0041715

Millero, F. J. (2010). Carbonate constants for estuarine waters. *Mar. Freshw. Res.* 61, 139–142. doi: 10.1071/MF09254

Mucci, A. (1983). The solubility of calcite and aragonite in seawater at various salinities, temperatures and one atmosphere total pressure. *Am. J. Sci.* 283, 780–799. doi: 10.2475/ajs.283.7.780

Murray, J. W. (2014). *Ecology and Palaeoecology of Benthic Foraminifera (Frontiers in Palaeobiology)*. New York, NY: Routledge. doi: 10.4324/9781315846101

Okazaki, R. R., Swart, P. K., and Langdon, C. (2013). Stress-tolerant corals of Florida Bay are vulnerable to ocean acidifcation. *Coral Reefs* 32, 671–683. doi: 10.1007/s00338-013-1015-3

Sargent, F. J., Leary, T. J., and Crewz, D. W. (1995). *Scarring of Florida's Seagrasses: Assessment and Management Options*. FMRI Technical Report TR-1. St. Petersburg, FL: Florida Department of Environmental Protection.

Schweitzer, P. N. (2011). *Combined Geologic Map Data for the Conterminous US. (Derived) From the USGS State Geologic Map Compilation*. Available at: https://mrdata.usgs.gov/geology/state

Troester, J. W., and White, W. B. (1986). Geochemical investigations of three tropical karst drainage basins in Puerto Rico. *Groundwater* 24, 475–482. doi: 10.1111/j.1745-6584.1986.tb01026.x

Uppstrom, L. R. (1974). The boron/chlorinity ratio of deep-sea water from the Pacific Ocean. *Deep Sea Res.* 21, 161–162. doi: 10.1016/0011-7471(74)90074-6

Uthicke, S., Momigliano, P., and Fabricius, K. E. (2013). High risk of extinction of benthic foraminifera in this century due to ocean acidification. *Sci. Rep.* 3:1769. doi: 10.1038/srep01769

Wang, Z. A., Wanninkhof, R., Cai, W.-J., Byrne, R. H., Hu, X., Peng, T.-H., et al. (2013). The marine inorganic carbon system along the Gulf of Mexico and Atlantic coasts of the United States: insights from a transregional coastal carbon study. *Limnol. Oceanogr.* 58, 325–342. doi: 10.4319/lo.2013.58.1.0325

Wanninkhof, R., Barbero, L., Byrne, R., Cai, W.-J., Huang, W.-J., Zhang, J.-Z., et al. (2015). Ocean acidification along the Gulf Coast and East Coast of the USA. *Contin. Shelf Res.* 98, 54–71. doi: 10.1016/j.csr.2015.02.008

Watson, D. F., and Philip, G. M. (1985). A refinement of inverse distance weighted interpolation. *Geoprocessing* 2, 315–327.

Weinmann, A. E., Rodder, D., Lotters, S., and Langer, M. R. (2013). Heading for new shores: projecting marine distribution ranges of selected larger foraminifera. *PLoS One* 8:e62182.doi: 10.1371/journal.pone.0062182

Yates, K. K., Rogers, C. S., Herlan, J. J., Brooks, G. R., Smiley, N. A., and Larson, R. A. (2014). Diverse coral communities in mangrove habitats suggest a novel refuge from climate change. *Biogeosciences* 11, 4321–4337. doi: 10.5194/bg-11-4321-2014

Yobbi, D. K., and Knochenmus, L. A. (1989). *Effects of River Discharge and High-Tide Stage on Salinity Intrusion in the Weeki Wachee, Crystal, and Withlacoochee River Estuaries, Southwest Florida*. USGS, Department of the Interior. Tallahassee, FL: United States Government Printing Office.

Conflict of Interest Statement: The authors declare that the research was conducted in the absence of any commercial or financial relationships that could be construed as a potential conflict of interest.

frontiers in Marine Science

ORIGINAL RESEARCH
published: 22 March 2019
doi: 10.3389/fmars.2019.00136

Decadal-Scale Acidification Trends in Adjacent North Carolina Estuaries: Competing Role of Anthropogenic CO_2 and Riverine Alkalinity Loads

Bryce R. Van Dam[1,2]* and Hongjie Wang[3,4]

[1] Institute of Marine Sciences, University of North Carolina at Chapel Hill, Chapel Hill, NC, United States, [2] Department of Biological Sciences, Florida International University, Miami, FL, United States, [3] School of Marine Science and Policy, University of Delaware, Newark, DE, United States, [4] Department of Physical and Environmental Sciences, Texas A&M University–Corpus Christi, Corpus Christi, TX, United States

OPEN ACCESS

Edited by:
David Koweek,
Carnegie Institution for Science (CIS),
United States

Reviewed by:
Yuichiro Takeshita,
Monterey Bay Aquarium Research
Institute (MBARI), United States
Xianghui Guo,
Xiamen University, China
Donald F. Boesch,
University of Maryland Center
for Environmental Science (UMCES),
United States

***Correspondence:**
Bryce R. Van Dam
vandam.bryce@gmail.com

Specialty section:
This article was submitted to
Global Change and the Future Ocean,
a section of the journal
Frontiers in Marine Science

Received: 15 November 2018
Accepted: 04 March 2019
Published: 22 March 2019

Citation:
Van Dam BR and Wang H (2019)
Decadal-Scale Acidification Trends
in Adjacent North Carolina Estuaries:
Competing Role of Anthropogenic
CO_2 and Riverine Alkalinity Loads.
Front. Mar. Sci. 6:136.
doi: 10.3389/fmars.2019.00136

Decadal-scale pH trends for the open ocean are largely monotonic and controlled by anthropogenic CO_2 invasion. In estuaries, though, such long-term pH trends are often obscured by a variety of other factors, including changes in net metabolism, temperature, estuarine mixing, and riverine hydrogeochemistry. In this study, we mine an extensive biogeochemical database in two North Carolina estuaries, the Neuse River estuary (NeuseRE) and New River estuary (NewRE), in an effort to deconvolute decadal-scale trends in pH and associated processes. By applying a Generalized Additive Mixed Model (GAMM), we show that temporal changes in NewRE pH were insignificant, while pH decreased significantly throughout much of the NeuseRE. In both estuaries, variations in pH were accompanied by increasing river discharge, and were independent of rising temperature. Decreases in bottom-water pH in the NeuseRE coincided with elevated primary production in surface waters, highlighting the importance of eutrophication on long-term acidification trends. Next, we used a simple mixing model to illustrate the impact of changing river discharge on estuarine carbonate chemistry. We found that increased riverine alkalinity loads to the NewRE likely buffered the impact of CO_2-intrusion-induced acidification. In the NeuseRE, however, elevated dissolved inorganic carbon loads further decreased the buffering capacity, exacerbating the effects of CO_2-intrusion-driven acidification. Taken together, the findings of this study show that future trajectories in estuarine pH will be shaped by complex interactions among global-scale changes in climate, regional-scale changes in precipitation patterns, and local-scale changes in estuarine biogeochemistry.

Keywords: estuary, ocean acidification, trend analysis, climate change, buffering, carbonate chemistry

INTRODUCTION

Anthropogenic activities have caused dramatic increases in atmospheric CO_2 levels, from a pre-industrial level of <300 ppm to the current value of 407 ppm (Keeling and Keeling Charles, 2017). Much of the open ocean is under-saturated in CO_2 with respect to the atmosphere, causing a net uptake of CO_2, mitigating approximately 30% of anthropogenic emissions (Le Quéré et al., 2016).

This absorption of atmospheric CO_2 is leading to the increase in aqueous CO_2 concentration $\{[CO_{2(aq)}]\}$, which affects the speciation of inorganic carbon in the ocean, shifting the following reaction (Eq. 1) toward the right, favoring the formation of H^+ and lowering the pH. Accordingly, anthropogenic CO_2 emissions have caused ocean pH to fall at a rate of approximately 0.001–0.0025 yr^{-1} (Doney et al., 2009; Bates et al., 2014; Takahashi et al., 2014).

Excess H^+ produced by the dissolution of $CO_{2(aq)}$ pairs with $CO_3{}^{2-}$ to form $HCO_3{}^-$, resulting in a net decrease in $[CO_3{}^{2-}]$ and saturation states (Ω) of various carbonate minerals, adding stress to marine calcifying organisms. This process is collectively known as ocean acidification, and may directly damage calcifying organisms, further decrease the fitness of commercially valuable groups, by directly damaging shells or compromising early development and survival.

$$CO_{2(aq)} + H_2O \rightleftharpoons H_2CO_3 \rightleftharpoons HCO_3^- + H^+ \rightleftharpoons CO_3^{2-} + 2H^+ \tag{1}$$

Over very long time scales (i.e., >100,000 years), it is expected that increased continental weathering and subsequent delivery of alkalinity via rivers will partially mitigate the coastal and open ocean acidification signal (Doney and Schimel, 2007; Müller et al., 2016). Over shorter time scales, though, riverine inputs of freshwater and related solutes may cause varied effects on the carbonate system in estuaries, resulting in contrasting pH trajectories (Aufdenkampe et al., 2011; Hu and Cai, 2013; Hu et al., 2015; Müller et al., 2016). For example, changing local water budgets resulted in a range of temporal trajectories in riverine alkalinity loading for a set of Northwest Gulf of Mexico estuaries, where estuaries experiencing decreasing alkalinity loads also became acidified (Hu et al., 2015). Similarly, long-term alkalinity increases in the Baltic sea have partially or wholly counteracted anthropogenic CO_2-induced acidification in that system (Müller et al., 2016). However, the impact of short-term variations in river discharge on the estuarine carbonate system is less clear (Mote et al., 2008; Phlips et al., 2011; Couldrey et al., 2016; Baumann and Smith, 2017; Siam and Eltahir, 2017).

A variety of biogeochemical processes will interact with these watershed-scale drivers, either enhancing or counteracting acidification trends in estuaries. For example, nutrient-enhanced primary production has been linked with elevated pH in well-mixed mesocosm experiments (Nixon et al., 2015), but net production and respiration are decoupled in stratified estuaries, where the latter process decreases bottom water pH (Feely et al., 2010; Cai et al., 2011; Waldbusser and Salisbury, 2014). Still, net ecosystem metabolism in productive coastal systems like seagrass beds has been suggested to lessen long-term coastal ocean acidification (Unsworth et al., 2012), but increase the short-term extremes in pH (Cyronak et al., 2018; Pacella et al., 2018). H_2S oxidation and subsequent H_2SO_4 additions may exacerbate acidification near the pycnocline of stratified systems (Cai et al., 2017). Anaerobic production of CO_2 and alkalinity in wetlands can act to simultaneously alkalize and acidify pore-water, leading to variable impacts on estuarine pH (Hu and Cai, 2011; Wang Z.A. et al., 2016). At the same time, estuarine waters are mixing with oceanic water that is also becoming enriched in CO_2 due to anthropogenic CO_2 emissions.

The above natural and anthropogenic processes will combine non-linearly to affect pH, to an extent that may be exacerbated by the typically poor buffering capacity of estuarine water (Feely et al., 2010; Cai et al., 2011; Hu and Cai, 2013; Jeffrey et al., 2016; Van Dam et al., 2018a). Future trajectories in estuarine acidification will depend on the interactions among a variety of complex drivers, including the invasion of anthropogenic CO_2, changes in freshwater delivery, and changes in net ecosystem metabolism. However, we do not yet know how these factors will interact over decadal time scales, or across different estuaries. The estuaries of eastern North Carolina, United States, offer a unique opportunity to compare the impacts of these factors on decadal-scale acidification trends. Both New and Neuse River estuaries, NC, experience the same climate, and have seen increases in river discharge that are of a similar magnitude over the past 10 years, but contrasting watersheds properties cause dissolved inorganic carbon (DIC) and total alkalinity (TA) loading to differ (Van Dam et al., 2018a). In this study, we investigate decadal trends in pH and associated parameters in these two adjacent estuaries, then use a simple modeling approach to examine the sensitivity of estuarine acidification to above three factors.

MATERIALS AND METHODS

Site Description

The Neuse River Estuary (NeuseRE) and New River Estuary (NewRE) are microtidal (tidal amplitude < 1 m), lagoonal systems located in the eastern North Carolina coastal plain (**Figure 1**), both of which have relatively long fresh water residence times [average 58 (±34) and 46 (±27) days, respectively (Van Dam et al., 2018a)]. Both estuaries are shallow, with average water depths of 1.8 and 2.7 m in the NewRE and NeuseRE, respectively. While the NewRE is connected directly with the coastal ocean through the New River inlet, a string of barrier islands (Outer Banks, NC) with narrow tidal inlets restricts water exchange between the NewRE and the ocean. The long residence time and limited tidal exchange has interacted with a history of anthropogenic nutrient enrichment to drive both estuaries toward eutrophy. Historically, average primary productivity (PPR) has been approximately 200–500 g C m^{-2} yr^{-1} in the NeuseRE (Boyer et al., 1993; Mallin et al., 1993) and <250 gC m^{-2} yr^{-1} in the NewRE (Mallin et al., 2005). A key difference between these two microtidal, lagoonal estuaries is their size; the surface area of the NeuseRE (352 km^2) is approximately 5 times that of the NewRE (79 km^2), while the Neuse River watershed (15,700 km^2) is over 15 times larger than that of the New River (1,024 km^2). In contrast with the heavily agricultural Neuse River watershed, much of the New River watershed contains impervious surfaces, causing river discharge in this system to be relatively 'flashy' in response to storm events (Hall et al., 2012; Peierls et al., 2012). Submarine groundwater discharge is a very small contributor to total freshwater loads in both

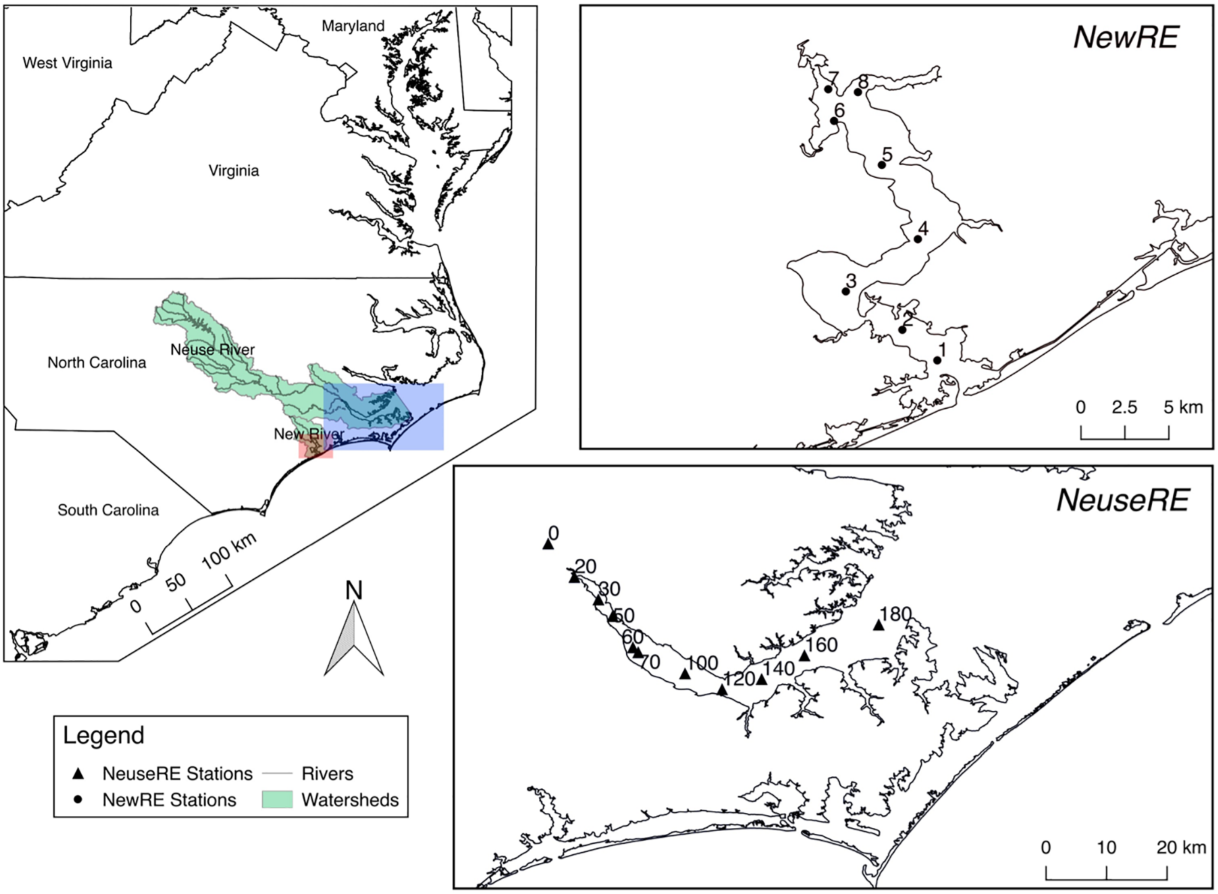

FIGURE 1 | Site map, including sampling stations for both estuaries, and watershed extents for both rivers.

NewRE (Crosswell et al., 2017) and NeuseRE (Fear et al., 2007; Null et al., 2011).

Long-Term Data Collection

Long-term data were acquired from two monitoring programs established in each estuary from 2005 to 2017. Associated with the Defense Coastal Estuarine Research Program (DCERP), monthly sample collection began in the NewRE in the Fall of 2007. The goal of this project was to assess the impacts of land use in the watershed on water quality in the NewRE. Likewise, bi-weekly to monthly sample collection occurred in the NeuseRE beginning in 1999, as a part of the Neuse River Estuary Modeling and Monitoring Project (ModMon). ModMon is a collaborative effort of both universities and the state of North Carolina, aiming at the collection of water-quality compliance data. For DCERP and ModMon programs, surface (∼0.2 m) and bottom-water (∼0.5 m above bottom) samples were collected at each station using a diaphragm pump, and were immediately stored in a cooler. For each surface sample, an estimate of phytoplankton PPR was made using the ^{14}C uptake method, and *in-vitro* Chlorophyll-a fluorescence (Chl-a IV) was determined using acetone extraction (Paerl et al., 1998; Hall et al., 2012). The ^{14}C uptake method generates PPR estimates that lie somewhere between gross and net PPR. This is because a fraction of the ^{14}C incorporated by phytoplankton is respired during the incubation period, and lost as CO_2 before the final scintillation count. However, this method has remained stable over time in both ModMon and DCERP programs, allowing us to reliably assess trends in PPR over time.

At each DCERP and ModMon station, vertical profiles of pH, dissolved oxygen (DO), salinity (Sal), and temperature (Temp) were collected at a vertical resolution of 0.5 m (YSI 6600 multi-parameter sonde, Yellow Springs Inc, Yellow Springs, OH). The pH sensor (YSI model 6561) was calibrated against NIST-traceable NBS buffers, and has a manufacturer's suggested accuracy of ±0.2 units, which is far less than the typical spatial variability in pH (Van Dam et al., 2018a). Once water samples were returned from the field, a small aliquot was immediately stored, unpreserved, in a 20 mL scintillation vial with no headspace, and was analyzed for DIC within 24 h using a Shimadzu TOC-5000A in inorganic carbon mode. Because DIC in these unpreserved water samples is often lower than when preserved with $HgCl_2$, or by filtration, we applied a correction factor (Crosswell et al., 2012) to DIC values obtained from the long-term monitoring dataset ($DIC = 7.18 + 1.16 \times DIC_{unpreserved}$). We then calculated TA from this corrected DIC value, pH, Temp, and Sal using CO2SYS

(Lewis and Wallace, 1998), with the carbonic acid dissociation constants of Millero (2010), and the NBS scale for pH.

Statistical Approach

We calculated trends in pH/PPR/Chl-a using a Generalized Additive Mixed Modeling (GAMM, Eq. 2), a method which has been previously applied to calculate multi-decadal fCO_2 trend in various coastal environments (Wang H. et al., 2016, 2017; Reimer et al., 2017). Briefly, a penalized spline was first used to fit the seasonal cycle, and a harmonic function was adopted to fit daily cycles, then linear regressions were used to model the variability resulting from salinity and DO change. Sampling date was also included in GAMM as a linear effect, and its coefficient represents the pH/PPR/Chl-a long-term change. The method also weighted the observations using explicit models for heteroscedasticity to account for an observed unequal variance in salinity.

$$\mathrm{pH/PPR/Chl-a} = f(\mathrm{seasonalcycle}) + f(\mathrm{dailycycle}) + f(\mathrm{DO, Sal}) + f(\mathrm{long-termtrend}) + \mathrm{error} \tag{2}$$

Note, the "best" model was selected based on smallest AICc values (**Supplementary Table S1** and **Supplementary Figure S1**). Trends were assessed for the time period 2005–2017 in the NeuseRE, and for 2007–2017 in the NewRE. Salinity and temperature trends were calculated after removing the seasonal cycle only. Pre-2005 data were not used for the NeuseRE because: (1) residuals were not normally distributed before 2005, (2) different pH probe was used before 2005, and data were more scattered, (3) surveys were conducted in early morning, causing pH measurements to be biased toward lower values (based on typical diel variations in these estuaries), and (4) data do not exist for the NewRE before 2007.

Box Model

In this study, we used a simple box model approach to address the relative importance of the following three factors on long term estuarine acidification trends: (1) continuous anthropogenic CO_2 invasion, (2) varying PPR, and (3) changing river discharge (and TA/DIC loads). This model is intended to represent average conditions over yearly to decadal-time scales, rather than shorter-term variations in pH, which can be very difficult to predict. As future changes in river discharge are very uncertain, we estimated a range of river discharge (Q_R) by estimating the average discharge (Q_R) from **Supplementary Table S2** over time, extrapolating forward 70 years, and backward 20 years. This range of Q_R (New River: 1.3–8.9 $m^3\ s^{-1}$, Neuse River: 82 – 221 $m^3\ s^{-1}$) is intended to include current conditions, and what could be expected for flood and drought years in the next century. The riverine end-member concentrations of DIC (DIC_R) was set based on the empirical relationships with Q_R determined in Van Dam et al., 2018b (**Supplementary Table S2**). We set the riverine TA (TA_R) value based on the linear relationship between measured DIC and calculated TA for the station closest to the river mouth, when salinity was <5 for the NewRE, or <2 for the NeuseRE. Those equations are also shown in **Supplementary Table S2**. The r^2 for these relationships were 0.96 for the NeuseRE, and 0.97 for the NewRE. We assumed a constant oceanic TA end-member (TA_O) of 2500 $\mu mol\ kg^{-1}$, and increasing oceanic DIC (DIC_O) as a function of increasing atmospheric CO_2 (i.e., $DIC_O \sim pCO_2, TA$). These end-member DIC and TA values were mixed within the estuary, allowing us to calculate pH under different atmospheric CO_2 levels.

After setting the end-member chemistry, we assumed that the main factors affecting DIC concentration in surface and bottom water was net ecosystem metabolism. The NewRE and NeuseRE are both stratified estuaries, where net ecosystem production and respiration are vertically decoupled, meaning that some fraction of net production in the surface is exported to bottom waters where it is respired. Hence, we used average net ecosystem productivity ($\overline{NEP}$, mol $m^{-2}\ yr^{-1}$) from Herrmann et al. (2015), and assumed that a certain fraction of net production was respired in bottom waters (R). Note that the sign of $\overline{NEP}$ was reversed from that given in Herrmann et al. (2015), such that positive values indicate net heterotrophy. Given the paucity of data regarding bottom-water respiration in these systems, we set R at 40% (R = 0.4 x$\overline{NEP}$). Variations in R do not affect the general trend of modeled pH with variations in Q_R or pCO_2, but does cause moderate changes in the absolute value of modeled pH. As an example of these variations, modeled pH results are shown for R values of 0.25 (a), 0.5 (b), and 0.75 (c) in **Supplementary Figure S4**.

Areal $\overline{NEP}$ was converted into a concentration change by the following equation where z_{ave} is the average water depth, τ_{FW} is the residence time (years), and F_{mix} is the mixing fraction, given by the ratio of Sal_E/Sal_O (i.e., F_{mix} = 10/35 = 0.29 for oligohaline region). Multiplying by F_{mix} scales the DIC loss due to air-water exchange from the whole estuary down to the region of interest.

$$\mathrm{NEP_E}\ (\mu\mathrm{M}) = 10^3 \times \left(\frac{\overline{\mathrm{NEP}} \times {}_{\mathrm{FW}} \times \mathrm{F_{Mix}}}{\mathrm{z_{ave}}}\right) \tag{3}$$

With DIC consumption/production terms defined, surface and bottom water DIC in the estuary (DIC_S and DIC_B respectively) was calculated assuming conservative mixing, with the addition of net metabolism and air-sea exchange:

$$\mathrm{DIC_S} = (\mathrm{DIC_O} \times \mathrm{F_{Mix}}) + (\mathrm{DIC_R} \times (1 - \mathrm{F_{Mix}})) - \mathrm{NEP_E} \tag{4}$$

$$\mathrm{DIC} = (\mathrm{DIC_O} \times \mathrm{F_{Mix}}) + \mathrm{DIC_R} \times (1 - \mathrm{F_{Mix}})) + (\mathrm{R}) \tag{5}$$

Total alkalinity in the estuary (TA_E) was determined by conservative mixing of river and ocean end-members. We also accounted for the small amount of TA production (consumption) that occurs during the production (remineralization) of Redfield organic matter, by assuming TA changes with DIC at a ratio of −17/106.

From these modeled TA and DIC values, estuarine pH (pH_{est}) was calculated in CO2SYS using the carbonic acid dissociation constants of Millero (2010), at a constant temperature of 20°C, very close to the median temperature in the NeuseRE (20.5°C)

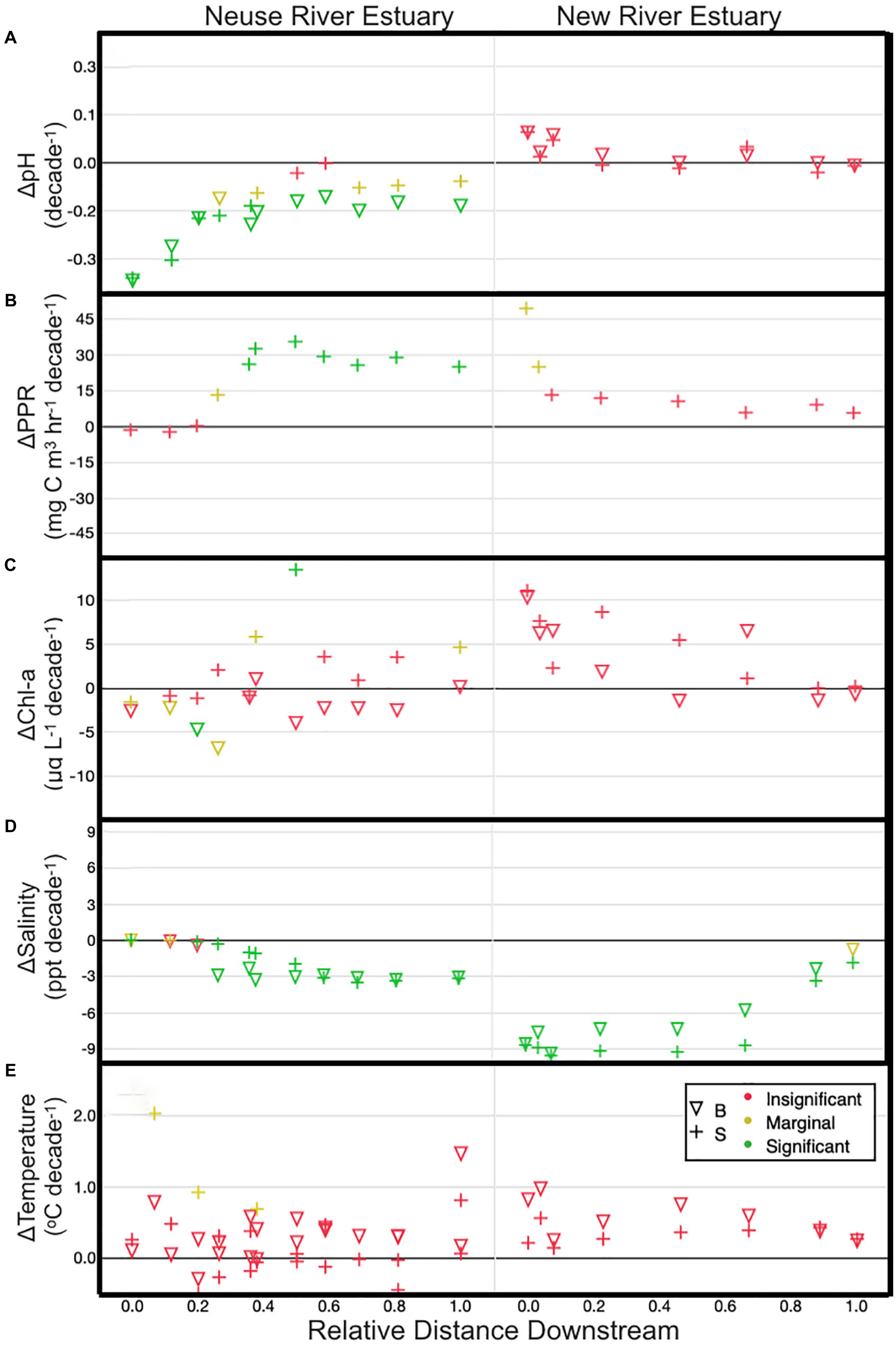

FIGURE 2 | Post-2005 trends for pH **(A)**, PPR **(B)**, Chl-a **(C)**, Salinity **(D)**, and Temperature **(E)** for surface (+) and bottom water (∇). Trends are shown relative to distance downstream, which is the distance from the head of the estuary divided by the total length of the estuary. Colors indicate the *p*-value for a *t*-test on the slope of the trend line (green: $p < 0.01$; yellow: $0.01 < p < 0.1$; red: $p > 0.1$).

and NewRE (20.8°C). A constant output temperature was used to control for the effect of changing temperature on pH and pCO_2.

RESULTS AND DISCUSSION

Physical Condition Change

From 1996 to 2017, Neuse river discharge at Ft Barnwell increased at an average rate of 1.55 m^3 s^{-2} yr^{-1}, or 2.8% yr^{-1}, while New River discharge at Gum Branch increased at 0.084 m^3 s^{-2} yr^{-1} (1.4% yr^{-1}) between 2007 and 2017. Variations in monthly averaged discharge during the Spring and Winter were significantly correlated with El Nino Southern Oscillation (ENSO) patterns, such that positive ENSO phase was associated with increases in discharge (**Supplementary Figure S2**). However, ENSO phase could not explain changes in discharge during the Fall and Summer. The observed increases in river discharge were reflected in a large and significant freshening trend in both estuaries. Averaged across all surface stations, salinity decreased at a rate of 0.002 to 0.35 yr^{-1} in the NeuseRE, and 0.18 to 0.96 yr^{-1} in the NewRE (**Figure 2D**). In both estuaries, trends in bottom water salinity followed those from surface water.

Despite generally non-significant changes in Chl-a (**Figure 2C**), PPR in the middle and lower NeuseRE increased significantly from 2005 to 2017, at a rate of approximately 30 mg C m^{-3} hr^{-1} $decade^{-1}$. Elevated river discharge has been shown to drive a seaward shift in the location of peak phytoplankton biomass (Peierls et al., 2012), so it is not surprising that increased river inputs were accompanied with elevated PPR in the lower NeuseRE (**Figure 2B**). Coinciding with this increasing surface water PPR in the NeuseRE, bottom water pH fell significantly at approximately ~0.02 yr^{-1} (0.2 $decade^{-1}$), while surface

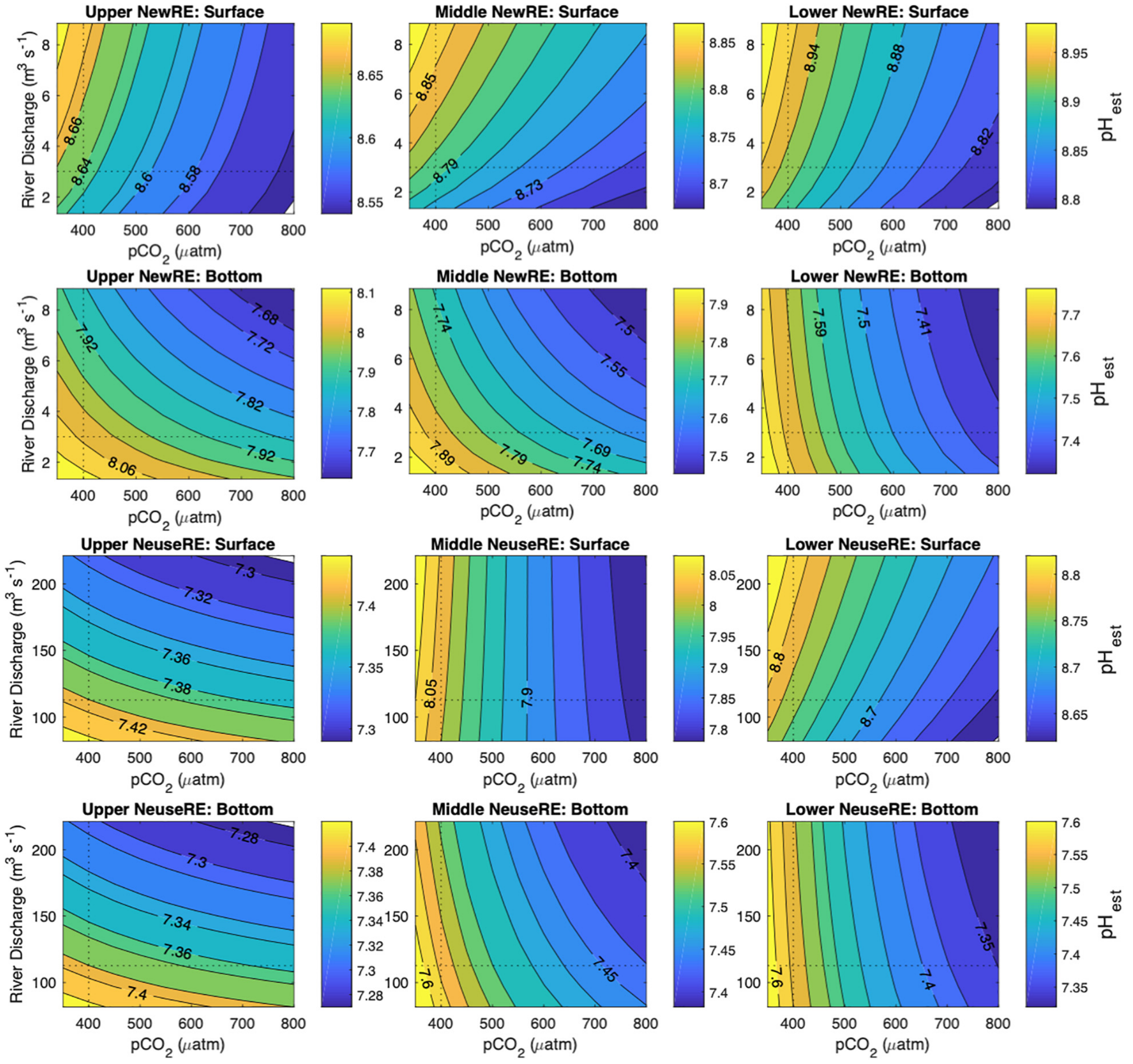

FIGURE 3 | Model pH_{est} as a function of atmospheric pCO_2 (µatm) and river discharge (m^3 s^{-1}), where pH_{est} values are shown by the colored contours. Model results are shown for surface and bottom estuarine boxes, for the regions described in the **Supplementary Material**.

water pH trends were generally non-significant. Trends in bottom water DO were not significantly different from zero in the NeuseRE (**Supplementary Figure S3**), indicating that the observed decreases in pH may have been accelerated by factors beyond aerobic decomposition.

Trends in both PPR and pH for the NewRE were not significant (**Figures 2A,B**). Meanwhile, changes in temperature over the study period were generally insignificant and variable, between −0.09 and 0.28°C yr^{-1} (average = 0.03 ± 0.06°C yr^{-1}), similar to the trends observed in the coastal ocean (Reimer et al., 2017). Because pH decreases with temperature (holding DIC and TA constant), it is possible to assess the thermal effect on pH changes. At a TA and DIC of 900 and 1000 μmol kg^{-1} respectively, an average temperature increase of 0.03°C yr^{-1} results in a calculated pH decrease of −0.00024 yr^{-1}. This is approximately ∼2 orders of magnitude below the observed trends in pH (**Figure 2A**), indicating that the effect of warming waters on acidification was negligible, relative to other factors.

Similar to the observed trend of acidification in the NeuseRE, which was accompanied by consistent DO, pH in the NewRE was stable (**Figure 2A**), while bottom water DO in the upper NewRE showed significant decreases (**Supplementary Figure S3**). This discrepancy between long term trends in DO and pH may be partially explained by the difference in air-water exchange for O_2 and CO_2, which is more rapid for O_2 than for CO_2. These counterintuitive trends in long-term acidification may be explained by changes in chemical buffering that served to accelerate acidification in the NeuseRE and to buffer acidification stress in the NewRE. Further explanation for this is given in the following section.

Box Model Results

In both estuaries, a doubling of oceanic pCO_2 from 400 to 800 μatm (reflecting estimated increases in atmospheric CO_2 over the next century) caused modeled surface water pH_{est} to fall by 0.094–0.14 in the NewRE, and by 0.037–0.23 in the NeuseRE. This modeled future decrease in pH over the next century corresponds to a rate of change of 0.004–0.023 $decade^{-1}$, which is within the range expected for the open ocean, but is an order of magnitude slower than the observed trend for the NeuseRE (**Figure 3**). This suggests that future trends in acidification will be driven by multiple interacting factors including the invasion of anthropogenic CO_2, and other factors including changing riverine TA loads or NEM. In the upper NeuseRE, elevated discharge was associated with decreasing surface water pH_{est} (pH_{est} at high Q_R − pH_{est} at low Q_R = ΔpH_{est} = −0.086). Throughout the rest of the NeuseRE, increases in Q_R corresponded with increasing surface pH_{est}, such that ΔpH_{est} was 0.019 and 0.045 across the forecasted range in Q_R, in the middle and lower segments, respectively. In the NewRE, surface pH_{est} always increased with Q_R, with ΔpH_{est} between 0.037 and 0.14.

To summarize, the invasion of anthropogenic CO_2 resulted in moderate decreases in modeled pH_{est}, but this acidification was buffered when accompanied by elevated river discharge. The buffering effect of riverine inputs was greatest in surface waters and appears to be larger in the NewRE than in the NeuseRE. This difference between estuaries is particularly pronounced in the upper, oligohaline regions of both estuaries, where increases in Q_R were accompanied by rising pH in the NewRE but decreasing pH in the NeuseRE. It is important to note that this difference in pH change between surface and bottom waters may be overestimated by the box model, which does not consider mixing between these two layers. However, this model does provide an indication that the pH in both estuaries are sensitive to variations in fresh water delivery.

Inputs of TA from the watershed, in excess of DIC loads, may help buffer CO_2-driven acidification. Hence, variations in the ratio of TA:DIC have been used to indicate changes in the ability of water to buffer changes in pH (Hu and Cai, 2011). As shown in **Figure 4**, the TA:DIC ratio decreases exponentially with Q_R in both rivers. This suggests that both DIC and TA concentration in the river is primarily driven by weathering inputs, which are progressively diluted by surface water as Q_R increases. However, TA appears to decrease more rapidly than DIC as Q_R increases, causing the ratio of TA:DIC to decrease with rising Q_R, converging on a value of ∼0.5 at high discharge (**Figure 4**). At low Q_R, TA:DIC was relatively high in the New River, occasionally exceeding 1:1. TA:DIC was always below 1:1 in the Neuse River. Decadal trends in the TA:DIC ratio were stable in the NewRE, but were significantly negative (decreasing trend) in much of the upper NeuseRE (**Supplementary Figure S3**), corresponding with the decreasing pH trend in that estuary.

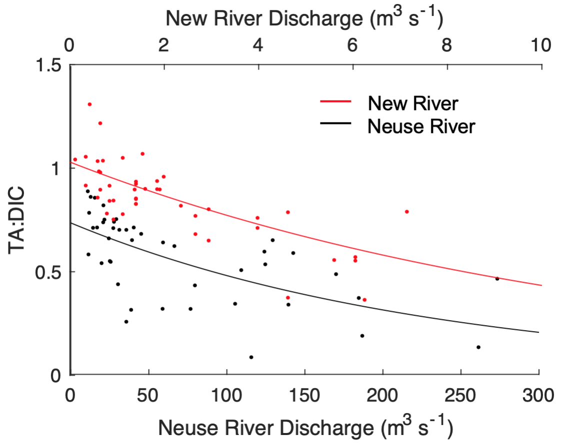

FIGURE 4 | Relationship between river endmember TA:DIC and discharge for the New (red points) and Neuse (black points) rivers. Exponential fits are of the form *f*(x) = a*exp(b*x), where the coefficients are *a* = 0.74 and *b* = −0.0043 for the Neuse River, and *a* = 1.03 and *b* = −0.086 for the New River. Water quality data (TA, pH, Temperature, Salinity) were obtained from STORET for the North Carolina Dept. of Environmental Quality site J7850000 (Neuse River near Ft Barnwell), and from sites 21NC01WQ-P0600000 and 21NC01WQ-P1200000 in the upper New River. Only matching pairs of TA, pH, temp, and salinity were used, yielding a relatively small set of data from 1990 to 1993. DIC was calculated from measured TA, pH, Temperature, and Salinity with CO2SYS. Matching discharge data were obtained from the USGS gage at Gum Branch for the New River (2093000), and the USGS gage at Kinston for the Neuse River (2089500).

To better understand the effect of changing river end-member TA:DIC on buffering within the estuary, we calculated pH across the estuarine salinity gradient (with CO2SYS) for a variety of river end-member TA:DIC ratios that fall within the range of **Figure 5A**. This assessment is intended to indicate potential pH values for an idealized estuary, and does not include DIC/TA production or consumption by net metabolic processes or air-water CO_2 exchange. When salinity is greater than ~20, carbonate chemistry is heavily controlled by mixing with well-buffered ocean water, thus, the decreasing riverine TA:DIC have limited effect on pH. However, when salinity falls below ~10, the impact of variable riverine TA:DIC ratios becomes more apparent, causing large changes in calculated pH (**Figure 5A**). Furthermore, because the ratio of TA:DIC in the coastal ocean is greater than 1 (at least in this case), scenarios where riverine TA:DIC is less than 1 result in a point where TA:DIC passes through 1:1 zone, where buffering is locally minimized (Hu and Cai, 2013). To more precisely quantify this process, we calculate a buffer factor (β_{DIC}), which can be expressed in partial differential form as in Egleston et al. (2010):

$$\beta_{\mathrm{DIC}} = \left(\partial \ln\left[\mathrm{H}^{+}\right] / \partial \mathrm{DIC}\right)^{-1} \tag{6}$$

Expressed in this manner, increases in β_{DIC} indicate an increased buffering capacity, or resistance to changes in pH with DIC additions. As seen in **Figure 5B**, β_{DIC} exhibits a non-monotonic relationship with salinity (when TA:DIC is < 1), such that buffering is minimized at a salinity of ~7 (riverine TA:DIC = 0.9) or ~12 (TA:DIC = 0.8). Hence, when riverine TA:DIC is less than 1, estuarine pH is particularly sensitive to additional DIC inputs, which can enter via changes in net metabolism, anthropogenic CO_2 inputs, etc. This is the case for the NeuseRE, where TA:DIC appears to always be less than 1. That the greatest pH decreases in the NeuseRE occurred near the river mouth (−0.3 decade^{-1}, **Figure 2A**) further supports the role of poorly buffered river water on estuarine pH trends. TA:DIC was relatively high in the New River (**Figure 4**), causing downstream pH in the estuary to be less sensitive to Q_R. This concept is further supported by decadal trends in the TA:DIC ratio, which decreased at a significant rate across much of the upper NeuseRE, and was stable across the entire NewRE (**Supplementary Figure S3**). To summarize, it appears that TA delivery from the watershed (in excess of DIC) helped to buffer acidification stress in the NewRE, while decadal decreases in TA relative to DIC served to diminish the buffering capacity of the NeuseRE, allowing significant pH decreases to occur.

Summary of Acidification Drivers

A vast and tangled array of factors contribute to temporal variations in estuarine pH. Given this complexity, we determined in a statistically robust manner, the magnitude and direction of decadal-scale biogeochemical trends for two adjacent estuaries.

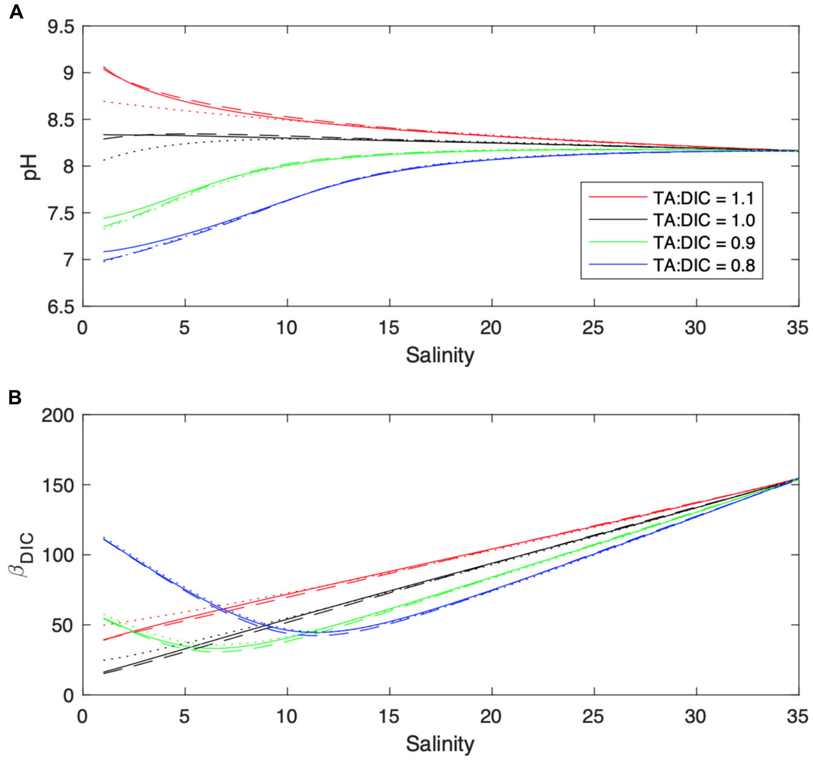

FIGURE 5 | Effect of varying river endmember TA:DIC ratios (1.1 = red, 1.0 = black, 0.9 = green, 0.8 = blue) on pH **(A)** and β_{DIC} (**B**, μmol kg^{-1}) within the estuary. The dashed lines show the effect of different H_2CO_3 dissociation constants on calculated $\mathrm{pH}_{\mathrm{est}}$ [solid line: Millero, 2010 (M10), dash line: Cai and Wang, 1998 (CW98), and dotted line: Lueker et al., 2000 (L00)].

Further, we identified which factors were the most important to the observed pH trends and determined if these factors differ between the two estuaries studied. While it is beyond the scope of this study to precisely quantify the many components affecting pH, we shed some light on the diverse drivers of estuarine acidification, a process that has gained interest in recent years.

Increases in river discharge [associated with ENSO activity (**Supplementary Figure S2**) during the Spring and Winter], coincided with a significant trend of acidification in the NeuseRE between 2005 and 2017. Acidification was greatest in bottom waters, concurrent with increased PPR in the surface, highlighting the importance of CO_2 inputs from net ecosystem respiration. Temporal trends in pH across the NewRE were small and not significant, despite moderate, but generally insignificant increases in phytoplankton biomass and productivity. Small, insignificant warming trends in both estuaries could not explain the observed bottom-water pH decrease. However, in the NewRE, this acidification 'pressure' was largely tempered by riverine loading of TA, which was higher relative to DIC. Inputs of TA from the Neuse River were smaller, however, leading to a weak buffer capacity that was more sensitive to autochthonous and allochthonous CO_2 inputs (**Figure 5**). While it is beyond the scope of this study to rigorously asses climate teleconnections like those between ENSO and annual-scale biogeochemical change, this topic may be of interest for future research, given the likely variations in ENSO with climate change.

Rising atmospheric CO_2 levels will act as a downward pressure on estuarine pH, but will be modified the net production or consumption of CO_2 by net ecosystem metabolism. Thus, in other stratified estuaries experiencing eutrophication, net respiratory inputs of CO_2 to bottom waters may interact with this anthropogenic CO_2 to geometrically lower pH. Meanwhile, concurrent change in river discharge (due to precipitation or human water consumption) have the potential to either enhance or ameliorate these acid inputs, although to an extent that varies according to differences in underlying lithology and hydrology. Hence, all estuaries experiencing future changes in river discharge may experience similar pH trajectories due to the interaction between atmospheric CO_2 inputs and riverine hydrogeochemistry. Local decision makers and stakeholders should consider these factors when considering management strategies aimed at coping with future estuarine acidification.

DATA AVAILABILITY

The DCERP (https://dcerp.rti.org/) and ModMon (http://paerllab.web.unc.edu/projects/modmon/products-and-applications/) datasets are published on the data sharing repository Figshare (https://figshare.com/articles/WQ_Datasets_-_Decadal_Acidification_Trends/7643195).

AUTHOR CONTRIBUTIONS

BVD and HW contributed equally to the conception and design of the study.

FUNDING

This research was funded by SERDP-DCERP project RC-2245, the North Carolina Department of Environmental Quality (ModMon Program), the Lower Neuse Basin Association, NC Sea Grant, and the UNC Water Resources Research Institute.

ACKNOWLEDGMENTS

We thank Hans Paerl, Betsy Abare, Jeremey Braddy, Karen Rossignol, and Randy Sloup of the University of North Carolina at Chapel Hill, Institute of Marine Sciences, for compiling and maintaining ModMon and DCERP databases. Xinping Hu offered valuable guidance during the preparation of this manuscript. We also thank the organizers of the 2017 Coastal and Estuarine Research Federation conference, at which the concept for this manuscript was conceived.

SUPPLEMENTARY MATERIAL

The Supplementary Material for this article can be found online at: https://www.frontiersin.org/articles/10.3389/fmars.2019.00136/full#supplementary-material

REFERENCES

Aufdenkampe, A. K., Mayorga, E., Raymond, P. A., Melack, J. M., Doney, S. C., Alin, S. R., et al. (2011). Riverine coupling of biogeochemical cycles between land, oceans, and atmosphere. *Front. Ecol. Environ.* 9:53–60. doi: 10.1890/100014

Bates, N., Astor, Y., Church, M., Currie, K., Dore, J., and Gonaález-Dávila, M. (2014). A time-series view of changing ocean chemistry due to ocean uptake of anthropogenic CO2 and ocean acidification. *Oceanography* 27, 126–141. doi: 10.5670/oceanog.2014.16

Baumann, H., and Smith, E. M. (2017). Quantifying metabolically driven pH and oxygen fluctuations in US nearshore habitats at diel to interannual time scales. *Estuaries Coasts* 41, 1102–1117. doi: 10.1007/s12237-017-0321-3

Boyer, J. N., Christian, R. R., and Stanleyl, D. W. (1993). Patterns of phytoplankton primary productivity in the Neuse River estuary, North Carolina, USA. *Mar. Ecol. Prog. Ser.* 97, 287–297. doi: 10.3354/meps097287

Cai, W. J., Hu, X., Huang, W. J., Murrell, M. C., Lehrter, J. C., and Lohrenz, S. E. (2011). Acidification of subsurface coastal waters enhanced by eutrophication. *Nat. Geosci.* 4, 766–770. doi: 10.1038/ngeo1297

Cai, W. J., Huang, W. J., Luther, G. W., Pierrot, D., Li, M., and Testa, J. (2017). Redox reactions and weak buffering capacity lead to acidification in the Chesapeake Bay. *Nat. Commun.* 8:369. doi: 10.1038/s41467-017-00417-7

Cai, W.-J., and Wang, Y. (1998). The chemistry, fluxes, and sources of carbon dioxide in the estuarine waters of the Satilla and Altamaha Rivers, Georgia. *Limnol. Oceanogr.* 43, 657–668. doi: 10.4319/lo.1998.43.4.0657

Couldrey, M. P., Oliver, K. I. C., Yool, A., Halloran, P. R., and Achterberg, E. P. (2016). On which timescales do gas transfer velocities control North Atlantic

CO2 flux variability? Global biogeochem. *Cycles* 30, 787–802. doi: 10.1002/2015GB005267

Crosswell, J. R., Anderson, I. C., Stanhope, J. W., Dam, B. V., Brush, M. J., and Ensign, S. (2017). Carbon budget of a shallow, lagoonal estuary: transformsink dynamics along the river-estuary-ocean continuum. *Limnol. Oceanogr.* 62, S29–S45. doi: 10.1002/lno.10631

Crosswell, J. R., Paerl, H. W., Wetz, M. S., and Hales, B. (2012). Air-water CO2 fluxes in the microtidal Neuse River Estuary, North Carolina. *J. Geophys. Res.* 117:12. doi: 10.1029/2012JC007925

Cyronak, T., Andersson, A. J., D'Angelo, S., Bresnahan, P., Davidson, C., and Griffin, A. (2018). Short-term spatial and temporal carbonate chemistry variability in two contrasting seagrass meadows: implications for pH buffering capacities. *Estuaries Coasts* 41, 1282–1296. doi: 10.1007/s12237-017-0356-5

Doney, S. C., Fabry, V. J., Feely, R. A., and Kleypas, J. A. (2009). Ocean acidification: the other CO2 problem. *Ann. Rev. Mar. Sci.* 1, 169–192. doi: 10.1146/annurev.marine.010908.163834

Doney, S. C., and Schimel, D. S. (2007). Carbon and climate system coupling on timescales from the precambrian to the anthropocene. *Annu. Rev. Environ. Resour.* 32, 31–66. doi: 10.1146/annurev.energy.32.041706.124700

Egleston, E. S., Sabine, C. L., and Morel, F. M. M. (2010). Revelle revisited: buffer factors that quantify the response of ocean chemistry to changes in DIC and alkalinity. *Global Biogeochem. Cycles* 24, 1–9. doi: 10.1029/2008GB003407

Fear, J. M., Paerl, H. W., and Braddy, J. S. (2007). Importance of submarine groundwater discharge as a source of nutrients for the Neuse River Estuary, North Carolina. *Estuaries Coasts* 30, 1027–1033. doi: 10.1007/BF02841393

Feely, R. A., Alin, S. R., Newton, J., Sabine, C. L., Warner, M., Devol, A., et al. (2010). The combined effects of ocean acidification, mixing, and respiration on pH and carbonate saturation in an urbanized estuary. *Estuar. Coast. Shelf Sci.* 88, 442–449. doi: 10.1016/j.ecss.2010.05.004

Hall, N. S., Paerl, H. W., Peierls, B. L., Whipple, A. C., and Rossignol, K. L. (2012). Effects of climatic variability on phytoplankton community structure and bloom development in the eutrophic, microtidal, New River Estuary, North Carolina, USA. *Estuar. Coast. Shelf Sci.* 117, 70–82. doi: 10.1016/j.ecss.2012.10.004

Herrmann, M., Najjar, R. G., Kemp, W. M., Alexander, R. B., Boyer, E. W., Cai, W.-J., et al. (2015). Net ecosystem production and organic carbon balance of U.S. East Coast estuaries: a synthesis approach. *Global Biogeochem. Cycles* 29, 96–111. doi: 10.1002/2013GB004736

Hu, X., and Cai, W. J. (2011). An assessment of ocean margin anaerobic processes on oceanic alkalinity budget. *Glob. Biogeochem. Cycles* 25, 1–11. doi: 10.1029/2010GB003859

Hu, X., and Cai, W. J. (2013). Estuarine acidification and minimum buffer zone. A conceptual study. *Geophys. Res. Lett.* 40, 5176–5181. doi: 10.1002/grl.51000

Hu, X., Pollack, J. B., McCutcheon, M. R., Montagna, P. A., and Ouyang, Z. (2015). Long-term alkalinity decrease and acidification of estuaries in northwestern Gulf of Mexico. *Environ. Sci. Technol.* 49, 3401–3409. doi: 10.1021/es505945p

Jeffrey, L. C., Maher, D. T., Santos, I. R., McMahon, A., and Tait, D. R. (2016). Groundwater, acid and carbon dioxide dynamics along a coastal wetland, lake and estuary continuum. *Estuaries Coasts* 39, 1325–1344. doi: 10.1007/s12237-016-0099-8

Keeling, R. F., and Keeling Charles, D. (2017). *Atmospheric Monthly In Situ CO2 Data - MaunaLoa Observatory, Hawaii. In Scripps CO2 Program Data. UC San Diego Library Digital Collections*. Available at: http://doi.org/10.6075/J08W3BHW

Le Quéré, C., Andrew, R. M., Canadell, J. G., Sitch, S., Korsbakken, J. I., and Peters, G. P. (2016). Global Carbon Budget 2016. *Earth Syst. Sci. Data Discuss.* 8, 605–649. doi: 10.5194/essd-8-605-2016

Lewis, E., and Wallace, D. (1998). *Program Developed for CO2 System Calculations*. Oak Ridge, TN: Carbon Dioxide Information Analysis Center. doi: 10.2172/639712

Lueker, T. J., Dickson, A. G., and Keeling, C. D. (2000). Ocean pCO2 calculated from dissolved inorganic carbon, alkalinity and equations K1 and K2: validation based on laboratory measurements of CO2 in gas and seawater at equilibrium. *Mar. Chem.* 70, 105–119. doi: 10.1016/S0304-4203(00)00022-0

Mallin, M., Paerl, H. W., Rudek, J., and Bates, P. (1993). Regulation of estuarine primary production by watershed rainfall and river flow. *Mar. Ecol. Prog. Ser.* 93, 199–203. doi: 10.3354/meps093199

Mallin, M. A., McIver, M. R., Wells, H. A., Parsons, D. C., and Johnson, V. L. (2005). Reversal of eutrophication following sewage treatment upgrades in the New River Estuary. North Carolina. *Estuaries* 28, 750–760. doi: 10.1007/BF02732912

Millero, F. J. (2010). Carbonate constants for estuarine waters. *Mar. Freshw. Res.* 61, 139–142. doi: 10.1071/MF09254

Mote, P. W., Parson, E., Hamlet, A. F., Keeton, W. S., Lettenmaier, D., and Mantua, N. (2008). Preparing for climatic change: the water, salmon, and forests of the Pacific Northwest. *Clim. Change* 61, 45–88. doi: 10.1023/A:1026302914358

Müller, J. D., Schneider, B., and Rehder, G. (2016). Long-term alkalinity trends in the Baltic Sea and their implications for CO2-induced acidification. *Limnol. Oceanogr.* 61, 1984–2002. doi: 10.1002/lno.10349

Nixon, S. W., Oczkowski, A. J., Pilson, M. E. Q., Fields, L., Oviatt, C. A., Hunt, C. W., et al. (2015). On the response of pH to inorganic nutrient enrichment in well-mixed coastal marine waters. *Estuaries Coasts* 38, 232–241. doi: 10.1007/s12237-014-9805-6

Null, K. A., Corbett, D. R., DeMaster, D. J., Burkholder, J. M., Thomas, C. J., Reed, R. E., et al. (2011). Porewater advection of ammonium into the Neuse River Estuary, North Carolina, USA. *Estuar. Coast. Shelf Sci.* 95, 314–325. doi: 10.1016/j.ecss.2011.09.016

Pacella, S. R., Brown, C. A., Waldbusser, G. G., Labiosa, R. G., and Hales, B. (2018). Seagrass habitat metabolism increases short-term extremes and long-term offset of CO2 under future ocean acidification. *PNAS* 115, 1–6. doi: 10.23719/1407616

Paerl, H. W., Pinckney, J., Fear, J., and Peierls, B. L. (1998). Ecosystem responses to internal and watershed organic matter loading: consequences for hypoxia in the eutrophying Neuse River Estuary, North Carolina, USA. *Mar. Ecol. Prog. Ser.* 166, 17–25. doi: 10.3354/meps166017

Peierls, B. L., Hall, N. S., and Paerl, H. W. (2012). Non-monotonic responses of phytoplankton biomass accumulation to hydrologic variability: a comparison of two coastal plain north carolina estuaries. *Estuaries Coasts* 35, 1376–1392. doi: 10.1007/s12237-012-9547-2

Phlips, E. J., Badylak, S., Hart, J., Haunert, D., Lockwood, J., and O'Donnell, K. (2011). Climatic influences on autochthonous and allochthonous phytoplankton blooms in a subtropical estuary, St. Lucie Estuary, Florida, USA. *Estuaries Coasts* 35, 335–352. doi: 10.1007/s12237-011-9442-2

Reimer, J. J., Wang, H., Vargas, R., and Cai, W.-J. (2017). Multidecadal fCO2 increase along the United States Southeast Coastal Margin. *J. Geophys. Res. Ocean* 122, 10061–10072. doi: 10.1002/2017JC013170

Siam, M. S., and Eltahir, E. A. B. (2017). Climate change enhances interannual variability of the Nile river flow. *Nat. Clim. Chang.* 7, 350–354. doi: 10.1038/nclimate3273

Takahashi, T., Sutherland, S. C., Chipman, D. W., Goddard, J. G., and Ho, C. (2014). Climatological distributions of pH, pCO2, total CO2, alkalinity, and CaCO3saturation in the global surface ocean, and temporal changes at selected locations. *Mar. Chem.* 164, 95–125. doi: 10.1016/j.marchem.2014.06.004

Unsworth, R. K. F., Collier, C. J., Henderson, G. M., and McKenzie, L. J. (2012). Tropical seagrass meadows modify seawater carbon chemistry: implications for coral reefs impacted by ocean acidification. *Environ. Res. Lett.* 7:024026. doi: 10.1088/1748-9326/7/2/024026

Van Dam, B. R., Crosswell, J. R., Anderson, I. C., and Paerl, H. W. (2018a). Watershed-Scale Drivers of Air-Water CO2Exchanges in Two Lagoonal North Carolina (USA) Estuaries. *J. Geophys. Res. Biogeosci.* 123, 271–287. doi: 10.1002/2017JG004243

Van Dam, B. R., Crosswell, J. R., and Paerl, H. W. (2018b). Flood-driven CO2 emissions from adjacent North Carolina estuaries during Hurricane Joaquin (2015). *Mar. Chem.* 207, 1–12. doi: 10.1016/j.marchem.2018.10.001

Waldbusser, G. G., and Salisbury, J. E. (2014). Ocean acidification in the coastal zone from an organism's perspective: multiple system parameters, frequency domains, and habitats. *Ann. Rev. Mar. Sci.* 6, 221–247. doi: 10.1146/annurev-marine-121211-172238

Wang, H., Hu, X., Cai, W. J., and Sterba-Boatwright, B. (2017). Decadal fCO2 trends in global ocean margins and adjacent boundary current-influenced areas. *Geophys. Res. Lett.* 44, 8962–8970. doi: 10.1002/2017GL074724

Wang, H., Hu, X., and Sterba-Boatwright, B. (2016). A new statistical approach for interpreting oceanic fCO2 data. *Mar. Chem.* 183, 41–49. doi: 10.1016/j.marchem.2016.05.007

Wang, Z. A., Kroeger, K. D., Ganju, N. K., Gonneea, M. E., and Chu, S. N. (2016). Intertidal salt marshes as an important source of inorganic carbon to the coastal ocean. *Limnol. Oceanogr.* 61, 1916–1931. doi: 10.1002/lno.10347

Conflict of Interest Statement: The authors declare that the research was conducted in the absence of any commercial or financial relationships that could be construed as a potential conflict of interest.

frontiers
in Marine Science

ORIGINAL RESEARCH
published: 14 March 2019
doi: 10.3389/fmars.2019.00062

Variability of Seawater Chemistry in a Kelp Forest Environment Is Linked to *in situ* Transgenerational Effects in the Purple Sea Urchin, *Strongylocentrotus purpuratus*

Umihiko Hoshijima*† and Gretchen E. Hofmann

Department of Ecology, Evolution and Marine Biology, University of California, Santa Barbara, Santa Barbara, CA, United States

Edited by:
Iris Eline Hendriks,
Universitat de les Illes Balears, Spain

Reviewed by:
Christopher Edward Cornwall,
Victoria University of Wellington,
New Zealand
Laura Ramajo,
Adolfo Ibáñez University, Chile

***Correspondence:**
Umihiko Hoshijima
uhoshiji@ucsc.edu;
umihoshijima@gmail.com

†Present address:
Umihiko Hoshijima,
Ecology and Evolutionary Biology,
University of California, Santa Cruz,
Santa Cruz, CA, United States

Specialty section:
This article was submitted to
Global Change and the Future Ocean,
a section of the journal
Frontiers in Marine Science

Received: 18 October 2018
Accepted: 05 February 2019
Published: 14 March 2019

Citation:
Hoshijima U and Hofmann GE (2019) Variability of Seawater Chemistry in a Kelp Forest Environment Is Linked to in situ Transgenerational Effects in the Purple Sea Urchin, Strongylocentrotus purpuratus. Front. Mar. Sci. 6:62. doi: 10.3389/fmars.2019.00062

While the value of giant kelp (*Macrocystis pyrifera*) as a habitat-forming foundation species is well-understood, it is unclear how they impact the oxygen concentration and pH of the surrounding seawater, and further, how such a dynamic abiotic environment will affect eco-evolutionary dynamics in a context of global change. Here, we profiled the nearshore kelp forest environment in Southern California to understand changes in dissolved oxygen (DO) and pH with high spatiotemporal resolution. We then examined transgenerational effects using sea urchins (*Strongylocentrotus purpuratus*) as our study organism. Using enclosures on the benthos, we conditioned adult sea urchins *in situ* at two locations – one inside the kelp forest and one outside the kelp forest. After a 11-week conditioning period timed to coincide with gametogenesis in the adults, the urchins were collected, spawned, and cultures of their progeny were raised in the laboratory in order to assess their performance to simulated ocean acidification. In terms of the physical observations, we observed significant changes in DO and pH not only when comparing sites inside and outside of the kelp forest, but also between surface and benthic sensors at the same site. DO and pH at the benthos differed in mean, the amplitude of the diel signal, and in the profile of background noise of the signal. Ultimately, these results indicated that both DO and pH were more predictably variable inside of the kelp forest environment. On the biological side, we found that adult sea urchins inside the kelp forest produced more protein-rich eggs that developed into more pH-resilient embryos. Overall, this study in a temperate kelp forest ecosystem is one of the first studies to not only observe biological response to highly characterized environmental variability *in situ*, but also to observe such changes in a transgenerational context.

Keywords: pH, dissolved oxygen, coastal variability, *Strongylocentrotus purpuratus*, sea urchin, kelp forest, *Macrocystis pyrifera*, transgenerational plasticity

INTRODUCTION

The role of macrophytes in raising the pH of seawater on a local scale while also locally increasing levels of dissolved oxygen (DO) (McLeod et al., 2011; Nielsen et al., 2018) has been recognized in a suite of coastal marine ecosystems (Hofmann et al., 2011; Unsworth et al., 2012; Guadayol et al., 2014; Hendriks et al., 2014; Baumann et al., 2015; Kline et al., 2015; Sorte and Bracken, 2015; Kapsenberg and Hofmann, 2016; Kroeker et al., 2016; Kwiatkowski et al., 2016; Kapsenberg et al., 2017; Silbiger and Sorte, 2018). These mean differences, as well as the increased diurnal variation of both pH and DO in these submerged underwater vegetation (SUV) systems has been observed in seagrasses (Unsworth et al., 2012; Hendriks et al., 2014; Oreska et al., 2017; Nielsen et al., 2018; Pacella et al., 2018) and kelp forest environments (Delille et al., 2009; Frieder et al., 2012; Britton et al., 2016; Kapsenberg and Hofmann, 2016), raising the question of whether these habitats could become a refuge for climate change in the near future (McLeod et al., 2011). While some studies strive to investigate this link by mimicking environmental variation in the lab (Alenius and Munguia, 2012; Dufault et al., 2012; Cornwall et al., 2013; Kim et al., 2013; Comeau et al., 2014; Frieder et al., 2014; Gradoville et al., 2014; Roleda et al., 2015; Britton et al., 2016; Clark and Gobler, 2016; Davidson et al., 2016; Eriander et al., 2016; Keppel et al., 2016; Li et al., 2016; Small et al., 2016), only a handful of studies in marine systems have directly investigated the ecological or biological consequences for metazoan residents of these macrophyte-dominated habitats (Smith, 2016). In this study, we aimed to close this gap in knowledge by examining how seawater conditions in Southern California kelp forests could affect transgenerational plasticity (TGP) in a key calcifying grazer species.

The physiochemical patterns in kelp forests along the California Current Large Marine Ecosystem (CCLME) have yielded observations that signal the significance of short spatial scales and temporal variation for this nearshore ecosystem (Frieder et al., 2012; Hofmann et al., 2013; Chan et al., 2017; Koweek et al., 2017). Particularly of note is the strong high-frequency covariation of pH and DO as multiple stressors in these nearshore environments (Frieder et al., 2012; Breitburg et al., 2015; Gunderson et al., 2016) that interact with a mosaic of coastal upwelling along the coastline (Chan et al., 2017). These patterns all suggest that adult organisms in the benthic environment, in particular, likely experience a range of pH as well as DO, and this gradient will vary in location and with proximity to macrophytes. Understanding such relationships will help to elucidate the future of these coastal oceans to complex environmental change (Gunderson et al., 2016; Vargas et al., 2017).

From a biological perspective, these variations in the abiotic environment have the potential to alter resident biota in both direct and indirect pathways, while also altering ecological-evolutionary dynamics. In metazoans, the variable and coupled pH/oxygen environment can interact to alter a suite of biological performance metrics including behavioral and physiological processes (Todgham and Stillman, 2013; Frieder et al., 2014; Stillman and Armstrong, 2015; Gunderson et al., 2016; Cornwall et al., 2018). In addition, more complex processes such as TGP may play a defining role in shaping the eco-evolutionary trajectory of nearshore organisms to future environmental conditions (Marshall, 2008; Salinas and Munch, 2012; Munday et al., 2013; Hofmann, 2017; Chirgwin et al., 2018). Here, processes such as maternal effects and TGP have the potential to alter the environmental tolerances of organisms on observable timescales more relevant to the rapid rate of global change, even potentially facilitating evolutionary rescue through an acceleration in genetic evolution (Price et al., 2003; Marshall et al., 2016). In this study, we investigated the potential for a predominant form of TGP, maternal effects, to alter the performance of an ecologically important kelp forest grazer's progeny (the purple sea urchin, *Strongylocentrotus purpuratus,* Pearse, 2006) in the presence or absence of a kelp forest environment in the CCLME.

The purple sea urchin has long been acknowledged as a key species in driving community-level dynamics, notably by grazing down canopy-forming kelp and creating urchin barrens as an alternate stable state (Pearse, 2006; Filbee-Dexter and Scheibling, 2014). As an invertebrate with aragonite spicules and tests potentially vulnerable to undersaturated ocean conditions (Wilt, 2002), the fate of *S. purpuratus* to future ocean change has been heavily studied in an attempt to predict its impact on the future nearshore environment along its range (Stumpp et al., 2011; Yu et al., 2011; Kelly et al., 2013; Wong et al., 2018). Furthermore, previous studies have already shown that transgenerational effects on progeny traits can arise from adult acclimation to current-day upwelling conditions (Wong et al., 2018). Thus, we anticipate that TGP may be impacted during gametogenesis conducted *in situ* in the variable nearshore environment of the kelp forest.

The principal objective of this study was to profile the pH and DO of the nearshore kelp forest environment, then to utilize *S. purpuratus* to investigate whether or not the presence or absence of this kelp forest environment would affect the quality of the offspring. We predict that the kelp forest may provide a more favorable environment for adult sea urchins, thus allowing for the generation of offspring more resilient and resistant to extremes of environmental conditions that could be created by natural processes (e.g., intense coastal upwelling or future ocean acidification).

MATERIALS AND METHODS

Deployment Site

Sensor deployments and the urchin caging experiment were co-located at a study site on Mohawk Reef (MKO) near Santa Barbara, CA, United States (**Figure 1**). MKO is a shallow, rocky temperate reef defined by kelp beds of giant kelp (*Macrocystis pyrifera*); although varying with year and season, these beds typically extend 300 m along-shore and from 120 to 200 m cross-shore (Gaylord et al., 2007). MKO is also a permanent long-term research site for the Santa Barbara Coastal Long-Term Ecological Research (SBC LTER) group, where the mediation of kelp forest dynamics by abiotic factors such as water

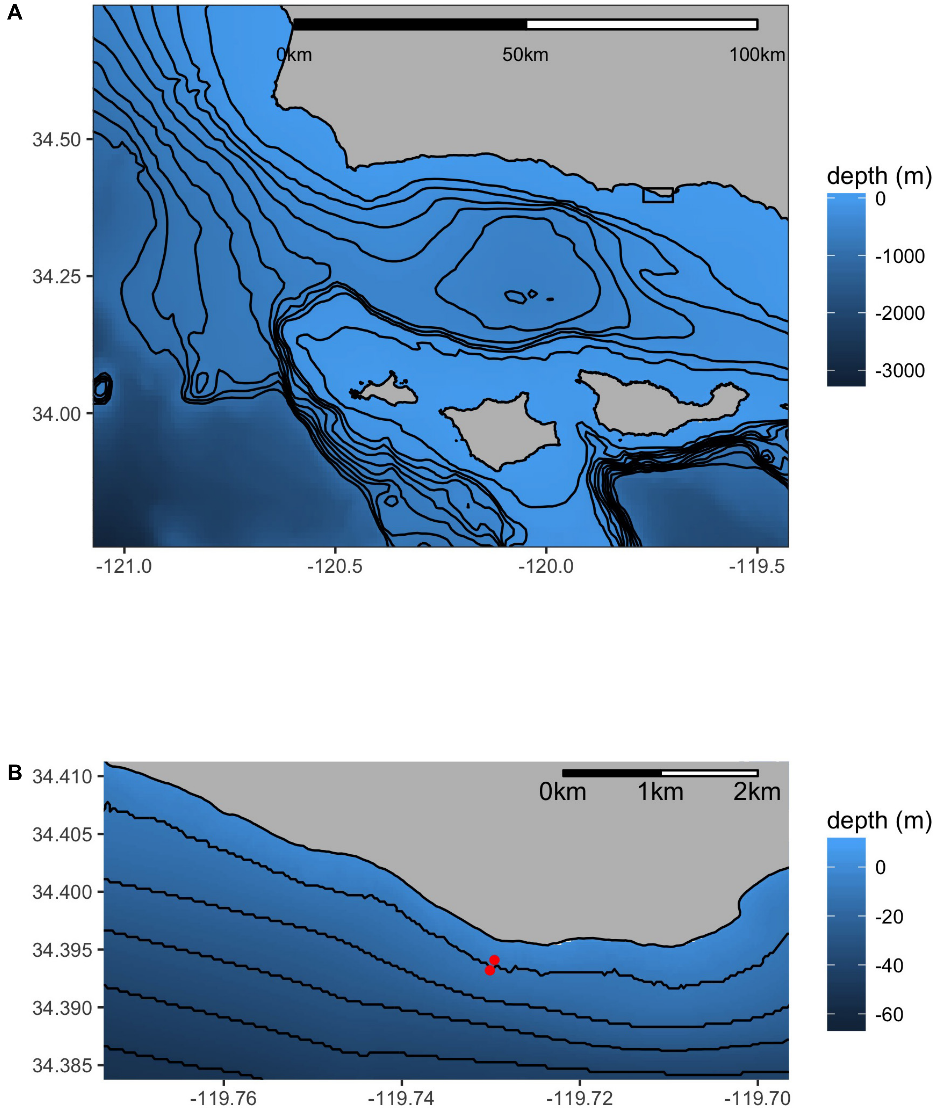

FIGURE 1 | Map of the research site – Mohawk Reef (MKO). The inset **(B)** details the sites relative to the coastline in close proximity (130 m apart). The "inside" site is northwest (inshore) of the "outside" site. Isobaths are 100 m **(A)** or 10 m **(B)**.

attenuation (Gaylord et al., 2007) and wave action (Reed et al., 2011) have been well-characterized.

The sensor deployments were located at one of two locations at MKO: the inshore site was situated inside of the kelp forest at a depth of 7 m (34.3941°N, 119.7296°W), while the offshore site was located outside of the kelp forest, in an area that completely lack kelp and had a sandy substrate at a depth of 11 m (34.3932°N, 119.7301°W). These two locations were <100 m apart, and will hereafter be referred to as the "inside" and "outside" locations, respectively (**Figure 1**).

Sensor Deployments

For this study of the kelp forest environment, three types of deployments, each with a different aim and sensor configuration, were conducted from June 2014 to December 2016. The details regarding each of the three deployments are described below:

Sensor Deployment 1: Dense Oxygen Sensor Deployments Inside and Outside of a Kelp Forest Environment

To understand the differences in daily changes of oxygen content inside and outside of the kelp forest environment, oxygen sensors (PME miniDOT®) were deployed at three different depths at each mooring: (1) just below the mean low tide on the buoy, (2) in the middle of the water column, and (3) 1 m off the bottom. Hereafter, these will be referred to as the "**top,**" "**middle,**" and "**bottom**" positions, respectively. Sensors were programmed to log every 10 min, and were deployed for 20 days (June 2–June 23, 2014). Sensors were retrieved and data were analyzed for patterns of oxygen dynamics as a function of depth and proximity to the kelp forest.

Sensor Deployment 2: Comparing Benthic pH–Oxygen Relationships Inside and Outside of a Kelp Forest Environment

To compare benthic relationships between pH, oxygen, and *in situ* temperature inside and outside of a kelp forest, SeapHOx® sensors (equipped with a Honeywell DuraFET® III pH electrode, an Aanderaa® 3835 oxygen optode, and Seabird® SBE-37 microCAT CTD) (Martz et al., 2010; McLaughlin et al., 2017) were deployed 1 m off the bottom at both the inside and outside spar buoy locations for 4 weeks (March 10–April 08, 2015). Sensors were programmed to log every 20 min. The relationship between pH and oxygen was modeled linearly following Frieder et al. (2012) due to the strong linearity of this theoretically non-linear relationship over the observed range.

Sensor Deployment 3: Seasonal Variation of pH and Oxygen in a Kelp Forest Environment

To ascertain the seasonal variation in the pH and oxygen dynamics in the kelp forest environment, an array of miniDOT® and SeapHOx® sensors were deployed at MKO from March 2016 to December 2016. Three miniDOT® sensors were placed inside of the kelp forest at the same three depths as in Deployment 1. Concurrently, one SeapHOx® sensor was placed 1 m off the bottom at the outside mooring, identical to the outside mooring site in Deployment 1. miniDOT® sensors were replaced approximately every 3 months, and SeapHOx® sensors were replaced approximately every 2 months. All sensors in deployment 3 were programmed to log every 20 min. Due to sensor failure, oxygen and temperature at the top of the water column at the inside mooring was not collected past August 03, 2016. Due to logistic constraints of deployment, pH, oxygen, and temperature at the bottom on the outside mooring was not collected past October 03, 2016.

Sensor Calibrations and Water Sampling

Sensors were deployed using established best practice techniques (Bresnahan et al., 2014; Kapsenberg and Hofmann, 2016; Rivest et al., 2016). Briefly, pH samples, coinciding with a sensor sampling timepoint, were collected during the sensor deployments using SCUBA to trigger GO-FLO sampling bottles (General Oceanics) underwater. These samples were immediately fixed with $HgCl_2$ at 0.02% and stored at 15°C until analyzed using a spectrophotometric pH assay (unpurified *m*-Cresol, Sigma-Aldrich®, assayed in a Shimadzu UV-1800 spectrophotometer at 730 nm, 578 nm, and 434 nm at 25°C) and an open-cell endpoint titration for total alkalinity (certified 0.1M HCl 0.6M NaCl titrant, using a Mettler-Toledo T50 autotitrator calibrated with a certified Tris buffer at 35‰ NaCl and pH 7) (Dickson et al., 2007). Total alkalinity was calculated from raw autotitrator electrode values using the R package *seacarb* (Gattuso et al., 2017), which was subsequently used to calculate pH for *in situ* conditions. These pH calibration samples were then used to calibrate the data using *seacarb*.

For oxygen measurements, multiple sensors were placed in the same flow-through sea table tanks to ensure precision before and after each deployment, and Winkler titrations were conducted to ensure accuracy after each deployment (Wetzel and Likens, 1991). Oxygen concentration was calculated from oxygen saturation using relationships from Weiss (1970) (R package *marelac* v.2.1.6) using salinity values from the long-term mooring time series maintained in the SBC LTER program's database (Washburn, 2018).

Adult Sea Urchin Outplants Paired With Oxygen Sensors

Adult sea urchins were collected from the kelp forest at MKO (under California Department of Fish and Wildlife Scientific Collecting permit #SC-1223) in August 2017. To ensure that the bulk of sea urchin gametogenesis occurred during the caged outplants, urchins were pre-spawned before outplants with an electric current (9 V DC for three 5-s shocks, Professor Kathy Foltz, UC Santa Barbara, personal communication). Shock spawning was preferred for this step, as it is a less invasive process than the KCl injection typically used for urchin spawning (Gago and Luís, 2011).

Urchin cages were constructed out of 1-inch PVC-coated welded wire fencing shaped into cylinders 50 cm in length and 30 cm in diameter. For this field experiment, 6 outplant cages were deployed using SCUBA: (1) three replicate cages were placed inside the kelp forest on the benthos, anchored to weights in ∼7 m of water, and (2) three cages were placed outside of the kelp forest on the benthos, attached to both weights and a 1 m sand anchor in ∼11 m of water. To begin the acclimatization period, each of the six cages was loaded with 10 adult sea urchins on August 27, 2017. Cages were revisited by SCUBA every 2 weeks and urchins were fed liberally with giant kelp, *Macrocystis pyrifera*, collected at MKO. Urchins were retrieved from the cages on November 14, 2017 after 79 days of acclimatization at MKO and brought back to laboratory seawater facilities at UC Santa Barbara for egg collection and the embryo culturing experiment. Each set of cages was paired with a miniDOT® oxygen sensor, which was programmed to collect oxygen data throughout the deployment period at 10-min intervals. During this period, one sensor deployed for this experiment failed (on the outside mooring). As a result, the data presented here were collected by an identical miniDOT® sensor deployed 1 m away (Washburn, 2018), a part of the SBC LTER sensor array at MKO.

Culturing the Early Stage Urchins Under Variable pCO_2 Conditions in the Laboratory

After 79 days of conditioning in the cages, adult urchins were collected on November 14, returned to the lab, and spawned within 24 h. Spawning was induced via injection of 1.0M KCl with intermittent shaking. For the fertilization step, eggs from five females from each maternal exposure treatment (inside vs. outside the kelp forest) were crossed with sperm from one male urchin from the same treatment. Care was taken to ensure that an identical number of eggs contributed from each female was represented in the pooled egg population. At this time, prior to fertilization, samples of eggs (n = 1,000 in three cryovials) were also collected for further analysis; these samples were flash frozen in liquid nitrogen and stored at −80°C prior to analyses. These eggs are designated as "**I**" or "**O**" for "Inside" and "Outside," corresponding to the location of the adults during conditioning in the field. In addition to these samples, egg yield from every spawned female was recorded as an estimate of fecundity. Test diameter was also measured to the nearest millimeter for all females.

For culturing, embryos were raised at 15°C using $p\text{CO}_2$ conditions chosen to reflect present-day relaxed and upwelling (Feely et al., 2008) conditions (400 μatm $p\text{CO}_2$ and 1000 μatm $p\text{CO}_2$, respectively). Gases of these CO_2 partial pressures were first created using mass-flow controllers (Sierra Manufacturing, SmartTrak 101 and 100L); they were then equilibrated in seawater using venturi injectors in 20L header tanks. Seawater from the header tanks was pumped to flow-through culturing tanks through irrigation drippers (Fangue et al., 2010). For each treatment, one header tank supplied three replicate flow-through culturing tanks in a pseudoreplicate design.

To calculate $p\text{CO}_2$ values, the carbonate system was parameterized by measuring spectrophotometric pH and total alkalinity titration as described earlier for sensor calibration samples, with the exception that the pH samples were not fixed with HgCl_2 and instead were analyzed immediately. These culturing conditions created in the laboratory setting are labeled "**L**" and "**H**" for "Low" and "High," and the crossed maternal conditioning and embryo treatments were named with a combination of these two codes: e.g., "**IL**" indicates embryos spawned from parents conditioned inside of the kelp forest, were then raised in a low-$p\text{CO}_2$ environment.

To assess the consequences of differential maternal environments on egg quality, three metrics were measured in collected eggs: **(1)** average egg length over three different axes (n = 30 per mother), **(2)** egg area (n = 30 per mother), and **(3)** total protein content (n = 3 tubes of 1,000 eggs per female). In addition, two measures were taken for each adult female urchin: **(1)** total number of eggs spawned after KCl injection, and **(2)** test diameter. Furthermore, to assess the impact of maternal conditioning on embryo traits and development, three metrics of hatched blastula embryos were measured: **(1)** embryo length over the major axis (n = 30 per replicate culture vessel), **(2)** embryo area (n = 30 per replicate culture vessel), and **(3)** embryo total protein content (n = 3 tubes of 1,000 embryos per replicate culture vessel).

Egg and Embryo Morphometrics

Eggs collected from the conditioned *S. purpuratus* females were preserved in 2% formalin in seawater, and imaged using a trinocular compound light microscope (Olympus BX50) equipped with a digital camera (Lumenera Infinity Lite), along with a computer running the associated imaging software (Infinity Capture v. 6.2.0). All samples were imaged within 30 days of the spawning event which occurred on November 15, 2017 and 40 images were captured for each egg sample.

Using these images for morphometric analysis, 30 eggs were measured from each female using ImageJ software (Schneider et al., 2012). In addition, 30 hatched blastula embryos were measured from each replicate embryo culturing vessel. For eggs, both average diameter and two-dimensional area were measured. As hatched blastula embryos are more ellipsoidal, the major axis (longest diameter that intersects the center) was chosen as a representative diameter. Two-dimensional area was also measured for these embryos (**Supplementary Figure 1**).

Biochemical Analyses

Three replicate tubes of 1,000 eggs were collected from each female for determination of total protein content. The tubes were gently centrifuged to pellet the eggs, excess seawater was removed, and the sample was then frozen in liquid nitrogen prior to storage at −80°C until use in further analysis. Three replicate tubes of 1,000 embryos were collected from each replicate embryo culturing vessel and preserved as described above for the eggs.

Embryos and eggs were processed using methods adapted from Prowse et al. (2007) and Byrne et al. (2008). Briefly, samples were re-suspended and sonicated in a lysis buffer (20 mM Tris-HCl, 130 mM NaCl, 5 mM EDTA, 1% Triton X-100, 1% Sigma-Aldrich Protease Inhibitor Cocktail, pH 7.6). The resulting homogenates were used in the BCA protein assay within 72 h of extraction. Protein content assays were performed using a microplate BCA protein assay (Catalog number 23225, Pierce Biotechnology) according to the manufacturer's instructions.

Data Analysis

All statistics and analysis were conducted using the R statistical software, as well as the R Studio IDE (RStudio Team, 2017).

Time Series Analysis

All power spectral density (PSD) estimates were conducted with five overlapping Hanning windows (50%) for 10 degrees of freedom (R package *signal*, v. 0.7–6) with 95% confidence intervals calculated from an inverse chi-square distribution. Beta statistics (β), or "environmental color" for time series were calculated monthly for DO values collected by each sensor for Deployment 3. After removing the diurnal signal using a moving average filter, β was calculated as the negative slope of the $\log_{10}$ – $\log_{10}$ spectral density plot (Marshall and Burgess, 2015), with larger values of β indicating that the variance of the signal was more biased toward lower frequencies. β was either calculated for the entire deployment (in the case of Deployments 1 and 2), weekly (in the case of Deployment 3), or monthly (in the case of the deployment paired with sea urchin outplants).

Wind data were taken from NOAA NBDC buoy #46054, which was the closest operational buoy for the duration of the field experiment[1], while current data were collected by the SBC LTER (Washburn, 2018) and averaged across all depths. Current data were rotated into principal axes (u = onshore positive, v = poleward positive), and wind stress was calculated from wind velocity (Large and Pond, 1981).

---

[1] https://www.ndbc.noaa.gov/

Egg Condition and Larval Culturing Analysis

Morphometric analysis, as well as biochemical analysis, were combined and visualized in tandem using a principal components analysis (PCA), and groupings were tested using a PERMANOVA.

RESULTS

Sensor Deployment 1: Dense Oxygen Sensor Deployments Inside and Outside of a Kelp Forest Environment

In general, levels of DO were significantly different inside and outside the kelp forest, as well as at each depth (**Figure 2**). This difference with depth was observed at both sites. Specifically, mean values for oxygen were significantly different for each sensor [repeated-measures ANOVA for time of day, $F_{(17725,5)} = 1789.5$, $p < 0.0001$; calculated with Satterthwaite approximation of degrees of freedom; all pairwise comparisons significant]. The sites inside of the kelp forest also exhibited a higher diurnal cycle of DO than those outside, with the top of the water column exhibiting the highest degree of diurnal variation, followed by the middle and bottom of the water column (**Figure 2D**). The differences in the β predictability index for each of these sites was significantly different (**Figure 2C**), with β being lower outside of the kelp forest, as well as in the middle of the water column.

All three positions in the water column also exhibited a significantly different diurnal pattern (sinusoidal fit, $p < 0.0001$ for both vertical position and mooring location), and these differences were also apparent in the PSD (**Figure 2D**). Overall, the combined significant differences in means and variation of these parameters highlighted a different oxygen regime for each of these sites and water column depths (**Figure 2B**).

Sensor Deployment 2: Comparing Benthic pH–Oxygen Relationships Inside and Outside of a Kelp Forest Environment

Here, we observed significantly different DO and pH at benthic sites inside and outside of the kelp forest environment. Specifically, the benthic site inside of the kelp forest exhibited stronger diurnal variation of DO as compared to the outside, similarly to what was observed in Sensor Deployment 1.

Examining the relationship between pH and DO yielded a tight correlation ($r^2 = 0.9313$, **Supplementary Figure 2**). The slope of this relationship was not significantly different between the two benthic sites [ANCOVA, $F_{(4166,1)} = 1.727$, $p = 0.1889$].

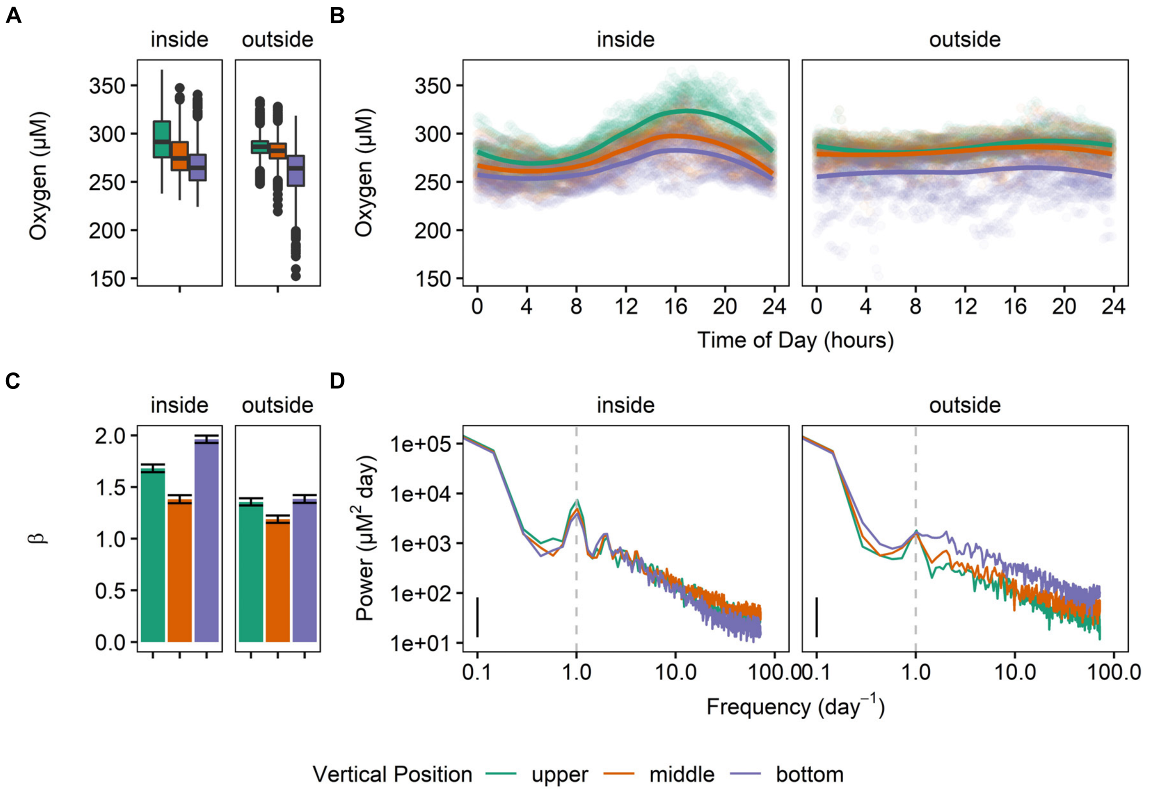

FIGURE 2 | Dissolved oxygen regimes at MKO for Deployment 1 (June 2 – June 23, 2014), where six oxygen sensors were deployed (two locations and three depths) inside and outside of the kelp forest. **(A)** Boxplots of the oxygen values, taken every 10 min. **(B)** Mean daily swings of oxygen. **(C)** β indexes calculated for the entirety of the deployment, after subtracting the diurnal signal. **(D)** Power spectra of the deployment for each sensor.

While the lines fit separately for the sensors exhibited a different intercept [$F_{(4166,1)} = 145.026$, $p < 0.001$], the discrepancy in the intercept was 0.01 pH units – within the margin of error of our spectrophotometric measurements, given an impure *m*-Cresol dye and operator error (Kapsenberg et al., 2015). Thus, data from both sites were used to fit the model correlating oxygen and pH in the nearshore environment, with a resulting relationship of $\mathrm{pH}_{\mathrm{total}} = 0.001718([O_2]) + 7.519$, with $[O_2]$ expressed in μM.

The power at the diurnal frequency (one cycle per day) was stronger inside of the kelp forest for DO, pH, and temperature (**Figure 3**), though not significantly. Notably, the benthic site inside of the kelp forest exhibited a slightly stronger (**Figure 3C**) diurnal cycle for both DO and pH, while the outside benthic site exhibited more high-frequency noise throughout this deployment. While oxygen and pH were slightly higher outside of the kelp forest on average, temperature was slightly lower (**Figure 3A**). There was also a significant increase in diurnal signal of pH and oxygen, as well as a decrease in the absolute values of pH, oxygen, and temperature, at the end of the deployment on April 6 (**Figure 3B**). This latter event also coincided with a change in wind stress (**Figure 3D**).

Sensor Deployment 3: Seasonal Variation of pH and Oxygen in a Kelp Forest Environment

At MKO, oxygen varied greatly with season with a 79 μM difference in monthly averages between July and November 2016 at the benthic site inside of the kelp forest. Specifically, DO peaked at 469 μM and declined to 125 μM over the course of the 6-month deployment (lowest and highest 10 values averaged). Using the linear equation derived from Deployment 2 (**Supplementary Figure 2**), this corresponded to a pH range of 8.32–7.73. This lowest extreme of pH and DO was observed outside of the kelp forest with a single SeapHOx® sensor (**Figure 4**), which captured a strong acidification event during March 2016 that was tied to a wind relaxation causing a strong poleward current.

Daily averages of oxygen, temperature, and pH (**Supplementary Table 1** and **Figure 5**) depicted a seasonally dynamic kelp forest environment, with seasonal upwelling (e.g., early April) as well as periods of comparatively static conditions (September onward, **Figure 6**). This strong seasonal variation was observed in tandem with the fine-scale variation between sites seen in Deployments 1 and 2 (**Figure 2** and

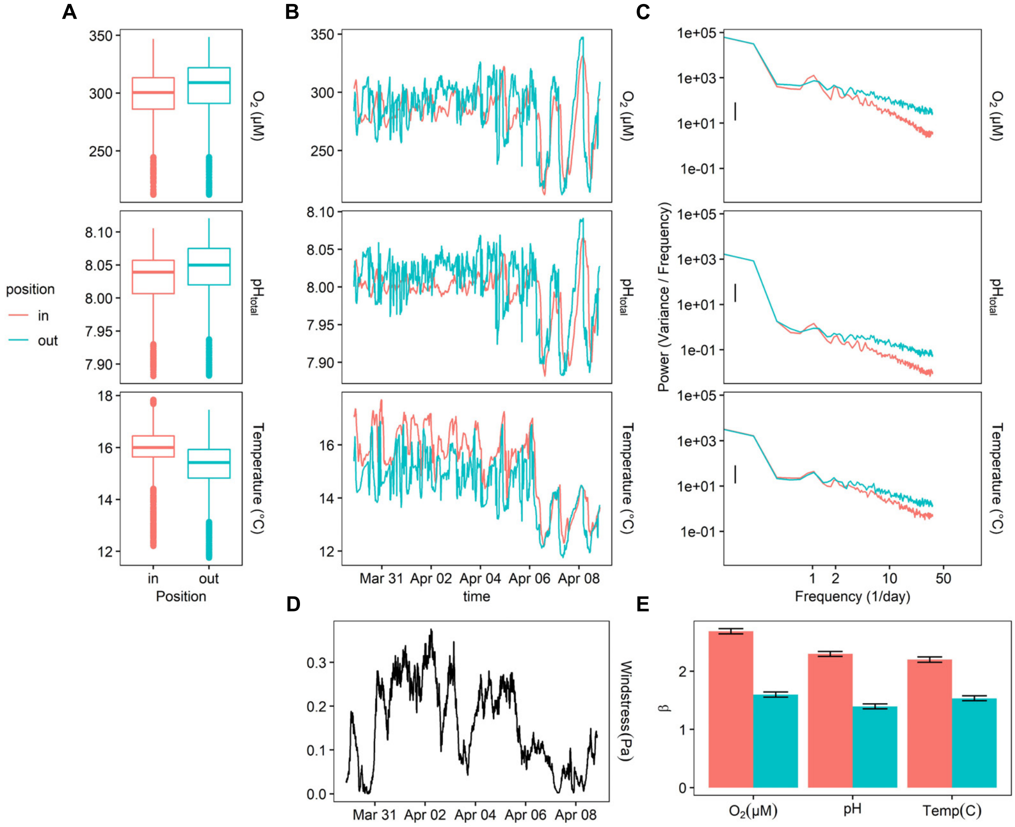

FIGURE 3 | Deployment 2 (March 10 – April 08, 2015) at MKO. **(A)** Boxplot of measured values for each sensor. **(B)** A 10-day representative sample of oxygen, temperature, and calculated pH data taken 1 m off the bottom, inside and outside of the kelp forest. **(C)** PSD of the entire deployment, for temperature and oxygen, **(D)** measurement of wind stress at the site, taken from NOAA NBDC #46054. **(E)**β indexes calculated for the entirety of the deployment, after subtracting the diurnal signal.

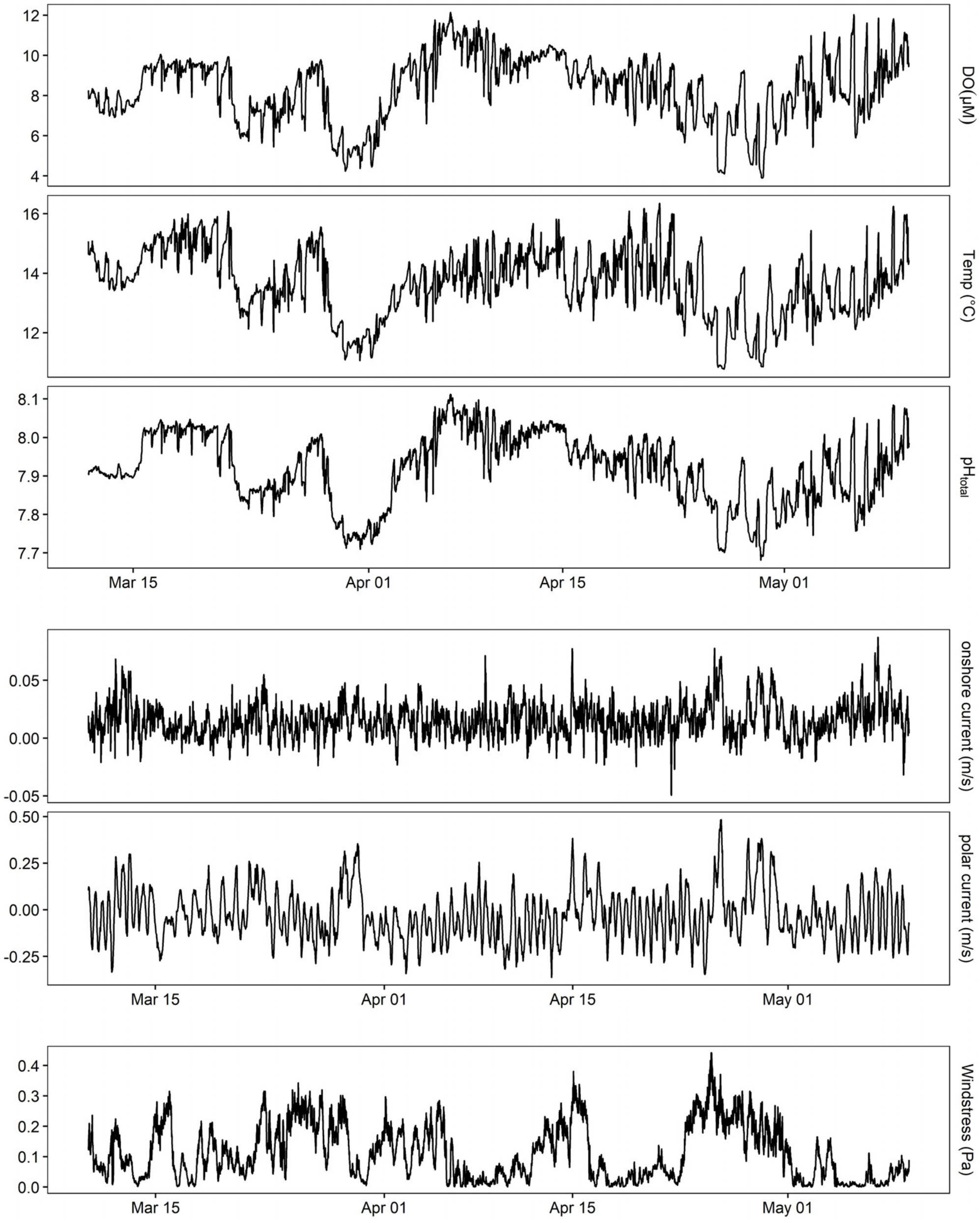

FIGURE 4 | pH, oxygen, and temperature outside of the kelp forest on the benthos at MKO during an extreme upwelling event for Deployment 3 (March–May 2016 shown). Also shown is ADCP data from the same site, rotated into principal components, and wind stress calculated from NOAA NBDC #46054.

Supplementary Figure 2); that is, a significantly higher absolute DO content inside of the kelp forest, but accompanied by relatively high diurnal variation. This diurnal variation varied by depth and season, peaking in the early summer (**Figure 6**). When examining diel patterns, daily variation in DO peaked on days in early summer, in concert with the maximum daily variation of pH, minimum mean pH, and maximum mean DO, but it was offset from the seasonality of temperature variation, which occurs in late summer to early fall (**Figure 6**). These data support the fact that the changes in pH and DO were largely not thermodynamically driven due to this temporal decoupling of maximum diel variation between temperature and DO/pH. Comparing the power spectra of two contrasting months (March vs. July) showed a pronounced difference in both the average diurnal peak in the signals, as well as a separation between the signals (**Supplementary Figure 3**), with the outside-bottom sensor displaying a significantly lower diurnal signal in the summer when the kelp forest is exhibiting the highest amount of productivity.

After removing this diurnal signal from the time series larger β values were found in the benthos inside of the kelp forest when

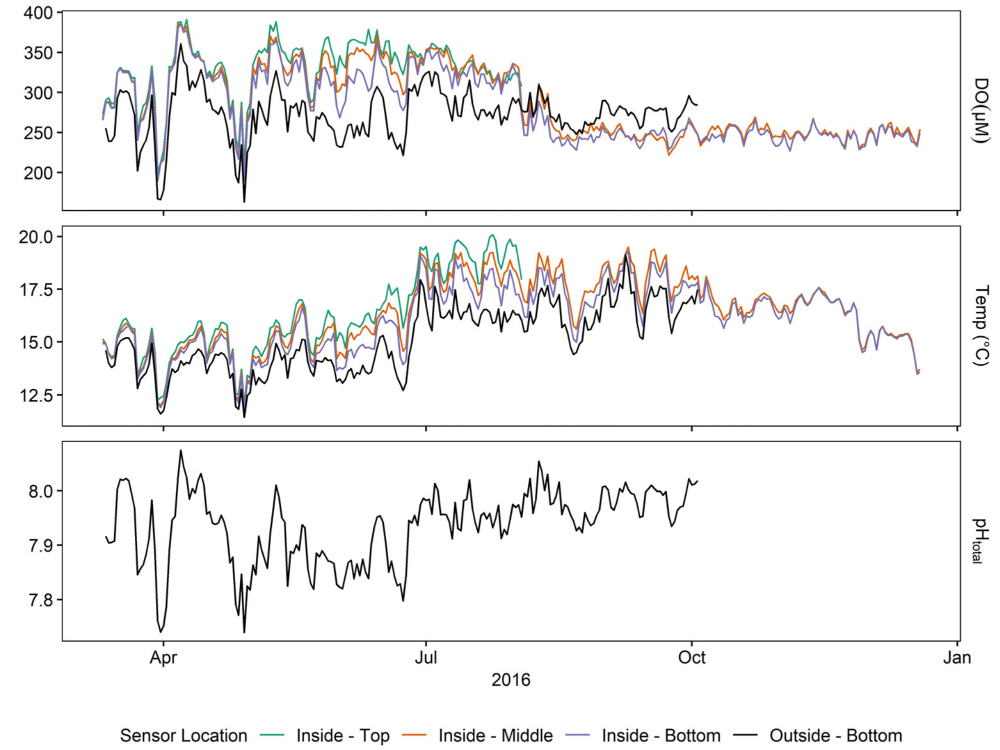

FIGURE 5 | Daily averages of oxygen, pH, and temperature at various sensors for Deployment 3 (March – December 2016).

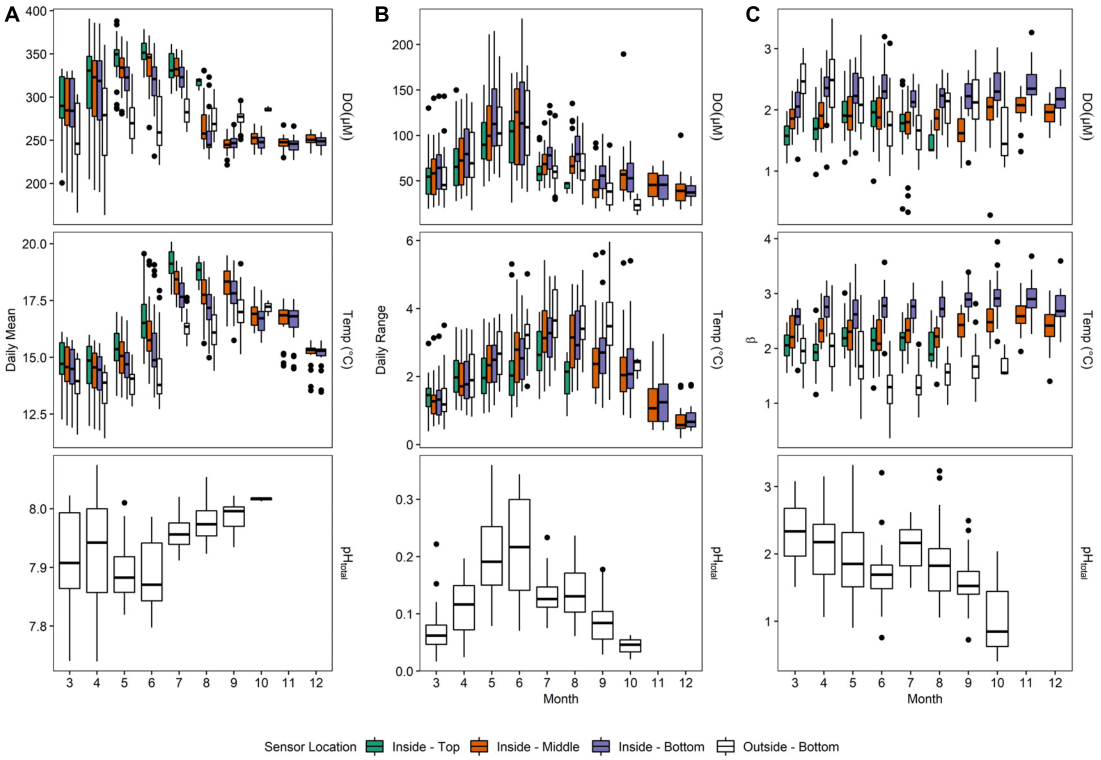

FIGURE 6 | Monthly means **(A)**, mean daily swings **(B)** and predictability indexes **(C)** for Deployment 3 (March – December 2016).

compared to outside the kelp forest (**Figure 6C**), indicating that the background variance was more predictable over time (i.e., shifted predominantly to lower frequencies) inside of the kelp forest compared to outside of the kelp forest.

In situ Conditioning of Adult Urchins Inside and Outside the Kelp Forest

The Environment: Oxygen and Temperature Regimes at the Field Site

In general, the oxygen and temperature regimes at the two study sites – inside and outside the kelp bed – (**Figure 7**) mirrored those observed during Deployment 3 in the previous year. This pattern was characterized by significantly different DO regimes as a function of the proximity to kelp, particularly in the frequency domain (**Figure 7C**).

While oxygen content varied significantly between the two sites [repeated-measures ANOVA, $F_{(10195,1)} = 505.04$, $p < 0.0001$], the mean difference in DO between these sites was small (245.94 ± 23.7 μM inside of the kelp forest, 250.41 ± 25.38 μM outside of the kelp forest, mean ± *SD*) (**Figure 7A**). Additionally, DO inside the kelp forest varied more strongly in the diurnal frequency peak, but less so at high frequencies. In contrast, the DO outside of the kelp forest environment was characterized by a lower diurnal variation, as well as more high-frequency variation. This pattern can be visually observed in the time series data (**Figure 7B**), where the DO inside of the kelp forest exhibited a more consistent sinusoidal pattern, while the DO outside of the kelp forest exhibited a more stochastic signal indicative of high-frequency variability. This was quantified through the environmental color statistic (**Figure 7H**), where higher values of β inside of the kelp forest indicate a higher bias toward lower-frequency environmental noise and thus a more predictable variation over time.

Temperature also varied in both harmonic content and absolute value. In absolute terms, temperature varied significantly between the two sites [repeated-measures ANOVA, $F_{(10050,1)} = 7032$, $p < 0.0001$], with the means differing by 0.6°C (17.60 ± 1.28°C inside of the kelp forest, 16.83 ± 1.42°C outside the kelp forest, mean ± *SD*) (**Figure 7D**). In the frequency spectrum, similar to the DO data, temperature exhibited high-frequency variability outside of the kelp forest in comparison to inside (**Figure 7F**). This degree of variation can be visualized as high-frequency noise in the representative time series data (**Figure 7E**). In contrast to DO, however, the diel variation of temperature inside the kelp forest was not notably different than that outside the kelp forest (**Figure 7F**).

Egg Characteristics, Morphometrics, and Protein Content

In terms of egg characteristics, the data showed that some morphometric characteristics of eggs covaried strongly regardless of maternal exposure; these were egg area and egg diameter (**Supplementary Figure 4**, linear regression $p < 0.0001$, $r^2 = 0.96$). Although we expect a square relationship between length and area if the shapes of the eggs were all identical, this relationship was fairly linear over the observed range of both metrics. In order to further explore this variation, these three measured metrics (egg diameter, egg area, and egg protein content) were combined and transformed using a PCA, the first two components of which are reported here (**Figure 8A**). With the PCA technique, correlates (e.g., egg diameter and egg area) can be accounted for and collapsed onto a primary axis. Here, eggs from females conditioned inside the kelp forest had higher total protein content, but were fewer in number (PERMANOVA, $p = 0.01$), while in contrast, eggs from females conditioned outside of the kelp forest were larger in number but less rich in protein (**Figure 8A**).

Embryo Characteristics, Morphometrics, and Protein Content

During the culturing run of 17 h, $p\text{CO}_2$ levels in the culturing vessels remained consistent to target values for each of the two treatments (target values = 400 μatm and 1,000 μatm, actual values = 413.59 ± 2.40 μatm $p\text{CO}_2$ and 987.59 ± 31.38 μatm $p\text{CO}_2$ – respectively). For these determinations, carbonate parameters were calculated based on alkalinity and salinity values taken on the second day of culturing (2,214.80 μmol kg^{-1} and 33.4‰, respectively).

These collected embryo data were visualized by PCA. Here, because two of the variables (protein content and embryo area) were orthogonal and corresponded well with PC1 and PC2, these original variables were used in analysis in lieu of the principal components.

Overall, there was a detectable effect of maternal conditioning in this study (**Figure 8B**). Embryos from females that performed gametogenesis outside the kelp, and then were raised under high $p\text{CO}_2$ conditions (abbreviated OH), had a larger body size than the other three treatments (IL and IH, or the offspring of mothers caged inside of the kelp forest and raised at either low or high $p\text{CO}_2$, and OL, the offspring of mothers caged outside the kelp forest and raised under low $p\text{CO}_2$). This was quantified as a significant effect of embryo area between treatments [$F_{(3,26)} = 11.156$, $p < 0.001$]. In addition, a *post hoc* test revealed a significant difference in the area of OH embryos compared to that of other treatments (FDR, $q = 0.05$). Lastly, there was a nearly significant effect of embryo protein content [$F_{(3,8)} = 2.81$, $p = 0.11$]. However, no significant pairwise comparisons were found with a *post hoc* test for false discovery rate (FDR; Benjamini and Hochberg, 1995).

DISCUSSION

The overall goal of this study was to characterize spatiotemporal variability of pH and DO in and around kelp forests at a range of timescales, from daily to seasonal, while comparing sites inside and outside of a kelp forest environment – then, to investigate the biological impacts of the spatiotemporal variability of physiochemical conditions around kelp forests. We found that the kelp forest environment provided a generally higher pH, higher DO environment throughout the water column, while also introducing a more predictable diel signal and diminishing high-frequency variation. These differences in physiochemical

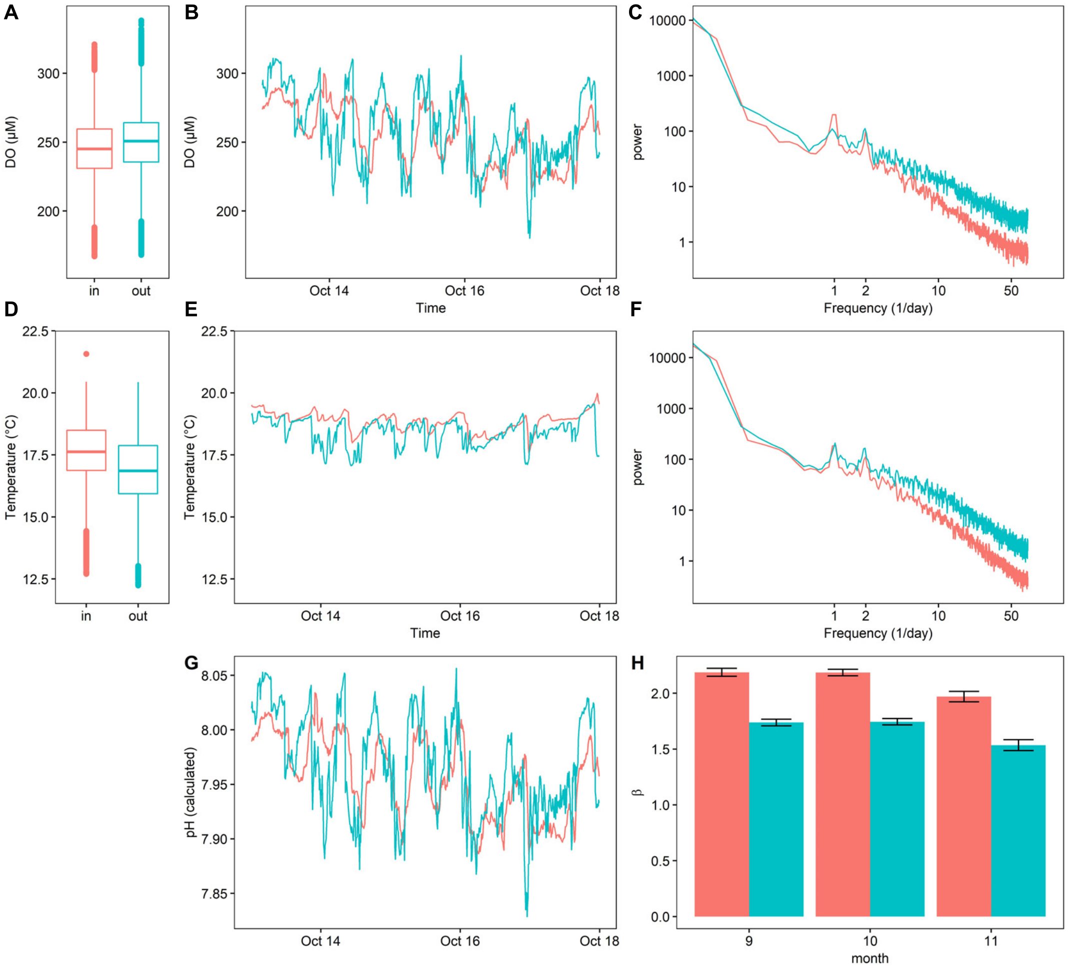

FIGURE 7 | Dissolved oxygen **(A–C)**, temperature **(D–F)**, and calculated pH **(G)** inside (red) and outside (blue) of a kelp forest environment, expressed as boxplots for the entire outplant **(A,D)**, a representative 5-day timeseries **(C,F)**, power spectra **(C,F)**, as well as calculated β indexes **(H)** (±SE).

conditions provided by the kelp forest appeared to impact characteristics of both the sea urchin eggs and early stage embryos, indicating that urchins develop more favorably and are more resistant to impacts of environmental variability when raised in environmental conditions that mimic that of a kelp forest.

Sensor Deployments

In general, we found significantly different regimes of oxygen and pH during this series of sensor deployments at MKO. The salient findings are: **(1)** DO and pH covaried strongly in the kelp forest environment, and both parameters can decrease to levels that could potentially affect organismal physiology, **(2)** pH and DO varied seasonally, both in daily means and in diel variation, and **(3)** this diel variation, as well as high-frequency variation, was significantly different inside and outside of the kelp forest. Overall, the patterns of DO and pH captured by this series of sensor deployments may have both biological and ecological consequences for marine biota in this nearshore environment (Breitburg et al., 2018).

While the most consistent trend throughout the deployments was the strong covariation of oxygen and pH (**Supplementary Figure 2**), the DO values observed in Deployment 3 included values down to 125 μM (3.9 mg/L) with 64 μM (2 mg/L) being the threshold for hypoxia for many species (Vaquer-Sunyer and Duarte, 2008). These low values were observed in March through May and were not observed in months with the highest daily variation (**Figure 5**). Such episodic, event-scale variations appear to be linked to the shoaling of upwelled water, as they are also coupled with low temperature (**Figures 2**, **5**). The most notable low pH event occurred in late March (**Figure 4**), and showed a regime of drastically decreased temperature, pH, and oxygen occurring simultaneously for several days. This was paired with a decrease in wind stress and a subsequent poleward flow of water. In contrast, the low, but more variable event on April 30 was accompanied by increased wind stress and a net onshore flow, which more likely indicates an upwelling event. Contextually, given that global ocean pH is expected to decrease ~0.2 units in the next 100 years (Feely et al., 2009), these dips pH (−0.3) in this time series are likely to play a large part in the future of this

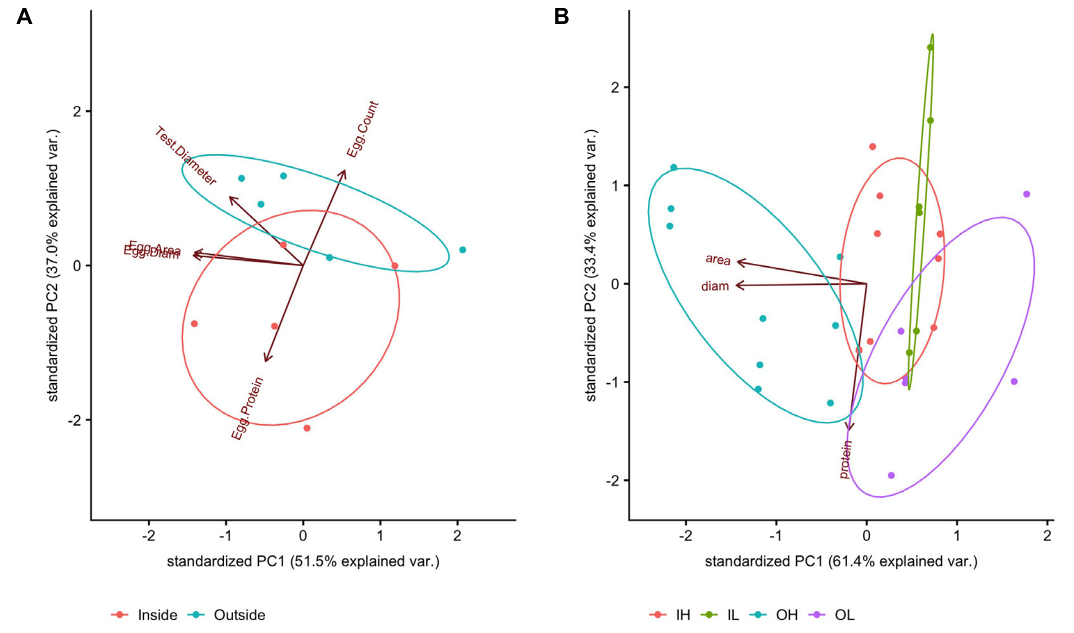

FIGURE 8 | PCA of measurements at the **(A)** egg level (egg average protein, egg area, egg diameter), averaged to match measurements at the individual female level (egg count, test diameter); PCA of measurements taken of **(B)** hatched blastula embryos (17 hpf). OH was significantly different from the other treatments (FDR *post hoc* test). Absolute values can be found in **Supplementary Table 2**.

coastal marine system (Gruber et al., 2012; Hofmann et al., 2013; Chan et al., 2017).

Although a DO value of 2 mg/L (or 64 μM), has long been used as a hypoxic threshold in the context of fisheries, this perspective has been re-visited with researchers noting that this concentration can be a drastic underestimation of sublethal and lethal thresholds of hypoxia when looking across taxa (Vaquer-Sunyer and Duarte, 2008). Here, marine fish and crustaceans have been noted to be the most vulnerable to hypoxia, and 4.6 mg/L (or 147 μM) is suggested as a precautionary 90-percentile value of survival, especially given that the ecosystem-level response to hypoxia is unpredictable and has been poorly studied (Steckbauer et al., 2011). In this time series, a value this low was seen most notably for 11 out of 22 h on April 30, and for over 12 continuous hours on April 26 (**Figure 4**). In addition, considering that these decreases in levels of DO are strongly linked to decreases in pH, the multiple stressor scenario of ocean acidification and hypoxia demands a more conservative cutoff for hypoxia (Gobler and Baumann, 2016) given that the interaction between these stressors is hard to predict and can differ even amongst closely related taxa (Crain et al., 2008; Przeslawski et al., 2015). For instance, in studies on red abalone in Monterey Bay (Kim et al., 2013), juveniles showed adverse effects when subjected to low pH (7.5) and low oxygen (5 mg L^{-1}), and the investigators attributed the majority of mortality to the hypoxia. This oxygen value was seen at MKO for 18 out of 62 h in early April, then again for 31 out of 80 h in late April 2016 (**Figure 4**). Overall, our data from the kelp forest indicate that resident taxa would encounter physiologically challenging conditions on a regular basis, even within taxa that are traditionally thought to be resilient to ocean change (Vaquer-Sunyer and Duarte, 2008).

Lastly, independent of these event-scale changes, DO values decreased with depth in the water column, and also decreased outside of the kelp forest along with pH (**Figures 2**, **5**). In general, pH and DO were very highly correlated in our study (**Supplementary Figure 2**). This strong coupling of these two factors has been previously observed, most recently in Frieder et al. (2012) which found a similar relationship except for a slightly different slope and an intercept difference with our margin of spectrophotometric pH error.

Seasonal Variation

The data collected in this study showed a seasonal variation of pH and DO in a kelp forest environment, as has been reported in other studies in California *Macrocystis* forests (Kapsenberg and Hofmann, 2016; Koweek et al., 2017). At MKO, seasonal variation was driven by both event-scale variation, as described above and displayed in **Figure 4**, and diurnal variation, as described below and displayed in **Figure 6**. In particular, the diurnal variation varied strongly with season, peaking in early summer. This was slightly earlier than the peak that was observed previously by Kapsenberg and Hofmann (2016), data that were collected in 2012–2015 at Anacapa Landing Cove, a site in the Santa Barbara Channel positioned on Anacapa Island further out in the Channel. In addition, seasonal variation of diel pH cycles was also generally higher than observed at the Channel Islands site in Kapsenberg and Hofmann (2016). Kapsenberg and Hofmann also observed very little change inter-annually in seasonal pH and oxygen. However, given that the sites on the

Northern coast of the Channel Islands experience little wind-driven upwelling, more variable interannual conditions could be expected on the mainland where abiotic conditions have a larger effect. To date, no other kelp forest sites have been instrumented to observe seasonal trends.

Diurnal and High-Frequency Variation in pH and DO

It is becoming increasingly clear that organismal exposure to pH and hypoxia cannot be completely encapsulated by discussing means and extremes, but that frequency of variation can play a strong factor (Cornwall et al., 2013). As expected, we found that pH and oxygen varied dramatically in this coastal system at MKO. The largest daily ranges of pH and DO were observed at middle and bottom of the kelp forest (**Figure 6**). One of the large drivers of this change in daily range was at a diel frequency, and corresponded to expected (but not measured) patterns of photosynthesis and respiration that would track availability of light in the water column. In all power spectra analyzed, the diurnal signal was the dominant periodic function, mirroring results from previous studies in the Southern California Bight (Frieder et al., 2012). Here, both mean DO and diel variation of DO decreased with depth in the water column (i.e., away from the kelp canopy), and decreased outside of the kelp forest (i.e., away from the kelp bed itself).

In addition to differences in diel variation, differences in high-frequency variation were observed both vertically in the water column as well as between sites. High-frequency variation of DO and temperature were observed on the benthos outside of the kelp forest (**Figure 2**). Thus, it appears that kelp forests offer an environment with a strong diel variation of DO and pH, but less high-frequency noise. This pattern is possibly caused by the dampening of water flow around kelp forests, which has been classified at this site in past studies (Gaylord et al., 2007). This change in physical flow likely contributes to the cleaner and stronger diurnal signal recorded inside of the kelp forest. The deeper, outside site could also be subject to different oceanographic processes, such as internal waves.

Comparison of Conditions Inside and Outside of a Kelp Forest Environment

This study compared a site inside of a kelp forest to one directly offshore, a site that lacked kelp and was characterized by sandy substrate. These sites were chosen as Frieder et al. (2012) observed higher gradients cross-shore compared to alongshore, and thus we expected to see a larger variation along this axis. With alongshore currents drastically stronger than cross-shore currents, it is intuitive that the physiochemical gradients would be stronger heading offshore.

Although Koweek et al. (2017) noted that depth was as great of an indicator of seawater chemistry change as horizontal distance, Frieder et al. (2012) observed that depth was a larger determinant of spatial pH difference than distance. Our study neither refutes nor supports these results, as the two sites were at different depths (7 m and 11 m). Choosing sites that were both different in depth and in kelp presence was intentional, as the main purpose of this study was to investigate the effect of the kelp forest on benthic communities. Regardless, we found a larger difference between the two sensors at the benthos than between the two sensors at the top and bottom of the water column (**Figure 2**).

In comparing the three available datasets on California kelp forests, differences in these systems are likely due to site-by-site differences, as well as sampling methodology. Koweek et al. (2017) sampled the water column from 9:00 to 12:00 local time, a time of day when vertical stratification of DO was the highest in the MKO deployments (**Figure 2**). It is likely that this sampling thus captured the vertical stratification of the kelp forest at its strongest point, which may partially explain why the study found large differences in water chemistry with depth. While Frieder et al. (2012) used autonomous pH sensors instead of the discrete sampling used by Koweek et al. (2017), most of their La Jolla kelp forest deployments were conducted in an area of the kelp forest at a 20 m depth. A larger effect of depth in these La Jolla kelp forests is not surprising as this is far beyond the extent of *Macrocystis* beds in the Santa Barbara Channel.

In summary, these results highlight the significance of kelp forests in mediating the pH and DO of the water column through the seasons. While these data help us understand another way that *Macrocystis* acts as a foundation species, one side note of importance is the consideration of the fate of giant kelp itself under future ocean conditions. To date, few studies have investigated the effect of future ocean conditions on *Macrocystis* physiology, and generally find no effect or a positive effect (Roleda et al., 2012; Leal et al., 2017). While kelp forests in the Santa Barbara Channel appear to be relatively resilient to extreme warming events (Reed et al., 2016), temperature is generally considered a limiting factor for kelp forest ranges (Wernberg et al., 2019) and kelp forests are generally declining globally (Krumhansl et al., 2016). Regardless, better understanding of the impact of kelp forests on the surrounding water column, as well as its surrounding "sphere of influence," will be a critical piece in predicting the fate of nearshore communities to future environmental change.

Co-locating *in situ* Biological Conditioning With Sensor Deployments

In support of this aspect of the study, we discerned that the presence of macrophytes was likely a large driving factor of DO and temperature variation at the study site. Biologically, we found that **(1)** sea urchin gametogenesis was affected *in situ* by these seawater conditions, and **(2)** this environmental variation also affected traits of the embryos raised using gametes from adult sea urchins conditioned at sites inside vs. outside the kelp forest. Overall, these results suggest that macrophytes may play a key role in the fate of sea urchins during a critical stage in their life history, potentially leading to ecosystem-level effects in the nearshore environment in the near future.

Evidence for Differential Exposure of Adults as a Function of the Presence of Kelp

At the two field sites, adult sea urchins were exposed to different regimes of DO and temperature. This differential experience *in situ* included not only a higher temperature and DO inside of the kelp forest, but also a noticeable difference in the frequency of variability between these two sites (**Figure 7**). Although pH was not directly measured during the urchin caging experiment, given the strong coupling between pH and DO (**Supplementary Figure 2**), we calculated approximate pH exposure for the deployment (**Figure 7**). One prominent difference is the color of the noise floor β (**Figure 7H**), which indicates that the kelp forest environment provided a more predictively variable environment during sea urchin gametogenesis.

Egg Characteristics After Parental Exposure

It is broadly understood that organisms exhibit physiological tolerances that reflect the abiotic variability in their environment, a process that could potentially play a large role in responding to anthropogenic environmental change (Sunday et al., 2011). However, it is less clear how this response to abiotic variation in nature could interact with TGP (Donelson et al., 2018). The results of this study begin to examine how the environment alters performance of the progeny via TGP, and further is a direct test of how this form of eco-evolutionary dynamic might play out in nature. In our comparison of kelp-rich vs. kelp-poor study sites, we observed that females conditioned outside of the kelp forest produced more gametes, but the eggs had a lower protein content. In comparison, females conditioned inside of the kelp forest spawned fewer gametes that were more protein-rich. Although subtle, the data hint at a possible tradeoff in maternal provisioning in response to the environmental variability encountered during gametogenesis. While some models and systems predict that adverse environments can be optimized for by generating fewer, larger eggs (Olofsson et al., 2009), other empirical studies posit that fitness can be maximized in harsh, unpredictable environments by creating many eggs with fewer resources, noting that resource-dependent fitness may not play a large role in more variable, unpredictable environments.

From a larval ecology perspective, *S. purpuratus* have planktotrophic larvae that derive a relatively small amount of their larval energy needs through maternal provisioning compared to direct developers and non-feeding larvae (Marshall and Keough, 2007). Because *S. purpuratus* early stages do not begin feeding until later in development (as pluteus at ~72 hpf, Strathmann, 1987), enhanced energy storage or maternal provisioning may play a significant role in the critical early life stages of this organism.

Lastly, while colder temperatures have been linked to larger optimal egg volume across taxa (Levitan, 2000; Pettersen et al., 2019), we did not see a significant difference in egg size as a function of parental conditioning. It appears that the tradeoff between protein content and egg number may play a larger role in larval success compared to egg size in this current study.

Embryo Response to $p\text{CO}_2$ Stress

While there was a negative correlation between egg size and protein content at the egg stage, there were no significant differences in protein between the maternal conditioning and embryo treatments at the hatched blastula stage (17 hpf). The differences between these treatments were largely driven by embryo size (**Figure 8B**). More specifically, it appears that embryos from females conditioned inside the kelp forest were not significantly different in size, regardless of their exposure to $p\text{CO}_2$ during culturing. However, hatched blastula embryos from females conditioned outside of the kelp forest exhibited a significantly different size in response to $p\text{CO}_2$ conditions, with those raised at higher $p\text{CO}_2$ conditions exhibiting an 8% larger area, on average, in comparison to those raised in the lower $p\text{CO}_2$ treatment.

Previous research has shown that early stage purple urchins are impacted by pH and oxygen change. However, the vast majority of this research has been conducted in the laboratory, and usually only examined the effects of high $p\text{CO}_2$/low pH using static treatment conditions. Additionally, many have focused on the impact of $p\text{CO}_2$ treatments on the energetic costs of skeletogenesis, finding that the larvae under high $p\text{CO}_2$ expend more energy (Stumpp et al., 2011) to create shorter spicules (Yu et al., 2011). Here, we review studies that investigated the energetic demands of earlier stages of *S. purpuratus,* specifically in a transgenerational context.

Prior research in our lab has examined TGP in purple urchins; these lab experiments were the motivation for the field component of this work. In the lab studies, we found evidence that the maternal environment affected gametogenesis. In one study, we found that adult female *S. purpuratus* held at static upwelling conditions in the laboratory (1,100 μatm $p\text{CO}_2$, 14°C) during gametogenesis had non-significantly 3.2% larger eggs than those from mothers raised in ambient conditions for the region (400 μatm, 17°C), with progeny sizes continuing to reflect this maternal effect (Wong et al., 2018). While the urchins conditioned outside of the kelp forest had both a lower temperature and higher extrapolated $p\text{CO}_2$ (derived from the known relationship between DO and pH at the region), the differences in absolute means of both pH and temperature between the field sites in this study were not as pronounced as those from Wong et al. (2018). Subsequently, the results presented here do not show a pronounced difference in egg size between maternal conditioning treatments.

In an additional study, we found that embryos from mothers acclimated to static upwelling conditions (1,150 μatm $p\text{CO}_2$, 13°C) were larger than the embryos from mothers acclimated to non-upwelling static conditions (500 μatm $p\text{CO}_2$, 17°C) (Wong et al., Unpublished). Overall, both studies show a clear effect of the maternal environment on gametogenesis. Regardless, not only can maternal effect change offspring characteristics, but it can also change the tolerance of offspring to environmental variability of $p\text{CO}_2$. In other studies, *S. purpuratus* has been shown to not alter its biochemical makeup in the face of experimental ocean acidification (Matson et al., 2012; Pan et al., 2015). However, it is becoming increasingly clear that studies that involve early developmental stages must take into account the genotype or the husbandry conditions of the adults, as both of these factors may play a major role in the biological response.

A suite of studies on fluctuating pH often find that changing the variance of pH can affect organism more than altering the mean. Fluctuating scenarios can vary on the species level, with even congenerics responding similarly to static conditions. This may be particularly important for benthic sessile organisms, that are dependent on the environment on which they settle. In contrast, any difference seen between these sites less than 100 m away can be traversed by most mobile organisms. If there is indeed a variation in preference for pH/DO regimes between species, then a heterogenous environment may provide a large opportunity for organisms to move to their regime of preference. Individual species must be more extensively surveyed in a multistressor framework to understand the vulnerability of coastal oceans to these ocean conditions (Gobler and Baumann, 2016). Overall, experiments that study the effect of pH variation on organisms generally show disparate results that do not form conclusive trends across taxa, and do not take into account the ability of the organism to move out of a stressful environment (Alenius and Munguia, 2012; Roleda et al., 2012; Kim et al., 2013; Frieder et al., 2014; Clark and Gobler, 2016; Davidson et al., 2016; Eriander et al., 2016; Keppel et al., 2016), with many of these studies utilizing pH and oxygen variability that generally reflect what is observed in this MKO kelp forest system. A more thorough understanding of both species physiology and community interactions will be critical in understanding the true prospect of kelp as a biomediator of global abiotic stressors.

CONCLUSION

Ultimately, this field experiment detected a within-generation plasticity (WGP) effect in response to development under high $p\mathrm{CO}_2$. Note however, that this response was mediated by transgenerational effects – in other words, the differential growth patterns of the embryos was based on the environmental experience of the mother. The concept that TGP can be a result of climate variability has been posited by Donelson et al. (2018). Here, the authors noted that TGP may be more advantageous in spatiotemporally stable regions where offspring can utilize parental cues. On the other hand, sea urchins in the CCLME are exposed to physiochemical conditions that can change over much shorter distances and time scales than larval dispersal. This makes the advantage of TGP less intuitive for this organism and its environment. In this case, the WGP of body size in response to $p\mathrm{CO}_2$ conditions may be explained as the result of the unpredictability of the maternal environment priming the larvae to be able to phenotypically respond to a large suite of conditions. This is supported by observations made by Wong et al. (2018) where the transcriptome changed in a manner that also suggests that female conditioning can prime the progeny to better respond to extreme abiotic conditions during development. Understanding the role of TGP in nature and the mechanisms that drive such a response are of great interest to the marine science research community at the moment (Ghalambor et al., 2007; Hofmann, 2017; Donelson et al., 2018), and this is one of very few studies that are designed to investigate this *in situ* (Murray et al., 2014).

While there is emerging evidence that the degree of pH fluctuation can modify the outcome of simulated ocean acidification experiments in laboratory-based mesocosms (Frieder et al., 2014; Roleda et al., 2015), it is unclear whether this difference in the frequency of variation will alter organismal response in nature. However, some field studies have begun to explore the ecological and biological consequences of pH variability for natural populations. In a study from Murray et al. (2014), early stage silverside fish (*Menidia menidia*) displayed different tolerances that correlated to the conditions the females experienced in the tidal marsh during the reproductive cycle. In a second study, Britton et al. (2016) found that a species of brown algae, *Ecklonia radiata,* was physiologically adapted to the diurnal pH/DIC conditions of its environment, and performed less optimally at either of the static pH treatments (pH 8.4 and pH 7.8) corresponding to the extremes of this diurnal variation. However, given that the response to diurnal pH variation was different across different algae (Roleda et al., 2015), or even congeneric invertebrates (Frieder et al., 2014), it is unclear how covarying pH and DO could influence TGP in *S. purpuratus*.

Overall, investigating the molecular basis for this plasticity over a multigenerational manipulation may be the key to ultimately understanding this variation in response (Foo and Byrne, 2016). Regardless, any phenotypic plasticity may play a critical component in the survival of marine species to rapid global change (Munday et al., 2013).

DATA AVAILABILITY

The datasets generated for this study, as well as the code for analysis, is available at the following doi: 10.17605/OSF.IO/A8N3P.

AUTHOR CONTRIBUTIONS

UH and GH conceived and designed the experiments and wrote the manuscript. UH, along with assistance from SBC LTER staff, performed field and lab work. UH performed the statistical analysis. Both authors have read and approved the submitted version.

FUNDING

This work was partially supported by awards to GH: the UC Climate Champion award from the University of California, and a grant from the United States National Science Foundation (NSF) (Award IOS-1656262). In addition, support for boating and sensor deployment and partial stipend support was provided by the Santa Barbara Coastal Long Term Ecological Research program (NSF award OCE-1232779; Director: Dr. Daniel Reed). In addition, UH was supported by an NSF Graduate Research Fellowship (NSF-1650144).

ACKNOWLEDGMENTS

We thank Dr. Robert Miller, Prof. Libe Washburn, Prof. Kathy Foltz, and Prof. Erika Eliason for input on the experiments.

We thank Clint Nelson for help during field deployments and support of the diving required to support the project. We also thank Dr. Marie Strader, Juliet Wong, Terence Leach, Logan Kozal, and Maddie Housh for assistance with urchin spawning and raising cultures of embryos.

SUPPLEMENTARY MATERIAL

The Supplementary Material for this article can be found online at: https://www.frontiersin.org/articles/10.3389/fmars.2019.00062/full#supplementary-material

REFERENCES

Alenius, B., and Munguia, P. (2012). Effects of pH variability on the intertidal isopod, *Paradella dianae*. *Mar. Freshw. Behav. Physiol.* 45, 245–259. doi: 10.1080/10236244.2012.727235

Baumann, H., Wallace, R. B., Tagliaferri, T., and Gobler, C. J. (2015). Large Natural pH, CO_2 and O_2 fluctuations in a temperate tidal salt marsh on diel, seasonal, and interannual time scales. *Estuar. Coasts* 38, 220–231. doi: 10.1007/s12237-014-9800-y

Benjamini, Y., and Hochberg, Y. (1995). Controlling the false discovery rate: a practical and powerful approach to multiple testing. *J. R. Stat. Soc. Ser. B Methodol.* 57, 289–300. doi: 10.1111/j.2517-6161.1995.tb02031.x

Breitburg, D., Levin, L. A., Oschlies, A., Grégoire, M., Chavez, F. P., Conley, D. J., et al. (2018). Declining oxygen in the global ocean and coastal waters. *Science* 359:eaam7240. doi: 10.1126/science.aam7240

Breitburg, D. L., Salisbury, J., Bernhard, J. M., Cai, W.-J., Dupont, S., Doney, S. C., et al. (2015). And on top of all that. Coping with ocean acidification in the midst of many stressors. *Oceanography* 28, 48–61. doi: 10.5670/oceanog.2015.31

Bresnahan, P. J., Martz, T. R., Takeshita, Y., Johnson, K. S., and LaShomb, M. (2014). Best practices for autonomous measurement of seawater pH with the Honeywell Durafet. *Methods Oceanogr.* 9, 44–60. doi: 10.1016/j.mio.2014.08.003

Britton, D., Cornwall, C. E., Revill, A. T., Hurd, C. L., and Johnson, C. R. (2016). Ocean acidification reverses the positive effects of seawater pH fluctuations on growth and photosynthesis of the habitat-forming kelp. *Ecklonia radiata. Sci. Rep.* 6:26036. doi: 10.1038/srep26036

Byrne, M., Prowse, T. A. A., Sewell, M. A., Dworjanyn, S., Williamson, J. E., and Vaïtilingon, D. (2008). Maternal provisioning for larvae and larval provisioning for juveniles in the toxopneustid sea urchin *Tripneustes gratilla*. *Mar. Biol.* 155, 473–482. doi: 10.1007/s00227-008-1045-5

Chan, F., Barth, J. A., Blanchette, C. A., Byrne, R. H., Chavez, F., Cheriton, O., et al. (2017). Persistent spatial structuring of coastal ocean acidification in the California Current System. *Sci. Rep.* 7:2526. doi: 10.1038/s41598-017-02777-y

Chirgwin, E., Marshall, D. J., Sgro, C. M., and Monro, K. (2018). How does parental environment influence the potential for adaptation to global change? *Proc. Biol. Sci.* 285:20181374. doi: 10.1098/rspb.2018.1374

Clark, H. R., and Gobler, C. J. (2016). Diurnal fluctuations in CO_2 and dissolved oxygen concentrations do not provide a refuge from hypoxia and acidification for early-life-stage bivalves. *Mar. Ecol. Prog. Ser.* 558, 1–14. doi: 10.3354/meps11852

Comeau, S., Edmunds, P. J., Spindel, N. B., and Carpenter, R. C. (2014). Diel pCO_2 oscillations modulate the response of the coral *Acropora hyacinthus* to ocean acidification. *Mar. Ecol. Prog. Ser.* 501, 99–111. doi: 10.3354/meps10690

Cornwall, C. E., Comeau, S., DeCarlo, T. M., Moore, B., D'Alexis, Q., and McCulloch, M. T. (2018). Resistance of corals and coralline algae to ocean acidification: physiological control of calcification under natural pH variability. *Proc. R. Soc. B Biol. Sci.* 285:20181168. doi: 10.1098/rspb.2018.1168

Cornwall, C. E., Hepburn, C. D., McGraw, C. M., Currie, K. I., Pilditch, C. A., Hunter, K. A., et al. (2013). Diurnal fluctuations in seawater pH influence the response of a calcifying macroalga to ocean acidification. *Proc. Biol. Sci.* 280:20132201. doi: 10.1098/rspb.2013.2201

Crain, C. M., Kroeker, K., and Halpern, B. S. (2008). Interactive and cumulative effects of multiple human stressors in marine systems. *Ecol. Lett.* 11, 1304–1315. doi: 10.1111/j.1461-0248.2008.01253.x

Davidson, M. I., Targett, T. E., and Grecay, P. A. (2016). Evaluating the effects of diel-cycling hypoxia and pH on growth and survival of juvenile summer flounder *Paralichthys dentatus*. *Mar. Ecol. Prog. Ser.* 556, 223–235. doi: 10.3354/meps11817

Delille, B., Borges, A. V., and Delille, D. (2009). Influence of giant kelp beds (Macrocystis pyrifera) on diel cycles of pCO_2 and DIC in the Sub-Antarctic coastal area. *Estuar. Coast. Shelf Sci.* 81, 114–122. doi: 10.1016/j.ecss.2008.10.004

Dickson, A. G., Sabine, C. L., and Christian, J. R. (2007). Guide to best practices for ocean CO_2 measurements. *PICES Spec. Publ.* 3:199.

Donelson, J. M., Salinas, S., Munday, P. L., and Shama, L. N. S. (2018). Transgenerational plasticity and climate change experiments: Where do we go from here? *Glob. Change Biol.* 24, 13–34. doi: 10.1111/gcb.13903

Dufault, A. M., Cumbo, V. R., Fan, T. Y., and Edmunds, P. J. (2012). Effects of diurnally oscillating pCO_2 on the calcification and survival of coral recruits. *Proc. Biol. Sci.* 279, 2951–2958. doi: 10.1098/rspb.2011.2545

Eriander, L., Wrange, A. L., and Havenhand, J. N. (2016). Simulated diurnal pH fluctuations radically increase variance in — but not the mean of — growth in the barnacle *Balanus improvisus*. *ICES J. Mar. Sci. J. Cons.* 73, 596–603. doi: 10.1093/icesjms/fsv214

Fangue, N. A., O'Donnell, M. J., Sewell, M. A., Matson, P. G., MacPherson, A. C., and Hofmann, G. E. (2010). A laboratory-based, experimental system for the study of ocean acidification effects on marine invertebrate larvae. *Limnol. Oceanogr. Methods* 8, 441–452. doi: 10.4319/lom.2010.8.441

Feely, R. A., Doney, S. C., and Cooley, S. R. (2009). Ocean Acidification: present conditions and future changes in a high-CO_2 world. *Oceanography* 22, 37–47. doi: 10.1098/rstb.2012.0442

Feely, R. A., Sabine, C. L., Hernandez-Ayon, J. M., Ianson, D., and Hales, B. (2008). Evidence for upwelling of corrosive "acidified" water onto the continental shelf. *Science* 320, 1490–1492. doi: 10.1126/science.1155676

Filbee-Dexter, K., and Scheibling, R. (2014). Sea urchin barrens as alternative stable states of collapsed kelp ecosystems. *Mar. Ecol. Prog. Ser.* 495, 1–25. doi: 10.3354/meps10573

Foo, S. A., and Byrne, M. (2016). Acclimatization and adaptive capacity of marine species in a changing ocean. *Adv. Mar. Biol.* 74, 69–116. doi: 10.1016/bs.amb.2016.06.001

Frieder, C. A., Gonzalez, J. P., Bockmon, E. E., Navarro, M. O., and Levin, L. A. (2014). Can variable pH and low oxygen moderate ocean acidification outcomes for mussel larvae? *Glob. Chang Biol.* 20, 754–764. doi: 10.1111/gcb.12485

Frieder, C. A., Nam, S. H., Martz, T. R., and Levin, L. A. (2012). High temporal and spatial variability of dissolved oxygen and pH in a nearshore California kelp forest. *Biogeosciences* 9, 3917–3930. doi: 10.5194/bg-9-3917-2012

Gago, J., and Luís, O. J. (2011). Comparison of spawning induction techniques on *Paracentrotus lividus*(Echinodermata: Echinoidea) broodstock. *Aquac. Int.* 19, 181–191. doi: 10.1007/s10499-010-9351-6

Gattuso, J.-P., Epitalon, J.-M., Lavigne, H., and Orr, J. (2017). *Seacarb: Seawawter Carbonate Chemistry*. Available at: https://CRAN.R-project.org/package = seacarb.

Gaylord, B., Rosman, J. H., Reed, D. C., Koseff, J. R., Fram, J., MacIntyre, S., et al. (2007). Spatial patterns of flow and their modification within and around a giant kelp forest. *Limnol. Oceanogr.* 52, 1838–1852. doi: 10.4319/lo.2007.52.5.1838

Ghalambor, C. K., McKAY, J. K., Carroll, S. P., and Reznick, D. N. (2007). Adaptive versus non-adaptive phenotypic plasticity and the potential for contemporary adaptation in new environments. *Funct. Ecol.* 21, 394–407. doi: 10.1111/j.1365-2435.2007.01283.x

Gobler, C. J., and Baumann, H. (2016). Hypoxia and acidification in ocean ecosystems: coupled dynamics and effects on marine life. *Biol. Lett.* 12:20150976. doi: 10.1098/rsbl.2015.0976

Gradoville, M. R., White, A. E., and Letelier, R. M. (2014). Physiological response of *Crocosphaera watsonii* to enhanced and fluctuating carbon dioxide conditions. *PLoS One* 9:e110660. doi: 10.1371/journal.pone.0110660

Gruber, N., Hauri, C., Lachkar, Z., Loher, D., Frolicher, T. L., and Plattner, G. K. (2012). Rapid progression of ocean acidification in the California Current System. *Science* 337, 220–223. doi: 10.1126/science.1216773

Guadayol, Ò, Silbiger, N. J., Donahue, M. J., and Thomas, F. I. M. (2014). Patterns in Temporal Variability of Temperature, Oxygen and pH along an Environmental Gradient in a Coral Reef. *PLoS One* 9:e85213. doi: 10.1371/journal.pone.0085213

Gunderson, A. R., Armstrong, E. J., and Stillman, J. H. (2016). Multiple stressors in a changing world: the need for an improved perspective on physiological responses to the dynamic marine environment. *Ann. Rev. Mar. Sci.* 8, 357–378. doi: 10.1146/annurev-marine-122414-033953

Hendriks, I. E., Olsen, Y. S., Ramajo, L., Basso, L., Steckbauer, A., Moore, T. S., et al. (2014). Photosynthetic activity buffers ocean acidification in seagrass meadows. *Biogeosciences* 11, 333–346. doi: 10.5194/bg-11-333-2014

Hofmann, G., Blanchette, C., Rivest, E., and Kapsenberg, L. (2013). Taking the pulse of marine ecosystems: the importance of coupling long-term physical and biological observations in the context of global change biology. *Oceanography* 26, 140–148. doi: 10.5670/oceanog.2013.56

Hofmann, G. E. (2017). Ecological epigenetics in marine metazoans. *Front. Mar. Sci* 4:4. doi: 10.3389/fmars.2017.00004

Hofmann, G. E., Smith, J. E., Johnson, K. S., Send, U., Levin, L. A., Micheli, F., et al. (2011). High-frequency dynamics of ocean pH: a multi-ecosystem comparison. *PLoS One* 6:e28983. doi: 10.1371/journal.pone.0028983

Kapsenberg, L., and Hofmann, G. E. (2016). Ocean pH time-series and drivers of variability along the northern Channel Islands, California, USA. *Limnol. Oceanogr.* 61. doi: 10.1002/lno.10264

Kapsenberg, L., Kelley, A. L., Shaw, E. C., Martz, T. R., and Hofmann, G. E. (2015). Near-shore Antarctic pH variability has implications for the design of ocean acidification experiments. *Sci. Rep.* 5:9638. doi: 10.1038/srep09638

Kapsenberg, L., Okamoto, D. K., Dutton, J. M., and Hofmann, G. E. (2017). Sensitivity of sea urchin fertilization to pH varies across a natural pH mosaic. *Ecol. Evol.* 7, 1737–1750. doi: 10.1002/ece3.2776

Kelly, M. W., Padilla-Gamino, J. L., and Hofmann, G. E. (2013). Natural variation and the capacity to adapt to ocean acidification in the keystone sea urchin *Strongylocentrotus purpuratus*. *Glob. Chang Biol.* 19, 2536–2546. doi: 10.1111/gcb.12251

Keppel, A. G., Breitburg, D. L., and Burrell, R. B. (2016). Effects of co-varying diel-cycling hypoxia and ph on growth in the juvenile eastern oyster. *Crassostrea virginica*. *PLoS One* 11:e0161088. doi: 10.1371/journal.pone.0161088

Kim, T. W., Barry, J. P., and Micheli, F. (2013). The effects of intermittent exposure to low-pH and low-oxygen conditions on survival and growth of juvenile red abalone. *Biogeosciences* 10, 7255–7262. doi: 10.5194/bg-10-7255-2013

Kline, D. I., Teneva, L., Hauri, C., Schneider, K., Miard, T., Chai, A., et al. (2015). Six month in situ high-resolution carbonate chemistry and temperature study on a coral reef flat reveals asynchronous pH and temperature anomalies. *PLoS One* 10:e0127648. doi: 10.1371/journal.pone.0127648

Koweek, D. A., Nickols, K. J., Leary, P. R., Litvin, S. Y., Bell, T. W., Luthin, T., et al. (2017). A year in the life of a central California kelp forest: physical and biological insights into biogeochemical variability. *Biogeosciences* 14, 31–44. doi: 10.5194/bg-14-31-2017

Kroeker, K. J., Sanford, E., Rose, J. M., Blanchette, C. A., Chan, F., Chavez, F. P., et al. (2016). Interacting environmental mosaics drive geographic variation in mussel performance and predation vulnerability. *Ecol. Lett.* 19, 771–779. doi: 10.1111/ele.12613

Krumhansl, K. A., Okamoto, D. K., Rassweiler, A., Novak, M., Bolton, J. J., Cavanaugh, K. C., et al. (2016). Global patterns of kelp forest change over the past half-century. *Proc. Natl. Acad. Sci. U.S.A.* 113, 13785–13790. doi: 10.1073/pnas.1606102113

Kwiatkowski, L., Gaylord, B., Hill, T., Hosfelt, J., Kroeker, K. J., Nebuchina, Y., et al. (2016). Nighttime dissolution in a temperate coastal ocean ecosystem increases under acidification. *Sci. Rep.* 6:22984. doi: 10.1038/srep22984

Large, W. G., and Pond, S. (1981). Oepn ocean momentum flux measurements in moderate to strong winds. *J. Phys. Oceanogr.* 11, 324–336. doi: 10.1175/1520-0485(1981)011<0324:OOMFMI>2.0.CO;2

Leal, P. P., Hurd, C. L., Fernández, P. A., and Roleda, M. Y. (2017). Ocean acidification and kelp development: reduced pH has no negative effects on meiospore germination and gametophyte development of *Macrocystis pyrifera* and *Undaria pinnatifida*. *J. Phycol.* 53, 557–566. doi: 10.1111/jpy.12518

Levitan, D. R. (2000). Optimal egg size in marine invertebrates: theory and phylogenetic analysis of the critical relationship between egg size and development time in echinoids. *Am. Nat.* 156, 175–192. doi: 10.1086/303376

Li, F., Wu, Y., Hutchins, D. A., Fu, F., and Gao, K. (2016). Physiological responses of coastal and oceanic diatoms to diurnal fluctuations in seawater carbonate chemistry under two CO_2 concentrations. *Biogeosciences* 13, 6247–6259. doi: 10.5194/bg-13-6247-2016

Marshall, D. J. (2008). Transgenerational plasticity in the sea: context-dependent maternal effects across the life history. *Ecology* 89, 418–427. doi: 10.1890/07-0449.1

Marshall, D. J., and Burgess, S. C. (2015). Deconstructing environmental predictability: seasonality, environmental colour and the biogeography of marine life histories. *Ecol. Lett.* 18, 174–181. doi: 10.1111/ele.12402

Marshall, D. J., Burgess, S. C., and Connallon, T. (2016). Global change, life-history complexity and the potential for evolutionary rescue. *Evol. Appl.* 9, 1189–1201. doi: 10.1111/eva.12396

Marshall, D. J., and Keough, M. J. (2007). The evolutionary ecology of offspring size in marine invertebrates. *Adv. Mar. Biol.* 53, 1–60. doi: 10.1016/S0065-2881(07)53001-4

Martz, T. R., Connery, J. G., and Johnson, K. S. (2010). Testing the Honeywell Durafet® for seawater pH applications. *Limnol. Oceanogr. Methods* 8, 172–184. doi: 10.4319/lom.2010.8.172

Matson, P. G., Yu, P. C., Sewell, M. A., and Hofmann, G. E. (2012). Development Under Elevated p CO 2 conditions does not affect lipid utilization and protein content in early life-history stages of the purple sea urchin. *Strongylocentrotus purpuratus*. *Biol. Bull.* 223, 312–327. doi: 10.1086/BBLv223n3p312

McLaughlin, K., Dickson, A., Weisberg, S. B., Coale, K., Elrod, V., Hunter, C., et al. (2017). An evaluation of ISFET sensors for coastal pH monitoring applications. *Reg. Stud. Mar. Sci.* 12, 11–18. doi: 10.1016/j.rsma.2017.02.008

McLeod, E., Chmura, G. L., Bouillon, S., Salm, R., Björk, M., Duarte, C. M., et al. (2011). A blueprint for blue carbon: toward an improved understanding of the role of vegetated coastal habitats in sequestering CO_2. *Front. Ecol. Environ.* 9, 552–560. doi: 10.1890/110004

Munday, P. L., Warner, R. R., Monro, K., Pandolfi, J. M., and Marshall, D. J. (2013). Predicting evolutionary responses to climate change in the sea. *Ecol. Lett.* 16, 1488–1500. doi: 10.1111/ele.12185

Murray, C. S., Malvezzi, A., Gobler, C. J., and Baumann, H. (2014). Offspring sensitivity to ocean acidification changes seasonally in a coastal marine fish. *Mar. Ecol. Prog. Ser.* 504, 1–11. doi: 10.3354/meps10791

Nielsen, K. J., Stachowicz, J. J., Boyer, K., Bracken, M., Chan, F., Chavez, F., et al. (2018). *Emerging Understanding of the Potential Role of Seagrass and Kelp as An Ocean Acidification Management Tool in California*. Oakland, CA: California Ocean Science Trust.

Olofsson, H., Ripa, J., and Jonzén, N. (2009). Bet-hedging as an evolutionary game: the trade-off between egg size and number. *Proc. R. Soc. B Biol. Sci.* 276, 2963–2969. doi: 10.1098/rspb.2009.0500

Oreska, M. P. J., McGlathery, K. J., and Porter, J. H. (2017). Seagrass blue carbon spatial patterns at the meadow-scale. *PLoS One* 12:e0176630. doi: 10.1371/journal.pone.0176630

Pacella, S. R., Brown, C. A., Waldbusser, G. G., Labiosa, R. G., and Hales, B. (2018). Seagrass habitat metabolism increases short-term extremes and long-term offset of CO 2 under future ocean acidification. *Proc. Natl. Acad. Sci. U.S.A.* 115, 3870–3875. doi: 10.1073/pnas.1703445115

Pan, T.-C. F., Applebaum, S. L., and Manahan, D. T. (2015). Experimental ocean acidification alters the allocation of metabolic energy. *Proc. Natl. Acad. Sci. U.S.A.* 112, 4696–4701. doi: 10.1073/pnas.1416967112

Pearse, J. S. (2006). Ecological role of purple sea urchins. *Science* 314, 940–941. doi: 10.1126/science.1131888

Pettersen, A. K., White, C. R., Bryson-Richardson, R. J., and Marshall, D. J. (2019). Linking life-history theory and metabolic theory explains the offspring size-temperature relationship. *Ecol. Lett.* 22, 518–526. doi: 10.1111/ele.13213

Price, T. D., Qvarnstrom, A., and Irwin, D. E. (2003). The role of phenotypic plasticity in driving genetic evolution. *Proc. R. Soc. B Biol. Sci.* 270, 1433–1440. doi: 10.1098/rspb.2003.2372

Prowse, T. A. A., Sewell, M. A., and Byrne, M. (2007). Fuels for development: evolution of maternal provisioning in asterinid sea stars. *Mar. Biol.* 153, 337–349. doi: 10.1007/s00227-007-0809-7

Przeslawski, R., Byrne, M., and Mellin, C. (2015). A review and meta-analysis of the effects of multiple abiotic stressors on marine embryos and larvae. *Glob. Chang Biol.* 21, 2122–2140. doi: 10.1111/gcb.12833

Reed, D., Washburn, L., Rassweiler, A., Miller, R., Bell, T., and Harrer, S. (2016). Extreme warming challenges sentinel status of kelp forests as indicators of climate change. *Nat. Commun.* 7:13757. doi: 10.1038/ncomms13757

Reed, D. C., Rassweiler, A., Carr, M. H., Cavanaugh, K. C., Malone, D. P., and Siegel, D. A. (2011). Wave disturbance overwhelms top-down and bottom-up control of primary production in California kelp forests. *Ecology* 92, 2108–2116. doi: 10.1890/11-0377.1

Rivest, E. B., O'Brien, M., Kapsenberg, L., Gotschalk, C. C., Blanchette, C. A., Hoshijima, U., et al. (2016). Beyond the benchtop and the benthos: dataset management planning and design for time series of ocean carbonate chemistry associated with Durafet®-based pH sensors. *Ecol. Inform.* 36, 209–220. doi: 10.1016/j.ecoinf.2016.08.005

Roleda, M. Y., Cornwall, C. E., Feng, Y., McGraw, C. M., Smith, A. M., and Hurd, C. L. (2015). Effect of Ocean Acidification and pH Fluctuations on the growth and development of coralline algal recruits, and an associated benthic algal assemblage. *PLoS One* 10:e0140394. doi: 10.1371/journal.pone.0140394

Roleda, M. Y., Morris, J. N., McGraw, C. M., and Hurd, C. L. (2012). Ocean acidification and seaweed reproduction: increased CO_2 ameliorates the negative effect of lowered pH on meiospore germination in the giant kelp *Macrocystis pyrifera* (Laminariales, Phaeophyceae). *Glob. Change Biol.* 18, 854–864. doi: 10.1111/j.1365-2486.2011.02594.x

RStudio Team (2017). *RStudio: Integrated Develpment for R*. Boston, MA: RStudio, Inc.

Salinas, S., and Munch, S. B. (2012). Thermal legacies: transgenerational effects of temperature on growth in a vertebrate: thermal transgenerational plasticity. *Ecol. Lett.* 15, 159–163. doi: 10.1111/j.1461-0248.2011.01721.x

Schneider, C. A., Rasband, W. S., and Eliceiri, K. W. (2012). NIH Image to ImageJ: 25 years of image analysis. *Nat. Methods* 9, 671–675. doi: 10.1038/nmeth.2089

Silbiger, N. J., and Sorte, C. J. B. (2018). Biophysical feedbacks mediate carbonate chemistry in coastal ecosystems across spatiotemporal gradients. *Sci. Rep* 8:796. doi: 10.1038/s41598-017-18736-6

Small, D. P., Milazzo, M., Bertolini, C., Graham, H., Hauton, C., Hall-Spencer, J. M., et al. (2016). Temporal fluctuations in seawater pCO_2 may be as important as mean differences when determining physiological sensitivity in natural systems. *ICES J. Mar. Sci. J. Cons.* 73, 604–612. doi: 10.1093/icesjms/fsv232

Smith, S. R. (2016). *Seagrasses as Potential Chemical Refugia for Acidification-Sensitive Bivalves*. Corvallis, OR: The Valley Library.

Sorte, C. J. B., and Bracken, M. E. S. (2015). Warming and Elevated CO_2 interact to drive rapid shifts in marine community production. *PLoS One* 10:e0145191. doi: 10.1371/journal.pone.0145191

Steckbauer, A., Duarte, C. M., Carstensen, J., Vaquer-Sunyer, R., and Conley, D. J. (2011). Ecosystem impacts of hypoxia: thresholds of hypoxia and pathways to recovery. *Environ. Res. Lett.* 6:025003. doi: 10.1088/1748-9326/6/2/025003

Stillman, J. H., and Armstrong, E. (2015). Genomics are transforming our understanding of responses to climate change. *Bioscience* 65, 237–246. doi: 10.1093/biosci/biu219

Strathmann, M. F. (1987). *Reproduction and Development of Marine Invertebrates of the Northern Pacific Coast*. Seattle: University of Washington Press.

Stumpp, M., Wren, J., Melzner, F., Thorndyke, M. C., and Dupont, S. T. (2011). CO_2 induced seawater acidification impacts sea urchin larval development I: elevated metabolic rates decrease scope for growth and induce developmental delay. *Comp. Biochem. Physiol. Mol. Integr. Physiol.* 160, 331–340. doi: 10.1016/j.cbpa.2011.06.022

Sunday, J. M., Bates, A. E., and Dulvy, N. K. (2011). Global analysis of thermal tolerance and latitude in ectotherms. *Proc. R. Soc. B Biol. Sci.* 278, 1823–1830. doi: 10.1098/rspb.2010.1295

Todgham, A. E., and Stillman, J. H. (2013). Physiological responses to shifts in multiple environmental stressors: relevance in a changing world. *Integr. Comp. Biol.* 53, 539–544. doi: 10.1093/icb/ict086

Unsworth, R. K. F., Collier, C. J., Henderson, G. M., and McKenzie, L. J. (2012). Tropical seagrass meadows modify seawater carbon chemistry: implications for coral reefs impacted by ocean acidification. *Environ. Res. Lett.* 7:024026. doi: 10.1088/1748-9326/7/2/024026

Vaquer-Sunyer, R., and Duarte, C. M. (2008). Thresholds of hypoxia for marine biodiversity. *Proc. Natl. Acad. Sci. U.S.A.* 105, 15452–15457. doi: 10.1073/pnas.0803833105

Vargas, C. A., Lagos, N. A., Lardies, M. A., Duarte, C., Manríquez, P. H., Aguilera, V. M., et al. (2017). Species-specific responses to ocean acidification should account for local adaptation and adaptive plasticity. *Nat. Ecol. Evol.* 1, 1–7. doi: 10.1038/s41559-017-0084

Washburn, L. (2018). *SBCLTER: Ocean: Currents and Biogeochemistry: Moored CTD and ADCP Data at Mohawk Reef (MKO), Ongoing Since 2005*. Available at: https://doi.org/10.6073/pasta/61ebe5fbec4663479ddae0eb5961d374. doi: 10.6073/pasta/61ebe5fbec4663479ddae0eb5961d374

Weiss, R. F. (1970). The solubility of nitrogen, oxygen and argon in water and seawater. *Deep Sea Res. Oceanogr. Abstr.* 17, 721–735. doi: 10.1016/0011-7471(70)90037-9

Wernberg, T., Krumhansl, K., Filbee-Dexter, K., and Pedersen, M. F. (2019). Status and Trends for the World's Kelp Forests. *World Seas* 3, 57–78. doi: 10.1016/B978-0-12-805052-1.00003-6

Wetzel, R. G., and Likens, G. E. (1991). *Limnological Analyses*, 2nd Edn. Berlin: Springer-Verlag. doi: 10.1002/rrr.3450070410

Wilt, F. H. (2002). Biomineralization of the Spicules of Sea Urchin Embryos. *Zool. Sci.* 19, 253–261. doi: 10.2108/zsj.19.253

Wong, J. M., Johnson, K. M., Kelly, M. W., and Hofmann, G. E. (2018). Transcriptomics reveal transgenerational effects in purple sea urchin embryos: adult acclimation to upwelling conditions alters the response of their progeny to differential *p* CO 2 levels. *Mol. Ecol.* 27, 1120–1137. doi: 10.1111/mec.14503

Yu, P. C., Matson, P. G., Martz, T. R., and Hofmann, G. E. (2011). The ocean acidification seascape and its relationship to the performance of calcifying marine invertebrates: laboratory experiments on the development of urchin larvae framed by environmentally-relevant pCO_2/pH. *J. Exp. Mar. Biol. Ecol.* 400, 288–295. doi: 10.1016/j.jembe.2011.02.016

Conflict of Interest Statement: The authors declare that the research was conducted in the absence of any commercial or financial relationships that could be construed as a potential conflict of interest.

frontiers in Marine Science

ORIGINAL RESEARCH
published: 06 March 2019
doi: 10.3389/fmars.2019.00099

Chesapeake Bay Inorganic Carbon: Spatial Distribution and Seasonal Variability

*Jean R. Brodeur[1], Baoshan Chen[1], Jianzhong Su[1,2], Yuan-Yuan Xu[1], Najid Hussain[1], K. Michael Scaboo[1], Yafeng Zhang[3], Jeremy M. Testa[4] and Wei-Jun Cai[1]**

[1] School of Marine Science and Policy, University of Delaware, Newark, DE, United States, [2] State Key Laboratory of Marine Environmental Science, Xiamen University, Xiamen, China, [3] School of Marine Science, Sun Yat-sen University, Guangzhou, China, [4] Chesapeake Biological Laboratory, University of Maryland Center for Environmental Science, Solomons, MD, United States

Edited by:
Andrea J. Fassbender,
Monterey Bay Aquarium Research Institute (MBARI), United States

Reviewed by:
Sophie Chu,
University of Washington, United States
Gregory J. Pelletier,
Washington State Department of Ecology, United States

***Correspondence:**
Wei-Jun Cai
wcai@udel.edu

Specialty section:
This article was submitted to Coastal Ocean Processes, a section of the journal Frontiers in Marine Science

Received: *16 August 2018*
Accepted: *19 February 2019*
Published: *06 March 2019*

Citation:
Brodeur JR, Chen B, Su J, Xu Y-Y, Hussain N, Scaboo KM, Zhang Y, Testa JM and Cai W-J (2019) Chesapeake Bay Inorganic Carbon: Spatial Distribution and Seasonal Variability. Front. Mar. Sci. 6:99. doi: 10.3389/fmars.2019.00099

Few estuaries have inorganic carbon datasets with sufficient spatial and temporal coverage for identifying acidification baselines, seasonal cycles and trends. The Chesapeake Bay, though one of the most well-studied estuarine systems in the world, is no exception. To date, there have only been observational studies of inorganic carbon distribution and flux in lower bay sub-estuaries. Here, we address this knowledge gap with results from the first complete observational study of inorganic carbon along the main stem. Dissolved inorganic carbon (DIC) and total alkalinity (TA) increased from surface to bottom and north to south over the course of 2016, mainly driven by seasonal changes in river discharge, mixing, and biological carbon dioxide (CO_2) removal at the surface and release in the subsurface. Upper, mid- and lower bay DIC and TA ranged from 1000–1300, 1300–1800, and 1700–1900 μmol kg^{-1}, respectively. The pH range was large, with maximum values of 8.5 at the surface and minimums as low as 7.1 in bottom water in the upper and mid-bay. Seasonally, the upper bay was the most variable for DIC and TA, but pH was more variable in the mid-bay. Our results reveal that low pH is a continuing concern, despite reductions in nutrient inputs. There was active internal recycling of DIC and TA, with a large inorganic carbon removal in the upper bay and at salinities < 5 most months, and a large addition in the mid-salinities. In spring and summer, waters with salinities between 10 and 15 were a large source of DIC, likely due to remineralization of organic matter and dissolution of $CaCO_3$. We estimate that the estuarine export flux of DIC and TA in 2016 was $40.3 \pm 8.2 \times 10^9$ mol yr^{-1} and $47.1 \pm 8.6 \times 10^9$ mol yr^{-1}. The estuary was likely a large sink of DIC, and possibly a weak source of TA. These results support the argument that the Chesapeake Bay may be an exception to the long-standing assumption that estuaries are heterotrophic. Furthermore, they underline the importance of large estuarine systems for mitigating acidification in coastal ecosystems, since riverine chemistry is substantially modified within the estuary.

Keywords: estuarine acidification, Chesapeake Bay, inorganic carbon, export flux, carbon budget

INTRODUCTION

Since industrialization, the oceans have absorbed at least 25% of anthropogenic carbon dioxide release due to fossil fuel combustion and land use change (Sabine et al., 2004; Le Quéré et al., 2017). Consequently, there has been a 30% increase in surface ocean acidity, a phenomenon called "ocean acidification" (Doney et al., 2009). Although there is global evidence of ocean acidification in open ocean waters (Bates et al., 2014), pH declines in estuaries have largely been attributed to eutrophication (Abril et al., 2004; Sarma et al., 2011). Eutrophication is the process by which additional inputs of organic matter derived from allocthonous transport and nutrient-fueled phytoplankton production stimulate respiration, lowering pH and oxygen in subsurface or downstream waters (Nixon, 1995). Anthropogenic nutrient runoff in rivers has been found to exert a larger influence on estuarine carbonate chemistry than ocean acidification (Borges and Gypens, 2010). The combination of acidification and eutrophication can result in an additional pH decline in estuaries, due to changes in buffering capacity (Cai et al., 2011; Breitburg et al., 2015). However inorganic carbon data for most estuarine systems are insufficient to define spatial and seasonal heterogeneity, which is necessary for establishing baseline pH information from which trends can be evaluated. This information gap is a serious obstacle for resource management in these economically and socially valuable systems.

The Chesapeake Bay is the largest estuarine system in the United States, with a main stem stretching 300 km long and 8–48 km wide, an average depth of 8 m, and a deep trench up to 50 m (Cerco and Cole, 1993). The water column is partially mixed and microtidal, with two-layer circulation and episodic winds dominating mixing processes (Li et al., 2005). The bay is usually divided into three major sections: an oligohaline, heterotrophic upper bay, containing the estuarine turbidity maximum; a mesohaline, generally autotrophic mid-bay, containing most of the hypoxic zone (Testa and Kemp, 2014); and a polyhaline lower bay with a balanced net metabolism (Kemp et al., 1997; Cornwell et al., 1999). Historically, one of the major water quality issues for the bay has been eutrophication, caused by an increasing human population in the watershed and land clearing and fertilization for agriculture (Kemp et al., 2005). The Chesapeake is particularly susceptible to eutrophication because of its long residence time of 90–180 days for freshwater and nutrients (Kemp et al., 2005) and circulation patterns that enhance recycling of nutrients (Boesch et al., 2001), which tends to stimulate high productivity. Many processes in the Chesapeake Bay vary strongly with season: stratification and hypoxia (Testa and Kemp, 2014); primary production, respiration, and sediment metabolism (Baird and Ulanowicz, 1989; Smith and Kemp, 1995; Cowan and Boynton, 1996); freshwater flow and sedimentation rates (Baird and Ulanowicz, 1989); groundwater recharge and nitrate leaching (Boesch et al., 2001); and wind direction and mixing (Li et al., 2005). This complex natural variability and anthropogenic eutrophication are obstacles to identifying the primary drivers of spatial and temporal variability in inorganic carbon.

Despite large public investments in the restoration of the Chesapeake Bay and ample study of nutrient, oxygen, and organic carbon cycling, few investigations have analyzed the inorganic carbon dynamics of the bay, making it difficult to ascertain the magnitude of carbon cycling, ocean acidification and eutrophication influences on changes in pH. Wong (1979) found that pH decreased with depth and increased with salinity in the James River and the lower Chesapeake Bay. He also found that TA was linearly related to salinity in the surface waters of the lower bay, but that there was a complex pattern of mixing and removal within the James River estuary. Raymond et al. (2000) determined that the York River estuary in the lower bay region was heterotrophic at most times and in most places, with strong seasonal patterns. Based on an analysis of historical pH data from a long-term monitoring program, Waldbusser et al. (2013) determined that daytime average surface pH declined over a 25-year period in polyhaline waters, but not in lower salinity regions. Cai et al. (2017) explored water column inorganic carbon dynamics at a station in the upper part of the mid-bay, focusing on pH minima in the sub-oxic zone and the implications for estuarine buffering. These studies raised important questions about whether there were significant, unobserved sources and sinks of TA in the bay that could not be resolved with existing observational data. However, there has been no previous study providing complete coverage of DIC, TA and pH distributions in the Chesapeake Bay.

The objective of this study was to measure the distribution of inorganic carbon across seasons (10 months) in the full Chesapeake Bay, and to better evaluate the bay-ocean carbon flux and vulnerability to estuarine acidification. Such studies are important for the management of valuable estuarine resources, as well as improving our understanding of spatial and seasonal changes and the underlying processes at local or regional scales for global ocean acidification research.

MATERIALS AND METHODS

Station and Cruise Information

Ten cruises were conducted in the Chesapeake Bay in 2016: four on the R/V *Rachel Carson* from May 4–6, June 6–10, August 8–12, and October 10–13; and six on the R/V *Randall T. Kerhin* from March 14–16, April 12–13, July 11–13, September 19–21, November 14–15, and December 12–14. *Carson* cruises, except for May, covered the main stem along the full longitudinal axis of the bay, while the *Kerhin* cruises took place solely in Maryland waters, with a southernmost point approximately at the latitude where the Potomac River meets the bay. Stations (**Figure 1**) were selected from existing Water Quality Monitoring stations designated through the collaboration between the States of Maryland and Virginia and the Chesapeake Bay Program[1]. We added an Atlantic Ocean site (AO1) in the mouth of the Bay at approximately 37.061°N, 75.856°W, and an additional site south of the Chesapeake Bay Bridge called Station 858 at approximately 38.962°N, 76.380°W [previously studied by Cai et al. (2017)].

---

[1] www.chesapeakebay.net

The upper bay stations start with the Susquehanna River (CB 1.1) and end with CB 3.2. The Susquehanna Flats are the shallow mudflats located between stations CB 1.1 and CB 2.1. The mid-bay stations start near the Bay Bridge at 39°N with CB 3.3 through CB 5.4. The lower bay stations start in Virginia waters south of the Potomac River mouth with CB 5.5 and end with AO1 in the Atlantic Ocean.

Susquehanna River DIC and TA were sampled monthly at United States Geological Survey site #01578310 in Conowingo, MD, United States. Discharge, temperature and calcium data were obtained from the USGS water quality data portal[2]. For March and April, the Susquehanna River was sampled at nearby Havre de Grace, MD (39.77278°N, 76.08639°W). The Maryland Department of Natural Resources measured Secchi depth, dissolved inorganic nutrients, chlorophyll-a, and performed hydrocasts for profiles of pH, oxygen, temperature, and salinity during the R/V *Kerhin* cruises[3].

Sampling Method and Laboratory Analysis

DIC and TA samples of 250 mL and pH samples of 100 mL were collected at multiple depths via a submersible pump and filtered through a cellulose acetate cartridge filter (pore size 0.45 μm) into a borosilicate glass bottle according to previously published methods (Huang et al., 2012). During the State of Maryland monitoring cruises (March, April, July, September, November, December), hereafter referred to as "DNR cruises," we sampled water at depths used for regular monitoring: surface, above and below the pycnocline (if present), and at the bottom. State officials determined the sampling depths by observing changes in salinity during the casts. For the May, June, August, and October cruises, subsequently referred to as "Carson cruises," we were able to sample at a higher vertical resolution, selecting depths where salinity, oxygen, pH, or partial pressure of CO_2 (pCO_2) profiles showed variation, resulting in more depths sampled per station overall during those months. All DIC samples were preserved with 50 μL of saturated mercuric chloride solution ($HgCl_2$) and refrigerated at 4°C until analysis (normally within 3–5 days). TA sample handling varied, depending on season and salinity, because $HgCl_2$ can cause acidifying reactions in very low salinity water ($S < 5$) or precipitate mercury sulfide (HgS) in anoxic water, releasing acid that may affect alkalinity (Hiscock and Millero, 2006; Cai et al., 2017). For March, April, November, and December DNR cruises, DIC and TA were measured from the same samples, preserved with 50 μL of saturated $HgCl_2$ solution and refrigerated at 4°C until analysis. During the Carson cruises, DIC and TA samples were taken in separate bottles and the TA samples were not preserved, but they were refrigerated at 4°C until analysis and analyzed at a nearby land-based lab within 24 h. During the July and September DNR cruises, all bottom water DIC and TA samples, and low salinity samples from stations CB 1.1 and CB 2.1, were taken separately, refrigerated at 4°C, and unpreserved TA samples analyzed within 72 h. pH samples were not preserved and were either measured immediately after sampling each station (Carson cruises) or refrigerated at 4°C and measured within 4–10 h of sampling (DNR cruises).

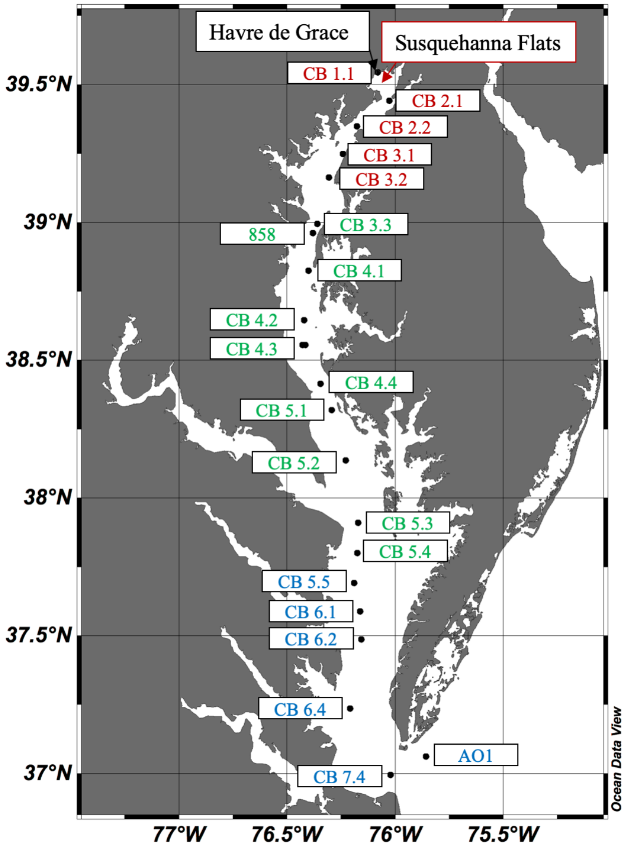

FIGURE 1 | Map of the Chesapeake Bay with stations sampled in 2016. The Upper Bay stations labeled in red include CB 1.1 through CB 3.2.; Mid-Bay stations in green are CB 3.3 through CB 5.4; and Lower Bay stations in blue are CB 5.5 through AO1. The Susquehanna River meets the bay at CB 1.1, the Potomac River near CB 5.3, and the James River near CB 7.4.

Dissolved inorganic carbon was measured by acidifying 1mL subsamples with phosphoric acid and quantifying the CO_2 gas released using an infrared analyzer (AS-C3, Apollo Scitech, Newark, DE, United States). TA was measured by open cell Gran titration (Dickson, 1981) with a semi-automatic titration system (AS-ALK2, Apollo Scitech, Newark, DE, United States). Measurements were calibrated against certified reference material produced by A.G. Dickson (Scripps Institution of Oceanography, San Diego, CA, United States). Further analytical detail is described in Huang et al. (2012). pH was measured on the NBS scale at 25°C using an Orion glass electrode calibrated against three NBS standard buffers (4, 7, and 10). Confidence intervals of 95% were calculated by finding the mean percentage error for DIC and TA (unit error for pH) in duplicate samples taken during all the cruises and then adding twice the standard error, which was determined by dividing the standard deviation among the errors by the square root of the number of duplicate pairs. The resulting 95% confidence interval for the sample collection and

---

[2] https://waterdata.usgs.gov/nwis/qw

[3] https://www.chesapeakebay.net/what/downloads/cbp_water_quality_database_1984_present

measurements are ±0.2% for DIC, ±0.3% for TA, and ±0.017 for pH (NBS). Because the analytical precision was about ±0.1% for three repeat DIC measurements and ±0.1 to 0.2% for two repeat TA measurements, the larger uncertainties are likely caused by the inherent sampling limitations of using a submersible pump.

Calculations for DIC and TA Net Export Flux

In order to analyze the distribution of DIC and TA in the bay, estimate the Chesapeake Bay flux of DIC and TA, and determine whether the estuary was a source or sink of inorganic carbon, we first had to calculate conservative DIC and TA values based on two endmember mixing between freshwater and seawater during estuarine transport. To do this, we plotted a line along the estuarine salinity gradient between riverine and oceanic DIC and TA values (Officer, 1979). For the Susquehanna River endmember DIC and TA values, we used monthly observational data at the Conowingo Dam (USGS Site #01578310), and in nearby Havre de Grace, MD, United States for March and April.

For the oceanic endmember, we calculated Mid-Atlantic Bight (MAB) surface layer values at 75.5°W and 36.5°N based on data from the Gulf of Mexico and East Coast Carbon cruises #1 (2007) and #2 (2012), and East Coast Ocean Acidification (ECOA) cruise (2015). Selected observations cover 17 months from 2011 to 2015. Salinity was obtained from Aquarius satellite data[4] and temperature values from Optimum Interpolation Sea Surface Temperature (OISST, v2)[5]. MAB TA was derived from ECOA cruise data using salinity based on the linear relationship $TA = (47.69(\pm 0.99) \times S) + 640.77(\pm 31.96)$, $r^2 = 0.95$, root-mean-square error = 19.6. The number of ECOA observations used was 131. For more information, studies using similar methods have recently been published, including one using the MAB data (Fassbender et al., 2017; Xu et al., 2017). MAB DIC was then calculated from seawater fugacity of CO_2 ($f CO_2$) from SOCAT (Bakker et al., 2016), the salinity-derived TA, temperature and salinity using CO2SYS (Lewis and Wallace, 1998).

We averaged the DIC, TA and salinity values for months that were sampled more than once during the 2011–2015 period. For the months of April and December, during which there was no data, we averaged the months before and after. We compared our calculated monthly MAB TA values with those previously published in order to validate the method (Signorini et al., 2013). Our values averaged just 5.2 μmol kg^{-1} higher (standard deviation 0.6, median 5.4). We also compared our calculated TA with the measured values at station AO1 in the bay mouth to further validate the equation, although we do not expect the two to be identical as this station is near the mouth and is likely affected by bay processes. Calculated TA values for the MAB salinity were 25.3 μmol kg^{-1} lower than those observed at AO1 in June, 30.0 μmol kg^{-1} lower in August, and 20.9 μmol kg^{-1} higher in October. Those differences are only 1% of the total TA value, demonstrating that the equation generates TA that is representative of the oceanic endmember and consistent over the seasonal cycle. Since the SOCAT $f CO_2$ and TA that is very similar to previously published and observed data were used to generate the DIC, we believe it is reasonable to use these values to represent the MAB in 2016.

Previous studies have estimated riverine DIC and TA fluxes to the ocean using an effective concentration (C*) describing what the values would be if all estuarine change was related to mixing, and the river discharge rate (Q) in the equation: $Flux = Q \times C^*$ (Officer, 1979; Cai et al., 2004; Joesoef et al., 2017). So, to estimate the Chesapeake Bay net estuarine export flux, we first calculated a monthly linear regression of the high salinity section of the data where TA was found to be mixed linearly with the oceanic endmember ($S \geq 20$ for most months, and > 15 in March and April, see **Figures 7–9**). Since there was no main stem cruise in January or February, we used the high salinity linear trend from December and March, respectively. Then we used the linear equation to extrapolate to zero salinity (C*), which would represent the expected Susquehanna River value if all of the estuarine change was related to the mixing of the two end members. When multiplied by the river discharge, this value gives us the bay export. Finally, we subtracted the extrapolated river values (the effective concentration, C*) from the measured riverine DIC and TA (C) and determined the difference related to estuarine processing. The difference was multiplied by the river discharge at the USGS station to determine the net internal accumulation, using the equation: $Q \times (C - C^*)$. Though there are significant subtidal estuarine flows of incoming and outgoing ocean water at the mouth of the bay, this method produces an estimate of the residual current because we extrapolate to zero salinity where tidal excursion is zero (residual current = river discharge, see Cai et al., 2004). However, our bay export flux could be up to 40% too low, as we did not add all other tributary discharge to the Susquehanna discharge (Q). Assuming the chemistry of other rivers are similar to the Susquehanna River, one could multiply the export flux estimated here by the ratio of the total river discharge to the Susquehanna River to derive the bay export flux. So, we also added the discharge for the Potomac and James Rivers in 2016 to the Susquehanna discharge (Q) value and estimated the full net estuarine export flux.

The most significant source of error in the net export estimation is due to the variability of the riverine DIC and TA flux, since the oceanic values were consistent and the analytical errors for the DIC and TA measurements were small. We addressed this by using a dataset of Susquehanna River sampling in 2016 that included multiple measurements per month to calculate the variation in DIC and TA. So, for the estimate of river variation, which we used as an error estimate for our export flux calculation, we used either the mean observed difference between the samples for a given month, or the mean difference for all the months, if the river was not sampled multiple times. The 2016 mean monthly variation was 97.4 μmol kg^{-1} for DIC and 105.3 μmol kg^{-1} for TA. We also tested the potential error related to the use of a high salinity trend for those months during which we did not have lower bay sampling by calculating the high salinity DIC and TA trend for June, August, and October with and without the lower bay stations and seeing the effect on the export estimate. In four of the six cases, the resultant export estimate was within the

---

[4] https://podaac.jpl.nasa.gov/aquarius

[5] https://www.esrl.noaa.gov/psd/data/gridded/data.noaa.oisst.v2.html

margin of error related to Susquehanna variation. However, when omitting the lower bay measurements, the calculated net DIC accumulation in June was a removal of 0.1×10^9 mol C yr^{-1}, when the one using the full bay data was an addition of $0.3 \pm 0.1 \times 10^9$ mol C yr^{-1}. The October net TA accumulation without the lower bay data was an addition of 0.5×10^9 mol C yr^{-1}, when the one using the full bay data was an addition of $0.3 \pm 0.1 \times 10^9$ mol C yr^{-1}. So, even though the majority of the tests showed the method to work appropriately, we have doubled the uncertainty for all of the export estimates for months in which there was no lower bay sampling. Finally, in order to explore the uncertainty in the oceanic value, we compared the effect of the difference in the calculated MAB TA and the published MAB TA on the effective concentration (C*). Using the October data and the two estimates, we calculated C* as explained in the previous paragraph. The previously published DIC and TA values generated C* values that were 11.9 μmol kg^{-1}, and 28.4 μmol kg^{-1} higher, respectively, an amount well within our uncertainty estimate for Susquehanna variability.

Upper Bay TA Removal

We investigated the surface chemical change between stations CB 1.1 and CB 2.1 in the Susquehanna Flats by calculating the impact of processes that result in DIC and TA change. First, we used the extended Redfield ratio (Redfield, 1934) ($106CO_2 + 16HNO_3 + H_3PO_4 + 122H_2O \leftrightarrow (CH_2O)_{106}(NH_3)_{16}(H_3PO_4) + 138O_2$ in conjunction with contemporaneous oxygen measurements to subtract the amount of DIC and TA change related to photosynthesis (assuming a photosynthetic quotient of 1, similar to that used by previous studies; Kemp et al., 1997). It was assumed that the surface waters were in equilibration with the atmosphere, and thus any change in oxygen was related to biological influence. Although this is not necessarily always the case, the stations are located close to one another and were sampled within an hour of each other, so we believe that any change in oxygen related to meteorological conditions would affect both stations. We also identified the DIC and TA change related to salinity differences between the stations by using the monthly mixing line equations to calculate the expected DIC and TA values and subtracted the mixing-related difference from the observed DIC and TA. Finally, we compared the ratio of the remaining TA to DIC change between stations to see if there was evidence of formation or dissolution of $CaCO_3$, which would result in removal or addition at a ratio of 2:1 ($Ca^{2+} + 2HCO_3^- \leftrightarrow CaCO_3 + CO_2 + H_2O$).

Calculations for Calcite Saturation State

Calcite saturation state values (Ω) were calculated from DIC and TA using CO2SYS version 2.1 (Lewis and Wallace, 1998). For the calculations, the following selections were made: K1 and K2 constants from Millero et al. (2006); $KHSO_4$ from Dickson et al. (1990); NBS pH Scale; and total boron from Uppström (1974). However, the method CO2SYS uses to calculate calcite saturation results in a saturation of zero at S = 0, which underestimates the fresh water saturation state, since the riverine calcium (Ca^{2+}) is neglected. So, we adjusted the CO2SYS calculated saturation state to account for riverine input of calcium using mean monthly [Ca^{2+}] from USGS measurements in 2016 (see Section "Station and Cruise Information" for USGS data source). First, we determined the calcium values calculated by CO2SYS, which uses constants from Mucci (1983), concentrations from Riley and Tongudai (1967), and the equation: $Ca^{2+}_{\text{ocean}} = (0.02128/40.087) \times (S/1.80655)$, where S = sample salinity. Then the river value was used in the following equation to determine the corrected saturation value: $\Omega_{\text{Corrected}} = \Omega_{\text{CO2SYS}} + (\Omega_{\text{CO2SYS}} \times (Ca^{2+}_{\text{river}}/Ca^{2+}_{\text{ocean}})$. For months where there were no USGS measurements (July, Sept., Nov.), we averaged the values from the month before and after. The correction is generally small: for the August data, it is an average addition of 0.25. However it is very important near the freshwater endmember.

Data Visualization

The station map (**Figure 1**), as well as the salinity, DIC, TA, and pH transects in **Figures 3–6** were created using Ocean Data View (Schlitzer, R., Ocean Data View, 2018)[6]. We used DIVA gridding with default options, including automatic scale lengths and color shading.

RESULTS

Seasonal and Spatial Distribution of DIC, TA, and pH

In 2016, the mean monthly discharge of the Susquehanna River was the lowest in a decade, only 776 m^3 s^{-1} compared with a 60-year average of 1153 m^3 s^{-1} (USGS data). The spring, peak freshwater discharge, or the "freshet," was similar to previous years, but occurred in February, two months earlier than average (**Figure 2**). The low freshwater input resulted in high salinity and a northward shift of the estuarine turbidity maximum (ETM) (**Figure 3**). The center of the ETM was defined by where the salinity of the S = 1 isohaline meets the bottom (Boynton et al., 1997), and confirmed by the shoaling of light penetration. The position of the ETM affects local carbonate chemistry by inhibiting primary productivity via reduced light penetration, which can result in less DIC consumption and lower pH.

The spring carbonate chemistry in the Chesapeake Bay was strongly influenced by the arrival of the freshet and the upper bay phytoplankton bloom. At the beginning of the freshet's influence on the bay, in March, DIC and TA increased down the bay at the surface with mixing but was largely uniform below 10 m (**Figure 4**). pH values in the upper bay were among the lowest all year (~7.2), even at the surface. The ETM was centered between stations CB 2.1 and CB 2.2, except for April, when the increasing impact of the freshet pushed it downstream between CB 2.2 and CB 3.1. In April, the freshet coincided with the breakdown of the vertical gradients in salinity (**Figure 3**), DIC and TA (**Figure 4**). During May, as seasonal stratification began, DIC and TA values increased with mixing down the bay at the surface and with depth, except for some removal in the subsurface photosynthesis maximum, and were relatively uniform below the pycnocline

---

[6] https://odv.awi.de

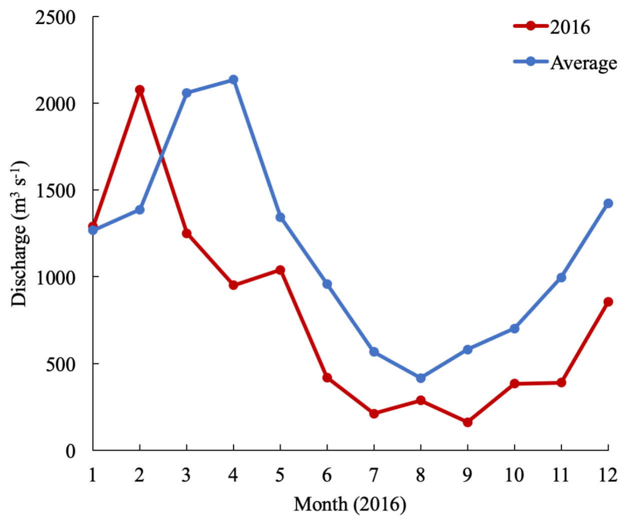

FIGURE 2 | Susquehanna River discharge in 2016 and averaged over 60 years of data collection (USGS data).

in the mid- and lower bays. pH declined with depth and was especially low in the mid-bay in May.

In the summer, the Chesapeake Bay was periodically hypoxic (State of Maryland Department of Natural Resources, 2016) and stratified in the main channel (**Figure 5**). The ETM center was between CB 2.1 and CB 2.2 in June, and between CB 1.1 and CB 2.1 in July and August, the lowest discharge months of the year. Low freshwater discharge resulted in increasing intrusion of ocean water over the season, indicated by increasing bottom water salinity, which also increased DIC and TA. In June, the DIC began to build up at depth in the mid-bay, due to the respiration of organic matter from the spring upper bay bloom. Bottom water pH decreased to a minimum value of ~7.0 to 7.1. July had similar patterns, with a reduction of the vertical gradient at some stations due to mixing and a very shallow pycnocline. Stations CB 2.1 and CB 2.2 (the 2nd and 3rd vertical profiles in the **Figure 5** plots), in the estuarine turbidity maximum, had much lower DIC and TA than CB 1.1, despite similar pH. In August, strong stratification, low freshwater input, and respiration resulted in very high and uniform DIC at depth. At the bottom in the lower bay, TA was particularly high, associated with high salinity water (**Figure 3**). For pH, the minimum was in the ETM and at depth in the mid-bay, due to respiration and possibly the oxidation of reduced chemical species when bottom water was mixed into the oxygenated middle depths, as previously identified during a mixing event in August (Cai et al., 2017). In August, pH at depth in the lower mid-bay and lower bay at around 38°N was high (~7.8–8.0), reflecting the influence of the oceanic endmember and mixing with high pH surface waters at the mouth.

In the early fall, water column chemistry was similar to the summer, but periodic and increasing wind-driven mixing events later reduced the vertical gradient of DIC and TA from over 300 μmol kg^{-1} in September to about 100 μmol kg^{-1}

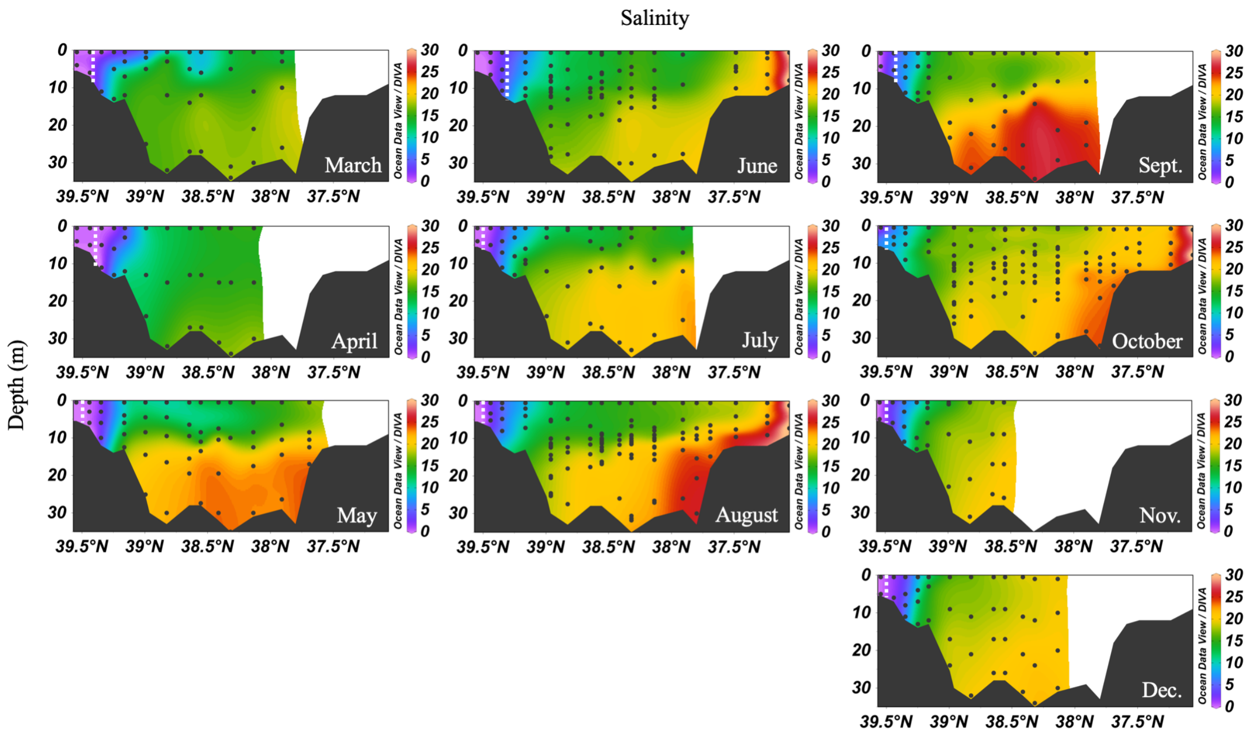

FIGURE 3 | Depth profiles of salinity in 2016. Note that the transect lengths differ. The dividing line between the upper and mid-bay is 39°N and the mid- and lower bay is about 37.75°N. The dashed white lines are the approximate center of the ETM.

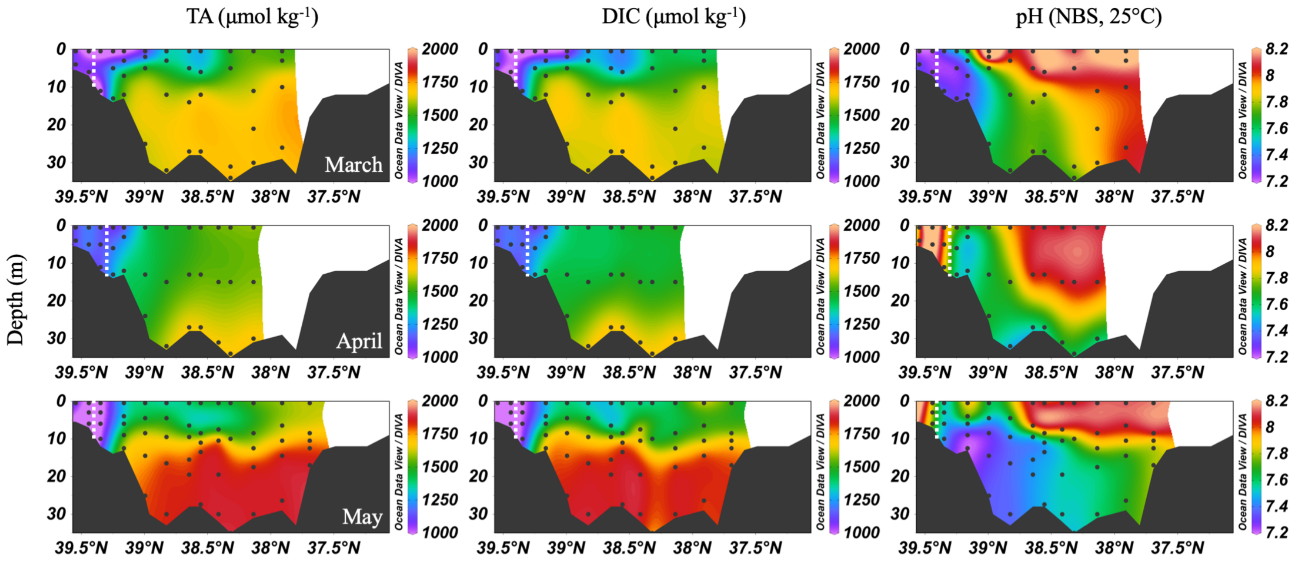

FIGURE 4 | Depth profiles of DIC, TA, and pH in spring, 2016. Note that the transect lengths differ. The dividing line between the upper and mid-bay is 39°N. The dashed white lines are the approximate center of the ETM.

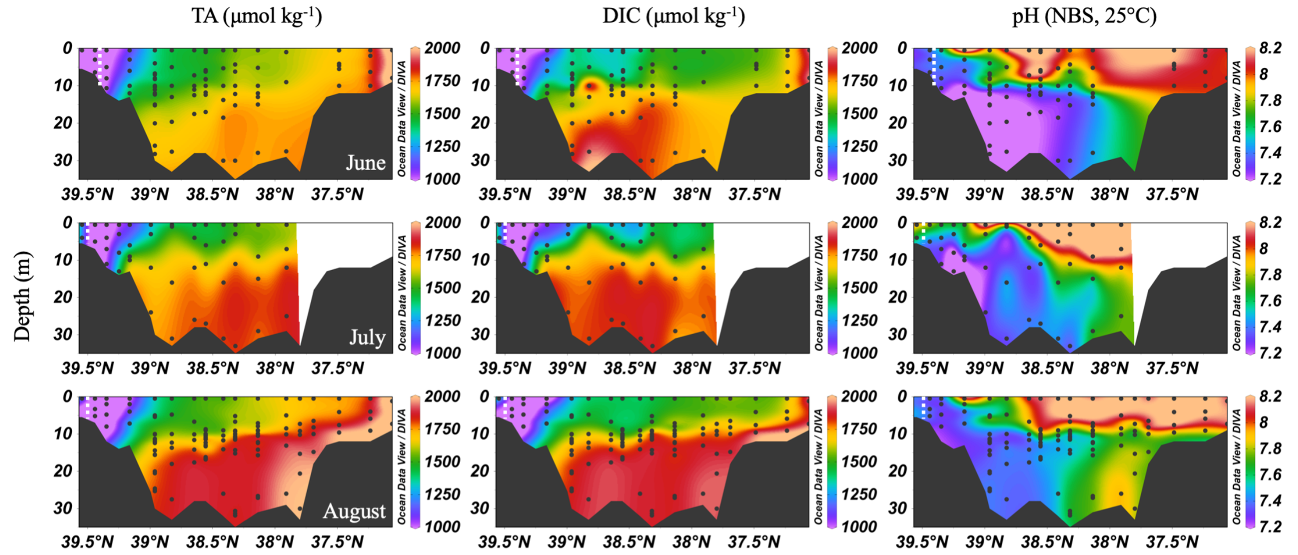

FIGURE 5 | Depth profiles of DIC, TA and pH in summer, 2016. Note that the transect lengths differ. The dividing line between the upper and mid-bay is 39°N and the mid- and lower bay is about 37.75°N. The dashed white lines are the approximate center of the ETM.

in December (**Figure 6**). The ETM was between CB 1.1 and CB 2.1 during the fall and winter. In September, pH was very low in the upper bay and with depth, likely a result of weakened stratification and overturn stimulating respiration and the oxidation of reduced species at depth. Later in the fall, the pH increased to the upper bay mean pH maximum (~7.9). Notably, high productivity was evident at the surface even as late as November, with a mean mid-bay surface pH of about 8.2, the seasonal maximum value and nearly as high as the overall surface maximum of 8.3 in July. One of the highest station vertical mean pH values, 8.15, was measured in December at CB 1.1.

As expected, mean DIC and TA increased with salinity in the Chesapeake Bay, so they increased from the upper bay to the lower bay and with depth (**Table 1**). The smallest difference in DIC and TA between the upper and mid-bay average, sectional values was in the fall/winter, in December: a minimum DIC difference of 162.5 μmol kg^{-1} (surface) and 322.6 μmol kg^{-1} (bottom); and a minimum TA difference of 279.2 μmol kg^{-1} (surface) and 348.9 μmol kg^{-1} (bottom). The December pH difference was just 0.11 at the surface and 0.02 at depth. The largest difference was in the summer, in August: with a DIC difference of 447.8 μmol kg^{-1} (surface) and

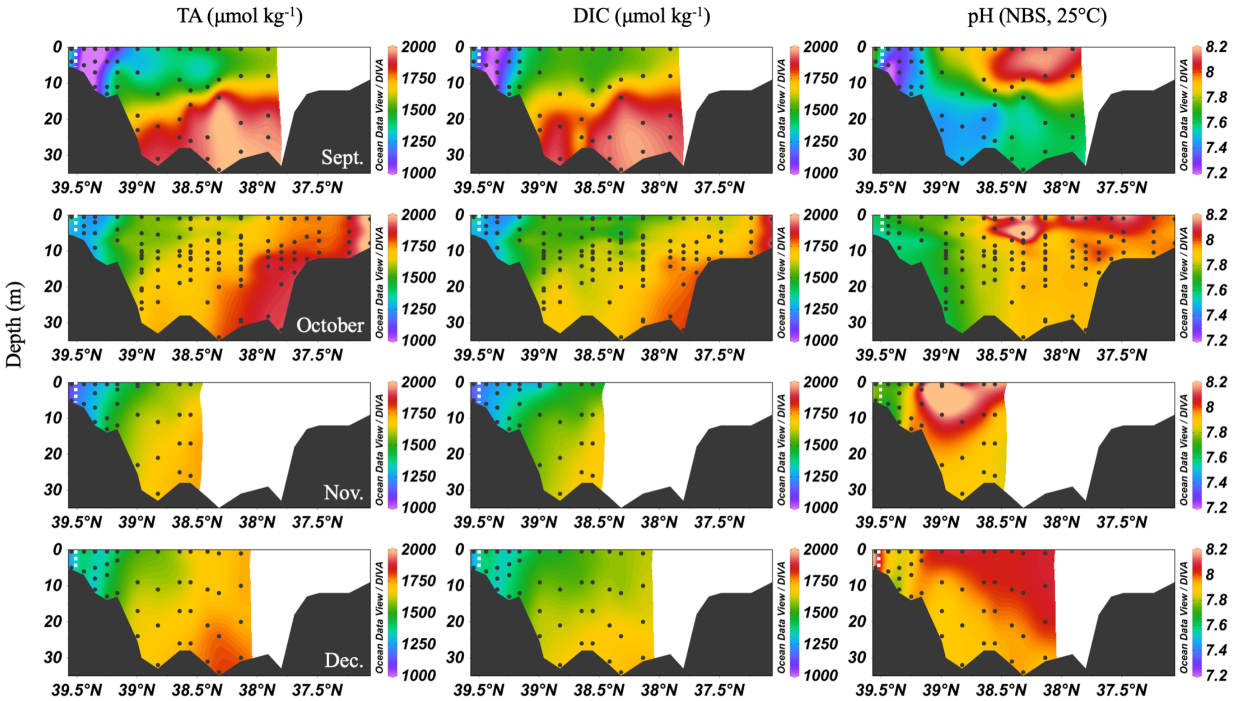

FIGURE 6 | Depth profiles of DIC, TA and pH in fall/winter, 2016. Note that the transect lengths differ. The dividing line between the upper and mid-bay is 39°N and the mid- and lower bay is about 37.75°N. The dashed white lines are the approximate center of the ETM.

TABLE 1 | Seasonal mean carbon parameters for bay regions in 2016.

Segment	Season	TA (μmol kg^{-1})		DIC (μmol kg^{-1})		pH (NBS, 25°C)		Ω Calcite	
		Surface	Bottom	Surface	Bottom	Surface	Bottom	Surface	Bottom
Upper Bay*	Spring	1052.3 ± 102.7	1220.8 ± 248.5	1061.4 ± 91.3	1251.9 ± 267.1	7.70 ± 0.24	7.50 ± 0.22	0.56 ± 0.24	0.43 ± 0.10
	Summer	989.8 ± 141.0	1100.6 ± 271.0	1001.4 ± 140.6	1162.5 ± 283.2	7.70 ± 0.35	7.31 ± 0.14	0.91 ± 0.94	0.31 ± 0.12
	Fall/Winter	1249.2 ± 100.9	1324.5 ± 151.3	1265.3 ± 91.2	1323.7 ± 132.7	7.74 ± 0.12	7.70 ± 0.12	1.31 ± 0.45	0.97 ± 0.32
Mid-Bay	Spring	1446.6 ± 103.1	1725.6 ± 47.5	1374.0 ± 79.2	1712.3 ± 44.2	8.07 ± 0.13	7.63 ± 0.11	2.12 ± 0.58	1.27 ± 0.51
	Summer	1504.6 ± 98.4	1800.9 ± 50.1	1391.0 ± 86.6	1839.7 ± 58.5	8.18 ± 0.14	7.43 ± 0.17	3.13 ± 0.76	0.93 ± 0.44
	Fall/ Winter	1571.4 ± 77.6	1780.1 ± 70.9	1508.6 ± 57.7	1721.5 ± 64.8	8.04 ± 0.09	7.80 ± 0.06	2.22 ± 0.58	1.84 ±0.25
Lower Bay	Summer	1902.5 ± 195.0	1994.2 ± 156.2	1723.5 ± 173.4	1875.7 ± 112.5	8.15 ± 0.08	7.94 ± 0.10	3.93 ± 0.35	2.97 ± 0.88
	Fall/ Winter	1866.9 ± 136.0	1904.8 ± 95.7	1724.6 ± 122.6	1791.4 ± 74.0	8.05 ± 0.07	7.94 ± 0.02	3.26 ± 0.30	2.90 ± 0.41

*The standard deviation reflects the spread among the station values in each bay segment. The upper bay includes stations CB 1.1–CB 3.2, the mid-bay CB 3.3–CB 5.4, and the lower bay CB 5.5 to AO1. Surface values include the shallowest sampling depth for each station, each month, typically 0.5 m. Bottom values include the deepest sampling depth for each station, each month, and varies with the bathymetry. *In March, April, May, and December, there was one supersaturated Ω value in the Upper Bay near the Susquehanna Flats, omitted here to present a representative segment-wide mean (see Section "Non-conservative Alkalinity in the Upper Bay" and* ***Table 3*** *for further discussion).*

847.5 μmol kg^{-1} (bottom); TA difference of 582.8 μmol kg^{-1} (surface) and 893.1 μmol kg^{-1} (bottom). The August pH difference was 0.49 at the surface and 0.21 at depth. The mid-bay and lower bay difference was also greater in summer and smaller in winter, though the DIC difference in summer was just half the TA difference, due to an enrichment of DIC in the bottom water of the mid-bay. pH increased 0.16 from the mid- to lower bay, but the difference in summer was about twice the value of the fall/winter. The saturation state of $CaCO_3$ typically increased with salinity and decreased with depth. The upper bay was generally undersaturated, except for some stations during the productive summer and during the fall/winter. The mid-bay was typically oversaturated at the surface year-round, and undersaturated at depth during the productive and stratified months. The lower bay was supersaturated with calcite during the summer and fall/winter.

Mixing Diagram Analysis of Inorganic Carbon Along the Salinity Gradient

We examined DIC and TA change along the salinity gradient by plotting a conservative mixing line between the two end members, the Susquehanna River and the Atlantic Ocean.

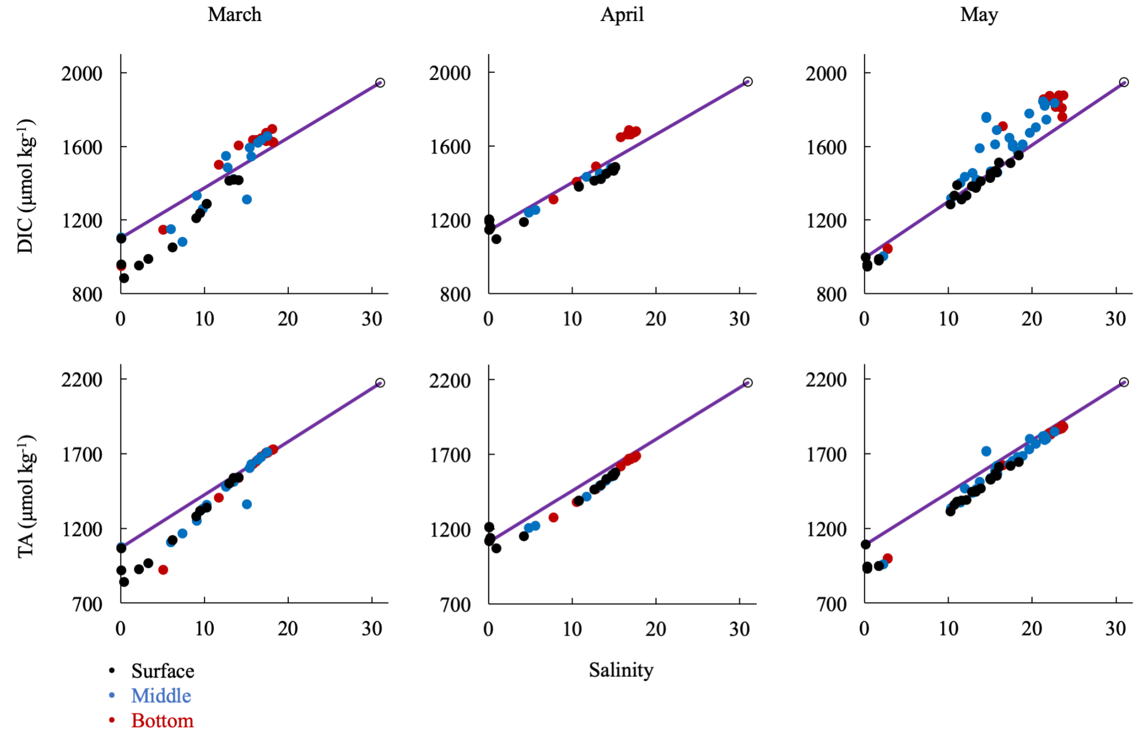

FIGURE 7 | Relationship of DIC and TA observations in the spring to the conservative mixing line. Black dots are surface water (shallowest samples, typically < 1 m), blue are mid-column, and red are bottom water (bottom samples, dependent on bathymetry). The open circle is the approx. bay mouth value at $S = 31$, derived from the mixing line equation. The 95% confidence intervals are smaller than the symbol.

Deviations from the line in the estuary indicate non-conservative behavior, with curvature below representing removal and above representing addition of the chemical species (Officer, 1979). Although the utility of the two-member model could be compromised if there were a third tributary, there is no other substantial freshwater source in the upper bay. Previous work has also found that many biogeochemical constituents are highly non-conservative in the Chesapeake Bay (Fisher et al., 1988).

In the spring (**Figure 7**), removal of DIC and TA was most significant at low salinity ($S < 5$), where the spring bloom begins (Malone et al., 1996), while DIC and TA changes were near conservative at middle ($5 < S < 15$) and higher salinities ($S > 15$). DIC was strongly influenced by biological activity, particularly through uptake at the surface, which was most dramatic in March, and enrichment via respiration in the bottom waters, most clearly seen beginning in May and continuing into the summer. Though the TA change with salinity was generally conservative in the spring, there was a large removal of alkalinity between CB 1.1 and CB 2.1, in an area called the Susquehanna Flats (approximately $S = 0$-2), that essentially resets the mixing line for the rest of the bay to Station CB 2.1 (see Section "Non-conservative Alkalinity in the Upper Bay" for more discussion). This region also often contained the ETM center, which may also contribute to TA removal. The exception was in April, when the freshet waters reached the bay with large inputs of riverine organic matter and sediments and diluted removal and addition signals (Schubel, 1968).

In the summer, when river discharge was lowest, ΔDIC and ΔTA from the conservative mixing line were very large, reflecting strong biological control on inorganic carbon (**Figure 8**). DIC was removed at low salinities and in the surface water and added in large amounts in the mid-salinities, reflecting the respiration signal in the sub-oxic boundary and at the bottom. TA was first removed in the low salinities via calcium carbonate ($CaCO_3$) formation and then added in the mid- and high salinities via $CaCO_3$ dissolution. The large addition of alkalinity via calcium carbonate dissolution in the respiration-dominated, higher-salinity waters below the pycnocline and in the mid- and lower bays is more apparent if the mixing line is drawn from station 2.1 (dotted lines in **Figure 8**). Over the year, conservative mixing related to salinity typically began at CB 2.1 instead of 1.1, due to the large chemical change across the Susquehanna Flats. Consequently, if the wrong freshwater endmember is used during the productive summer, TA could appear to be conservatively mixed in the mid- and high salinities, when it is in fact recycled.

Large removals or additions of alkalinity continued into the early fall with the breakdown of stratification (**Figure 9**). September had a similar DIC and TA pattern as the summer months. In October, there was a general addition of DIC and TA with increasing salinity south of the upper bay removal. Notably, there was a large alkalinity addition at mid-salinities and in the mid-bay in September and October that correlates with evidence of a small bloom (increase in oxygen and pH and decrease in DIC). Then, in November and December, the

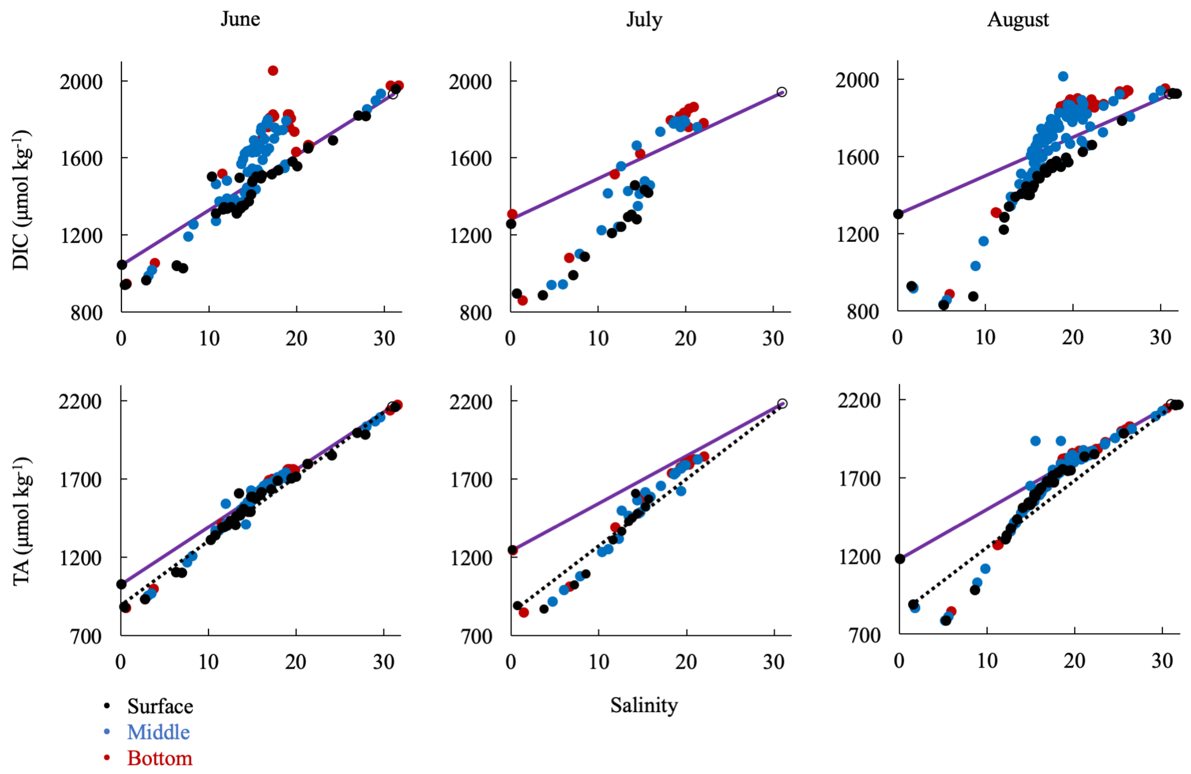

FIGURE 8 | Relationship of DIC and TA observations in the summer to the conservative mixing line. Black dots are surface water (shallowest samples, typically < 1 m), blue are mid-column, and red are bottom water (bottom samples, dependent on bathymetry). The open circle is the approx. bay mouth value at $S = 31$, derived from the mixing line equation. The 95% confidence intervals are smaller than the symbol. The dotted lines show mixing from CB 2.1 to the oceanic end member.

upper bay removal was absent. In fact, there appeared to be a source near the Susquehanna Flats in December, possibly due to $CaCO_3$ dissolution after the end of summer submerged aquatic vegetation (SAV) production in the upper bay. This is especially interesting since there was consistent inorganic carbon removal during the other 8 months studied. Both months showed a non-linear, concave mixing curve that seems to describe removal of DIC and TA in the mid-salinities. The similarities of the DIC and TA curves and the fact that surface, middle, and bottom water are all on the same line eliminate several potential processes such as CO_2 degassing or biological production, which would reduce DIC but not TA, and sulfide oxidation, which would reduce TA, but not DIC. It is possible that the Susquehanna River values suddenly increased before sampling or additional freshwater was mixed in the mid-bay, via precipitation and groundwater or other tributaries.

DIC and TA Net Estuarine Export Flux

As with other biogeochemical constituents in the Chesapeake Bay, the net estuarine export flux of DIC is positively correlated to Susquehanna River discharge, which is highest in winter and spring (**Table 2**). We calculated riverine DIC and TA flux using USGS monthly mean discharge data (Q) and monthly measurements of DIC and TA (C) in the following equation: $Flux = Q^{*}C$. The estimated Susquehanna River DIC and TA flux in 2016 was $27.5 \pm 2.7 \times 10^9$ and $26.9 \pm 2.6 \times 10^9$ mol C yr^{-1}, respectively. The maximum river flux was in February, during the freshet, and the minimum in September, the month with the lowest discharge. We used the Susquehanna River to represent all riverine input, because it is the most significant tributary of the Chesapeake Bay, representing over 60% of the total freshwater input, though the Potomac (19%) and James (13%) are other large tributaries (Zhang et al., 2015). So, our riverine flux estimate represents a minimum, potentially resulting in an underestimation of estuarine removal. The James River has been found to have little impact on lower bay chemistry (Wong, 1979; Fisher et al., 1988), so it is reasonable to assume a negligible contribution of DIC and TA. While the Potomac River has higher discharge than the James, previous studies have found that its chemistry differs from the Susquehanna only on the order of seasonal variation in the Susquehanna River (Fisher et al., 1988), and that it has little impact on the main stem, since most of the river constituents are processed in the sub-estuary (Boynton et al., 1995). The Susquehanna values should not be significantly different from the Potomac River, since their values and biogeochemical processes are likely similar. So, only the difference in concentrations between the two rivers would matter in the C^* and net internal accumulation calculations, and that difference would likely be a small amount, potentially within the uncertainty estimate we use to account for Susquehanna River

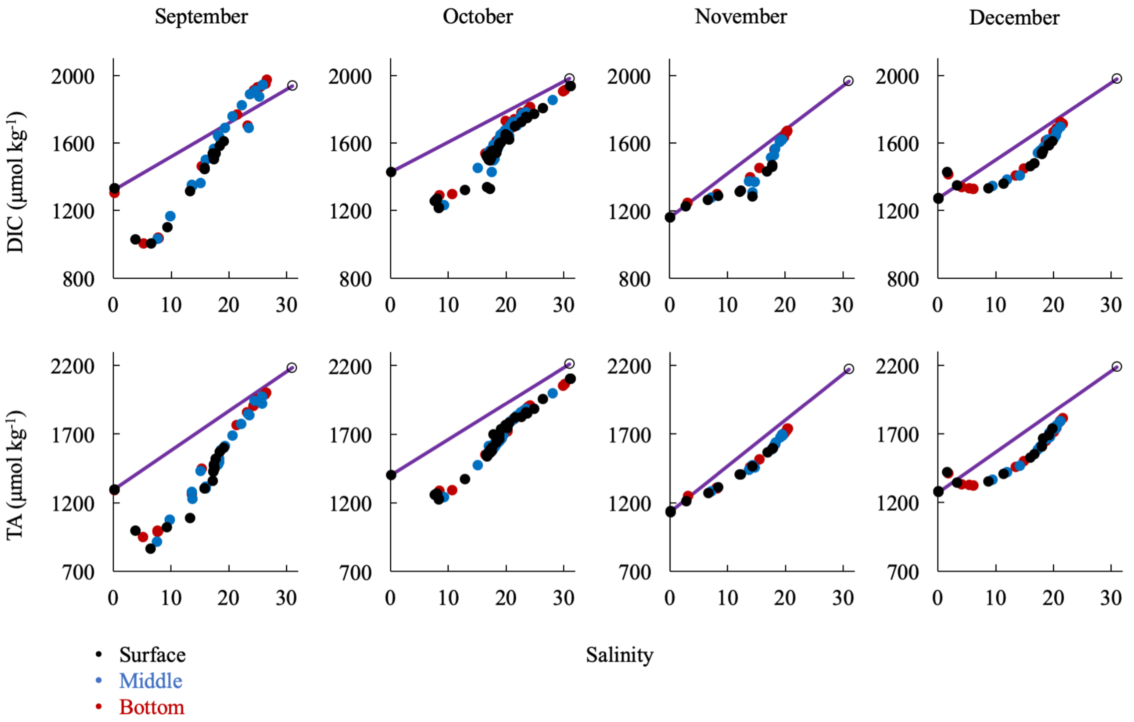

FIGURE 9 | Relationship of DIC and TA observations in the fall/winter to the conservative mixing line. Black dots are surface water (shallowest samples, typically < 1 m), blue are mid-column, and red are bottom water (bottom samples, dependent on bathymetry). The open circle is the approx. bay mouth value at *S* = 31, derived from the mixing line equation. The 95% confidence intervals are smaller than the symbol.

TABLE 2 | Estimated Susquehanna River inorganic carbon flux, Chesapeake Bay net export to the coastal ocean, and net internal accumulation in 2016.

Month (2016)	Discharge (m^3 s^{-1})	River Values (µmol kg^{-1})		Susquehanna River Flux (10^9 mol C)		Bay Export (10^9 mol C)		Net Internal Accumulation (10^9 mol C)	
		DIC	TA	DIC	TA	DIC	TA	DIC	TA
January*	1290	846.0	827.6	2.9 ± 0.1	2.9 ± 0.0	2.1 ± 0.1	2.6 ± 0.1	–0.8	–0.3
February*	2077	1128.2	1071.9	5.9 ± 1.0	5.6 ± 1.0	5.1 ± 1.9	5.4 ± 2.1	–0.8	–0.2
March	1251	1125.4	1089.9	3.8 ± 0.3	3.6 ± 0.4	3.2 ± 0.7	3.6 ± 0.7	–0.5	–0.1
April	951	1047.2	1098.3	2.6 ± 0.3	2.7 ± 0.0	1.8 ± 0.5	2.8 ± 0.0	–0.7	0.1
May	1040	965.2	951.4	2.7 ± 0.1	2.7 ± 0.3	1.1 ± 0.2	2.5 ± 0.5	–1.5	–0.1
June	419	1256.2	1173.1	1.4 ± 0.1	1.3 ± 0.1	1.7 ± 0.1	1.5 ± 0.1	0.3	0.2
July	211	1464.5	1411.3	0.8 ± 0.0	0.8 ± 0.0	0.8 ± 0.0	1.0 ± 0.1	–0.1	0.2
August	288	1459.8	1441.4	1.1 ± 0.1	1.1 ± 0.1	1.1 ± 0.1	1.3 ± 0.1	–0.1	0.2
September	162	1391.5	1345.1	0.6 ± 0.0	0.6 ± 0.0	0.7 ± 0.1	0.8 ± 0.1	0.1	0.2
October	383	1488.4	1436.1	1.5 ± 0.1	1.5 ± 0.1	1.8 ± 0.2	1.8 ± 0.2	0.3	0.3
November	390	1086.4	1053.6	1.1 ± 0.1	1.1 ± 0.1	1.1 ± 0.2	1.2 ± 0.3	0.0	0.1
December	855	1335.6	1322.2	3.1 ± 0.5	3.0 ± 0.5	3.6 ± 1.0	4.0 ± 0.9	0.6	0.9
All				27.5 ± 2.7	26.9 ± 2.6	24.3 ± 5.1	28.4 ± 4.9	–3.2	1.5

**There were no cruises during these months, so the December high salinity trend was used for the January extrapolation and the March trend for February.*

variation. If we scale up the discharge to account for the all three rivers, the riverine DIC and TA fluxes are 46.0 ± 4.4 × 10^9 and 44.7 ± 4.6 × 10^9 mol C yr^{-1}.

Next, we used Susquehanna River and Mid-Atlantic Bight DIC and TA values to estimate the net estuarine export flux and found that the Chesapeake Bay was a sink of inorganic carbon in 2016 (**Table 2**). At high salinities in the lower bay, near the ocean endmember, DIC and TA are generally mixed conservatively with salinity. So, we used a linear regression of the high salinity measurements for each month ($S > 20$, except for March and April, when we used > 15) to extrapolate to zero salinity, representing what the river values would be if the change along the bay was solely due to mixing of the endmembers. We multiplied the extrapolated river value (C*) by the river discharge (Q) to determine the estuarine export flux as in the following equation:$Flux = Q \times C^*$. Note that by this approach, we extrapolated to zero the integrated biological non-linear addition or removal during the entire estuarine mixing process. This extrapolation allows us to use the river discharge and avoid the necessity of knowing the residual water flux at the bay mouth (Officer, 1979; Cai and Wang, 1998; Cai et al., 2004; Joesoef et al., 2017). Then, the difference between the extrapolated and measured river values represent either estuarine addition, if positive, or removal, if negative. However, such internal addition or removal is also subject to subsequent modification by air-water gas exchange.

The estimated net export of DIC and TA in 2016 was $24.3 \pm 5.1 \times 10^9$ mol C yr^{-1} and $28.4 \pm 4.9 \times 10^9$ mol C yr^{-1}. The annual estuarine DIC removal was $-3.2 \pm 5.1 \times 10^9$ mol C yr^{-1} and TA addition was $1.5 \pm 4.9 \times 10^9$ mol C yr^{-1}, making the Chesapeake Bay a sink of riverine DIC and a potential weak source of TA to the coastal ocean. However, the above net estuarine export is based on the Susquehanna discharge alone. If we scale up the numbers to account for the additional tributary discharge in order to see more realistic total DIC and TA export numbers, the net estuarine export flux is $40.3 \pm 8.2 \times 10^9$ and $47.1 \pm 8.6 \times 10^9$ mol C yr^{-1}, meaning there was a DIC removal of $-5.7 \pm 8.2 \times 10^9$ mol C yr^{-1}, and a TA addition of $2.4 \pm 8.2 \times 10^9$ mol C yr^{-1}. The monthly bay net export flux and the net internal production were also highly variable, related to temperature differences in atmospheric exchange and biological activity. In the late winter, spring and summer, the bay was typically a sink of inorganic carbon, though it may have been a weak source in June. A previous study found a reduction of net productivity in June and related it to higher relative respiration due to a lag between the fading spring bloom and the build-up of summer phytoplankton assemblages (Kemp et al., 1997), which would explain this result. Maximum DIC removal was in May, during the spring bloom, while maximum DIC addition was in December, when the water was colder, enhancing atmospheric CO_2 invasion and reducing biological activity. Maximum TA addition was also in December, but maximum removal was in January. This seems to be a contradiction since both are during the winter season. However, January had nearly twice the freshwater discharge of December. Unfortunately, we do not have cruise data for January to compare to December, and we used the December high salinity trend for the January flux estimate. Greater resolution of the January and February conditions bay-wide would be needed to resolve the apparent conflict.

Finally, we generated an estimated carbon budget for the Chesapeake Bay (**Figure 10**), using published net ecosystem metabolism (NEM) (Smith and Kemp, 1995; Kemp et al., 1997) and atmospheric flux estimates (Shen et al., 2019). Notably, these studies found the bay to be net autotrophic and an atmospheric CO_2 sink (12.0×10^9 mol CO_2 yr^{-1}), consistent with our findings on inorganic carbon flux. We calculated a range of biological DIC removal using the lower end and average estimates of the NEM range, 33 and 50 g C m^{-2} yr^{-1}, and a total bay area of 5514×10^6 m^2. The resulting biological DIC removal would be -15.2 to -23.0×10^9 mol DIC yr^{-1}. Using our riverine flux estimate, the total CO_2 flux from riverine and atmospheric sources was 58.0×10^9 mol DIC yr^{-1}, and when the export is subtracted, the remaining amount is -17.7×10^9 mol DIC yr^{-1}, which falls within the published NEM range. We did not explicitly estimate benthic inorganic carbon flux in our budget, though its impact on the water column was addressed via our mass-balance method, and the NEM estimate included benthic metabolism. So, if the NEM was higher than the lower-end estimate that balances our budget, potential sources of additional CO_2 could include benthic respiration, groundwater or any difference between the Susquehanna River DIC and TA values used in the estimate and the concentrations in the smaller tributaries.

Non-conservative Alkalinity in the Upper Bay

The mixing plots showed substantial and persistent inorganic carbon removal in the upper bay between stations CB 1.1 and CB 2.1. This area has experienced a large increase in SAV, shown to substantially modify local chemistry by removing total nitrogen, raising pH and improving water clarity (Gurbisz and Kemp, 2014; Orth et al., 2017). To investigate this further, we separated out the various processes that could have contributed during the months when both stations were sampled (**Table 3**). First, we used oxygen data from Maryland Department of Natural Resources monitoring cruises and Redfield stoichiometry to determine the apparent photosynthetic/respiratory contribution to the change in DIC and TA between the stations. We assumed that all oxygen changes were related to biological activity and not meteorological forcing, since the stations are located near one another and were sampled within an hour of each other. Then, we used the conservative mixing lines to calculate the ΔDIC and ΔTA related to increased salinity at CB 2.1. Finally, we examined the TA:DIC ratio of the remaining change between stations because when $CaCO_3$ is formed or dissolved, the ratio of the change in TA to DIC is 2:1.

During the spring bloom and freshet, the TA: DIC ratio was high. In March, oxygen increased and DIC and TA decreased by 141.5 and 149.1 μmol kg^{-1}, likely due to photosynthesis. Yet, pH was unchanged and calcite saturation declined, though it was still undersaturated. In April, oxygen also increased between stations, however TA and DIC were added (46.2 and 94.8 μmol kg^{-1}, respectively). There was also a fivefold increase in carbonate saturation from undersaturated to supersaturated and pH that could support the hypothesis of $CaCO_3$ formation in the flats. The carbonate saturation returns to the CB 1.1 value at station CB 2.2, further evidence that the change is related to a process in the flats that may impact chemistry at a later time or in a difference place, as with the transport of carbonate minerals. During this month, the center of the ETM was further south, between CB 2.2 and CB 3.1, so it was not affecting the values. During the other months, the change in DIC and TA was near a TA:DIC ratio of 1, and the presence of the ETM generally resulted in expected declines in oxygen, saturation and pH, as well as addition of DIC and TA. However,

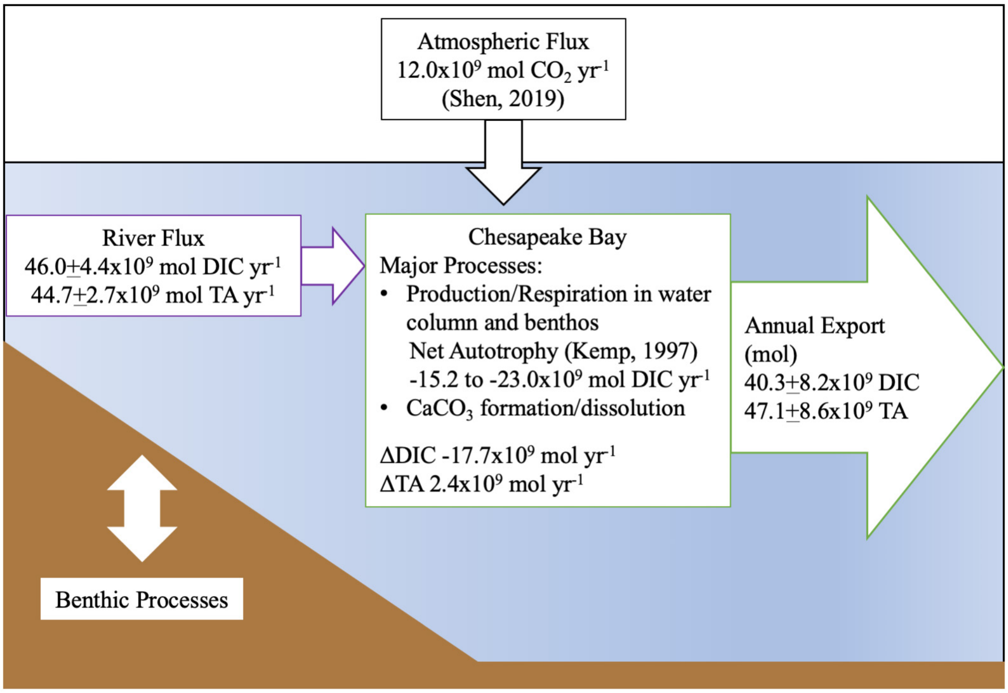

FIGURE 10 | Summary of estimated riverine DIC and TA flux into the Chesapeake Bay and estuarine export to the Atlantic Ocean in 2016. The atmospheric flux estimate is from Shen et al. (2019) and the metabolic rate estimate from Kemp et al. (1997).

TABLE 3 | Change in surface water chemistry across the Susquehanna Flats between CB 1.1 and CB 2.1.

Station	Parameter	March	April	July	September	November	December
CB 1.1	DIC (μmol kg^{-1})	1099.1	1145.2	1256.8	1332.1	1159.9	1274.4
	TA (μmol kg^{-1})	1067.4	1119.2	1247.8	1296.1	1131.8	1278.2
	pH (NBS)	7.2	7.9	7.9	7.7	7.8	8.2
	$\Omega_{Calcite}$	0.46	0.59	1.31	0.74	0.73	15.82
	O$_2$(μmol kg^{-1})	650.3	706.4	527.1	451.4	631.5	812.5
	TA:DIC	0.97	0.98	0.99	0.97	0.98	1.00
CB 2.1	DIC (μmol kg^{-1})	957.6	1191.4	896.7	1028.5	1226.1	1429.0
	TA (μmol kg^{-1})	918.3	1214.0	889.9	996.7	1212.0	1419.3
	pH (NBS)	7.2	8.4	7.8	7.5	7.7	7.9
	$\Omega_{Calcite}$	0.29	2.93	0.70	0.40	0.78	2.60
	O$_2$(μmol kg^{-1})	706.4	731.6	476.6	443.7	611.5	761.6
	TA:DIC	0.96	1.02	0.99	0.97	0.99	0.99
ΔDIC (μmol kg^{-1})	Total	−141.5	46.2	−360.1	−303.6	66.2	154.6
	Biological	−43.2	−19.4	38.9	5.9	15.4	39.2
	Mixing	0.0	0.0	12.8	71.7	70.3	34.2
ΔTA (μmol kg^{-1})	Total	−149.1	94.8	−357.9	−299.4	80.2	141.1
	Biological	6.7	3.0	−6.1	−0.9	−2.4	−6.1
	Mixing	0.0	0.0	18.2	103.5	90.5	44.4
ΔpH (NBS)		0.0	0.5	−0.1	−0.3	−0.1	−0.3
ΔO$_2$ (μmol kg^{-1})		56.1	25.1	−50.5	−7.6	−20.1	−50.9
ΔSalinity		0	0	0.6	3.6	2.7	1.5
$\Delta\Omega_{Calcite}$		−0.17	2.34	−0.61	−0.34	0.05	−13.22
TA:DIC of change		1.6	1.4	0.9	1.1	0.4	1.3
ETM center present?		No	No	Yes	Yes	Yes	Yes

Negative numbers represent a decrease across the flats and positive numbers an increase. The error for ΔDIC and ΔTA is <10 μmol kg^{-1}, twice the 95% confidence interval of the measurements. The error for ΔpH is 0.034.

November had a very low ratio, potentially related to coupled denitrification and nitrification, which are at maximum rates during the fall (McCarthy et al., 1984; Kemp et al., 1990; Lee et al., 2015; Testa et al., 2018) and is positively correlated with suspended particles as in the ETM (Damashek et al., 2016). Given the non-conservative behavior of inorganic carbon in this region, and minimal buffering resulting in relatively large changes in conditions with changes in the carbonate parameters, higher resolution study is needed, particularly given the lack of measurements within the flats area, the potential for nitrogen-related effects on alkalinity, and the analytical complications associated with the periodic presence of the ETM.

DISCUSSION

This study describes the seasonal main stem inorganic carbon distribution in the Chesapeake Bay for the first time. Generally, DIC and TA increased from surface to bottom and north to south, bay-wide, and pH decreased from surface to bottom and increased from north to south. The pattern reflects the two-layer, density-driven circulation and seasonal stratification (Li et al., 2005). Surface DIC and TA varied most over the study period because of variance in the freshwater flow, and thus salinity, though wind-driven mixing and biological activity caused seasonal changes in values. Below 15 m, average DIC and TA values were spatially consistent in the deepest parts of the main stem all year. At the surface, CO_2 was removed for biological production, and then it was released in the bottom water with respiration, causing $CaCO_3$ dissolution. This means that inorganic carbon was usually non-conservative in the bay due to biological uptake, similar to other biogeochemical constituents (Fisher et al., 1988). In terms of annual variation, the upper bay was the most variable for DIC and TA, but pH was more variable in the mid-bay. Spring was characterized by the arrival of the freshet and the beginning of the phytoplankton bloom in the upper bay. Despite large removals of DIC and TA, pH remained very low, likely related to low buffering capacity and the respiration of riverine organic material and estuarine phytoplankton. Stratification began in May, lowering pH in the mid-bay and at depth. In the summer, low discharge and stratification caused a build-up of DIC at depth and low pH, though productivity was high at the surface. In early fall, the break-down of stratification reduced the vertical gradient of DIC and TA and lowered pH, likely as reduced chemical species from the bottom were oxidized and respiration stimulated by an injection of organic material and nutrients (Lee et al., 2015; Cai et al., 2017). This detailed seasonal and spatial analysis helps to establish a baseline that can be used in the future to identify any changes in pH from eutrophication or ocean acidification.

Strong modification of the riverine flux of inorganic carbon occurred in the portion of the upper bay in which the Susquehanna Flats SAV bed is found, while downstream of CB 2.1 there was a clear pattern of linear mixing of TA over the estuarine salinity gradient. Non-conservative behavior of alkalinity in the early stages of estuarine mixing has previously been attributed to dissolution of $CaCO_3$ causing TA addition (Abril et al., 2003, 2004). It has also been established that the organic alkalinity contribution is controlled by pH in the early stages of mixing and then becomes conservative with respect to salinity change (Cai and Wang, 1998). April measurements suggest $CaCO_3$ precipitation and downstream dissolution, because of the high TA to DIC removal ratio and large pH and calcite saturation state increase over the flats area. However, an inorganic carbon study in the Flats is needed to resolve the issue, as well as greater resolution of the organic alkalinity contribution. Non-conservative behavior of TA in the fall and winter is likely due to a different process. Unfortunately, we have limited winter data to establish a robust high salinity trend and consequently more reliable export estimates during the fall and winter, an important time interval when TA addition was highest as percentage of river input. During the winter months, the data at all depths are in an odd concave curve, suggesting removal due to either a physical process or one affecting the full water column via vertical mixing, like sedimentary flux. The timing is coincident with maximum nitrification and denitrification rates (Kemp et al., 1990; Lee et al., 2015), so it is possible the DIC and TA addition in the low salinities and uptake in the mid-salinities during this time is in part related to nitrogen cycling. The ETM was also in the low salinity Susquehanna Flats area during the fall, which may further enhance nitrification (Damashek et al., 2016). Then, the removal with increasing salinity would be related to competing processes of photosynthesis and denitrification. Mid-bay surface removal of DIC and increased pH support the idea of an increase in productivity stimulated by nitrate addition. Another potential explanation of the alkalinity removal could be buried ferrous sulfide (FeS) oxidizing and releasing acid to the water column as low river discharge is correlated with an increase in lower bay sulfate reduction rates (Marvin-DiPasquale et al., 2003).

Many previous studies have estimated that estuaries are typically heterotrophic, with significant degassing of CO_2 to the atmosphere (Raymond et al., 2000; Caffrey, 2004; Borges et al., 2005; Chen and Borges, 2009), but the Chesapeake Bay may be an exception to that pattern. It was also argued that neglecting seasonal change and an over-reliance on measurements in low salinity waters where degassing is high could be causing significant over-estimation of estuarine heterotrophy (Cai, 2011). The Chesapeake Bay in 2016 demonstrates the validity of these cautionary points. Estuarine processing of the riverine inorganic carbon flux was strongly seasonal, with active biological removal in the spring and summer and addition later in the year. At the same time, there was a strong spatial gradient, so despite extremely high pCO_2 found in the low salinities (Cai et al., 2017), the large surface area of highly productive areas like the mid-bay and the flanks of the main stem (Kemp et al., 1997) as well as the long water residence time, allowed biological removal to compensate for the high DIC in 2016. Caffrey (2004) found that large estuaries, like the Chesapeake Bay, were closer to having a balanced metabolism than smaller estuaries, and that the surrounding habitat had a significant effect, with SAV beds increasing autotrophy. So, the regrowth of the SAV beds in recent years may have had an important effect on carbon cycling in the bay and explain the finding of net autotrophy. Furthermore, if the

Chesapeake Bay is not an exception and other large estuaries are also currently autotrophic, coastal acidification models will need to be updated to reflect this point.

Kemp et al. (1997) estimated net ecosystem metabolism in the Chesapeake Bay and also proposed that it was autotrophic. They found that biologically mediated fluxes were unusually important in the bay, given its large size and long water residence time. Our mixing curves support that finding, showing that strong biological forcing on inorganic carbon was a regular feature of the system during the spring, summer and early fall, resulting in non-linear behavior of DIC and TA. While our study does not estimate net ecosystem metabolism directly, our finding that the upper bay was frequently a DIC and TA sink seems to contradict their assertion that the upper Bay is net heterotrophic, however, there are two reasons this may not be contradictory. First, since the 1997 study, the recovery of SAV in the upper bay may have changed the net metabolism to autotrophic during the growing season and would certainly affect their assumptions about plant contributions to organic carbon (Gurbisz and Kemp, 2014). Second, we note some limited evidence for a potential abiotic pathway for the removal of inorganic carbon, via precipitation of $CaCO_3$, which would allow for net heterotrophy alongside DIC and TA removal. Using the lower published estimate for NEM resulted in a balanced budget, and there is some evidence that the modern Chesapeake Bay has lower productivity in 2016 than 1997. First, Kemp omitted data from years that diverged from average conditions, while 2016 was a dry year. Less discharge, combined with reductions in nitrogen inputs and chlorophyll (Zhang et al., 2018) and nitrogen removal by SAV beds that have grown in area by 50 km^2 since 1998 (Gurbisz and Kemp, 2014; Orth et al., 2017), likely resulted in reduced eutrophication and consequently, lower productivity in the mesohaline and polyhaline regions. So, our net export flux estimates are compatible with the previous organic carbon budget. Overall TA flux was found to be nearly conservative in the estuary, when the error estimate is considered. So, this study is not in conflict with previous calculations that the bay is an alkalinity sink (Waldbusser et al., 2013), despite our conclusion that it may have been a weak source in 2016.

This study is the first full bay, main stem observational inorganic carbon study, which will allow for better assessment and modeling of acidification. We found that there was substantial internal recycling of DIC and TA in the bay, and, notably, that TA was frequently non-conservative in the upper bay. 2016 may have been a "best-case" year for minimal Chesapeake Bay acidification, with low river discharge leading to a lower spring hypoxic volume, though pH was still often very low at depth. Efforts to reduce nutrient and sediment loading, which are leading to a resurgence of SAV growth in the upper bay, could be helping to increase the bay's resilience to acidification by enabling substantial upper bay removal of riverine nitrogen and DIC. However, the interplay of river discharge, submerged vegetation, and the location of the ETM in the upper bay created a complex pattern of DIC and TA flux that complicates efforts to use riverine alkalinity to model bay conditions. We estimated that the bay was autotrophic in 2016, making it an important asset for mitigating anthropogenic CO_2 inputs via the atmosphere and land use in the watershed. These findings, which suggest that the Chesapeake Bay is an exception to many of the assumptions about estuaries, highlight the importance of considering seasonal and spatial distributions of DIC and TA in estuarine systems when refining coastal acidification models.

DATA AVAILABILITY

The raw data supporting the conclusions of this manuscript will be made available by the authors, without undue reservation, to any qualified researcher.

AUTHOR CONTRIBUTIONS

JB did most of sample collection and measurements, as well as writing the article. W-JC and JT designed the NOAA study and assisted with writing. JT was co-chief scientist on the *Carson* cruises. BC was co-chief scientist on the *Carson* cruises and checked data quality. JS participated on the May *Carson* cruise, measured May TA, and checked the flux calculations. Y-YX measured TA in August and October and provided MAB data. NH measured salinity during *Carson* cruises, assisted with TA measurements periodically, collected March samples and measured March pH, and provided Susquehanna River data. KS participated in all of the *Carson* cruises. YZ participated on the June *Carson* cruise and measured June TA.

FUNDING

This work was supported by NOAA grant NA15NOS4780190. JB was also supported by Delaware NSF EPSCoR grant NSF EPS-01814251.

ACKNOWLEDGMENTS

We would like to thank the Maryland Department of Natural Resources for allowing JB on their monitoring cruises and for their data, and the crews of the R/V *Randall T. Kerhin* and R/V *Rachel Carson* for making the fieldwork possible. This is UMCES publication #5571.

REFERENCES

Abril, G., Commarieu, M. V., Maro, D., Fontugne, M., Guérin, F., and Etcheber, H. (2004). A massive dissolved inorganic carbon release at spring tide in a highly turbid estuary. *Geophys. Res. Lett.* 31:L09316. doi: 10.1029/2004GL019714

Abril, G., Etcheber, H., Delille, B., Frankignoulle, M., and Borges, A. V. (2003). Carbonate dissolution in the turbid and eutrophic Loire estuary. *Mar. Ecol. Prog. Ser.* 259, 129–138. doi: 10.3354/meps259129

Baird, D., and Ulanowicz, R. E. (1989). The seasonal dynamics of the chesapeake bay ecosystem. *Ecol. Monogr.* 59, 329–364. doi: 10.2307/1943071

Bakker, D. C. E., Pfeil, B., Landa, C. S., Metzl, N., O'Brien, K. M., Olsen, A., et al. (2016). A multi-decade record of high-quality fCO2data in version 3 of the Surface Ocean CO2Atlas (SOCAT). *Earth Syst. Sci. Data* 8, 383–413. doi: 10.5194/essd-8-383-2016

Bates, R. N., Astor, Y. M., Church, J. M., Currie, K., Dore, J. E., González-Dávila, M., et al. (2014). A time-series view of changing surface ocean chemistry due to ocean uptake of anthropogenic CO2 and ocean acidification. *Oceanography* 27, 126–141. doi: 10.5670/oceanog.2014.16

Boesch, D. F., Brinsfield, R. B., and Magnien, R. E. (2001). Chesapeake bay eutrophication: scientific understanding, ecosystem restoration, and challenges for agriculture. *J. Environ. Qual.* 30, 303–320. doi: 10.2134/jeq2001.302303x

Borges, A. V., Delille, B., and Frankignoulle, M. (2005). Budgeting sinks and sources of CO2 in the coastal ocean: diversity of ecosystems counts. *Geophys. Res. Lett.* 32, 2–5. doi: 10.1029/2005GL023053

Borges, A. V., and Gypens, N. (2010). Carbonate chemistry in the coastal zone responds more strongly to eutrophication than ocean acidification. *Limnol. Oceanogr.* 55, 346–353. doi: 10.4319/lo.2010.55.1.0346

Boynton, W. R., Boicourt, W., Brandt, S., Hagy, J., Harding, L., Houde, E., et al. (1997). *Interactions Between Physics and Biology in the Estuarine Turbidity Maximum (ETM) of Chesapeake Bay, USA*. Copenhagen: ICES.

Boynton, W. R., Garber, J. H., Summers, R., and Kemp, W. M. (1995). Inputs, transformations, and transport of nitrogen and phosphorus in chesapeake bay and selected tributaries. *Estuaries* 18, 285–314. doi: 10.2307/1352640

Breitburg, D. L., Salisbury, J., Bernhard, J. M., Cai, W., Dupont, J. S., Doney, S. C., et al. (2015). And on top of all that Coping with ocean acidification in the midst of many stressors. *Oceanography* 28, 48–61. doi: 10.1017/CBO9781107415324.004

Caffrey, J. M. (2004). Factors controlling net ecosystem metabolism in U.S. estuaries. *Estuaries* 27, 90–101. doi: 10.1007/BF02803563

Cai, W., Dai, M., Wang, Y., Zhai, W., Huang, T., Chen, S., et al. (2004). The biogeochemistry of inorganic carbon and nutrients in the Pearl River estuary and the adjacent Northern South China Sea. *Cont. Shelf Res.* 24, 1301–1319. doi: 10.1016/j.csr.2004.04.005

Cai, W. J. (2011). Estuarine and coastal ocean carbon paradox: CO2 sinks or sites of terrestrial carbon incineration? *Ann. Rev. Mar. Sci.* 3, 123–145. doi: 10.1146/annurev-marine-120709-142723

Cai, W. J., Hu, X., Huang, W. J., Murrell, M. C., Lehrter, J. C., Lohrenz, S. E., et al. (2011). Acidification of subsurface coastal waters enhanced by eutrophication. *Nat. Geosci.* 4, 766–770. doi: 10.1038/ngeo1297

Cai, W. J., Huang, W. J., Luther, G. W., Pierrot, D., Li, M., Testa, J., et al. (2017). Redox reactions and weak buffering capacity lead to acidification in the Chesapeake Bay. *Nat. Commun.* 8, 1–12. doi: 10.1038/s41467-017-00417-7

Cai, W.-J., and Wang, Y. (1998). The chemistry, fluxes, and sources of carbon dioxide in the estuarine waters of the Satilla and Altamaha Rivers. *Georgia. Limnol. Oceanogr.* 43, 657–668. doi: 10.4319/lo.1998.43.4.0657

Cerco, C. F., and Cole, T. (1993). 3-dimensional eutrophication model of Chespeake Bay. *J. Environ. Eng.* 119, 1006–1025. doi: 10.1061/(ASCE)0733-9372(1993)119:6(1006)

Chen, C. A., and Borges, A. V. (2009). Reconciling opposing views on carbon cycling in the coastal ocean: continental shelves as sinks and near-shore ecosystems as sources of atmospheric CO2. *Deep Sea Res. II* 56, 578–590. doi: 10.1016/j.dsr2.2008.12.009

Cornwell, J. C., Kemp, W. M., and Kana, T. M. (1999). Denitrification in coastal ecosystems: methods, environmental controls, and ecosystem level controls, a review. *Aquat. Ecol.* 33, 41–54. doi: 10.1023/A:1009921414151

Cowan, J. L. W., and Boynton, W. R. (1996). Sediment-water oxygen and nutrient exchanges along the longitudinal axis of chesapeake bay: seasonal patterns, controlling factors and ecological significance. *Estuaries Coasts* 19, 562–580. doi: 10.2307/1352518

Damashek, J., Casciotti, K. L., and Francis, C. A. (2016). Variable nitrification rates across environmental gradients in turbid, nutrient-rich estuary waters of San Francisco Bay. *Estuaries Coasts* 39, 1050–1071. doi: 10.1007/s12237-016-0071-7

Dickson, A. G. (1981). An exact definition of total alkalinity and a procedure for the estimation of alkalinity and total inorganic carbon from titration data. *Deep Sea Res. A* 28, 609–623. doi: 10.1016/0198-0149(81)90121-7

Dickson, A. G., Wesolowski, D. J., Palmer, D. A., and Mesmer, R. E. (1990). Dissociation constant of bisulfate ion in aqueous sodium chloride solutions to 250°C. *J. Phys. Chem.* 94, 7978–7985. doi: 10.1021/j100383a042

Doney, S. C., Fabry, V. J., Feely, R. A., and Kleypas, J. A. (2009). Ocean acidification: the other CO_2 problem. *Ann. Rev. Mar. Sci.* 1, 169–192. doi: 10.1146/annurev.marine.010908.163834

Fassbender, A. J., Alin, S. R., Feely, R. A., Sutton, A. J., Newton, J. A., and Byrne, R. H. (2017). Estimating total alkalinity in the washington state coastal zone: complexities and surprising utility for ocean acidification research. *Estuaries Coasts* 40, 404–418. doi: 10.1007/s12237-016-0168-z

Fisher, T. R., Harding, L. W., Stanley, D. W., and Ward, L. G. (1988). Phytoplankton, nutrients, and turbidity in the Chesapeake, Delaware, and Hudson estuaries. *Estuar. Coast. Shelf Sci.* 27, 61–93. doi: 10.1016/0272-7714(88)90032-7

Gurbisz, C., and Kemp, W. M. (2014). Unexpected resurgence of a large submersed plant bed in Chesapeake Bay: analysis of time series data. *Limnol. Oceanogr.* 59, 482–494. doi: 10.4319/lo.2014.59.2.0482

Hiscock, W. T., and Millero, F. J. (2006). Alkalinity of the anoxic waters in the Western Black Sea. *Deep Sea Res. Part II* 53, 1787–1801. doi: 10.1016/j.dsr2.2006.05.020

Huang, W.-J. J., Wang, Y., and Cai, W.-J. (2012). Assessment of sample storage techniques for total alkalinity and dissolved inorganic carbon in seawater. *Limnol. Ocean Methods* 10, 711–717. doi: 10.4319/lom.2012.10.711

Joesoef, A., Kirchman, D. L., Sommerfield, C. K., and Cai, W. C. (2017). Seasonal variability of the inorganic carbon system in a large coastal plain estuary. *Biogeosciences* 14, 4949–4963. doi: 10.5194/bg-14-4949-2017

Kemp, W. M., Boynton, W. R., Adolf, J. E., Boesch, D. F., Boicourt, W. C., Brush, G., et al. (2005). Eutrophication of Chesapeake Bay: historical trends and ecological interactions. *Mar. Ecol. Prog. Ser.* 303, 1–29. doi: 10.3354/meps303001

Kemp, W. M., Sampou, P., Caffrey, J., Mayer, M., Henriksen, K., and Boynton, W. R. (1990). Ammonium recycling versus denitrification in Chesapeake Bay sediments. *Limnol. Oceanogr.* 35, 1545–1563. doi: 10.4319/lo.1990.35.7.1545

Kemp, W. M., Smith, E. M., Marvin-DiPasquale, M., and Boynton, W. R. (1997). Organic carbon balance and net ecosystem metabolism in Chesapeake Bay. *Mar. Ecol. Prog. Ser.* 150, 229–248. doi: 10.3354/meps150229

Le Quéré, C., Andrew, R. M., Friedlingstein, P., Sitch, S., Pongratz, J., Manning, A. C., et al. (2017). Global Carbon Budget 2017. *Earth Syst. Sci. Data* 10, 405–448. doi: 10.5194/essd-2017-123

Lee, D. Y., Owens, M. S., Crump, B. C., and Cornwell, J. C. (2015). Elevated microbial CO2 production and fixation in the oxic/anoxic interface of estuarine water columns during seasonal anoxia. *Estuar. Coast. Shelf Sci.* 164, 65–76. doi: 10.1016/j.ecss.2015.07.015

Lewis, E., and Wallace, D. (1998). *Program Developed for CO2 System Calculations. Ornl/Cdiac-105*. Available at: https://pubs.usgs.gov/of/2010/1280/pdf/ofr_2010-1280.pdf. doi: 10.2172/639712

Li, M., Zhong, L., and Boicourt, W. C. (2005). Simulations of Chesapeake Bay estuary: sensitivity to turbulence mixing parameterizations and comparison with observations. *J. Geophys. Res. Ocean* 110, 1–22. doi: 10.1029/2004JC002585

Malone, T. C., Conley, D. J., Fisher, T. R., Glibert, P. M., Harding, L. W., and Sellner, K. G. (1996). Scales of nutrient-limited phytoplankton productivity in Chesapeake Bay. *Estuaries* 19:371. doi: 10.2307/1352457

Marvin-DiPasquale, M. C., Boynton, W. R., and Capone, D. G. (2003). Benthic sulfate reduction along the Chesapeake Bay central channel. II. Temporal controls. *Mar. Ecol. Prog. Ser.* 260, 55–70. doi: 10.3354/meps260055

McCarthy, J. J., Kaplan, W., and Nevins, J. L. (1984). Chesapeake Bay nutrient and plankton dynamics. 2. Sources and sinks of nitrite. *Limnol. Oceanogr.* 29, 84–98. doi: 10.4319/lo.1984.29.1.0084

Millero, F. J., Graham, T. B., Huang, F., Bustos-Serrano, H., and Pierrot, D. (2006). Dissociation constants of carbonic acid in seawater as a function of salinity and temperature. *Mar. Chem.* 10, 80–94. doi: 10.1016/j.marchem.2005.12.001

Mucci, A. (1983). The solubility of calcite and aragonite in seawater at various salinities, temperatures, and one atmosphere total pressure. *Am. J. Sci.* 283, 780–799. doi: 10.2475/ajs.283.7.780

Nixon, S. W. (1995). Coastal marine eutrophication: a definition, social causes, and future concerns. *Ophelia* 41, 199–219. doi: 10.1080/00785236.1995.10422044

Officer, C. B. (1979). Discussion of the behaviour of nonconservative dissolved constituents in estuaries. *Estuar. Coast. Mar. Sci.* 9, 91–94. doi: 10.1016/0302-3524(79)90009-4

Orth, R. J., Dennison, W. C., Lefcheck, J. S., Gurbisz, C., Hannam, M., Keisman, J., et al. (2017). Submersed aquatic vegetation in chesapeake bay: sentinel species in a changing world. *Bioscience* 67, 698–712. doi: 10.1093/biosci/bix058

Raymond, P. A., Bauer, J. E., and Cole, J. J. (2000). Atmospheric CO_2 evasion, dissolved inorganic carbon production, and net heterotrophy in the York River estuary. *Limnol. Oceanogr.* 45, 1707–1717. doi: 10.4319/lo.2000.45.8.1707

Redfield, A. C. (1934). "On the proportions of organic derivatives in sea water and their relation to the composition of plankton," in *James Johnstone Memorial Volume*, ed. R. J. Daniel (Liverpool: Liverpool University Press), 176–192.

Riley, J. P., and Tongudai, M. (1967). The major cation/chlorinity ratios in sea water. *Chem. Geol.* 2, 263–269. doi: 10.1016/0009-2541(67)90026-5

Sabine, C. L., Feely, R. A., Gruber, N., Key, R. M., Lee, K., Bullister, J. L., et al. (2004). The oceanic sink for anthropogenic CO2. *Science* 305, 367–371. doi: 10.1126/science.1097403

Sarma, V. V. S. S., Kumar, N. A., Prasad, V. R., Venkataramana, V., Appalanaidu, S., Sridevi, B., et al. (2011). High CO2 emissions from the tropical Godavari estuary (India) associated with monsoon river discharges. *Geophys. Res. Lett.* 38:4. doi: 10.1029/2011GL046928

Schubel, J. R. (1968). Turbidity maximum of the northern chesapeake bay. *Science* 161, 1013–1015. doi: 10.1126/science.161.3845.1013

Shen, C., Testa, J. M., Li, M., Cai, W.-J., Waldbusser, G. G., Ni, W., et al. (2019). Controls on carbonate system dynamics in a coastal plain estuary: a modelling study. *J. Geophys. Res. Biogeosci.* 124, 61–78. doi: 10.1029/2018JG004802

Signorini, S. R., Mannino, A. Jr., Najjar, R. G., Friedrichs, M. A. M., Cai, W., Salisbury, J., et al. (2013). Surface ocean pCO2 seasonality and sea-air CO2 flux estimates for the North American east coast. *J. Geophys. Res. Ocean* 118, 5439–5460. doi: 10.1002/jgrc.20369

Smith, E. M., and Kemp, W. M. (1995). Seasonal and regional variations in plankton community production and respiration for Chesapeake Bay. *Mar. Ecol. Prog. Ser.* 116, 217–231. doi: 10.3354/meps116217

State of Maryland Department of Natural Resources (2016). *Hypoxia Report*. Available at: http://dnr.maryland.gov/waters/bay/Pages/Hypoxia-Reports.aspx

Testa, J. M., and Kemp, W. M. (2014). Spatial and temporal patterns of winter-spring oxygen depletion in Chesapeake Bay bottom water. *Estuaries Coasts* 37, 1432–1448. doi: 10.1007/s12237-014-9775-8

Testa, J. M., Kemp, W. M., and Boynton, W. R. (2018). Season-specific trends and linkages of nitrogen and oxygen cycles in Chesapeake Bay. *Limnol. Oceanogr.* 63, 2045–2064. doi: 10.1002/lno.10823

Uppström, L. R. (1974). The boron/chlorinity ratio of deep-sea water from the Pacific Ocean. *Deep Res. Oceanogr. Abstr.* 21, 161–162. doi: 10.1016/0011-7471(74)90074-6

Waldbusser, G. G., Powell, E. N., and Mann, R. (2013). Ecosystem effects of shell aggregations and cycling in coastal waters: an example of Chesapeake Bay oyster reefs. *Ecology* 94, 895–903. doi: 10.1890/12-1179.1

Wong, G. T. F. (1979). Alkalinity and pH in the southern Chesapeake Bay and the James River estuary. *Limnol. Oceanogr.* 24, 970–977. doi: 10.4319/lo.1979.24.5.0970

Xu, Y. Y., Cai, W. J., Gao, Y., Wanninkhof, R., Salisbury, J., Chen, B., et al. (2017). Short-term variability of aragonite saturation state in the central Mid-Atlantic Bight. *J. Geophys. Res. Ocean* 122, 4274–4290. doi: 10.1002/2017JC012901

Zhang, Q., Brady, D. C., Boynton, W. R., and Ball, W. P. (2015). Long-term trends of nutrients and sediment from the nontidal Chesapeake Watershed: an assessment of progress by river and season. *J. Am. Water Resour. Assoc.* 51:15. doi: 10.1111/1752-1688.12327

Zhang, Q., Murphy, R. R., Tian, R., Forsyth, M. K., Trentacoste, E. M., Keisman, J., et al. (2018). Chesapeake Bay's water quality condition has been recovering: insights from a multimetric indicator assessment of thirty years of tidal monitoring data. *Sci. Total Environ.* 637–638, 1617–1625. doi: 10.1016/j.scitotenv.2018.05.025

Conflict of Interest Statement: The authors declare that the research was conducted in the absence of any commercial or financial relationships that could be construed as a potential conflict of interest.

frontiers
in Marine Science

ORIGINAL RESEARCH
published: 25 January 2019
doi: 10.3389/fmars.2018.00520

Carbon Isotopic Fractionation in Organic Matter Production Consistent With Benthic Community Composition Across a Coral Reef Flat

David A. Koweek[1]*, Atleigh Forden[1], Rebecca Albright[1,2], Yuichiro Takeshita[1,3], David A. Mucciarone[4], Aaron Ninokawa[5] and Ken Caldeira[1]

[1] Department of Global Ecology, Carnegie Insitution for Science, Stanford, CA, United States, [2] Department of Invertebrate Zoology, California Academy of Sciences, San Francisco, CA, United States, [3] Monterey Bay Aquarium Research Institute, Moss Landing, CA, United States, [4] Department of Earth System Science, Stanford University, Stanford, CA, United States, [5] Bodega Marine Laboratory, University of California, Davis, Davis, CA, United States

OPEN ACCESS

Edited by:
Eric 'Pieter Achterberg,
GEOMAR Helmholtz Center for Ocean
Research Kiel, Germany

Reviewed by:
Matheus Carvalho,
Southern Cross University, Australia
Benoit Thibodeau,
The University of Hong Kong,
Hong Kong

***Correspondence:**
David A. Koweek
dkoweek@carnegiescience.edu

Specialty section:
This article was submitted to
Marine Biogeochemistry,
a section of the journal
Frontiers in Marine Science

Received: 12 April 2018
Accepted: 21 December 2018
Published: 25 January 2019

Citation:
Koweek DA, Forden A, Albright R,
Takeshita Y, Mucciarone DA,
Ninokawa A and Caldeira K (2019)
Carbon Isotopic Fractionation in
Organic Matter Production Consistent
With Benthic Community Composition
Across a Coral Reef Flat.
Front. Mar. Sci. 5:520.
doi: 10.3389/fmars.2018.00520

Carbon fluxes on coral reefs (net community production and net community calcification) aggregate the collective activity of all coral reef community members. This integrated approach provides powerful community-level insights, but is unable to resolve the finer-scale contributions of different reef functional groups to the community-scale rates. Tools are required to disaggregate the community-scale approaches and evaluate the performance of co-existing reef functional groups. Such assessments are necessary to improve forecasts of coral reef responses to global and local environmental change. We present results from a coral reef field study on One Tree Island reef in the Great Barrier Reef, off northeastern Australia, in September-October 2016 where we combined observations of total alkalinity, dissolved inorganic carbon (DIC), and the stable isotopic composition of dissolved inorganic carbon ($\delta^{13}C_{DIC}$) to estimate carbon isotopic fractionation during organic matter formation. Portions of the reef with greater abundance of non-calcifying algae fractionated DIC ~5‰ more (stronger preference for ^{12}C) during organic metabolism than did portions of the reef with a greater abundance of calcifiers. These results were consistent across a wide range of assumed isotopic fractionation factors for net calcification. We attribute the observed differences in carbon isotopic fractionation to the metabolic activities of the ecological community underlying each section of the reef, rather than to environmental factors such as light availability or water temperature. The patterns in carbon isotopic fractionation were generally consistent with inferred ratios of calcification to primary production in each reef zone, giving further confidence to our inference that differences in carbon isotopic fractionation may be related to differences in the ecological community on small spatial scales.

Keywords: coral reefs, stable isotopes, carbonate chemistry, calcification, primary production, Great Barrier Reef, marine chemistry, biogeochemistry

1. INTRODUCTION

Field studies of coral reef community metabolism (also called ecosystem metabolism) have greatly improved our collective understanding of coral reef ecosystems since they began over 60 years ago (Sargent and Austin, 1949; Odum, 1953; Odum and Odum, 1955). Together, these studies have illuminated variability in net photosynthetic and calcification rates over a range of timescales, including interannual (Kinsey, 1978; Silverman et al., 2012; Shaw et al., 2015; Yeakel et al., 2015; Kwiatkowski et al., 2016), seasonal (Falter et al., 2012; Shaw et al., 2012; Albright et al., 2013), daily (Nakamura and Nakamori, 2008; Albright et al., 2015), and even hourly (Shamberger et al., 2011; Koweek et al., 2015b; Takeshita et al., 2016). Environmental data collected alongside the metabolic rate data has helped us understand the community-scale dependence of primary production on light availabilty (Gattuso et al., 1993), the close correlation between rates of net production and net calcification (Shaw et al., 2012; McMahon et al., 2013; Albright et al., 2015), and the relative roles of benthic processes in controlling the biogeochemical variability experienced on coral reefs over diel timescales (Andersson and Gledhill, 2013).

Net community production (NCP: gross primary production minus community respiration) and net community calcification (NCC: calcification minus dissolution) have most commonly been estimated by measuring changes, or anomalies, in dissolved inorganic carbon (DIC) or dissolved oxygen (O_2) and total alkalinity (TA) over some portion of reef, along with an estimate of the water volume and timescale over which the biogeochemical anomaly took place (Odum and Odum, 1955; Barnes, 1983). NCC estimates rely on the well-documented ratio of approximately 2:1 changes in TA to changes in DIC (Smith and Key, 1975) and assume that NCP does not change TA (Kinsey, 1978). NCP rates calculated using DIC anomalies need to be corrected for DIC changes due to calcification and air/sea gas exchange. These so-called anomaly techniques have strength because of their ability to integrate the activity of all members of the coral reef community into a single rate estimate. However, this integrated approach to metabolic rate estimates is unable to resolve the contributions of different reef functional groups such as corals, macroalgae, calcifying algae, etc. to community-scale metabolic rates. Improved linkages between between the coral reef ecological community and coral reef community metabolic rates are needed to improve our understanding of coral reef ecosystem function.

Recent evidence supports the hypothesis that bulk biogeochemical measurements of seawater chemistry (DIC and TA) may be reflective of the ecological community composition (Lantz et al., 2014; Cyronak et al., 2018) and that variations in biogeochemical variability can be related to the coral and algal cover in a reef community through the metabolic activity of these reef community members (Page et al., 2016). However, coral cover effects on biogeochemical variability through coral metabolic activities are complex. Using mesocosms and corals from Bermuda, Page et al. (2017) showed that variations in coral cover between 40 percent and 80 percent had no effect on biogeochemical variability. Conversely, using mesocosms and corals from Hawai'i Page et al. (2017) showed that nighttime pH decreases from respiration scaled with percent coral cover, but that daytime pH increases from gross production were not dependent on percent coral cover. Clearly work remains to better understand the linkages between benthic community composition, NCC and NCP, and resulting biogeochemical variability. A new suite of biogeochemical tracers could continue to improve our understanding of coral reef ecosystem function by allowing us to zoom in from an aggregated community perspective to better understand the contributions of different functional groups to the community metabolism. These tracers could include coral metabolomic profiles (Sogin et al., 2014), environmental DNA (Stat et al., 2017), and stable isotopic tracers.

Variations in the stable isotopic composition of dissolved inorganic carbon ($\delta^{13}C_{DIC}$) are driven by variations in carbon isotopic fractionation (ϵ) among members of the coral reef community and thus may yield insights into modern biogeochemical cycling in coral reefs that are unavailable from measurements of DIC and TA alone. Although there has been a long history of using $\delta^{13}C_{DIC}$ and $\delta^{13}C_{CO_2}$ to study global ocean processes, these measurements have not been applied often to study coral reef metabolism. $\delta^{13}C_{DIC}$ may act as a powerful tracer of reef community metabolic activities by reflecting the isotopic fractionation of the various carbon fluxes occuring within reefs, and specifically in ways that are not captured by measured TA and DIC anomalies alone. For example, photosynthesis results in the preferential uptake of ^{12}C, leaving seawater DIC enriched in the heavier ^{13}C isotope. The degree of this fractionation, which is dependent upon the rate of uptake and the photosynthetic pathway involved (Hayes, 1993; Carvalho et al., 2015), can range from 10‰ to 30‰ in reef organisms with the organic tissue isotopically depleted relative to the seawater (Smith et al., 1985). Calcification typically involves far less carbon isotopic fractionation, which can either leave the carbonate skeletons of corals and calcifying algae isotopically enriched or depleted relative to the seawater DIC by ~0‰ to 3‰ (Smith et al., 1985; Gischler et al., 2009). Such large differences in carbon isotopic fractionation between photosynthesis and calcification have previously been exploited to estimate reef-scale rates of NCP using reef-scale isotopic fractionation factors (Smith and Kroopnick, 1981), but little effort has been expended to move from reef-scale fractionation toward finer scales of ecological and biogeochemical relevance.

In this study we continue to explore carbon isotopic fractionation of DIC on coral reefs using a reef flat in the Great Barrier Reef as a case study. We hypothesized that portions of the reef community featuring a greater abundance of non-calcifiers would more strongly fractionate DIC than portions of the reef featuring a greater abundance of calcifiers, and that such differences would result in distinct spatial patterns of $\delta^{13}C_{DIC}$ that can be traced back to the underlying benthic communities. We inferred carbon isotopic fractionation during organic matter formation from variations in $\delta^{13}C_{DIC}$, TA, and DIC as water flowed over the reef flat. Our results show that carbon isotopic fractionation on the reef reflects the metabolic activities of the underlying ecological community, but work remains to unlock the full potential of $\delta^{13}C_{DIC}$ as a biogeochemical tracer.

2. METHODS

2.1. Study Site and Sampling Protocol–a Study of Opportunity

Seawater samples were collected from a reef flat on One Tree Island (OTI) in the southern Great Barrier Reef (**Figure 1**) in September to October 2016 in conjunction with the Albright et al. (2018) CO_2 enrichment experiment. As discussed in Albright et al. (2018), OTI features a ponded lagoon system such that free surface gradients exist between lagoons at low tide, causing a gravitational flow from one lagoon to another. Slow, unidirectional flow over this shallow reef flat at low tide creates an excellent environment to make coral reef biogeochemical measurements. We sampled natural abundance $\delta^{13}C_{DIC}$, DIC, and TA across the reef flat on days (n = 10) when the Albright et al. (2018) experiment was not adding CO_2 to the reef. Because this was largely a study of opportunity that leveraged the resources already in place for the CO_2 enrichment experiment, the study site, time of year, and sampling locations were determined by factors outside the direct control of this study.

The reef flat study area was approximately 32 m wide (perpendicular to the direction of flow) by 25 m long (parallel to the direction of flow). The mean depth of the front zone during sampling was 0.15 m and mean depth of the back zone was 0.08 m. Samples were collected along three lines perpendicular to the direction of water flow across the water. The front line was near the leading edge of the border, the middle line bisected the study area, and the back line defined the trailing edge of the study area (**Figure 1**). Along each of the three lines, sampling locations were marked into the reef prior to the start of the field season in order to ensure day-to-day consistency in sampling location. The front line had 9 sampling positions approximately normally distributed about the middle of the study area, the middle line had 11 sampling positions and the back line had 15 sampling positions, each also normally distributed about the center of the study area. The sampling stations were centered in the middle of the study area to best track the fate of the released CO_2 and Rhodamine WT in the concurrent CO_2 enrichment experiment (Albright et al., 2018), which were both released upstream of the midpoint of the front line. Approximately one hour after low tide, seawater samples were collected by a field team of 6 people (2 people per line) who used water pumps to rapidly sample the study area, typically in less than 5 min, by moving from the edges of each line toward the midpoint. Seawater samples were pumped directly into pre-rinsed 500 mL borosillicate bottles taped entirely black to minimize any photosynthetic activity prior to water chemistry analysis. Despite having a sampling design optimized for conditions outside the direct scope of this study, we believe that this study presents a unique opportunity to pair a highly sampled reef flat (n = 35 samples across a 32 x 25 m area) with a detailed survey of the ecological community and environmentally

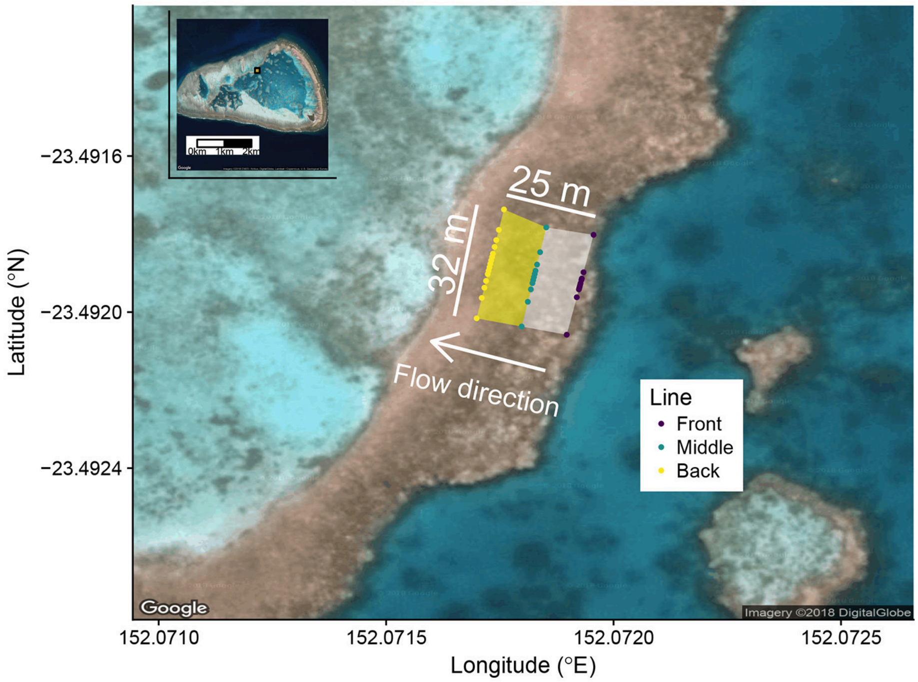

FIGURE 1 | Google Earth image of the study site with One Tree Island as an inset in the upper left corner. The orange rectangle with black border in the inset shows the location of the study site within One Tree Island. Colored dots show the position of all sampling locations. The front zone is defined between the front and middle lines (white shaded area). The back zone is defined between the middle and back lines (yellow shaded area). The white arrow shows the direction of gravitational flow from First Lagoon to Third Lagoon at low tide due to ponding.

relevant data sets (e.g., PAR). As such, we argue that this study offers value because of its ability to pair $\delta^{13}C_{DIC}$ measurements with their ecological and environmental controls.

2.1.1. Ecological Community Survey

Benthic surveys were conducted to characterize the ecological community following Albright et al. (2018). The methodology is briefly summarized here. Five transects running parallel to the direction of flow were evenly spaced across the study site. Top-down photographs of 0.25 m^2 quadrats were taken each meter along the transect. Coral Point Count software was used to randomly select 15 points per quadrat, which were then classified into one of six functional groups: (1) coral, (2) coralline algae, (3) sand, pavement, and rubble, (4) macroalgae, (5) turf algae, and (6) unknown. Results from each quadrat were aggregated into transect-wide results, which were averaged to establish representative community composition metrics for the front and back zones.

2.2. Analytical Chemistry

Field samples were immediately transferred to a shore-based laboratory for geochemical analysis. As described in Albright et al. (2018) samples were analyzed for pH using spectrophotometry and TA using a Metrohm 855 robotic autotitrator. TA samples were monitored for accuracy using Certified Reference Materials (CRMs) provided by the laboratory of Andrew Dickson (Scripps Insitution of Oceanography). DIC was calculated from pH and TA at 20°C (the constant temperature of the spectrophotometric pH measurements) using field-based measurements of salinity from SBE37 MicroCAT C-T Recorders (Sea-Bird Scientific, Inc.) following the equations and best practices described in Riebesell et al. (2010). Aliquots of the original 500 mL samples were filtered following protocols specified in Bockmon and Dickson (2014) into 30 mL serum vials (Wheaton Inc.) for later stable isotopic analysis. These samples were preserved through addition of 20 μL of saturated mercuric chloride solution within 2 to 3 h of sample collection, and were sealed with rubber septa and tin or aluminum crimp tops.

Stable isotope samples were analyzed at the Stanford University Stable Isotope Biogeochemistry Laboratory (SIBL). The custom methodology used to analyze the samples is briefly described here with additional details available in the SI. Aqueous samples were converted into a gaseous stream for analysis in a Finnigan Delta+ isotope-ratio mass spectrometer (IRMS) with a ConFloII open split interface using a modified version of the sample acidification and delivery system first described by Long et al. (2011). Samples were acidified through addition of 100 μL of 10 percent concentrated phosphoric acid (H_3PO_4) and passed through both a 2′ Nafion drier and a magnesium perchlorate ($Mg(ClO)_4$) trap to remove water prior to delivery to the IRMS via a CO_2-free stream of H_2 gas (**Figure S2**). The IRMS was calibrated daily using injections of an independentally calibrated reference CO_2 gas. IRMS performance was monitored through daily analysis of CRMs (Batch 153) as well as replicate filtered aliquots of seawater collected from a a single, well-mixed batch on site at OTI (henceforth referred to as OTI reef water). Note that while the CRMs are typically used to calibrate carbonate chemistry measurements, we used them only as a filtered, stable, internally consistent batch of water in order to assess our sample precision throughout the duration of our analysis. Details on the calibration and quality assurance procedures can also be found in the SI. All reported values of $\delta^{13}C_{DIC}$ are relative to the Vienna Pee Dee Belemnite (VPDB) standard.

2.2.1. Analytical Uncertainty

Instrumental precision on 185 injections of the CO_2 reference gas over the course of the ~6 weeks of sample analysis was 0.09‰ (1 S.D.). Precision on 255 replicates of the CRMs was 0.12‰ (1 S.D.). Finally, replicate analysis of 155 aliquots of OTI reef water originating from 36 replicate bottles yielded a precision of 0.12‰ (1 S.D.). Average daily precision for both the CRMs and OTI reef water was better than 0.04‰. Errors from the different standards (reference gas injections, CRMs, and OTI reef water) were independent of one another based on an analysis of daily means for each type of standard. The small difference in error between the reference CO_2 injections and the CRMs suggests little additional analytical error attributable to acidifying the seawater into a gaseous CO_2 stream. The negligible difference between the analytical error of the CRMs and the OTI reef water replicates, which were held in 36 separate bottles, indicates no significant error attributable to bottle effects.

We cross-validated our analytical methods with the the laboratory of Paul Quay at the University of Washington (UW). We aggregated some of our internal standard (OTI reef water) and split the samples between bottles to be run at SIBL and those to be sent to UW. SIBL samples had a $\delta^{13}C_{DIC}$ mean ± S.D. of –0.75 ± 0.05‰ (n = 10). UW samples had a $\delta^{13}C_{DIC}$ mean ± S.D. of –0.72 ± 0.01‰ (n = 3). The strong agreement between the two laboratories supports the accuracy of the $\delta^{13}C_{DIC}$ analytical method used in this study.

2.3. Isotopic Calculations

The isotopic mass balance of water flowing across each zone can be expressed as:

$$\begin{aligned} DIC_o\, F\, \delta^{13}C_{DIC_o} \;&=\; DIC_i\, F\, \delta^{13}C_{DIC_i} + A(-NCC\, \delta^{13}C_{CaCO_3} \\ &-\; NCP\, \delta^{13}C_{OM}) \end{aligned} \tag{1}$$

where the subscripts "o" and "i" stand for "outgoing" (left hand side) and "incoming" (right hand side), respectively, F is the mass flux of water over the study site (in $kg\ s^{-1}$) and A is the study site area (m^2). NCC, or net community calcification, is defined as:

$$NCC = \frac{F}{A}\left(\frac{\overline{TA_i} - \overline{TA_o}}{2}\right) \tag{2}$$

and NCP, or net community production, is defined as:

$$NCP = \frac{F}{A}\left(\overline{DIC_i} - \overline{DIC_o}\right) - NCC \tag{3}$$

where the overbars on incoming and outgoing TA and DIC signify line-averaged mean values. Based on the flow direction during low tides, in the front zone the outgoing line was the middle line and the incoming line was the front line. In the back zone, the outgoing line was the back line and incoming line was the middle line. We ignored any effects from air-sea gas exchange in Equation (3) because preliminary calculations revealed small (<5 $\mu mol\ kg^{-1}$) air-sea CO_2 gradients, which were much smaller than the observed DIC and TA gradients generated during flow across the reef flat zones (see section 3).

We define isotopic fractionation factors (ϵ_{P-S}) as $\delta_{product} = \delta_{substrate} + \epsilon$ such that positive isotopic fractionation factors ($\epsilon > 0$) indicate an enrichment in the product relative to the substrate and vice versa for negative isotopic fractionation factors. The factor for NCP is $\delta^{13}C_{OM} = \delta^{13}C_{DIC} + \epsilon_{OM}$ and the factor for NCC is $\delta^{13}C_{CaCO_3} = \delta^{13}C_{DIC} + \epsilon_{CaCO_3}$ where "OM" stands for "organic matter," recognizing that each of these ϵ's represent the net process (i.e., photosynthesis-respiration and calcification-dissolution) and aggregate across all contributors of the reef community.

Substituting Equations (2) and (3) into Equation (1) (as well as using the short-hand $\overline{\Delta TA} = \overline{TA_i} - \overline{TA_o}$, $\overline{\Delta DIC} = \overline{DIC_i} - \overline{DIC_o}$, and $\overline{\Delta\delta^{13}C_{DIC}} = \overline{\delta^{13}C_{DIC_i}} - \overline{\delta^{13}C_{DIC_o}}$) allows us to express the isotope balance using $\overline{\Delta TA}$, $\overline{\Delta DIC}$, and $\overline{\Delta\delta^{13}C_{DIC}}$:

$$\begin{aligned} DIC_o\,\delta^{13}C_{DIC_o} = {} & DIC_i\,\delta^{13}C_{DIC_i} - \big[\,\overline{\Delta TA}/2\ \left(\delta^{13}C_{DIC_i} + \epsilon_{CaCO_3}\right) \\ & + \ \big[\left(\overline{\Delta DIC} - \overline{\Delta TA}/2\right)\left(\delta^{13}C_{DIC_i} + \epsilon_{OM}\right)\big]\big] \end{aligned} \tag{4}$$

Note that Equation (4) is independent of mass flow, F, and depends only on changes in TA, DIC, and $\delta^{13}C_{DIC}$ between two lines oriented normal to the direction of flow. We re-arrange Equation (4) to isolate ϵ_{OM}:

$$\epsilon_{OM}\left(\overline{\Delta DIC} - \overline{\Delta TA}/2\right) = DIC_o\,\overline{\Delta\delta^{13}C_{DIC}} - \overline{\Delta TA}/2\,\epsilon_{CaCO_3} \tag{5}$$

We calculated ϵ_{OM} from Equation (5) for fixed values of ϵ_{CaCO_3} ranging from –5‰ to 5‰. We chose this range in ϵ_{CaCO_3} to reflect the inorganic $\delta^{13}C$ of reef materials, which typically ranges ± 3–5‰ (Smith et al., 1985; Gischler et al., 2009).

Finally, we wanted to explore how variations ΔTA, ΔDIC, ϵ_{CaCO_3}, and ϵ_{OM} influence $\delta^{13}C_{DIC}$ fractionation. The change in $\delta^{13}C_{DIC}$ as the water flows through a given area, $\Delta\delta^{13}C_{DIC}$, can be expressed by re-arranging Equation (5):

$$\overline{\Delta\delta^{13}C_{DIC}} = \frac{\epsilon_{OM}\left(\overline{\Delta DIC} - \overline{\Delta TA}/2\right) + \epsilon_{CaCO_3}\left(\overline{\Delta TA}/2\right)}{DIC_o} \tag{6}$$

We held DIC_o constant in order to explore the effects the geochemical changes and isotope effects on the $\Delta\delta^{13}C_{DIC}$. We set DIC_o equal to the mean DIC leaving the front zone through the ten days of observation (1,907 $\mu mol\ kg^{-1}$). For simplicity, we henceforth refer to $\overline{\Delta DIC}$, $\overline{\Delta TA}$, and $\overline{\Delta\delta^{13}C_{DIC}}$ as ΔDIC, ΔTA, and $\Delta\delta^{13}C_{DIC}$, respectively.

2.4. Uncertainty Analysis

We calculated the standard error in ΔDIC, ΔTA, and $\Delta\delta^{13}C_{DIC}$ between two lines as $S.E._{\Delta} = \sqrt{\left(\sigma_i/\sqrt{n_i}\right)^2 + \left(\sigma_o/\sqrt{n_o}\right)^2}$ where σ_i and n_i were the standard deviation and number of samples of the incoming line, respectively, and σ_o and n_o were the standard deviation and number of samples of the outgoing line, respectively, for each zone and for each day. We calculated the standard error in the ratio $\Delta TA/\Delta DIC$ as $S.E._{\Delta TA/\Delta DIC} = \frac{\Delta TA}{\Delta DIC}\sqrt{\left(\frac{S.E._{\Delta TA}}{\Delta TA}\right)^2 + \left(\frac{S.E._{\Delta DIC}}{\Delta DIC}\right)^2}$ where ΔTA and ΔDIC are the mean estimates for each zone on each day, and where $S.E._{\Delta TA}$ and $S.E._{\Delta DIC}$ are the standard errors for ΔTA and ΔDIC, respectively, for each zone on each day.

We calculated ϵ_{OM} using the daily mean ΔDIC, ΔTA, and $\Delta\delta^{13}C_{DIC}$ within each zone on each day (**Figure S1**), but we chose to focus on bootstrap estimates of ϵ_{OM} for both the front and back zones. We bootstrapped the ϵ_{OM} estimates using linear regression since Equation (5) takes the form $\beta x = Y$ where $\beta = \epsilon_{OM}$. We bootstrapped the ϵ_{OM} estimates for both the front and back zones 10,000 times drawing from the original 10 observations (daily mean ΔDIC, ΔTA, $\Delta\delta^{13}C_{DIC}$, and $\overline{DIC_o}$ for each zone on each day). The bootstrap generated ϵ_{OM} estimates less sensitive to the results of any given day than did the individual ϵ_{OM} calculated using the data from only a single day. Since we were interested in evaluating the differences in ϵ_{OM} between zones for the purposes of understanding the degree to which they reflect the benthic community composition, we felt justified in using the more temporally integrated approach to estimating the average ϵ_{OM} within each zone. After we completed the bootstrap, we calculated the difference in ϵ_{OM} between the front and back zones ($\Delta\epsilon$) for equivalent bootstrap iterations (same sample index used to calculate ϵ_{OM} in both the front and back zones), resulting in 10,000 estimates of $\Delta\epsilon$ for each value of ϵ_{CaCO_3}.

3. RESULTS

3.1. Coral Reef Community Composition

Calcifiers (defined as the percent cover of coral and coralline algae) were less abundant in the front zone than in the back zone (21 percent vs. 41 percent) (**Figure 2**). Non-calcifying algae (defined as macroalgae plus turf algae) were more abundant in the front zone relative to the back zone (48 percent vs. 35 percent). A small fraction (<0.5 percent) of the ecological community in the back zone consisted of sponges and other organisms that were not classified. We omitted these two categories from **Figure 2** for clarity.

3.2. DIC, TA, and $\delta^{13}C_{DIC}$ Variability

DIC ranged from 1,683 $\mu mol\ kg^{-1}$ to 2,008 $\mu mol\ kg^{-1}$ across the study, with strong day-to-day variability in daily DIC minima and less variability in DIC maxima. DIC became depleted moving from the front to the middle to the back lines, although the magnitude of depletion depended upon the position on the line (**Figure 3**). Sampling positions south of the study area midpoint in **Figure 1** (positive values along the line) generally exhibited greater DIC depletion than did those located north of the study area center line (negative values). This pattern was generally consistent across all three lines, although the front line tended to exhibit more DIC variability than did the middle and back lines. Similar patterns in TA along the sampling lines emerged as those observed in the DIC data

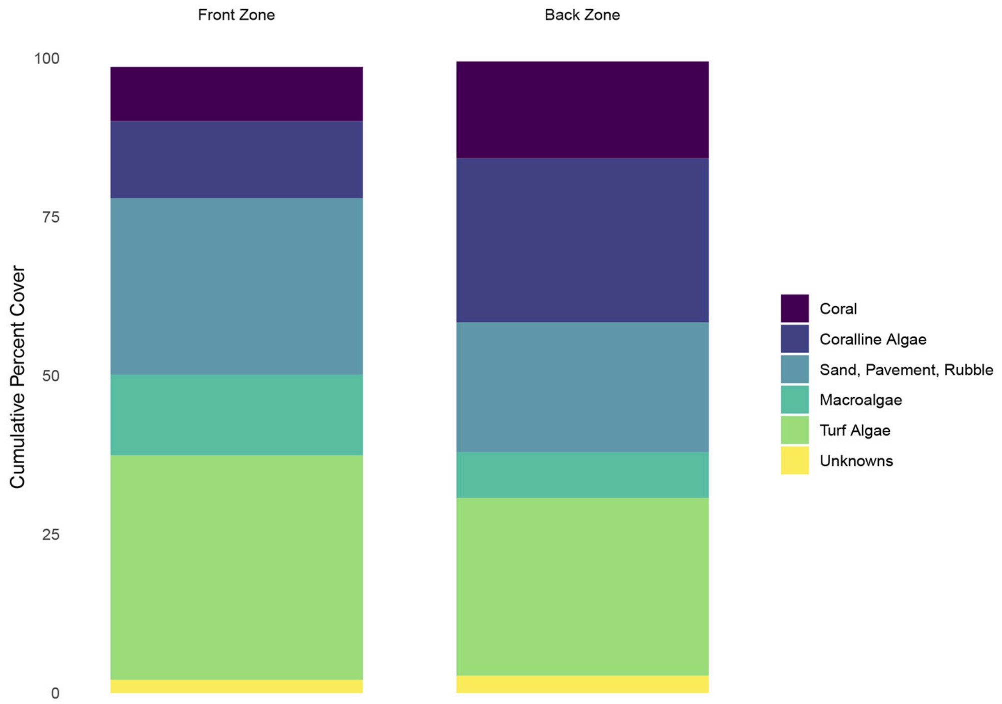

FIGURE 2 | Ecological community composition of the front and back zones on the reef. Calcifers (corals and coralline algae) are show in opaque, while the other functional groups are shown in semi-transparent color to highlight the differences in calcifier abundance between the two zones.

(**Figure 4**). TA had a smaller observed range in concentration than did DIC (2,134 $\mu mol\ kg^{-1}$–2,295 $\mu mol\ kg^{-1}$). The DIC and TA data from 03-October-2016 exhibited small-to-negligible depletion moving across the study site. We attribute this outlier to exceptionally low photosynthetically active radiation (PAR), which we believe led to reduced biological uptake of DIC and TA by reducing light available for photosynthesis and subsequent calcification. The PAR measurements on 03-October-2016 were made at 15:51 hrs local time with a PAR value of 169 $\mu mol\ m^{-2}\ s^{-1}$. In comparison, average PAR during the sampling periods was 1112 $\pm$ 175 $\mu mol\ m^{-2}\ s^{-1}$ (mean $\pm$ S.E.) (Albright et al., 2018).

$\delta^{13}C_{DIC}$ values typically spanned –0.5‰ to 1.4‰ with a few exceptions for more isotopically depleted samples (**Figure 5**). One back line sample on 03-October-2016 was less than –3‰ and one front line sample on 16-October-2016 was less than –2‰. These two samples, along with the other isotopically light samples, corresponded to high DIC (**Figure 6**). $\delta^{13}C_{DIC}$ showed greater along-line and along-flow variability than did DIC or TA which often obscured overall trends of isotopic enrichment during flow across the reef. Some sampling days, such as 12-September-2016, 15-September-2016, and 13-October-2016, revealed clearer spatial patterns in $\delta^{13}C_{DIC}$ enrichment during transit across the reef flat. Other days, such as 30-September-2016 and 16-October-2016, showed less consistent patterns in $\delta^{13}C_{DIC}$ during transit across the reef. Line-averaged patterns of isotopic enrichment helped reveal a clearer pattern of average isotopic enrichment during flow across the reef flat (**Figure 5**).

Mean ΔDIC ranged from –6 to 91 $\mu mol\ kg^{-1}$. The only negative ΔDIC value occurred on 03-October-2016, although 18-September-2106 also featured $\Delta DIC < 25\ \mu mol\ kg^{-1}$. ΔDIC was generally consistent between the front and back zone, but differences between the two zones of up to ~25$\mu mol\ kg^{-1}$ were observed early in the study (**Figure 7A**). Front zone ΔDIC was greater than back zone ΔDIC on 6 sampling days (including 03-October-2016). ΔTA was positive in both zones on all sampling days (**Figure 7B**) and ranged from 5 to 35 $\mu mol\ kg^{-1}$. Front zone and back zone ΔTA were of similar magnitudes and showed similar patterns across the sampling days. Back zone ΔTA exceeded front zone ΔTA on 6 sampling days. Mean $\Delta\delta^{13}C_{DIC}$ ranged from 0.12 to –0.73 ‰ (**Figure 7C**; note that $\Delta\delta^{13}C_{DIC}$ is usually negative since $\Delta\delta^{13}C_{DIC} = \delta^{13}C_{DIC_i} - \delta^{13}C_{DIC_o}$). $\Delta\delta^{13}C_{DIC}$ estimates were characterized by high variability, although the mean estimates showed a consistent pattern on enrichment. On all 10 sampling days, front zone $\Delta\delta^{13}C_{DIC} < 0$ and on 9 of the 10 sampling days, back zone $\Delta\delta^{13}C_{DIC} < 0$. The only day for which the back zone $\Delta\delta^{13}C_{DIC} > 0$ was 03-October-2016.

We calculated $\Delta TA/\Delta DIC$ because of it has long been used to reveal the relative importance of calcification and primary production on coral reefs (Suzuki and Kawahata, 2003; Andersson and Gledhill, 2013; Cyronak et al., 2018) with higher values signifying greater rates of calcification relative to primary production (**Figure 7D**). $\Delta TA/\Delta DIC$ was typically between 0.25 and 0.5, although the back zone $\Delta TA/\Delta DIC$ on 18-September-2016 was slighly higher (0.87). $\Delta TA/\Delta DIC$

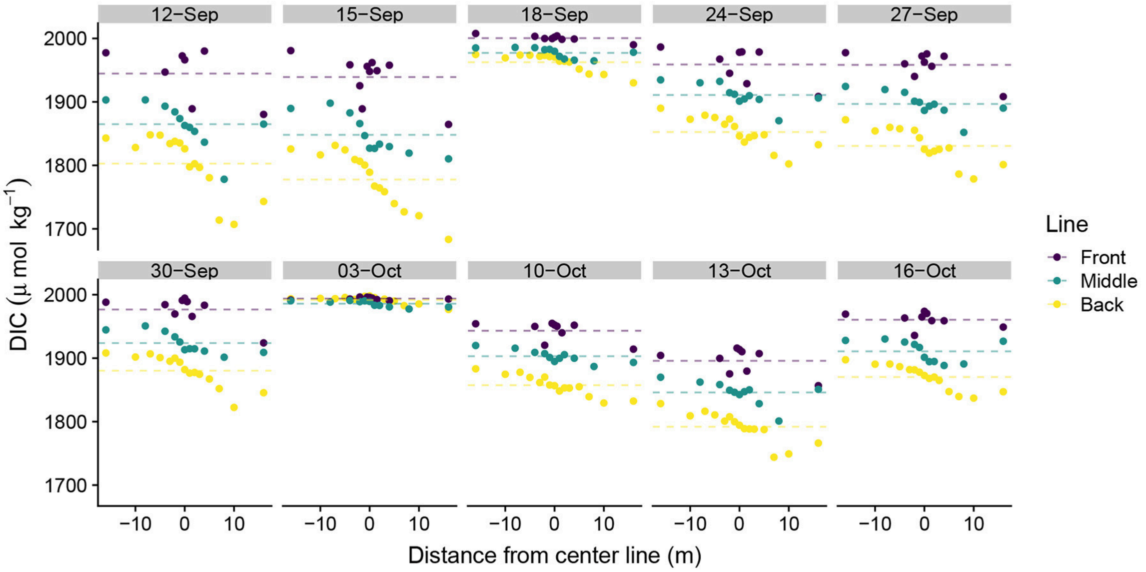

FIGURE 3 | Spatial distribution of dissolved inorganic carbon measurements. Spatial distance values less than zero are located north of the center line and distance values greater than zero are located south of the center line in **Figure 1**. Dotted lines show line-averaged DIC.

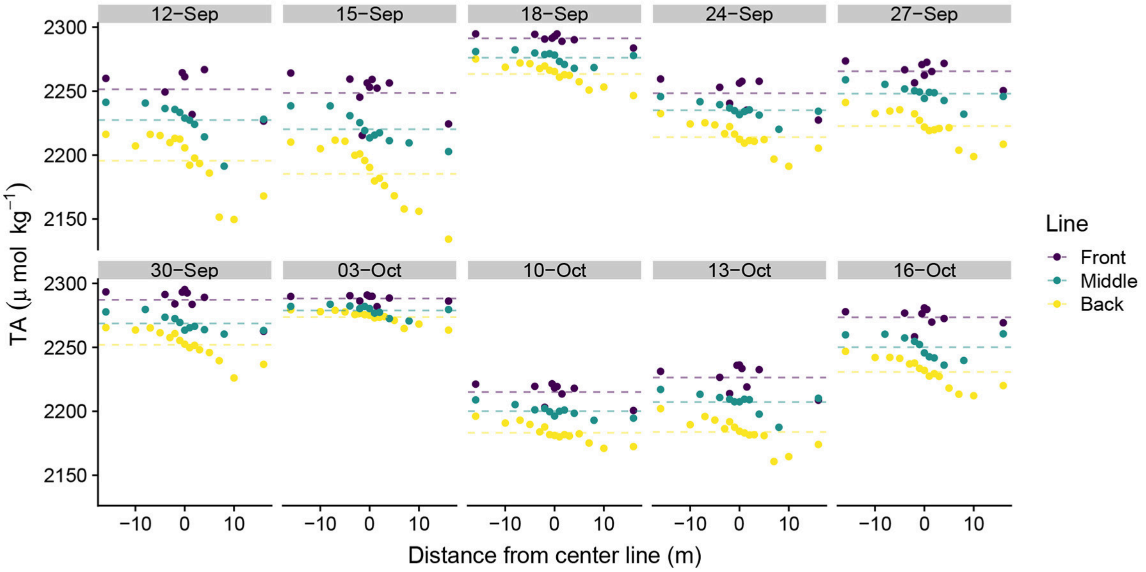

FIGURE 4 | Spatial distribution of total alkalinity measurements. Spatial distance values less than zero are located north of the center line and distance values greater than zero are located south of the center line in **Figure 1**. Dotted lines show line-averaged TA.

values on 03-October-2016 deviated from the patterns observed during the other nine sampling days, no doubt driven by the small $|\Delta DIC|$, which led to large positive and negative values of $\Delta TA/\Delta DIC$ because the ratio is sensitive to the magnitude of the denominator. We converted $\Delta TA/\Delta DIC$ to NCC/NCP using the formula $NCC/NCP = m/(2 - m)$ where m is $\Delta TA/\Delta DIC$ (Koweek et al., 2015a). Front zone NCC/NCP was 0.24 ± 0.03 and back zone NCC/NCP was 0.33 ± 0.06 (both mean ± S.E., excluding the data from O3-October-2016). The NCC/NCP calculations were consistent with expectations from the ecological survey (greater abundance of calcifiers in the back zone) with the uncertainty surrounding the estimates reflective of the uncertainty in the underlying ΔTA and ΔDIC data.

3.3. Isotopic Fractionation Factors

Mean ϵ_{OM} in the front zone spanned −16‰ to −14‰ while the mean back zone estimates ranged from –12‰ to –9‰ (**Figure 8A**). Mean ϵ_{OM} estimates showed minor sensitivity to

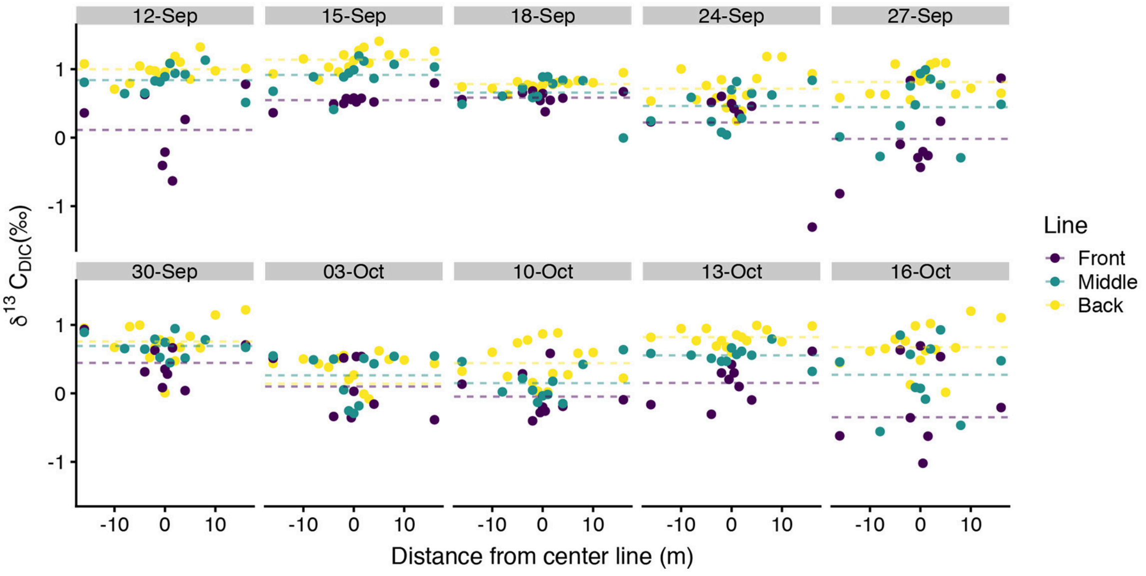

FIGURE 5 | Spatial distribution of $\delta^{13}C_{DIC}$ measurements. Spatial distance values less than zero are located north of the center line and distance values greater than zero are located south of the center line in **Figure 1**. Dotted lines show line-averaged $\delta^{13}C_{DIC}$. Two anomalously low $\delta^{13}C_{DIC}$ samples, one on 03-October-2016 and the other on 16-October-2016, extend beyond the y-axis of this plot and are shown in **Figure 6**.

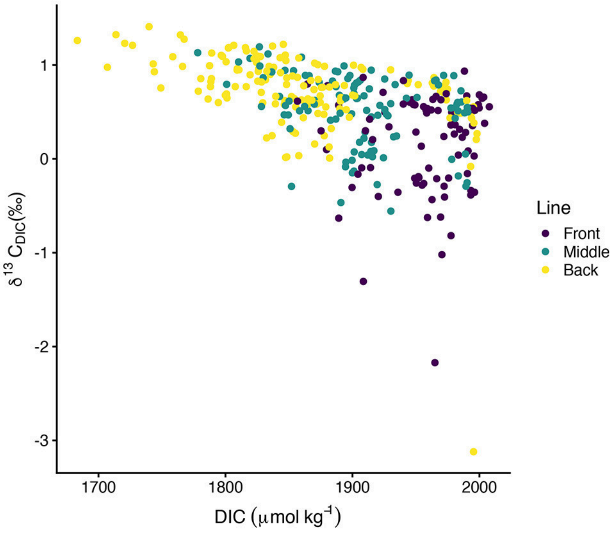

FIGURE 6 | Scatter plot of $\delta^{13}C_{DIC}$ vs. DIC.

the ϵ_{CaCO_3} value considered, with decreasing ϵ_{OM} at increasing ϵ_{CaCO_3} in both zones. However, the effect of ϵ_{CaCO_3} on mean ϵ_{OM} was small (2‰ and 3‰ in the front zone and back zone, respectively). Bootstrapped estimates of ϵ_{OM} in the front zone spanned −25‰ to −8‰ and in the back zone ranged from −20‰ to −4‰. (**Figure 8A**). Inclusion of the anomalous data from 03-October-2016 undoubtably increased the ranges on the ϵ_{OM} estimates, so we view these ranges from the bootstrapping as conservative. Back zone ϵ_{OM} was, on average, approximately 5‰ higher than front zone ϵ_{OM}, independent of the ϵ_{CaCO_3} value considered. Greater than 99 percent of the 10,000 bootstrap estimates of $\Delta\epsilon$ for each value of ϵ_{CaCO_3} were greater than 0 (**Figure 8B**).

3.4. Combining Δ s and ϵ s

We explored how ϵ_{CaCO_3} and ϵ_{OM} across the range of ΔTA and ΔDIC observed in this study affected $\Delta\delta^{13}C_{DIC}$ because differences in $\delta^{13}C_{DIC}$ must be observable in order to use differences in ϵ's to trace metabolic activity on a reef (**Figure 9**). When both ΔTA and ΔDIC are near the lower end of values observed in this data set (10 and 25 $\mu mol\ kg^{-1}$, respectively, **Figure 7A**), the calculated ϵ_{OM} at fixed values of ϵ_{CaCO_3} for the front and back zone result in estimates of $\Delta\delta^{13}C_{DIC}$ that were ~−0.15‰ and ~−0.11‰, respectively, a difference of only ~0.04‰ (**Figure 9A**). This difference between the two $\Delta\delta^{13}C_{DIC}$ estimates lies below instrumental precision thresholds, thus the ϵ's of the front and back zones would fail to fractionate $\delta^{13}C_{DIC}$ at detectable differences for the same ΔTA and ΔDIC. Since the isotope effects run parallel to the contour lines of constant $\Delta\delta^{13}C_{DIC}$ in **Figure 9A**, the $\Delta\delta^{13}C_{DIC}$ across both zones is approximately constant across the range of considered ϵ's.

In conditions with high ΔTA and low ΔDIC (30 $\mu mol\ kg^{-1}$ and 25 $\mu mol\ kg^{-1}$, respectively), the $\Delta\delta^{13}C_{DIC}$ contour lines are more steeply sloped (**Figure 9B**). At low values of ϵ_{CaCO_3} (~−5‰), $\Delta\delta^{13}C_{DIC}$ for the front zone is ~−0.12‰ and for the back zone is ~−0.08‰ for ϵ_{OM} values calculated from the data. Again, these differences between front zone and back zone $\delta^{13}C_{DIC}$ fractionation are likely too small for analytical instrumentation to detect. At the high end of ϵ_{CaCO_3} values considered, the $\Delta\delta^{13}C_{DIC}$ for the front zone and back zone

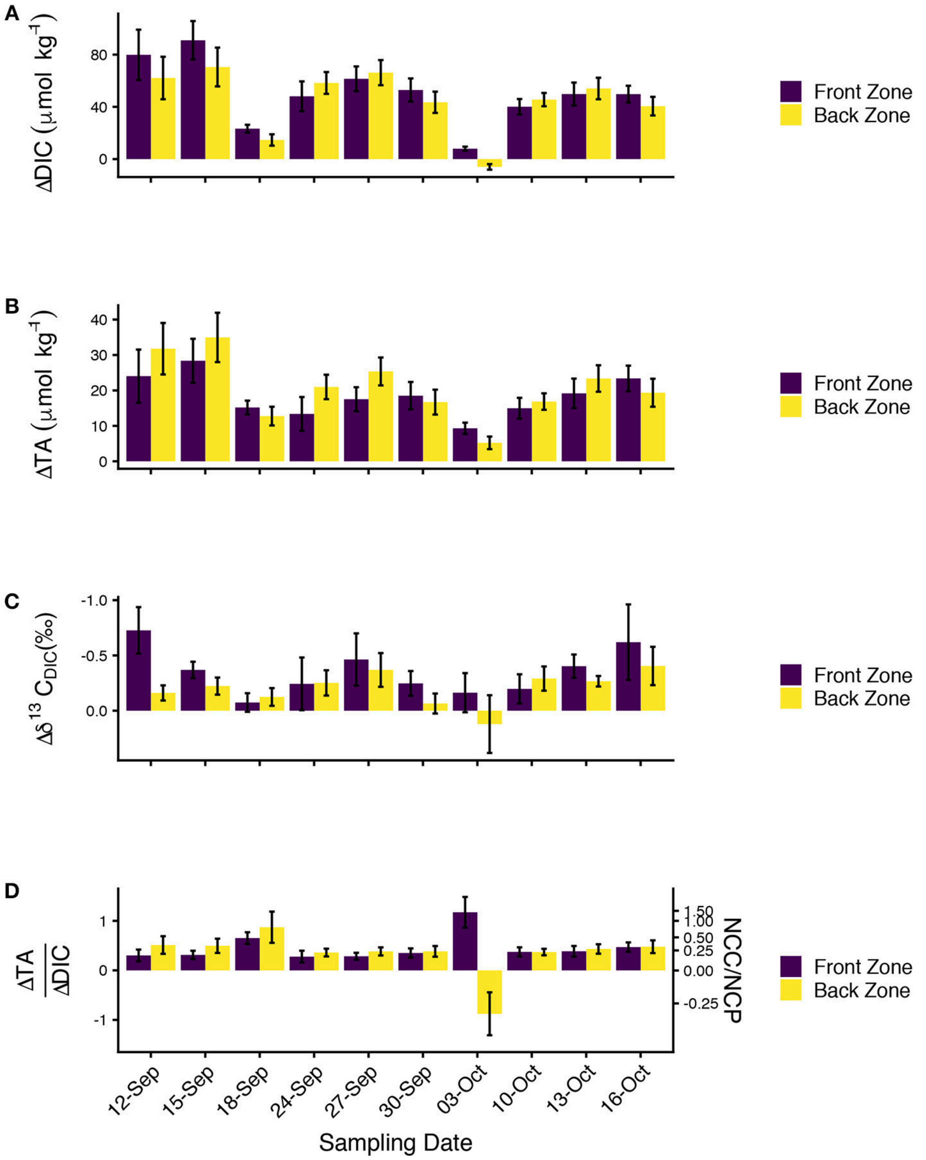

FIGURE 7 | **(A)** ΔDIC, **(B)** ΔTA, **(C)** $\Delta\delta^{13}C_{DIC}$, and **(D)** $\Delta TA/\Delta DIC$ for the front (purple) and back (yellow) zones for all ten sampling days showing biogeochemical changes in water chemistry due to community metabolism. All data are presented as mean ± S.E. Note that the y-axis on **(C)** is reversed for consistency with the other plots. The second axis on **(D)** shows the ratio of net community calcification (NCC) to net community production (NCP) inferred from the $\Delta TA/\Delta DIC$ data.

decrease to ~–0.05‰ and ~–0.03‰, respectively. $\Delta\delta^{13}C_{DIC}$ for the front zone, and especially for the back zone, decreased below instrumental limits of detection. Positive ϵ_{CaCO_3} offsets the $\delta^{13}C_{DIC}$ enrichment created by $\epsilon_{OM} < 0$, which explains how the estimates of $\Delta\delta^{13}C_{DIC}$ in **Figure 9B** decrease toward analytical precision limits as ϵ_{CaCO_3} becomes increasingly positive.

In conditions with high ΔDIC (80 $\mu mol\ kg^{-1}$) the front zone $\Delta\delta^{13}C_{DIC}$ was ~–0.5‰ to ~–0.6‰ and the back zone $\Delta\delta^{13}C_{DIC}$ was ~–0.4‰, resulting in differences of $\Delta\delta^{13}C_{DIC}$ between the two zones of between 0.15‰ and 0.2‰ (**Figures 9C,D**). High ΔDIC drives detectable differences in $\Delta\delta^{13}C_{DIC}$ between the front zone and back zone. This condition was consistent for both the low and high ΔTA explored in this analysis (**Figures 9C,D**). High ΔDIC was necessary to distinguish between $\Delta\delta^{13}C_{DIC}$ estimated using ϵ_{OM} from the front and back zones because of the small difference in ϵ_{OM} between the front and back zones (~5‰).

4. DISCUSSION

4.1. Consideration of ϵ's

We found substantially different ϵ_{OM} between two ecologically distinct zones on a coral reef flat. In the front zone, where algae constituted nearly 50 percent of the benthic community and calcifiers contributed accounted for less than 25 percent of

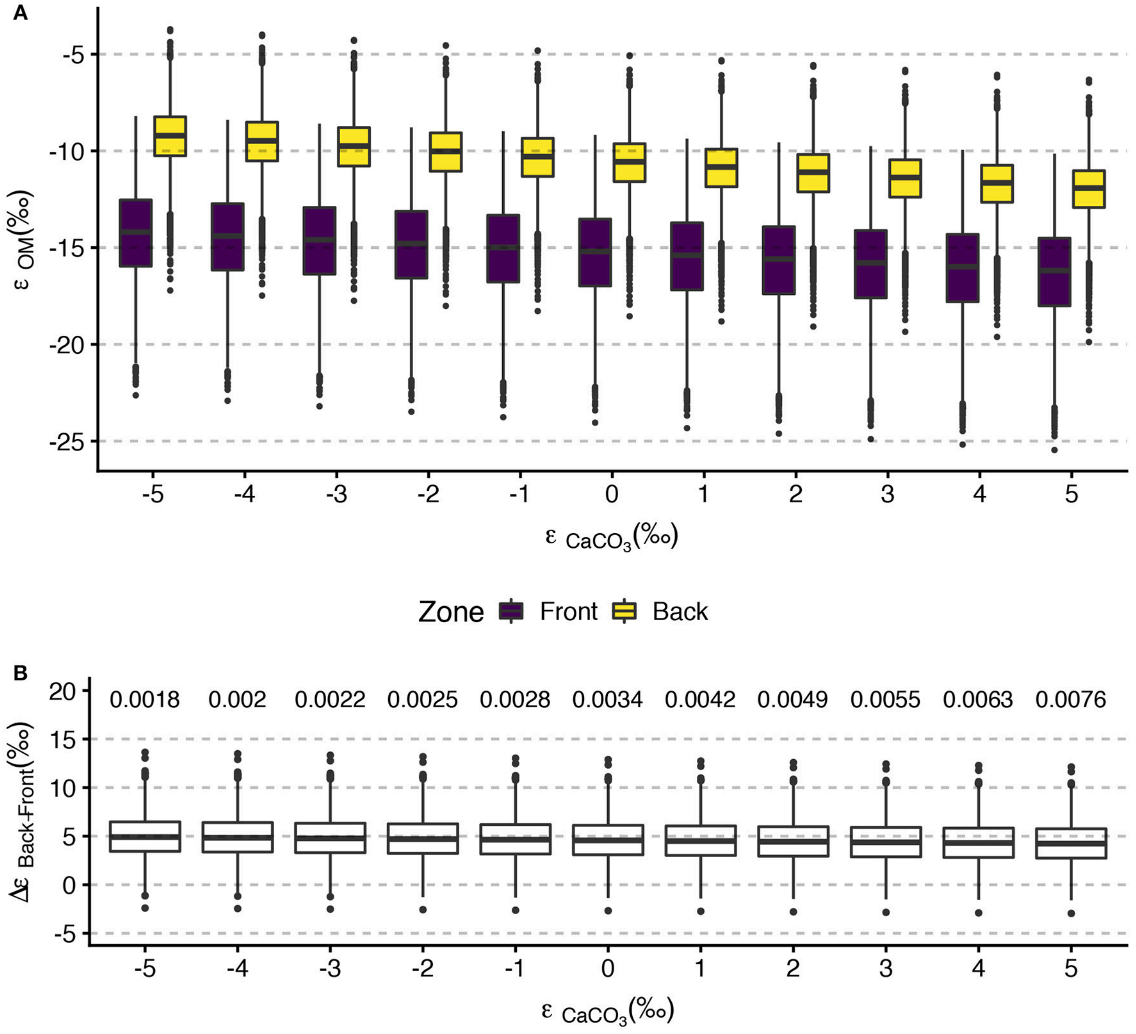

FIGURE 8 | Tukey boxplots of **(A)** front zone and back zone bootstrapped ϵ_{OM} estimates for selected ϵ_{CaCO_3} values and **(B)** $\Delta\epsilon_{OM}$ between the back zone and front zone show the greater isotopic fractionation in the front zone relative to the back zone. Bootstrap values were calculated using mean ΔTA, ΔDIC, and $\Delta\delta^{13}C_{DIC}$ on all sampling days. Boxplots in **(A)** are set at integer values of ϵ_{CaCO_3} and are offset for clarity. The numerical values above $\Delta\epsilon_{OM}$ display the proportion of bootstrap iterations less than or equal to 0.

the benthic community, ϵ_{OM} was –16‰ to –14‰. In the back zone, where the abundance of calcifiers grew to ~40 percent and the algal abundance dropped to 35 percent, ϵ_{OM} increased to between –12‰ and –9‰. Since these two zones were sampled concurrently and at approximately the same depth, we cannot attribute the differences in fractionation to environmental factors such as time of day at sampling, light availability, water depth, and water temperature. Instead, we attribute these differences to the underlying ecological community. That is, we observed greater (more negative) ϵ_{OM} in the section the reef with more algae relative to the section of the reef with more calcifiers, regardless of the assumed ϵ_{CaCO3} value. We hypothesize that the greater isotopic fractionation observed in the front zone was due to the prevalence of C_3 photosynthesis among marine algae (Koch et al., 2013). C_3 photosynthesis fractionates at approximately –25‰ to –29‰ (O'Leary, 1988). Photosynthetic isotopic fractionation in corals can be quite variable at –10‰ to –30‰ (Hayes, 1993; Carvalho et al., 2015), but is, on average, more positive than the fractionation found in marine algae. Thus, we hypothesize that the greater relative abundance of algae resulted in greater isotopic fractionation in the front zone relative to the back zone. Linking the variations in the ecological community to differences in ϵ_{OM} on a real reef system is an important step toward constraining the set of physical and biological conditions under which $\delta^{13}C_{DIC}$ variability may act as a suitable biogeochemical tracer on reefs.

Our estimates of ϵ_{OM} in both the front and back zones are within range of other reported values. Smith and Kroopnick (1981) calculated a community-scale isotope effect (ϵ) of −18.6‰, which is more $\delta^{13}C_{DIC}$ fractionation than our ϵ_{OM}

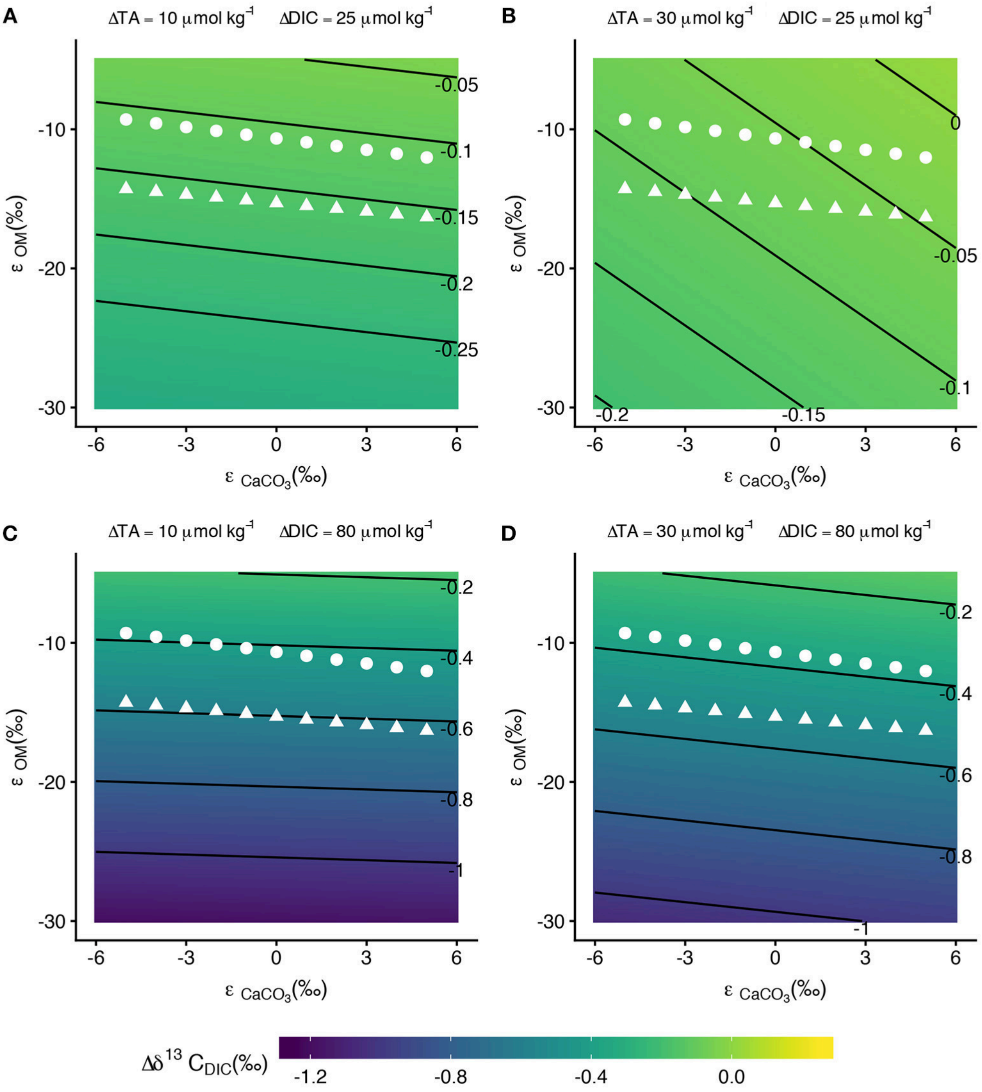

FIGURE 9 | Contour plots of $\Delta\delta^{13}C_{DIC}$ as functions of ϵ_{CaCO_3} and ϵ_{OM} for different values of ΔTA and ΔDIC. The white points on the plots show the mean ϵ_{OM} values from bootstrapping at selected ϵ_{CaCO_3} values for the front zone (triangles) and back zone (circles). Contours lines in **(A,B)** are spaced by 0.05 ‰ while contour lines in **(C,D)** are spaced by 0.2 ‰. With the exception of high ΔTA and low ΔDIC **(B)**, $\Delta\delta^{13}C_{DIC}$ is relatively insensitive to ϵ_{CaCO_3}.

values. However, directly comparing the ϵ_{OM} in this study to Smith and Kroopnick's (1981) ϵ is difficult because Smith and Kroopnick (1981) did not separate their estimates of $\delta^{13}C_{DIC}$ fractionation into ϵ_{OM} and ϵ_{CaCO_3}. If one assumed a negative value for ϵ_{CaCO_3} in Smith and Kroopnick's (1981) data, their ϵ_{OM} would be less negative than their community-scale ϵ and vice-versa. Applying the range of ϵ_{CaCO_3} considered in this study (−5‰ to 5‰) to the Smith and Kroopnick (1981) ϵ would result in a range of ϵ_{OM} between −23.6‰ to −13.6‰, which is lower, but still overlaps, with our ϵ_{OM}. Carvalho et al. (2015) similarly defined a community-scale DIC isotopic fractionation factor that aggregated photosynthesis and biogenic calcification, but excluded respiration and carbonate dissolution. They documented a much larger range in isotopic fractionation than we observed in our bootstrap analysis, however their mean isotope effect estimates tended to converge between −15‰ and −10‰. Given that our observed $\delta^{13}C_{DIC}$ did not diverge far from 0, the ϵ_{OM} reported here should be close to the $\delta^{13}C$ of organic matter in members of the reef community. Heikoop et al. (2000) found coral tissue $\delta^{13}C$ from a pan-tropical data set ranged from −16‰ to −10‰. Smith (Smith et al., 1985) found that reef organic material (plankton, benthic macroalgae, and corals) $\delta^{13}C_{DIC}$ ranged from −28‰ to −12‰. This collective evidence of similarity between reef material organic $\delta^{13}C$ and our estimates of ϵ_{OM} gives confidence in our estimates.

ϵ_{OM} as calculated in this study is an imperfect representation of the many carbon fluxes occuring simultaneously on reef systems. ϵ_{OM} aggregates the isotopic fractionation due to all photosynthesis, and their respective pathways, as well as all respiratory processes (including those of fish and other mobile organisms). Photosynthetic preference for either CO_2 or HCO_3^- will also affect estimates of ϵ_{OM} because of the equilibrium fractionation between CO_2 and HCO_3^- ($\epsilon_{CO_2-HCO_3^-}$ ~−10‰) (Zeebe and Wolf-Gladrow, 2001), as well as the different photosynthetic pathways and degrees of "leakage" between photosynthetic cells and the ambient seawater (Carvalho et al., 2015). Algal respiration may exhibit some small isotopic fractionation (~3‰), with resulting changes reflected in the $\delta^{13}C_{DIC}$ (Carvalho and Eyre, 2011). We also ignored any potential contributions of air/sea CO_2 fluxes to the $\delta^{13}C_{DIC}$ variability because we calculated small air/sea CO_2 fluxes. However, these fluxes contribute to $\delta^{13}C_{DIC}$ variability because of the known fractionation between DIC and CO_2 in the atmosphere ($\epsilon_{DIC-CO_{2atm}}$ ~8‰ to 10‰, temperature-dependent) (Zhang et al., 1995).

We regret that we were unable to sample during nighttime hours because nighttime samples would have been useful for quantifying respiratory fluxes of DIC and the changes in $\delta^{13}C_{DIC}$ associated with replenishment from isotopically light respired CO_2. Such information may have helped us partition the photosynthetic and respiratory contributions to ϵ_{OM}. As an example, we observed exceptionally low $\delta^{13}C_{DIC}$ values on 03-October-2016 and 16-October-2016. We attribute these anomalously isotopically light samples to accumulation of respiratory CO_2 during their transit across the reef (**Figure 6**). Water moving over the reef flat did not travel above an impermeable benthic substrate, but rather traveled through a semi-permeable substrate due to holes and cracks in the substrate, as well as areas of sediment cover. Visual inspection of the flow paths by following the fate of the released Rhodamine WT during this study revealed flow through through these cracks in the shallow back zone of the study area. These two exceptionally isotopically light samples may have been sampled after traveling through gaps and cracks in the benthic substrate, during which time the water accumulated respiratory CO_2 from the metabolic activity of organisms living within the benthic substrate. Independent estimates of the ϵ for community respiration would have allowed us to more rigorously test this hypothesis.

Our ϵ_{OM} estimates are for one reef flat during one season in one year. Future work should expand the sampling to account for potential seasonal and inter-annual variations in metabolism, and ϵ_{OM}, within individual reef systems. Sampling across multiple reef systems will add independent observations and increase the statistical rigor with which hypotheses about the connections between benthic community composition and ϵ's can be tested.

4.2. $\Delta\delta^{13}C_{DIC}$ Model Assumptions

We developed our model of $\Delta\delta^{13}C_{DIC}$ (Equation 6) in order to explore the combination of ΔDIC, ΔTA, and ϵ's necessary to drive observable and differentiable changes in $\Delta\delta^{13}C_{DIC}$. We constrained the model using ranges in ΔDIC and ΔTA observed in the study, along with calculated values of ϵ_{OM} across a conservative range of assumed ϵ_{CaCO3} values. However, Equation (6) also shows that $\Delta\delta^{13}C_{DIC}$ is inversely proportional to DIC_o. While we did not consider DIC_o variability in **Figure 9**, incorporating realistic variability in DIC_o (comparing the middle and back lines) of ~5 percent (**Figure 3**) would lead to differences in $\Delta\delta^{13}C_{DIC}$ estimates of up to 0.03‰ to 0.04‰ (at high ΔDIC and ΔTA). While this difference is small, it can amplify or attentuate the differences in $\Delta\delta^{13}C_{DIC}$ between different sections of a reef depending upon the configuration of the benthic community. For instance, DIC_o leaving the back zone (the back line DIC) was less than the front zone DIC_o (the middle line DIC). Holding everything else constant, these differences in DIC_o would act to increase the $\Delta\delta^{13}C_{DIC}$ in the back zone relative to the front zone. However, since the front zone already had stronger $\delta^{13}C_{DIC}$ fractionation due to its greater algal abundance, the net effect would be to decrease the differences in $\Delta\delta^{13}C_{DIC}$ between the front zone and back zone (at equivalent ΔDIC and ΔTA).

4.3. Study Limitations and Future Considerations

A few aspects of the study design hindered our ability to develop further inference into the controls on carbon isotopic fractionation at our study site. First, we were unable to make flow speed estimates across our study site which prevented us from being able to calculate NCC and NCP from our ΔDIC and ΔTA in the two zones (Equation 2). As described above, the study site was shallow during sampling periods, and this inhibited the use of current meters for flow speed estimates during sampling. While we assumed steady-state equivalent mass fluxes of water across both zones during the short sampling period (<5 min), direct estimates of the water flow would have allowed us to evaluate this assumption in Equation (4), and therefore, potentially refine our ϵ_{OM} estimates. Future work would be enhanced by direct measurements of flow speed and directionality throughout the study site. As discussed in Cyronak et al. (2018), ΔTA and ΔDIC measurements are useful for understanding individual reef metabolism, but having NCC and NCP estimates greatly facilitates inter-reef comparisons.

Second, we observed high $\delta^{13}C_{DIC}$ variability along and across our sampling lines (**Figures 5–7**). As we have described above, this study was largely a study of opportunity conducted concurrently with the Albright et al. (2018) CO_2 enrichment study and therefore the study site and sampling locations were pre-determined. A longer reef flat as a study site would have resulted in longer contact time between the reef community and the overlying water, which presumably would have decreased the variability in $\Delta\delta^{13}C_{DIC}$, ΔTA, and ΔDIC estimates, resulting in better estimates of ϵ_{OM}. Our simple model of $\Delta\delta^{13}C_{DIC}$ (**Figure 9**) provides a starting point for choosing sampling locations sufficiently far enough apart to generate observable ΔTA, ΔDIC, and $\Delta\delta^{13}C_{DIC}$. Our along-line $\delta^{13}C_{DIC}$ variability highlighted the high spatial heterogeneity present in reef environments, possibly due to lateral variations in flow rate, and thus contact time with the benthic community as the water flowed over the reef. However, the cause of these along-line variations cannot be determined conclusively without flow rate measurements. The across-line and along-line variability highlight the need for more lateral sampling during flow respirometry-style studies, which often oversimplify coral reef biogeochemical processes as one-dimensional along the flow path.

4.4. Summary

We explored small-scale spatial variations in ϵ_{OM} along a reef flat in the Great Barrier Reef. The ecological survey of the study site revealed differences in calcifier and algal abundance between the two zones of the reef flat, with the front zone featuring a lower percent cover of calcifiers and a higher percent cover of non-calcifying algae when compared to the back zone (**Figure 2**). $\delta^{13}C_{DIC}$ had high variability, but revealed a consistent pattern of enrichment during transit across the reef, with front zone ϵ_{OM} exhibiting ~5‰ greater enrichment than the back zone (**Figure 8**). The ϵ_{OM} estimates complemented the $\Delta TA/\Delta DIC$ data, and inferred NCC/NCP, which generally exhibited a greater ratio of calcification to primary production in the back zone relative to the front zone. At the upper end of the observed ΔTA and ΔDIC, ϵ_{OM} estimates between the front and back zone have the potential to yield observable differences in $\delta^{13}C_{DIC}$ enrichment. $\delta^{13}C_{DIC}$ is most likely to act as an additional useful biogeochemical tracer on coral reefs when the ϵ's, ΔTA, ΔDIC, and hydrodynamic conditions are well characterized.

DATA AVAILABILITY STATEMENT

Data used in this study is publicly avaiable at: https://github.com/dkoweek/one_tree_island_DIC_isotope_data.

AUTHOR CONTRIBUTIONS

DAK conceived the study with input from KC. DAK, RA, YT, AN, and KC collected samples on a field expedition led by RA and KC. RA conducted the ecological survey. YT and AN analyzed carbonate chemistry data. DAM and AF developed the stable isotope analytical methods with AF analyzing the samples and DAM processing the isotopic data. DAK led the overall data analysis. DAK wrote the paper with input from all co-authors.

ACKNOWLEDGEMENTS

We thank Paul Quay and Johnny Stutsman at the University of Washington for their assistance with cross-validation of our analytical methods. Conversations with Jennifer Johnson, Shawna Foo, and Philip Brodrick helped improve an earlier version of this manuscript. Kenny Wolfe, Lilian Caldeira, Tanya Rivlin, Roberta Johnson, Yana Nebuchina, Jordan Young, and the One Tree Island Research Station staff provided field assistance. We thank the reviewers whose comments improved earlier versions of this manuscript.

SUPPLEMENTARY MATERIAL

The Supplementary Material for this article can be found online at: https://www.frontiersin.org/articles/10.3389/fmars.2018.00520/full#supplementary-material

REFERENCES

Albright, R., Benthuysen, J., Cantin, N. E., Caldeira, K., and Anthony, K. R. (2015). Coral reef metabolism and carbon chemistry dynamics of a coral reef flat. *Geophys. Res. Lett.* 42, 3980–3998. doi: 10.1002/2015GL063488

Albright, R., Langdon, C. J., and Anthony, K. R. (2013). Dynamics of seawater carbonate chemistry, production, and calcification of a coral reef flat, central Great Barrier Reef. *Biogeosciences* 10, 6747–6758. doi: 10.5194/bg-10-6747-2013

Albright, R., Takeshita, Y., Koweek, D. A., Ninokawa, A., Wolfe, K., Rivlin, T., et al. (2018). Carbon dioxide addition to coral reef waters suppresses net community calcification. *Nature* 555, 516–519. doi: 10.1038/nature25968

Andersson, A. J., and Gledhill, D. (2013). Ocean acidification and coral reefs: effects on breakdown, dissolution, and net ecosystem calcification. *Annu. Rev. Mar. Sci.* 5, 321–348. doi: 10.1146/annurev-marine-121211-172241

Barnes, D. J. (1983). Profiling coral reef productivity and calcification using pH and oxygen electrodes. *J. Exp. Mar. Biol. Ecol.* 66, 149–161.

Bockmon, E. E., and Dickson, A. G. (2014). A seawater filtration method suitable for total dissolved inorganic carbon and pH analyses. *Limnol. Oceanogr. Methods* 12, 191–195. doi: 10.4319/lom.2014.12.191

Carvalho, M. C., and Eyre, B. D. (2011). Carbon stable isotope discrimination during respiration in three seaweed species. *Mar. Ecol. Prog. Ser.* 437, 41–49. doi: 10.3354/meps09300

Carvalho, M. C., Santos, I. R., Maher, D. T., Cyronak, T., McMahon, A., Schulz, K. G., et al. (2015). Drivers of carbon isotopic fractionation in a coral reef lagoon: predominance of demand over supply. *Geochim. Cosmochim. Acta* 153, 105–115. doi: 10.1016/j.gca.2015.01.012

Cyronak, T., Andersson, A. J., Langdon, C. J., Albright, R., Bates, N. R., Caldeira, K., et al. (2018). Taking the metabolic pulse of the world's coral reefs. *PLoS ONE* 13:e0190872. doi: 10.1371/journal.pone.0190872

Falter, J. L., Lowe, R. J., Atkinson, M. J., and Cuet, P. (2012). Seasonal coupling and de-coupling of net calcification rates from coral reef metabolism and carbonate chemistry at Ningaloo Reef, Western Australia. *J. Geophys. Res. Oceans* 117, 1–14. doi: 10.1029/2011JC007268

Gattuso, J.-P., Pichon, M., Delesalle, B., and Frankignoulle, M. (1993). Community metabolism and air-sea CO_2 fluxes in a coral reef ecosystem (Moorea, French Polynesia). *Mar. Ecol. Prog. Ser.* 96, 259–267. doi: 10.3354/meps096259

Gischler, E., Swart, P. K., and Lomando, A. J. (2009). Stable isotopes of carbon and oxygen in modern sediments of carbonate platforms, barrier reefs, atolls and ramps: patterns and implications. *Int. Assoc. Sedimentol. Spec. Publ.* 41, 61–74. doi: 10.1002/9781444312065.ch5

Hayes, J. (1993). Factors controlling ^{13}C contents of sedimentary organic compounds: principles and evidence. *Mar. Geol.* 113, 111–125.

Heikoop, J., Dunn, J., Risk, M., Tomascik, T., Schwarz, H., Sandeman, I., et al. (2000). δ^{15}N and δ^{13}C of coral reef tissue show significant inter-reef variation. *Coral Reefs* 19, 189–193. doi: 10.1007/s003380000092

Kinsey, D. W. (1978). Productivity and calcification estimates using slack-water periods and field enclosures. *Monogr. Oceanogr. Methodol.* 5, 439–468.

Koch, M., Bowes, G., Ross, C., and Zhang, X. H. (2013). Climate change and ocean acidification effects on seagrasses and marine macroalgae. *Global Change Biol.* 19, 103–132. doi: 10.1111/j.1365-2486.2012.02791.x

Koweek, D. A., Dunbar, R. B., Monismith. S. G., Mucciarone. D. A., Woodson. C. B., and Samuel. L. (2015a). High-resolution physical and biogeochemical variability from a shallow back reef on Ofu, American Samoa: an end-member perspective. *Coral Reefs* 34, 979–991. doi: 10.1007/s00338-015-1308-9

Koweek, D. A., Dunbar, R. B., Rogers, J. S., Williams, G. J., Price, N. N., Mucciarone, D. A., et al. (2015b). Environmental and ecological controls of coral community metabolism on Palmyra Atoll. *Coral Reefs* 34, 339–351. doi: 10.1007/s00338-014-1217-3

Kwiatkowski, L., Albright, R., Hosfelt, J., Nebuchina, Y., Ninokawa, A., Rivlin, T., et al. (2016). Interannual stability of organic to inorganic carbon production on a coral atoll. *Geophys. Res. Lett.* 43, 3880–3888. doi: 10.1002/2016GL068723

Lantz, C. A., Atkinson, M. J., Winn, C. W., and Kahng, S. E. (2014). Dissolved inorganic carbon and total alkalinity of a Hawaiian fringing reef: chemical techniques for monitoring the effects of ocean acidification on coral reefs *Coral Reefs* 33, 105–115. doi: 10.1007/s00338-013-1082-5

Long, M. C., Dunbar, R. B., Tortell, P. D., Smith, W. O., Mucciarone, D. A., and DiTullio, G. R. (2011). Vertical structure, seasonal drawdown, and net community production in the Ross Sea , Antarctica. *J. Geophys. Res. Oceans* 116, 1–19. doi: 10.1029/2009JC005954

McMahon, A., Santos, I. R., Cyronak, T., and Eyre, B. D. (2013). Hysteresis between coral reef calcification and the seawater aragonite saturation state. *Geophys. Res. Lett.* 40, 4675–4679. doi: 10.1002/grl.50802

Nakamura, T., and Nakamori, T. (2008). Estimation of photosynthesis and calcification rates at a fringing reef by accounting for diurnal variations and the zonation of coral reef communities on reef flat and slope: a case study for the Shiraho reef, Ishigaki Island, southwest Japan. *Coral Reefs* 28, 229–250. doi: 10.1007/s00338-008-0454-8

Odum, E. P. (1953). *Fundamentals of Ecology*. Philadelphia, PA: Saunders.

Odum, H. T., and Odum, E. P. (1955). Trophic structure and productivity ofa windward coral reef community on Eniwetok Atoll. *Ecol. Monogr.* 25, 291–320.

O'Leary, M. H. (1988). Carbon isotopes in photosynthesis. *Bioscience* 38, 328–336.

Page, H. N., Andersson, A. J., Jokiel, P. L., Rodgers, K. S., Lebrato, M., Yeakel, K. L., et al. (2016). Differential modification of seawater carbonate chemistry by major coral reef benthic communities. *Coral Reefs* 35, 1311–1325. doi: 10.1007/s00338-016-1490-4

Page, H. N., Courtney, T. A., Collins, A., Carlo, E. H. D., and Andersson, A. J. (2017). Net community metabolism and seawater carbonate chemistry scale non-intuitively with coral cover. *Front. Mar. Sci.* 4:161. doi: 10.3389/fmars.2017.00161

Riebesell, U., Fabry, V. J., Hansson, L., and Gattuso, J.-P. (2010). *Guide to Best Practices for Ocean Acidification Research and Data Reporting.* Luxembourg: European Union.

Sargent, M. C., and Austin, T. S. (1949). Organic productivity of an atoll *Eos Trans. Am. Geophys. Union* 30, 245–249.

Shamberger, K. E. F., Feely, R. A., Sabine, C. L., Atkinson, M. J., DeCarlo, E., Mackenzie, F. T., et al. (2011). Calcification and organic production on a Hawaiian coral reef. *Mar. Chem.* 127, 64–75 doi: 10.1016/j.marchem.2011.08.003

Shaw, E. C., McNeil, B. I., and Tilbrook, B. (2012). Impacts of ocean acidification in naturally variable coral reef flat ecosystems. *J. Geophys. Res. Oceans* 117, 1–14. doi: 10.1029/2011JC007655

Shaw, E. C., Phinn, S. R., Tilbrook, B., and Steven, A. (2015). Natural in situ relationships suggest coral reef calcium carbonate production will decline with ocean acidification. *Limnol. Oceanogr.* 60, 777–788. doi: 10.1002/lno.10048

Silverman, J., Kline, D. I., Johnson, L., Rivlin, T., Schneider, K., Erez, J., et al. (2012). Carbon turnover rates in the One Tree Island reef: a 40-year perspective. *J. Geophys. Res. Biogeosci.* 117, 1–16. doi: 10.1029/2012JG001974

Smith, S. V., and Key, G. (1975). Carbon dioxide and metabolism in marine environments. *Limnol. Oceanogr.* 20, 493–495. doi: 10.4319/lo.1975.20.3.0493

Smith, S. V., and Kroopnick, P. (1981). Carbon-13 isotopic fractionation as a measure of aquatic metabolism. *Nature* 294, 252–253.

Smith, S. V., Schneider, R. C., and Tribble, G. W. (1985). "Carbon isotopic balance in coral reef ecosystems,"in *Proceedings of the Fifth International Coral Reef Congress, Vol. 3* (Tahiti), 445–450.

Sogin, E. M., Anderson, P., Williams, P., Chen, C. S., and Gates, R. D. (2014). Application of ^{1}H-NMR metabolomic profiling for reef-building corals. *PLoS ONE* 9:e111274. doi: 10.1371/journal.pone.0111274

Stat, M., Huggett, M. J., Bernasconi, R., Dibattista, J. D., Berry, T. E., Newman, S. J., et al. (2017). Ecosystem biomonitoring with eDNA: metabarcoding across the tree of life in a tropical marine environment. *Sci. Rep.* 7, 1–11. doi: 10.1038/s41598-017-12501-5

Suzuki, A., and Kawahata, H. (2003). Carbon budget of coral reef systems: an overview of observations in fringing reefs, barrier reefs and atolls in the Indo-Pacific regions. *Tellus B* 55, 428–444. doi: 10.1034/j.1600-0889.2003.01442.x

Takeshita, Y., McGillis, W. R., Briggs, E. M., Carter, A. L., Donham, E. M., Martz, T. R., et al. (2016). Assessment of net community production and calcification of a coral reef using a boundary layer approach. *J. Geophys. Res. Oceans* 121, 5655–5671. doi: 10.1002/2016JC011886

Yeakel, K. L., Andersson, A. J., Bates, N. R., Noyes, T. J., Collins, A., and Garley, R. (2015). Shifts in coral reef biogeochemistry and resulting acidification linked to offshore productivity. *Proc. Natl. Acad. Sci. U.S.A.* 112, 14512–14517. doi: 10.1073/pnas.1507021112

Zeebe, R. E., and Wolf-Gladrow, D. A. (2001). *Carbon Dioxide in Seawater: Equilibrium, Kinetics, and Isotopes*. ed D Halpern. Elsevier Ltd.

Zhang, J., Quay, P., and Wilbur, D. (1995). Carbon isotope fractionation during gas-water exchange and dissolution of CO_2. *Geochim. Cosmochim. Acta* 59, 107–114.

Conflict of Interest Statement: The authors declare that the research was conducted in the absence of any commercial or financial relationships that could be construed as a potential conflict of interest.

frontiers in Marine Science

ORIGINAL RESEARCH
published: 15 January 2019
doi: 10.3389/fmars.2018.00536

Marine CO_2 Patterns in the Northern Salish Sea

Wiley Evans[1]*, Katie Pocock[1], Alex Hare[1], Carrie Weekes[1], Burke Hales[2], Jennifer Jackson[1], Helen Gurney-Smith[3], Jeremy T. Mathis[4], Simone R. Alin[5] and Richard A. Feely[5]

[1] Hakai Institute, Heriot Bay, BC, Canada, [2] College of Earth, Ocean, and Atmospheric Sciences, Oregon State University, Corvallis, OR, United States, [3] St. Andrews Biological Station, Fisheries and Oceans Canada, St. Andrews, NB, Canada, [4] Arctic Research Program, National Oceanic and Atmospheric Administration, Silver Spring, MD, United States, [5] Pacific Marine Environmental Laboratory, National Oceanic and Atmospheric Administration, Seattle, WA, United States

OPEN ACCESS

Edited by:
Tyler Cyronak,
University of California, San Diego,
United States

Reviewed by:
Matthew Paul Humphreys,
University of East Anglia,
United Kingdom
Jens Daniel Müller,
Leibniz Institute for Baltic Sea
Research (LG), Germany

***Correspondence:**
Wiley Evans
wiley.evans@hakai.org

Specialty section:
This article was submitted to
Coastal Ocean Processes,
a section of the journal
Frontiers in Marine Science

Received: 03 October 2018
Accepted: 31 December 2018
Published: 15 January 2019

Citation:
Evans W, Pocock K, Hare A,
Weekes C, Hales B, Jackson J,
Gurney-Smith H, Mathis JT, Alin SR
and Feely RA (2019) Marine CO_2
Patterns in the Northern Salish Sea.
Front. Mar. Sci. 5:536.
doi: 10.3389/fmars.2018.00536

Marine carbon dioxide (CO_2) system data has been collected from December 2014 to June 2018 in the Northern Salish Sea (NSS; British Columbia, Canada) and consisted of continuous measurements at two sites as well as spatially- and seasonally distributed discrete seawater samples. The array of CO_2 observing activities included high-resolution CO_2 partial pressure (pCO_2) and pH_T (total scale) measurements made at the Hakai Institute's Quadra Island Field Station (QIFS) and from an Environment Canada weather buoy, respectively, as well as discrete seawater measurements of pCO_2 and total dissolved inorganic carbon (TCO_2) obtained during a number of field campaigns. A relationship between NSS alkalinity and salinity was developed with the discrete datasets and used with the continuous measurements to highly resolve the marine CO_2 system. Collectively, these datasets provided insights into the seasonality in this historically under-sampled region and detail the area's tendency for aragonite saturation state (Ω_{arag}) to be at non-corrosive levels (i.e., $\Omega_{arag} > 1$) only in the upper water column during spring and summer months. This depth zone and time period of reprieve can be periodically interrupted by strong northwesterly winds that drive short-lived (~1 week) episodes of high-pCO_2, low-pH, and low-Ω_{arag} conditions throughout the region. Interannual variability in summertime conditions was evident and linked to reduced northwesterly winds and increased stratification. Anthropogenic CO_2 in NSS surface water was estimated using data from 2017 combined with the global atmospheric CO_2 forcing for the period 1765 to 2100, and projected a mean value of 49 ± 5 μmol kg^{-1} for 2018. The estimated trend in anthropogenic CO_2 was further used to assess the evolution of Ω_{arag} and pH_T levels in NSS surface water, and revealed that wintertime corrosive Ω_{arag} conditions were likely absent pre-1900. The percent of the year spent above $\Omega_{arag} = 1$ has dropped from ~98% in 1900 to ~60% by 2018. Over the coming decades, winter pH_T and spring and summer Ω_{arag} are projected to decline to conditions below identified biological thresholds for select vulnerable species.

Keywords: ocean acidification, coastal CO_2 chemistry, aragonite saturation state, anthropogenic CO_2, long-term assessment

INTRODUCTION

The marine carbon dioxide (CO_2) system in coastal settings is influenced by a host of processes that are unique to the land-ocean boundary (e.g., freshwater inputs, coastal upwelling and downwelling circulations, benthic-pelagic coupling, eutrophication, and the uptake of anthropogenic CO_2) and create a complicated mosaic of spatially and temporally varying seawater CO_2 conditions (Feely et al., 2016; Chan et al., 2017) that hinders long-term trend detection in the absence of lengthy observational records (Sutton et al., 2018). Resolving the downward trajectories of seawater pH and carbonate ion (CO_3^{2-}) concentration that result from the uptake of anthropogenic CO_2, termed ocean acidification (OA; Caldeira and Wickett, 2003; Feely et al., 2004; Orr et al., 2005), is of specific interest because of the anticipated impacts on marine ecosystems and the services they provide (Cooley et al., 2009; Doney et al., 2012), as well as downstream economic consequences by jeopardizing food security and fisheries revenue, and destabilizing coastal communities (Cooley and Doney, 2009; Ekstrom et al., 2015; Mathis et al., 2015; Seung et al., 2015). Understanding secular change in CO_2 system parameters associated with OA is critical in order to forecast the ecological implications, however, the effort is significantly impaired in coastal settings that contain sparse CO_2 system information in the context of large inherent dynamic variability.

The Salish Sea is one of the largest inland seas on the North American Pacific Coast, is bi-national with a shared border between the United States of America (Washington State) and Canada (British Columbia, BC), and consists of a collection of straits, sounds, and inlets; the largest waterways being: Strait of Juan de Fuca, Puget Sound, and the Strait of Georgia. The Northern Salish Sea (NSS) is defined here as the Strait of Georgia and peripheral waterways north of Lasqueti Island and south of Quadra Island (**Figure 1**). The along-axis of the NSS is oriented ~50° west of true north, and the distance spanned along this axis is ~110 km. The NSS cross-axis is narrower and spans ~50 km at its widest point (near Baynes Sound; **Figure 1**). The maximum depth of the NSS is ~350 m and deep water exchange with the open shelf is thought to mainly occur via a flow pathway over ~100 m sills in the southern Strait of Georgia (Masson, 2002; Johannessen et al., 2014). Deep water renewal occurs annually during summer and maximal surface water residence times are at most a few months (Masson, 2002; Pawlowicz et al., 2007). The NSS is bounded by coastal mountains on both Vancouver Island and mainland BC, such that wind patterns are highly channelized (i.e., oriented along channel; **Figure 1**) with predominantly northwesterly winds in summer and southeasterly winds in winter (Bakri et al., 2017). The Fraser River is the dominant freshwater source to the southern Salish Sea, with peak discharge near 10,000 $m^3\ s^{-1}$ during the summer snow/ice melt freshet (Masson and Cummins, 2004). Fraser River water flow-weighted mean total alkalinity (TA) is ~700 $\mu mol\ kg^{-1}$, with higher values during lower flow states (Voss et al., 2014). Numerous smaller river systems also likely play an important role, particularly in the NSS, that collectively stratify the upper water column and allow for high spring and summer phytoplankton biomass accumulation and rates of primary production (Masson and Peña, 2009). The NSS also houses the majority of the shellfish aquaculture industry lease sites in BC (Haigh et al., 2015), and serves as an important region for migrating salmon traveling through the Discovery Islands to the open North Pacific (Journey et al., 2018).

Marine CO_2 dynamics have not been well documented for the NSS beyond the information gained from periodic research cruises (Ianson et al., 2016) and limited underway observations from ships-of-opportunity (Evans et al., 2012; Tortell et al., 2012). A greater wealth of information exists for the central and southern Salish Sea, that collectively describe surface CO_2 system variability that is driven by large seasonal oscillations in primary productivity, freshwater delivery, and localized zones of intense tidal mixing (Feely et al., 2010; Evans et al., 2012; Tortell et al., 2012; Ianson et al., 2016; Fassbender et al., 2018). In deep Salish Sea water, total dissolved inorganic carbon (TCO_2) concentrations are high due to organic matter remineralization combined with restricted connectivity to the open continental shelf (Feely et al., 2010; Johannessen et al., 2014; Ianson et al., 2016). Nonetheless, as importantly noted by Fassbender et al. (2018), TA and TCO_2 concentrations are lower within the Salish Sea relative to the open North Pacific, however, the ratio of these two parameters (i.e., TA:TCO_2) is closer to 1, and therefore these waters are more weakly buffered (Egleston et al., 2010) than open North Pacific water. Weaker buffering capacity results in an amplified response of pH, CO_2 partial pressure (pCO_2), and aragonite saturation state (Ω_{arag}; where $\Omega_{arag} = \left[CO_3^{2-}\right]\left[Ca^{2+}\right]/K_{sp(arag)}$, and $K_{sp(arag)}$ is the aragonite-specific solubility product) to changes in TCO_2. A TA:TCO_2 ratio near 1 also sets the tendency for seawater to be corrosive to aragonite (i.e., $\Omega_{arag} < 1$). Seasonally, the entire Salish Sea water column has been observed to be corrosive to aragonite during winter, while during productive spring and summer months, Ω_{arag} increases in the surface layer (<20 m) to saturated levels (Feely et al., 2010; Ianson et al., 2016; Fassbender et al., 2018).

A number of organisms residing in the Salish Sea may be sensitive to currently observed Ω_{arag} and pH_T (total scale) conditions. Research has shown that Ω_{arag} during first shell development was a determining factor for growth and survival of larval *Crassostrea gigas* (Pacific oyster), and an Ω_{arag} value of 1.7 was determined to be the "break-even" point for commercial larvae production (Barton et al., 2012; Barton et al., 2015). *C. gigas* larval biomass production within the Whiskey Creek Hatchery on the Oregon coast was zero below this value (Barton et al., 2012). More detailed experimental work has revealed acute stress in juvenile *C. gigas*, *Mytilus galloprovincialis* (Mediterranean mussel), and *M. californianus* (California mussel) at Ω_{arag} values of 1.2 and 1.5, respectively (Waldbusser et al., 2014, 2015). Collectively, these studies highlight that Ω_{arag} levels above the thermodynamic threshold of 1 can negatively impact vulnerable early life stages of these species, with the duration and frequency of exposure to such adverse conditions also being important factors (Waldbusser and Salisbury, 2014). These vulnerable species reside in the NSS with Ω_{arag} values above these thresholds only in the

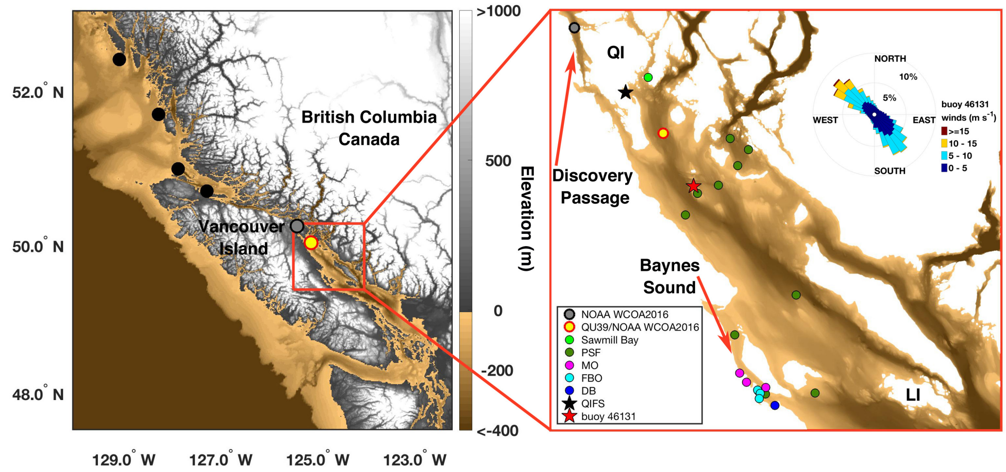

FIGURE 1 | Sampling locations on the British Columbia (BC) coast **(left)** and in the Northern Salish Sea (NSS; red box in **left** and **right**). **(Left)** Shows locations occupied during the NOAA West Coast Ocean Acidification Cruise (WCOA2016) on the BC central coast (black), in Discovery Passage (gray), and in the NSS (red-outlined yellow circle). **(Right)** Shows locations in the NSS, defined here as waters extending from Quadra Island (QI) to Lasqueti Island (LI). The black star marks the Quadra Island Field Station (QIFS), and the red star marks Environment Canada weather buoy 46131. The Hakai Institute routinely samples the NSS station occupied during the NOAA WCOA2016 cruise (known as QU39). Additional sites were occupied by citizen science groups: light green dot = Sawmill Bay Shellfish Company, dark green dots = Pacific Salmon Foundation Citizen Science Program (PSF), magenta dots = Mac's Oysters, Ltd. (MO), light blue dots = Fanny Bay Oysters (FBO), and dark blue dot = Vancouver Island University Deep Bay Field Station(DB). The wind rose in the right panel is hourly data from buoy 46131 collected between August 1997 to September 2018. Elevation shown in the left panel is from the Strait of Juan de Fuca 36 arc-second MHW Coastal Digital Elevation Model (https://data.noaa.gov/metaview/page?xml=NOAA/NESDIS/NGDC/MGG/DEM/iso/xml/541.xml&view=getDataView&header=none#Credit), and depth below sea surface in the right panel is from the British Columbia 3 arc-second Bathymetric Digital Elevation Model (https://data.noaa.gov/metaview/page?xml=NOAA/NESDIS/NGDC/MGG/DEM/iso/xml/4956.xml&view=getDataView&header=none). The color scale for depth below sea surface is the same between the two panels.

surface layer during spring and summer months (Feely et al., 2010; Ianson et al., 2016; Fassbender et al., 2018). Similarly, pelagic species, such as *Euphausia pacifica* (krill; McLaskey et al., 2016) and *Limacina helicina* (thecosome pteropod; Bednarsek et al., 2017) may also be impacted by currently observed conditions. For instance, there is experimental evidence that *E. pacifica* larval development and survival is reduced at pH_T levels of 7.69 (McLaskey et al., 2016), values already seen in the region (Feely et al., 2010; Ianson et al., 2016; Fassbender et al., 2018). Efforts to model this area have focused on the southern domain (Moore-Maley et al., 2016; Bianucci et al., 2018), but highlight that the stability of favorable surface layer CO_2 conditions during summer can be disrupted by episodic variability.

In this paper, we will describe a growing NSS high-resolution dataset from the Hakai Institute's Quadra Island Field Station (QIFS) that began in late 2014 in conjunction with other datasets collected by an array of observing activities that occurred during 2016 and 2017. These datasets collectively highlight important characteristics of the region, including perpetually low-Ω_{arag} at depth and large surface ocean variability across seasonal and sub-seasonal timescales. We also present estimates of anthropogenic CO_2 for NSS surface water spanning the start of the Industrial Revolution (e.g., 1765) to the end of the 21st century. Using this information, we assess the changes in Ω_{arag} and pH_T over ~2.5 centuries and consider the passing of key biological thresholds during this period.

MATERIALS AND METHODS

The approach applied here relied on developing a compilation of spatially- and seasonally distributed discrete seawater temperature, salinity, pCO_2, and TCO_2 measurements. The full marine CO_2 system was determined using these data as detailed below (see section "Discrete Seawater Sample Analyses"). A selected set of measurements was used to examine deep-water conditions within the NSS relative to the open continental shelf. Then, using the full suite of measurements, a relationship between alkalinity and salinity was constructed for the NSS. This relationship was then coupled with high-resolution surface measurements of salinity, temperature, and pCO_2 or pH_T collected at QIFS (see section "Autonomous Analytical Systems at the Quadra Island Field Station") or from the Environment Canada weather buoy 46131 (see section "Buoy-of-Opportunity Continuous Observations"), respectively (**Figure 1**), to characterize surface CO_2 system variability over a 3.5-year period. Anthropogenic CO_2 was then estimated (see section "Estimation of Anthropogenic CO_2") and used to assess the long-term trends in NSS surface water Ω_{arag} and pH_T. Ancillary datasets used in this manuscript are described in **Supplementary Text 1**.

Discrete Seawater Sample Analyses

Discrete seawater samples were collected during a number of field campaigns that occurred in 2016 and 2017 in the NSS (**Figure 1** and **Supplementary Table S1**), including: (1) citizen science efforts by Sawmill Bay Shellfish Company, Fanny Bay Oysters, Mac's Oysters Ltd., and the Pacific Salmon Foundation's (PSF) Citizen Science Program; (2) occupations of the Hakai Institute's oceanographic station QU39; (3) the 2016 United States National Oceanic and Atmospheric Administration (NOAA) West Coast OA Cruise (NOAA WCOA2016); and (4) shore-side sampling at the Vancouver Island University Deep Bay Marine Field Station. Seawater was collected using 350 mL amber soda-lime glass bottles that were filled either by hand (for the case of most citizen science groups) or using a Niskin bottle (for the cases of PSF, QU39, and NOAA WCOA2016) with care not to introduce bubbles. Sample bottles were rinsed three times with sample, filled from the bottom to leave ∼3 mL of headspace, fixed with 200 μl of a solution of saturated mercuric chloride, and crimp-sealed using polyurethane-lined metal caps. The effect of using soda-lime over borosilicate bottles was tested by comparing alkalinity determined (as described below) from triplicate surface and 500 m seawater samples stored in each bottle type for 100 and 126 days, respectively. No significant difference between the alkalinity of seawater stored in borosilicate or soda-lime glass bottles was evident at the end of either storage period (two sample *t*-test *p*-value for surface and 500 m water was 0.26 and 0.47, respectively). Triplicate sample sets were collected routinely in order to assess potential sampling uncertainty (estimated to be ∼8 μmol kg^{-1} for triplicate alkalinity determinations computed over all datasets). Sampling by the citizen scientist organizations involved using NIST traceable thermometers (VWR PN 23609-176) to record *in situ* temperature with 0.2°C factory reported accuracy. *In situ* temperature and salinity were recorded by conductivity-temperature-depth (CTD) profilers either coupled with a Niskin bottle rosette (NOAA WCOA2016) or used just prior to Niskin bottle collection for samples collected by the Hakai Institute at station QU39. Niskin bottles deployed on a line for the PSF and QU39 field campaigns were tripped with messengers, and CTD data were extracted from the preceding profile for the Niskin bottle collection depth (for QU39 only). Niskin bottle target depth was determined using an A.G.O Environmental Ltd EWC-6 Electronic Wire Counter Module (or similar) and verified using RBRSolo[2] pressure sensors. Accuracy in hitting target depths was 2.6 ± 3.8 m, with largest inaccuracy occurring at the deepest depths. With the exception of the NOAA WCOA2016 data where CTD salinity co-occurred with the seawater sample collection, seawater sample salinity was measured using a YSI MultiLab 4010-1 with a MultiLab IDS 4310 conductivity and temperature sensor that is calibrated using the known salinity from CO_2 certified reference materials (CRMs; provided by A. Dickson at Scripps Institute of Oceanography). The uncertainty in salinity determinations from the calibrated probe was estimated to be 0.11 based on the standard deviation about a mean difference of 0.01 between measured and known CRM salinity and the standard deviation between station QU39 sample YSI salinity and CTD salinity.

For all the above listed datasets, discrete seawater sample analysis for TCO_2 and pCO_2 was conducted on a Burke-o-Lator (BoL) pCO_2/TCO_2 analyzer at QIFS by acidification with 1 N hydrochloric acid followed by flow-balanced gas stripping for TCO_2 (Hales et al., 2004; Bandstra et al., 2006) and recirculated-headspace gas equilibration for pCO_2 (Hales et al., 2004). Our protocol for TCO_2 and pCO_2 analysis followed methods published previously (Hales et al., 2005; Barton et al., 2012; Hales et al., 2016) with some slight modification to the degree at which CRMs were processed and how quality control was conducted[1]. CO_2 mole fractions (xCO_2) were detected in the analytical gas stream, either evolved following acidification and stripped for the TCO_2 analysis stream or recirculated through the pCO_2 headspace gas loop, by non-dispersive infrared (NDIR) absorbance using a gas analyzer (LI-COR LI840A CO_2/H_2O) housed within the BoL's electronics box. Both TCO_2 and pCO_2 were measured from the same seawater sample, with TCO_2 measured first in a process that took ∼2.5 min and consumed ∼50 mL of sample. TCO_2 measurements were calibrated using liquid standards, which were solutions of Na_2CO_3 and $NaHCO_3$ in deionized water that had been prepared to have target TCO_2 values (nominally 800, 1600, and 2400 μmol kg^{-1}) with alkalinity adjusted to give solution pCO_2 near that of ambient room air. The liquid standards were stored in gas-impermeable bags, and were analyzed, along with a set of gas standards (see section "Autonomous Analytical Systems at the Quadra Island Field Station"), in conjunction with each group of samples analyzed in a day. The order of analyses that would occur was: (1) gas standards, (2) liquid standards, (3) triplicate TCO_2 analysis of a CRM bottle, (4) TCO_2 and pCO_2 analyses on a battery of typically 20–30 samples, (5) triplicate TCO_2 analysis of the same CRM bottle as well as a pCO_2 analysis following the last TCO_2 measurement (that had been resealed between analyses), (6) liquid standards, and finally (7) gas standards. In this way, gas and liquid calibration curves were generated at the start and end of a sample analysis sequence, linearly interpolated over the time period of sample analysis (usually <8 h), and then used to calibrate the TCO_2 and pCO_2 analyses. Post-calibration TCO_2 samples were converted to units of μmol kg^{-1} using the sample density based on the salinity and temperature at the time of analysis. Sample temperature at the time of analysis was recorded using NIST traceable thermometers (VWR PN 23609-176). pCO_2 was measured with the BoL following the TCO_2 analysis by recirculating a closed loop of headspace gas through the seawater sample (by bubbling with an aquarium air diffuser) for a period of 10 min in order to ensure full equilibration of the headspace gas. Post-calibration pCO_2 measurements were converted from xCO_2 to pCO_2 using ambient laboratory total pressure. A correction factor was applied to the TCO_2 data based on the analyses of CRMs of known TCO_2 content (batch numbers 151, 157, 169, and 174). Each triplicate CRM run in the analysis sequence listed above was averaged, and the ratio of known to measured average TCO_2 content was interpolated over the time period of the analysis sequence and subsequently used to correct measured sample TCO_2. Typical correction factors for TCO_2 analysis range between 0.99 and 1.01, with deviations from the ideal value of 1.00 related to the accuracy of liquid standard preparation. The standard deviation in CRM triplicate runs was used as a metric of analytical uncertainty, computed

---

[1] http://dx.doi.org/10.21966/1.521066

here to be 0.3%. Analysis temperature, salinity, TCO_2, and pCO_2 were used to compute seawater sample alkalinity, however, a final adjustment was needed to obtain the correct alkalinity that accounted for the change in TCO_2 induced by the bubbling of headspace gas through the sample volume (Wanninkhof and Thoning, 1993). *In situ* pCO_2, pH_T, and Ω_{arag} were then computed using the MATLAB version of CO2SYS (Van Heuven et al., 2011) with alkalinity, TCO_2, *in situ* temperature, salinity, and pressure as inputs. Calculations were done with nutrient concentrations omitted, and using the carbonic acid dissociation constants of Lueker et al. (2000), the bisulfate dissociation constant of Dickson et al. (1990), the boron/chlorinity ratio of Uppström (1974), and the aragonite solubility constant from Mucci (1983) with no adjustment for a potential non-zero Ca^{2+} intercept. Alkalinity ($Alk_{inorganic}$) consisted of carbonate, bicarbonate, borate, hydroxide, and hydrogen ions, all of which can be calculated from the direct measurements of pCO_2 and TCO_2. Note that TA is $Alk_{inorganic}$ plus the contributions for phosphate, silicate, and organic acids, which here are assumed to be negligible such that TA $\approx$ $Alk_{inorganic}$. Lastly, there is no parameter-specific CRM available for pCO_2, therefore we assessed the analytical uncertainty of that measurement based on the comparison of known CRM TA and that calculated from measured TCO_2 and pCO_2. The comparison between certified and calculated TA points to an analytical uncertainty of ∼1.5%, however, we note that this determination is based on pCO_2 analyses of CRM bottles that had been opened and resealed <8 h before analysis. Also, the headspace in the CRM had increased since opened as well as flushed with ambient room air. Because of these reasons, we expect that the uncertainty listed above is over- estimated and that the true uncertainty is likely ≤1%.

Autonomous Analytical Systems at the Quadra Island Field Station

Near-continuous pCO_2 measurements made on surface (1 m) seawater from Hyacinthe Bay, adjacent to the QIFS (**Figure 1**), were collected using two analytical systems over the course of this study: (1) the Sunburst Sensors Shipboard Underway pCO_2 Environmental Recorder ($SUPERCO_2$) from December 18, 2014 to April 6, 2016, and (2) the BoL from April 6, 2016 to June 1, 2018. Seawater pCO_2 data produced by both systems were calculated from corrected measurements of wet air xCO_2 made following standardization protocols described by Pierrot et al. (2009) with the system theory and calculations presented by Hales et al. (2004) and Evans et al. (2015). Seawater was drawn from a 2-inch diameter polypropylene tube positioned approximately 50 m from shore at ∼150 l min^{-1} using a Pentair Aquatic Eco-systems Sparus 3HP pump (or similar). Most seawater was diverted back to sea, while an analysis seawater stream was drawn tangentially off the main supply and diverted through the instrumentation configured within a shore-side flow-through laboratory at ∼4 l min^{-1}. Within the laboratory, unaltered seawater continuously flowed first through a Sea-Bird Electronics SBE 45 MicroTSG Thermosalinograph, and then through a seawater equilibrator before being returned to sea.

Equilibrator design differed slightly between the two systems. The $SUPERCO_2$ used both primary and make-up air showerhead equilibrators (Takahashi, 1961) in order to pre-equilibrate any (make-up) air drawn into the primary equilibrator via the presence of a slight vacuum pressure. The BoL pre-equilibrated make-up air by direct contact with seawater running vertically down the wetted-wall of the equilibrator drain pipe, further isolated from the ambient air by a ‘P trap’ to the ultimate water exit from the system. The BoL equilibrator did not have a showerhead, but instead diverted incoming seawater over a flat plate surrounded by porous tubing that delivered headspace gas with vigorous bubbling into the seawater stream. Both equilibrator designs were found to have response times (e-folding times) on the order of 2 min determined by sequentially injecting high and low concentration standard gas directly into the equilibrators and tracking the return to equivalent pre-disturbance levels. Equilibrators for both systems supplied equilibrated carrier gas (marine air) to a LI840A housed within an electronics box. The $SUPERCO_2$ system diverted a split from the recirculation headspace gas flow at a rate of ∼50 ml min^{-1}, which was made-up through the pre-equilibrated make-up air line, while the BoL system circulated the entire headspace flow through the LI840A in a quasi-closed-loop configuration. Pressure and temperature were continuously monitored in the equilibrators using either Honeywell or Omega Pressure Sensors and Fast Response Resistance Temperature Detectors, respectively. Unaltered marine air was drawn from 0.25-inch polyethylene tubing that connected a vented water trap positioned outside of the shore-side laboratory to the analytical systems coincident with the detector standardization sequence. The detector was calibrated with gasses of known gravimetric mol/mol mixing ratio of CO_2 in ultrapure air. Equilibrated carrier gas, standard gasses of known mixing ratio (three for the $SUPERCO_2$ = 150.4, 453, and 750 ppm; four for the BoL = 153.3, 451, 752, and 1515 ppm; formerly Scott-Marin Inc., now Praxair Distribution Inc.), and unaltered marine air were all plumbed to provide gas flow to the electronics boxes of both systems. Computers with National Instruments LabVIEW software controlled data acquisition from the thermosalinograph, the pressure and temperature sensors, and the LI840A, while also controlling Valco Instruments Co. Inc. (VICI) multi-port actuators that cycled between the gas streams plumbed to the electronics box. None of the gas streams were dried prior to analysis, and measurements were made at 0.5 and 1 Hz on the $SUPERCO_2$ and BoL, respectively.

The prescribed measurement schemes controlled by the software differed slightly between the two systems. Software on the $SUPERCO_2$ was initially set to supply equilibrated carrier gas from the primary equilibrator to the LI840A continuously for 240 min, then cycle the actuators to consecutively allow the three standard gas streams and unaltered marine air to be measured for 90 s each at ∼100 ml min^{-1} before returning to sample the carrier gas equilibrated with seawater pCO_2. After the 1st weeks of operation, the time between standardization sequences was increased to once per day as the high degree of standardization typically employed on research cruise was not necessary. From each sequence of standard gas measurements, the final 20 s of data in the 90 s interval before the actuator changed position was averaged and then used to construct a linear fit of the LI840A response to each gas standard in the sequence. These steps were conducted using custom MATLAB programs. LabVIEW software controlling the BoL cycled through gas standards and unaltered marine air every 720 min, at which time gas flowed during each step of the sequence for 60 s before a 20 s averaging window occurred. Unlike for the $SUPERCO_2$, LabVIEW software running the BoL computed the linear fit of a calibration sequence and stored this information in a calibration file. Corrected atmospheric xCO_2, as part of the aforementioned gas standard sequence, and atmospheric pressure measurements from the LI840A were used to compute atmospheric pCO_2 and stored in the BoL calibration file. The linear fits constructed with data from both systems for each calibration sequence were then interpolated in time between standard gas sequences in order to produce temporally resolved calibration functions. These functions were then used to calibrate the raw xCO_2 measurements of both the seawater equilibrated carrier gas and unaltered marine air, with an adjustment on the order of 1%. Corrected seawater xCO_2 was subsequently adjusted for any under- or over-pressurization in the equilibrator using the ratio of equilibrator-to-vented LI840A cell pressure, and then converted to pCO_2 using atmospheric pressure measured by the LI840A. The seawater pCO_2, temperature, and salinity (reported here on the Practical Salinity Scale, PSS-78; dimensionless) data were quality controlled by removing obvious aberrant measurements, and then bin-averaged in 5-min interval bins.

Although residence time within the mostly submerged seawater supply line was minimal (~2 min), warming was assessed on two separate occasions by comparing temperature from the thermosalinograph with measurements made using a SBE 56 Temperature Sensor affixed to the end of the seawater intake line during two ~20-day periods starting in early October and late November 2017. The SBE 56 data revealed a trivial amount of warming (averaging ~0.2 ± 0.1°C over both ~20-day deployments) that would result in a slight positive bias for pCO_2 by <1%. This bias, combined with a consistently observed 2 ppm uncertainty in xCO_2 determinations revealed by the comparison of calibrated standard gas readings to the known values, equated to ~1.5% uncertainty for pCO_2. CO_2 system parameters were then computed using the bin-averaged data with $Alk_{inorganic}$ estimated using a regional $Alk_{inorganic}$-salinity relationship using a MATLAB version of CO2SYS (Van Heuven et al., 2011) with the series of constants described previously.

Buoy-of-Opportunity Continuous Observations

A Sea-Bird Electronics SeaFET V1 Ocean pH sensor was used during two deployments on the Environment Canada weather buoy 46131 (**Figure 1**) between summer and autumn in 2016 and 2017. These deployments occurred in collaboration with PSF who deployed a Sea-Bird Electronics SBE 37 MicroCAT to record seawater temperature and salinity from the platform. Both units were placed in protective stainless steel cages and hung off the surface buoy with chain to 1 m depth. Copper tape and copper guards were used to prevent biofouling of the units during deployment. The SeaFET went through a near 10-day period of pre-conditioning within a test tank filled with NSS surface water prior to each deployment. At this stage, the response of both internal and external electrodes was tracked and the deployment settings were configured. The SeaFET was set to sample every 30 min throughout each deployment. Here, we only report data generated using the SeaFET's internal electrode.

Once deployed, the SeaFET was allowed to condition for a period of 10–14 days before discrete seawater samples were collected adjacent to the sensor for TCO_2 and pCO_2 analysis on the QIFS BoL. Discrete seawater samples were collected using Niskin bottles deployed to 1 m depth alongside the sensor at the time of a sampling event, and analyzed as described above. Calibration coefficients for each electrode were then re-calculated using the average *in situ* pH_T of triplicate discrete samples and the corresponding electrode voltage reading (equations detailed in Sea-Bird Scientific SeaFET Product Manual 2.0.0.), resulting in an adjustment from the factory calibration of ~0.03%. The calibration coefficients were calculated following any major sensor maintenance such as battery change or annual service, which occurred four times over the course of the deployments. Additional discrete samples were collected during service visits approximately once every 2 months throughout the deployment period to validate the single-point calibration. The offset between validation sample and SeaFET pH was 0.005 ± 0.001 averaged over both deployments, indicating no observable drift. The *in situ* calibration coefficients, along with temperature data from the co-located SBE 37 were used to convert SeaFET electrode voltage readings to *in situ* pH_T measurements. Same as for the QIFS analytical systems, CO_2 system parameters were then computed using a regional $Alk_{inorganic}$-salinity relationship with the series of constants described previously and a MATLAB version of CO2SYS (Van Heuven et al., 2011).

Estimation of Anthropogenic CO_2

The ΔTCO_2 approach (Sabine et al., 2002; Takeshita et al., 2015; Pacella et al., 2018) was employed to calculate anthropogenic CO_2 in NSS surface water. This approach makes the following assumptions: (1) the difference between surface seawater TCO_2 and the TCO_2 level expected if surface seawater pCO_2 were in equilibrium with the atmosphere at the current TA, termed $\Delta TCO_{2,diseq}$, is constant in time, (2) variability in temperature, salinity, and TA is also constant in time. The ΔTCO_2 approach has advantages over the commonly used ΔpCO_2 approach (Feely et al., 2010; Harris et al., 2013; Evans et al., 2015; Hales et al., 2016; Sutton et al., 2016; Pacella et al., 2018) because it captures Revelle Factor-driven changes in seawater pCO_2 seasonal dynamic ranges (Fassbender et al., 2018; Feely et al., 2018; Landschützer et al., 2018; Laruelle et al., 2018), meaning that amplified changes in pCO_2 per unit change in TCO_2 are captured, thereby subsequently not manifested in amplified unrealistic TCO_2 variability and so likely producing a more robust estimate of anthropogenic CO_2. We used 14-day low-pass (LOESS) filtered daily data from 2017 to compute $\Delta TCO_{2,diseq}$ with the following formulation:

$$\Delta TCO_{2,diseq} = TCO_{2,2017} - TCO_2\left(\text{atm } pCO_{2,2017}, TA\right)$$

where $TCO_2\left(\text{atm } pCO_{2,2017}, TA\right)$ is the TCO_2 concentration calculated at the 2017 mean atmospheric pCO_2 and TA levels. Then using this $\Delta TCO_{2,diseq}$ term, we computed TCO_2 for each day of each year between 1765 and 2100 as:

$$TCO_{2,yr} = TCO_{2,yr}\left(\text{atm } pCO_{2,yr},\ TA\right) + \Delta TCO_{2,diseq}$$

where $TCO_{2,yr}\left(\text{atm } pCO_{2,yr},\ TA\right)$ was determined using atmospheric pCO_2 from the RCP 8.5 (Riahi et al., 2011) "business as usual" record from 1765 to 2100 (**Supplementary Text 1**). Finally, anthropogenic CO_2 for each day of each year was calculated as:

$$\text{anthropogenic } CO_2 = TCO_{2,yr} - TCO_{2,1765}$$

Uncertainty in calculated anthropogenic CO_2 has been shown to be 10% (Sabine et al., 2002).

RESULTS

NSS Alk*inorganic*-Salinity Relationship and CO_2 System Uncertainties

Over 250,000 marine CO_2 system measurements have been collected over the course of this study spanning December 18, 2014 to June 1, 2018 (**Supplementary Table S1**). The data collected highly resolve each season over 3.5 years, with the majority of observations occurring in the surface layer where the largest seasonal dynamic range was evident. The establishment of a NSS Alk*inorganic*-salinity relationship was an integral tool developed using the discrete datasets and utilized with the continuous records. A total of 1360 seawater samples collected over the seven field campaigns and spanning the full water column, all seasons (**Supplementary Table S1**), and a broad range of salinity (1.4–30.9) conditions were used to construct this relationship (**Figure 2**). The uncertainty in this relationship, as indicated by the root mean square error (RMSE), was 22.47 μmol kg^{-1}. The Alk*inorganic*-salinity relationship presented here spanned a much broader salinity range than a comparable TA-S relationship developed using data from the coastal zone around Washington State including the southern Salish Sea [(Fassbender et al., 2016); salinity 20–35]. These two relationships are more consistent at the higher salinity range and diverge at the lower salinity range.

The NSS Alk*inorganic*-salinity relationship was used with direct CO_2 system measurements (either pCO_2 or pH_T) to determine the full marine CO_2 system. However, it is important to consider how our measurement and relationship uncertainties propagate to uncertainties in the derived parameters (**Supplementary Table S2**). Using the reported measurement uncertainties detailed above with a MATLAB CO2SYS error propagation routine that includes uncertainty in the carbonic acid dissociation constants (Orr et al., 2018), we determined the uncertainty in derived CO_2 system parameters relative to the mean conditions observed during this study. The full CO_2 system was determined by three sets of parameter pairs: (1) continuous pCO_2 with Alk*inorganic* derived from our regional Alk*inorganic*-salinity relationship [Alk*inorganic*(S); **Figure 2**], (2) continuous pH_T with Alk*inorganic* (S), and (3) discrete TCO_2 and pCO_2. Of these three sets of pairings, Ω_{arag} determined by continuous pH_T from the SeaFET sensor combined with Alk*inorganic* (S) had the largest uncertainty of 0.039 or 3%. Unsurprisingly, the discrete TCO_2 and pCO_2 pair had the lowest Ω_{arag} uncertainty of 0.031 or 2%. The close agreement between uncertainties from all three pairings (**Supplementary Table S2**), even with an RMSE of 22.47 μmol kg^{-1} in the Alk*inorganic*-salinity relationship (**Figure 2**), indicated that uncertainty in continuous pCO_2 or pH was a larger contributor than uncertainty in our Alk*inorganic*-salinity relationship to the uncertainty in derived Ω_{arag} (Fassbender et al., 2016). These reported uncertainties were nearly an order of magnitude lower than the ±0.2 Ω_{arag} uncertainty threshold prescribed by the California Current Acidification Network (C-CAN; McLaughlin et al., 2015) and the Global Ocean Acidification Observing Network (GOA-ON; Newton et al., 2015) required for "weather" quality data that can link changes in marine ecosystems to changes in the marine CO_2 system.

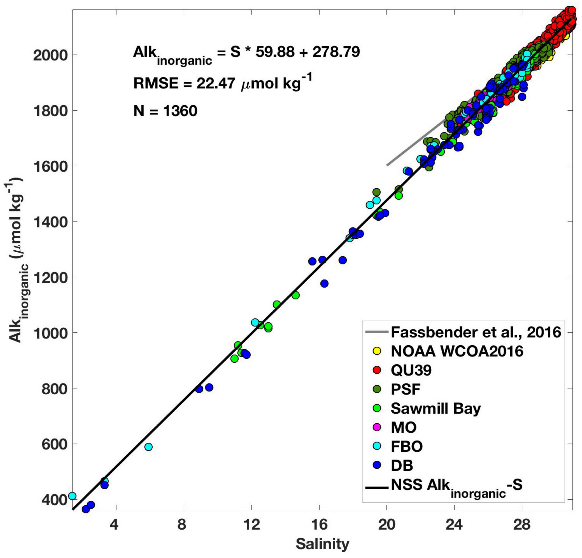

FIGURE 2 | Relationship between alkalinity (Alk*inorganic*; μmol kg^{-1}) and salinity (black line; Alk*inorganic* = S * 59.88 + 278.79; RMSE = 22.47 μmol kg^{-1}) developed using 1360 discrete measurements of pCO_2, TCO_2, temperature, and salinity collected at oceanographic and aquaculture sites in the NSS (color matched with position in **Figure 1**) between 2016 and 2017. Also shown for comparison is the relationship from Fassbender et al. (2016; gray line) that was constructed using data collected over a salinity range from 20 to 35.

NSS Deep Water Conditions Relative to the Open Continental Shelf

Measurements made at depth (i.e., >50 m) during both the NOAA WCOA2016 cruise and from occupations of oceanographic station QU39 illustrate a key aspect of deep water in the NSS that sets this domain apart from conditions found at similar depths on the open continental shelf (**Figure 3**); the NSS was observed to be continually corrosive below the depth zone influenced by surface dynamics. Six near-shore stations were occupied during the NOAA WCOA2016 cruise in a transect that spanned the open continental shelf, Discovery Passage, and the NSS (**Figure 1**). Surface variability across the transect reflected a spectrum of conditions related to CO_2 drawdown by phytoplankton, freshwater dilution, and vertical mixing that extended deeper into the water column on the open continental shelf but limited to <50 m. Below this depth, salinity, $Alk_{inorganic}$, and TCO_2 were all higher on the open continental shelf compared to values found within the NSS (**Figure 3**). However, $Alk_{inorganic}$:TCO_2 was lower in the NSS, and this condition is a key determinant in setting pCO_2, pH_T, and Ω_{arag} levels. At salinity at and above the NSS mean (26.26) with $Alk_{inorganic}$:TCO_2 near 1, pH_T and Ω_{arag} have nominal values of 7.5 and 0.6, respectively. Therefore, it is unsurprising that the water column below the surface layer (>50 m) with $Alk_{inorganic}$:TCO_2 near 1 has Ω_{arag} near 0.6 (**Figure 3**). $Alk_{inorganic}$:TCO_2 equal to 1 also marks the condition where pCO_2, pH_T, and Ω_{arag} will change the most with incrementally increasing TCO_2 (Egleston et al., 2010). As anthropogenic TCO_2 addition continues beyond this equivalency point, per unit changes in pCO_2, pH_T, and Ω_{arag} will decrease. The conditions found at depth during the NOAA WCOA2016 cruise closely align with the seasonally resolved average for ≥150 m samples collected at station QU39 between January 2016 and December 2017 (**Figure 3**; *n* = 206), indicating perennially low-Ω_{arag} deep water in the NSS.

NSS Surface Water Variability

Variability was pronounced in NSS surface water, with large dynamic ranges of temperature, salinity, and CO_2 system parameters on seasonal and sub-seasonal time scales. The seasons were defined here with December through February as winter, March through May as spring, June through August as summer, and September through November as autumn. SST varied from ~6°C in winter to ~20°C in summer, while salinity was less seasonally varying with low values, minima near 20, during short-lived freshwater events and high values, maxima near 30, during summertime mixing events (either vertically mixed locally or transported laterally to the measurement location) that drove concurrent low-pH_T and high-pCO_2 conditions. Wintertime pCO_2 and pH_T were near 700 μatm and 7.8, respectively, with generally lower variability relative to the summer months. The standard deviation of wintertime pCO_2 was less than 70 μatm for all years. The transition from winter CO_2 conditions in spring was rapid and marked by the occurrence of the spring phytoplankton bloom that drew down surface pCO_2 well below equilibrium with the atmosphere. The timing of this initial drawdown varied by ~6 weeks; observed to occur as early as the start of March in 2015 and as late as late April in 2017. Spring bloom-driven low-pCO_2 conditions were disrupted in 2015, 2016, and 2018 by late season southeasterly winds. Summertime levels were generally more variable, with seasonal pCO_2 standard deviations of 140 and 100 μatm in 2015 and 2016, respectively. During 2017, summertime variability was lower, however, with

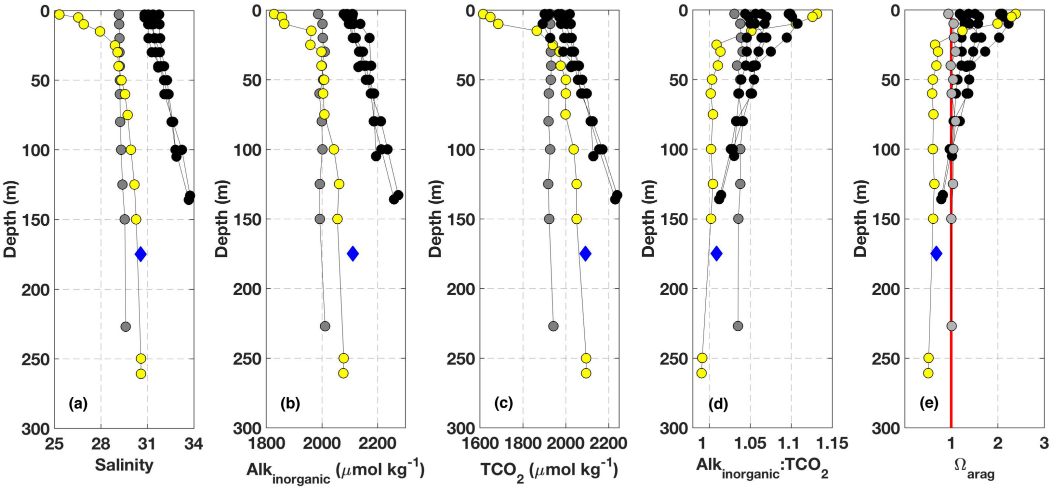

FIGURE 3 | Observations from the NOAA WCOA2016 cruise in June 2016 color-coded by area as shown in **Figure 1**: data from the BC open continental shelf are black, the data from Discovery Passage are gray, and data from the NSS (QU39) are yellow. The data shown are: **(A)** salinity, **(B)** $Alk_{inorganic}$ (μmol kg^{-1}), **(C)** TCO_2 (μmol kg^{-1}), **(D)** $Alk_{inorganic}$:TCO_2, and **(E)** Ω_{arag}. The vertical red line in **(E)** marks Ω_{arag} = 1. Also shown are averages from seasonally resolved data collected at station QU39 from depths ≥ 150 m between January 2016 and December 2017 (blue diamonds; *n* = 206). The deep-water averages (±standard deviation) for salinity, $Alk_{inorganic}$, TCO_2, $Alk_{inorganic}$:TCO_2, and Ω_{arag} were 30.58 ± 0.25, 2112 ± 24 μmol kg^{-1}, 2093 ± 31 μmol kg^{-1}, 1.009 ± 0.008, and 0.68 ± 0.09, respectively.

a seasonal standard deviation of 40 μatm. pCO_2 and pH_T levels during periods of assumed highest primary productivity and subsequent CO_2 drawdown reaching to near 100 μatm and up to 8.50, respectively. During observed summertime short-lived mixing events, pH_T went down to as low as 7.65 and pCO_2 up to near 1000 μatm. These seasonal and sub-seasonal signals were evident in both the QIFS and buoy 46131 records, platforms located ∼26 km apart (**Figure 1**), which provided an indication of spatial coherence in the observed patterns (**Figure 4**). However, summertime high-CO_2 events did not occur each year; summertime surface pCO_2 in 2015 and 2016, but not in 2017, episodically reached or exceeded levels observed during wintertime (see section "The Lack of High-CO_2 Summertime Conditions in

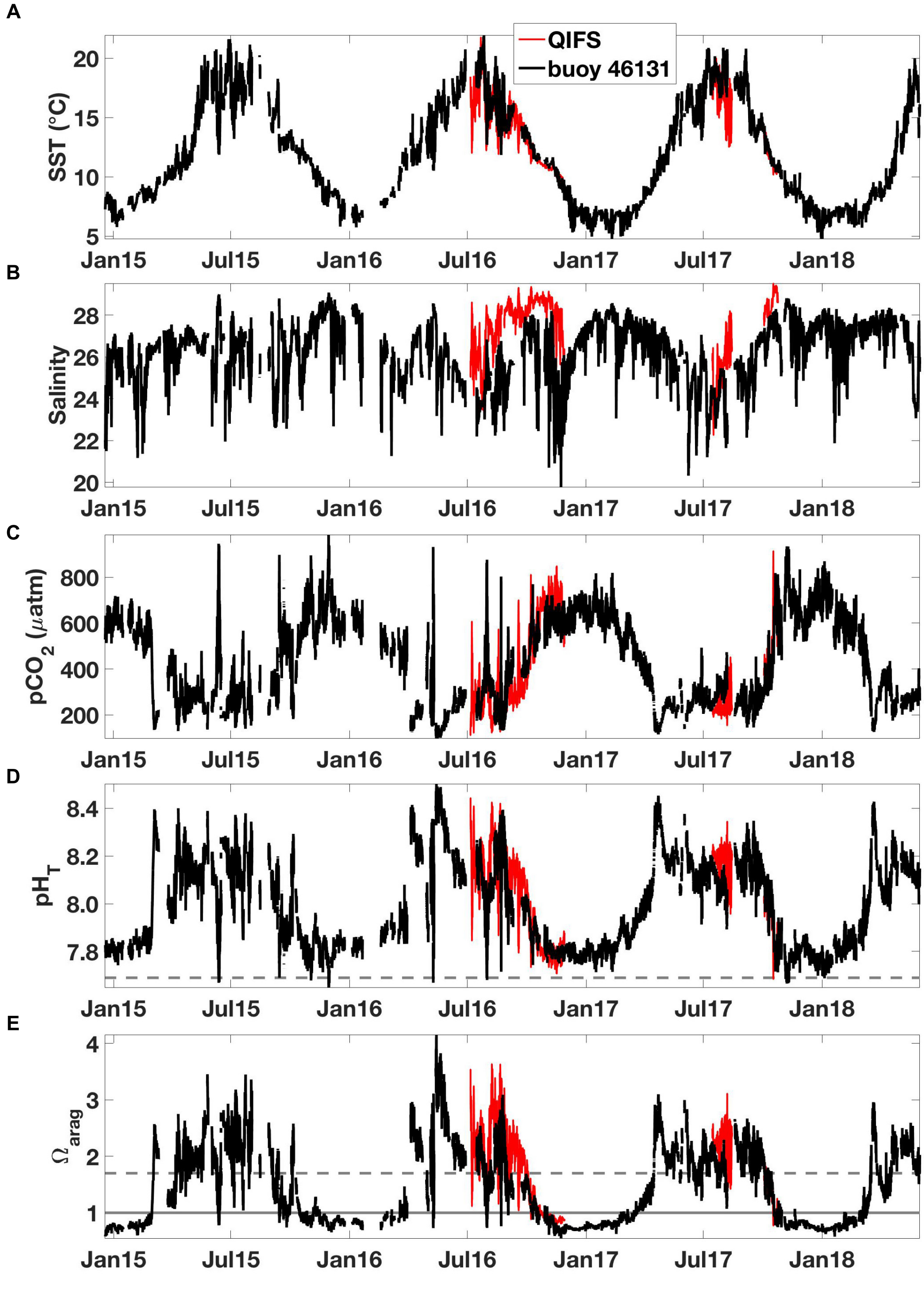

FIGURE 4 | High-resolution observations of **(A)** SST (°C), **(B)** salinity, **(C)** pCO_2 (μatm), **(D)** pH_T, and **(E)** Ω_{arag} from the QIFS (black) and Environment Canada buoy 46131 (red). The horizontal line in **(D)** marks pH_T = 7.69, and the horizontal lines in **(E)** mark Ω_{arag} = 1 (solid gray) and Ω_{arag} = 1.7 (dashed gray).

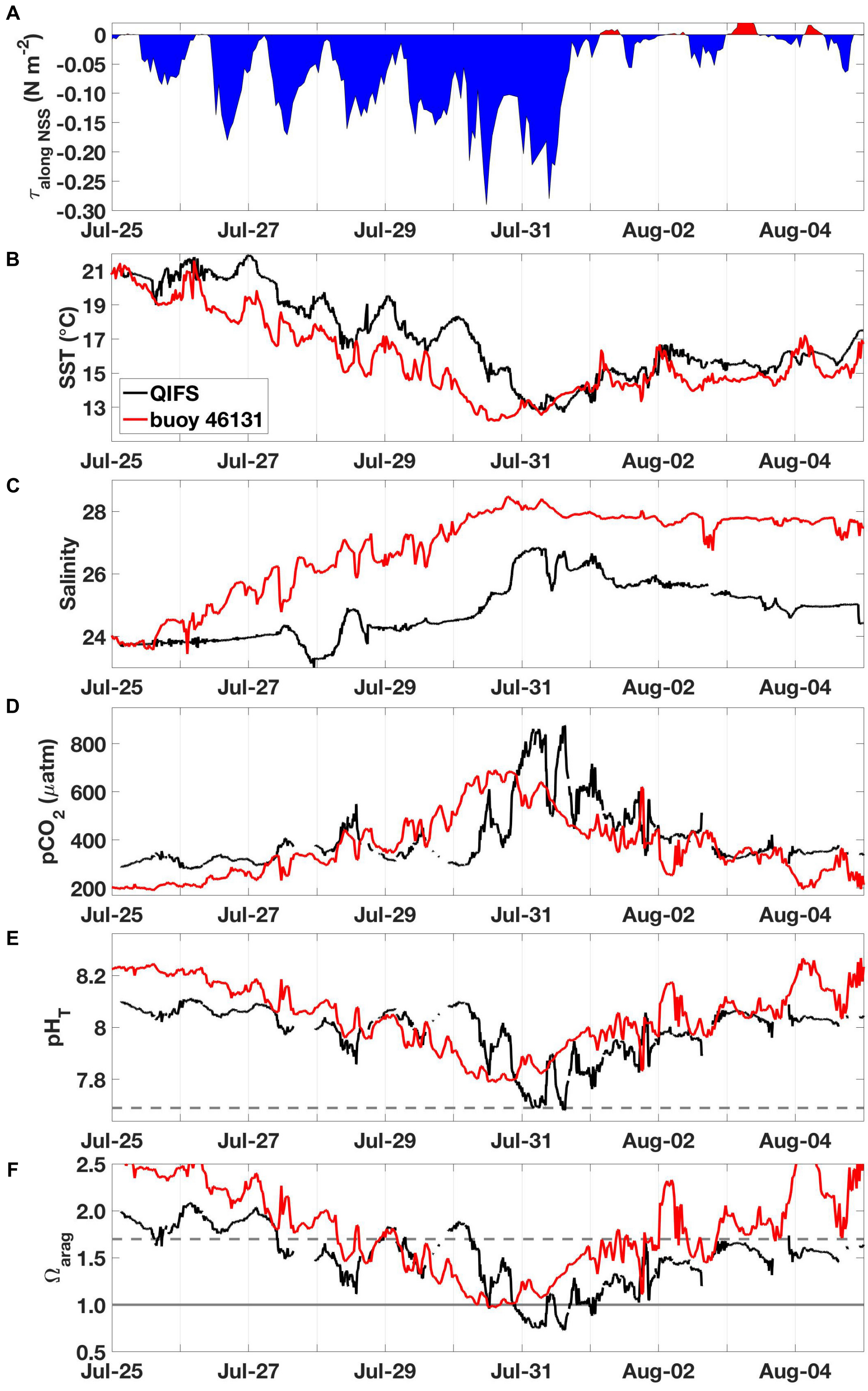

FIGURE 5 | Observations made during the July 2016 high-CO_2 event, including: **(A)** along-axis wind stress ($\tau_{along\ NSS}$; N m^{-2}) from buoy 46131, **(B)** SST (°C) from QIFS and buoy 46131, **(C)** salinity from QIFS and buoy 46131, **(D)** seawater pCO_2 (μatm) from QIFS and buoy 46131, **(E)** pH_T from QIFS and buoy 46131, and **(F)** Ω_{arag} from QIFS and buoy 46131. All QIFS data are black while buoy 46131 data are red. The horizontal line in **(E)** marks pH_T = 7.69, and the horizontal lines in **(F)** mark Ω_{arag} = 1 (solid gray) and Ω_{arag} = 1.7 (dashed gray).

2017"). Autumn marks the transition back to wintertime conditions, however, evidence of late season pCO_2 drawdown likely associated with a phytoplankton bloom occurred in 2015.

Combined meteorological and oceanographic records from QIFS and buoy 46131 over the duration of a high-CO_2 event in July 2016 revealed the significance of wind forcing as a driver for the occurrence of vertical mixing and subsequently observed large CO_2 system variability (**Figure 5**). Using the wind records from buoy 46131 adjusted to 10 m (Hsu et al., 1994), wind stresses were computed along the main axis of the NSS (**Figure 1**) with drag coefficients determined using the relationship of Smith et al. (1991). Wind stresses became negative (indicating northwesterly winds) on July 25, and strengthened over a ~5-day period. The surface ocean response to the intensifying negative along-axis wind stress was a concurrent decrease in SST, an increase in salinity, and a >400 µatm increase in pCO_2 at both QIFS and buoy 46131 (**Figure 5**), which were indications of strong vertical mixing. pH_T dropped at QIFS to below the observed wintertime levels (7.65), and surface water $\Omega_{arag} \leq 1$ was evident at both sites prior to the wind stress abating. By August 1, intense along-axis wind stress associated with strong (i.e., >5 m s^{-1}) wind speeds had completely abated, with pCO_2, pH_T, and Ω_{arag} returning to near pre-disturbance levels by August 4. However, salinity stayed elevated and SST warmed only marginally by 2–3°C during this period of rapidly transitioning CO_2 system parameters. A similar vertical mixing and high-CO_2 event was observed in 2015, and showed a consistent time evolution to the 2016 event described above (although CO_2 observations were limited to QIFS; **Supplementary Figure S1**). Satellite SST observations captured both the 2015 and 2016 events and showed 6–8°C of cooling that occurred broadly over the entire NSS over ~6 days (**Figure 6** and **Supplementary Figure S2**).

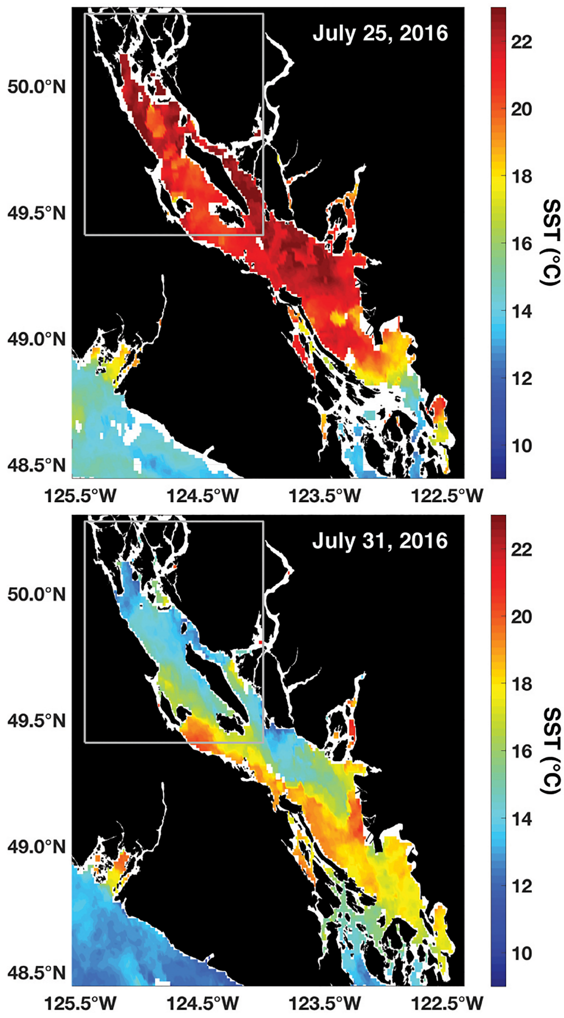

FIGURE 6 | NOAA Polar Operational Environmental Satellite (POES) Advanced Very High Resolution Radiometer (AVHRR) daily average (night and day passes) 1.1 km SST (°C) at the start **(top)** and peak **(bottom)** of the July 2016 high-CO_2 event. The gray box marks the NSS as outlined in **Figure 1**.

Anthropogenic CO_2 in NSS Surface Water

Calculations of annual mean anthropogenic CO_2 in NSS surface water show a steady increase since the Industrial Revolution (~1765) with intensifying growth rates beginning after 1950 (**Supplementary Figure S3**) that reflects the evolving pace of increasing atmospheric CO_2 levels. Annual minima and maxima of anthropogenic CO_2 values, with variance largely associated with the vertical mixing of sub-surface water with a lower anthropogenic CO_2 content, diverged from the corresponding annual means toward the end of the 21st century. As mentioned previously, these estimates were based on 2017 observations when observations of high-CO_2 were reduced, and hence lack of strongest vertical mixing events that would accompany the lowest anthropogenic CO_2. However, calculations of mean anthropogenic CO_2 were less sensitive than the variance to the year of input data used in the computation. Calculations using 2015 data resulted in a slightly broader range of annual minima and maxima values with no significant difference in mean estimates. Mean anthropogenic CO_2 estimated for 2018 was 49 ± 5 µmol kg^{-1}. By comparison, the mean value for 2008 was 41 ± 4 µmol kg^{-1} and close to the value reported by Feely et al. (2010) for the Main Basin in Puget Sound during summer (36 µmol kg^{-1}; **Supplementary Figure S3**). The difference between these two estimates, which is marginally outside of the expected 10% uncertainty, may be related to one or both of the following two factors: (1) the difference between estimating anthropogenic CO_2 using the ΔpCO_2 approach versus the ΔTCO_2 approach (see Supporting Information by Pacella et al., 2018), and (2) building estimations using high-resolution datasets versus data from infrequent research cruises. However, it is important to note that these determinations fall below estimated levels for BC open continental shelf surface water (Feely et al., 2016), and that differences in buffering capacity between the open continental shelf, Puget Sound, and the NSS contribute to driving the expected regional differences in estimated anthropogenic CO_2 (Sabine et al., 2004).

DISCUSSION

CO_2 Dynamics in the NSS

The rigorous evaluation of NSS CO_2 dynamics presented here was reliant on dedicated high-resolution monitoring sites combined with frequent and spatially distributed discrete sample collection by a number of organizations. This combination of assets produced data that highlight perpetually corrosive conditions at depth as well as dynamic variability across a range of time scales at the surface. Continuously corrosive conditions in deep water is an important feature of this setting, as a number of marine organisms have experimentally been shown to exhibit sensitivities, in terms of reduced calcification (Kroeker et al., 2013; Bednarsek et al., 2017) and slower growth (McLaskey et al., 2016), at the currently observed levels. Perpetually corrosive conditions have not been seen on the open continental shelf, where deep water (165 m) Ω_{arag} can vary from 0.8 to 2.4 (Harris et al., 2013). An $Alk_{inorganic}$:TCO_2 near 1 sets the corrosive state of NSS deep water, and high organic carbon input (Johannessen et al., 2014) and annual deep water renewal (Masson, 2002; Pawlowicz et al., 2007) both act to maintain a state of elevated TCO_2 relative to $Alk_{inorganic}$. This pattern is consistent with observations made in Puget Sound (Feely et al., 2010) where deep water exchange with the open continental shelf is restricted and corrosive conditions dominate. Such corrosive hot spots likely serve as important areas to gauge organismal and ecosystem response to OA.

Baseline information across a broad range of time scales, afforded by continuous high-resolution datasets such as shown here, is needed to understand current marine CO_2 "weather" conditions and how these might relate to projected CO_2 "climate" scenarios (Waldbusser and Salisbury, 2014). Surface-oriented forcing (i.e., wind-driven vertical mixing, seawater CO_2 drawdown via primary productivity, freshwater addition and stratification) drove large dynamic ranges of surface water CO_2 parameters in the NSS (**Figure 4**). Such surface dynamics are not unique to this area, and similarly large ranges have been reported for the southern Salish Sea (Feely et al., 2010; Ianson et al., 2016; Fassbender et al., 2018). However, information has been scarce on the importance of high-frequency variability; the summertime wind events shown here in the NSS resulted in CO_2 system "weather" variation in pCO_2, Ω_{arag}, and pH_T that surpassed the seasonal dynamic ranges of these parameters in less than a week (**Figure 4**) and likely over the entire domain, as indicated by satellite SST observations (**Figure 6**).

Large summer wind-driven variability did not occur each year in the NSS, and this may have far-reaching ecosystem-level implications. For instance, following the 2016 wind event, super-saturated dissolved oxygen levels >60 μmol kg^{-1} were observed beginning ~1 week after the maximum in seawater pCO_2 (**Supplementary Figure S4**). In addition, the trajectory of SST, salinity, and pCO_2 over the 4 days following the occurrence of maximal seawater pCO_2 during the 2016 event suggests a strong biological response (**Figure 5**). At buoy 46131 during this interval, salinity was stable while SST warmed by ~3°C. Driven by solubility alone, this warming should have increased pCO_2 by ~80 μatm. However, seawater pCO_2 decreased over the 4 days from 700 to 200 μatm. Sea-air CO_2 exchange alone cannot explain this precipitous drop in pCO_2 to undersaturated levels with respect to the atmosphere. Even with a sustained maximal sea-air CO_2 exchange of ~1 mmol m^{-2} hr^{-1} (data not shown but observed during the 2016 event), it would take >200 days to equilibrate a 20 m surface layer with the SST, salinity, and pCO_2 levels observed during the event. These biogeochemical lines of evidence suggest a strong primary productivity response to wind-driven high-CO_2 events in the NSS. While this variability may stimulate productivity, with potentially food web implications, it also means short-term exposure to adverse conditions for marine life vulnerable to low-Ω_{arag} and low-pH_T (Waldbusser and Salisbury, 2014; McLaskey et al., 2016; Bednarsek et al., 2017).

The Lack of High-CO_2 Summertime Conditions in 2017

Important NSS interannual variability was revealed by the lack of high-CO_2 summertime conditions in 2017 that had been observed in 2015 and 2016 associated with strong northwesterly wind events. The drivers of this variability at the regional scale can be assessed by examining the rate of energy transfer from the winds to the surface ocean (Denman and Miyake, 1973) and how this input compares to the potential energy needed to mix the upper water column (Hauri et al., 2013), which is related to the stratification (**Supplementary Text 2**). The significance of a single summertime wind event equates to the integrated rate of energy transfer over the duration of the event, with an event defined here as wind conditions over 5 m s^{-1} that resulted in energy transfer ≥ 0.19 mJ m^{-2} s^{-1} at a mean drag coefficient of 0.00128 and an air density of 1.22 kg m^{-3}. High-CO_2 events in 2015 and 2016 (**Supplementary Figures S1, S2** and **Figures 5**, **6**) were each associated with instances where energy from the winds overcame upper ocean stratification (**Figure 7**), however, these conditions did not occur in 2017. In 2017, wind strength was inadequate to overcome the nearly 50% higher potential energy requirement needed to mix the upper 20 m. While weaker winds in 2017 clearly played a role in not forcing high-CO_2, the energy needed to mix the upper water column, and hence the stratification, was significantly higher (**Figure 7**). Greater freshwater content in the NSS during 2017 (**Figure 8**), calculated following the relationship from Proshutinsky et al. (2009), increased the energy needed to mix the surface water column (**Figure 7**) and halted any potential influence from the weaker winds to drive high-CO_2 conditions. Given that El Niño winters in BC are typically warmer and drier (Shabbar et al., 1997), and that 2015 and 2016 were both warm years, we speculate that there may be a relationship whereby El Niño winters set the stage for reduced freshwater content in the NSS during summer, enabling the upper water column to be more easily mixed by northwesterly winds. Although only tenuously

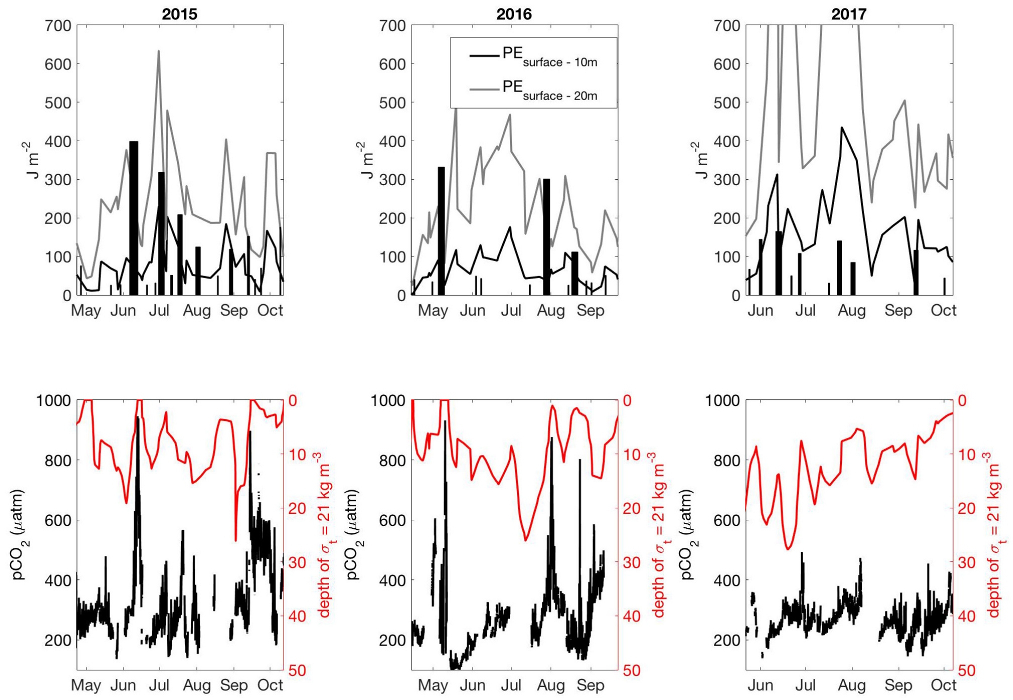

FIGURE 7 | Top row is the integrated rate of energy transfer ($J\ m^{-2}$; bars) over the duration of wind events observed between the spring and fall transitions (**Supplementary Figure S5**) in 2015 **(left)**, 2016 **(middle)**, and 2017 **(right)**. The width of the bars equates to the duration of the wind event. The top panels also show the potential energy needed to mix the upper water column (surface to 10 m in black, surface to 20 m in gray). Lower panel is surface water pCO_2 from QIFS (black) and the depth of the 21 $kg\ m^{-3}$ density anomaly (σ_t) surface.

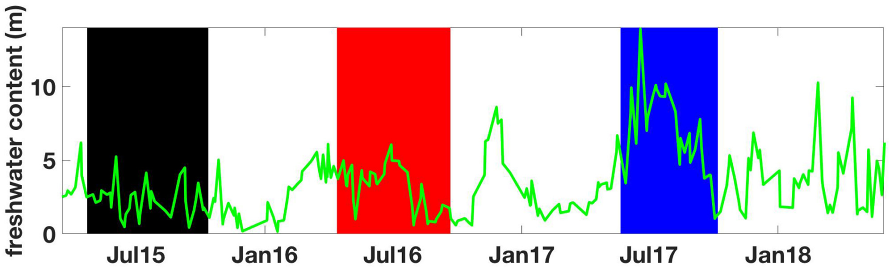

FIGURE 8 | Freshwater content at QU39 from March 18, 2015 to June 1, 2018 computed using a reference salinity of 29.1 following the relationship from Proshutinsky et al. (2009). Vertical shaded areas mark the time periods between spring and fall transitions color-coded to match the years shown in **Supplementary Figures S5**, **S6**.

supported by the 3.5 years of data presented here, the growing QIFS dataset will help to further elucidate this potential pattern on summertime surface CO_2 variability.

Crossing CO_2 System Thresholds in the NSS

The variability of surface NSS CO_2 parameters was maximal during summer, and year-to-year differences in the drivers of summertime variability were important and linked to the combined influences of northwesterly wind events and freshwater content, as shown above. Increasing anthropogenic CO_2 content (**Supplementary Figure S3**) under the "business as usual" scenario will shift the system further to less favorable conditions for marine life sensitive to low-Ω_{arag} and/or low-pH_T exposure. Using TCO_2 estimated for each year in the anthropogenic CO_2 calculation, we derived Ω_{arag} and pH_T for NSS surface water spanning 1765 to the end of the 21st century (**Figure 9**). As mentioned above, the calculation is based on data from 2017; therefore the seasonal dynamics are slightly biased toward less variable Ω_{arag} and pH_T conditions due to the lack of observed summertime wind-driven vertical mixing that year (**Figure 4**). Nonetheless, our analysis shows that NSS surface water was consistently above the thermodynamic threshold of $\Omega_{arag} = 1$ at the start of the Industrial Revolution. Observed wintertime surface water $\Omega_{arag} < 1$ (**Figure 4**) was shown

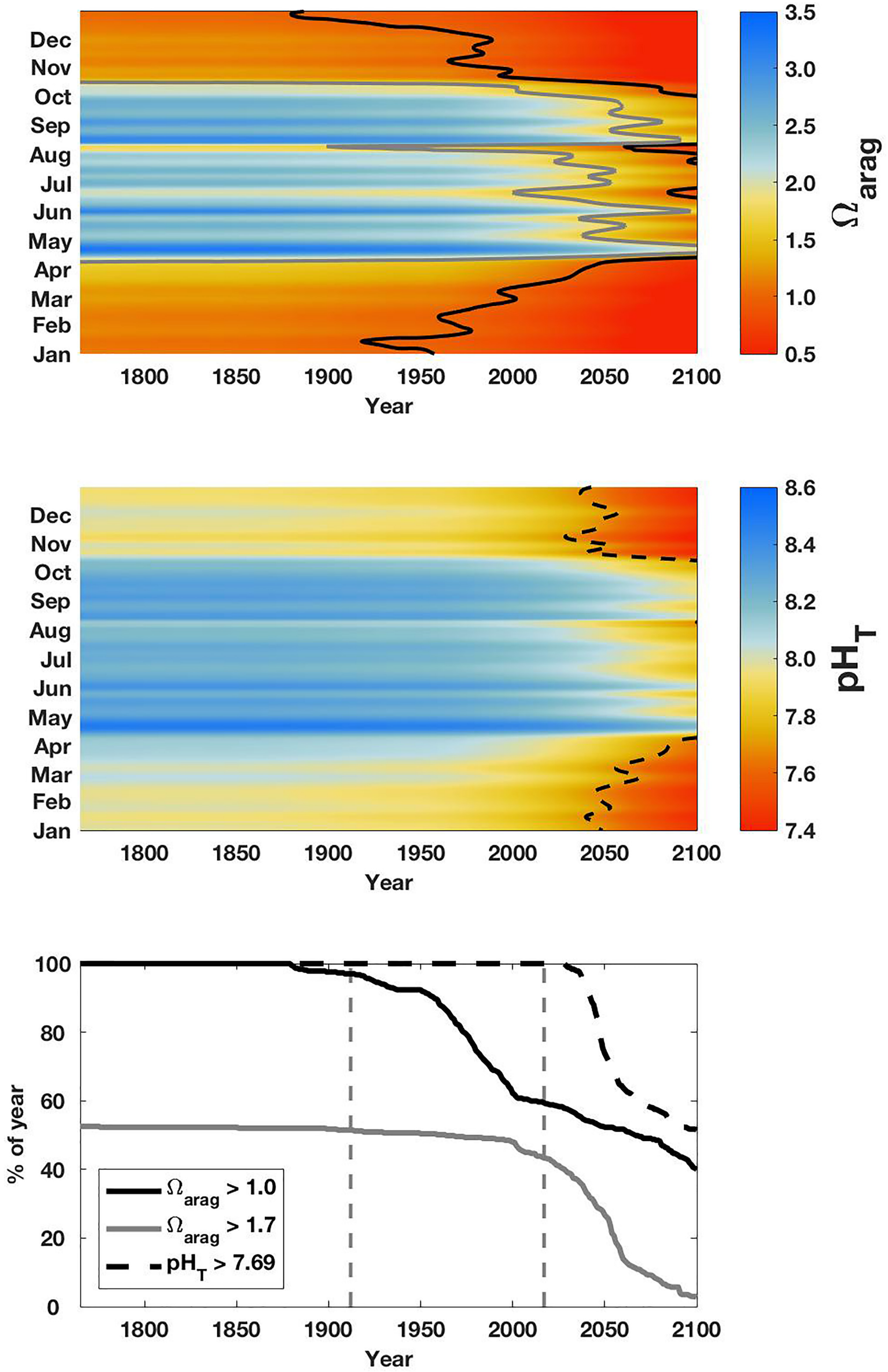

FIGURE 9 | Projections from 1765 to 2100 of surface water Ω_{arag} **(top)**, pH_T **(middle)**, and the percent of the year with values above key thresholds (bottom): Ω_{arag} = 1 (black), Ω_{arag} = 1.7 (gray), and pH_T = 7.69 (dashed black). These thresholds are highlighted in the upper panels. 2017 QIFS data used in these projections were smoothed using a 14-day LOESS filter.

to have developed only over the last century (**Figure 9**); a change that has occurred simultaneously with the development of *C. gigas* culture in BC beginning in ∼1900 (Quayle, 1988).

Surface conditions during winter may have always been below the "break-even" point for larval biomass production of Ω_{arag} = 1.7 (**Figure 9**), as well as near levels shown experimentally to induce stress in the larvae of *C. gigas*, *M. galloprovincialis*, and *M. californianus* larvae (Waldbusser et al., 2014, 2015). It should be noted that winter periods are generally typified by the absence of larvae and reduced adult shellfish growth (Gosling, 2003). However, crossing the thermodynamic threshold in winter marks the shift toward a seasonal full water column corrosive environment. Spring CO_2 drawdown, which initiates with variable timing, establishes a refugia only in the surface layer that can be disrupted by episodic forcing and then subsequently breaks down in autumn. The biological implications of this contemporary window of non-corrosive conditions are unknown and require immediate further study, albeit point to a reduction in suitable habitat for vulnerable resident prey species (i.e., *L. helicina*; Bednarsek et al., 2014) and reduced calcification (Kroeker et al., 2013) with potential implications for shell-forming populations.

The shift in winter Ω_{arag} conditions was shown in our assessment to cross the thermodynamic Ω_{arag} threshold earlier than the shift in pH_T to levels low enough to potentially slow *E. pacifica* larval development (McLaskey et al., 2016). Beginning in 2030, the percent of the year above $pH_T = 7.69$ rapidly decreases (**Figure 9**), representing the onset of surface conditions that may impact *E. pacifica* larvae. This increased pressure on *E. pacifica* survival could subsequently lead to indirect ecosystem effects by way of reducing an important prey item for many species of salmon in the study area (Brodeur et al., 2007). Near the same time as when winter pH_T conditions drop below this threshold for *E. pacifica*, summertime Ω_{arag} values above 1.7 also rapidly decline, marking a transition to perennially stressful levels for vulnerable larval shellfish species with potential impacts for population stability and ecosystem structure.

Limitations of Long-Term Assessment

Our estimation of changing NSS surface water Ω_{arag} and pH_T shows the time scales over which thermodynamic and biological thresholds will be crossed (**Figure 9**). However, cautionary notes must be made. First, our analysis utilized the "business as usual" emissions trajectory, and would over-estimate shifting Ω_{arag} and pH_T conditions over the remainder of the century if global CO_2 emissions decrease. Second, the calculations assumed consistency in SST, salinity, and $Alk_{inorganic}$ variance. In coastal settings, this assumption can be violated, such as seen in the Gulf of Maine (Salisbury and Jönsson, 2018) and Baltic Sea (Müller et al., 2016). While warming in Strait of Georgia surface water has been estimated to be $\sim 1°C\ century^{-1}$ (Riche et al., 2014), which would have a ~1% impact on projected Ω_{arag} and pH_T, unaccounted for variance in salinity and $Alk_{inorganic}$ is an unknown and requires further investigation. For comparison, the observed alkalinity increase in the central Baltic Sea compensated CO_2-induced acidification by almost 50% and stabilized Ω_{arag} over a 2-decade period (Müller et al., 2016). Third, our approach assumed constant seasonality in $\Delta TCO_{2,diseq}$; an assumption that could be prone to failure in the presence of increasing eutrophication. Fourth, while experimental work has identified some Ω_{arag} and pH_T thresholds, the combined impact of the projected chemical changes with additional environmental stressors, such as warming, hypoxia, marine pollutants, will be an important determinant for adaptive capacity. The ability for vulnerable marine organisms to adapt will be a function of the rate of environmental change, population plasticity, and genetic selection processes (Sunday et al., 2014). Adaptive capacity will ultimately determine whether the passage of experimentally determined biological Ω_{arag} and pH_T thresholds negatively impacts vulnerable organisms and the ecosystems they reside in.

AUTHOR CONTRIBUTIONS

WE, KP, AH, and CW carried out all CO_2 data collection presented in this study. BH provided guidance on analytical system operation. WE and BH established data handling protocols. WE, JJ, and AH analyzed interannual variability in NSS surface CO_2. WE and HG-S initially developed CO_2 observing at QIFS. JM provided the instrumentation as well as the SeaFET used on Environment Canada buoy 46131. WE, SA, and RF conducted data collection from NOAA WCOA2016. WE wrote the manuscript. All authors provided input to the text.

FUNDING

This work was provided by the Tula Foundation, with some instruments and ship-time provided by partnering agencies including the National Oceanic and Atmospheric Administration.

ACKNOWLEDGMENTS

We would like to acknowledge that this study occurred within the traditional territories of the Heiltsuk, the Wuikinuxv, the Kwakwaka'wakw, and the Coast Salish peoples. We would like to thank the numerous citizen scientists, Vancouver Island University Deep Bay Marine Field Station staff, and Hakai Institute field technicians who collected many of the seawater samples and CTD data used in this study. We would also like to thank the Pacific Salmon Foundation and Environment Canada for the opportunity to deploy instrumentation on weather buoy 46131. We thank the captain and crew of the NOAA ship Ronald H. Brown used during WCOA2016. We are extremely appreciative of the Tula Foundation for supporting the research presented here. SA and RF thank the NOAA Ocean Acidification Program for their support of this research. We would like to thank two reviewers for their valued and constructive comments that helped to improve this manuscript. Contribution number 4849 from the Pacific Marine Environmental Laboratory of NOAA.

SUPPLEMENTARY MATERIAL

The Supplementary Material for this article can be found online at: https://www.frontiersin.org/articles/10.3389/fmars.2018.00536/full#supplementary-material

REFERENCES

Bakri, T., Jackson, P., and Doherty, F. (2017). A synoptic climatology of strong along-channel winds on the Coast of British Columbia. Canada. *Int. J. Climatol.* 37, 2398–2412. doi: 10.1002/joc.4853

Bandstra, L., Hales, B., and Takahashi, T. (2006). High-frequency measurements of total CO2: method development and first oceanographic observations. *Mar. Chem.* 100, 24–38. doi: 10.1016/j.marchem.2005.10.009

Barton, A., Hales, B., Waldbusser, G., Langdon, C., and Feely, R. A. (2012). The Pacific oyster, *Crassostrea gigas*, shows negative correlation to naturally elevated carbon dioxide levels: implications for near-term ocean acidification effects. *Limnol. Oceanogr.* 57, 698–710. doi: 10.4319/lo.2012.57.3.0698

Barton, A., Waldbusser, G. G., Feely, R. A., Weisberg, S. B., Newton, J. A., Hales, B., et al. (2015). Impacts of coastal acidification on the Pacific Northwest shellfish industry and adaptation strategies implemented in response. *Oceanography* 28, 146–159. doi: 10.5670/oceanog.2015.38

Bednarsek, N., Feely, R. A., Reum, J. C., Peterson, B., Menkel, J., Alin, S. R., et al. (2014). Limacina helicina shell dissolution as an indicator of declining habitat suitability owing to ocean acidification in the California Current Ecosystem. *Proc. Biol. Sci.* 281:20140123. doi: 10.1098/rspb.2014.0123

Bednarsek, N., Feely, R. A., Tolimieri, N., Hermann, A. J., Siedlecki, S. A., Waldbusser, G. G., et al. (2017). Exposure history determines pteropod vulnerability to ocean acidification along the US West Coast. *Sci. Rep.* 7:4526. doi: 10.1038/s41598-41017-03934-z

Bianucci, L., Long, W., Khangaonkar, T., Pelletier, G., Ahmed, A., Mohamedali, T., et al. (2018). Sensitivity of the regional ocean acidification and carbonate system in Puget Sound to ocean and freshwater inputs. *Elem. Sci. Anth.* 6:22. doi: 10.1525/elementa.151

Brodeur, R., Daly, E. A., Sturdevant, M. V., Miller, T. W., Moss, J. H., Thiess, M. E., et al. (2007). Regional comparisons of juvenile salmon feeding in coastal Marine waters off the West Coast of North America. *Am. Fish. Soc. Symp.* 57, 183–203.

Caldeira, K., and Wickett, M. E. (2003). Anthropogenic carbon and ocean pH. *Nature* 425:365. doi: 10.1038/425365a

Chan, F., Barth, J. A., Blanchette, C. A., Byrne, R. H., Chavez, F. P., Cheriton, O., et al. (2017). Persistent spatial structuring of coastal ocean acidification in the California Current System. *Sci. Rep.* 7:2526. doi: 10.1038/s41598-41017-02777-y

Cooley, S. R., and Doney, S. C. (2009). Anticipating ocean acidification's economic consequences for commercial fisheries. *Environ. Res. Lett.* 4, 1–8. doi: 10.1088/1748-9326/1084/1082/024007

Cooley, S. R., Kite-Powell, H. L., and Doney, S. C. (2009). Ocean acidification's potential to alter global marine ecosystem services. *Oceanography* 22, 172–181. doi: 10.5670/oceanog.2009.106

Denman, K. L., and Miyake, M. (1973). Behavior of the mean wind, the drag coefficient, and the wave field in the open ocean. *J. Geophyis. Res.* 78, 1917–1931. doi: 10.1029/JC078i012p01917

Dickson, A., Wesolowski, D. J., Palmer, D. A., and Mesmer, R. E. (1990). Dissociation constant of bisulfate ion in aqueous sodium chloride solutions to 250 °C. *J. Phys. Chem.* 94, 7978–7985. doi: 10.1021/j100383a042

Doney, S. C., Ruckelshaus, M., Duffy, J. E., Barry, J. P., Chan, F., English, C. A., et al. (2012). Climate change impacts on marine ecosystems. *Ann. Rev. Mar. Sci.* 4, 11–37. doi: 10.1146/annurev-marine-041911-111611

Egleston, E. S., Sabine, C. L., and Morel, F. M. M. (2010). Revelle revisited: buffer factors that quantify the response of ocean chemistry to changes in DIC and alkalinity. *Glob. Biogeochem. Cycles* 24:GB1002. doi: 10.1029/2008GB003407

Ekstrom, J. A., Suatoni, L., Cooley, S. R., Pendleton, L. H., Waldbusser, G. G., Cinner, J. E., et al. (2015). Vulnerability and adaptation of US shellfisheries to ocean acidification. *Nat. Clim. Chang.* 5, 207–214. doi: 10.1038/nclimate2508

Evans, W., Hales, B., Strutton, P. G., and Ianson, D. (2012). Sea-air CO2 fluxes in the western Canadian coastal ocean. *Prog. Oceanogr.* 101, 78–91. doi: 10.1016/j.pocean.2012.1001.1003

Evans, W., Mathis, J. T., Ramsay, J., and Hetrick, J. (2015). On the frontline: tracking ocean acidification in an alaskan shellfish hatchery. *PLoS One* 10:e0130384. doi: 10.1371/journal.pone.0130384

Fassbender, A. J., Alin, S. R., Feely, R. A., Sutton, A. J., Newton, J., Krembs, C., et al. (2018). Seasonal carbonate chemistry variability in marine surface waters of the Pacific Northwest. *Earth Syst. Sci. Data* 10, 1367–1401. doi: 10.1371/journal.pone.0089619

Fassbender, A. J., Alin, S. R., Feely, R. A., Sutton, A. J., Newton, J. A., and Byrne, R. H. (2016). Estimating total alkalinity in the washington state coastal zone: complexities and surprising utility for ocean acidification research. *Estuaries Coasts* 40, 404–418. doi: 10.1007/s12237-12016-10168-z

Feely, R. A., Alin, S. R., Carter, B., Bednarsek, N., Hales, B., Chan, F., et al. (2016). Chemical and biological impacts of ocean acidification along the west coast of North America. *Estuarine Coastal Shelf Sci.* 183, 260–270. doi: 10.1016/j.ecss.2016.08.043

Feely, R. A., Alin, S. R., Newton, J., Sabine, C. L., Warner, M., Devol, A., et al. (2010). The combined effects of ocean acidification, mixing, and respiration on pH and carbonate saturation in an urbanized estuary. *Estuarine Coastal Shelf Sci.* 88, 442–449. doi: 10.1016/j.ecss.2010.05.004

Feely, R. A., Okazaki, R. R., Cai, W. J., Bednarsek, N., Alin, S. R., Byrne, R. H., et al. (2018). The combined effects of acidification and hypoxia on pH and aragonite saturation in the coastal waters of the California current ecosystem and the northern Gulf of Mexico. *Cont. Shelf Res.* 152, 50–60. doi: 10.1016/j.csr.2017.11.002

Feely, R. A., Sabine, C. L., Lee, K., Berelson, W., Kleypas, J., Fabry, V. J., et al. (2004). Impact of anthropogenic CO$_2$ on the CaCO$_3$ System in the oceans. *Science* 305, 362–366. doi: 10.1126/science.1097329

Gosling, E. (2003). *Bivalve Molluscs: Biology, Ecoogy and Culture*. Malden, MA: Blackwell Publishing, Inc. doi: 10.1002/9780470995532

Haigh, R., Ianson, D., Holt, C. A., Neate, H. E., and Edwards, A. M. (2015). Effects of ocean acidification on temperature coastal marine ecosystems and fisheries in the Northeast Pacific. *PLoS One* 10:e0117533. doi: 10.1371/journal.pone.0117533

Hales, B., Chipman, D., and Takahashi, T. (2004). High-frequency measurements of partial pressure and total concentration of carbon dioxide in seawater using microporous hydrophobic membrane contactors. *Limnol. Oceanogr.* 2, 356–364. doi: 10.4319/lom.2004.2.356

Hales, B., Suhrbier, A., Waldbusser, G. G., Feely, R. A., and Newton, J. A. (2016). The carbonate chemistry of the "Fattening Line," Willapa Bay, 2011-2014. *Estuaries Coasts* 40, 173–186. doi: 10.1007/s12237-12016-10136-12237

Hales, B., Takahashi, T., and Bandstra, L. (2005). Atmospheric CO2 uptake by a coastal upwelling system. *Glob. Biogeochem. Cycles* 19:GB1009. doi: 10.1029/2004GB002295

Harris, K. E., Degrandpre, M. D., and Hales, B. (2013). Aragonite saturation state dynamics in a coastal upwelling zone. *Geophys. Res. Lett.* 40, 2720–2725. doi: 10.1002/grl.50460

Hauri, C., Winsor, P., Juranek, L. W., Mcdonnell, A. M. P., Takahashi, T., and Mathis, J. T. (2013). Wind-driven mixing causes a reduction in the strength of the continental shelf carbon pump in the Chukchi Sea. *Geophys. Res. Lett.* 40, 5932–5936. doi: 10.1002/2013GL058267

Hsu, S. A., Meindl, E. A., and Gilhousen, D. B. (1994). Determining the power-law wind-profile exponent under near-neutral stability conditions at sea. *J. Appl. Meteorol.* 33, 757–765. doi: 10.1175/1520-0450(1994)033<0757:DTPLWP>2.0.CO;2

Ianson, D., Allen, S. E., Moore-Maley, B. L., Johannessen, S. C., and Macdonald, R. W. (2016). Vulnerability of a semienclosed estuarine sea to ocean acidification in contrast with hypoxia. *Geophys. Res. Lett.* 43, 5793–5801. doi: 10.1002/2016GL068996

Johannessen, S. C., Masson, D., and Macdonald, R. W. (2014). Oxygen in the deep strait of Georgia, 1951-2009: the roles of mixing, deep-water renewal, and remineralization of organic carbon. *Limnol. Oceanogr.* 59, 211–222. doi: 10.4319/lo.2014.59.1.0211

Journey, M. L., Trudel, M., Young, G., and Beckman, B. R. (2018). Evidence of depressed growth of juvenile Pacific salmon (Oncorhynchus) in Johnstone and Queen Charlotte Straits, British Columbia. *Fish. Oceanogr.* 27, 174–183. doi: 10.1111/fog.12243

Kroeker, K. J., Kordas, R. L., Crim, R., Hendriks, I. E., Ramajo, L., Singh, G. S., et al. (2013). Impacts of ocean acidification on marine organisms: quantifying sensitivities and interactions with warming. *Glob. Chang. Biol.* 19, 1884–1896. doi: 10.1111/gcb.12179

Landschützer, P., Gruber, N., Bakker, D. C. E., Stemmler, I., and Six, K. D. (2018). Strengthening seasonal marine CO2 variations due to increasing atmospheric CO2. *Nat. Clim. Chang.* 8, 146–150. doi: 10.1038/s41558-41017-40057-x

Laruelle, G. G., Cai, W. J., Hu, X., Gruber, N., Mackenzie, F. T., and Regnier, P. (2018). Continental shelves as a variable but increasing global sink for atmospheric carbon dioxide. *Nat. Commun.* 9:454. doi: 10.1038/s41467-41017-02738-z

Lueker, T. J., Dickson, A. G., and Keeling, C. D. (2000). Ocean pCO2 calculated from dissolved inorganic carbon, alkalinity, and equations for K1 and K2: validation based on laboratory measurements of CO2 in gas and seawater at equilibrium. *Mar. Chem.* 70, 105–119. doi: 10.1016/S0304-4203(00)00022-0

Masson, D. (2002). Deep water renewal in the strait of Georgia. *Estuarine Coastal Shelf Sci.* 54, 115–126. doi: 10.1006/ecss.2001.0833

Masson, D., and Cummins, P. F. (2004). Observations and modeling of seasonal variability in the straits of Georgia and Juan de Fuca. *J. Mar. Res.* 62, 491–516. doi: 10.1357/0022240041850075

Masson, D., and Peña, A. (2009). Chlorophyll distribution in a temperature estuary: the strait of Georgia and Juan de Fuca Striat. *Estuarine Coastal Shelf Sci.* 82, 19–28. doi: 10.1016/j.ecss.2008.12.022

Mathis, J. T., Cooley, S. R., Lucey, N., Colt, S., Ekstrom, J., Hurst, T., et al. (2015). Ocean acidification risk assessment for Alaska's fishery sector. *Prog. Oceanogr.* 136, 71–91. doi: 10.1016/j.pocean.2014.07.001

McLaskey, A. K., Keister, J. E., Mcelhany, P., Brady Olson, M., Busch, D. S., Maher, M., et al. (2016). Development of *Euphausia pacifica* (krill) larvae is impaired under pCO2 levels currently observed in the Northeast Pacific. *Mar. Ecol. Prog. Ser.* 555, 65–78. doi: 10.3354/meps11839

McLaughlin, K., Weisberg, S., Dickson, A., Hofmann, G., Newton, J., Aseltine-Neilson, D., et al. (2015). Core principles of the california current acidification network: linking chemistry, physics, and ecological effects. *Oceanography* 25, 160–169. doi: 10.5670/oceanog.2015.39

Moore-Maley, B. L., Allen, S. E., and Ianson, D. (2016). Locally driven interannual variability of near-surface pH and ΩA in the strait of Georgia. *J. Geophys. Res.* 121, 1600–1625. doi: 10.1002/2015JC011118

Mucci, A. (1983). The solubility of calcite and aragonite in seawater at various salinities, temperatures, and one atmosphere total pressure. *Am. J. Sci.* 283, 780–799. doi: 10.2475/ajs.283.7.780

Müller, J. D., Schneider, B., and Rehder, G. (2016). Long-term alkalinity trends in the Baltic Sea and their implications for CO2-induced acidification. *Limnol. Oceanogr.* 61, 1984–2002. doi: 10.1002/lno.10349

Newton, J. A., Feely, R. A., Jewett, E. B., Williamson, P., and Mathis, J. (2015). *Global Ocean Acidification Observing Network: Requirements and Governance Plan*. Available at: http://goa-on.org/documents/resources/GOA-ON_2nd_edition_final.pdf

Orr, J. C., Epitalon, J.-M., Dickson, A. G., and Gattuso, J.-P. (2018). Routine uncertainty propagation for the marine carbon dioxide system. *Mar. Chem.* 207, 84–107. doi: 10.1016/j.marchem.2018.10.006

Orr, J. C., Fabry, V. J., Aumont, O., Bopp, L., Doney, S. C., Feely, R. A., et al. (2005). Anthropogenic ocean acidification over the twenty-first century and its impact on calcifying organisms. *Nature* 437, 681–686. doi: 10.1038/nature04095

Pacella, S. R., Brown, C. A., Waldbusser, G. G., Labiosa, R. G., and Hales, B. (2018). Seagrass habitat metabolism increases short-term extremes and long-term offset of CO2 under future ocean acidification. *Proc. Natl. Acad. Sci. U.S.A.* 115, 3870–3875. doi: 10.1073/pnas.1703445115

Pawlowicz, R., Riche, O., and Halverson, M. (2007). The circulation and residence time of the strait of georgia using a simple mixing-box approach. *Atmos. Ocean* 45, 173–193. doi: 10.3137/ao.450401

Pierrot, D., Neill, C., Sullivan, K., Castle, R., Wanninkhof, R., Lüger, H., et al. (2009). Recommendations for autonomous underway pCO2 measuring systems and data-reduction routines. *Deep Sea Res. II* 56, 512–522. doi: 10.1016/j.dsr2.2008.12.005

Proshutinsky, A., Krishfield, R., Timmermans, M.-L., Toole, J., Carmack, E., Mclaughlin, F., et al. (2009). Beaufort Gyre freshwater reservoir: state and variability from observations. *J. Geophyis. Res.* 114:C00A10. doi: 10.1029/2008JC005104

Quayle, D. B. (1988). "Pacific oyster culture in British Columbia," in *Canadian Bulletin of Fisheries and Aquatic Sciences 218*, ed. Department of Fisheries and Oceans (Ottawa, ON: Department of Fisheries and Oceans).

Riahi, K., Rao, S., Krey, V., Cho, C., Chirkov, V., Fischer, G., et al. (2011). RCP 8.5 – A scenario of comparatively high greenhouse gas emissions. *Clim. Chang.* 109, 33–57. doi: 10.1007/s10584-011-0149-y

Riche, O., Johannessen, S. C., and Macdonald, R. W. (2014). Why timing matters in a coastal sea: trends, variability and tipping points in the Strait of Georgia, Canada. *J. Mar. Syst.* 131, 36–53. doi: 10.1016/j.jmarsys.2013.11.003

Sabine, C. L., Feely, R. A., Gruber, N., Key, R. M., Lee, K., Bullister, J. L., et al. (2004). The oceanic sink for anthropogenic CO2. *Science* 305, 367–371. doi: 10.1126/science.1097403

Sabine, C. L., Feely, R. A., Key, R. M., Bullister, J. L., Millero, F. J., Lee, K., et al. (2002). Distribution of anthropogenic CO2 in the Pacific Ocean. *Glob. Biogeochem. Cycles* 16, 30–31. doi: 10.1029/2001GB001639

Salisbury, J. E., and Jönsson, B. F. (2018). Rapid warming and salinity changes in the Gulf of Maine alter surface ocean carbonate parameters and hide ocean acidification. *Biogeochemistry* 141, 401–418. doi: 10.1007/s10533-018-0505-3

Seung, C. K., Dalton, M. G., Punt, A. E., Poljak, D., and Foy, R. (2015). Economic impacts of changes in an alaska crab fishery from ocean acidification. *Clim. Chang. Econ.* 6:1550017. doi: 10.1142/S2010007815500177

Shabbar, A., Bonsal, B., and Khandekar, M. (1997). Canadian precipitation patterns associated with the southern oscillation. *J. Clim.* 10, 3016–3027. doi: 10.1175/1520-0442(1997)010<3016:CPPAWT>2.0.CO;2

Smith, S. D., Anderson, R. J., Oost, W. A., Kraan, C., Maat, N., Decosmo, J., et al. (1991). Sea surface wind stress and drag coefficients: the HEXOS results. *Boundary-Layer Meteorology* 60, 109–142. doi: 10.1007/BF00122064

Sunday, J. M., Calosi, P., Dupont, S., Munday, P. L., Stillman, J. H., and Reusch, T. B. (2014). Evolution in an acidifying ocean. *Trends Ecol. Evol.* 29, 117–125. doi: 10.1016/j.tree.2013.11.001

Sutton, A. J., Feely, R. A., Maenner-Jones, S., Musielewicz, S., Osborne, J., Dietrich, C., et al. (2018). Autonomous seawater pCO2 and pH time series from 40 surface buoys and the emergence of anthropogenic trends. *Earth Syst. Sci. Data Discuss.* doi: 10.5194/essd-2018-5177

Sutton, A. J., Sabine, C. L., Feely, R. A., Cai, W. J., Cronin, M. F., Mcphaden, M. J., et al. (2016). Using present-day observations to detect when anthropogenic change forces surface ocean carbonate chemistry outside preindustrial bounds. *Biogeosciences* 13, 5065–5083. doi: 10.5194/bg-13-5065-2016

Takahashi, T. (1961). Carbon dioxide in the atmosphere and in atlantic ocean water. *J. Geophyis. Res.* 66, 477–494. doi: 10.1029/JZ066i002p00477

Takeshita, Y., Frieder, C. A., Martz, T. R., Ballard, J. R., Feely, R. A., Kram, S., et al. (2015). Including high-frequency variability in coastal ocean acidification projections. *Biogeosciences* 12, 5853–5870. doi: 10.1371/journal.pone.0085117

Tortell, P. D., Merzouk, A., Ianson, D., Pawlowicz, R., and Yelland, D. R. (2012). Influence of regional climate forcing on surface water pCO2, ΔO2/Ar and dimethylsulfide (DMS) along the southern British Columbia coast. *Cont. Shelf Res.* 47, 119–132. doi: 10.1016/j.csr.2012.07.007

Uppström, L. R. (1974). The boron/chlorinity ratio of deep-sea water from the pacific ocean. *Deep Sea Res. Oceanogr. Abstracts* 21, 161–162. doi: 10.1016/0011-7471(74)90074-6

Van Heuven, S., Pierrot, D., Rae, J. W. B., Lewis, E., and Wallace, D. W. R. (2011). "MATLAB program developed for CO_2 system calculations," in *ORNL/CDIAC-105b*, ed. Carbon Dioxide Information Analysis Center (Oak Ridge, TN: Department of Energy).

Voss, B. M., Peucker-Ehrenbrink, B., Eglinton, T. I., Fiske, G., Wang, Z. A., Hoering, K. A., et al. (2014). Tracing river chemistry in space and time: dissolved inorganic constituents of the Fraser River. Canada. *Geochim. Cosmochim. Acta* 124, 283–308. doi: 10.1016/j.gca.2013.09.006

Waldbusser, G. G., Hales, B., Langdon, C., Haley, B. A., Schrader, P., Brunner, E. L., et al. (2015). Ocean acidification has multiple modes of action on bivalve larvae. *PLoS One* 10:e0128376. doi: 10.1371/journal.pone.0128376

Waldbusser, G. G., Hales, B., Langdon, C. J., Haley, B. A., Schrader, P., Brunner, E. L., et al. (2014). Saturation-state sensitivity of marine bivalve larvae to ocean acidification. *Nat. Clim. Chang.* 5, 273–280. doi: 10.1038/nclimate2479

Waldbusser, G. G., and Salisbury, J. E. (2014). Ocean acidification in the coastal zone from an organism's perspective: multiple system parameters, frequency domains, and habitats. *Ann. Rev. Mar. Sci.* 6, 221–247. doi: 10.1146/annurev-marine-121211-172238

Wanninkhof, R., and Thoning, K. (1993). Measurement of fugacity of CO2 in surface water using continuous and discrete sampling methods. *Mar. Chem.* 44, 189–204. doi: 10.1016/0304-4203(93)90202-Y

Conflict of Interest Statement: The authors declare that the research was conducted in the absence of any commercial or financial relationships that could be construed as a potential conflict of interest.

frontiers
in Marine Science

ORIGINAL RESEARCH
published: 09 January 2019
doi: 10.3389/fmars.2018.00508

Modeled Effect of Coastal Biogeochemical Processes, Climate Variability, and Ocean Acidification on Aragonite Saturation State in the Bering Sea

Darren J. Pilcher[1,2]*, Danielle M. Naiman[2,3], Jessica N. Cross[2], Albert J. Hermann[1,2], Samantha A. Siedlecki[4], Georgina A. Gibson[5] and Jeremy T. Mathis[6]

[1] Joint Institute for the Study of the Atmosphere and Ocean, University of Washington, Seattle, WA, United States, [2] NOAA Pacific Marine Environmental Laboratory, NOAA, Seattle, WA, United States, [3] Jacobs School of Engineering, University of California, San Diego, San Diego, CA, United States, [4] Department of Marine Sciences, University of Connecticut, Groton, CT, United States, [5] International Arctic Research Center, University of Alaska Fairbanks, Fairbanks, AK, United States, [6] Georgetown University, Washington, DC, United States

OPEN ACCESS

Edited by:
Andrea J. Fassbender,
Monterey Bay Aquarium Research
Institute (MBARI), United States

Reviewed by:
Raffaele Bernardello,
Barcelona Supercomputing Center,
Spain
Diane Lavoie,
Department of Fisheries and Oceans
(Canada), Canada

***Correspondence:**
Darren J. Pilcher
darren.pilcher@noaa.gov

Specialty section:
This article was submitted to
Marine Biogeochemistry,
a section of the journal
Frontiers in Marine Science

Received: 12 July 2018
Accepted: 19 December 2018
Published: 09 January 2019

Citation:
Pilcher DJ, Naiman DM,
Cross JN, Hermann AJ, Siedlecki SA,
Gibson GA and Mathis JT (2019)
Modeled Effect of Coastal
Biogeochemical Processes, Climate
Variability, and Ocean Acidification on
Aragonite Saturation State
in the Bering Sea.
Front. Mar. Sci. 5:508.
doi: 10.3389/fmars.2018.00508

The Bering Sea is highly vulnerable to ocean acidification (OA) due to naturally cold, poorly buffered waters and ocean mixing processes. Harsh weather conditions within this rapidly changing, geographically remote environment have limited the quantity of carbon chemistry data, thereby hampering efforts to understand underlying spatial-temporal variability and detect long-term trends. We add carbonate chemistry to a regional biogeochemical model of the Bering Sea to explore the underlying mechanisms driving carbon dynamics over a decadal hindcast (2003–2012). The results illustrate that coastal processes generate considerable spatial variability in the biogeochemistry and vulnerability of Bering Sea shelf water to OA. Substantial seasonal biological productivity maintains high supersaturation of aragonite on the outer shelf, whereas riverine freshwater runoff loaded with allochthonous carbon decreases aragonite saturation states (Ω_{Arag}) to values below 1 on the inner shelf. Over the entire 2003–2012 model hindcast, annual surface Ω_{Arag} decreases by 0.025 – 0.04 units/year due to positive trends in the partial pressure of carbon dioxide ($p\mathrm{CO}_2$) in surface waters and dissolved inorganic carbon (DIC). Variability in this trend is driven by an increase in fall phytoplankton productivity and shelf carbon uptake, occurring during a transition from a relatively warm (2003–2005) to cold (2010–2012) temperature regime. Our results illustrate how local biogeochemical processes and climate variability can modify projected rates of OA within a coastal shelf system.

Keywords: ocean acidification, aragonite saturation, Bering Sea, climate variability, coastal carbon cycling, coastal biogeochemistry, freshwater inputs

INTRODUCTION

The global ocean has absorbed ∼41% of all anthropogenic carbon dioxide (CO_2) emissions resulting from the combustion of fossil fuels and industrial processes (Khatiwala et al., 2009), thereby mitigating some of the warming associated with climate change. When CO_2 dissolves in seawater, it can react with water molecules to form a weak acid, carbonic acid (H_2CO_3).

The dissociation of this acid shifts the marine carbonate system, generating a decline in surface pH and reduced carbonate saturation states (Ω), a process referred to as ocean acidification (OA). This process is expected to negatively impact the growth and survival of a wide-range of marine organisms, particularly marine calcifiers (Doney et al., 2009; Kroeker et al., 2013). OA has already generated a pH decline of 0.1 units globally, equivalent to a ~30% increase in acidity since the beginning of the Industrial Revolution (Orr et al., 2005). High-latitude regions are particularly vulnerable to this expected change as these waters are already naturally low in carbonate ion concentrations, due to ocean circulation patterns and the effect of colder water temperatures increasing CO_2 gas solubility (Fabry et al., 2009).

The Bering Sea is one of the most productive marine ecosystems in the world and supports a $3 billion annual U.S. fishery that constitutes approximately 40% of all U.S. commercial fish landings (Wiese et al., 2012). Many of the marine organisms that comprise this ecosystem are vulnerable to OA, posing a large risk to Alaskan commercial and subsistence fisheries (Mathis et al., 2015a). Bivalves such as the Pacific Oyster (*Crassostrea gigas*) display reduced growth and survival rates under conditions of low pH and Ω (Barton et al., 2012; Waldbusser et al., 2015). Survival rates of larval and juvenile red king crab (*Paralithodes camtschaticus*) and tanner crab (*Chionoecetes bairdi*) are also negatively impacted at lower pH (Long et al., 2013; Long et al., 2016), which may lead to significant reductions in catch and profits for these fisheries (Punt et al., 2016). Pelagic fish appear to have relatively greater resilience to direct impacts of OA. For instance, no significant negative impacts from OA have been found for walleye Pollock (*Gadus chalcogrammus*) larval and juvenile growth rates (Hurst et al., 2012; Hurst et al., 2013). However, pelagic fish may still be vulnerable due to indirect effects of OA on the food web, particularly by reducing prey abundance and behavior. Pteropods are an important prey source for many subarctic and arctic fish species and are already exhibiting shell dissolution due to OA in the Southern Ocean (Orr et al., 2005; Bednarsek et al., 2012).

Many of these biological experiments testing organismal response to OA consist of monitoring the organism in a controlled setting of constant low pH/high CO_2 water. However, the natural environment displays substantial spatial-temporal variability, particularly in dynamic coastal settings where the underlying biogeochemistry is impacted by a range of land, ocean, and atmosphere processes. For example, freshwater runoff from terrestrial (Semiletov et al., 2016) and glacial (Evans et al., 2014; Siedlecki et al., 2017) sources, in addition to wind-driven upwelling (Feely et al., 2008) produce localized regions of corrosive water conditions on seasonal timeframes. Thus, while long-term trends in open ocean pH are expected to emerge within a 10–15 years timeframe (Rodgers et al., 2015; Sutton et al., 2017), trends in coastal pH have been substantially more difficult to detect (Duarte et al., 2013). Nonetheless, these coastal regions are a variable but increasing sink of atmospheric CO_2 (Laruelle et al., 2018), suggesting that OA is occurring. Furthermore, the interplay of these coastal processes with OA can produce accelerated rates of pH decline compared to the open oceans (Chavez et al., 2017; Carstensen et al., 2018).

The remote geographic location, harsh winters, and large spatial extent of the Bering Sea shelf are additional challenges that observational field campaigns in this region face. Nonetheless, previous work stemming from the 2008 to 2010 Bering Sea Ecosystem Study (BEST) and Bering Sea Integrated Research Project (BSIERP) cruises illustrated distinctive variability, even at low spatial-temporal resolution, and greatly expanded our understanding of the underlying carbon cycle and vulnerability to OA (Wiese et al., 2012; Mathis et al., 2015b). Similar to other high-latitude regions, the Bering Sea shelf has a highly seasonal carbon cycle, with periods of carbon efflux to the atmosphere in winter and carbon influx to the ocean in summer and fall (Cross et al., 2014). Net carbon uptake on annual timeframes results from substantial summer-fall biological productivity, especially along the outer shelf "green belt" region where mixing processes supply off shelf nitrate and coastally derived iron (Mathis et al., 2010; Bates et al., 2011; Cross et al., 2012; Lomas et al., 2012). This organic carbon eventually sinks and is remineralized by bacteria at depth, producing conditions of aragonite undersaturation ($\Omega_{\text{Arag}} < 1$) in bottom waters for at least several months starting in June (Mathis et al., 2014). Periods of aragonite undersaturation have also been observed in surface waters along the inner Bering Sea Shelf, near sources of freshwater runoff from the Yukon and Kuskokwim rivers (Mathis et al., 2011). This river runoff is supersaturated with terrestrial-derived carbon and supports significant respiration and net heterotrophic conditions in nearshore coastal waters (Striegl et al., 2007; Cross et al., 2012). The Bering Sea shelf also displays substantial interannual variability in sea ice extent and water temperature due to natural climate variability. This variability has recently coalesced into 4–5 years regimes of persistent cold, high sea ice (e.g., 2007–2012) or warm, low sea ice (e.g., 2001–2005) conditions, which have had significant effects on the Bering Sea ecosystem (Stabeno et al., 2012; Heintz et al., 2013; Eisner et al., 2014). This physical variability likely also produces substantial variability in the biogeochemistry and carbonate system, however, the available data are insufficient to resolve this effect (Mathis et al., 2010; Cross et al., 2012).

Computational regional models grounded in observable data have emerged as a useful tool to help elucidate spatial-temporal variability due to their much finer spatial and temporal resolution (Xue et al., 2016; Siedlecki et al., 2017). A regional physical-biological model was developed as part of BEST-BSIERP and utilized in previous work to understand biophysical variability and project changes to the Bering Sea ecosystem under future climate change scenarios (Gibson and Spitz, 2011; Hermann et al., 2016) Here, we add carbonate chemistry to this Bering Sea model and run a 10-year hindcast simulation from 2003 to 2012. The 2003–2012 timeframe was selected as it: (1) provides a full decadal timeframe, (2) encompasses the 2008–2010 period when shipboard measurements of TA and DIC were collected throughout the Bering Sea shelf, and (3) also encompasses both a warm (2003–2005) and a cold (2010–2012) temperature regime. The purpose of this hindcast simulation is to elucidate (1) the underlying mechanisms of spatial variability in Ω_{Arag}, (2) the impact of climate variability on the shelf carbon

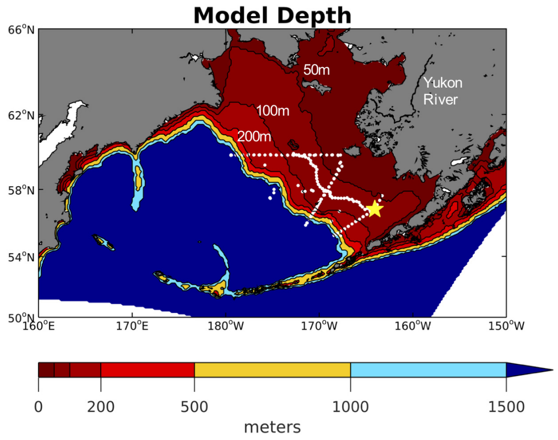

FIGURE 1 | Model domain with contoured color shading for model depth. The contour lines for the 50, 100, and 200 m isobaths are also labeled as these represent the generalized boundaries for the inner, middle, and outer Bering Sea shelf domains. White dots signify station locations from the 2008–2010 BEST-BSIERP cruises and the yellow star signifies the locating of the M2 mooring.

cycle, and (3) how this climate variability impacts the expected rate of OA.

MATERIALS AND METHODS

Physical Model Description

We use the Regional Ocean Modeling System (ROMS; Shchepetkin and McWilliams, 2005; Haidvogel et al., 2008) configured to the Bering Sea by Hermann et al. (2013) following an implementation for the Northeast Pacific (NEP-5) described by Danielson et al. (2011). This configuration (known as the "Bering10K" model) has ∼10km spatial horizontal resolution with 10 vertical layers (**Figure 1**). The use of 10 sigma-coordinate vertical layers significantly decreases model run time, while still maintaining many of the physical and biological dynamics produced by a 60-vertical layer implementation (Hermann et al., 2013). The Bering10K model simulates both sea ice (Budgell, 2005) and tidal mixing. The version used here includes recent corrections to the ice thermodynamics terms, which improved the seasonal timing of ice formation and retreat. The Climate Forecast System Reanalysis (CFSR; Saha et al., 2010) and subsequent CFSv2 operational analysis (CFSv2; Saha et al., 2014) provide the atmospheric forcing of air temperature, winds, specific humidity, rainfall, and shortwave and longwave radiation.

Biogeochemical Model Description

We use the biological model developed as part of the BEST program by Gibson and Spitz (2011) (BEST-NPZD). This model contains 12 total pelagic state variables (**Figure 2**) – large and small phytoplankton, microzooplankton, small and large copepods, euphausiids, jellyfish, iron, nitrate, ammonium, and slow (1 m/day) and fast (10 m/day) sinking detritus. Coupled to this pelagic model is a 3-component ice-biology submodel which simulates ice algae, nitrate, and ammonium within the bottom 2 cm of the ice. Benthic processes are simulated in a 2-component benthic submodel consisting of benthic fauna and benthic detritus. Phytoplankton and detritus that sinks out of the bottom water layer enters the benthic detritus component. Of this flux, 20% is removed to simulate burial and off-shelf

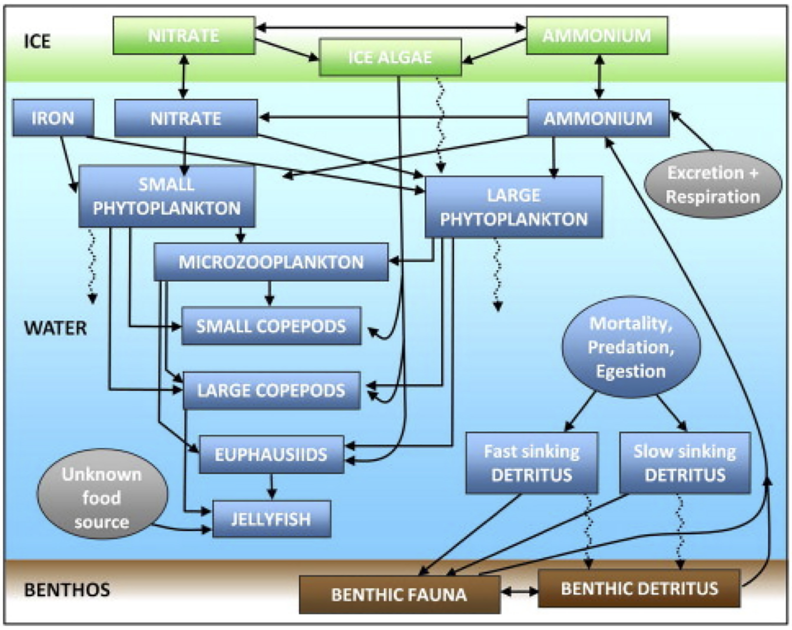

FIGURE 2 | Schematic diagram of the model ecosystem structure, reprinted from Gibson and Spitz (2011) with permission from Elsevier.

transport, based on observations at the M2 mooring (**Figure 1**; Gibson and Spitz, 2011). An additional 1% is removed due to de-nitrification, which is relatively low in the Bering Sea (Gibson and Spitz, 2011).

We add dissolved inorganic carbon (DIC) and total alkalinity (TA) cycling to this existing biological model, following the framework of Fennel et al. (2008) for DIC and Siedlecki et al. (2017) for TA. The model is coded in units of carbon and is converted to nitrogen when necessary (e.g., for nitrate, ammonium, TA) following a constant C:N ratio of 106:16 (Sarmiento and Gruber, 2006). The time evolution of DIC is as follows:

$$\frac{\partial DIC}{\partial t} = remin * D – P_i * \mu_i(Light,\ N) + Resp\,(P_i) + Z_i * Graz_i(P_i) + advection + diffusion \quad (1)$$

$$\left.\frac{\partial DIC}{\partial t}\right|_{bottom} = \frac{1}{\Delta z}\left(w_D \left.\frac{dD}{dz}\right|_{z=bottom}\right) \quad (2)$$

$$\left.\frac{\partial DIC}{\partial t}\right|_{surface} = \frac{V_{CO2}}{\Delta z} * [CO_2]_{sol} * ([CO_2]_{air} - [CO_2]|_{z=surface}) \quad (3)$$

$$V_{CO2} = 0.31u^2\left(\frac{Sc}{660}\right)^{-0.5} \quad (4)$$

where *remin* is the detrital (*D*) remineralization rate, *P* is the phytoplankton group, μ is the phytoplankton growth rate which is a function of light and nutrients (*N*), *Resp* is the respiration rate, *Z* is the zooplankton group, *Graz* is the zooplankton grazing rate, w_D is the sinking rate of 1 m/day for slow sinking detritus and 10 m/day for fast sinking detritus, $[CO_2]_{sol}$ is the CO_2 solubility calculated from Weiss (1974), V_{CO2} is the gas transfer velocity, *u* is the wind speed, Δz is the vertical thickness of the model grid cell, z = bottom is the bottom water model grid cell, and *Sc* is the Schmidt number from Wanninkhof (1992). The atmospheric CO_2 concentration ($[CO_2]_{air}$) is set to a spatially mean value at monthly time resolution from 2002 to 2012, calculated for the Bering Sea from the NOAA Earth System Research Laboratory's CarbonTracker 2016 product (CT2016; Peters et al., 2007). Atmospheric CO_2 increases from 370 μatm to 393 μatm over the 10-year model hindcast.

Alkalinity cycling follows many of the same processes as DIC, except with the addition of nitrification and the lack of air-sea exchange:

$$\frac{\partial TA}{\partial t} = P_i * \mu_i(Light,\ NO_3) - P_i * \mu_i(Light,\ NH_4) + remin * D + resp(P_i) + Z_i * Graz_i(P_i) - 2 * Nitrif + advection + diffusion \quad (5)$$

$$\left.\frac{\partial TA}{\partial t}\right|_{bottom} = \frac{1}{\Delta z}\left(w_D \left.\frac{dD}{dZ}\right|_{z=bottom}\right) \quad (6)$$

where *Nitrif* is nitrification. Phytoplankton uptake of nitrate (NO_3^-) increases TA while the uptake of ammonium (NH_4^+) decreases TA (Brewer and Goldman, 1976; Goldman and Brewer, 1980; Zeebe and Wolf-Gladrow, 2001; Siedlecki et al., 2017). Nitrification decreases TA due to the production of H^+ from the conversion of ammonium to nitrate (Brewer and Goldman, 1976).

DIC and TA are not explicitly simulated within the ice sub-model, however, surface layer DIC and TA concentrations are directly modified by ice algae growth, in order to ensure mass conservation. For example, growth of ice algae decreases surface water DIC, which is then transferred back to the water column following ice algae senescence, grazing, or sinking. A caveat of this simplified approach is that it ignores any additional dynamics between sea ice and TA/DIC, which may have significant local effects in Arctic environments. For example, the formation of ikaite crystals in sea ice can have a greater impact on surface water $p\mathrm{CO}_2$ concentrations than ice algae production (Rysgaard et al., 2012; Moreau et al., 2014). To our knowledge, this effect has not been quantified in a 3D biogeochemical model, so we leave this to future work. The presence of sea ice also acts to inhibit the magnitude of the air-sea CO_2 flux according to the percentage of the grid cell covered by ice. For example, a grid cell that is 40% covered with sea ice will have the flux magnitude reduced by 40%.

Boundary Conditions

Oceanic horizontal open boundary conditions are interpolated from the CFSR/CFSv2 global model reanalysis/analysis (for all physical state variables) and climatological estimates (for BEST-NPZ state variables). Values for TA and DIC are derived from empirical relationships with salinity, calculated from shipboard data collected as part of the BEST-BSIERP program from 2008 to 2010. Sampling typically occurred between April and July, with an additional late September to early October cruise in 2009. The values are calculated using the following robust linear regressions:

$$S < 32.6 \quad DIC = 58.5^{*}S + 191.2 \quad (7)$$

$$S \geq 32.6 \quad DIC = 140.4^{*}S - 2478.7 \quad (8)$$

$$S < 33.6 \quad TA = 49.6^{*}S + 600.6 \quad (9)$$

$$S \geq 33.6 \quad TA = 141.8^{*}S - 2494.4 \quad (10)$$

TABLE 1 | Seasonal concentrations of DIC and TA in freshwater runoff.

	May–Jun	July–October	November–April
DIC (mmol/m^3)[a]	1517	1937	4202
TA (mmol/m^3)[b]	1269	1557	2812

[a] *DIC data were collected by Striegl et al. (2007) and summarized by Mathis et al. (2011).* [b] *TA data were collected from the Pan-Arctic River Transport of Nutrients, Organic Matter, and Suspended Sediments Project [PARTNERS] (2010) dataset. Both DIC and TA data are from the mouth of the Yukon River.*

This method was previously employed by Siedlecki et al. (2017) for the Gulf of Alaska, which yielded similar fits, suggesting that the fits are robust throughout the region. All of the fits display strong R^2 values (0.75–0.95), except for the DIC fit at salinity values less than 32.6 psu (R^2 = 0.21). This fit can be moderately improved by increasing the value of the salinity cutoff between the two fits, however, this leads to a discontinuity where the two regressions intersect. This discontinuity can generate substantial differences in DIC values between two very similar salinities and is therefore less suitable for our purpose of simulating the model boundary conditions.

Freshwater terrestrial runoff reduces salinity in nearshore gridpoints, with monthly climatological magnitude calculated from Dai et al. (2009). The freshwater runoff also has a seasonally varying concentration of DIC and TA following data collected from the mouth of the Yukon River (**Table 1**). The Yukon River supplies a substantial portion of the total freshwater runoff to the Bering Sea, and is therefore a reasonable representation of total runoff flux of DIC and TA to the Bering Sea. Model water column iron, nitrate, and ammonium are relaxed to climatological values on a 1-year timescale in order to reduce any long-term drift issues that may develop on decadal model timeframes (Hermann et al., 2013). Climatology values are based on observational data collected in the Bering Sea (e.g., BEST-BSIERP), with some additional tuning based on model ecosystem development and multidecadal hindcast analysis (Gibson and Spitz, 2011; Hermann et al., 2013). This climatological relaxation was found to have no discernable impact on 4-year timeframes, but is essentially for multidecadal runs (Hermann et al., 2013). Model surface salinity values are relaxed to monthly values from the Polar Science Center Hydrographic Climatology (PHC; Steele et al., 2001), using the same 1-year relaxation timescales as was used for the nutrients. Model initial conditions for all prognostic variables except TA and DIC are interpolated from a long-term spinup of the Bering10K model, started in 1970 and fully described in Hermann et al. (2013). Initial conditions for TA and DIC are calculated from the salinity regressions.

Model Skill Assessment

We use observational shipboard data collected during the 2008–2010 BEST-BSIERP cruises for model validation. These data were collected during the spring (April/May) and summer (June/July) seasons, with an additional fall (September/October) sampling in 2009. The sampling covered three cross-shelf transects and one line along the 70 m isobath (**Figure 1**). Model output is compared to co-located discrete measurements of temperature, salinity, nitrate, DIC, and TA. Values of $p\mathrm{CO}_2$ and Ω_{Arag} were calculated from TA and DIC by Cross et al. (2012, 2013) using CO2SYS version 1.05 (Lewis and Wallace, 1998). Model comparisons to observed data are summarized with target diagrams (Jolliff et al., 2009). Target diagrams allow for easy visualization of a model's bias and variance compared to the observed data. Location on the y-axis indicates either a positive (Y > 0) or negative (Y < 0) model bias, while location on the x-axis (calculated as the normalized unbiased RMSD between model and data, multiplied by the sign of modeled minus observed standard deviation) indicates whether the model has a larger (X > 0) or smaller (X < 0) standard deviation compared to the observed data. The radial distance from the origin is also related to the modeling efficiency metric (MEF; Stow et al., 2009). Model fields that lie within the circle have a MEF value of less than 1, indicating better than average model performance as compared to using the mean of the observations. A "perfect" fit would result in all points at $X = 0$, $Y = 0$.

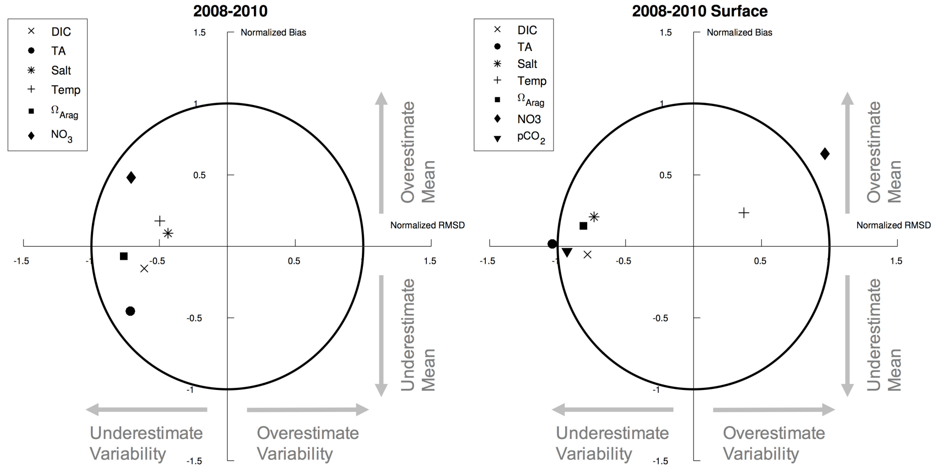

FIGURE 3 | Target diagrams for model variables compared to observed variables from the 2008–2010 BEST-BSIERP cruises for **(left)** the full water column and **(right)** surface layer. *X*-axis is the normalized unbiased RMSD between model and data, multiplied by the sign of the difference between modeled standard deviation and observed standard deviation. *Y*-axis is the normalized mean bias between model and data. The symbol locations thus illustrate whether the model contains a positive ($Y > 0$) or negative ($Y < 0$) bias, whether the model standard deviation is larger ($X > 0$) or smaller ($X < 0$) compared to the observations, and the normalized unbiased RMSD between model and data (absolute value of *X*).

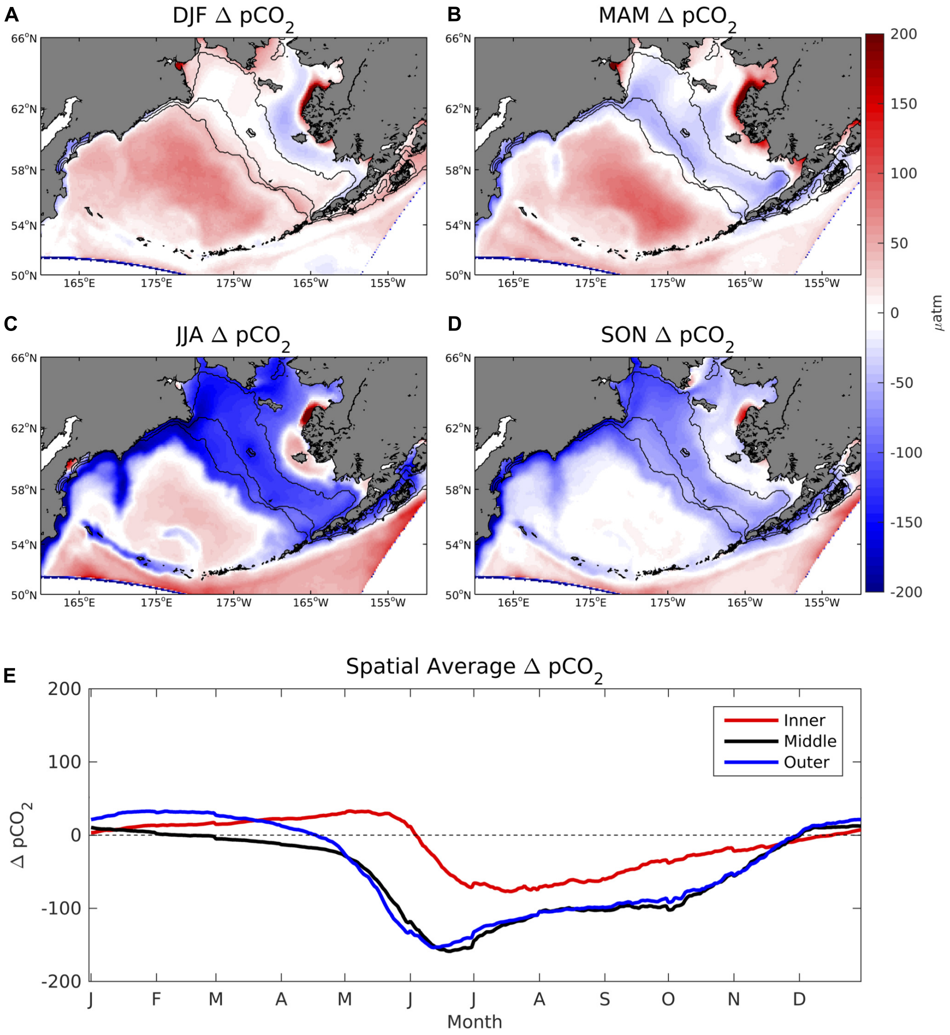

FIGURE 4 | (A–D) Seasonal plots of model ΔpCO_2 averaged over the 2003–2012 timeframe and **(E)** time series of area-weighted spatial mean ΔpCO_2 for the three shelf domains, denoted by the 50, 100, and 200 m isobath lines shown in **Figure 1**.

Model Hindcast Setup

The model hindcast was run from 2002 to 2012. The year 2002 serves as the model spin-up year for the DIC and TA tracers, therefore we only display results from 2003 to 2012. To ensure sufficient model spin-up, we also tested using two consecutive years of 2002 forcing, but found no substantial subsequent model differences compared to the single year of 2002 forcing. Upon model completion, the model output is re-gridded from the curvilinear, sigma-coordinate grid to a regular latitude-longitude-depth grid to facilitate plotting and comparison to observational data.

RESULTS

Model Performance

The Bering10K model with the BEST-NPZD ecosystem model has been previously validated and utilized in a variety of studies exploring biophysical variability in the Bering Sea in both hindcast and decadal projection simulations (Gibson and Spitz, 2011; Hermann et al., 2013, 2016; Ortiz et al., 2016). The model version presented in this manuscript incorporates updated algorithms for the vertical absorption of shortwave radiation in the water column and sea ice growth described in Hermann et al. (2016). These updated algorithms significantly improved model-data comparisons of water temperature and sea ice coverage. The model does contain a few previously described biases, including a late sea ice retreat and colder water temperatures in the northern regions (Hermann et al., 2016). This late sea ice retreat also delays the timing of the spring bloom and tends to generate somewhat lower total phytoplankton biomass in spring and greater biomass in fall (Ortiz et al., 2016). The model version used in the present study also includes recent corrections to the ice thermodynamics terms, which reduce but do not completely eliminate these biases (K. Kearney, personal communication).

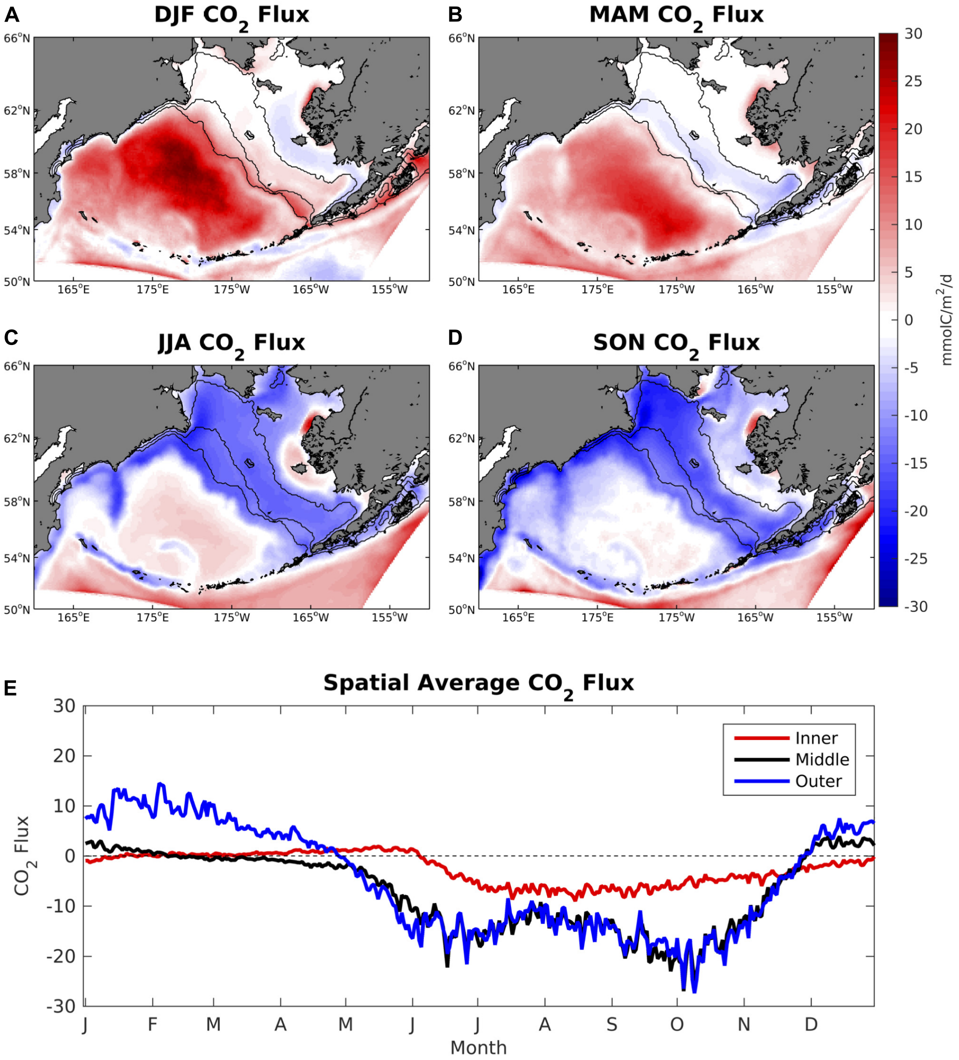

FIGURE 5 | (A–D) Seasonal plots of model air-sea CO_2 flux averaged over the 2003–2012 timeframe and **(E)** time series of area-weighted spatial mean CO_2 flux for the three shelf domains. A positive value signifies a flux of carbon from the ocean to the atmosphere.

Most model fields compare well with the observations and fall within the MEF < 1 circle, suggesting that the model is skillful at reproducing the observed system (**Figure 3**). The lack of any significant mean biases suggest that the model is especially useful for simulating mean-state conditions, particularly near the surface. Only surface TA and NO_3^- values fall outside of the circle, underestimating and overestimating the observed variability respectively. This bias in variability for surface NO_3^- suggests that the model may be producing more variability in nutrient transport or primary productivity. The biases described above by Ortiz et al. (2016) support the latter mechanism. However, if primary productivity variability is overestimated, we may also expect to see an overestimate in DIC variability. On the contrary, DIC variability is underestimated. Thus, either this mechanism is not present, is not of sufficient magnitude to produce a similar bias in DIC, or is compensated by additional factors governing DIC variability (e.g., TA, air-sea CO_2 flux, solubility).

Seasonal and Spatial Patterns

The direction of the air-sea flux of CO_2 is determined by the gradient between the pCO_2 of the surface ocean (pCO_2^{ocn}) of the atmosphere (pCO_2^{atm}). Here we define this gradient as the ΔpCO_2 ($pCO_2^{ocn} - pCO_2^{atm}$), where a negative value indicates a flux direction from the atmosphere into the ocean. Thus, regions of negative ΔpCO_2 are associated with regions of net ocean carbon uptake.

Values of ΔpCO_2 are generally neutral on the Bering Sea shelf throughout most of the winter and spring, but become largely negative in summer and fall (**Figure 4**). In particular, June–October ΔpCO_2 values are strongly undersaturated with respect to the atmosphere, typically ranging from −100 to −200 μatm. However, much of the coastal ocean

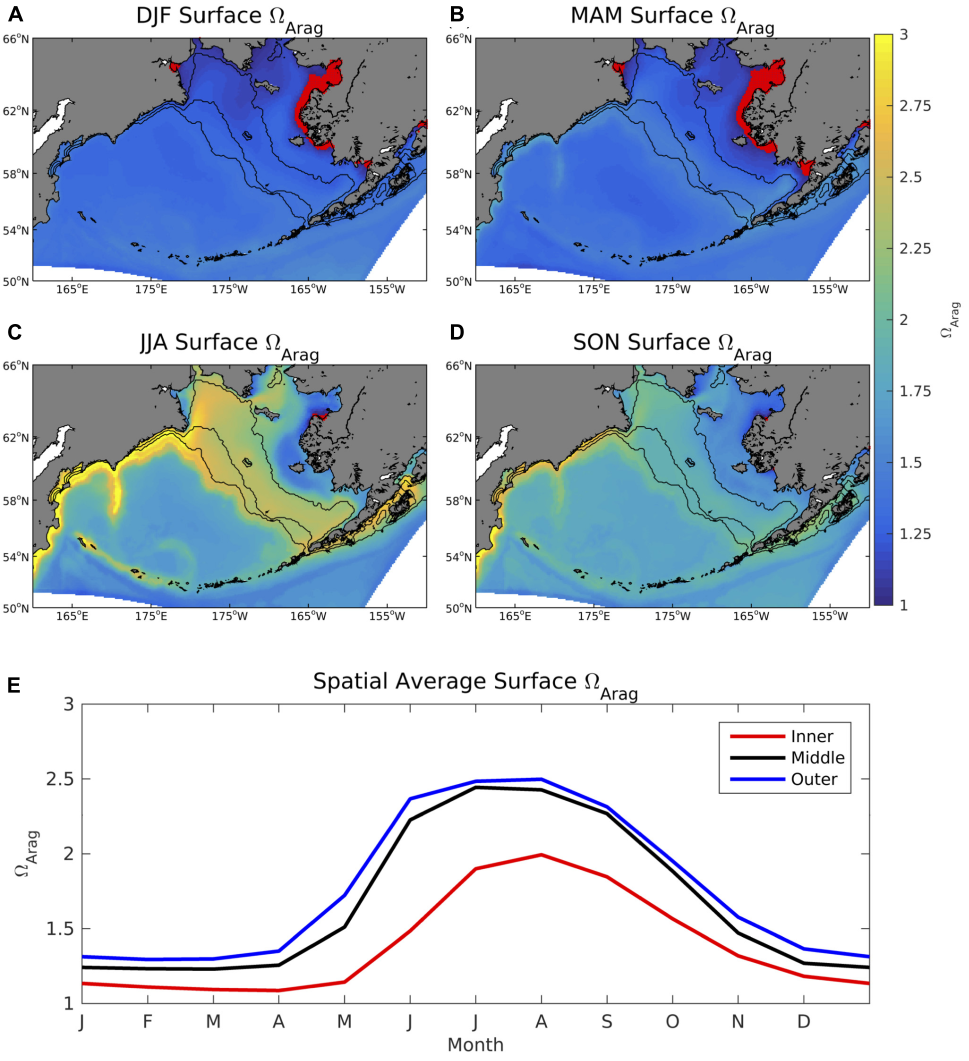

FIGURE 6 | (A–D) Seasonal plots of model surface Ω_{Arag} averaged over the 2003–2012 timeframe and **(E)** time series of area-weighted spatial mean Ω_{Arag} for the three shelf domains The red dots signify locations where $\Omega_{Arag} < 1$.

near western Alaska and Nunivak Island contains positive $\Delta p\text{CO}_2$ values, particularly near the Yukon River delta. In the deep-water basin off of the Bering Sea shelf, $\Delta p\text{CO}_2$ remains slightly positive or neutral for nearly the entire year. CO_2 flux values display a similar seasonal pattern but with differences in relative magnitude due to the influence of wind speed and sea ice (**Figure 5**). For example, sea ice inhibits air-sea exchange on the inner and middle coastal shelf during winter and spring months, leading to relatively low CO_2 flux values. Conversely, frequent storms and strong wind speeds produce substantial positive CO_2 flux values of 20–30 mmolC/m^2/day in the deep Bering Sea basin despite relatively low $\Delta p\text{CO}_2$ values ($\sim$ 25–50 µatm).

Values of surface Ω_{Arag} are relatively low throughout winter and spring, with values in coastal regions along the western Alaskan shoreline consistently below 1 (**Figure 6**). Ω_{Arag} values increase to 2–3 during summer and fall for most of the Bering Sea shelf, except for coastal regions near Nunivak Island and the Yukon River delta where Ω_{Arag} remains less than 2 and less than 1 in a few isolated locations. Bottom water Ω_{Arag} values are lower compared to the surface and display a more subdued seasonal cycle compared to surface Ω_{Arag} (**Figure 7**). Coastal waters along the western Alaskan shoreline are persistently undersaturated in aragonite through winter and spring similar to surface waters, however, coastal regions near Siberia are also undersaturated for large portions of the year. Regions along the middle and outer Bering Sea shelf also display an inverse seasonal cycle compared to surface Ω_{Arag}. That is, bottom water Ω_{Arag} values *decrease* during the winter-summer transition, as opposed to surface Ω_{Arag} values which increase.

The spatial differences between the inner and outer Bering Sea shelf also manifest on annual timescales, with important implications to the underlying carbon chemistry (**Figure 8**). Salinity, DIC, and TA are all substantially lower along the inner shelf compared to the rest of the model domain, and particularly

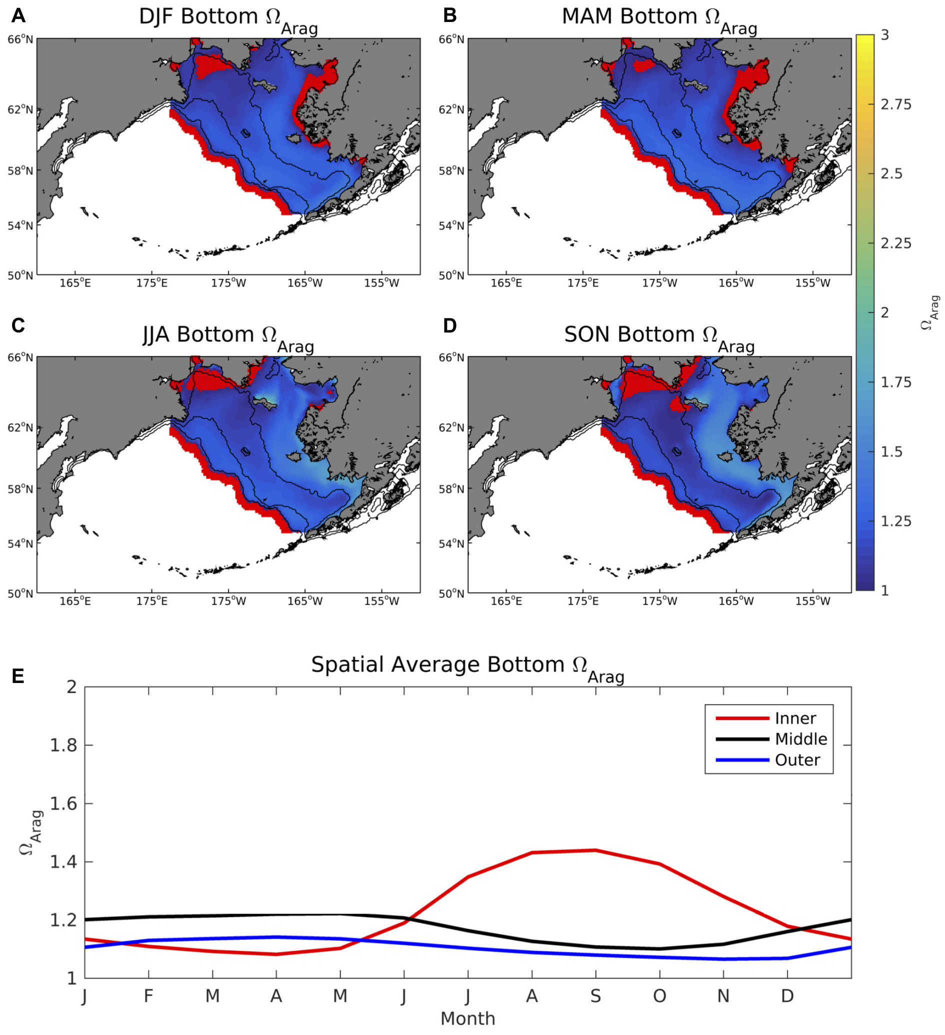

FIGURE 7 | (A–D) Seasonal plots of model bottom water Ω_{Arag} averaged over the 2003–2012 timeframe and **(E)** time series of area-weighted spatial mean bottom Ω_{Arag} for the three shelf domains. The red dots signify locations where $\Omega_{Arag} < 1$. Regions deeper than the Bering Sea coastal shelf break (>1500 m) are whited out.

within Norton Sound, indicative of outflow from the neighboring Yukon River delta. Plotting the TA/DIC ratio (**Figure 8E**) illustrates the relative buffering capacity of the water, with lower values indicating a reduced buffering capacity. Values along the inner shelf are relatively lower compared to the outer shelf, indicating this reduced buffering capacity. The spatial pattern of the TA/DIC ratio correlates very strongly with the spatial pattern in Ω_{Arag} ($r = 0.996$, **Figure 8F**), illustrating the utility of this ratio in identifying regions of corrosive water conditions. Relatively low phytoplankton productivity on the inner shelf and high productivity on the outer shelf (**Figure 8B**) further contributes to the spatial pattern of this ratio through changes in DIC.

Warm and Cold Regimes

The model hindcast timeframe covers two distinct observed temperature regimes: a period of warm, relatively low sea ice extent years (2003–2005) and a period of cold, relatively high sea ice extent years (2010–2012). Surface water temperatures during the cold regime are generally 1–2°C colder throughout most of the shelf region, and up to 4°C colder along the southeastern middle and outer shelf domains (**Figures 9A–C**). Similarly, sea ice extent is 20–40% greater during the cold regime (**Figures 9D–F**). Primary production increases for the outer shelf and the northwestern shelf, but remains largely unchanged or slightly decreases through most of the inner shelf and for Bristol Bay (**Figures 9G–I**). Surface salinity slightly decreases for the outer and middle shelf, but slightly increases for the inner shelf (**Figures 9J–L**). During the transition from a warm to a cold period, surface Ω_{Arag} decreases by ∼ 0.2 units throughout most of the Bering Sea shelf, with locations south of Nunivak Island and in Bristol Bay decreasing by up to 0.3 units (**Figures 10A–C**). Surface Ω_{Arag} also decreases in the Bering Sea Basin, though to a lesser extent (∼0.1 units) compared to the shelf. Surface DIC increases by 20 mmol/m^3 for most of the shelf, with a smaller increase of 5–10 mmol/m^3 along the shelf break region (**Figures 10D–F**). However, the area around

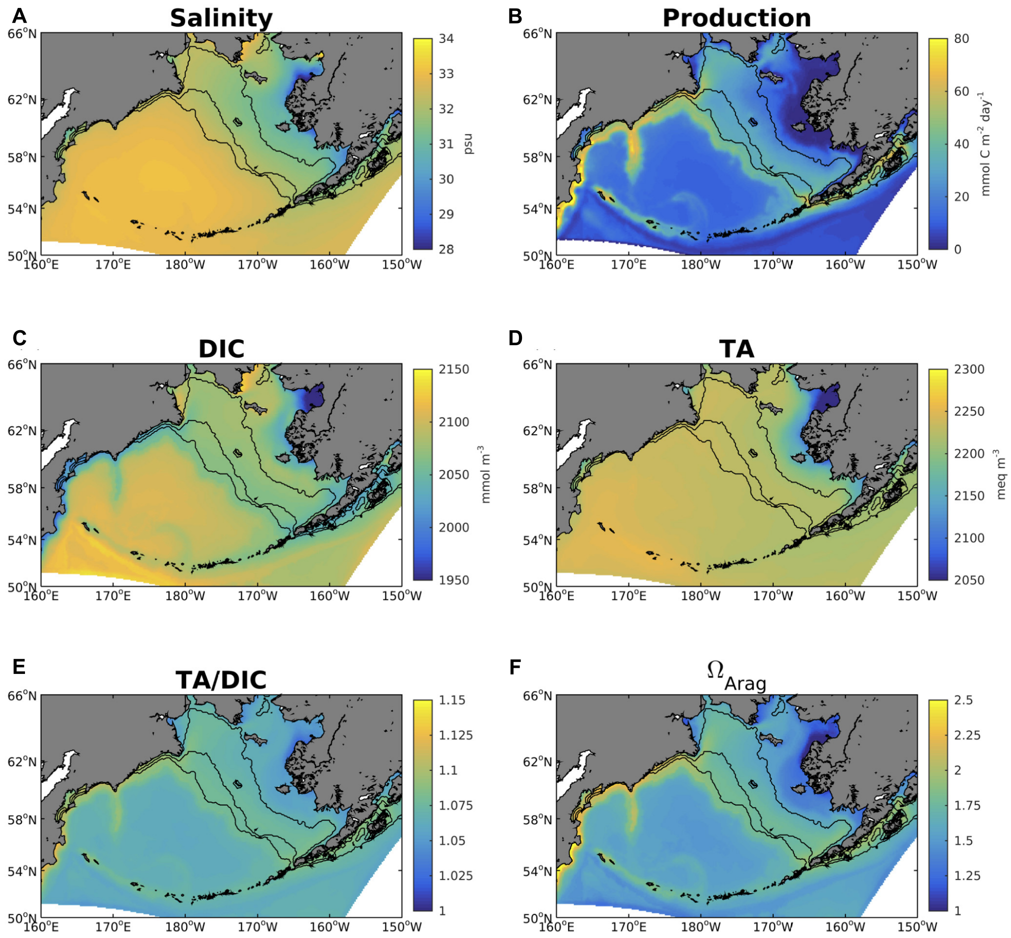

FIGURE 8 | Annual average plots of model **(A)** surface salinity, **(B)** primary production integrated over the top 200 m of the water column, **(C)** surface DIC, **(D)** surface TA, **(E)** surface TA/DIC ratio, and **(F)** surface Ω_{Arag}. All variables are averaged over the 2003–2012 timeframe.

Nunivak Island remains largely unchanged. Surface TA remains relatively unchanged for the middle and outer coastal shelf, but decreases by ~20 meq/m^3 for large portions of the inner shelf near Nunivak Island (**Figures 10G–I**). The change in air-sea CO_2 flux is more spatially heterogeneous than the change in Ω_{Arag} and DIC (**Figures 10J–L**). Following a similar pattern to primary production (**Figures 9G–I**), CO_2 flux becomes more negative (i.e., increased ocean carbon uptake) over the outer and northwestern shelf regions, but more positive over the inner shelf. In particular, the outer shelf region near the Aleutian Island chain transitions from a neutral or weak carbon source to a significant carbon sink. Carbon efflux from the deep Bering Sea basin also decreases, though the region remains a significant carbon source on annual timeframes.

Decadal Trends

Statistically significant trends (p-value < 0.05) of decreasing Ω_{Arag} are evident throughout most of the Bering Sea shelf, with magnitudes ranging from 0.025 – 0.04 units/year (**Figure 11**). These regions also correspond to significant positive trends in DIC of 2.5 – 4.0 mmol/m^3/year. Localized regions of negative trends in TA of −2.5 to −5.0 mmol/m^3/year are also present in the southeastern inner shelf. Trends in pCO_2 and ΔpCO_2 are largely positive along the inner and northwestern middle Bering Sea shelf, but large portions of the outer and southeastern middle shelf display a negative trend, particularly for ΔpCO_2. These areas of significant negative ΔpCO_2 trends correspond to regions of significant negative trends in CO_2 flux, indicating an increase in ocean carbon uptake.

The negative trends in CO_2 flux drive positive trends in surface pCO_2 and DIC, along with a substantial increase in the total carbon uptake of the entire Bering Sea shelf (**Figure 12**). Surface ocean pCO_2 largely follows the estimated, expected increase in ocean pCO_2 based on the air-sea pCO_2 disequilibrium calculated in 2002 and the increase in atmospheric CO_2 over the model hindcast timeframe (**Figure 12A**). We then recalculate DIC using CO2SYS and the ocean pCO_2 values calculated in **Figure 12A** (dashed line), along with model TA, salinity, and temperature (**Figure 12B**). This allows for comparison between the model increase in surface DIC and the expected increase in DIC, calculated from the increase in ocean pCO_2 associated with the increase in atmospheric CO_2. The goal is to understand the extent

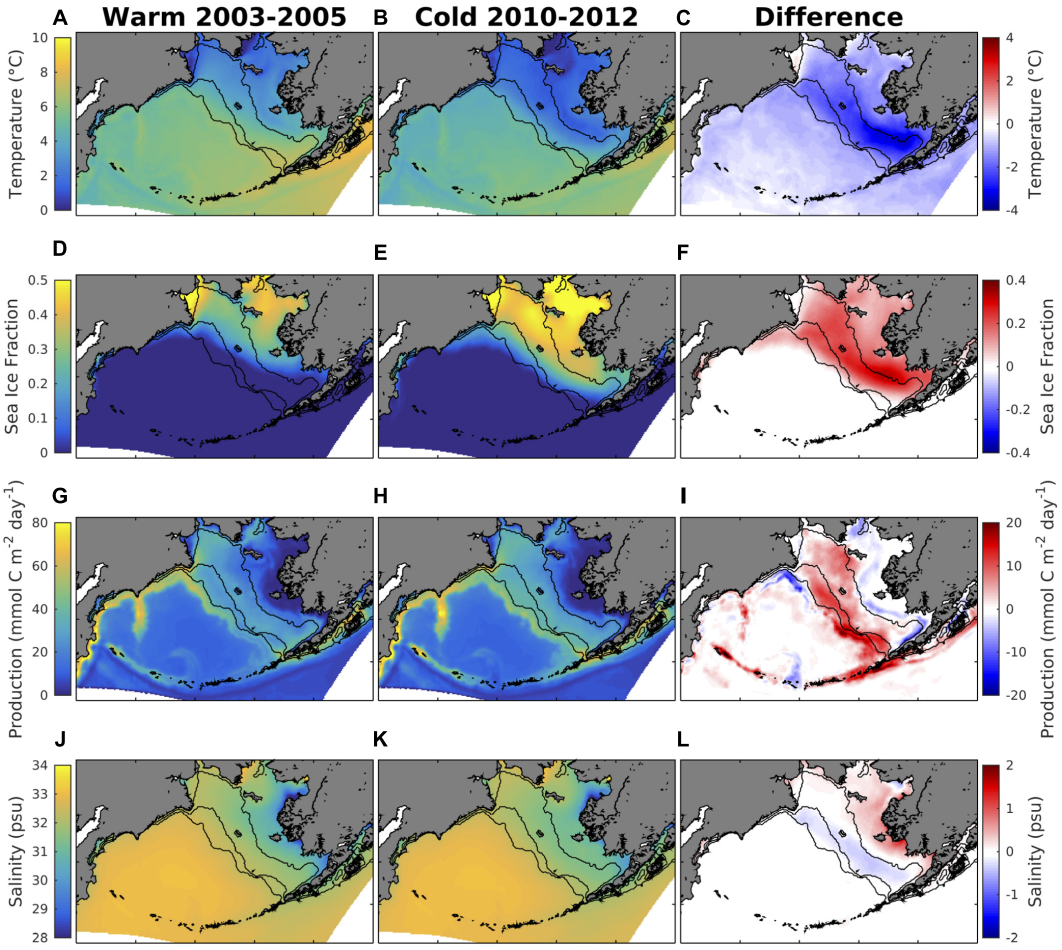

FIGURE 9 | (left) Model annual mean variables averaged over the warm and (middle) cold temperature regimes, and (right) the difference generated by the transition from warm to cold conditions. **(A–C)** Surface temperature, **(D–F)** fraction of grid cell covered by sea ice, **(G–I)** production integrated over the top 200 m of the water column, and **(J–L)** surface salinity.

to which the change in model $p\text{CO}_2$ and DIC is driven by the increase in atmospheric CO_2. **Figure 12B** illustrates that the two values track closely, similar to **Figure 12A**. Shelf annual total carbon uptake increases from 15.9 TgC/year in 2003 to 26.3 TgC/year in 2012, and total benthic carbon increases slightly from 2.61 TgC in 2003 to 2.78 TgC in 2012 (**Figures 12D,E**). Surface Ω_{Arag} decreases from 1.7 to 1.5, while bottom Ω_{Arag} decreases from 1.2 to 1.1. Thus, the decrease at the surface is approximately twice as great as the decrease at the bottom.

DISCUSSION

The model simulates significant spatial variability in carbonate chemistry on the Bering Sea shelf, resulting from local biogeochemical processes. The inner shelf region contains low values of Ω_{Arag}, with some areas near the Yukon Delta and Norton Sound experiencing nearly year-round $\Omega_{\text{Arag}} < 1$ conditions. These corrosive water conditions result from river inputs of terrestrial carbon from the Yukon River combined with low coastal productivity, which both drive a reduced TA/DIC ratio. Previous studies using shipboard data have also noted relatively low productivity and Ω_{Arag} waters along the inner shelf (Mathis et al., 2011; Cross et al., 2014), though the corrosive conditions in Norton Sound are difficult to verify due to a lack of data. Norton Sound contains a relatively small red king crab fishery, but the life cycle of these crab is largely unknown (Norton Sound Economic Development Corporation [NSEDC], 2016). The sound may therefore be a natural analog to future OA conditions and an ideal location for experimental testing on the impacts of OA on red king crab growth, survival, and adaptability. However, observational data are first needed to verify these corrosive water conditions.

In contrast to the inner shelf, the middle and outer shelf regions have greater values of Ω_{Arag}, particularly during the summer and fall, due to substantial productivity and minimal influence of freshwater runoff. While this productivity boosts Ω_{Arag} in surface waters, carbon remineralization at depth generates bottom water Ω_{Arag} values close to 1. This result is supported by observational evidence (Mathis et al., 2014) and is

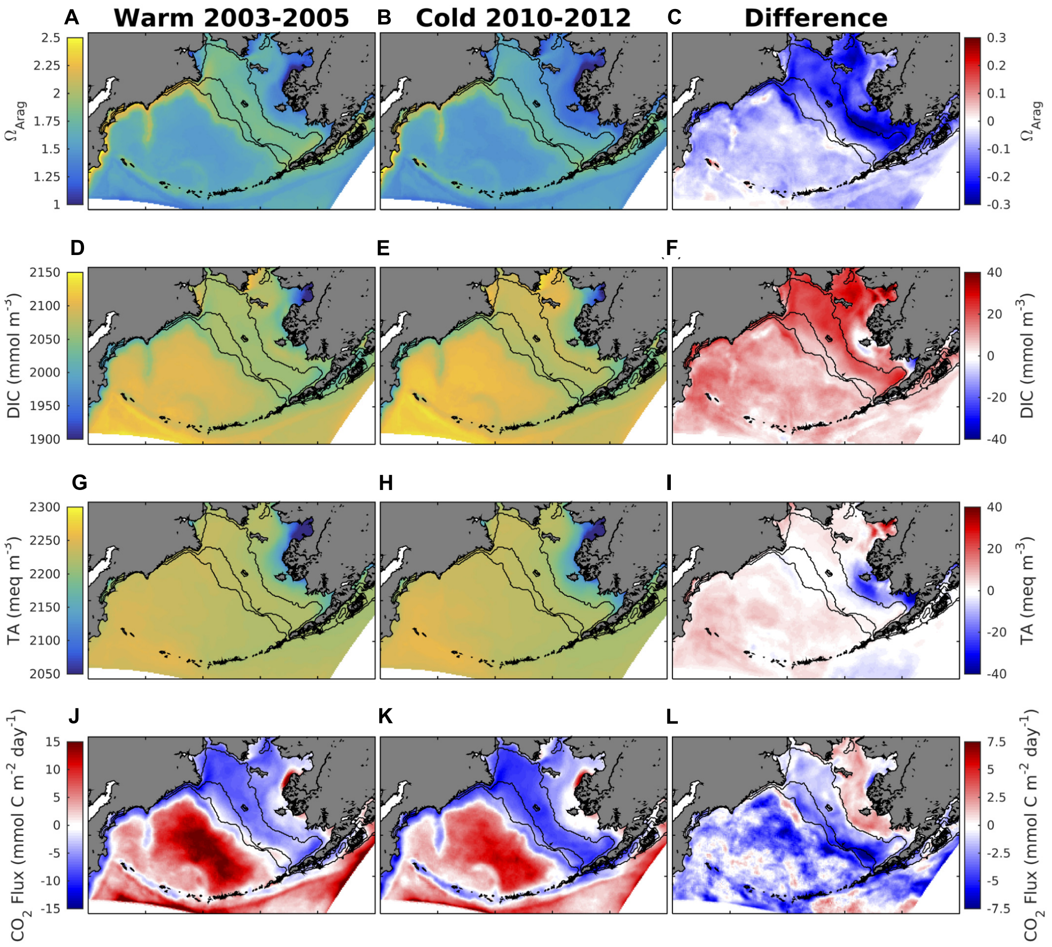

FIGURE 10 | (left) Model annual mean variables averaged over the warm and (middle) cold temperature regimes, and (right) the difference generated by the transition from warm to cold conditions. **(A–C)** Surface Ω_{Arag}, **(D–F)** surface DIC, **(G–I)** surface TA, and **(J–L)** air-sea CO_2 flux (where a positive value indicates a flux out of the ocean).

noteworthy because the region is home to substantial tanner and red king crab fisheries, which are negatively impacted at Ω_{Arag} values less than 1 (Long et al., 2013; Mathis et al., 2015a; Long et al., 2016). Furthermore, while summer and fall surface Ω_{Arag} is highly saturated due to productivity, winter and early spring values are much lower at 1.0–1.5. Thus, while productivity may buffer Ω_{Arag} against OA during the summer and fall, biological organisms are still highly vulnerable to winter and early spring conditions as Ω_{Arag} values are already near 1.

Modeled total annual carbon uptake for the Bering Sea shelf is 15–25 TgC/year, which is within the 2–67 TgC/year range of previous estimates, but is significantly greater than the most recent estimate of 6.8 TgC/year (Cross et al., 2014). This difference between the latter estimate and the model results from substantially greater modeled carbon uptake in fall. Cross et al. (2014) report average CO_2 flux values of −5.0 and −0.48 mmolC/m^2/day in September and October respectively, whereas model average flux values are between −10 and −15 mmolC/m^2/day for these months. These higher magnitude model flux values are caused by a fall phytoplankton bloom, generated by vertical mixing of nutrients under still-optimal light and temperature conditions (**Figure 13**). Similar fall blooms are observed on the eastern Bering Sea shelf (Sigler et al., 2014) and reproduced in other biogeochemical models (Cheng et al., 2016), but their prevalence has received less attention compared to the spring bloom. This fall biological drawdown is not apparent to the same extent in the Cross et al. (2014) analysis, though they still calculate a pCO_2 drawdown of 50–100 µatm in September and October due to biological productivity. The data are also sparser in September and October compared to the spring and summer months, primarily consisting of a north-south transect line from the Aleutian Islands to the Bering Strait. In this transect, relatively larger ΔpCO_2 of ∼150 µatm are located on the outer and middle shelf region south of Nunivak Island, similar to the region of enhanced model primary productivity. It is possible that the finer spatial and temporal resolution of the model is capturing this fall productivity signal that is largely absent in the observed pCO_2 data, though the model is also likely biased considering the stronger magnitude fall bloom (Ortiz et al., 2016).

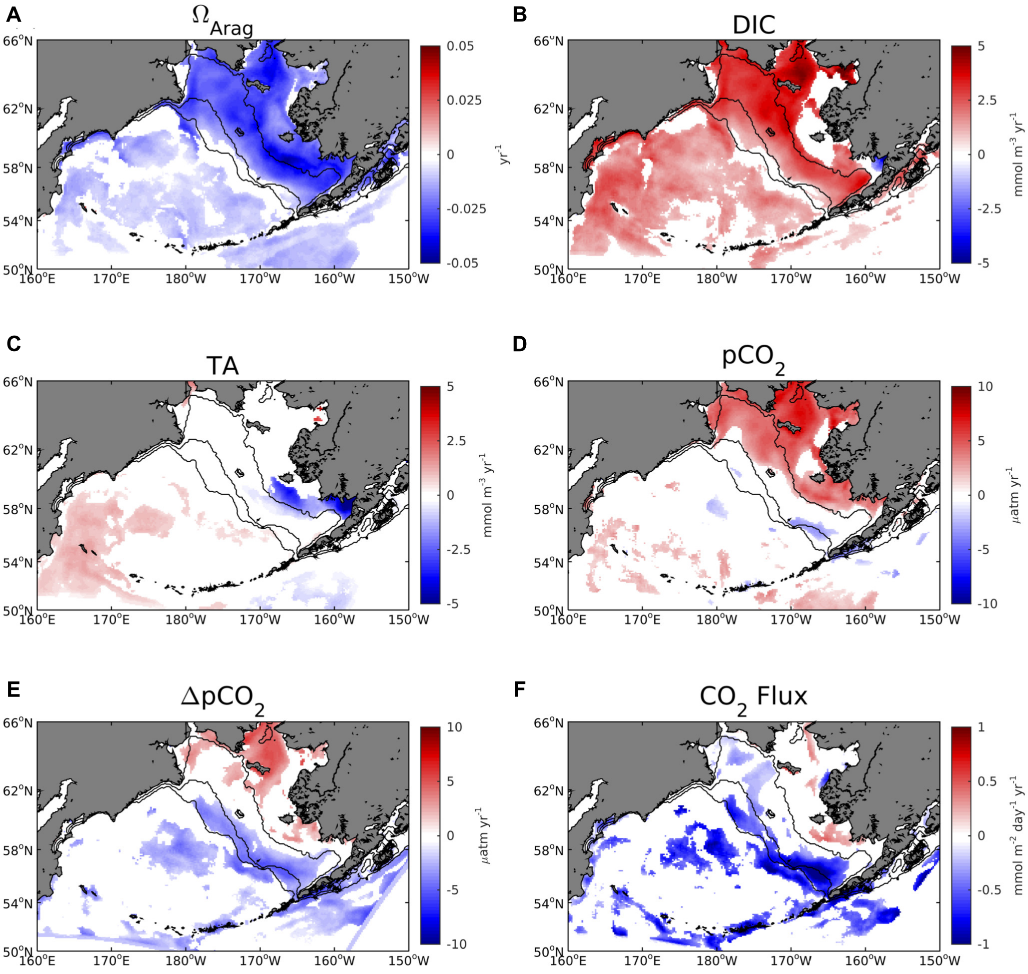

FIGURE 11 | Linear trends in annual average surface model **(A)** Ω_{Arag}, **(B)** DIC, **(C)** TA, **(D)** pCO_2, **(E)** ΔpCO_2, and **(F)** air-sea CO_2 flux. Linear trends are calculated using the 2003–2012 timeframe. Only trend values that are significant at the 95% confidence level are displayed.

The strengthening of this fall phytoplankton bloom is also the primary mechanism behind the ~10 TgC/year increase in total carbon uptake from 2003 to 2012. This is a substantial increase in total carbon uptake over only a 10-year timeframe, though we note that this change equates to approximately one-sixth of the total variability between the various observationally based estimates for Bering Sea shelf carbon uptake. Comparing **Figures 9**, **10** illustrates that the increase in carbon uptake is co-located with the increase in primary production in outer shelf regions. Colder water temperatures will also decrease pCO_2 values which can generate enhanced ocean carbon uptake by enhancing negative ΔpCO_2 values. Indeed, the regions of greatest increasing carbon uptake (i.e., the southeastern outer shelf) are located where both mechanisms (i.e., increased productivity and colder temperatures) are present. Though there is a slight decreasing trend in annual wind speed (~0.05 m/s/year) through large portions of the coastal shelf, the trend is not statistically significant. The substantial increase in ice cover during the cold period can also impact shelf carbon uptake by further inhibiting air-sea exchange and by meltwater dilution of surface DIC and TA concentrations. The latter mechanism is evident by the freshening of the outer shelf waters during the cold period (**Figure 9L**), though the effect is not as apparent with DIC and TA. Implementing mechanistic connections between sea ice formation/melt and DIC and TA concentrations (e.g., Rysgaard et al., 2012) that are currently not included in our model may help resolve this connection for future work.

Previous studies have noted significant variability in temperature and sea ice extent between the 2003–2005 and 2010–2012 timeframes, which likely impacted the marine ecosystem (Stabeno et al., 2012). There is considerable debate regarding whether warmer water temperatures and reduced sea ice extent will increase or decrease primary productivity (Lomas et al., 2012; Brown and Arrigo, 2013; Eisner et al., 2014; Banas et al., 2016; Liu et al., 2016). In the Bering Sea, warmer years have been tied to reduced large copepod and euphausiid populations and subsequent weaker summer/fall lipid content and survival of age-0 walleye Pollock and Pacific cod recruits, which consume the copepods and euphausiids (Hunt et al., 2011; Mueter et al., 2011; Stabeno et al., 2012). However, this response

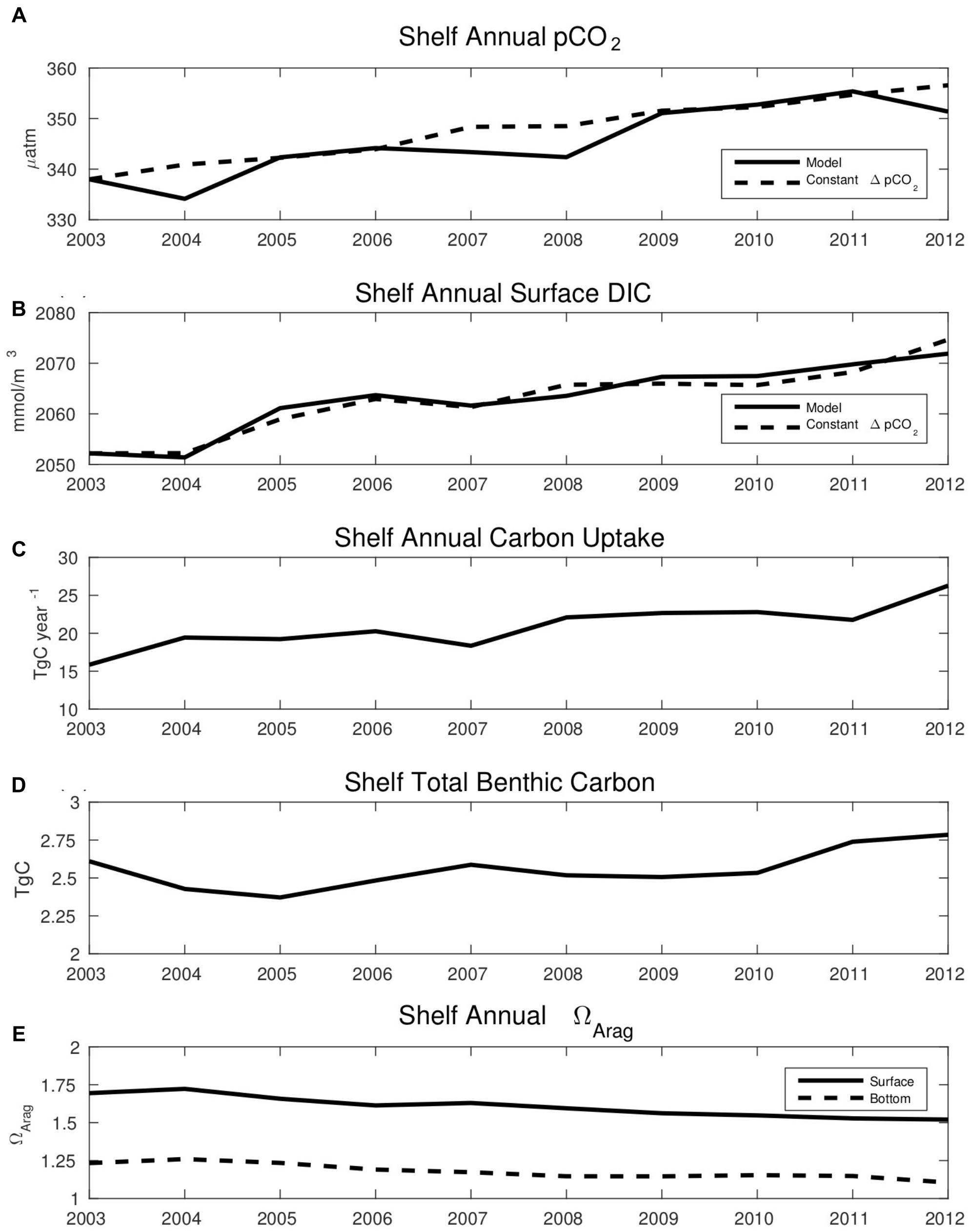

FIGURE 12 | Time series plots of annual average model **(A)** surface ocean $p\mathrm{CO}_2$ and **(B)** surface DIC. The dashed line in **(A)** represents the expected increase in surface ocean $p\mathrm{CO}_2$ based on the model air-sea $p\mathrm{CO}_2$ disequilibrium in 2003, combined with the yearly increase in atmospheric CO_2. The dashed line in **(B)** represents the excepted increase in surface ocean DIC, calculated from the expected surface $p\mathrm{CO}_2$ values shown in the dashed line of **(A)**, and the model values of total alkalinity, salinity, and temperature. **(C)** Total ocean carbon uptake and **(D)** total benthic carbon over the entire Bering Sea shelf. **(E)** Annual average values of surface Ω_{Arag} (solid line) and bottom water Ω_{Arag} (dashed line).

is thought to be tied specifically to the strength of the spring diatom bloom supporting spring zooplankton populations (e.g., copepods and euphausiids) as opposed to annual net productivity. Our model results suggest that warmer years are less productive overall, though with slightly more productivity on the inner shelf. A similar response with zooplankton (i.e., warmer temperatures generating less zooplankton overall, but slightly more on inner shelf) was noted by Hermann et al. (2016) in climate change projections out to 2040 using the Bering10K model. Thus, we expect that the modeled increase in primary productivity from 2003 to 2012 is temporary and will revert to lower values with the return of warm conditions and future warming.

For this study, our primary interest in productivity stems from the biogeochemical connection to the carbonate system. An increase in productivity and carbon export can decrease surface

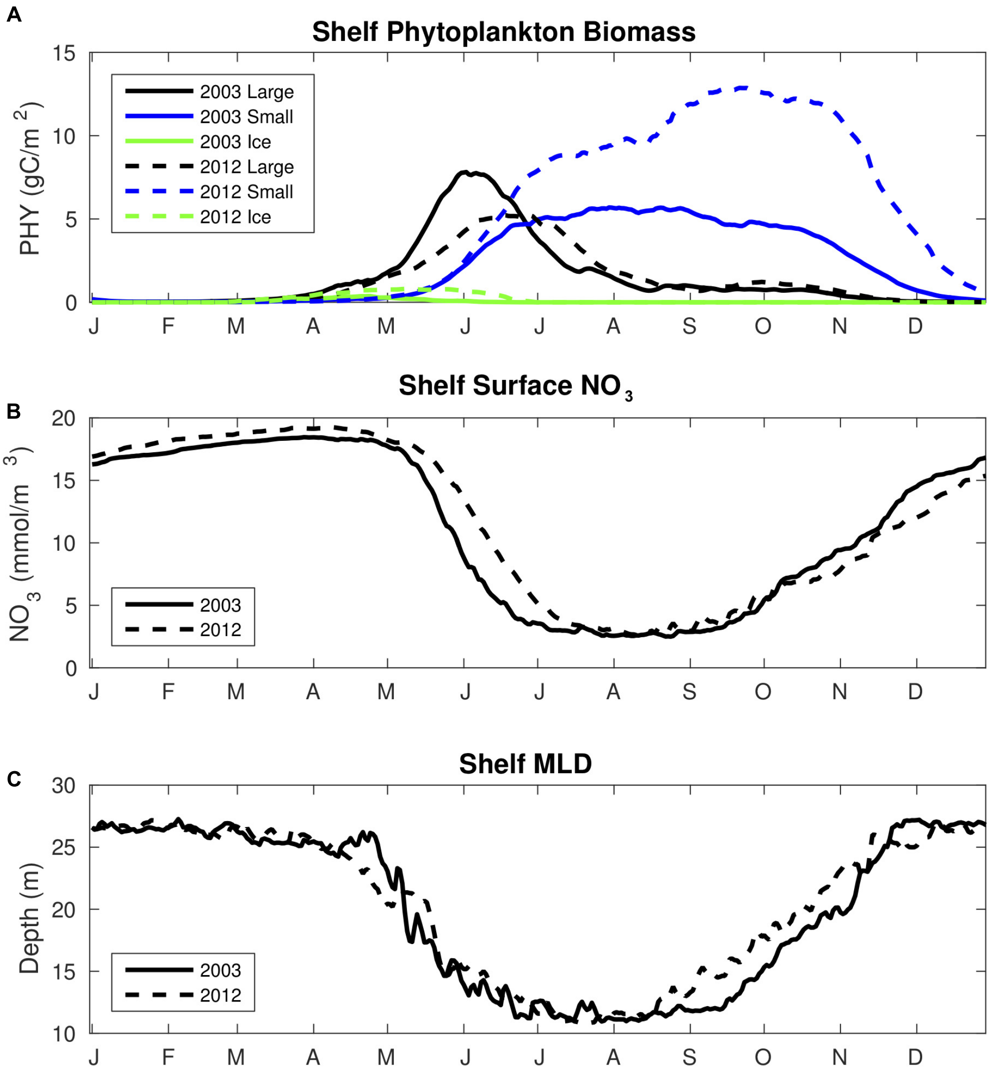

FIGURE 13 | Time series plots of area-weighted spatial mean **(A)** 30 m column integrated phytoplankton biomass, **(B)** surface NO_3^-, and **(C)** mixed layer depth for model year 2003 and 2012. Phytoplankton biomass is divided into the large phytoplankton (black line), small phytoplankton (blue line), and ice algae (green line) functional groups.

DIC concentrations, and thereby mask the expected increase in surface DIC and corresponding decrease in Ω_{Arag} due to OA. However, shelf DIC increases at a rate similar to that expected due to increasing atmospheric CO_2 (**Figure 12**). This increase in DIC accounts for the rapid decrease in Ω_{Arag}, but it is perhaps less intuitive as to why the DIC is increasing at a rate comparable to the expected rate from increasing atmospheric CO_2, despite the increase in productivity. This discrepancy results from the composition (i.e., small phytoplankton) and fall timing of the increase in productivity. For instance, the cold period drives enhanced negative ΔpCO_2 values in fall due to colder water temperature and increased productivity. However, this productivity is in the form of small phytoplankton, which have a significantly slower sinking rate compared to large phytoplankton (0.05 m/day vs. 1.0 m/day, respectively). Thus, this organic carbon is not permanently buried (**Figure 12D**), but rather remineralized back to DIC during the winter and retained in the water column due to ice inhibition of air-sea exchange. This process combined with the increase in atmospheric CO_2 results in a net annual increase in DIC, despite the increased productivity.

It is possible that the model is overestimating the trend in productivity and thereby shelf carbon uptake, which would exacerbate the previously described mechanism. Ortiz et al. (2016) noted that model fall productivity is likely biased high, particularly due to strong small phytoplankton blooms. These fall blooms are further enhanced during the cold period, due to relatively deeper mixed layer depths and enhanced vertical transport of sub-surface nitrate. The colder period is also defined by a comparatively weaker spring diatom bloom, leaving more nitrate in the summer surface layer for small phytoplankton (**Figure 13**). Model surface DIC does not contain a significant bias though, suggesting a reasonable seasonal biological drawdown of carbon. Surface NO_3^- is the only model variable that displays much greater variability compared to the observations (**Figure 3**), though model NO_3^- is also biased somewhat high compared to the observations, which is not what we would expect if model productivity is biased high. Ammonium inhibition of nitrate uptake could also lead to the higher nitrate concentrations, though this process is modeled to prevent the complete limitation of nitrate uptake at high ammonium concentrations (Gibson and Spitz, 2011).

Over the 10-year model hindcast, statistically significant increasing trends in surface ocean DIC and $p\mathrm{CO}_2$, along with a decreasing trend in Ω_{Arag} are apparent throughout most of the Bering Sea shelf. These are the long-term changes expected due to OA. That these trends emerge within a 10-year timeframe is surprising considering the highly variable coastal setting and substantial temperature variability. The transition from warm to cold water conditions acts to *decrease* surface ocean $p\mathrm{CO}_2$ values, due to increased gas solubility and primary production. Yet, surface ocean $p\mathrm{CO}_2$ values largely increase at a rate comparable to that expected due to increasing atmospheric CO_2 (**Figures 11**, **12**). For $p\mathrm{CO}_2$, the temperature driven signal and the atmospheric CO_2 driven signal act in opposition. Conversely, both colder water temperatures and increasing atmospheric CO_2 act to *decrease* Ω_{Arag} values. For Ω_{Arag}, the transition from a warm to cold regime acts to accelerate the decreasing trend. Comparing **Figures 9C**, **10C** illustrates that the region of greatest temperature decrease in the southeastern middle shelf corresponds to the region of greatest Ω_{Arag} decrease. However, warm conditions returned to the Bering Sea starting in 2014 (Duffy-Anderson et al., 2017), thus this mechanism likely did not continue.

The Community Earth System Model (CESM) projects that, under RCP 8.5, annual average surface Ω_{Arag} will decrease by an additional 0.70 units by the end of the century and reach the saturation threshold (i.e., $\Omega_{\mathrm{Arag}} < 1$) by 2062 (Mathis et al., 2015a). If extrapolated forward in time, our model results suggest a faster timeline, with annual average Ω_{Arag} values < 1 by 2040. However, this estimate is highly uncertain due to the simplistic extrapolation method and likely biased by significant variability encapsulated within our model timeframe. Furthermore, observed and modeled spatial variability suggests that this timeframe may vary by up to several decades between different shelf regions. Future work will utilize ESM output to dynamically downscale OA projections using the Bering10K model (Hermann et al., 2016; Wallhead et al., 2017). This method will reduce the uncertainty of these critical threshold years and provide information on their spatial variance throughout the Bering Sea.

CONCLUSION

We use a regional model of the Bering Sea to illustrate how coastal biogeochemical processes and climate variability impact aragonite saturation state over a 10-year timeframe. Freshwater runoff from the Yukon River reduces surface Ω_{Arag} values to < 1 from December-May along the inner shelf region, particularly in Norton Sound. Conversely, substantial primary productivity increases Ω_{Arag} values to >2 along the outer shelf and shelf break regions, though Ω_{Arag} still decreases to ~ 1.5 during winter months. A shift from relatively warm, low sea ice conditions (2003–2005) to relatively cold, high sea ice conditions (2010–2012) produces a significant increase in fall productivity and ocean carbon uptake throughout the outer shelf region. Surface DIC increases at a rate of 2.5–4.0 mmol/m^3/year and surface Ω_{Arag} decreases at a rate of 0.025 – 0.04 units/year. These trends are statistically significant throughout most of the middle and inner shelf domains, though they are likely enhanced by the transition from the warm to cold period. Nonetheless, these trends are relatively greater than those observed for the open ocean, illustrating how high-latitude coastal shelf regions serve as hotspots of global change. Future work will utilize statistical downscaling to project these changes through 2100 in order to determine critical threshold years for persistent annual Ω_{Arag} undersaturation and variability in this projected change between the inner and outer shelf regions.

AUTHOR CONTRIBUTIONS

DP and JM conceived the project. DP and DN were responsible for the model simulations, analysis, and producing the manuscript figures. JC provided the observational data. AH provided the model forcing fields. AH, SS, and GG provided guidance and support for model development. DP wrote the first draft of the manuscript. All authors provided feedback and contributed to the final manuscript.

FUNDING

Part of this research was performed while DP held a National Research Council Research Associateship award at the Pacific Marine Environmental Laboratory. Funding was provided by the NOAA Arctic Research Program and through the Joint Institute for the Study of the Atmosphere and Ocean (JISAO) NOAA Cooperative Agreement NA15OAR4320063 (2015–2020). Funding for DN was provided by the NOAA Hollings Scholarship Program. This is PMEL contribution number 4802 and JISAO contribution number 2018-0158. Model output data supporting the conclusions of this manuscript will be made available by the authors, without undue reservation, to any qualified researcher.

ACKNOWLEDGMENTS

We would like to acknowledge high-performance computing support from Yellowstone (ark:/85065/d7wd3xhc) provided by NCAR's Computational and Information Systems Laboratory, sponsored by the National Science Foundation. Use of the Yellowstone system was provided by a postdoctoral allocation for DP.

REFERENCES

Banas, N. S., Zhang, J., Campbell, R. G., Sambrotto, R. N., Lomas, M. W., Sherr, E., et al. (2016). Spring plankton dynamics in the Eastern Bering Sea, 1971-2050: mechanisms of interannual variability diagnosed with a numerical model. *J. Geophys. Res. Oceans.* 121, 1476–1501. doi: 10.1002/2015JC011449

Barton, A., Hales, B., Waldbusser, G. G., Langdon, C., and Feely, R. A. (2012). The *Pacific oyster*, *Crassostrea gigas*, shows negative correlation to naturally elevated carbon dioxide levels: implications for near-term ocean acidification effects. *Limnol. Oceanogr.* 57, 698–710. doi: 10.4319/lo.2012.57.3.0698

Bates, N. R., Mathis, J. T., and Jeffries, M. A. (2011). Air-sea CO_2 fluxes on the bering sea shelf. *Biogeoscience* 8, 1237–1253. doi: 10.5194/bg-8-1237-2011

Bednarsek, N., Tarling, G. A., Bakker, D. C. E., Fielding, S., Jones, E. M., Venables, H. J., et al. (2012). Extensive dissolution of live pteropods in the Southern Ocean. *Nat. Geosci.* 5, 881–885. doi: 10.1038/NGEO1635

Brewer, P. G., and Goldman, J. C. (1976). Alkalinity changes generated by phytoplankton growth. *Limnol. Oceanogr.* 21, 108–117. doi: 10.4319/lo.1976.21.1.0108

Brown, Z. W., and Arrigo, K. R. (2013). Sea ice impacts on spring bloom dynamics and net primary production in the Eastern Bering Sea. *J. Geophys. Res. Oceans* 118, 43–62. doi: 10.1029/2012JC008034

Budgell, W. P. (2005). Numerical simulation of ice-ocean variability in the Barents Sea region: towards dynamical downscaling. *Ocean Dyn.* 55, 370–387. doi: 10.1007/s10236-005-0008-3

Carstensen, J., Chierici, M., Gustaffson, B. G., and Gustafsson, E. (2018). Long-term and seasonal trends in estuarine and coastal carbonate systems. *Global Biogeochm. Cycles* 32, 497–513. doi: 10.1002/2017GB005781

Chavez, F. P., Pennington, J. T., Michisaki, R. P., Blum, M., Chavez, G. M., Friederich, J., et al. (2017). Climate variability and change: response of a coastal ocean ecosystem. *Oceanography* 30, 128–145. doi: 10.5670/oceanog.2017.429

Cheng, W., Curchitser, E., Stock, C., Hermann, A., Cokelet, E., Mordy, C., et al. (2016). What processes contribute to the spring and fall bloom co-variability on the Eastern Bering Sea shelf? *Deep-Sea Res. II* 134, 128–140. doi: 10.1016/j.dsr2.2015.07.009

Cross, J. N., Mathis, J. T., and Bates, N. R. (2012). Hydrographic controls on net community production and total organic carbon distributions in the eastern Bering Sea. *Deep-Sea Res. II* 6, 98–109. doi: 10.1016/j.dsr2.2012.02.003

Cross, J. N., Mathis, J. T., Bates, N. R., and Byrne, R. H. (2013). Conservative and non-conservative variations of total alkalinity on the southeastern Bering Sea shelf. *Mar. Chem.* 154, 110–112. doi: 10.1016/j.marchem.2013.05.012

Cross, J. N., Mathis, J. T., Lomas, M. W., Moran, S. B., Baumann, M. S., Shull, D. H., et al. (2014). Integrated assessment of the carbon budget in the southeastern Bering Sea. *Deep-Sea Res. II* 109, 112–124. doi: 10.1016/j.dsr2.2014.03.003

Dai, A., Qian, T., Trenberth, K. E., and Milliman, J. D. (2009). Changes in continental freshwater discharge from 1948-2004. *J. Climate* 22, 2773–2791. doi: 10.1175/2008JCLI2592.1

Danielson, S. L., Curchitser, E. N., Hedstrom, K. S., Weingartner, T. J., and Stabeno, P. J. (2011). On ocean and sea ice modes of variability in the Bering Sea. *J. Geophys. Res.* 116:C12034. doi: 10.1029/2011JC007389

Doney, S. C., Fabry, V. J., Feely, R. A., and Kleypas, J. A. (2009). Ocean acidification: the other CO_2 problem. *Annu. Rev. Mar. Sci.* 1, 169–192. doi: 10.1146/annurev.marine.010908.163834

Duarte, C. M., Hendriks, I. E., Moore, T. S., Olsen, Y. S., Steckbauer, A., Ramajo, L., et al. (2013). Is ocean acidification an open-ocean syndrome? Understanding anthropogenic impacts on seawater pH. *Estuaries Coasts* 36, 221–236. doi: 10.1007/s12237-013-9594-3

Duffy-Anderson, J. T., Stabeno, P. J., Siddon, E. C., Andrews, A. G., Cooper, D. W., Eisner, L. B., et al. (2017). Return of warm conditions in the southeastern bering sea: phytoplankton – Fish. *PLoS One* 12:e0178955. doi: 10.1371/journal.pone.0178955

Eisner, L. B., Napp, J. M., Mier, K. L., Pinchuk, A. I., and Andrews, A. G. III. (2014). Climate-mediated changes in zooplankton community structure for the eastern Bering Sea. *Deep Sea Res. Part II Top. Stud. Oceanogr.* 109, 157–171. doi: 10.1016/j.dsr2.2014.03.004

Evans, W., Mathis, J. T., and Cross, J. N. (2014). Calcium carbonate corrosivity in an Alaskan inland sea. *Biogeoscience* 11, 365–379. doi: 10.5194/bg-11-365-2014

Fabry, V. J., McClintock, J. B., Mathis, J. T., and Grebmeier, J. M. (2009). Ocean acidification at high latitudes: the bellwether. *Oceanography* 22, 160–171.

Feely, R. A., Sabine, C. L., Hernandez-Ayon, J. M., Ianson, D., and Hales, B. (2008). Evidence for upwelling of corrosive "acidified" water onto the continental shelf. *Science* 320, 1490–1492. doi: 10.1126/science.1155676

Fennel, K., Wilkin, J., Previdi, M., and Najjar, R. (2008). Denitrification effects on air-sea CO_2 flux in the coastal ocean: simulations for the northwest North Atlantic. *Geophys. Res. Lett.* 35:L24608. doi: 10.1029/2008GL036147

Gibson, G. A., and Spitz, Y. H. (2011). Impacts of biological parameterization, initial conditions, and environmental forcing on parameter sensitivity and uncertainty in a marine ecosystem model for the Bering Sea. *J. Mar. Sys.* 88, 214–231. doi: 10.1016/j.jmarsys.2011.04.008

Goldman, J. C., and Brewer, P. G. (1980). Effect of nitrogen source and growth rate on phytoplankton-mediated changes in alkalinity. *Limnol. Oceanogr.* 25, 352–357.

Haidvogel, D. B., Arango, H., Budgell, W. P., Cornuelle, B. D., Curchitser, E., Di Lorenzo, E., et al. (2008). Ocean forecasting in terrain-following coordinates: formulation and skill assessment of the Regional Ocean Modeling System. *J. Comput. Phys.* 227:3624. doi: 10.1016/j.jcp.2007.06.016

Heintz, R. A., Siddon, E. C., Farley, E. V. Jr., and Napp, J. M. (2013). Correlation between recruitment and fall condition of age-0 pollock (*Theragra chalcogramma*) from the eastern Bering Sea under varying climate conditions. *Deep-Sea Res. II* 94, 150–156. doi: 10.1016/j.dsr2.2013.04.006

Hermann, A. J., Gibson, G. A., Bond, N. A., Curchitser, E. N., Hedstrom, K., Cheng, W., et al. (2013). A multivariate analysis of observed and modeled biophysical variability on the Bering Sea shelf: *Multidecadal hindcasts* (1970-2009) and forecasts (2010-2040). *Deep-Sea Res. II* 94, 121–139. doi: 10.1016/j.dsr2.2013.04.007

Hermann, A. J., Gibson, G. A., Bond, N. A., Curchitser, E. N., Hedstrom, K., Cheng, W., et al. (2016). Projected future biophysical states of the Bering Sea. *Deep-Sea Res. II* 134, 30–47. doi: 10.1016/j.dsr2.2015.11.001

Hunt, G. L. Jr., Coyle, K. O., Eisner, L. B., Farley, E. V., Heintz, R. A., et al. (2011). Climate impacts on eastern Bering Sea foodwebs: a synthesis of new data and an assessment of the Oscillating Control Hypothesis. *ICES J. Mar. Sci.* 68, 1230–1243. doi: 10.1093/icesjms/fsr036

Hurst, T. P., Fernandex, E. R., and Mathis, J. T. (2013). Effects of ocean acidification on hatch size and larval growth of walleye Pollock (*Theragra chalcogramma*). *ICES J. Mar. Sci.* 70, 812–822. doi: 10.1093/icesjms/fst053

Hurst, T. P., Fernandez, E. R., Mathis, J. T., Miller, J. A., Stinson, C. M., and Ahgeak, E. F. (2012). Resiliency of juvenile walleye Pollock to projected levels of ocean acidification. *Aquat. Biol.* 17, 247–259. doi: 10.3354/ab00483

Jolliff, J. K., Kindle, J. C., Shulman, I., Penta, B., Friedrichs, M. A. M., Helber, R., et al. (2009). Summary diagrams for coupled hydrodynamic-ecosystem model skill assessment. *J. Mar. Syst.* 76, 64–82. doi: 10.1016/j.jmarsys.2008.05.014

Khatiwala, S., Primeau, F., and Hall, T. (2009). Reconstruction of the history of anthropogenic CO_2 concentrations in the ocean. *Nature* 462, 346–349. doi: 10.1038/nature08526

Kroeker, K. J., Kordas, R. L., Crim, R., Hendriks, I. E., Ramajo, L., Singh, G. S., et al. (2013). Impacts of ocean acidification on marine organisms: quantifying sensitivities and interaction with warming. *Glob. Change Biol.* 19, 1884–1896. doi: 10.1111/gcb.12179

Laruelle, G. G., Cai, W.-J., Hu, Z., Gruber, N., Mackenzie, F. T., and Regnier, P. (2018). Continental shelves as a variable but increasing global sink of atmospheric carbon dioxide. *Nat. Comm.* 9:454. doi: 10.1038/s41467-017-02738-z

Lewis, E. R., and Wallace, D. W. R. (1998). *Program Developed for* CO_2 *System Calculations. Rep. BNL-61827*. Oak Ridger, TN: U.S. Dep. of Energy, Oak Ridge Natl. Lab., Carbon Dioxide Inf. Anal. Cent.

Liu, C. L., Zhai, L., Zeeman, S. I., Eisner, L. B., Gann, J. C., Mordy, C. W., et al. (2016). Seasonal and geographic variations in modeled primary production and phytoplankton losses from the mixed layer between warm and cold years on the eastern Bering Sea shelf. *Deep-Sea Res. II* 134, 141–156. doi: 10.1016/j.dsr2.2016.07.008

Lomas, M. W., Moran, S. B., Casey, J. R., Bell, D. W., Tiahlo, M., Whitefield, J., et al. (2012). Spatial and seasonal variability of primary production on the Eastern Bering Sea shelf. *Deep-Sea Res. II* 65–70, 126–140. doi: 10.1016/j.dsr2.2012.02.010

Long, W. C., Swiney, K. M., and Foy, R. J. (2016). Effects of high pCO_2 on Tanner crab reproduction and early life history, Part II: carryover effects on larvae from oogenesis and embryogenesis are stronger than direct effects. *ICES J. Mar. Sci.* 73, 836–848. doi: 10.1093/icesjms/fsv251

Long, W. C., Swiney, K. M., Harris, C., Page, H. N., and Foy, R. J. (2013). Effects of ocean acidification on juvenile red king crab (*Paralithodes camtschaticus*) and tanner crab (*Chionoecetes bairdi*) Growth, condition, calcification, and survival. *PLoS One* 8:e60959. doi: 10.1371/journal.pone.0060959

Mathis, J. T., Cooley, S. R., Lucey, N., Colt, S., Ekstrom, J., Hurst, T., et al. (2015a). Ocean acidification risk assessment for Alaska's fishery sector. *Prog. Oceanogr.* 136, 71–91. doi: 10.1016/j.pocean.2014.07.001

Mathis, J. T., Cross, J. N., Evans, W., and Doney, S. C. (2015b). Ocean acidification in the surface waters of the Pacific-Arctic boundary regions. *Oceanography* 28, 122–135. doi: 10.5670/oceanog.2015.36

Mathis, J. T., Cross, J. N., and Bates, N. R. (2011). Coupling primary production and terrestrial runoff to ocean acidification and carbonate mineral suppression in the eastern Bering Sea. *J. Geophys. Res.* 116:C02030. doi: 10.1029/2010JC006453

Mathis, J. T., Cross, J. N., Bates, N. R., Moran, S. B., Lomas, M. W., Mordy, C. W., et al. (2010). Seasonal distribution of dissolved inorganic carbon and net community production on the Bering Sea shelf. *Biogeoscience* 7, 1769–1787. doi: 10.5194/bg-7-1769-2010

Mathis, J. T., Cross, J. N., Monacci, N., Feely, R. A., and Stabeno, P. (2014). Evidence of prolonged aragonite undersaturations in the bottom waters of the southern Bering Sea shelf from autonomous sensors. *Deep-Sea Res. II* 109, 125–133. doi: 10.1016/j.dsr2.2013.07.019

Moreau, S., Vancoppenolle, M., Delille, B., Tison, J.-L., Zhou, J., Kotovitch, M., et al. (2014). Drivers of inorganic carbon dynamics in first-year sea ice: a model study. *J. Geophys. Res. Oceans* 120, 2121–2128. doi: 10.1002/2014JC010388

Mueter, F. J., Bond, N. A., Ianelli, J. N., and Hollowed, A. B. (2011). Expected declines in recruitment of walleye Pollock (*Theragra chalcogramma*) in the eastern Bering Sea under future climate change. *ICES J. Mar. Sci.* 68, 1284–1296. doi: 10.1093/icesjms/fsr022

Norton Sound Economic Development Corporation [NSEDC] (2016). *Annual Report 2016*. Anchorage, AK: Norton Sound Economic Development Corporation.

Orr, J. C., Fabry, V. J., Aumont, O., Bopp, L., Doney, S. C., Feely, R. A., et al. (2005). Anthropogenic ocean acidification over the twenty-first century and its impact on calcifying organisms. *Nature* 437, 681–686. doi: 10.1038/nature04095

Ortiz, I., Aydin, K., Hermann, A. J., Gibson, G. A., Punt, A. E., Wiese, F. K., et al. (2016). Climate to fish: synthesizing field work, data and models in a 39-year retrospective analysis of seasonal processes on the eastern Bering Sea shelf and slope. *Deep-Sea Res. II* 134, 390–412. doi: 10.1016/j.dsr2.2016.07.009

Pan-Arctic River Transport of Nutrients, Organic Matter, and Suspended Sediments Project [PARTNERS]. (2010). *Arctic River Biogeochemistry Data Set*. Available at http://ecosystems.mbl.edu/partners/

Peters, W., Jacobson, A. R., Sweeney, C., Andrews, A. E., Conway, T. J., Masarie, K., et al. (2007). An atmospheric perspective on North American carbon dioxide exchange: CarbonTracker. *Proc. Natl. Acad. Sci. U.S.A.* 104, 18925–18930. doi: 10.1073/pnas.0708986104

Punt, A. E., Foy, R. J., Dalton, M. C., Long, W. C., and Swiney, K. M. (2016). Effects of long-term exposure to ocean acidification conditions on future southern Tanner crab (*Chionoecetes bairdi*) fisheries management. *ICES J. Mar. Sci.* 73, 849–864. doi: 10.1093/icesjms/fsv205

Rodgers, K. B., Lin, J., and Frölicher, T. L. (2015). Emergence of multiple ocean ecosystem drivers in a large ensemble suite with an Earth system model. *Biogeoscience* 12, 3301–3320. doi: 10.5194/bg-12-3301-2015

Rysgaard, S., Glud, R. N., Lennert, K., Cooper, M., Halden, N., Leakey, R. J. G., et al. (2012). Ikaite crystals in melting sea ice – implications for pCO_2 and pH levels in arctic surface waters. *Cryosphere* 6, 901–908. doi: 10.5194/tc-6-901-2012

Saha, S., Moorthi, S., Wu, X., Wang, J., Nadiga, S., Tripp, P., et al. (2010). The NCEP climate forecast system reanalysis. *Bull. Am. Meteorol. Soc.* 91, 1015–1057. doi: 10.1175/2010BAMS3001.1

Saha, S., Moorthi, S., Wu, X., Wang, J., Nadiga, S., Tripp, P., et al. (2014). The NCEP climate forecast system version 2. *J. Climate* 27, 2185–2208. doi: 10.1175/JCLI-D-12-00823.1

Sarmiento, J. L., and Gruber, N. (2006). *Ocean Biogeochemical Dynamics*. Princeton, NJ: Princeton University Press, 526.

Semiletov, I., Pipko, I., Gustafsson, Ö., Anderson, L. G., Sergienko, V., Pugach, S., et al. (2016). Acidification of East siberian arctic shelf waters through addition of freshwater and terrestrial carbon. *Nat. Geosci.* 9, 361–365. doi: 10.1038/NEGO2695

Shchepetkin, A. F., and McWilliams, J. C. (2005). The regional oceanic modeling system (ROMS): a split-explicit, free-surface, topography-following-coordinate oceanic model. *Ocean Modell.* 9, 347–404. doi: 10.1016/j.ocemod.2004.08.002

Siedlecki, S. A., Pilcher, D. J., Hermann, A., Coyle, K., and Mathis, J. T. (2017). The importance of freshwater to spatial variability of aragonite saturation state in the Gulf of Alaska. *J. Geophys. Res. Oceans* 122, 8482–8502. doi: 10.1002/2017JC012791

Sigler, M. F., Stabeno, P. J., Eisner, L. B., Napp, J. M., and Mueter, F. J. (2014). Spring and fall phytoplankton blooms in a productive subarctic ecosystem, the eastern Bering Sea, during 1995-2011. *Deep-Sea Res. II* 109, 71–83. doi: 10.1016/j.dsr2.2013.12.007

Stabeno, P. J., Kachel, N. B., Moore, S. E., Napp, J. M., Sigler, M., Yamaguchi, A., et al. (2012). Comparison of warm and cold years on the southeastern Bering Sea shelf and some implications for the ecosystem. *Deep-Sea Res. II* 6, 31–45. doi: 10.1016/j.dsr2.2012.02.020

Steele, M., Morley, R., and Ermold, W. (2001). PHC: a global ocean hydrography with a high-quality arctic ocean. *J. Climate* 14, 2079–2087. doi: 10.1175/1520-04422001014<2079:PAGOHW<2.0CO;2

Stow, C. A., Jolliff, J., McGillicuddy, D. J., Doney, S. C., Allen, J. I., Friedrichs, M. A. M., et al. (2009). Skill assessment for coupled biological/physical models of marine systems. *J. Mar. Syst.* 76, 4–15. doi: 10.1016/j.jmarsys.2008.03.011

Striegl, R. G., Dornblaser, M. M., Aiken, G. R., Wickland, K. P., and Raymond, P. A. (2007). Carbon export and cycling by the Yukon, Tanana, and Porcupine rivers, Alaska, 2001-2005. *Water Resour. Res.* 43:W02411. doi: 10.1029/2006WR005201

Sutton, A. J., Wanninkhof, R., Sabine, C. L., Feely, R. A., Cronin, M. F., and Weller, R. A. (2017). Variability and trends in surface seawater pCO_2 and CO_2 flux in the Pacific Ocean. *Geophys. Res. Lett.* 44, 5627–5636. doi: 10.1002/2017GL073814

Waldbusser, G. G., Hales, B., Langdon, C. J., Haley, B. A., Schrader, P., Brunner, E. L., et al. (2015). Saturation-state sensitivity of marine bivalve larvae to ocean acidification. *Nat. Climate Change* 5, 273–280. doi: 10.1038/NCLIMATE2479

Wallhead, P. J., Bellerby, R. G. J., Silyakova, A., Slagstad, D., and Polukhin, A. A. (2017). Bottom water acidification and warming on the western eurasian arctic shelves: dynamical downscaling projections. *J. Geophys. Res. Oceans* 122, 8126–8144. doi: 10.1002/2017JC013232

Wanninkhof, R. (1992). Relationship between wind speed and gas exchange over the ocean. *J. Geophys. Res. Oceans* 97, 7373–7382. doi: 10.1029/92JC00188/

Weiss, R. (1974). Carbon dioxide in water and seawater: the solubility of a non-ideal gas. *Mar. Chem.* 2, 203–215. doi: 10.1016/0304-4203(74)90015-2

Wiese, F. K., Van Pelt, T. I., and Wiseman, W. J. (2012). Bering sea linkages. *Deep-Sea Res. II* 6, 2–5. doi: 10.1016/j.dsr2.2012.03.001

Xue, Z., He, R., Fennel, K., Cai, W.-J., Lohrenz, S., Huang, W.-J., et al. (2016). Modeling pCO_2 variability in the Gulf of Mexico. *Biogeoscience* 13, 4359–4377. doi: 10.5194/bg-13-4359-2016

Zeebe, R., and Wolf-Gladrow, D. (2001). CO_2 *in Seawater: Equilibrium, Kinetics, Isotopes, Elsevier Oceanograph Series*, 65. Amsterdam: Elsevier.

Conflict of Interest Statement: The authors declare that the research was conducted in the absence of any commercial or financial relationships that could be construed as a potential conflict of interest.

frontiers
in Marine Science

METHODS
published: 20 August 2018
doi: 10.3389/fmars.2018.00286

Improved Post-processing of Eddy-Covariance Data to Quantify Atmosphere–Aquatic Ecosystem CO_2 Exchanges

Tatsuki Tokoro and Tomohiro Kuwae*

Coastal and Estuarine Research Group, Port and Airport Research Institute, Yokosuka, Japan

The capture of carbon by aquatic ecosystems and its sequestration in sediments has been studied as a potential method for mitigating the adverse effects of climate change. However, the evaluation of *in situ* atmospheric CO_2 fluxes is challenging because of the difficulty in making continuous measurements over areas and for periods of time that are environmentally relevant. The eddy covariance method for estimating atmospheric CO_2 fluxes is the most promising approach to address this concern. However, methods to process the data obtained from eddy covariance measurements are still being developed, and the estimated air-water CO_2 fluxes have large uncertainties and differ from those obtained using conventional methods. In this study, we improved the post-processing procedure for the eddy covariance method to reduce the uncertainty in the measured air-water CO_2 fluxes. Our procedure efficiently removes low-quality fluxes using a combination of filtering methods based on the received signal strength indicator of the eddy covariance sensor, the normalized standard deviation of atmospheric CO_2 and water vapor concentrations, and a high-pass filter. The improved eddy covariance fluxes revealed diurnal and semi-diurnal cycles and a significant relationship with water fCO_2, patterns that were not observed from the results before filtering. Although there were still differences with indirect conventional measurements like the bulk formula method, the methods used in this study should improve the accuracy of carbon flow estimates at sites with complex terrains like coastal areas.

Keywords: CO_2 flux, eddy covariance, post-processing, aquatic ecosystems, indirect conventional method

Edited by:
Yuichiro Takeshita,
Monterey Bay Aquarium Research Institute, United States

Reviewed by:
Melissa Ward,
University of California, Davis, United States
Byron Walter Blomquist,
University of Colorado Boulder, United States

***Correspondence:**
Tatsuki Tokoro
tokoro-t@pari.go.jp

Specialty section:
This article was submitted to Coastal Ocean Processes, a section of the journal Frontiers in Marine Science

Received: *27 March 2018*
Accepted: *27 July 2018*
Published: *20 August 2018*

Citation:
Tokoro T and Kuwae T (2018) Improved Post-processing of Eddy-Covariance Data to Quantify Atmosphere–Aquatic Ecosystem CO_2 Exchanges. Front. Mar. Sci. 5:286. doi: 10.3389/fmars.2018.00286

INTRODUCTION

Aquatic environments are considered critical to the mitigation of adverse climate change effects because of their ability to store atmospheric CO_2. Previous studies have estimated that the ocean absorbs approximately one-fourth of the CO_2 emitted by anthropogenic activities (IPCC, 2013). However, the effect of shallow aquatic ecosystems on atmospheric CO_2 remains a controversial topic. Several previous studies, after taking into account carbon inputs from land, have concluded that shallow aquatic ecosystems are sources of atmospheric CO_2 (e.g., Gazeau et al., 2005; Borges et al., 2006; Chen et al., 2013). In contrast, some autotrophic, shallow aquatic ecosystems have been reported to be net sinks for atmospheric CO_2 (e.g., Schindler et al., 1997; Tokoro et al., 2014).

In situ measurements of atmospheric CO_2 fluxes are necessary for precise analysis of carbon cycling in aquatic environments. CO_2 fluxes in aquatic environments are difficult to determine because of the variability of several factors, including concentrations of CO_2 in the water and air and the physical characteristics of the atmosphere and water surface. Several methods have been proposed for measuring *in situ* CO_2 fluxes. Because each of these methods works best at a different combination of spatial and temporal scales and is associated with different costs and technical difficulties, a variety of methods have been applied to different aquatic environments (e.g., oceans, estuaries, and lakes) to assess rates of aquatic carbon cycling.

Methods of estimating air-water CO_2 fluxes can be assigned to one of two categories: (1) indirect estimations based on CO_2 concentration gradients just below the water surface (Lewis and Whitman, 1924) or from the renewal rate of a very small body of water (Danckwerts, 1951) and (2) direct estimations. With either of the indirect methods, the CO_2 flux is calculated from the product of the difference in the CO_2 fugacity (fCO_2) between air and water, the CO_2 solubility, and a physically regulated parameter called the transfer velocity. Because the transfer velocity cannot be estimated directly, empirical and hydrodynamic models for estimating transfer velocities have been proposed (Garbe et al., 2014).

At the present time, the empirical model is primarily used for evaluating aquatic CO_2 fluxes because of the difficulty in applying the hydrodynamic model. In the empirical model, the regulating factor for transfer velocity has been identified from several direct CO_2 measurements by using tracers such as ^{14}C and SF_6 (e.g., Broecker and Peng, 1982; Ho et al., 2014) or water-tank experiments (e.g., Komori et al., 1993). Based on these results, several empirical equations have been formulated manly for the open ocean fluxes. The wind speed above the water surface is a metric of one regulating factor (e.g., Liss and Merlivat, 1986; Wanninkhof, 1992; Ho et al., 2006). In the case of shallow systems, water velocity fields and depths also have been used to estimate the gas transfer velocity (O'Conner and Dobbins, 1958; Borges et al., 2004).

However, the relationship between the gas transfer velocity and such environmental parameters is affected by the topography (depth, bottom roughness, distance from the land, etc.) and is site-specific (e.g., Tokoro et al., 2008) especially at coastal area because the physical conditions near the water surface that unambiguously regulate the gas transfer velocity are functions of the topography, even under the same wind and current conditions. Furthermore, application of the empirical method is limited by its poor temporal and spatial coverage. Moreover, the determination in most previous studies of air-water CO_2 fluxes as snapshots that did not account for diurnal changes or annual cycles resulted in considerable uncertainty and bias (Kuwae et al., 2016). In brackish environments in particular, temporal variability of water fCO_2 is significant, and because the carbonate buffer effect is weak, fluctuations of fCO_2 become very large (Zeebe and Wolf-Gladrow, 2001). Use of empirical methods to carry out a comprehensive analysis of dynamic carbon cycling in aquatic environments with large spatial and temporal variability would therefore be very costly and require much effort.

Another method for evaluating air-water CO_2 fluxes is direct measurement of *in situ* fluxes. One such technique involves use of a chamber floating on the water surface (e.g., Frankignoulle, 1988; Tokoro et al., 2008). The floating chamber method is used to determine the air-water CO_2 flux from continuous measurements of CO_2 concentrations in the air inside a hollow, box-shaped device floating on the water surface. Although this method is the easiest of the direct methods to use in shallow coastal waters because of its relative simplicity, like the empirical method it is poorly suited for obtaining long-term measurements over wide areas.

Another direct measurement technique is the eddy covariance (EC) method, which is commonly used to determine mass and heat fluxes in terrestrial environments and has recently been used to estimate air-water fluxes of greenhouse gases (e.g., Tsukamoto et al., 2004). The determination of the EC CO_2 flux is based on the micrometeorological behavior of atmospheric eddy diffusion and is calculated from the covariance of atmospheric CO_2 concentrations and vertical wind speeds measured at high frequency (more than 10 Hz). Because EC measurements can be performed automatically and represent the flux over a large area, the EC method can be used to obtain a detailed analysis of CO_2 fluxes.

Despite the promise of EC measurements, their application in aquatic environments remains challenging (Tsukamoto et al., 2004; Rutgersson and Smedman, 2010; Vesala, 2012; Blomquist et al., 2013; Ikawa and Oechel, 2014; Kondo et al., 2014; Landwehr et al., 2014). The main difficulty is that the air-water CO_2 flux is small compared with the air-land CO_2 flux (Vesala, 2012; Landwehr et al., 2014).

There are several other problems in addition to the small fluxes in using EC measurements in aquatic environments. The uncertainty of EC measurements has been attributed to the spatial and temporal heterogeneity of water (Mørk et al., 2014). The EC flux is calculated as the average within a measurement area called the "footprint," which can range from several hundred meters to several kilometers windward from the measurement point (e.g., Schuepp et al., 1990). Therefore, EC fluxes at heterogeneous water sites are different from the fluxes determined by methods that estimate the CO_2 flux in an area of only several square meters (e.g., the empirical method and floating chamber method). The inflow of terrestrial air can cause unnatural temporal changes in the atmospheric CO_2 concentration and spatial heterogeneity at the measurement site. It is therefore necessary to account for the characteristics of the aquatic environment and carry out post-processing (Leinweber et al., 2009) to avoid large uncertainties or biases in EC flux calculations. Relevant procedures include use of a statistical test based on the short-term variance of CO_2 and vertical wind speed and measurement of the integral turbulent characteristics of vertical wind and air temperature (Mauder and Foken, 2004).

In this study, we improved a post-processing procedure for aquatic EC measurements that excludes low-quality data and corrects unnatural changes in EC measurements by using a series of data-filtering steps. The improved process is based on the idea that the unnatural changes during flux measurements causes spikes, drifts, offsets, and long-term variation of the CO_2 and H_2O raw data. We compared the results calculated with our procedure to those obtained using conventional EC post-processing procedures along with an existing EC filtering procedure and a parameter of the indirect model. We then discuss the differences among these post-processing methods with respect to the regulating factors of aquatic CO_2 fluxes.

METHODS

Field Measurements

Continuous EC measurement data were used for the evaluation of the post-processing procedure and analysis of atmospheric-aquatic ecosystem CO_2 exchanges. The data were collected from a brackish lagoon in Japan (the Furen Lagoon, **Figure 1**) from 28 May to 21 October 2014, during which time the water surface was not frozen. Most of the study area (57.4 km^2) was covered by seagrass meadows (mainly *Zostera marina*). The water was shallow (1–2 m), except in a channel that connected the eastern and western basins of the lagoon (approximately 5 m deep). Freshwater flows into the western basin through several rivers that run through the surrounding grass farms, and seawater is exchanged through the lagoon mouth, which opens to the Okhotsk Sea. A previous study has found that the air-water CO_2 flux in the lagoon is affected by changes of salinity caused by the inflow of river water and tides as well as by changes of dissolved inorganic carbon resulting from biological processes such as photosynthesis (Tokoro et al., 2014). The measurement platform was built at the same site used in that previous study (43°19.775′ N, 145°15.463′ E); the effects of photosynthesis and changes in salinity are most notable at this location in the lagoon (Tokoro et al., 2014).

The EC devices used in this study were as follows. Atmospheric CO_2 concentrations and water vapor were measured with an open-path sensor (LI-7500A, LI-COR, USA). The three-dimensional (3D) wind velocity, air temperature, and atmospheric pressure were measured with a 3D sonic anemometer (CSAT-3, Campbell Scientific, USA). The data were logged and managed by a SMARTFlux system (LI-COR, USA). The open-path sensor and the wind velocimeter were attached to the platform approximately 3.0–5.5 m above the water surface (the height varied with the tide). The sampling rate for all data was 10 Hz, and the fluxes (CO_2, water vapor, and heat) were calculated as averages over 30-min intervals. Batteries and solar panels were attached to the platform as power sources. Battery replacement, data collection, and device maintenance were performed approximately every 2 weeks. Water temperature and salinity were measured continuously with a conductivity-temperature sensor (Compact-CT, Alec, Japan).

Conventional Calculation and Post-processing of Fluxes

The conventional EC flux calculation method (hereafter PP1) is described in this section, for comparison with the proposed improved procedure introduced in the next section. The air-water CO_2 flux (F) was calculated every 30 min using the following equation:

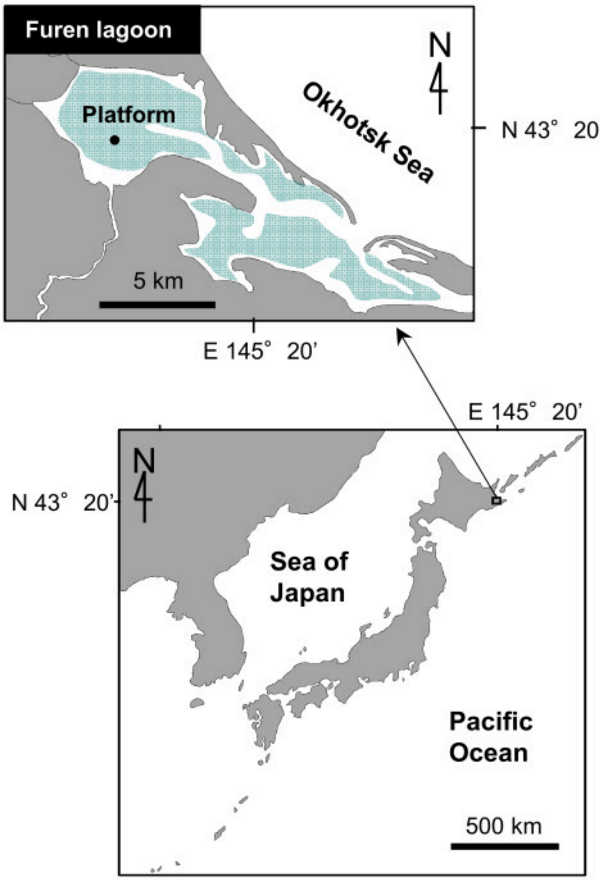

FIGURE 1 | Location of the measurement site (Furen Lagoon, Hokkaido, Japan). The lagoon is shallow (1–2 m). Green area indicates seagrass meadows. Eddy covariance (EC) measurements were performed on the platform in 2014.

$$F = \overline{\rho_c' w'} \cdot F_1 + \mu \frac{\rho_c}{\rho_d} \overline{\rho_v' w'} \cdot F_1 + \rho_c \left(1 + \mu \frac{\rho_v}{\rho_d}\right) \frac{\overline{T_a' w'}}{T_a} \cdot F_2 \quad (1)$$

where the coefficients F_1 and F_2 are correction terms based on the transfer functions that correct for the frequency attenuation of the air-sea CO_2 flux caused by the response time of the sensor, path-length averaging, sensor separation, signal processing, and flux-averaging time (Massman, 2000). The first term on the right-hand side of Eq. (1) is the product of F_1 and the uncorrected air-sea CO_2 flux calculated as the covariance of the CO_2 density ρ_c and the vertical wind speed w (the bar and the prime indicate the mean and the deviation from the mean, respectively). The second and third terms are the Webb-Pearman-Leuning (WPL) correction of latent heat and sensible heat, respectively (Webb et al., 1980). The other variables in Eq. (1) are defined as follows: ρ_d is dry air density, ρ_v is water vapor density, T_a is air temperature, and μ is the ratio of the molar weight of dry air to that of water vapor. The footprint (measurement area) depends on several factors, including the measurement height, wind speed, atmospheric stability, and measurement site roughness (10^{-4} cm) (Schuepp et al., 1990; Kondo, 2000). This footprint was several hundred meters on the windward side of the measurement site.

The deviation of each parameter in Eq. (1) was calculated by subtracting the 30 min average from the instantaneous data after deleting obviously low-quality data (e.g., negative values of CO_2 or water vapor concentration). Other corrections to the raw data included coordinate rotation of the 3D wind component (double rotation; Lee et al., 2004), time lag of the measurement due to the separation of the CO_2 sensor and the wind velocimeter (covariance maximization; Lee et al., 2004), exclusion of wind data contaminated by the wind velocimeter frame, and correction of the measurement noise (Vickers and Mahrt, 1997) based on the default settings of the data management software (EddyPro 5.1.1, LI-COR, USA).

For comparison with our improved post-processing procedure described in the next section, a conventional post-processing was applied to the PP1 data. The conventional post-processing was the statistical test using the short-term variation of CO_2 concentrations and vertical wind speeds, and the integral turbulent characteristics of vertical wind speed and air temperature (Mauder and Foken, 2004; hereafter, the test is designated the "TK2" from the software package). The TK2 test has been widely implemented in several software applications, including EddyPro. We used the optional EddyPro output with default setting.

Improved Post-processing Procedure

After calculating the EC flux using conventional post-processing as described in Sect. 2.2 (PP1), we recalculated the EC flux using our improved post-processing procedure (called PP2 hereafter; **Figure 2**). The PP2 procedure is based mainly on excluding low-quality data and high-pass (HP) filtering. It is also focused on aquatic environments in which the spatial and temporal variations of atmospheric CO_2 are large. The procedure combines a series of filtering methods based on the received signal strength indicator (RSSI) of the EC sensor, the normalized standard deviation (nSD) of the atmospheric CO_2 and water vapor concentrations, and HP filtering detrending of the raw CO_2 signal.

The RSSI, obtained from the CO_2 sensor of the EC measurement instrumentation every 30-min, indicates the available signal strength of the sensor. This parameter has been used to assess the validity of the measurement. In this study, we used the RSSI to filter the CO_2 data. First, data in the 30 min time series were excluded if their RSSI was low. The RSSI threshold for exclusion was set to 90% in this study because the number of data remaining after the RSSI filtering rapidly decreased at thresholds above this value (e.g., 91 and 78% of the data remained at RSSI thresholds of 90 and 95%, respectively).

Second, criteria for excluding low-quality fluxes were identified. Low-quality fluxes were identified from unnatural discontinuous change in the CO_2 and vapor data, which might cause the interference to CO_2 measurement. Such data were excluded based on the normalized standard deviation (nSD), calculated as follows: (1) calculate the SD of 10 Hz CO_2 and vapor concentration for every 30 min measurement; (2) divide each CO_2 and vapor SD by the mean RSSI-filtered CO_2 and vapor concentration during the entire measurement period (CO_2: 16.02 mmol m^{-3}, water vapor: 548.10 mmol m^{-3}), respectively; and (3) take the larger value of the divided CO_2 or vapor SD for every 30 min measurement. For the determination of the threshold, we checked the ten most extreme outliers of the CO_2 fluxes, which were probably low-quality, and we confirmed whether they were actually low-quality or not by visual confirmation of whether there were unnatural discontinuous change, or extreme values (negative concentration or values that differed from natural values by more than a factor of 1000). We found that the nSD threshold eliminated all of the actually low-quality data among these top ten outliers. In this case, we set the nSD threshold value to the lowest value among the ten low-quality data (0.050).

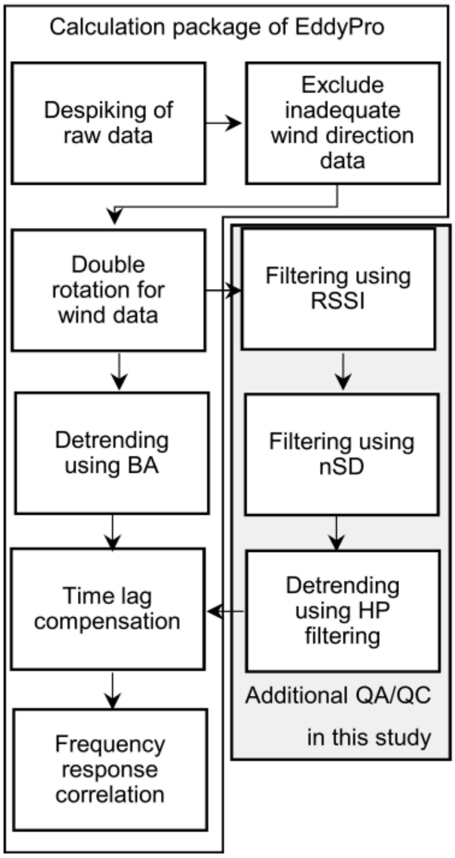

FIGURE 2 | Post-processing methods for EC flux calculations. The EC CO_2 flux was calculated by using conventional post-processing (PP1) in EddyPro. The corrections involved in PP1 have been described in previous publications (e.g., Lee et al., 2004). Detrending was performed by using block averaging (BA). Our new post-processing method (PP2) included two data-filtering steps based on the received signal strength indication of the CO_2 sensor and the standard deviation of the CO_2 and water vapor concentrations divided by the corresponding average standard deviation during the measurement period (nSD). Detrending in PP2 was performed by using high-pass filtering (Massman, 2000).

Finally, HP filtering was applied to detrend the raw concentration deviations in Eq. (1), in place of simple mean subtraction used in the PP1 procedure. This procedure corrected relatively long-term (several minutes to 30 minutes) variations in CO_2 or water vapor concentrations that were independent of eddy fluctuations and were caused by the temporal and spatial heterogeneity of the atmospheric mass. HP filtering is often applied to measurements in a complex environment; however, incorrect application of HP filtering results in underestimation of fluxes (Lee et al., 2004). HP filtering was applied by using an exponential moving average as follows:

$$x_i' = (1 - A)\, x'_{i-1} + A x_i$$
$$A = e^{-\left(1/f_\tau\right)}, \qquad (2)$$

where x_i and x_i' are an instantaneous datum and filtered datum for PP2 at time i, respectively. The latter parameter is plugged in the Eq. (1) as the deviation from the mean. The parameter τ is the time constant of the exponential moving average, which was determined to be 150 s in a previous study (McMillen, 1988). This value means 1, 50, and 99% of the CO_2 fluxes (cospectrum of CO_2 and vertical wind speed) are reduced at frequencies lower than 1/15, 1/150, and 1/1,500 Hz, respectively (Massman, 2000). Therefore, the effect of long-term variation of CO_2 in each measurement (during 30 min = 1/1,800 Hz) could be excluded. HP filtering was applied to all of the measured instantaneous data (i.e., 3D wind velocity, air temperature, CO_2 and water vapor concentrations, and atmospheric pressure). The parameter f is the sampling frequency (10 Hz).

Regulation Factor in the Indirect Model

In the indirect model, flux is calculated as the product of the gas transfer velocity, the CO_2 solubility in water, and the difference in CO_2 fugacity between air and water (Lewis and Whitman, 1924). However, the method of estimating the gas transfer velocity has varied and should probably be site-specific in coastal areas, as described above. The estimation should be inaccurate at our site, in particular, where the water depth was very shallow and seagrass was abundant. We therefore decided to compare the difference in CO_2 fugacity ($\Delta f CO_2$) with EC data as a theoretical regulating factor of air-water CO_2 flux.

The measurements were performed during the daytime on 29 May, 15 July, and 21 September 2014 for comparison with the EC measurements. The water samples used to determine CO_2 fugacity in water ($fCO_{2\text{water}}$) were collected just below the water surface (up to 20 cm below the water surface) to measure the concentration of CO_2 where direct gas exchange with air occurs. The sampling was performed within the EC footprint (estimated from Schuepp et al., 1990) for purposes of comparing the CO_2 fugacity and EC fluxes. The sampling points were determined from the wind direction and the distance from the platform measured using a hand-held GPS unit (Venture HC, Garmin, USA; see **Table S1**). The water fCO_2 was determined from the total alkalinity and the dissolved inorganic carbon content of the water sample using a batch-type carbonate measurement system (ATT-05, Kimoto electrics, Japan) and the CO2SYS program (Pierrot et al., 2006). The CO_2 fugacity in air ($fCO_{2\text{air}}$) was calculated from the CO_2 concentration, air temperature, pressure, and humidity measured by the EC devices.

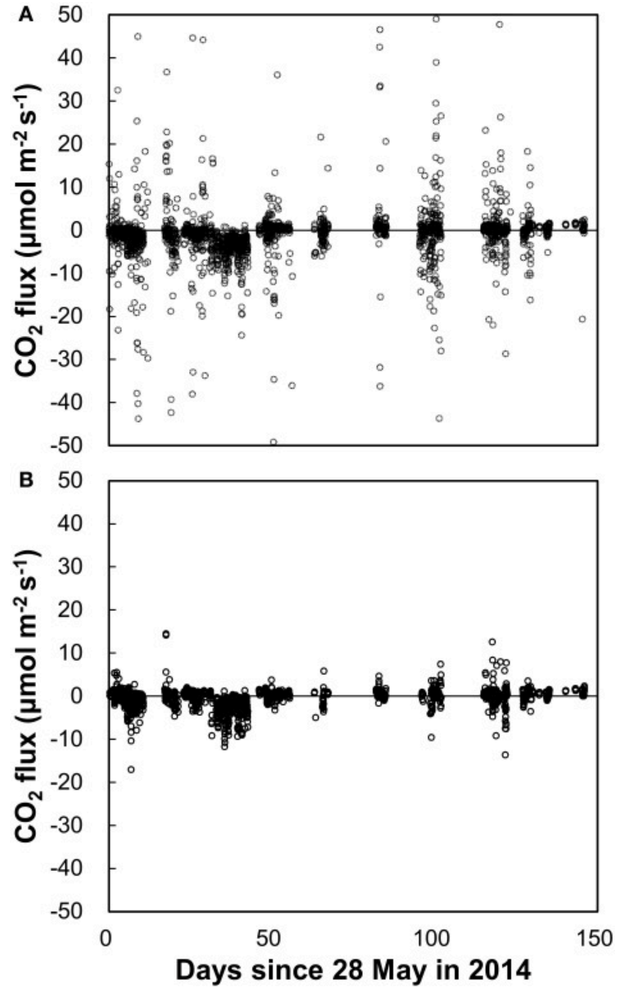

FIGURE 3 | EC CO_2 fluxes with **(A)** PP1 (mean: −1.93 μmol m^{-2} s^{-1}, SD: 52.4 μmol m^{-2} s^{-1}, n = 2,502) and with **(B)** PP2 (mean: −0.54 μmol m^{-2} s^{-1}, SD: 2.2 μmol m^{-2} s^{-1}, n = 1,833). Several data points in panel **(A)** are off the scale and not shown for comparison with **(B)**, in which all data are shown.

RESULTS

PP1 Data and TK2 Test

During the deployment period, 4,464 flux data points corresponding to 2,232 h were obtained; 1971 of those data points (44%) were excluded as low-quality data after PP1 application. The mean and SD of the EC CO_2 fluxes were−1.93 and 52.4 μmol m^{-2} s^{-1}, respectively. **Figure 3A** shows the retained CO_2 flux data.

Examples of PP1 measurements were some extremely high values of the CO_2 fluxes. The largest positive CO_2 flux (release to atmosphere) was 156.51 μmol m^{-2} s^{-1} at 2:00 on 23 June (day 56). The largest negative CO_2 flux (uptake of atmospheric CO_2) was −217.93 μmol m^{-2} s^{-1} at 22:00 on 4 October (day 129). These fluxes were more than three orders of magnitude larger than the average of the measured EC fluxes. **Figure 4** shows the instantaneous atmospheric CO_2 concentration, water vapor concentration, and the cumulative covariance between CO_2 and vertical wind speed during the times when the CO_2 fluxes were most positive or most negative. Among the most positive data, spikes and discontinuities were observed in the atmospheric CO_2 and water vapor concentrations, despite the prior correction applied by the PP1 processing. On the other hand, shifts of atmospheric CO_2 and vapor were observed during the first 5 min for the most negative data. On the other hand, shifts of atmospheric CO_2 and vapor were observed during the first 5 min for the most negative data, leading to two unnatural fluctuations in the flux during the first 5 min. This fluctuation in the computed flux was caused by the cross-sensitivity (interference between CO_2 and vapor measurement) given the unnatural change of vapor and the inverse correlation between CO_2 and vapor. The cumulative covariance indicated that the covariance at certain periods (0–5 min) contributed significantly to the total cumulative covariance.

The TK2 test flagged the best quality data (flagged "0" in the EddyPro output), the general quality data (flagged "1"), and wrong data that should be discarded (flagged "2"). The mean and SD after removal of the data flagged "2" from PP1 were −2.53 and 57.2 μmol m^{-2} s^{-1}, respectively (196 data removed). The mean and SD after removal of the data flagged "1" and "2" from PP1 (only data flagged "0" were retained) were −2.15 and 4.48 μmol m^{-2} s^{-1}, respectively (1395 data removed).

PP2 Data

Figure 3B shows the EC CO_2 flux data subjected to PP2 (RSSI, nSD, and HP filtering). Of the 2,493 total data points remaining after PP1, approximately 234 (9%) were excluded by RSSI filtering. Subsequent nSD filtering removed 426 additional data points (17%); approximately 73% of the measurement data remained after this filtering. The mean and SD of the EC CO_2 flux after PP2 were −0.54 and 2.2 μmol m^{-2} s^{-1}, respectively. For comparison, the mean and SD obtained by block averaging, not HP filtering, were −1.02 and 2.74 μmol m^{-2} s^{-1}, respectively.

The number of data remaining after PP2 was almost the same during the day and night, but the average value of the flux shifted to positive in the daytime. This shift was observed after HP filtering in PP2 but not after excluding data with the nSD (**Figure 5**). Cumulative fluxes showed an influx in the summer season and an efflux in autumn and winter (**Figure 6**). The trend was the same between PP1 and PP2 data, but a large jump at around 30 days was absent from the PP2 data.

Figure 7 shows the nSD for the EC CO_2 flux data. There was no significant relationship between the nSD and atmospheric parameters (air temperature, water vapor, atmospheric CO_2 concentration, wind speed and wind direction; the multiple correlation coefficient was 0.23) and water parameters (salinity, water temperature and water depth; $r = 0.25$). However, a nSD of more than 0.3 was observed only when atmospheric conditions were relatively stratified and humid. Water vapor around the EC devices may therefore have contaminated the CO_2 measurement.

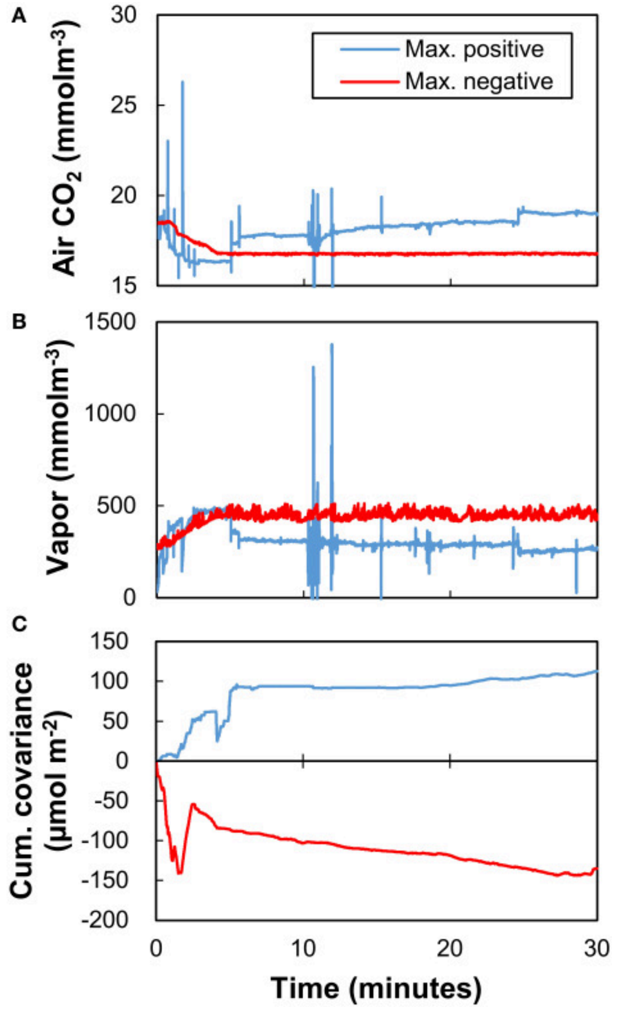

FIGURE 4 | Instantaneous values of **(A)** atmospheric CO_2 concentration, **(B)** water vapor (atmospheric H_2O) concentration, and **(C)** cumulative covariance of atmospheric CO_2 concentration and vertical wind speed calculated with PP1 when the CO_2 fluxes showed the largest positive value (156.5 μmol m^{-2} s^{-1}; blue) and the largest negative value (–217.9 μmol m^{-2} s^{-1}; red). Note that the covariance was not equal to the CO_2 flux because there was no Webb-Pearman-Leuning correction.

The nSD and TK2 test produced consistent results. Among the best quality data based on the TK2 test (flagged "0" in EddyPro), the nSD was the lowest and equal to 0.043 ± 0.133 (average ± SD, $n = 1{,}098$). In contrast, the nSD was 0.062 ± 0.209 ($n = 1{,}199$) among the general qualified data (flagged "1") and was the highest, 0.090 ± 0.340 ($n = 512$), among wrong qualified data (flagged "2"). Meanwhile, the nSD after PP1 and PP2 were 0.057 ± 0.207 ($n = 2{,}493$) and 0.024 ± 0.011 ($n = 1{,}833$), respectively. However, the large SD showed that the TK2 test and the nSD filtering were not completely consistent.

Figure 8 shows an example of the results in which the difference of CO_2 fluxes between before and after HP filtering was

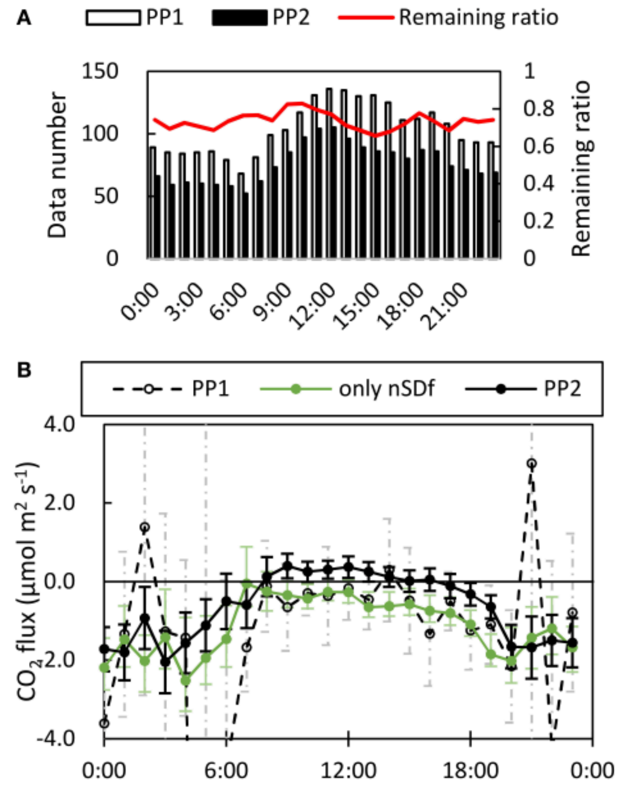

FIGURE 5 | Changes in **(A)** the number of data points and **(B)** average value of diurnal flux by filtering. Some plots of data after PP1 were omitted for clarity. The remaining ratio of the flux data after PP2 (red line) was almost the same between daytime and nighttime. In contrast, the average value in the daytime shifted to positive (efflux). The shift was caused by high-pass filtering (black solid line and closed circles), not the filtering using nSD (dashed line and open circles to green data). The error bars mean the 95% confidential limit.

a maximum (measured at 8:00 on day 84, August 21). These data were not excluded by the RSSI and nSD filtering (RSSI = 100%, nSD = 2.07×10^{-2}), thus it was not thought to be low-quality in spite of the spikes in the raw data and co-spectrum. The trend showed by the concentration of atmospheric CO_2 over the 30-min time interval indicated that the block average could not extract appropriate eddy movements from the time-series data. The normalized cospectrum of CO_2 concentration and vertical wind speed showed that the cospectrum density at low frequency before HP filtering was very large and not convergent. The implication is that the measurement was not appropriate, because the average flux value should have changed if the measurement period was shorter or longer than 30 min. However, the density after HP filtering was reduced and convergent. The filtering thus successfully excluded the effect caused by the variation of atmospheric CO_2 concentrations.

Difference in CO_2 Fugacity in the Indirect Model

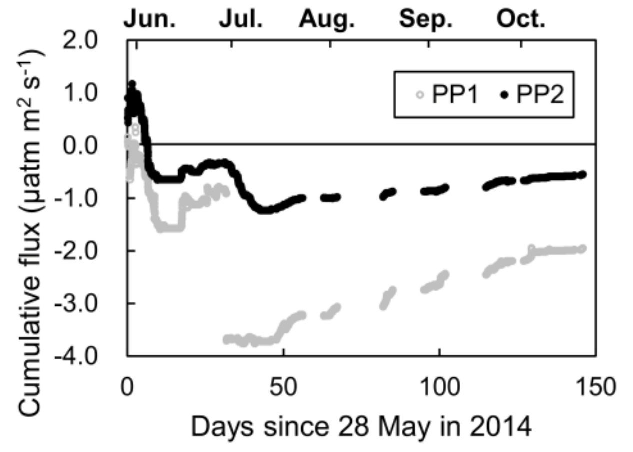

FIGURE 6 | Cumulative EC flux after PP1 and PP2. The data during the gap period due to bad weather conditions were not counted. The seasonal trends of the fluxes were roughly the same, except for the large change around 30 days after the measurements started. This comparison shows that the PP2 did not bias the seasonal trend and improved the continuity.

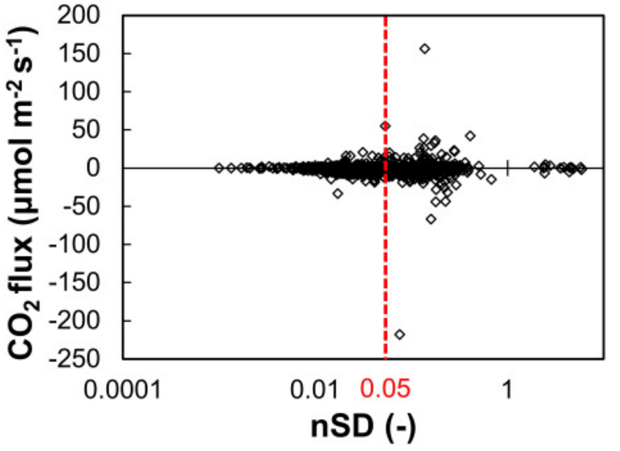

FIGURE 7 | Comparison between the effects of the filtering parameter and the CO_2 flux after the RSSI filtering procedure. The threshold (broken red line) was determined so as to remove the confirmed low-quality data. Normalized standard deviation (nSD) is the standard deviation over 30-min interval divided by the average during the entire measurement period (threshold = 0.05; 74% of data retained).

The measured differences in CO_2 fugacity showed spatial and seasonal variations (see **Table S1**). The means and SDs were 469.21 ± 732.29 μatm ($n = 18$) on 29 May (day 1), 2890.51 ± 1013.98 μatm ($n = 18$) on 15 July (day 48), and −247.73 ± 53.49 μatm ($n = 10$) on 21 September (day 115). The correlation of the fCO_2 was insignificant with PP1 data ($P>0.4$) while was significant with PP2 data ($P < 10^{-3}$).

DISCUSSION

Identifying and removing bad parameters is a longstanding issue in the application of direct EC flux measurements. This paper presents two methods for identifying low-quality flux values

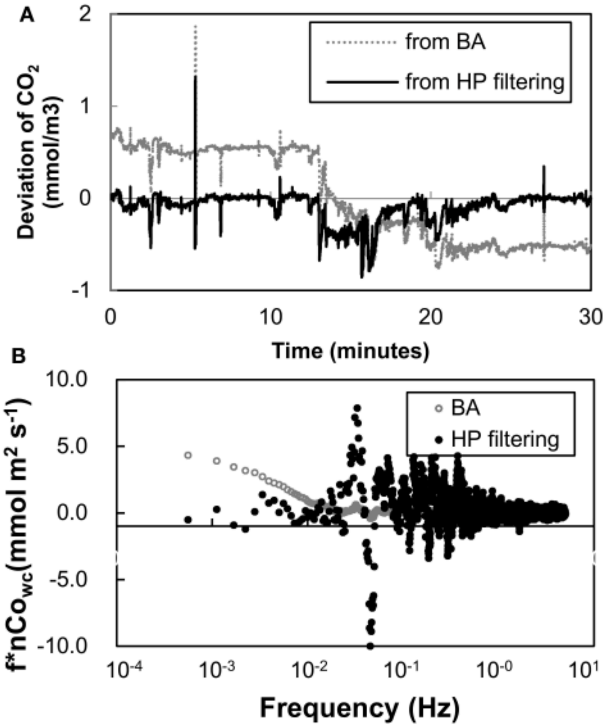

FIGURE 8 | Examples of the deviation calculations of atmospheric CO_2 concentration **(A)** and the cospectrum of atmospheric CO_2 concentration and vertical wind speed **(B)**. The cospectrum density was normalized by each covariance of CO_2 and vertical wind speed.

and a high-pass filtering procedure for detrending low-frequency variability in the raw data prior to computing covariance.

Our filtering method, PP2, successfully excluded low-quality fluxes. The SD was decreased by a factor of 24 (52.4 μmol m^{-2} s^{-1} in PP1 to 2.2 μmol m^{-2} s^{-1} in PP2). While the atmospheric CO_2 uptake rate calculated via PP1 measurements (−1.93 μmol m^{-2} s^{-1}) was reduced in magnitude by 72% after PP2 to −0.54 μmol m^{-2} s^{-1}.

Removing only the wrong data (flagged "2") with the TK2 test was inadequate for the comparison because the SD was almost the same as before filtering. Given the complex situation at the measurement site, only the best quality data (flagged "0") should be used for the comparison with the PP2 procedure (mean and SD were −2.15 and 4.48 μmol m^{-2} s^{-1}, respectively). The largest difference between the flagged "0" data and PP2 data was the mean CO_2 flux during the measurement period. Unfortunately, there was not a large difference between these data during the water fCO_2 measurement period. It was therefore difficult to evaluate which data were reliable by the indirect model or other flux estimation. However, the uptake rate based on the PP2 data would be more consistent with the range of atmospheric CO_2 uptake rates reported in previous coastal studies by the indirect method and the direct measurement using the floating chamber method (e.g., Borges et al., 2005; Chen et al., 2013; Laruelle et al., 2013); the most negative CO_2 flux ever reported was −1.08 μmol m^{-2} s^{-1} during spring in the Baltic Sea (Chen et al., 2013). In addition, the data in **Figure 4**, which were the largest positive and negative flux after PP1 should also support the validity of PP2. The data has unnatural spikes and fluctuations by the cross-sensitivity and was removed by PP2 while the data was flagged "1" by TK2 and passed by usual application of TK2. This is an example of higher accuracy of PP2 than that of TK2 in this study. These results indicate that the thresholds of the RSSI and nSD in this study were valid although they determined by arbitral criteria. Given that the theoretical identification of signal and noise is still discussing in many field like informatics, the PP procedure in this study should be practical and basically applicable to the EC flux at several coastal area.

The diurnal and seasonal variations during the measurement period were not affected by the RSSI and HP filtering (**Figures 5**, **6**). In the case of the diurnal cycle, the positive shift in the daytime was caused by HP filtering, not by excluding low-quality data based on the RSSI and nSD. This positive shift is inferred because HP filtering did not affect the WPL terms in Eq. 1, which were based on heat fluxes and usually positive, relative to the covariance term of CO_2 and vertical wind. In contrast, the similar trend of the seasonal cycles showed that the PP2 did not bias monthly temporal variations. Rather, PP2 improved the continuity of the seasonal trend by removing the large jump at about 30 days.

Even after the exclusion of low-quality outliers by PP2, no significant relationship between CO_2 fluxes and environmental parameters could be discerned, in similar to the case with the nSD ($r = 0.23$ and 0.33 for atmospheric and water parameters). On the other hand, filtering contributed to the time-series analysis. The normalized power spectrum of the EC CO_2 fluxes after PP1 displayed large, noise-like fluctuations at high frequencies (**Figure 9**), and thus any suggestion of peaks in the time series was obscured. After PP2, however, the noise-like fluctuations were smaller, and two peaks associated with semi-diurnal (∼12.5 h) and diurnal (∼24 h) time intervals were apparent. On the other hand, such peaks were obscure in the spectrum from TK2 "0" data. The fCO_2 variations in the lagoon, which are among the parameters that regulate air-water CO_2 fluxes, have been confirmed to be related to mixing of lagoon water with freshwater coming from rivers and with biological processes such as photosynthesis (Tokoro et al., 2014). Given that the former and latter phenomena are caused by the semi-diurnal tidal cycle and diel changes of irradiance, respectively, the peaks in the power spectrum are consistent with the results of Tokoro et al. (2014). This consistency is a good demonstration of the utility of the PP2. The positive value of the average CO_2 flux in the daytime (**Figure 5**) indicates that the effect of mixing with freshwater was larger than the effect of photosynthesis during the measurement period. This was because the average water depth was the shallowest around noon due to the tidal condition at the site in spring and summer when most of the experiment was performed.

The most of EC data that were inconsistent with ΔfCO_2 in terms of their signs (plus or minus) were excluded by PP2 (**Figure 10**). Although EC data and ΔfCO_2 cannot be compared directly, the sign should be consistent, because other parameters

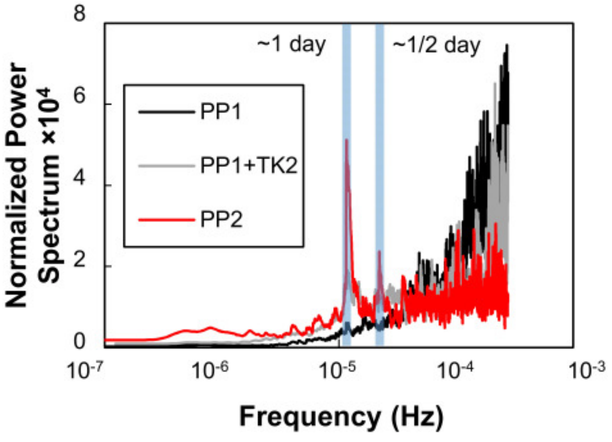

FIGURE 9 | Power spectra of CO_2 flux with PP1 (black line), PP1 with TK2 (blue line) and PP2 (red line). The spectra were normalized using the variances of CO_2 flux for the entire measurement period after each calculation. The shaded areas indicate the frequency around the 24 h diurnal cycle (left) and 12.5 h tidal cycle (right). Average CO_2 flux data during the entire measurement period were used to replace missing CO_2 flux data.

in the indirect model (the gas transfer velocity and solubility) are always positive. Furthermore, the linear relationship between the EC data and ΔfCO_2, which is suggested in the indirect model, was highly significant ($P < 10^{-3}$) after PP2 but was insignificant ($P > 0.4$) only after PP1. However, the EC fluxes estimated with PP2 did not always agree with the estimation by the indirect model. Because the $fCO_{2\text{water}}$ is theoretically never negative, a theoretical maximum negative flux can be calculated by arbitrarily setting fCO_2 equal to zero and using the largest estimation of the gas transfer velocity. The maximum negative flux calculated in this way with the gas transfer velocity estimated in several studies (Wanninkhof, 1992; Borges et al., 2004; Mørk et al., 2014) was $-6.16\ \mu\text{mol m}^{-2}\ \text{s}^{-1}$ at 15:00 on 30 May (day 2), when the maximum wind speed was recorded ($11.9\ \text{m s}^{-1}$). Forty-seven EC flux data points (3% of all data) indicated even lower fluxes. Because the maximum negative value was the theoretical limit with the indirect model, some of the EC fluxes cannot be explained by only the indirect model.

Similar inconsistencies between air-water CO_2 fluxes calculated with the EC method and other conventional methods have been reported in several studies (e.g., Tsukamoto et al., 2004; Rutgersson and Smedman, 2010). In the case of coastal measurements, water side convection due to vertical temperature gradients within the water column has been postulated to enhance the gas transfer velocity (Rutgersson and Smedman, 2010). However, such an enhancement has not been previously observed with direct flux measurements using a floating chamber at our site (Tokoro et al., 2014). Because the very shallow water depth (less than 2 m) at our site cannot explain any enhancement by the Rutgersson's model, we suspect that water side convection was not the main reason for the inconsistency of the fluxes.

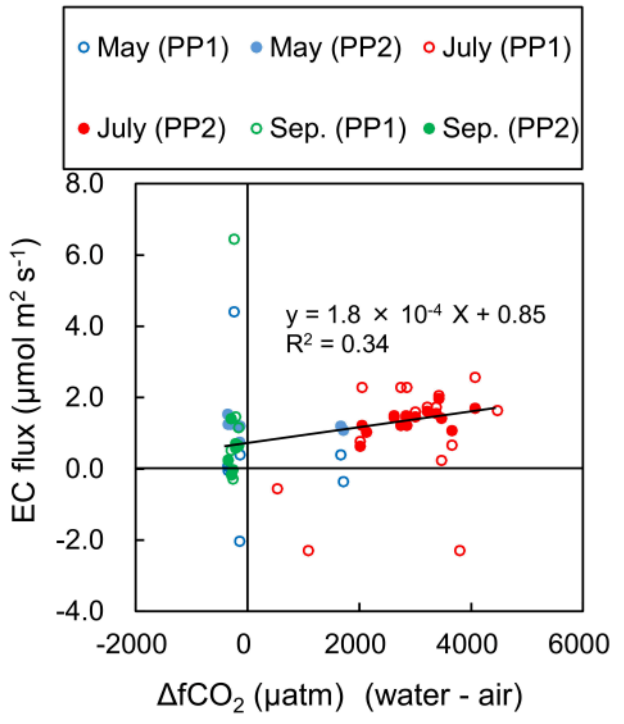

FIGURE 10 | Comparison of ΔfCO_2 (water minus air), EC flux with PP1 and EC flux with PP2. Significant linear relationship (solid line; $P < 10^{-3}$) was observed after PP2, but not after PP1 ($P >$ 0.4).

TABLE 1 | Summary of the differences in fluxes calculated by the eddy covariance and bulk formula methods.

	Eddy covariance	Bulk formula
Major sources of uncertainty	- Cross sensitivity - Long-term variation (minutes) of CO_2 and water vapor concentrations in air	- Wind-dependent formula - Heterogeneity of measurement site
Vegetation on the water surface	- effect included	- effect not included

On the assumption that the EC fluxes obtained with PP2 were valid, the discrepancy between the EC and the indirect estimation was also postulated to reflect the limitations of the indirect model. One consideration with respect to the limitations of the indirect model is that seagrass leaves, which reached the water surface during low tide at the study site, might have affected the physical and chemical conditions at the water surface (Watanabe and Kuwae, 2015). The indirect model assumes that the CO_2 flux is caused by the CO_2 concentration gradient just below the water surface. The indirect model should therefore not be applied when seagrass is present on the water surface. A previous study that investigated the radiocarbon isotopic signatures of seagrass at the study site indicated that of the total CO_2 assimilated by the seagrass, 0–40% (mean = 17%) originated from the atmosphere and the rest from the water (Watanabe and Kuwae, 2015). The implication is that there is enhanced uptake of atmospheric CO_2 (rather than uptake through the water column) by seagrass when seagrass leaves are on the water surface. Atmospheric CO_2 is therefore directly taken up within a thin film of water over the seagrass leaves, but this seagrass-driven CO_2 flux is not included in the indirect model using the gas transfer velocity.

In summary, we attribute the discrepancy between the EC and conventional indirect model to (1) major technical uncertainties in both methods and (2) limitations of the indirect model related to the presence of vegetation on the water surface (**Table 1**). The latter one may cause the actual CO_2 flux to be larger than the indirect estimation in aquatic systems that have large amounts of vegetation. Determination of the contribution of aquatic ecosystems to mitigating the adverse effects of climate change will require consideration of all processes related to atmosphere-aquatic ecosystem exchange. For this purpose, the EC CO_2 flux should be a more robust indicator than the indirect estimation, which includes only processes related to air-water exchanges. Improving the EC method and the post-processing procedure are therefore essential for a re-evaluation of atmosphere-aquatic ecosystem CO_2 gas exchanges and comprehensive analyses of the contributions of aquatic environments to mitigating the adverse effects of climate change.

AUTHOR CONTRIBUTIONS

TT associated main part of the measurement and the analysis. TK supported the field measurement, and discussed with TT about the analysis of this study.

ACKNOWLEDGMENTS

We thank K. Watanabe, H. Moki, E. Miyoshi, and S. Montani for help with the field work and F. Kondo and H. Ikawa for helpful comments. This study was supported by a Grant-in-Aid for Challenging Exploratory Researches (no. 24656316 and 26630251) from the Japan Society for the Promotion of Science and a Strategic R&D Area Project (S-14) of the Environmental Research and Technology Development Fund (Strategic Research on Global Mitigation and Local Adaptation to Climate Change).

SUPPLEMENTARY MATERIAL

The Supplementary Material for this article can be found online at: https://www.frontiersin.org/articles/10.3389/fmars.2018.00286/full#supplementary-material

REFERENCES

Blomquist, B. W., Huebert, B. J., Fairall, C. W., Bariteau, L., Edson, J. B., Hare, J. E., et al. (2013). Advances in air-sea CO_2 flux measurement by eddy correlation. *Bound. Lay. Meteorol.* 152, 245–276. doi: 10.1007/s10546-014-9926-2

Borges, A. V., Delille, B., and Frankignoulle, M. (2005). Budgeting sinks and sources of CO_2 in the coastal ocean: diversity of ecosystems counts. *Geophys. Res. Lett.* 32:L11460. doi: 10.1029/2005GL023053

Borges, A. V., Schiettecatte, L. S., Abril, G., Delille, B., and Gazeau, F. (2006). Carbon dioxide in European coastal waters. *Estuar. Coast. Shelf Sci.* 70, 375–387. doi: 10.1016/j.ecss.2006.05.046

Borges, A. V., Vanderborght, J. P., Schiettecatte, L. S., Gazeau, F., Ferrón-Smith, S., Delille, B., et al. (2004). Variability of the gas transfer velocity of CO_2 in a macrotidal estuary (the Scheldt). *Estuaries* 27, 593–603. doi: 10.1007/BF02907647

Broecker, W. S., and Peng, T.-H. (1982). *Tracers in the Sea, the Lamont-Doherty Geological Observatory*. New York, NY: Eldigio Press.

Chen, C. T. A., Huang, T. H., Chen, Y. C., Bai, Y., He, X., and Kang, Y. (2013). Air-sea exchanges of coin the world's coastal seas. *Biogeosciences* 10, 6509–6544. doi: 10.5194/bg-10-6509-2013

Danckwerts, P. V. (1951). Significant of liquid-film coefficient in gas absorption. *Ind. Eng. Chem*. 43, 1460–1467.

Frankignoulle, M. (1988). Field-measurements of air sea CO_2 exchange. *Limnol. Oceangr*. 33, 313–322.

Garbe, C. S., Rutgersson, A., Boutin, J., de Leeuw, G., Delille, B., Fairall, W., et al. (2014). *Open-Atmosphere Interaction of Gases and Particles*. Heidelberg: Springer, 55–122.

Gazeau, F., Duarte, C. M., Gattuso, J. P., Barrón, C., Navarro, N., Ruiz, S., et al. (2005). Whole-system metabolism and CO_2 fluxes in a Mediterranean Bay dominated by seagrass beds (Palma Bay, NW Mediterranean). *Biogeosciences* 2, 43–60.doi: 10.5194/bg-2-43-2005

Ho, D. T., Ferrón, S., Engel, V. C., Larsen, L. G., and Barr, J. D. (2014). Air-water gas exchange and CO_2 flux in a mangrove-dominated estuary. *Geophys. Res. Lett*. 41, 108–113.doi: 10.1002/2013GL058785

Ho, D. T., Law, C. S., Smith, M. J., Schlosser, P., Harvey, M., and Hill, P. (2006). Measurement of air-sea gas exchange at high wind speeds in the Southern Ocean: implications for global parametrization. *Geophys. Res. Lett*. 33:L11661.doi: 10.1029/2006GL026817

Ikawa, H., and Oechel, C. (2014). Temporal variations in air-sea CO_2 exchange near large kelp beds near San Diego, California. *J. Geophys. Res. Oceans* 120, 50–63.doi: 10.1002/2014JC010229

IPCC (2013). *Climate Change 2013: The Physical Science Basis.* eds T. F. Stocker, D. Qin, G. K. Plattner, M. Tignor, S. K. Allen, J. Boschung, A. Nauels, Y. Xia, V. Bex and P. M. Midgley (Cambridge, UK; New York, NY: Cambridge University Press).

Komori, S., Nagaosa, R., and Murakami, Y. (1993). Turbulent structure and heat and mass transfer mechanism at a gas-liquid interface in a wind-wave tunnel. *Appl. Sci. Res*. 51, 423–427.

Kondo, F., Ono, K., Mano, M., Miyata, A., and Tsukamoto, O. (2014). Experimental evaluation of water vapor cross-sensitivity for accurate eddy covariance measurement of CO_2 flux using open-path CO_2/H_2O gas analysers. *Tellus B* 66:23803.doi: 10.3402/tellusb.v66.23803

Kondo, J. (2000). *Atmospheric Science near the Ground Surface.* Tokyo: University of Tokyo Press.

Kuwae, T., Kanda, J., Kubo, A., Nakajima, F., Ogawa, H., Sohma, A., et al. (2016). Blue carbon in human-dominated estuarine and shallow coastal systems. *Ambio* 45, 290–301. doi: 10.1007/s13280-015-0725-x

Landwehr, S., Miller, S. D., Smith, M. J., Saltzman, E. S., and Ward, B. (2014). Analysis of the PKT correction for direct CO_2 flux measurements over the ocean. *Atmos. Chem. Phys*. 14, 3361–3372. doi: 10.5194/acp-14-3361-2014

Laruelle, G. G., Dürr, H. H., Lauerwald, R., Hartmann, J., Slomp, C. P., Goossens, N., et al. (2013). Global multi-scale segmentation of continental and coastal waters from the watersheds to the continental margins. *Hydrol. Earth. Syst. Sci.* 17, 2029–2051. doi: 10.5194/hess-17-2029-2013

Lee, X., Massman, W., and Law, B. (eds) (2004). Handbook of Micrometeorology-A *Guide for Surface Flux Measurement and Analysis,* Dordrecht: Kluwer Academic Publishers.

Leinweber, A., Gruber, N., Frenzel, H., Friederich, G. E., and Chavez, F. P. (2009). Diurnal carbon cycling in the surface ocean and lower atmosphere of Santa Monica Bay, California. *Geophys. Res. Lett.* 36:L08601. doi: 10.1029/2008GL037018

Lewis, W. K., and Whitman, W. (1924). Principle of gas absorption. *Ind. Eng. Chem*. 16, 1215–1220.

Liss, P. S., and Merlivat, L. (1986). *The Role of Air-Sea Exchange in Geochemical Cycling*. Boston, MA: Reidel, 113–129.

Massman, W. J. (2000). A simple method for estimating frequency response corrections for eddy covariance systems. *Agr. Forest Meteorol*. 104, 185–198. doi: 10.1016/S0168-1923(00)00164-7

Mauder, M., and Foken, T. (2004). *Documentation and Instruction Manual of the Eddy Covariance Software Package TK2.* Bayreuth: University of Bayreuth.

McMillen, R. T. (1988). An eddy correlation technique with extended applicability to non-simple terrain. *Bound. Lay. Meteorol*. 43, 231–245.

Mørk, E. T., Sørensen, L. L., Jensen, B., and Sejr, M. K. (2014). Air-Sea CO_2 gas transfer velocity in a shallow estuary. *Bound. Lay. Meteorol*. 151, 119–138. doi: 10.1007/s10546-013-9869-z

O'Conner, D. J., and Dobbins, W. E. (1958). Mechanism of reaeration in natural streams. *Trans. Am. Soc. Civ. Eng*. 123, 641–684.

Pierrot, D., Lewis, E., and Wallace, D. W. S. (2006). *MS Excel Program Developed for CO2 System Calculations*. Oak Ridge, TN: Oak Ridge National Laboratory.

Rutgersson, A., and Smedman, A. (2010). Enhanced air-sea CO_2 transfer due to water-side convection. *J. Mar. Sys*. 80, 125–134. doi: 10.1016/j.jmarsys.2009.11.004

Schindler, D. E., Carpenter, S. R., Cole, J. J., Kitchell, J. F., and Pace, M. L. (1997). Influence of food web structure on carbon exchange between lakes and the atmosphere. *Science* 277, 248–251.

Schuepp, P. H., Leclerc, M. Y., MacPherson, J. I., and Desjardins, R. L. (1990). Footprint prediction of scalar fluxes from analytical solutions of the diffusion equation. *Bound. Lay. Meteorol*. 50, 355–373.

Tokoro, T., Hosokawa, S., Miyoshi, E., Tada, K., Watanabe, K., Montani, S., et al. (2014). Net uptake of atmospheric CO_2 by coastal submerged aquatic vegetation. *Glob. Change Biol*. 20, 1873–1884. doi: 10.1111/gcb.12543

Tokoro, T., Kayanne, H., Watanabe, A., Nadaoka, K., Tamura, H., Nozaki, K., et al. (2008). High gas-transfer velocity in coastal regions with high energy-dissipation rates. *J. Geophys. Res. Oceans* 113:C11006. doi: 10.1029/2007JC004528

Tsukamoto, O., Takahashi, S., Kono, T., Yamashita, E., Murata, A., and Ishida, H. (2004). "Eddy covariance co2 flux measurements over open ocean," in *Paper Presented at the 13th Symposium on the Interaction of the Sea and Atmosphere* (Boston, MA: American Meteorological Society), 8–13.

Vesala, T. (2012). "Eddy covariance measurements over lakes," in *Eddy Covariance: A Practical Guide to Measurement and Data Analysis*, eds M. Aubinet, T. Vesala, and D. Papale (Dordrecht: Springer), 365–376.

Vickers, D., and Mahrt, L. (1997). Quality control and flux sampling problems for tower and aircraft data. *J. Atmos. Ocean. Tech*. 14, 512–526.

Wanninkhof, R. (1992). Relationship between wind speed and gas exchange over the ocean. *J. Geophys. Res*. 97, 7373–7382.

Watanabe, K., and Kuwae, T. (2015). Radiocarbon isotopic evidence for assimilation of atmospheric CO_2 by the seagrass *Zostera marina*. *Biogeosciences* 12, 6251–6258.doi: 10.5194/bg-12-6251-2015

Webb, E. K., Pearman, G. I., and Leuning, R. (1980). Correction of flux measurements for density effects due to heat and water vapour transfer. *Q. J. Roy. Meteor. Soc*. 106, 85–100.

Zeebe, R. E., and Wolf-Gladrow, D. (2001). *Seawater: Equilibrium, Kinetics, Isotope.* Amsterdam: Elsevier, 85–140.

Conflict of Interest Statement: The authors declare that the research was conducted in the absence of any commercial or financial relationships that could be construed as a potential conflict of interest.

frontiers in Marine Science

ORIGINAL RESEARCH
published: 24 May 2018
doi: 10.3389/fmars.2018.00181

The Dynamics of Coral-Algal Interactions in Space and Time on the Southern Great Barrier Reef

Kristen T. Brown[1,2,3]*, *Dorothea Bender-Champ*[1,3], *Andreas Kubicek*[1,3], *Rene van der Zande*[1,2,3], *Michelle Achlatis*[1,2,3], *Ove Hoegh-Guldberg*[1,2,3] and *Sophie G. Dove*[1,2,3]

[1] Coral Reef Ecosystems Lab, School of Biological Sciences, University of Queensland, St. Lucia, QLD, Australia, [2] Global Change Institute, University of Queensland, St. Lucia, QLD, Australia, [3] ARC Centre for Excellence for Coral Reef Studies, University of Queensland, St. Lucia, QLD, Australia

Globally, tropical coral reefs are being degraded by human activities, and as a result, reef-building corals have declined while macroalgae have increased. Recent work has focused on measuring macroalgal abundance in response to anthropogenic stressors. To accurately evaluate the effects of human impacts, however, it is necessary to understand the effects of natural processes on reef condition. To better understand how coral reef communities are influenced by natural processes, we investigated how spatial and seasonal changes in environmental conditions (temperature and PAR) influence benthic community structure, and the composition and frequency of coral-algal interactions across eight distinct zones and over a 23-month period at Heron reef on the southern Great Barrier Reef. Hard coral cover and macroalgal density showed distinct spatio-temporal variations, both within and between zones. Broad hard coral cover was significantly higher at the reef slope sites compared to the lagoon and was not significantly influenced by season. The composition and biomass of macroalgae increased in spring and declined in summer, with maximum macroalgal abundance corresponding with average temperatures of between 22 and 24°C and average 24 h PAR of 300–500 μmol qanta m^{-2} s^{-1}. Changes in macroalgal biomass further influenced the composition and frequency of coral-algal interactions, however the incidence of coral-algal contact was best explained by coral cover. The results presented here emphasize that natural levels of macroalgae and coral-algal interactions are context-specific, and vary not only with-in zones, but in somewhat predictable seasonal cycles. Further, these results emphasize that the frequency of coral-algal interactions is dependent on hard coral, not just macroalgal cover, and an increase in coral-algal interactions does not necessarily translate to degradation of coral reefs.

Keywords: coral-algal interactions, seasonality, macroalgae, environmental drivers, spatial variation, coral reef

Edited by:
Tyler Cyronak,
University of California, San Diego,
United States

Reviewed by:
Maggy Nugues,
Ecole Pratique des Hautes Etudes,
Université de Sciences Lettres de
Paris, France
Heather N. Page,
Mote Marine Laboratory,
United States

***Correspondence:**
Kristen T. Brown
kristen.brown@uq.edu.au

Specialty section:
This article was submitted to
Global Change and the Future Ocean,
a section of the journal
Frontiers in Marine Science

Received: *04 April 2018*
Accepted: *07 May 2018*
Published: *24 May 2018*

Citation:
Brown KT, Bender-Champ D,
Kubicek A, van der Zande R,
Achlatis M, Hoegh-Guldberg O and
Dove SG (2018) The Dynamics of
Coral-Algal Interactions in Space and
Time on the Southern Great Barrier
Reef. Front. Mar. Sci. 5:181.
doi: 10.3389/fmars.2018.00181

INTRODUCTION

Many coral reefs are shifting away from coral dominance to assemblages that include macroalgae (Pandolfi et al., 2003; McManus and Polsenberg, 2004; Hughes et al., 2007). As a result, investigations into the drivers of coral-algal phase shifts have focused on disturbed ecosystems, where anthropogenic stressors (i.e., overfishing, eutrophication) are contributing to the proliferation of macroalgae and an increase in coral-algal competition (Hughes, 1994; Burkepile and Hay, 2006; Hughes et al., 2007; Littler and Littler, 2007; Smith et al., 2010). In order to understand the effects of human impacts, it is first necessary to understand how macroalgae respond to natural processes and to include more dynamic indicators of reef condition, such as coral-algal interactions (Connell et al., 2004; Bruno et al., 2014; Flower et al., 2017). Very few studies, however, have investigated natural drivers of the spatio-temporal dynamics of macroalgal biomass and its effect on coral-algal competition in the absence of anthropogenic influence (Bruno et al., 2014; Sangil and Guzman, 2016).

The natural state of macroalgae varies in space and time due to a combination of biotic (i.e., competition and herbivory) and abiotic (i.e., wave action and temperature) processes (Steneck and Dethier, 1994; Connell et al., 2004; Bruno et al., 2014). Spatially, macroalgae display distinct within and between reef patterns in biomass and community composition (Diaz-Pulido et al., 2007; Wismer et al., 2009). Macroalgae also show marked seasonal dynamics, primarily due to strong seasonal oscillations in temperature and light (Glenn et al., 1990; Ateweberhan et al., 2006; Fulton et al., 2014). The effects of spatio-temporal variability on tropical macroalgae, however, have mostly been inferred from the occurrence of seasonal peaks and have principally focused on large, conspicuous species (i.e., *Sargassum*) that bloom in the austral summer (Vuki and Price, 1994; McCook, 1997; Lefèvre and Bellwood, 2010). Comparatively, little is known about a large proportion of macroalgae, which predominantly grow in the austral autumn, winter and spring (Price, 1989; Rogers, 1996, 1997; Schaffelke and Klumpp, 1997). Furthermore, environmental factors do not operate independently, and investigations into how temperature and light interact to influence macroalgal seasonality have been less clear (Mathieson and Dawes, 1986; Fong and Zedler, 1993; Ferrari et al., 2012).

One apparent consequence of an increase in macroalgal abundance is a shift in the intensity of coral-algal competition (Connell et al., 2004; Diaz-Pulido et al., 2009; Haas et al., 2010). Competition between coral and macroalgae for limiting resources (i.e., space and light) can lead to reductions in coral growth and survival (Tanner, 1995; Clements et al., 2018), which have serious implications for the structure and function of coral reef ecosystems. An increase in macroalgal abundance leads to an increase in coral-algal interactions (Hughes, 1989, 1994; Bonaldo and Hay, 2014). Understanding how natural seasonal shifts in macroalgae influence the composition and frequency of coral-algal contact is critical for reef management (i.e., macroalgal removal programs), but remains unexplored.

Heron reef (23.442°S, 151.914°E), a platform reef located ~50 km off the coast of Queensland in the Great Barrier Reef (GBR), represents a unique location to study natural variation in macroalgae and coral-algal interactions for several reasons. The high-latitude and offshore location within the GBR Marine Park indicate that seasonal fluctuations are pronounced and major anthropogenic influences such as overfishing and water quality degradation (i.e., sedimentation, eutrophication) are comparatively minor (De'ath et al., 2012). The southern, offshore reefs were the least affected GBR region from the cumulative footprint of the last three major coral bleaching events (Hughes et al., 2017), and since 1992, have experienced only one major damage-inducing cyclone in 2009 (Connell et al., 1997; Woolsey et al., 2012). Within Heron reef, specific geomorphological zones include a gamut of naturally variable benthic communities subject to distinct diel and seasonal changes in seawater conditions (Phinn et al., 2012; Georgiou et al., 2015). As such, Heron reef is an ideal ecosystem to explore the influence of natural environmental drivers on fluctuations in benthic cover and coral-algal interactions across a complete reef system.

Here, we test the following hypotheses concerning spatio-temporal fluctuations in benthic cover and the influence on the composition and frequency of coral-algal interactions:

1. Benthic community composition is expected to vary across geomorphological zones, with higher coral cover and lower macroalgal cover on the reef slope compared to the lagoon.
2. The abundance of macroalgae, rather than coral cover, is expected to fluctuate seasonally.
3. Commoner species are expected to have more coral-algal interactions than rare species, and because coral is expected to vary by zone, and macroalgae by season, the frequency of coral-algal interactions is expected to vary by zone and season.
4. Since competition for space only occurs between neighbors, greater coral-algal interactions are expected to occur when abiotic substrate is limited and hard coral and/or macroalgal cover is high.

MATERIALS AND METHODS

Study Sites

Surveys were performed at Heron Island, southern Great Barrier Reef across the 23-month study period between January 2015 and November 2016. To measure seasonal variation, a total of eight expeditions were undertaken representing each austral season twice. Eight sites were chosen to encompass the distinct geomorphological habitats of Heron reef (Phinn et al., 2012) (**Figure 1**). Four reef slope sites were selected at two different depths (5 and 8 m) on the northeast and southwest of Heron reef: Fourth Point 5 m (F5), Fourth Point 8 m (F8), Harry's Bommie 5 m (H5), and Harry's Bommie 8 m (H8) (**Figure 1**). The northeast of Heron reef is the exposed side, subject to extreme wave forces during cyclones, whereas the southwest rim is sheltered from waves generated by both the SE trade winds and extreme wave action of cyclones by Wistari reef (Bradbury and Young, 1981; Connell et al., 1997, 2004). The northeast study area is the only area investigated located outside of the Marine National Park management zone, where fishing is permitted. One site was selected on the reef crest (Reef Crest, RC), and within the lagoon, three sites were chosen [Reef Flat (RF), Shallow Lagoon (SL), Deep Lagoon (DL)] (**Figure 1**). The lagoonal study area is shallow and periodically isolated at low tide, resulting in extreme diel fluctuations in seawater conditions (Kinsey and Kinsey, 1967; Potts and Swart, 1984; Georgiou et al., 2015).

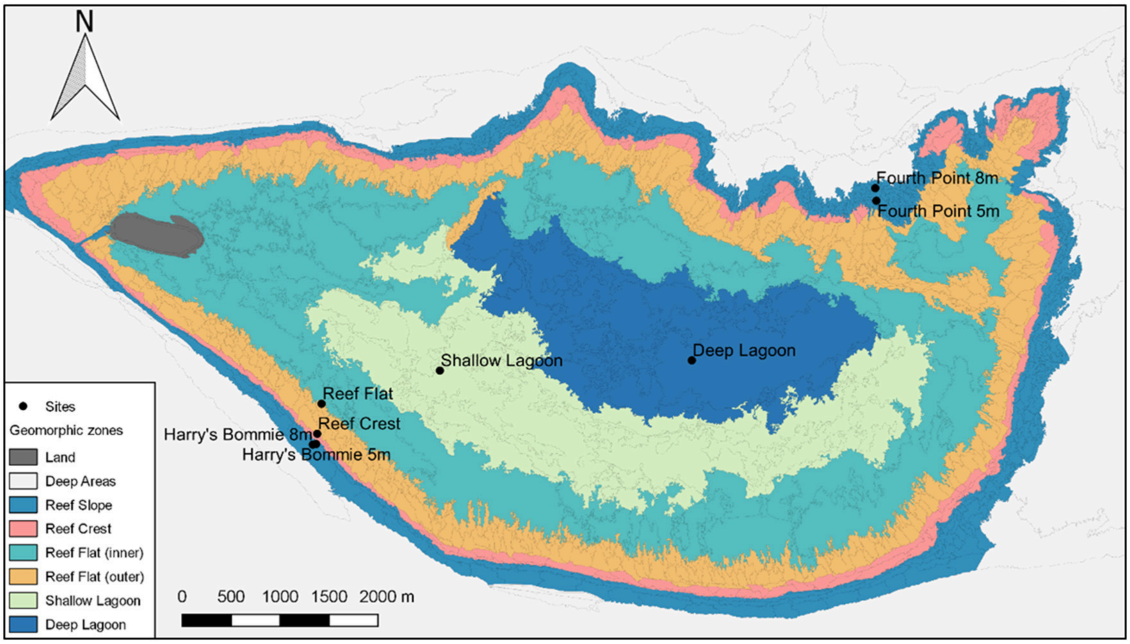

FIGURE 1 | Geomorphic zones of Heron reef, southern Great Barrier Reef. Surveyed sites are indicated by name. Map data provided by Phinn et al. (2012).

Benthic Community Composition and Coral-Algal Interactions

Benthic community composition and frequencies of coral-algal contact were recorded using the method described by Brown et al. (2017). At each site, 3 × 15 m transects were established coursing north, east and west from a central reference point. Benthic community composition was measured by recording percent cover from thirty 0.25 m^2 quadrats per transect *in situ*, totalling 90 quadrats per site. Benthic community composition was determined from 22 categories, with the four central categories consisting of hard coral, other invertebrates, macroalgae, and abiotic substrate. Commonly encountered coral families were chosen, representing a range of growth forms: *Acropora-Isopora* (ACR-ISO, including tabular/corymbose/branching/columnar varieties); *Montipora* (MON); Pocilloporidae (POCI); Poritidae-massive (PORM); Poritidae-encrusting/plating varieties (PORE); Poritidae-branching (PORB); Favidae-Lobophyllidae (FAV-LOB); and other hard corals (including non-scleractinian corals). Macroalgae were differentiated as: fleshy macroalgae (i.e., *Sargassum*, *Laurencia intricata*), *Halimeda*, turf algae/cyanobacteria assemblages, and articulate/crustose coralline algae (ACA/CCA). Turf algae/cyanobacteria assemblages were distinguished as macroscopic assemblages that were generally >3 mm in height (Birrell et al., 2005). "Other invertebrates" included organisms such as soft corals, giant clams, sea cucumbers, and all other invertebrates (i.e., sponges, ascidians). "Abiotic substrate" was divided into sand/sediment, coral rubble, recently dead hard coral, and "bare" rock (i.e., epithetic algal community with turf height <3 mm) (see definitions in Brown et al., 2017).

Along the same transects, a 1 m belt (0.5 m on either side) of the transect line was examined and any coral colonies physically touching macroalgae were documented (Brown et al., 2017). A single coral colony (i.e., corals with more than one corallite) could be involved in multiple competitive interactions with different macroalgal taxa or groups (Swierts and Vermeij, 2016). The types of interacting corals and macroalgae were recorded to genus level, with the exception of cyanobacteria, turf algae, and crustose coralline algae, which generally cannot be identified to genus level *in situ* (Steneck and Dethier, 1994).

To calculate the frequency of coral-algal contact, all coral colonies occurring along a transect, regardless of macroalgal contact, were counted. The total number of interactions per coral colony, allowing for multiple interactions per coral colony, was then determined by site and season by dividing the number of coral-algal interactions by the total number of coral colonies occurring per transect (i.e., number of interactions per coral). To calculate the most frequently encountered coral-algal interactions at each site, the five most abundant coral-algal interactions were established in each season. To visualize differences in interacting macroalgal taxa or groups by site and season, the total number of interactions were summed by macroalgal taxa or groups and divided by the total number of observed interactions so that the sum of all macroalgal components was 100%.

Environmental Variables

Variation in seawater temperature (°C) and irradiance (µmol quanta m^{-2} s^{-1}) were monitored continuously from July 2015 to November 2016 (Figure S1). Seawater temperatures were measured hourly, and photosynthetic active radiation (PAR) were integrated over hourly intervals at all sites by use of Conductivity Temperature Depth units (CTD; SBE 16*plus* V2 SEACAT) fitted with an auxiliary PAR sensor (Satlantic/ECO-PAR sensor, WET Labs). At Fourth Point 8 m, seawater temperature (HOBO Pendant UA-001-64, Onset) and PAR (Odyssey PAR sensor, Dataflow Systems Ltd) were recorded using other sensors. All PAR sensors were fitted with copper coating to prevent biofouling, cleaned *in situ* at least monthly, and removed every 3 months to clean thoroughly, exchange batteries, and download the data.

Statistical Analyses

Statistical analyses were conducted using R version 3.3.2 software (R Core Team, 2014), and plots were produced using the package *ggplot2* (Wickham, 2016). Differences in benthic community composition and coral-algal interaction composition were analyzed using permutational MANOVAs (PERMANOVA), with the fixed effects of site and season using the adonis function in the *vegan* package. Resemblance matrices were obtained using Bray-Curtis dissimilarity and 9,999 permutations. Significant PERMANOVA results were explored by running separate two-way ANOVAs on explicit benthic categories. Differences in the frequency of coral-algal contact were also explored using a two-way ANOVA. The categorical factors contained the following levels: season (spring, summer, autumn, winter) and site (H8, H5, RC, RF, SL DL, F5, F8). Transects were used as replicates. Data were tested and met the assumptions for homogeneity of variance (Levene's test) and normality of distribution (Normal Q-Q plots). Significant interactive effects were followed by pairwise comparison with Tukey *post-hoc* tests.

All generalized additive models (GAMs) were applied to data sets using the package *mgcv* (Wood, 2006). In all models, the number of knots were restricted ($k = 4$) to produce conservative models and avoid overfitting. To quantify the response of the frequency of coral-algal contact to benthic cover, three GAMs were fit using hard coral, macroalgae, and abiotic substrate as predictor variables.

To explore the response of macroalgal abundance to seasonal changes in environmental conditions, we fit all possible model combinations using seasonally averaged temperature (°C; mean of hourly measurements) and PAR (μmol quanta m^{-2} s^{-1}; mean of 24-h measurements) as predictor variables (**Table 1**). Cyclic penalized cubic regression splines (cc) and tensor product interactions (ti) were chosen as the smoothers for the separate covariates and interactions terms, respectively. The model requires interaction terms because the combined effect of both predictor variables differs from their separate effect (Wood, 2006). The model structure was developed using a stepwise procedure: temperature was added first, followed by irradiance, and finally the interaction term (Yi et al., 2016). These models were compared using the Akaike Information Criterion Corrected (AICc). A three-dimensional "perspective" plot was generated using the *vis.gam* function in the *mgcv* package.

RESULTS

Effects of Site and Season on Benthic Community Composition

Benthic community composition was significantly influenced by both site [PERMANOVA, $F_{(1,\,167)} = 58.37$, $p < 0.0001$] and season [PERMANOVA, $F_{(1,\,167)} = 2.105$, $p = 0.039$]. Broad hard coral cover was significantly higher at the reef slope sites compared to the lagoon and was not significantly influenced by season (**Table 2**). Specific hard coral functional groups showed distinct spatial patterns, but not seasonal patterns interactive or otherwise (**Table 2**). *Acropora-Isopora* was the most abundant across Heron reef, with the highest cover on the reef slope and reef crest (**Table 2**). *Montipora* was highest on the southwest reef slope and was nearly absent in the lagoon (**Table 2**). The family of hard coral Pocilloporidae was found at every site (**Table 2**). The different growth forms of the coral family Poritidae showed variable spatial patterns, with the highest density of Poritidae-branching and Poritidae-massive occurring at the Deep Lagoon; and generally low levels of Poritidae-plating/encrusting across Heron reef (**Table 2**). Massive corals of the families Favidae-Lobophyllidae were found at every site, with the greatest abundance observed on the southwest side of Heron reef (**Table 2**).

Fleshy macroalgal cover varied by both site and season, with the highest cover observed in the lagoon and in spring (**Table 2**, **Figure 2**). *Halimeda* cover varied by site, with significantly higher cover on the north side of Heron reef (**Table 2**, **Figure 2**). The cover of crustose/articulate coralline algae (CCA/ACA) also significantly varied by site, with the highest cover observed on the reef crest (**Table 2**, **Figure 2**). Turf algae/cyanobacteria assemblages were influenced by both site and season, with cover generally highest on the reef slope and significantly lower in winter (**Table 2**, **Figure 2**). Abiotic substrate cover was highest in the lagoon and did not significantly vary with season (**Table 2**).

Effect of Temperature and Irradiance on Macroalgal Abundance

AICc indicated that the best-fit GAM incorporated both temperature and irradiance to best explain macroalgal abundance. Maximum macroalgal abundance corresponded with average temperature of between 22 and 24°C and average 24 h PAR of 300–500 μmol quanta m^{-2} s^{-1} (**Figure 3**). Two smaller peaks were observed when average 24 h PAR was 150–300 μmol quanta m^{-2} s^{-1} and average temperatures were $\sim$21 and $\sim$26°C. At the warmest observed temperature ($\sim$26°C) and highest observed light intensity (24 h PAR: 400–500 μmol quanta m^{-2} s^{-1}), macroalgal abundance was lowest (**Figure 3**).

Effect of Site and Season on the Frequency and Composition of Coral-Algal Interactions

The frequency of coral-algal contact was highest at the Reef Flat and Shallow Lagoon [ANOVA, $F_{(1,\,160)} = 26.9$, $p < 0.00001$, *post-hoc*: SL = IRF > F8 = DL > F5 = RC > H8 = H5] and was

TABLE 1 | Average benthic community composition, temperature and irradiance by season and site from Heron Island, southern Great Barrier Reef.

Season	Site	Hard coral	*SD*	Macroalgae	*SD*	Abiotic	*SD*	Temperature	*SD*	PAR	*SD*
Autumn	Deep lagoon	15.51	5.9	26.22	14.7	60.67	19.6	25.70	1.33	151.67	248.85
Autumn	Fourth point 5 m	61.25	9.4	19.37	2.9	21.33	11.0	26.14	1.08	157.09	240.38
Autumn	Fourth point 8 m	25.73	11.0	31.21	6.8	45.67	8.9	26.54	1.07	45.85	68.92
Autumn	Harry's Bommie 5 m	78.26	2.5	8.72	3.7	14.56	4.2	26.06	0.98	51.67	82.63
Autumn	Harry's Bommie 8 m	70.49	9.7	7.84	2.9	21.12	10.0	25.81	1.04	43.71	75.20
Autumn	Harry's tower	50.48	15.7	20.97	6.3	29.92	17.2	25.78	1.24	155.25	269.85
Autumn	Inner reef flat	16.87	3.5	21.43	6.0	64.04	7.9	25.68	1.26	338.19	498.50
Autumn	Shallow lagoon	2.21	1.3	28.42	7.5	69.69	7.8	26.10	1.23	112.02	181.38
Spring	Deep lagoon	14.18	6.5	32.28	23.1	55.39	29.6	23.46	1.42	223.13	319.99
Spring	Fourth point 5 m	66.03	10.1	16.72	2.2	18.83	10.0	23.07	0.97	220.43	319.10
Spring	Fourth point 8 m	24.64	9.2	37.67	8.2	40.14	2.9	23.49	1.02	61.68	88.36
Spring	Harry's Bommie 5 m	81.22	3.7	8.75	3.1	11.81	2.6	22.99	1.03	103.36	152.94
Spring	Harry's Bommie 8 m	77.33	8.8	6.08	1.8	17.61	9.4	23.08	0.97	97.76	142.94
Spring	Harry's tower	54.00	14.9	19.61	5.0	28.11	17.3	23.25	1.27	242.38	390.00
Spring	Inner reef flat	16.83	3.7	27.11	4.5	58.53	7.0	23.19	1.27	461.43	637.05
Spring	Shallow lagoon	2.25	1.7	36.78	12.5	61.69	13.8	23.42	1.47	230.19	389.56
Summer	Deep lagoon	13.50	7.3	21.28	15.1	67.78	22.0	26.95	1.00	176.54	269.66
Summer	Fourth point 5 m	62.56	9.0	21.50	2.3	17.17	9.0	26.43	0.78	197.57	284.99
Summer	Fourth point 8 m	25.28	8.8	29.17	3.2	47.00	7.6	26.79	0.76	73.88	106.13
Summer	Harry's Bommie 5 m	74.56	6.9	8.50	4.2	18.44	9.9	26.57	0.71	99.26	138.49
Summer	Harry's Bommie 8 m	76.39	8.4	7.33	2.8	16.83	5.8	26.57	0.68	89.09	127.10
Summer	Harry's tower	60.00	14.3	15.78	2.3	25.83	15.2	26.60	0.99	181.79	286.85
Summer	Inner reef flat	19.89	3.1	22.00	1.2	60.89	3.8	26.74	1.11	514.94	698.59
Summer	Shallow lagoon	4.00	1.4	19.39	3.2	77.11	4.0	26.95	1.25	283.09	444.79
Winter	Deep lagoon	15.53	6.3	28.08	18.2	59.08	23.0	21.43	0.87	145.33	242.85
Winter	Fourth point 5 m	62.00	10.9	19.92	2.5	19.42	10.3	21.82	0.79	127.16	216.47
Winter	Fourth point 8 m	24.92	10.5	26.63	5.3	50.56	9.4	22.04	0.75	37.12	59.35
Winter	Harry's Bommie 5 m	74.75	6.0	8.36	3.6	18.33	8.3	21.78	0.67	47.51	86.87
Winter	Harry's Bommie 8 m	69.97	20.0	8.22	5.1	19.09	9.2	21.81	0.71	46.79	76.39
Winter	Harry's tower	53.92	16.1	18.64	7.2	29.25	18.5	21.80	0.92	154.20	287.75
Winter	Inner reef flat	17.46	1.8	20.19	1.5	64.94	3.2	21.70	0.95	264.40	425.55
Winter	Shallow lagoon	2.69	1.8	36.36	11.0	61.61	12.0	21.68	0.88	128.35	301.12

Hard coral, macroalgae, and abiotic composition are percent cover (mean ± SD; n = 3) at each site in each austral season. Other invertebrate cover not reported. Temperature (°C) values are seasonal averages (mean ± SD) of measurements recorded at hourly intervals, and photosynthetic active radiation (PAR, μmol quanta m^{-2} s^{-1}) values are seasonal averages (mean ± SD) of 24-h measurements.

significantly reduced in summer [ANOVA, $F_{(1,\,160)} = 3.42$, $p = 0.01$, *post-hoc*: autumn = winter = spring > summer] (**Figure 4**).

A total of 207 unique coral-algal interactions were observed across all transects, representing 30 coral and 21 macroalgal taxa or groups (Table S1). The composition of coral-algal interactions was significantly affected by site [PERMANOVA, $F_{(1,\,63)} = 6.51$, $p = 0.0001$] and season [PERMANOVA, $F_{(1,\,62)} = 1.33$, $p = 0.028$]. Depending on seasonal shifts in coral-algal interactions, each site could have up to 20 unique coral-algal interactions, with the 10 most abundant displayed (**Figure 5**). Generally, the most abundant coral taxa were the most commonly encountered coral interacting with macroalgae (**Figure 5**). For macroalgae, interactions with *Halimeda* were frequently encountered at the reef crest and northeast side of Heron reef (**Figure 5**). Turf algae were the most abundant macroalgae interacting with coral at southwest side of Heron reef (**Figure 5**). In the lagoon, frequently encountered coral-algal interactions fluctuated seasonally (**Figure 5**).

Modeling the Effect of Benthic Cover on the Frequency of Coral-Algal Interactions

Relationships between the number of coral-algal interactions to hard coral cover (edf: 2.58, $F = 23.21$, $p < 0.00001$), macroalgal cover (edf: 2.89, $F = 11.5$, $p < 0.00001$), and abiotic substrate cover (edf: 1.92, $F = 8.664$, $p = 0.0001$) were non-linear and resembled parabolic, sinusoidal, and exponential decay curves, respectively (**Figure 6**). Hard coral cover explained 29.6% of the deviance in coral-algal interaction frequency, macroalgal cover explained 17.1% and abiotic substrate cover explained 11.6%. The greatest number of coral-algal interactions occurred when coral cover was ∼50%, macroalgal cover was ∼20%, and abiotic cover remained less than ∼30% (**Figure 6**).

TABLE 2 | Results of the statistical analyses (two-way ANOVAs) on benthic community composition.

Response variable	Factor(s)	*df*	*F*	*p*	*Post-hoc*
Hard coral (broad)	Site	7,136	207.49	<0.00001	H8 = H5 > F5 > RC > F8 > RF = DL > SL
	Season	3,136	0.585	0.63	
	Site × season	21,136	0.305	0.99	
Acropora-Isopora	Site	7,136	93.5	<0.00001	H8 = H5 = RC > F5 > F8 > RF > DL= SL
	Season	3,136	0.32	0.81	
	Site × season	21,136	0.25	1	
Montipora	Site	7,136	236.6	<0.00001	H8 > H5 = F5 > F8 = RC = RF = DL= SL
	Season	3,136	0.83	0.48	
	Site × season	21,136	0.76	0.76	
Pocilloporidae	Site	7,136	18.3	<0.00001	DL = F5 = RC > RF = H5 = H8 = F8 = SL
	Season	3,136	0.15	0.93	
	Site × season	21,136	0.32	0.99	
Poritidae (branching)	Site	7,136	42.3	<0.00001	DL > RF = F5 = H8 = F8 = H5 = HT = SL
	Season	3,136	0.77	0.51	
	Site × season	21,136	0.97	0.5	
Poritidae (massive)	Site	7,136	10.9	<0.00001	H5 = DL = RC > F5 > H8 = F8 = RF = SL
	Season	3,136	0.25	0.86	
	Site × season	21,136	0.32	0.99	
Poritidae (plating/encrusting)	Site	7,136	4.1	<0.00001	H5 > H8 = RC = F5 = F8 = RF = DL= SL
	Season	3,136	2.7	0.05	
	Site × season	21,136	1.49	0.09	
Favidae-Lobophyllidae	Site	7,136	53.1	<0.00001	H5 = H8 > F5 > RC = RF = SL = DL = F8
	Season	3,136	0.077	0.97	
	Site × season	21,136	0.46	0.98	
Fleshy macroalgae	Site	7,136	39.2	<0.00001	SL > RF = DL > RC = F8 = F5 = H8 = H5
	Season	3,136	4.78	0.003	spring = winter > autumn = summer
	Site × season	21,136	1.3	0.17	
Halimeda	Site	7,136	92.6	<0.00001	F8 > F5 > DL = RC = RF = SL > H8 = H5
	Season	3,136	0.15	0.93	
	Site × season	21,136	0.53	0.95	
Crustose/articulate coralline algae (CCA/ACA)	Site	7,136	23.5	<0.00001	RC > DL = F8 > F5 > H5 = RF = SL = H8
	Season	3,136	1.3	0.29	
	Site × season	21,136	0.31	0.99	
Turf algae/cyanobacteria	Site	7,136	12.5	<0.00001	F8 = H8 = H5 = RC > RF > DL = F5 = SL
	Season	3,136	5.02	0.002	spring = summer = autumn > winter
	Site × season	21,136	1.2	0.27	
Abiotic (broad)	Site	7,136	57.75	<0.00001	SL = RF = DL > F8 > RC = F5 = H5 = H8
	Season	3,136	1.27	0.29	
	Site × season	21,136	0.325	0.99	

DISCUSSION

Tropical coral reefs worldwide are degrading due to human activities. In many cases, reef-building corals have declined and macroalgae have become more prevalent (McManus and Polsenberg, 2004). Recent work has focused on measuring macroalgal abundance in response to anthropogenic stressors (Hughes et al., 2007; Littler and Littler, 2007; Smith et al., 2010). To evaluate the effects of human impacts, however, it is first necessary to understand the effects of natural processes on reef condition (Bruno et al., 2014; Flower et al., 2017).

The results presented here highlight the key observation that natural levels of macroalgae and coral-algal interactions are context-specific, and do not only vary within zones, but also within the context of well-known seasonal cycles. Distinct spatio-temporal changes in temperature and light controlled the abundance of macroalgae, with macroalgal biomass peaking in spring and decreasing in summer. Given the important role that macroalgae and coral-algal interactions play in structuring coral reef ecosystems, these results indicate that frequent reef monitoring should be encouraged within and between zones to detect potential changes and avoid a loss of important

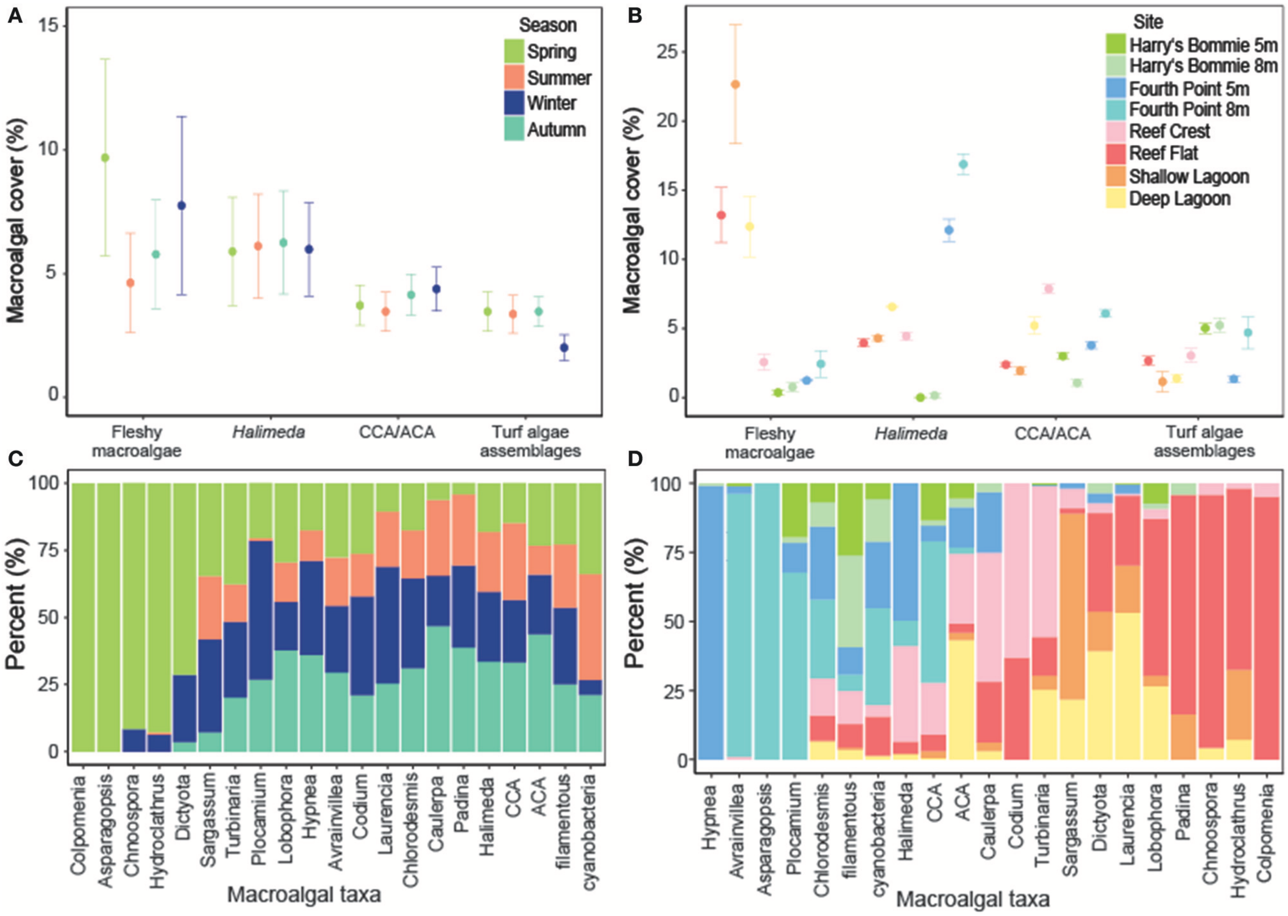

FIGURE 2 | The cover of macroalgae and the composition of macroalgal taxa or groups by season and site. **(A)** Percent cover (mean ± SE; $n = 3$) of broad macroalgal taxa or groups by season. **(B)** Percent cover (mean ± SE; $n = 3$) of broad macroalgal taxa or groups by site. **(C)** Seasonal differences in the composition of interacting macroalgal taxa or groups. **(D)** Differences in the composition of interacting macroalgal taxa or groups by site. The total number of interactions were summed by macroalgal taxa or groups and divided by the total number of interactions so that the sum of all macroalgal components was 100%.

information relating to the trajectory and resilience of coral reef ecosystems.

The benthic community composition varied distinctly across the geomorphological zones, which was expected (Hatcher, 1988; Phinn et al., 2012). Within the reef slope, however, differences in benthic community composition were revealed between the northeast and southwest sides of Heron reef. Regardless of depth, the southwest was characterized by very high hard coral cover (∼80%) and low turf algal cover, indicating a healthy reef condition with high herbivory and low nutrients (Littler and Littler, 2007). On the northeast side, community composition varied by depth, with high hard coral cover (∼60%) at 5 m and at 8 m, comparatively low and uniform branching *Acropora* cover (∼20%), high macroalgal cover and high amounts of coral rubble. Large decreases in coral cover at Heron reef over the 40-year period from the 1960s to the 1990s have been directly attributable to the localized effects of cyclones at particular locations (Connell et al., 1997, 2004). In 2009, waves from cyclone Hamish struck the northern side of Heron reef (Woolsey et al., 2012). The reduction in coral cover and increase coral rubble observed in this study suggest that the northeast reef slope at 8 m sustained localized damage due to the cyclone's impact. The long-term study of Connell et al. (2004) indicates that recovery to ∼20% coral cover on the northeast slope can occur in ∼5 years post-cyclone, particularly when seeded from displaced fragments of fast-growing branching *Acropora*, which is consistent with these findings.

In addition to reduced coral cover and increased coral rubble, macroalgal cover was higher on the northeast side of Heron reef. On both the southwest and northeast slope, fleshy macroalgal cover remained very low (<2%). The cover of the calcifying macroalgae *Halimeda*, however, was significantly higher on the exposed side. *Halimeda* is highly vulnerable to herbivory by fishes in the families Scaridae and Acanthuridae, suggesting an increase in biomass may be due to a reduction in these fish populations (Ferrari et al., 2012; Castro-Sanguino et al., 2016). Although herbivorous fish abundances were not directly measured, the northeast study area is the only area investigated outside of the Marine National Park management zone, where fishing is permitted. Furthermore, the reduction in coral cover due to cyclone damage may have led to a decline in structural complexity, further reducing fish populations (Wilson et al., 2008), and ultimately leading to a greater abundance of *Halimeda*.

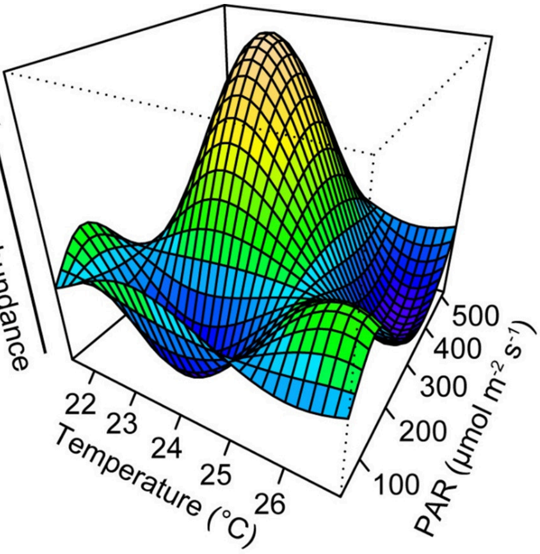

FIGURE 3 | Three-dimensional graphic output from generalized additive model (GAM) with temperature and irradiance as predictors of macroalgal abundance. Temperature (°C) values are seasonal averages of measurements recorded at hourly intervals, and photosynthetic active radiation (PAR, µmol quanta m^{-2} s^{-1}) values are seasonal averages of 24-h measurements. Plot was generated using the *vis.gam* function in the *mgcv* package (Wood, 2006).

The lagoonal geomorphological zones were distinctly different from the reef slope, characterized by low hard coral cover, high macroalgal biomass and high cover of sand. Coral cover on the Heron reef flat has historically ranged between 0 and 20%, which is consistent with our observations of coral cover (∼18%) (Connell et al., 2004). Although hard corals are believed to be sensitive to environmental extremes, recent studies have shown that corals are able to persist in marginal conditions of lagoon habitats (Camp et al., 2017) and increased temperature variability reduces the likelihood of coral bleaching (Safaie et al., 2018). Instead, persistently low coral cover in the Heron lagoon appears to be due to reduced coral recruitment due to the lack of hard substrate (Connell et al., 2004). In the shallow lagoon, hard substrates were present, but mostly as unconsolidated rubble banks, resulting in the lowest observed coral cover (<5%) on Heron reef (Fox et al., 2003). At the reef flat and deep lagoon, there was a greater availability of suitable stabilized substrate, giving rise to a higher abundance of corals (Morrissey, 1980). Competition for space with macroalgae may further prevent coral recruitment, with dense macroalgal populations blanketing the benthos and pre-empting coral settlement (Birrell et al., 2008). Average fleshy macroalgal cover ranged from 15 to 25% within the lagoon, which was facilitated by reduced grazing pressure due to periodic isolation at low tide (Hatcher and Larkum, 1983; McCook, 1997), reduced water movement and wave energy (Dollar, 1982), and decreased competition with reef-building corals (Diaz-Pulido and McCook, 2004).

Broad macroalgal abundance showed pronounced seasonal variations, and the seasonality of macroalgae tracked closely with spatio-temporal changes in temperature and light availability.

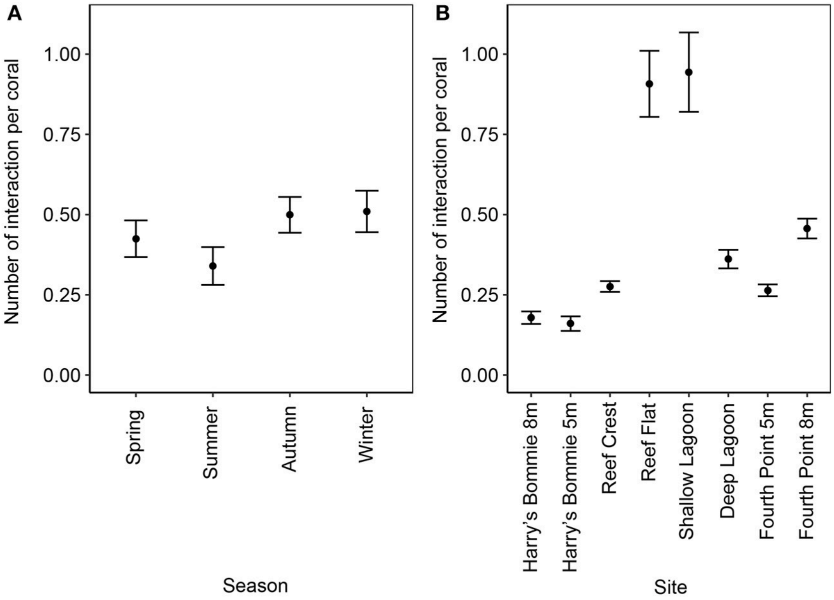

FIGURE 4 | Frequency of coral-algal contact by season and site. **(A)** Seasonal differences in frequency of coral-algal contact (mean ± SE; $n = 48$). **(B)** Variation in the frequency of coral-algal contact by site (mean ± SE; $n = 24$). The total number of coral-algal interactions, allowing for multiple interactions per coral, was determined per transect and divided by the total number of corals along the transect.

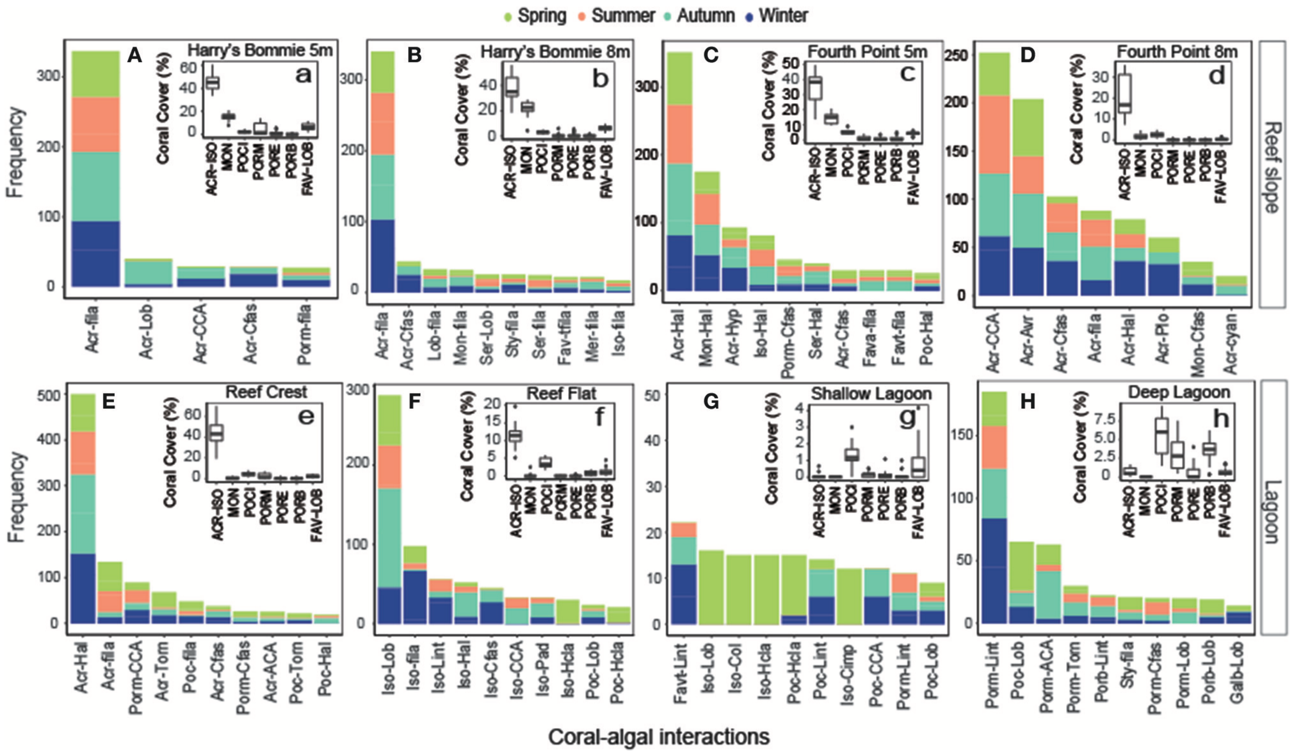

FIGURE 5 | Frequency of coral-algal interactions by site with inset displaying coral cover. For each site **(A–H)**, the most frequently encountered coral-algal interactions were established, by combining the five most abundant coral-algal interactions from each season. Only the top 10 most dominant are displayed here (where applicable). Coral-algal interactions are abbreviated listing the coral first and macroalgae second. Inset (a-h) displays boxplots (minimum, 25th percentile, median, 75th percentile, and maximum; $n = 24$) of hard coral functional group abundance. **(A–H)** abbreviations: Coral: Acr, *Acropora*; Fava, *Favia*; Favt, *Favites*; Galb, *Galaxea* (branching); Iso, *Isopora*; Lob, *Lobophyllia*; Mer, *Merulina*; Mon, *Montipora*; Poc, *Pocillopora*; Porb, *Porites* (branching); Porm, *Porites* (massive); Ser, *Seriatopora*; Sty, *Stylophora* Macroalgae: ACA, articulate coralline algae; Avr, *Avrainvillea*; CCA, crustose coralline algae; Cfas, *Chlorodesmis fastigiata*; Cimp, *Chnoospora implexa*; Col, *Colpomenia*; cyan, cyanobacteria; fila, turf; Hal, *Halimeda*; Hcla, *Hydroclathrus clathratus*; Hyp, *Hypnea*; Lint, *Laurencia intricata*; Lob, *Lobophora*; Pad, *Padina*; Plo, *Plocamium*; Torn, *Turbinaria ornate.* a-h abbreviations: ACR-ISO, *Acropora-Isopora*; MON, *Montipora*; POCI, Pocilloporidae; PORM, Poritidae (massive); PORB, Poritidae (branching); PORE, Poritidae (encrusting); FAV-LOB, Favidae-Lobophyllidae.

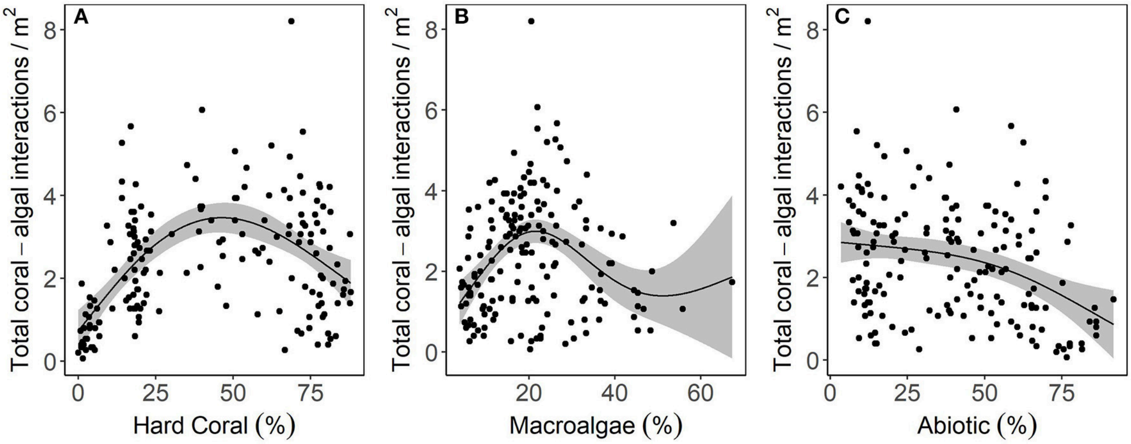

FIGURE 6 | The effect of benthic cover on the frequency of coral-algal interactions based on fitted parameter estimates ± 95% confidence intervals (shaded). The effect of **(A)** hard coral, **(B)** macroalgae, and **(C)** abiotic substrate on the frequency of coral-algal interactions. In each case, a generalized additive model (GAM) with integrated smoothness estimation was fit using the package *mgcv* (Wood, 2006).

The highest cover of fleshy macroalgae was observed in shallow, lagoonal environments in spring and was significantly lower in summer. Turf algal/cyanobacteria assemblages, on the other hand, were nearly absent in the winter, reflecting a preference toward warmer temperatures (O'Neil et al., 2012). Field observations were further supported by the modeled abundance of macroalgae using temperature and irradiance as predictors. Moderate temperature and high light, corresponding to spring temperature and shallow reef flat habitats, gave rise to the greatest macroalgal biomass. The lowest abundance of macroalgae was observed when both temperature and light were highest, corresponding with summer temperatures and high light environments. While seawater temperature and light have long been considered important drivers of macroalgal seasonality, the relationship between the two variables has been unclear (Mathieson and Dawes, 1986; Fong and Zedler, 1993). These results yield a unique perspective on the interaction of light and temperature on macroalgal abundance, revealing a complex, non-linear response across environmental gradients. Further, these findings emphasize that natural levels of macroalgal abundance are context-specific, and vary not only within zones, but in somewhat predictable seasonal cycles. When investigating macroalgal abundance, both spatial and seasonal variability must be considered, particularly as seasonality in macroalgal abundance can impact a reef's trajectory and resilience (Diaz-Pulido et al., 2009).

In addition to macroalgal cover, the composition and frequency of coral-algal interactions showed distinct spatio-temporal variation. Commoner species are expected to have more interactions than rare species (Connell et al., 2004). On the reef slope, *Acropora* was the most abundant coral genera, resulting in the greatest number of interactions with macroalgae. On the southwest side of Heron reef, the most widespread interaction was between *Acropora* and turf algal assemblages. Many of these interactions were algal lawns cultivated by territorial damselfish (i.e., *Stegastes* sp.), whose aggressive behavior can reduce grazing pressure and allow dense turf algal mats to persist (Potts, 1977; Bruno et al., 2014). While these interactions were frequently observed, a very small proportion of other coral-algal interactions were encountered and the incidence of coral-algal contact was the lowest on all of Heron reef. On the northeast side of Heron reef, the frequency of coral-algal contact was significantly higher, with a greater diversity of coral-algal interactions principally driven by interacting macroalgal taxa or groups. Interactions with *Halimeda* were common, reflecting the significantly higher abundance of this macroalga in the study area. Although fleshy macroalgal cover remained very low (<5%), interactions between four genera of fleshy macroalgae, *Plocamium*, *Hypnea*, *Avrainviella*, and *Asparagopsis*, were principally encountered on the northeast reef slope at 8 m. These taxa were observed selectively growing at the bases and among the branches of *Acropora* colonies, suggesting these interactions were occurring more than expected. The unique habitat within the *Acropora* canopy may provide refuge from herbivores or a reduction in water movement and in doing so, limit the ability of these macroalgal taxa to grow beyond the branches of the coral (Hay, 1986; Jompa and McCook, 2003b; Castro-Sanguino et al., 2016).

The composition of coral-algal interactions in the lagoon differed considerably from the reef slope. Commonly observed lagoonal taxa *Isopora*, *Pocillopora*, and *Porites* were the most abundant in the reef flat, shallow lagoon, and deep lagoon, respectively (Morrissey, 1980; Tanner, 1995). Similar to the reef slope, the dominant coral taxa were coral species that most frequently interacted with macroalgae. Unlike the reef slope, however, the composition of interactions in the lagoon varied seasonally, reflecting a seasonal shift in the macroalgal community. Several macroalgal taxa were observed interacting with corals only in the lagoon including fleshy macroalgal taxa *Turbinaria*, *Sargassum*, *Padina*, and *Lobophora*, which is consistent with previously reported spatial variation (Tanner, 1995; Rogers, 1997; Diaz-Pulido et al., 2007). A subset, *Hydroclathrus*, *Colopomenia*, *Chnoospora,* and *Dictyota*, were observed predominantly in spring, reflecting their ephemeral seasonality (Price, 1989; Rogers, 1997; Schaffelke and Klumpp, 1997; Diaz-Pulido et al., 2007). These results highlight the unique seasonality of macroalgal taxa, even within the same functional group, and demonstrate that shifts in macroalgal taxa influence the composition of coral-algal interactions. Future studies should consider the seasonality of individual macroalgal taxa when investigating coral-algal competition.

While on modern reefs it is believed that an increase in coral-algal interactions is synonymous with processes associated with reef degradation (Smith et al., 1981; Lewis, 1986; Hughes, 1989, 1994; Bonaldo and Hay, 2014), the highest frequency of coral-algal interactions observed here were associated with healthy, spatially heterogeneous coral reef assemblages. Since competition for space takes place only between neighbors, coral-algal interactions would be expected to occur more often when abiotic space is low (Brown et al., 2017) and coral (Connell et al., 2004) or macroalgal cover are high (Smith et al., 1981; Lewis, 1986; Hughes, 1989, 1994; Bonaldo and Hay, 2014). Our results show that the greatest number of coral-algal interactions on Heron reef occur when coral cover is ~50%, macroalgal cover is ~20%, and abiotic cover remains less than ~30%. Even though macroalgal abundance fluctuated naturally from as low as 1% to as high as 60% cover, an increase in macroalgal cover over 20% did not translate into an increase in coral-algal interactions, which is similar to some previous studies (Jompa and McCook, 2003a; Brown et al., 2017) and in contrast to others (Smith et al., 1981; Lewis, 1986; Hughes, 1989, 1994; Bonaldo and Hay, 2014). Instead, coral cover was the best predictor of the coral-algal interaction frequency. When coral cover was low (<25%), there were fewer coral-algal interactions. This reduction in coral-algal interactions corresponded with an increase in both macroalgae and abiotic substrate cover, suggesting less coral-algal interactions indicate reduced coral cover. When coral cover was very high (>70%), however, there were also fewer coral-algal interactions. As coral cover increases over ~50%, the number of coral-coral interactions increases exponentially (Connell et al., 2004), suggesting that when coral cover is high, interactions between corals themselves is the principle form of competition. These results emphasize that the frequency of coral-algal interactions is dependent on the abundance of hard coral, not just macroalgal cover, and an increase in coral-algal interactions does not necessarily translate to degradation of coral reefs.

Macroalgae and their interactions with corals are more relevant than ever, especially given the rapidly shifting tropical coral reef ecosystem dynamics. Ideally, reef-monitoring will take place during the same time of year and at the same location. Due to logistical constraints (i.e., weather, financial), however, coral reef monitoring often occurs in response to a disturbance and rarely ever considers seasonal and spatial variability. The results presented here emphasize that natural levels of macroalgae and coral-algal interactions are context-specific, and vary not only with-in zones, but in somewhat predictable seasonal cycles. Variation in temperature and light play a key role in the abundance of tropical macroalgae, and future work should explore to what extent these thresholds are reached at large spatial scales to improve quantitative models of the biomass of macroalgae on coral reefs. The complexity of macroalgal and coral-algal dynamics across this one reef system further highlight the need for future studies to consider inter-seasonal variability across zones and illustrate the difficulty in determining the baseline condition of well-studied ecosystems. Now more than ever, seasonal and long-term studies are needed to avoid a loss of important information associated with the trajectory and resilience of coral reef ecosystems.

DATA AVAILABILITY STATEMENT

The datasets generated/analyzed for this study can be found as an electronic notebook on (https://github.com/imkristenbrown) with scripts available through https://github.com/imkristenbrown.

AUTHOR CONTRIBUTIONS

KB, DB-C, AK, SD, and OH-G: designed the study; KB, DB-C, AK, RvdZ, and MA: carried out the study and collected field data; KB, DB-C, and SD: performed statistical analyses; KB: wrote the first draft of the manuscript, and all authors contributed substantially to the interpretation and final version of the paper. All authors agreed to be listed and gave final approval for publication.

FUNDING

This work was supported by the Australian Research Council (ARC) LP110200874 (SD and OH-G), the ARC Centre of Excellence for Coral Reef Studies CE140100020 (SD and OH-G), and an ARC Laureate Fellowship FL120100066 (OH-G). It was also supported by the Holsworth Wildlife Research Endowment-Equity Trustees Charitable Foundation and the Ecological Society of Australia (KB), the PADI Foundation (KB) and a XL Catlin Seaview Survey scholarship (KB).

ACKNOWLEDGMENTS

We would like to thank the numerous volunteers for support in the field including Matheus A. Mello-Athayde, Tania Kenyon, Camille Rémond, Bonnie Lewis, Heather Middleton, Catherine Kim, and Aaron Chai, colleagues of the Coral Reef Ecosystem Laboratory, and the staff of Heron Island Research Station. Research was conducted under GBR Marine Park Authority Limited Impact Research permit #UQ008/2014c.

SUPPLEMENTARY MATERIAL

The Supplementary Material for this article can be found online at: https://www.frontiersin.org/articles/10.3389/fmars.2018.00181/full#supplementary-material

REFERENCES

Ateweberhan, M., Bruggemann, J., and Breeman, A. (2006). Effects of extreme seasonality on community structure and functional group dynamics of coral reef algae in the southern Red Sea, (Eritrea). *Coral Reefs* 25, 391–406. doi: 10.1007/s00338-006-0109-6

Birrell, C. L., McCook, L. J., and Willis, B. L. (2005). Effects of algal turfs and sediment on coral settlement. *Mar. Pollut. Bull.* 51, 408–414. doi: 10.1016/j.marpolbul.2004.10.022

Birrell, C. L., McCook, L. J., Willis, B. L., and Diaz-Pulido, G. A. (2008). Effects of benthic algae on the replenishment of corals and the implications for the resilience of coral reefs. *Oceanogr. Mar. Biol. Annu. Rev.* 46, 25–63. doi: 10.1201/9781420065756.ch2

Bonaldo, R. M., and Hay, M. E. (2014). Seaweed-coral interactions, variance in seaweed allelopathy, coral susceptibility, and potential effects on coral resilience. *PLoS ONE* 9:e85786. doi: 10.1371/journal.pone.0085786

Bradbury, R., and Young, P. (1981). The effects of a major forcing function, wave energy, on a coral reef ecosystem. *Mar. Ecol. Prog. Series* 5, 229–241. doi: 10.3354/meps005229

Brown, K. T., Bender-Champ, D., Bryant, D. E. P., Dove, S., and Hoegh-Guldberg, O. (2017). Human activities influence benthic community structure and the composition of the coral-algal interactions in the central Maldives. *J. Exp. Mar. Biol. Ecol.* 497, 33–40. doi: 10.1016/j.jembe.2017.09.006

Bruno, J. F., Precht, W. F., Vroom, P. S., and Aronson, R. B. (2014). Coral reef baselines: how much macroalgae is natural? *Mar. Pollut. Bull.* 80, 24–29. doi: 10.1016/j.marpolbul.2014.01.010

Burkepile, D. E., and Hay, M. E. (2006). Herbivore vs. nutrient control of marine primary producers: context-dependent effects. *Ecology* 87, 3128–3139. doi: 10.1890/0012-9658(2006)87[3128:HVNCOM]2.0.CO;2

Camp, E. F., Nitschke, M. R., Rodolfo-Metalpa, R., Houlbreque, F., Gardner, S. G., Smith, D. J., et al. (2017). Reef-building corals thrive within hot-acidified and deoxygenated waters. *Sci. Rep.* 7:2434. doi: 10.1038/s41598-017-02383-y

Castro-Sanguino, C., Lovelock, C., and Mumby, P. J. (2016). The effect of structurally complex corals and herbivory on the dynamics of Halimeda. *Coral Reefs* 35, 1–13. doi: 10.1007/s00338-016-1412-5

Clements, C. S., Rasher, D. B., Hoey, A. S., Bonito, V. E., and Hay, M. E. (2018). Spatial and temporal limits of coral-macroalgal competition: the negative impacts of macroalgal density, proximity, and history of contact. *Mar. Ecol. Prog. Ser.* 586, 11–20. doi: 10.3354/meps12410

Connell, J. H., Hughes, T. P., and Wallace, C. C. (1997). A 30-year study of coral abundance, recruitment, and disturbance at several scales in space and time. *Ecol. Monogr.* 67, 461–488. doi: 10.1890/0012-9615(1997)067[0461:AYSOCA]2.0.CO;2

Connell, J. H., Hughes, T. P., Wallace, C. C., Tanner, J. E., Harms, K. E., and Kerr, A. M. (2004). A long-term study of competition and diversity of corals. *Ecol. Monogr.* 74, 179–210. doi: 10.1890/02-4043

De'ath, G., Fabricius, K. E., Sweatman, H., and Puotinen, M. (2012). The 27–year decline of coral cover on the great barrier reef and its causes. *Proc. Natl. Acad. Sci. U.S.A.* 109, 17995–17999. doi: 10.1073/pnas.1208909109

Diaz-Pulido, G., and McCook, L. J. (2004). Effects of live coral, epilithic algal communities and substrate type on algal recruitment. *Coral Reefs* 23, 225–233. doi: 10.1007/s00338-004-0370-5

Diaz-Pulido, G., McCook, L. J., Dove, S., Berkelmans, R., Roff, G., Kline, D. I., et al. (2009). Doom and boom on a resilient reef: climate change, algal overgrowth and coral recovery. *PLoS ONE* 4:e5239. doi: 10.1371/journal.pone.0005239

Diaz-Pulido, G., McCook, L. J., Larkum, A. W., Lotze, H. K., Raven, J. A., Schaffelke, B., et al. (2007). "Vulnerability of macroalgae of the great barrier reef to climate change," in *Climate change and the Great Barrier Reef,* eds P. A. Marshall and J. Johnson (Townsville: Great Barrier Reef Marine Park Authority), 153–192.

Dollar, S. (1982). Wave stress and coral community structure in Hawaii. *Coral Reefs* 1, 71–81. doi: 10.1007/BF00301688

Ferrari, R., Gonzalez-Rivero, M., Ortiz, J. C., and Mumby, P. J. (2012). Interaction of herbivory and seasonality on the dynamics of Caribbean macroalgae. *Coral Reefs* 31, 683–692. doi: 10.1007/s00338-012-0889-9

Flower, J., Ortiz, J. C., Chollett, I., Abdullah, S., Castro-Sanguino, C., Hock, K., et al. (2017). Interpreting coral reef monitoring data: a guide for improved management decisions. *Ecol. Indic.* 72, 848–869. doi: 10.1016/j.ecolind.2016.09.003

Fong, P., and Zedler, J. B. (1993). Temperature and light effects on the seasonal succession of algal communities in shallow coastal lagoons. *J. Exp. Mar. Biol. Ecol.* 171, 259–272. doi: 10.1016/0022-0981(93)90008-C

Fox, H. E., Pet, J. S., Dahuri, R., and Caldwell, R. L. (2003). Recovery in rubble fields: long-term impacts of blast fishing. *Mar. Pollut. Bull.* 46, 1024–1031. doi: 10.1016/S0025-326X(03)00246-7

Fulton, C. J., Depczynski, M., Holmes, T. H., Noble, M. M., Radford, B., Wernberg, T., et al. (2014). Sea temperature shapes seasonal fluctuations in seaweed biomass within the Ningaloo coral reef ecosystem. *Limnol. Oceanogr.* 59, 156–166. doi: 10.4319/lo.2014.59.1.0156

Georgiou, L., Falter, J., Trotter, J., Kline, D. I., Holcomb, M., Dove, S. G., et al. (2015). pH homeostasis during coral calcification in a free ocean CO2 enrichment (FOCE) experiment, Heron Island reef flat, Great Barrier Reef. *Proc. Natl. Acad. Sci. U.S.A.* 112, 13219–13224. doi: 10.1073/pnas.1505586112

Glenn, E., Smith, C., and Doty, M. (1990). Influence of antecedent water temperatures on standing crop of a *Sargassum* spp.-dominated reef flat in Hawaii. *Mar. Biol.* 105, 323–328. doi: 10.1007/BF01344302

Haas, A., El-Zibdah, M., and Wild, C. (2010). Seasonal monitoring of coral–algae interactions in fringing reefs of the Gulf of Aqaba, Northern Red Sea. *Coral Reefs* 29, 93–103. doi: 10.1007/s00338-009-0556-y

Hatcher, B. G. (1988). Coral reef primary productivity: a beggar's banquet. *Trends Ecol. Evol.* 3, 106–111. doi: 10.1016/0169-5347(88)90117-6

Hatcher, B. G., and Larkum, A. W. D. (1983). An experimental analysis of factors controlling the standing crop of the epilithic algal community on a coral reef. *J. Exp. Mar. Biol. Ecol.* 69, 61–84. doi: 10.1016/0022-0981(83)90172-7

Hay, M. E. (1986). Associational plant defenses and the maintenance of species diversity: turning competitors into accomplices. *Am. Nat.* 128, 617–641. doi: 10.1086/284593

Hughes, T. P. (1989). Community structure and diversity of coral reefs: the role of history. *Ecology* 70, 275–279. doi: 10.2307/1938434

Hughes, T. P. (1994). Catastrophes, phase shifts, and large-scale degradation of a Caribbean coral reef. *Science* 265, 1547–1551. doi: 10.1126/science.265.5178.1547

Hughes, T. P., Kerry, J. T., Álvarez-Noriega, M., Álvarez-Romero, J. G., Anderson, K. D., Baird, A. H., et al. (2017). Global warming and recurrent mass bleaching of corals. *Nature* 543, 373–377. doi: 10.1038/nature21707

Hughes, T. P., Rodrigues, M. J., Bellwood, D. R., Ceccarelli, D., Hoegh-Guldberg, O., McCook, L., et al. (2007). Phase shifts, herbivory, and the resilience of coral reefs to climate change. *Curr. Biol.* 17, 360–365. doi: 10.1016/j.cub.2006.12.049

Jompa, J., and McCook, L. J. (2003a). Contrasting effects of turf algae on corals: massive *Porites* spp. are unaffected by mixed-species turfs, but killed by the red alga *Anotrichium tenue. Mar. Ecol. Prog. Series* 258, 79–86. doi: 10.3354/meps258079

Jompa, J., and McCook, L. J. (2003b). Coral–algal competition: macroalgae with different properties have different effects on corals. *Mar. Ecol. Prog. Ser.* 258, 87–95. doi: 10.3354/meps258087

Kinsey, D., and Kinsey, E. (1967). Diurnal changes in oxygen content of the water over the coral reef platform at Heron, I. *Mar. Freshw. Res.* 18, 23–34. doi: 10.1071/MF9670023

Lefèvre, C. D., and Bellwood, D. R. (2010). Seasonality and dynamics in coral reef macroalgae: variation in condition and susceptibility to herbivory. *Mar. Biol.* 157, 955–965. doi: 10.1007/s00227-009-1376-x

Lewis, S. M. (1986). The role of herbivorous fishes in the organization of a Caribbean reef community. *Ecol. Monogr.* 56, 183–200. doi: 10.2307/2937073

Littler, M. M., and Littler, D. S. (2007). Assessment of coral reefs using herbivory/nutrient assays and indicator groups of benthic primary producers: a critical synthesis, proposed protocols, and critique of management strategies. *Aquat. Conserv. Mar. Freshw. Ecosyst.* 17, 195–215. doi: 10.1002/aqc.790

Mathieson, A. C., and Dawes, C. J. (1986). Photosynthetic responses of Florida seaweeds to light and temperature: a physiological survey. *Bull. Mar. Sci.* 38, 512–524.

McCook, L. (1997). Effects of herbivory on zonation of *Sargassum* spp. within fringing reefs of the central Great Barrier Reef. *Mar. Biol.* 129, 713–722. doi: 10.1007/s002270050214

McManus, J. W., and Polsenberg, J. F. (2004). Coral–algal phase shifts on coral reefs: ecological and environmental aspects. *Prog. Oceanogr.* 60, 263–279. doi: 10.1016/j.pocean.2004.02.014

Morrissey, J. (1980). Community structure and zonation of microalgae and hermatypic corals on a fringing reef flat of magnetic island (Queensland, Australia). *Aquat. Bot.* 8, 91–139. doi: 10.1016/0304-3770(80)90045-5

O'Neil, J. M., Davis, T. W., Burford, M. A., and Gobler, C. J. (2012). The rise of harmful cyanobacteria blooms: the potential roles of eutrophication and climate change. *Harmful Algae* 14, 313–334. doi: 10.1016/j.hal.2011.10.027

Pandolfi, J. M., Bradbury, R. H., Sala, E., Hughes, T. P., Bjorndal, K. A., Cooke, R. G., et al. (2003). Global trajectories of the long-term decline of coral reef ecosystems. *Science* 301, 955–958. doi: 10.1126/science.1085706

Phinn, S. R., Roelfsema, C. M., and Mumby, P. J. (2012). Multi-scale, object-based image analysis for mapping geomorphic and ecological zones on coral reefs. *Int. J. Remote Sens.* 33, 3768–3797. doi: 10.1080/01431161.2011.633122

Potts, D. C. (1977). Suppression of coral populations by filamentous algae within damselfish territories. *J. Exp. Mar. Biol. Ecol.* 28, 207–216. doi: 10.1016/0022-0981(77)90092-2

Potts, D. C., and Swart, P. K. (1984). Water temperature as an indicator of environmental variability on a coral reef. *Limnol. Oceanogr.* 29, 504–516. doi: 10.4319/lo.1984.29.3.0504

Price, I. (1989). Seaweed phenology in a tropical Australian locality (Townsville, North Queensland). *Botan. Mar.* 32, 399–406. doi: 10.1515/botm.1989.32.5.399

Rogers, R. (1997). Brown algae on Heron reef fiat, Great Barrier Reef, Australia: spatial, seasonal and secular variation in cover. *Botan. Mar.* 40, 113–118. doi: 10.1515/botm.1997.40.1-6.113

Rogers, R. W. (1996). Spatial, seasonal and secular patterns in the cover of green algae on Heron reef flat, Great Barrier Reef, Australia. *Botan. Mar.* 39, 415–420. doi: 10.1515/botm.1996.39.1-6.415

Safaie, A., Silbiger, N. J., McClanahan, T. R., Pawlak, G., Barshis, D. J., Hench, J. L., et al. (2018). High frequency temperature variability reduces the risk of coral bleaching. *Nat. Commun.* 9:1671. doi: 10.1038/s41467-018-04074-2

Sangil, C., and Guzman, H. M. (2016). Macroalgal communities on multi-stressed coral reefs in the Caribbean: long-term changes, spatial variations, and relationships with environmental variables. *J. Sea Res.* 117, 7–19. doi: 10.1016/j.seares.2016.09.001

Schaffelke, B., and Klumpp, D. (1997). Biomass and productivity of tropical macroalgae on three nearshore fringing reefs in the central Great Barrier Reef, Australia. *Botan. Mar.* 40, 373–384. doi: 10.1515/botm.1997.40.1-6.373

Smith, J. E., Hunter, C. L., and Smith, C. M. (2010). The effects of top–down versus bottom–up control on benthic coral reef community structure. *Oecologia* 163, 497–507. doi: 10.1007/s00442-009-1546-z

Smith, S. V., Kimmerer, W. J., Laws, E. A., Brock, R. E., and Walsh, T. W. (1981). Kaneohe Bay sewage diversion experiment: perspectives on ecosystem responses to nutritional perturbation. *Pac. Sci.* 35, 279–395.

Steneck, R. S., and Dethier, M. N. (1994). A functional group approach to the structure of algal-dominated communities. *Oikos* 69, 476–498. doi: 10.2307/3545860

Swierts, T., and Vermeij, M. J. (2016). Competitive interactions between corals and turf algae depend on coral colony form. *PeerJ* 4:e1984. doi: 10.7717/peerj.1984

Tanner, J. E. (1995). Competition between scleractinian corals and macroalgae: an experimental investigation of coral growth, survival and reproduction. *J. Exp. Mar. Biol. Ecol.* 190, 151–168. doi: 10.1016/0022-0981(95)00027-O

R Core Team (2014). *R: A Language and Environment for Statistical Computing.* Vienna: R Foundation for Statistical Computing.

Vuki, V. C., and Price, I. R. (1994). Seasonal changes in the Sargassum populations on a fringing coral reef, Magnetic Island, Great Barrier Reef region, Australia. *Aquat. Bot.* 48, 153–166. doi: 10.1016/0304-3770(94)90082-5

Wickham, H. (2016). *ggplot2: Elegant Graphics for Data Analysis*. Houston: Springer.

Wilson, S., Fisher, R., Pratchett, M., Graham, N., Dulvy, N., Turner, R., et al. (2008). Exploitation and habitat degradation as agents of change within coral reef fish communities. *Glob. Chang. Biol.* 14, 2796–2809. doi: 10.1111/j.1365-2486.2008.01696.x

Wismer, S., Hoey, A. S., and Bellwood, D. R. (2009). Cross-shelf benthic community structure on the Great Barrier Reef: relationships between macroalgal cover and herbivore biomass. *Mar. Ecol. Prog. Ser.* 376, 45–54. doi: 10.3354/meps07790

Wood, S. (2006). *Generalized Additive Models: An Introduction With R*. Boca Raton, FL: CRC press.

Woolsey, E., Bainbridge, S. J., Kingsford, M. J., and Byrne, M. (2012). Impacts of cyclone Hamish at one tree reef: integrating environmental and benthic habitat data. *Mar. Biol.* 159, 793–803. doi: 10.1007/s00227-011-1855-8

Yi, Y., Sun, J., and Zhang, S. (2016). A habitat suitability model for Chinese sturgeon determined using the generalized additive method. *J. Hydrol.* 534, 11–18. doi: 10.1016/j.jhydrol.2015.12.055

Conflict of Interest Statement: The authors declare that the research was conducted in the absence of any commercial or financial relationships that could be construed as a potential conflict of interest.

frontiers
in Marine Science

ORIGINAL RESEARCH
published: 22 May 2018
doi: 10.3389/fmars.2018.00175

Coral Reef Carbonate Chemistry Variability at Different Functional Scales

Yuichiro Takeshita[1]*, **Tyler Cyronak**[2], **Todd R. Martz**[2], **Theodor Kindeberg**[2] **and Andreas J. Andersson**[2]

[1] Monterey Bay Aquarium Research Institute, Moss Landing, CA, United States, [2] Scripps Institution of Oceanography, University of California, San Diego, La Jolla, CA, United States

There is a growing recognition for the need to understand how seawater carbonate chemistry over coral reef environments will change in a high-CO_2 world to better assess the impacts of ocean acidification on these valuable ecosystems. Coral reefs modify overlying water column chemistry through biogeochemical processes such as net community organic carbon production (NCP) and calcification (NCC). However, the relative importance and influence of these processes on seawater carbonate chemistry vary across multiple functional scales (defined here as space, time, and benthic community composition), and have not been fully constrained. Here, we use Bermuda as a case study to assess (1) spatiotemporal variability in physical and chemical parameters along a depth gradient at a rim reef location, (2) the spatial variability of total alkalinity (TA) and dissolved inorganic carbon (DIC) over distinct benthic habitats to infer NCC:NCP ratios [< several km^2; rim reef vs. seagrass and calcium carbonate ($CaCO_3$) sediments] on diel timescales, and (3) compare how TA-DIC relationships and NCC:NCP vary as we expand functional scales from local habitats to the entire reef platform (10's of km^2) on seasonal to interannual timescales. Our results demonstrate that TA-DIC relationships were strongly driven by local benthic metabolism and community composition over diel cycles. However, as the spatial scale expanded to the reef platform, the TA-DIC relationship reflected processes that were integrated over larger spatiotemporal scales, with effects of NCC becoming increasingly more important over NCP. This study demonstrates the importance of considering drivers across multiple functional scales to constrain carbonate chemistry variability over coral reefs.

Keywords: coral reef biogeochemistry, carbonate chemistry variability, bermuda, beams, NCP and NCC

OPEN ACCESS

Edited by:
Anas Ghadouani,
University of Western Australia, Australia

Reviewed by:
Ruy Kenji Papa De Kikuchi,
Universidade Federal da Bahia, Brazil
Wei-dong Zhai,
Shandong University, China

****Correspondence:***
Yuichiro Takeshita
yui@mbari.org

Specialty section:
This article was submitted to Coastal Ocean Processes, a section of the journal Frontiers in Marine Science

Received: *13 January 2018*
Accepted: *02 May 2018*
Published: *22 May 2018*

Citation:
Takeshita Y, Cyronak T, Martz TR, Kindeberg T and Andersson AJ (2018) Coral Reef Carbonate Chemistry Variability at Different Functional Scales. Front. Mar. Sci. 5:175. doi: 10.3389/fmars.2018.00175

INTRODUCTION

Coral reefs provide ecosystem services worth trillions of dollars (Costanza et al., 2014) that are threatened by local (e.g., overfishing, eutrophication, sedimentation) and global anthropogenic stressors (e.g., climate change and ocean acidification; Hoegh-Guldberg et al., 2007; Wilkinson, 2008; Hughes et al., 2017). Coral reefs are thought to be particularly vulnerable to ocean acidification, largely because the ecosystem foundation is built from biogenically precipitated calcium carbonate ($CaCO_3$) (Kleypas et al., 1999; Kleypas and Yates, 2009). Numerous experimental studies have demonstrated decreases in coral calcification rates (Chan and Connolly, 2013) and increases in rates of $CaCO_3$ substrate and sediment dissolution (Andersson et al., 2009; Cyronak et al., 2013) under increasing seawater CO_2 concentrations and decreasing pH. Thus, ocean acidification poses a direct threat to the ability of coral reef ecosystems to maintain positive $CaCO_3$ accretion (Eyre et al., 2014). However, extrapolating and scaling these experimental results to *in situ* community and ecosystem scales poses multiple challenges (Andersson et al., 2015; Edmunds et al., 2016).

One of the challenges when making projections on how coral reefs will respond to ocean acidification on an ecosystem scale is the tightly coupled feedback between water column chemistry and benthic metabolic processes (Anthony et al., 2011; Kleypas et al., 2011; Albright et al., 2013; Andersson and Gledhill, 2013; Shaw et al., 2015; Takeshita, 2017). Coral reefs modulate the overlying seawater chemistry through two main metabolic processes: net community production (NCP) and net community calcification (NCC). NCP describes the balance of primary production and total respiration, whereas NCC describes the balance of calcification and $CaCO_3$ dissolution. Metabolically driven variability of pH in many coral reef habitats over diel and/or seasonal timescales is often significantly larger than the projected mean decline in the open ocean due to ocean acidification over the next century. In addition to reef metabolism, reef pH variability is strongly modified by physical properties such as geomorphology, flow trajectory, flow rates and residence time, which alter properties such as biomass to water volume ratio and the contact time between seawater and the benthos (Falter et al., 2013; Lowe and Falter, 2015). However, the relative importance of these drivers and how they influence seawater carbonate chemistry variability over multiple functional scales, defined here as space, time, and benthic community composition, in the natural environment is not fully constrained.

Traditionally, NCP and NCC have been calculated by measuring changes in TA and DIC while characterizing residence time and water volume (Gattuso et al., 1996; Venti et al., 2012; Albright et al., 2015). This complicates our ability to study the feedbacks between benthic metabolism and carbonate chemistry variability, as both are derived from the same set of discrete measurements. Thus, an independent assessment of NCP and NCC would be useful. Recently, Takeshita et al. (2016) reported an autonomous system that simultaneously measures NCP and NCC using a boundary layer gradient flux approach. They observed significantly different ratios of NCC to NCP (NCC:NCP) over two different benthic communities, one dominated by calcifiers and the other dominated by non-calcifiers, directly demonstrating the effects of benthic community composition on metabolic ratios *in situ*. However, the relationship between benthic metabolism and water column chemistry was not assessed in that study. Here, we used the Bermuda coral reef platform as a case study to examine benthic metabolism and the variability of carbonate chemistry across multiple functional scales. Bermuda is a highly suitable location to conduct this study, as historical spatial data exist on the ecosystem scale (Andersson et al., 2014; Yeakel et al., 2015), residence time over the reef platform is constrained (Venti et al., 2012), and multiple estimates of NCC exist using independent approaches (Bates et al., 2010; Courtney et al., 2016, 2017). Seawater chemistry measurements were made across spatial scales ranging from a single point on a rim reef to the entire reef platform (10's of km^2) over varying benthic communities, and over short-term (hourly to diel) and long-term (seasonal to interannual) time scales. We directly measured NCC and NCP using a gradient flux approach on the rim reef (Takeshita et al., 2016), and compared NCC:NCP to that inferred from discrete total alkalinity (TA) and dissolved inorganic carbon (DIC) measurements taken around this community. We also examined how patterns of TA and DIC changed on the community scale over different benthic habitats (i.e., a coral dominated rim reef vs. a seagrass bed), and compared the community scale metabolic footprints to those observed across the whole platform. This sampling approach allowed us to assess the variability in seawater carbonate chemistry and the NCC to NCP ratio across multiple functional scales.

METHODS

Study Sites

The study was performed on the Bermuda coral reef platform in July, 2015. Specifically, sensors were deployed and discrete samples were taken near Hog Reef (32.457°N 64.845°W) located ∼16 km northwest of the Bermuda Institute of Ocean Sciences (BIOS) research station, and in Bailey's Bay (32.350°N, 64.725°W), located ∼3 km west of BIOS (**Figure 1**). Depth across Hog Reef ranged from ∼4 to 25 m, with water depth increasing offshore toward northwest. Typically there is a MAPCO2 buoy that autonomously measures pCO_2 at Hog Reef (T3; **Figure 1**), however, it was not operating at the time of this study due to maintenance. The benthic community composition from this site has been reported previously (MEP, 2007; Courtney et al., 2016) and consists of $27 \pm 5\%$ hard coral, $16 \pm 2\%$ soft coral, $35 \pm 3\%$ macroalgae, $20 \pm 4\%$ turf algae, and $<5\%$ of sediments, rubble, and coralline algae. Bailey's Bay is a semi-enclosed bay, with water depth ranging from 1 to 3 m. Carbonate sediments dominate the bay with patches of increasing seagrass density occurring in the northeastern portion of the bay, predominantly composed of *Thalassia testudinum*. Carbonate chemistry data from Bailey's Bay have been reported previously (Cyronak et al., 2018a).

Autonomous Sensor Array

Autonomous sensors were deployed between July 12 and 30, 2015 at stations T2, T3, and T4, ranging in depth from ∼4.5 m (T2) to 18.5 m (T4) (**Table 1**). pH was measured using either a SeaFET or SeapHOx (Bresnahan et al., 2014), based on the Honeywell Durafet combination electrode (Martz et al., 2010; Takeshita et al., 2014). SeapHOxes were deployed at T2 and T4, providing pH, O_2, temperature, pressure, and salinity measurements every 15 min. At T3, pH, temperature (SeaFET), and photosynthetically active radiation (PAR; Wetlabs ECO-PAR) were measured. The pH sensors were calibrated pre-deployment in a holding tank overnight by collecting discrete samples for DIC and TA ($n = 2$) and using CO2SYS to calculate tank pH with equilibrium constants measured by Mehrbach et al. (1973), refit by Lueker et al. (2000). The accuracy of the sensor pH is estimated to be ± 0.015. Samples for DIC and TA were collected alongside the

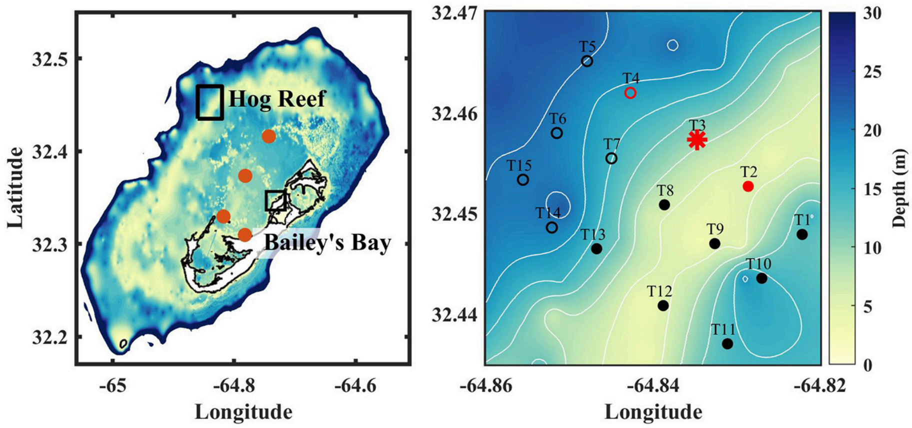

FIGURE 1 | (Left) Bathymetry of the Bermuda coral reef platform. Water depth >200 m is represented as white. Brown circles represent the four time series stations where monthly surface discrete samples for DIC and TA were taken between 2007 and 2012 (Andersson et al., 2014). Hog reef and Bailey's Bay are outlined in black. **(Right)** Bathymetry of Hog reef; contours are every 3 m. Stations for the spatial survey are shown as black circles. Open circles represent deep stations (> 10 m) that were not included in the regression analysis of TA-DIC data (see main text). Red circles indicate sensor deployment sites; BEAMS was deployed at T3 (red star).

TABLE 1 | Summary of sensor deployments for this study.

Site name	Depth (m)	Sensors deployed	Parameters measured
T2	4.5	SeapHOx	pH, O_2, T, S, P (17 days)
T3	7	SeaFET; Wetlabs PAR,	pH, T, PAR (17 days)
		BEAMS	O_2, S, NCC, NCP (3 days)
T4	18.5	SeapHOx	pH, O_2, T, S, P (17days)

sensors at the time of recovery to assess sensor drift, and no drift was detected for any of the sensors. pH is reported on the total scale at *in situ* conditions.

BEAMS

Benthic NCP and NCC at T3 were measured for 3 days between July 26 and 29, 2015 at 10 min intervals using the Benthic Ecosystem and Acidification Measurement System (BEAMS). BEAMS was deployed at 7 m depth. The details of this approach are explained elsewhere (McGillis et al., 2011; Takeshita et al., 2016), but will be summarized here. Gradients of O_2, TA, and current velocity in the benthic boundary layer were used to calculate benthic NCP and NCC. The gradient in TA was estimated using simultaneous measurements of pH and O_2 (Barnes, 1983; Takeshita et al., 2016), assuming a net photosynthetic quotient (Q) of 1, defined as $\Delta CO_2/\Delta O_2$. Studies from reefs worldwide have demonstrated that this ratio is near 1 in coral reefs (Kinsey, 1985; Falter et al., 2012). The pH and O_2 at 20, 40, and 70 cm above the benthos were measured by sequentially pumping seawater from the respective heights through a single SeapHOx. The current velocity profile with 5 cm resolution was measured using an Aquadopp High Resolution 1 MHz current profiler at 1 Hz sampling frequency; current velocity profiles were averaged for 5 min to obtain a mean current velocity at 1 m above benthos, U_0, and the friction velocity, u_*. The mean drag coefficient, C_D at this site was 0.012 ± 0.002. ($C_D = u_*^2/U_0^2$), which is in broad agreement with other reef measurements (Reidenbach et al., 2006; McGillis et al., 2011; Takeshita et al., 2016). NCP and NCC are reported in mmol O_2 m^{-2} h^{-1} and mmol $CaCO_3$ m^{-2} h^{-1}, respectively. NCP-Irradiance and NCC-Irradiance curves were established by fitting an exponential relationship to the observed metabolic rates (Takeshita et al., 2016).

Spatial Surveys for Surface Carbonate Chemistry

Surface DIC and TA samples were collected from 15 different stations, encompassing roughly 1.5 × 3 km area of Hog Reef (**Figure 1**). Three total spatial surveys were conducted for DIC and TA, one in the morning (~09:00) and afternoon (~15:00) on July 27, 2015, and one in the morning (~10:00) on July 29, 2015. All samples were collected within 1.5 h for each sampling interval. In addition to these spatial surveys, two transects between T1 and T5 were undertaken on July 13 (~17:00) and July 17 (~16:00).

Surface DIC and TA samples were collected in 250 ml borosilicate glass bottles. The bottles were rinsed with seawater three times before submerging to ~30 cm below the surface to collect the samples. The samples were preserved and stored following standard protocols (Dickson et al., 2007). Temperature, salinity, and oxygen were measured using a YSI Pro 2030 meter (Xylem) at each sampling location. DIC was analyzed using an Automated Infrared Inorganic Carbon Analyzer (AIRICA, Marianda, Inc.) equipped with a LI-COR infrared CO_2 analyzer. Total alkalinity was determined by open-cell potentiometric acid titration using an 876 Dosimat (Metrohm) and Ecotrode Plus pH electrode (Metrohm) (Dickson et al., 2007). All samples were measured within 6 months of collection. Accuracy and precision of the measurements were assessed through routine measurements of Certified Reference Materials, provided by Prof.

A. Dickson at Scripps Institution of Oceanography (Dickson et al., 2003). Accuracy was within ± 3 μmol kg $^{-1}$ for both DIC and TA, whereas precision calculated as the standard deviation of replicate CRMs was ± 1.7 μmol kg $^{-1}$ ($n = 41$) and ± 2.7 μmol kg $^{-1}$ ($n = 18$), respectively. DIC and TA were normalized to salinity of 36.5 (Andersson et al., 2014), and the slope between nDIC and nTA was determined using a model II linear regression. The variability of carbonate chemistry at reef platform functional scale was assessed using data collected monthly between 2007 and 2012 at four time series sites across the Bermuda reef platform (Andersson et al., 2014; **Figure 1**).

RESULTS

Autonomous Sensor Array and Temporal Variability

Observed trends and variability in temperature, pH, and O_2 were nearly identical between T2 and T3, whereas T4 was distinctly different from these stations (**Figure 2**). The mean temperature, salinity, pH, and O_2 were similar at all sites (**Table 2**). Clear diel cycles in O_2 and pH were observed at T2 and T3, with average diel ranges of 43 ± 12 (1σ) μmol kg^{-1} and 0.056 ± 0.016, respectively. The diel cycles were smaller at T4, with an average diel range of 22 ± 12 μmol kg^{-1} and 0.034 ± 0.017 for O_2 and pH, respectively.

Large, episodic shifts in O_2 and pH were observed at T4 (e.g., July 14 and July 27), coincident with sharp changes in temperature and salinity. During these events, as observed on July 14, O_2 and pH shifted by up to 30 μmol kg^{-1} and 0.08 within an hour, respectively. Overall, salinity was consistently around 36.6 for the first half of the deployment and decreased by ~0.6 during the second half of the deployment. A reduction in PAR and temperature associated with stormy weather was observed between July 23 and 26. Between July 26 and 29, salinity at T4 (15 m depth) was significantly higher and temperature slightly lower than at T2 and T3, indicating stratification.

Benthic NCC and NCP From BEAMS

A clear, consistent diel cycle in both NCP and NCC was observed, with positive NCP and NCC observed during the day, and negative NCP and variable NCC (positive or negative) near 0 observed during the night (**Figure 3**). On average, daytime NCP was 5.2 ± 9.2 (1 σ) mmol O_2 m^{-2} h^{-1}, and reached as high as 31.6 mmol O_2 m^{-2} h^{-1} during peak daylight, whereas average daytime NCC was 3.8 ± 2.7 (1 σ) mmol $CaCO_3$ m^{-2} h^{-1}, and reached as high as 11.4 mmol $CaCO_3$ m^{-2} h^{-1}. On average, nighttime NCP was −11.7 ± 5.5 mmol O_2 m^{-2} h^{-1}, whereas nighttime NCC was 0.0 ± 2.8 mmol $CaCO_3$ m^{-2} h^{1}. Given that the precision of the BEAMS approach is ~3 mmol O_2 (or $CaCO_3$) m^{-2} h^{-1} (Takeshita et al., 2016), it cannot be quantitatively established whether Hog Reef experienced net dissolution at night. If NCC was calculated assuming $Q = 1.1$, then the average nighttime NCC becomes −1.4 ± 3.5 mmol $CaCO_2$ m^{-2} h^{-1}, indicating net dissolution during the night. However, since Q was not quantified during this study, this remains a source of uncertainty in the reported NCC. At the hourly scale, it is sometimes difficult to separate the biogeochemical processes from transient physical signals. For example, a negative anomaly for NCP and a positive anomaly for NCC were observed on the night of the 27th (**Figure 3A**). Although the origin of these signals remains unclear, they likely represent a physical process that temporarily negated the steady-state turbulent boundary layer assumption inherent in the gradient flux approach. In contrast, as discussed below, daytime transient signals associated with light are often well-understood and reflected in the measured NCC and NCP as one might expect. We have chosen to report daily integrated values here, and do not focus on the sub-daily patterns beyond their qualitative description.

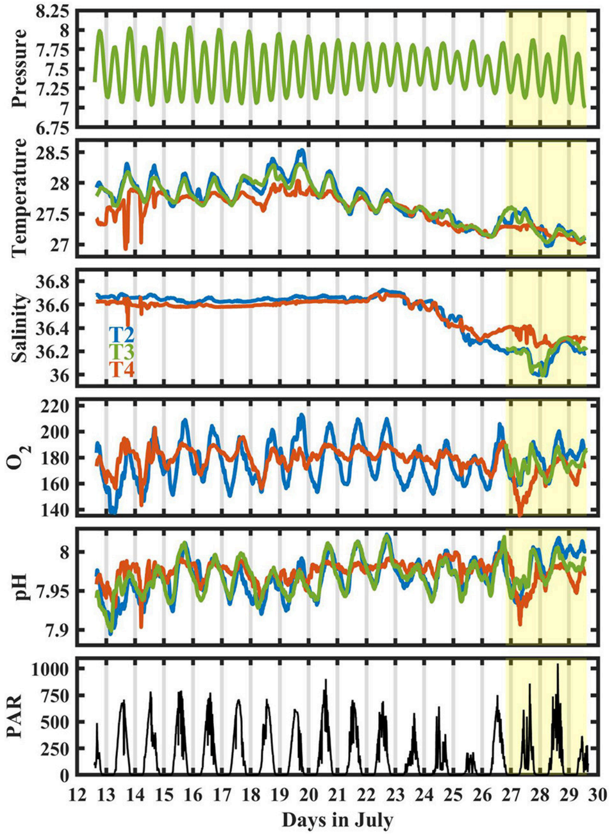

FIGURE 2 | Time series at T2 (blue), T3 (green), and T4 (red) for pressure [dBar], temperature [Celsius], salinity, O_2 [μmol kg^{-1}], pH [total scale], and PAR at 11 m at T3 [μmol photons m^{-2} s^{-1}]. Only pressure at T3 is shown for clarity. Shaded yellow represents when BEAMS was deployed.

TABLE 2 | Mean ± 1 σ of temperature [Celsius], salinity, pH [total], and O_2 [μmol kg^{-1}] from T2, T3, and T4.

Parameter	T2	T3	T4
Temperature	27.69 ± 0.35	27.68 ± 0.32	27.56 ± 0.26
Salinity	36.53 ± 0.20	-	36.5 ± 0.13
pH	7.97 ± 0.024	7.97 ± 0.022	7.97 ± 0.014
O_2	176 ± 15	-	173 ± 10

*Statistics for salinity and O_2 at T3 are not presented because of the short deployment duration (see **Figure 2**).*

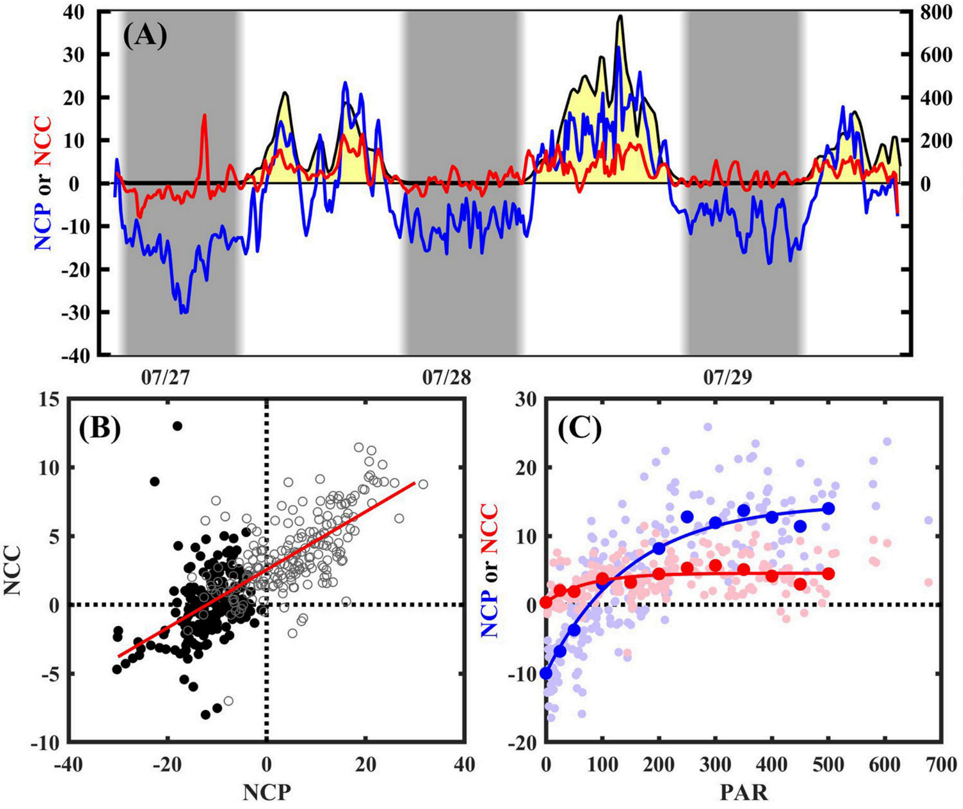

FIGURE 3 | (A) Benthic NCP (blue; mmol O_2 m^{-2} h^{-1}), NCC (red; mmol $CaCO_3$ m^{-2} h^{-1}), and PAR (shaded yellow; µmol photons m^{-2} s^{-1}) measured every 10 min at site T3. Gray background represents night time. **(B)** NCP vs. NCC during the day (open gray circles) and night (black circles). Model II regression is shown in red, with slope = 0.21 ± 0.01 (R^2 = 0.48) **(C)** NCP-Irradiance (blue) and NCC-Irradiance (red) curve for daytime data. Small dots are individual measurements, whereas larger solid dots represent binned averages (0, 25, 50, then every 50 until 500). Solid lines represent fit.

A positive, linear relationship between NCC and NCP was observed (**Figure 3B**), with a slope of 0.21 ± 0.01 ($R^2 = 0.48$). This slope changed to 0.08 ± 0.01 and 0.33 ± 0.01 when Q = 0.9 and 1.1, respectively. Both NCC and NCP were strongly correlated to light, and followed a simple exponential relationship (Platt et al., 1980; Takeshita et al., 2016):

$$NCC = 4.23\left(1 - e^{\frac{-0.0584PAR}{4.23}}\right) - 0.347$$

$$NCP = 24.7\left(1 - e^{\frac{-0.166PAR}{24.7}}\right) - 9.97$$

The metabolic rates were dynamic and sensitive to changes in PAR, and effects were observed within minutes. For example, a sharp decrease followed by an increase in both NCC and NCP occurred concomitantly with changes in PAR associated with a passing rain-storm around noon on July 27 (**Figure 3A**). During this time, net respiration was observed for a brief period, while NCC decreased to near zero. Diel integrated NCP (ΣNCP) and NCC (ΣNCC) for July 27 and 28 were −123 and 38 mmol O_2 m^{-2} d^{-1}, and 45 and 63 mmol $CaCO_3$ m^{-2} d^{-1}, respectively. Both net heterotrophy and autotrophy over the course of a diel cycle were observed, whereas net calcification was observed for the duration of both days. The uncertainty for ΣNCP and ΣNCC is estimated to be ± 13 mmol O_2 m^{-2} d^{-1} and ± 15 mmol $CaCO_3$ m^{-2} d^{-1}, respectively (Takeshita et al., 2016).

Spatial Surveys

The results for the spatial surveys at Hog Reef are summarized in **Table 3** and **Figure 4**. In general, temporal variability across the survey area followed a diel cycle, where on average, higher nDIC and lower O_2 were observed during the morning (7/27 09:00 and 7/20 10:00) compared to the afternoon (7/27 16:00). Spatial distributions of O_2 and DIC were inversely correlated (R^2 = 0.80) whereas correlations between DIC and TA were less pronounced (R^2 = 0.43; **Figure 5**). The slope of nTA and nDIC regression was 0.35 ± 0.24, which equates to a NCC:NCP of 0.21 (**Figure 6**), the same as the NCC:NCP ratio of 0.21 determined from BEAMS measurements. Samples taken from deep sites (water depth > 10 m; shown as open circles in **Figure 4**) were not included in the regression, because the water column at these sites was stratified at this time (**Figure 2**), thus, the benthic reef metabolism would have small or delayed effects on the water chemistry at the surface.

TABLE 3 | Mean ± 1 σ of nDIC [μmol kg^{-1}], nTA [μmol kg^{-1}], pH [total scale], O_2 [μmol kg^{-1}], Temperature [Celsius], and Salinity for the three spatial surveys at Hog Reef.

Parameter	7/27/2015 09:00	7/27/2015 16:00	7/29/2015 10:00
nDIC	2046 ± 9	2037 ± 4	2044 ± 6
nTA	2347 ± 8	2353 ± 10	2347 ± 5
pH	7.99 ± 0.022	8.01 ± 0.015	7.99 ± 0.009
O_2	172 ± 7	182 ± 3	173 ± 6
Temperature	27.4 ± 0.10	27.3 ± 0.12	27.1 ± 0.04
Salinity	36.46 ± 0.05	36.32 ± 0.09	36.5 ± 0.08

DISCUSSION

Temporal Variability

Clear diel cycles in O_2 and pH were observed at all sensor sites, suggesting that organic carbon metabolism was the dominant driver in chemical variability at Hog Reef. This is supported by a stronger correlation between O_2 and DIC ($R^2 = 0.80$) relative to TA and DIC ($R^2 = 0.43$) from spatial surveys (**Figure 5**). The magnitude of biologically-driven diel variability in chemistry is a function of the imbalance of NCC and NCP, metabolic rates, water depth, and residence time. Greater imbalance of NCC and NCP, higher metabolic rates and longer residence times lead to larger changes in seawater chemistry, whereas increasing water depth proportionally reduces the changes, assuming a well-mixed water column. Qualitatively, the benthic cover at T4 was similar to that at the shallower sites, yet, T4 had a significantly smaller diel amplitude for both pH and O_2 (**Figure 2**). This is mainly because T4 was the deepest site, and thus, the chemical signatures of the metabolic fluxes were diluted over a larger water column. It is worth noting that chemical variability at T4 was significantly affected by episodic events linked to transient physical processes (e.g., internal waves) as observed on July 14th (and July 27th) where O_2 and pH decreased by > 30 μmol kg^{-1} and 0.08, respectively, within an hour coincident with sudden drops in temperature and salinity (**Figure 2**). This highlights the importance of episodic physical processes influencing high frequency temporal chemical variability over coral reefs.

Projections on how high frequency, diel pH variability at these sites will be affected in a future high CO_2 world are dependent on a number of factors. First, changes in the relative proportion of NCC to NCP could either increase or decrease diel fluctuations in pH, where a lower NCC:NCP would lead to larger variability (Andersson and Gledhill, 2013). It is commonly hypothesized that NCC:NCP will decrease in the future due to shifts from coral to algae-dominated states (Hoegh-Guldberg et al., 2007; Enochs et al., 2015) and reductions in NCC due to ocean acidification (Chan and Connolly, 2013; Albright et al., 2016, 2018). These changes will most likely increase the difference between the daily extreme values relative to the mean pH due to increasing dominance by NCP over NCC, although, nighttime pH could be partially buffered due to increasing $CaCO_3$ dissolution (Page et al., 2016). Furthermore, increased CO_2 due to ocean acidification will lead to larger diel cycles in pH due to decreased buffering capacity of seawater (Jury et al., 2013; Shaw et al., 2013; Takeshita et al., 2015).

Benthic Metabolic Rates

Short term BEAMS measurements demonstrated that NCC and NCP were tightly coupled over multiple days (**Figure 3B**), which is consistent with previous observations from various coral reefs (McMahon et al., 2013; Albright et al., 2015; Shaw et al., 2015; Takeshita et al., 2016). The NCC:NCP based on a model II regression between the two parameters was 0.21 ± 0.01, though this ratio calculated from O_2 and pH measurements is dependent on the assumed Q, and varies between 0.08 and 0.33 when Q is set equal to 0.9 and 1.1, respectively (**Figure 3**). While previous studies from reefs worldwide demonstrate that Q is near 1 (Kinsey, 1985; Falter et al., 2012), the assumed Q remains a source of uncertainty of the calculated NCC from the BEAMS approach. Simultaneous measurements of pH, O_2, and TA in an enclosure would allow direct observations of Q, however, properly sealing such enclosures in a natural reef environment is challenging (Nakamura and Nakamori, 2008), especially on hard substrate like at Hog Reef. Alternatively, simultaneous measurements of the pH, O_2, and TA gradients in the turbulent benthic boundary layer would also quantify Q, as chemical gradients in the turbulent boundary layer are driven by benthic metabolism. However, autonomous TA sensing technology still remains in the prototype phase and is not widely available (Crespo et al., 2012; Spaulding et al., 2014; Briggs et al., 2017).

The ΣNCC determined from BEAMS (45 and 63 mmol $CaCO_3$ m^{-2} d^{-1}) was scaled up to an annual rate in order to compare with previously reported NCC rates at Hog Reef (Courtney et al., 2016). The seasonal variability in NCC was modeled by assuming that NCC at Hog Reef followed the standardized seasonal growth rate derived from colonies of *D. labyrinthiformis* and *P. astreoides* at Hog Reef over 2 years [Equation 1 in (Courtney et al., 2016)]. The standardized growth rate curve was multiplied by 37.65 mmol $CaCO_3$ m^{-2} d^{-1} so that ΣNCC from the growth curve equaled the mean ΣNCC from BEAMS (53.5 ± 15 mmol $CaCO_3$ m^{-2} d^{-1}) on July 28th. The BEAMS-based annual NCC rate was 14.3 ± 4.0 mol $CaCO_3$ m^{-2} year^{-1} (or 1.43 ± 0.40 kg $CaCO_3$ m^{-2} year^{-1}), which is in broad agreement with previously reported annual NCC rates using census-based (2.35 ± 1.01 kg $CaCO_3$ m^{-2} year^{-1}) and chemistry-based (2.23 ± 1.02 kg $CaCO_3$ m^{-2} year^{-1}) approaches (Courtney et al., 2016). However, given the limited deployment length of BEAMS during this study and the large variability in diel, seasonal, and interannual metabolic rates over coral reefs (Falter et al., 2008, 2012; Yeakel et al., 2015; Takeshita et al., 2016), caution needs to be exercised in the interpretation of these results. We suspect that the BEAMS-based annual NCC estimated here may be skewed low due to heavy rainfall on the first day of deployment, which depressed daytime NCC (**Figure 3**). Longer term deployment of BEAMS over seasonal to annual timescales would provide a more robust estimate of annual NCC rates, and the environmental drivers across multiple temporal scales ranging from hourly to seasonal timescales.

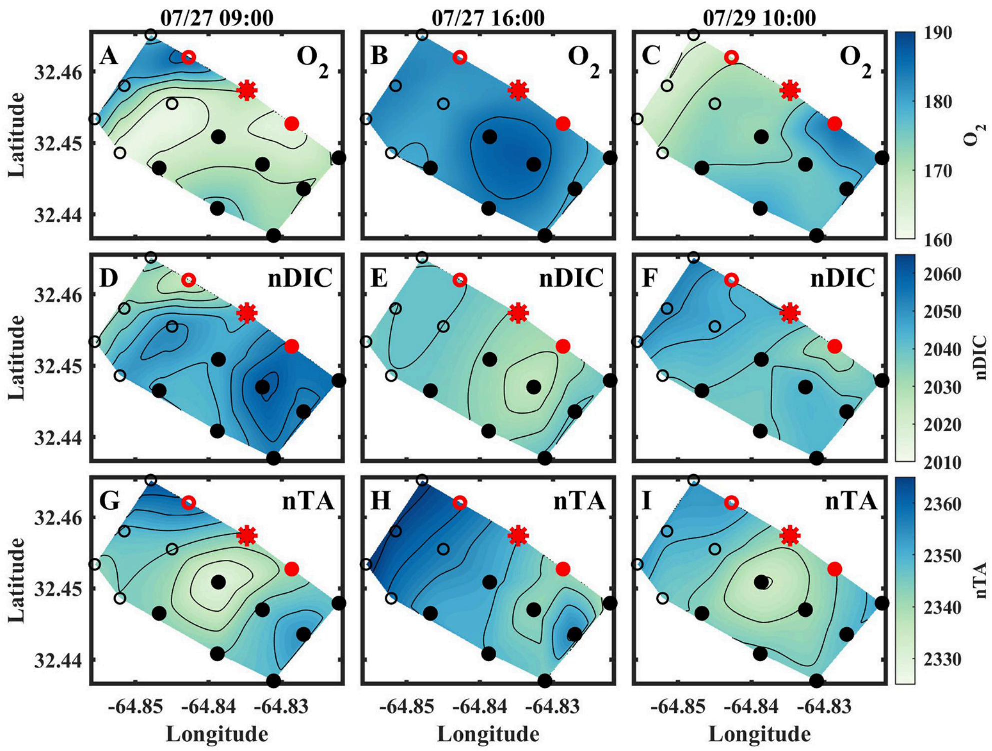

FIGURE 4 | Spatial contour plots for O_2 [μmol kg^{-1}] **(A–C)**, nDIC [μmol kg^{-1}] **(D–F)**, and nTA [μmol kg^{-1}] **(G–I)** from the morning of July 27 (left column), afternoon of July 27 (middle column), and morning of July 29 (right column). Contours are 5 μmol kg^{-1} for all plots. Red indicates where sensors were deployed, and the red star indicates where BEAMS was deployed.

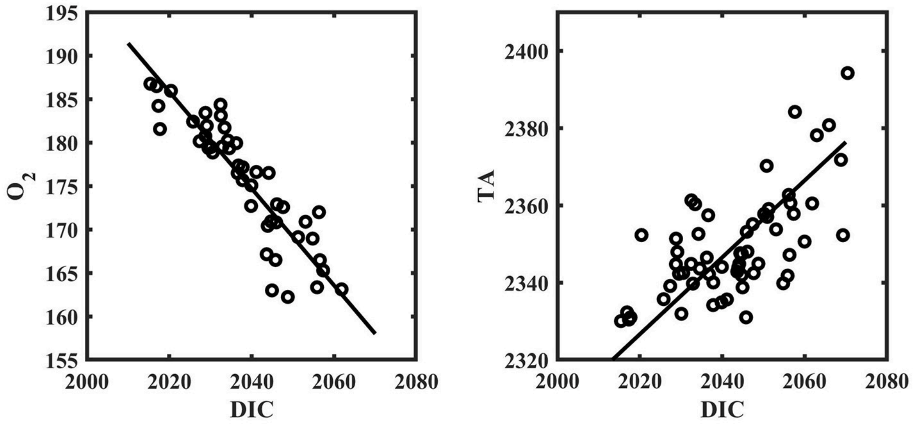

FIGURE 5 | O_2 [μmol kg^{-1}] vs. DIC [μmol kg^{-1}] (left) and TA [μmol kg^{-1}] vs. DIC [μmol kg^{-1}] (right) from spatial survey data around Hog Reef. Solid line represents model II regression. All samples from the spatial surveys are included.

Spatial Variability

The relationship between TA and DIC has been proposed as an approach to calculate NCC:NCP over benthic communities, as NCC and NCP alter TA and DIC in known ratios (Deffeyes, 1965; Suzuki and Kawahata, 2003; Andersson and Gledhill, 2013; Cyronak et al., 2018b). Consequently, TA-DIC relationships reflect the relative balance of the inorganic to organic carbon cycles, which are functions of the community composition and metabolic rates. Higher slopes in TA vs. DIC indicate a higher NCC:NCP, and can be calculated using a simple equation (Koweek et al., 2015). Distinct TA-DIC relationships have been observed for well-defined communities in mesocosms with larger slopes for calcifying (e.g., corals, sediments, and calcifying algae) relative to non-calcifying communities (e.g., fleshy algae), and

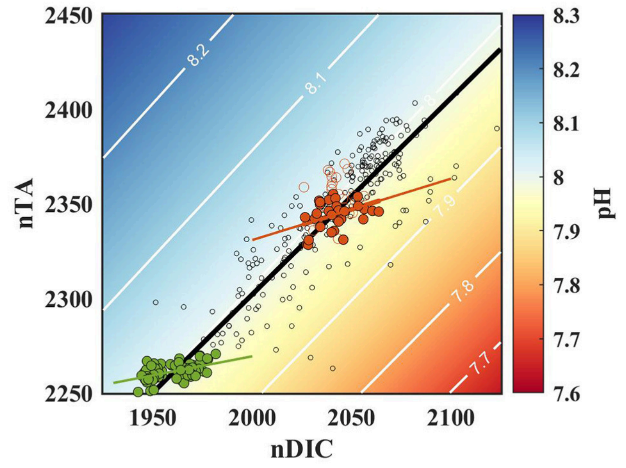

FIGURE 6 | Salinity normalized (36.5) nDIC and nTA at Hog Reef (red circles), Bailey's Bay (green circles), and across the Bermuda coral reef platform between 2007 to 2012 (open black circles), and the resulting seawater pH (contours; salinity = 36.5, temperature = 27.5°C). Open red circles represent data from deep stations, and were not included in the model II regression. Solid red, green, and black lines represent model II regression for the Hog Reef, Bailey's Bay, and the reef platform, respectively.

intermediate slopes for mixed communities of calcifiers and non-calcifiers (Anthony et al., 2013; Page et al., 2016; Lantz et al., 2017). However, it is not clear at what spatiotemporal scales TA and DIC samples should be collected in order to obtain a robust estimate of NCC:NCP in natural environments. At Hog Reef, we had an independent estimate of NCC:NCP from BEAMS, enabling us to assess this approach. When data were combined from all spatial surveys (spanning several km^2 and multiple days), the derived NCC:NCP from TA-DIC data (0.21) was in agreement with direct measurements from BEAMS (0.21). However, linear regressions performed on individual surveys resulted in inconsistent estimates of the NCC:NCP, ranging from −2 to 2.1. This is most likely because multiple processes affect the carbonate chemistry variability on short temporal and small spatial scales of a few km^2, such as local metabolic rates, advection, and mixing. Furthermore, metabolic rates are highly dynamic and can change drastically over minutes to hours, as demonstrated during the storm event on July 27 (**Figure 3**). The metabolic rates do not necessarily change at a constant ratio during these rapid events, as positive NCC and negative NCP were observed during this storm. One of our spatial surveys followed this rain-storm, most likely contributing to the variability observed in the slope of TA to DIC between individual surveys. Nonetheless, despite this variability from survey to survey, the slope of TA to DIC was consistent with the metabolic rates determined from BEAMS when data were taken over sufficiently large spatial scales and multiple days. This demonstrates the critical importance of collecting TA-DIC samples at the appropriate spatiotemporal scales to obtain accurate estimates of NCC:NCP over a given benthic community.

There are additional considerations when using this approach to assess NCC:NCP over specific benthic communities. For example, advection of a different water mass into the survey area could introduce chemical changes that do not reflect local benthic metabolism, but rather the signature of upstream communities. Thus, it is important to characterize the upstream chemical TA-DIC signature and carefully consider the dominant flow trajectory and mixing across multiple habitats (Watanabe et al., 2006). In addition, water depth can also affect the interpretation of TA-DIC relationship in several ways. First, deeper sites have a higher potential for stratification, as was observed at Hog Reef (open circles in **Figure 4**). When stratified, benthic chemical fluxes are not represented in surface samples and should not be included in regression analysis to determine benthic NCC:NCP of a specific community. Alternatively, samples could be collected near the bottom to minimize this effect and/or throughout the water column to characterize the vertical gradients for which actual fluxes could be approximated in certain environments (Andersson et al., 2007). Second, the magnitude of variability (but not the TA-DIC slope) is dependent on water depth and flow rates, as shallower depth and slower flow rates will allow for larger accumulation of chemical signatures. This has been well characterized and observed on reef flat environments (Shaw et al., 2012; McMahon et al., 2013; Kwiatkowski et al., 2016). A larger range in TA and DIC will lead to more robust linear regression results, and thus lower uncertainty in NCC:NCP. Such considerations are important for choosing appropriate study sites, defining the spatiotemporal scale of a study, and in interpreting TA-DIC and NCC:NCP data from various environments.

Variability of Carbonate Chemistry Over Multiple Functional Scales

There is a growing recognition of the importance of examining biogeochemical processes across different functional scales (i.e., across time, space, and different benthic communities) on coral reefs to get a comprehensive understanding of the natural variability of seawater carbonate chemistry, the metabolic function of different habitats (e.g., net calcifying vs. net dissolving), and their ability to alleviate or exacerbate ocean acidification (Cyronak et al., 2018b). To place the current results into a broader context, we compared the TA-DIC relationships from Hog Reef with TA-DIC relationships from Bailey's Bay (similar spatiotemporal scales but different benthic communities) and across the entire Bermuda reef platform.

Spatial surveys were conducted at Hog Reef and Bailey's Bay (Cyronak et al., 2018a) over similar spatiotemporal scales (several days, and 100 s of m^2 to several km^2), with the major difference being the benthic community composition. Hog Reef has a higher abundance of calcifying organisms relative to Bailey's Bay, implying there should be a higher NCC:NCP at Hog Reef (Page et al., 2016; Lantz et al., 2017). As expected, the TA-DIC slope was higher at Hog reef (0.35; NCC:NCP = 0.21) relative to Bailey's Bay (0.20; NCC:NCP = 0.10), most likely explained by the different benthic communities between the two sites (**Figure 6**). These results demonstrate that carbonate chemistry variability on small spatial scales over diel timescales follow a TA-DIC relationship that is determined by local benthic metabolic processes (red and green line in **Figure 6**). However, the magnitude of change along this TA-DIC ratio is driven by metabolic rates that are strongly dependent on many other factors including light intensity (Gattuso et al., 1996; Takeshita et al., 2016), residence time, and water depth (Falter et al., 2013).

When we expand the spatiotemporal scale to the entire Bermuda reef platform, a different pattern for TA and DIC emerges (**Figure 6**). Andersson et al. (2014) presented surface TA and DIC data that were collected monthly at four time series stations across the reef platform between 2007 and 2012 (**Figure 1**), shown as black circles in **Figure 6**. The residence time over the Bermuda platform increases closer to shore, and was on the order of several days to a week near the time series stations (Venti et al., 2012). The sampling stations were chosen in locations that were not in the direct vicinity of highly productive benthic communities to minimize influence from local benthic fluxes. Therefore, the platform-scale data represent chemical variability that results from processes integrated over days to more than a week across multiple habitats around the reef platform, and thus, TA and DIC depletion is strongly correlated with residence time (Venti et al., 2012). The slope of the TA-DIC relationship at the platform-scale was 1.05 ± 0.04 (NCC:NCP = 1.1), which follows an isoline of pH at constant temperature and salinity, maintaining relatively constant pH as water traverses across the reef platform over multiple days. This is in contrast to both Hog Reef and Bailey's Bay, where TA-DIC relationships had a significantly lower slope which intersects pH-isolines, leading to clear diel cycles in pH (**Figure 2**). The platform-scale samples were collected monthly, which is significantly longer than the residence time of the water, yet a consistent slope in TA-DIC was observed. This implies that NCC:NCP at this spatiotemporal scale remains relatively consistent over seasonal to interannual timescales, although variability associated with larger scale oceanic and climatic process such as the North Atlantic Oscillation (NAO) is evident (Yeakel et al., 2015).

The TA-DIC slope on the platform-scale was significantly higher than at Hog Reef and Bailey's Bay, consistent with patterns observed from reefs globally, where TA-DIC slopes were typically higher when collected over larger spatial scales (Cyronak et al., 2018b). The larger slope is most likely driven by the longer residence time of seawater, i.e., the integration length for NCC and NCP. The metabolic ratios that determine the slope of TA-DIC are integrated over multiple days on the platform scale, whereas they represent instantaneous metabolic ratios on diel timescales over specific benthic habitats at Hog Reef and Bailey's Bay. In general, NCC:NCP increases with longer integration time because the influence of NCC on carbonate chemistry becomes more important than NCP when integrated over multiple days (Gattuso et al., 1999; Falter et al., 2013). This is because daytime organic production is nearly balanced by nighttime respiration over a diel cycle (i.e., ΣNCP $\sim$0) (Kinsey, 1985; Gattuso et al., 1999; Falter et al., 2012), whereas NCC remains consistently positive over a day (ΣNCC > 0) (**Figure 3**). Therefore, if the residence time of the water is > 1 day, the chemical signature of ΣNCC accumulates disproportionately over ΣNCP, leading to a higher slope in TA-DIC. Given that the residence time for the platform-scale data were several days to a week (Venti et al., 2012), the TA-DIC slope was higher than those from smaller spatial surveys representing variability over diel cycles. It is possible that air-sea CO_2 exchange plays a role on the platform scale, since gas exchange becomes more important with longer residence time. The effect of gas exchange would be to push the TA-DIC relationship toward a pCO_2 isoline near atmospheric concentration. However, previous analysis has demonstrated that gas exchange plays a significantly smaller role than metabolism in Bermuda (Yeakel et al., 2015) and from reefs worldwide (Frankignoulle et al., 1996; Watanabe et al., 2006; Falter et al., 2013), thus it only plays a minor role in driving DIC variability on the platform scale.

The carbonate chemistry at any given point in time and space on the reef is determined through a combination of drivers that simultaneously operate across multiple functional scales. The platform-scale processes can be thought of as determining the "upstream" properties for different sections of the reef depending on location and recirculation patterns, whereas metabolism on local scales induces additional high frequency variability on diel timescales determined by benthic community composition, depth, and residence time. This poses a challenge for predicting future pH (or any CO_2 parameter of interest) on coral reefs because it requires understanding of how biogeochemical feedbacks due to changes in benthic metabolism and physical processes interact across different spatiotemporal scales. For example, if the platform-scale ΣNCC:ΣNCP decreases, pH would increase as water travels across the reef platform, leading to a potential partial offset in ocean acidification on the platform-scale (Andersson et al., 2014). However, the TA-DIC relationship at the platform-scale is determined by multiple processes including the large-scale oceanographic processes such as the NAO (Yeakel et al., 2015) or Pacific Decadal Oscillation (PDO) (Pelejero et al., 2005) affecting rates and ratios of benthic metabolism across multiple habitats (Andersson et al., 2014; Andersson, 2015), making accurate predictions elusive but not unattainable. At the local-scale, a decrease in NCC:NCP due to changes in benthic community composition toward more algae-dominated states (Hoegh-Guldberg et al., 2007) would lead to larger diel cycles in pH. Understanding the relative strengths and interactions of such feedbacks is critical to project future seawater carbonate chemistry conditions on coral reefs.

CONCLUSIONS

The main objective of this study was to present carbonate chemistry variability and the relative importance of NCC:NCP affecting TA-DIC relationships across multiple functional scales, which is critical to better understand the implications of future acidification to coral reefs. At the community-scale [several km^2 over day(s)], TA-DIC relationships were driven by local metabolism and community composition, where higher slopes of TA-DIC were observed at Hog Reef (coral reef) relative to Bailey's Bay (seagrass bed). The inferred NCC:NCP at Hog Reef using the TA-DIC data was in agreement with an independent measurement of benthic metabolism using a gradient flux approach when averaged over multiple days. The TA-DIC relationship had a significantly higher slope at the platform-scale, where the chemical variability reflected processes that were integrated over longer periods. This is most likely because the contribution from NCC on TA-DIC changes becomes increasingly important over NCP over longer integration timescales (Falter et al., 2013; Cyronak et al., 2018b). The results presented here demonstrate that drivers of carbonate chemistry variability cannot be viewed in isolation, but must be interpreted in the context of how they interact across overlapping functional scales.

AUTHOR CONTRIBUTIONS

YT, TC, TM, and AA: contributed to the development, planning, data collection, data analysis and interpretation; TK: analyzed and quality controlled the discrete samples. All authors contributed to the writing of the manuscript.

ACKNOWLEDGMENTS

This work was funded by the National Science Foundation grants CRI-OA 1316047 (YT, TM), OCE 12-55042 (AA), and OCE 14-16518 (AA). TC gratefully thanks the Scripps postdoctoral scholarship for their support. YT thanks the Dave & Lucile Packard Foundation for supporting YT. We would like to thank Ashley Cyronak for helping with the sample collection. BEAMS, spatial surveys, and autonomous sensor data are available at BCO- DMO under project BEAMS.

REFERENCES

Albright, R., Caldeira, L., Hosfelt, J., Kwiatkowski, L., Maclaren, J. K., Mason, B. M., et al. (2016). Reversal of ocean acidification enhances net coral reef calcification. *Nature* 531, 362–365. doi: 10.1038/nature17155

Albright, R., Langdon, C., and Anthony, K. R. N. (2013). Dynamics of seawater carbonate chemistry, production, and calcification of a coral reef flat, Central Great Barrier Reef. *Biogeosciences* 10, 7641–7676, doi: 10.5194/bgd-10-7641-2013

Albright, R., Benthuysen, J., Cantin, N., Caldeira, K., and Anthony, K. (2015). Coral reef metabolism and carbon chemistry dynamics of a coral reef flat. *Geophys. Res. Lett.* 42, 3980–3988. doi: 10.1002/2015GL063488

Albright, R., Takeshita, Y., Koweek, D. A., Ninokawa, A., Wolfe, K., Rivlin, T. et al. (2018). Carbon dioxide addition to coral reef waters suppresses net community calcification. *Nature* 555, 516–519. doi: 10.1038/nature25968

Andersson, A. J., Kline, D. I., Edmunds, P. J., Archer, S. D., Bednaršek, N., Carpenter, R. C., et al. (2015), Understanding ocean acidification impacts on organismal to ecological scales. *Oceanography* 25, 16–27. doi: 10.5670/oceanog.2015.27

Andersson, A. J. (2015). A fundamental paradigm for coral reef carbonate sediment dissolution. *Front. Mar. Sci.* 2:52. doi: 10.3389/fmars.2015.00052

Andersson, A. J., and Gledhill, D. (2013). Ocean acidification and coral reefs: effects on breakdown, dissolution, and net ecosystem calcification. *Ann. Rev. Mar. Sci.* 5, 321–348. doi: 10.1146/annurev-marine-121211-172241

Andersson, A. J., Yeakel, K. L., Bates, N. R., and de Putron, S. J. (2014). Partial offsets in ocean acidification from changing coral reef biogeochemistry. *Nat. Clim. Change* 4, 56–61. doi: 10.1038/nclimate2050

Andersson, A. J., Bates, N. R., and Mackenzie, F. T. (2007). Dissolution of carbonate sediments under rising pCO2 and ocean acidification: observations from devil's hole, bermuda. *Aquat. Geochem.* 13, 237–264. doi: 10.1007/s10498-007-9018-8

Andersson, A. J., Kuffner, I. B., Mackenzie, F. T., Jokiel, P. L., Rodgers, K. S., and Tan, A. (2009). Net loss of $CaCO_3$ from a subtropical calcifying community due to seawater acidification: mesocosm-scale experimental evidence. *Biogeosciences* 6, 1811–1823. doi: 10.5194/bg-6-1811-2009.

Anthony, K. R. N., Diaz-Pulido, G., Verlinden, N., Tilbrook, B.,and Andersson, A. J. (2013). Benthic buffers and boosters of ocean acidification on coral reefs. *Biogeosciences* 10, 4897–4909. doi: 10.5194/bg-10-4897-2013

Anthony, K. R. N., Kleypas, J. A., and Gattuso, J.-P. (2011). Coral reefs modify their seawater carbon chemistry - implications for impacts of ocean acidification. *Glob. Change Biol.* 17, 3655–3666. doi: 10.1111/j.1365-2486.2011.02510.x

Barnes, D. J. (1983). Profiling coral reef productivity and calcification using pH and oxygen electrodes. *J. Exp. Mar. Bio. Ecol.* 66, 149–161. doi: 10.1016/0022-0981(83)90036-9

Bates, N. R., Amat, A., and Andersson, A. J. (2010). Feedbacks and responses of coral calcification on the Bermuda reef system to seasonal changes in biological processes and ocean acidification. *Biogeosciences* 7, 2509–2530. doi: 10.5194/bg-7-2509-2010

Bresnahan, P. J., Martz, T. R., Takeshita, Y., Johnson, K. S., and, LaShomb, M. (2014). Best practices for autonomous measurement of seawater pH with the Honeywell Durafet. *Methods Oceanogr.* 9, 44–60. doi: 10.1016/j.mio.2014.08.003

Briggs, E. M., Sandoval, S., Erten, A., Takeshita, Y., Kummel, A. C., and Martz, T. R. (2017). Solid state sensor for simultaneous measurement of total alkalinity and pH of seawater. *ACS Sens.* 2, 1302–1309. doi: 10.1021/acssensors.7b00305

Chan, N. C., and Connolly, S. R. (2013). Sensitivity of coral calcification to ocean acidification: a meta-analysis. *Glob. Change Biol.* 19, 282–290. doi: 10.1111/gcb.12011

Costanza, R., de Groot, R., Sutton, P., van der Ploeg, S., Anderson, S. J., Turner, I., et al. (2014). Changes in the global value of ecosystem services. *Glob. Environ. Change* 26, 152–158. doi: 10.1016/j.gloenvcha.2014.04.002

Courtney, T. A., Andersson, A. J., Bates, N. R., Collins, A., Cyronak, T., de Putron, S. J., et al. (2016). Comparing chemistry and census-based estimates of net ecosystem calcification on a rim reef in bermuda. *Front. Mar. Sci.* 3:181. doi: 10.3389/fmars.2016.00181

Courtney, T. A., Lebrato, M., Bates, N. R., Collins, A., de Putron, S. J., Garley, R., et al. (2017). Environmental controls on modern scleractinian coral and reef-scale calcification. *Sci. Adv.* 3:e1701356. doi: 10.1126/sciadv.1701356

Crespo, G. A., Ghahraman Afshar, M.,and Bakker, E. (2012). Direct detection of acidity, alkalinity, and pH with membrane electrodes. *Anal. Chem.* 84, 10165–10169. doi: 10.1021/ac302868u

Cyronak, T., Andersson, A. J., Langdon, C., Albright, R., Bates, N. R., Caldeira, K. (2018b). Taking the metabolic pulse of the world's coral reefs. *PLoS ONE* 13:e0190872. doi: 10.1371/journal.pone.0190872

Cyronak, T., Andersson, A. J., D'Angelo, S., Bresnahan, P., Davidson, C., White, A., et al. (2018a). Short-term spatial and temporal carbonate chemistry variability in two contrasting seagrass meadows: implications for pH buffering capacities. *Estuar. Coasts* doi: 10.1007/s12237-017-0356-5. [Epub ahead of print].

Cyronak, T., Santos, I. R., and Eyre, B. D. (2013). Permeable coral reef sediment dissolution driven by elevated p CO 2 and pore water advection. *Geophys. Res. Lett.* 40, 4876–4881. doi: 10.1002/grl.50948

Deffeyes, K. S. (1965). Carbonate equilibria: a graphic and algebraic approach1. *Limnol. Oceanogr.* 10, 412–426. doi: 10.4319/lo.1965.10.3.0412

Dickson, A. G., Sabine, C. L., and Christian, J. R., Eds. (2007). *Guide to Best Practices for Ocean CO_2 Measurements*. PICES Special Publication. 3.

Dickson, A. G., Afghan, J. D., and Anderson, G. C. (2003). Reference materials for oceanic CO_2 analysis: a method for the certification of total alkalinity. *Mar. Chem.* 80, 185–197. doi: 10.1016/S0304-4203(02)00133-0

Edmunds, P. J., Comeau, S., Lantz, C., Andersson, A., Briggs, C., Cohen, A., et al. (2016). Integrating the effects of ocean acidification across functional scales on tropical coral reefs. *Bioscience* 66:biw023. doi: 10.1093/biosci/biw023

Enochs, I. C., Manzello, D. P., Donham, E. M., Kolodziej, G., Okano, R., Johnston, L., et al. (2015). Shift from coral to macroalgae dominance on a volcanically acidified reef. *Nat. Clim. Change* 5, 1–9. doi: 10.1038/nclimate2758.

Eyre, B. D., Andersson, A. J., and Cyronak, T. (2014). Benthic coral reef calcium carbonate dissolution in an acidifying ocean. *Nat. Clim. Change* 4, 969–976. doi: 10.1038/nclimate2380

Falter, J. L., Lowe, R. J., Atkinson, M. J., and Cuet, P. (2012). Seasonal coupling and de-coupling of net calcification rates from coral reef metabolism and carbonate chemistry at Ningaloo Reef, Western Australia. *J. Geophys. Res. Ocean.* 117, 1–14. doi: 10.1029/2011JC007268

Falter, J. L., Lowe, R. J., Atkinson, M. J., Monismith, S. G., and Schar, D. W. (2008). Continuous measurements of net production over a shallow reef community using a modified Eulerian approach. *J. Geophys. Res.* 113, 1–14. doi: 10.1029/2007JC004663

Falter, J. L., Lowe, R. J., Zhang, Z., and McCulloch, M. (2013). Physical and biological controls on the carbonate chemistry of coral reef waters: effects of metabolism, wave forcing, sea level, and geomorphology. *PLoS ONE* 8:e53303. doi: 10.1371/journal.pone.0053303

Frankignoulle, M., Gattuso, J. P., Biondo, R., Bourge, I., Copin-Montegut, G., and Pichon, M. (1996). Carbon fluxes in coral reefs. 2. eulerian study of inorganic carbon dynamics and measurement of air-sea CO_2 exchanges. *Mar. Ecol. Prog. Ser.* 145, 123–132. doi: 10.3354/meps145123

Gattuso, J. P., Allemand, D., and Frankignoulle, M. (1999). Photosynthesis and calcification at cellular, organismal and community levels in coral reefs: a review on interactions and control by carbonate chemistry. *Am. Zool.* 39, 160–183. doi: 10.1093/icb/39.1.160

Gattuso, J. P., Pichon, M., Delesalle, B., Canon, C., and Frankignoulle, M. (1996). Carbon fluxes in coral reefs. I. Lagrangian measurement of community metabolism and resulting air-sea CO_2 disequilibrium. *Mar. Ecol. Prog. Ser.* 145, 109–121. doi: 10.3354/meps145109

Hoegh-Guldberg, O., Mumby, P. J., Hooten, A. J., Steneck, R. S., Greenfield, P., Gomez, E., et al. (2007). Coral reefs under rapid climate change and ocean acidification. *Science* 318, 1737–1742. doi: 10.1126/science.1152509

Hughes, T. P., Barnes, M. L., Bellwood, D. R., Cinner, J. E., Cumming, G. S., Jackson, J. B. C., et al. (2017). Coral reefs in the Anthropocene. *Nature* 546, 82–90. doi: 10.1038/nature22901

Jury, C. P., Thomas, F. I. M., Atkinson, M. J., and Toonen, R. J. (2013). Buffer capacity, ecosystem feedbacks, and seawater chemistry under global change. *Water* 5, 1303–1325. doi: 10.3390/w5031303

Kinsey, D. W. (1985). Metabolism, calcification and carbon production: 1 systems level studies. *Fifth Int. Coral Reef Congr.* 4, 505–526.

Kleypas, J. A., Buddemeier, R. W., Archer, D., Gattuso, J.-P., Langdon, C., and Opdyke, B. N. (1999). Geochemical consequences of increased atmospheric carbon dioxide on coral reefs. *Science* 284, 118–120. doi: 10.1126/science.284.5411.118

Kleypas, J. A., Anthony, K. R. N., and Gattuso, J.-P. (2011). Coral reefs modify their seawater carbon chemistry - case study from a barrier reef (Moorea, French Polynesia). *Glob. Change Biol.* 17, 3667–3678. doi: 10.1111/j.1365-2486.2011.02530.x

Kleypas, J., and Yates, K. (2009). Coral reefs and ocean acidification. *Oceanography* 22, 108–117. doi: 10.5670/oceanog.2009.101

Koweek, D. A., Dunbar, R. B., Monismith, S. G., Mucciarone, D. A., Woodson, C. B., and Samuel, L. (2015). High-resolution physical and biogeochemical variability from a shallow back reef on Ofu, American Samoa: an end-member perspective. *Coral Reefs* 34, 979–991. doi: 10.1007/s00338-015-1308-9

Kwiatkowski, L. R., Albright, J., Hosfelt, Y., Nebuchina, A., Ninokawa, T., Rivlin, T., et al. (2016). Interannual stability of organic to inorganic carbon production on a coral atoll. *Geophys. Res. Lett.* 43, 3880–3888. doi: 10.1002/2016GL068723

Lantz, C. A., Carpenter, R. C., Comeau, S., and Edmunds, P. J. (2017). Organisms composing an experimental coral reef community from mo'orea, french polynesia, exhibit taxon-specific net production: net calcification ratios. *Front. Mar. Sci.* 4:298. doi: 10.3389/fmars.2017.00298

Lowe, R. J., and Falter, J. L. (2015). Oceanic forcing of coral reefs. *Ann. Rev. Mar. Sci.* 7, 43–66. doi: 10.1146/annurev-marine-010814-015834

Lueker, T. J., Dickson, A. G., and Keeling, C. D. (2000). Ocean pCO_2 calculated from dissolved inorganic carbon, alkalinity, and equations for K1 and K2: validation based on laboratory measurements of CO_2 in gas and seawater at equilibrium. *Mar. Chem.* 70, 105–119. doi: 10.1016/S0304-4203(00)00022-0

Martz, T. R., Connery, J. G., and Johnson, K. S. (2010). Testing the honeywell durafet for seawater pH applications. *Limnol. Oceanogr. Methods* 8, 172–184. doi: 10.4319/lom.2010.8.172

McGillis, W. R., Langdon, C., Loose, B., Yates, K. K., and Corredor, J. (2011). Productivity of a coral reef using boundary layer and enclosure methods. *Geophys. Res. Lett.* 38, 1–5. doi: 10.1029/2010GL046179

McMahon, A., Santos, I. R., Cyronak, T., and Eyre, B. D. (2013). Hysteresis between coral reef calcification and the seawater aragonite saturation state. *Geophys. Res. Lett.* 40, 4675–4679. doi: 10.1002/grl.50802

Mehrbach, C., Culberson, C. H., Hawley, J. E., and Pytkowicz, R. M. (1973). Measurement of the apparent dissociation constants of carbonic acid in seawater at atmospheric pressure. *Limnol. Oceanogr.* 18, 897–907. doi: 10.4319/lo.1973.18.6.0897

MEP (2007). *Marine Environmental Program Annual Report, 2006-2007*. Bermuda Institute of Ocean Sciences. 80.

Nakamura, T., and Nakamori, T. (2008). Estimation of photosynthesis and calcification rates at a fringing reef by accounting for diurnal variations and the zonation of coral reef communities on reef flat and slope: a case study for the Shiraho reef, Ishigaki Island, southwest Japan. *Coral Reefs* 28, 229–250. doi: 10.1007/s00338-008-0454-8

Page, H. N., Andersson, A. J., Jokiel, P. L., Rodgers, K. S., Lebrato, M., Bahr, K. D., et al. (2016). Differential modification of seawater carbonate chemistry by major coral reef benthic communities. *Coral Reefs* 35, 1311–1325. doi: 10.1007/s00338-016-1490-4

Pelejero, C., Calvo, E., McCulloch, M. T., Marshall, J. F., Gagan, M. K., Opdyke, J. M., et al. (2005). Ocean science: preindustrial to modern interdecadal variability in coral reef pH. *Science* 309, 2204–2207. doi: 10.1126/science.1113692

Platt, T., Gallegos, C. L., and Harrison, W. G. (1980). Photoinibition of photosynthesis in natural assemblages of marine phytoplankton. *J. Mar. Res.* 38, 687–701.

Reidenbach, M. A., Monismith, S. G., Koseff, J. R., Yahel, G., and Genin, A. (2006). Boundary layer turbulence and flow structure over a fringing coral reef. *Limnol. Oceanogr.* 51, 1956–1968. doi: 10.4319/lo.2006.51.5.1956

Shaw, E. C., McNeil, B. I., and Tilbrook, B. (2012). Impacts of ocean acidification in naturally variable coral reef flat ecosystems. *J. Geophys. Res.* 117:C03038. doi: 10.1029/2011JC007655

Shaw, E. C., McNeil, B. I., Tilbrook, B., Matear, R., and Bates, M. L. (2013). Anthropogenic changes to seawater buffer capacity combined with natural reef metabolism induce extreme future coral reef CO2 conditions. *Glob. Change Biol.* 19, 1632–1641. doi: 10.1111/gcb.12154

Shaw, E. C., Phinn, S. R., Tilbrook, B., and Steven, A. (2015). Natural *in situ* relationships suggest coral reef calcium carbonate production will decline with ocean acidification. *Limnol. Oceanogr.* 60, 777–788. doi: 10.1002/lno.10048

Spaulding, R. S., DeGrandpre, M. D., Beck, J. C., Hart, R. D., Peterson, B., De Carlo, E.H., et al. (2014). Autonomous *in situ* measurements of seawater alkalinity. *Environ. Sci. Technol.* 48, 9573–9581. doi: 10.1021/es501615x

Suzuki, A., and Kawahata, H. (2003). Carbon budget of coral reef systems: an overview of observations in fringing reefs, barrier reefs and atolls in the Indo-Pacific regions. *Tellus Ser. B Chem. Phys. Meteorol.* 55, 428–444. doi: 10.1034/j.1600-0889.2003.01442.x

Takeshita, Y. (2017). Understanding feedbacks between ocean acidification and coral reef metabolism. *J. Geophys. Res. Ocean.* 122, 1639–1642. doi: 10.1002/2017JC012740

Takeshita, Y., Frieder, C. A., Martz, T. R., Ballard, J. R., Feely, R. A., Smith, J. E., et al. (2015). Including high-frequency variability in coastal ocean acidification projections. *Biogeosciences* 12, 5853–5870. doi: 10.5194/bg-12-5853-2015

Takeshita, Y., Martz, T. R., Johnson, K. S., and Dickson, A. G. (2014). Characterization of an ion sensitive field effect transistor and chloride ion selective electrodes for pH measurements in seawater. *Anal. Chem.* 86, 11189–11195. doi: 10.1021/ac502631z

Takeshita, Y. W., McGillis, E. M., Briggs, A. L., Carter, E. M., Donham, T. R., Smith, J. E. et al. (2016). Assessment of net community production and calcification of a coral reef using a boundary layer approach. *J. Geophys. Res. Ocean.* 121, 5655–5671. doi: 10.1002/2016JC011886

Venti, A. D., Kadko, A. J., Andersson, C., Langdon, C., and Bates, N. R. (2012). A multi-tracer model approach to estimate reef water residence times. *Limnol. Oceanogr. Methods* 10, 1078–1095. doi: 10.4319/lom.2012.10.1078

Watanabe, A. H., Kayanne, H., Hata, S., Kudo, K., Nozaki, K., Yamano, H., et al. (2006). Analysis of the seawater CO_2 system in the barrier reef-lagoon system of Palau using total alkalinity-dissolved inorganic carbon diagrams. *Limnol. Oceanogr.* 51, 1614–1628, doi: 10.4319/lo.2006.51.4.1614

Wilkinson, C. (2008). *Status of Coral Reefs of the World: 2008*. Townsville, QLD: Global Coral Reef Monitoring Network and Reef and Rainforest Research Centre.

Yeakel, K. L., Andersson, A. J., Bates, N. R., Noyes, T. J., Collins, A., and Garley, R. (2015). Shifts in coral reef biogeochemistry and resulting acidification linked to offshore productivity, *Proc. Natl. Acad. Sci. U.S.A.* 112, 14512–14517, doi: 10.1073/pnas.1507021112

Conflict of Interest Statement: The authors declare that the research was conducted in the absence of any commercial or financial relationships that could be construed as a potential conflict of interest.

Advantages of publishing in Frontiers

OPEN ACCESS

Articles are free to read
for greatest visibility
and readership

FAST PUBLICATION

Around 90 days
from submission
to decision

HIGH QUALITY PEER-REVIEW

Rigorous, collaborative,
and constructive
peer-review

TRANSPARENT PEER-REVIEW

Editors and reviewers
acknowledged by name
on published articles

Frontiers
Avenue du Tribunal-Fédéral 34
1005 Lausanne | Switzerland

Visit us: www.frontiersin.org
Contact us: info@frontiersin.org | +41 21 510 17 00

REPRODUCIBILITY OF RESEARCH

Support open data
and methods to enhance
research reproducibility

DIGITAL PUBLISHING

Articles designed
for optimal readership
across devices

FOLLOW US

@frontiersin

IMPACT METRICS

Advanced article metrics
track visibility across
digital media

EXTENSIVE PROMOTION

Marketing
and promotion
of impactful research

LOOP RESEARCH NETWORK

Our network
increases your
article's readership